

IIUM ENGINEERING JOURNAL

Volume 22

Number 1

January 2021



**IIUM
Press**

INTERNATIONAL ISLAMIC UNIVERSITY MALAYSIA

ISSN: 1511-788X E-ISSN: 2289-7860

<http://journals.iium.edu.my/ejournal>

IUM ENGINEERING JOURNAL

CHIEF EDITOR

Ahmad Faris Ismail, IIUM, Malaysia

TECHNICAL EDITOR

Sany Izan Ihsan, IIUM, Malaysia

EXECUTIVE EDITOR

AHM Zahirul Alam, IIUM, Malaysia

ASSOCIATE EDITOR

Nor Farahidah Za'bah, IIUM, Malaysia

LANGUAGE EDITOR

Lynn Mason, Malaysia

COPY EDITOR

Hamzah Mohd. Salleh, IIUM, Malaysia

EDITORIAL BOARD MEMBERS

Abdullah Al-Mamun, IIUM, Malaysia
Abdumalik Rakhimov, IIUM, Malaysia
Ali Sophian, IIUM, Malaysia
Erwin Sulaeman, IIUM, Malaysia
Hanafy Omar, Saudi Arabia
Hazleen Anuar, IIUM, Malaysia
Konstantin Khanin, University of Toronto, Canada
Ma'an Al-Khatib, IIUM, Malaysia
Md Zahangir Alam, IIUM, Malaysia
Meftah Hrairi, IIUM, Malaysia
Mohamed B. Trabia, United States
Mohammad S. Alam, Texas A&M University-Kingsville, United States
Mustafizur Rahman, National University Singapore, Singapore
Ossama Abdulkhalik, Michigan Technological University, United States
Othman O Khalifa, IIUM, Malaysia
Razi Nalim, IUPUI, Indianapolis, Indiana, United States
Rosminazuin AB. Rahim, IIUM, Malaysia
Waqar Asrar, IIUM, Malaysia

AIMS & SCOPE OF IUMENGINEERING JOURNAL

The **IUM Engineering Journal**, published biannually (January and July), is a carefully refereed international publication of International Islamic University Malaysia (IIUM). Contributions of high technical merit within the span of engineering disciplines; covering the main areas of engineering: Electrical and Computer Engineering; Mechanical and Manufacturing Engineering; Automation and Mechatronics Engineering; Material and Chemical Engineering; Environmental and Civil Engineering; Biotechnology and Bioengineering; Engineering Mathematics and Physics; and Computer Science and Information Technology are considered for publication in this journal. Contributions from other areas of Engineering and Applied Science are also welcomed. The IUM Engineering Journal publishes contributions under *Regular papers and Invited review papers*. It also welcomes contributions that address solutions to the specific challenges of the developing world, and address science and technology issues from an Islamic and multidisciplinary perspective.

REFEREES' NETWORK

All papers submitted to IUM Engineering Journal will be subjected to a rigorous reviewing process through a worldwide network of specialized and competent referees. Each accepted paper should have at least two positive referees' assessments.

SUBMISSION OF A MANUSCRIPT

A manuscript should be submitted online to the IIUM-Engineering Journal website at <http://journals.iium.edu.my/ejournal>. Further correspondence on the status of the paper could be done through the journal website.

INTERNATIONAL ADVISORY COMMITTEE

A. Anwar, United States
Abdul Latif Bin Ahmad, Malaysia
Farzad Ismail, USM, Pulau Pinang, Malaysia
Hanafy Omar, Saudi Arabia
Hany Ammar, United States
Idris Mohammed Bugaje, Nigeria
K.B. Ramachandran, India
Kunzu Abdella, Canada
Luis Le Moyne, ISAT, University of Burgundy, France
M Mujtaba, United Kingdom
Mohamed AI-Rubei, Ireland
Mohamed B Trabia, United States
Syed Kamrul Islam, United States
Tibor Czigany, Budapest University of Technology and Economics, Hungary
Yiu-Wing Mai, The University of Sydney, Australia.

Published by:

IIUM Press,
International Islamic University Malaysia
Jalan Gombak, 53100 Kuala Lumpur, Malaysia
Phone (+603) 6421-5014, Fax: (+603) 6421-6298

Whilst every effort is made by the publisher and editorial board to see that no inaccurate or misleading data, opinion or statement appears in this Journal, they wish to make it clear that the data and opinions appearing in the articles and advertisement herein are the responsibility of the contributor or advertiser concerned. Accordingly, the publisher and the editorial committee accept no liability whatsoever for the consequence of any such inaccurate or misleading data, opinion or statement.

ISSN 1511 - 788X



IIUM Engineering Journal
ISSN: 1511-788X E-ISSN: 2289-7860

IUM ENGINEERING JOURNAL
Volume 22, Issue 1, January 2021
<https://doi.org/10.31436/iiumej.v22i1>

Table of Contents

EDITORIAL	i
CHEMICAL AND BIOTECHNOLOGY ENGINEERING	
1447: A NOVEL DIMENSIONALITY REDUCTION APPROACH TO IMPROVE MICROARRAY DATA CLASSIFICATION	1
<i>Mohammed Hamim, Ismail El Moudden, Mounir Ouzir, Hicham Moutachaouik and Mustapha Hain</i>	
CIVIL AND ENVIRONMENTAL ENGINEERING	
1446: INFLUENCE OF FIBREGLASS MESH ON PHYSICAL PROPERTIES OF LIGHTWEIGHT FOAMCRETE	23
<i>Anisah Mat Serudin, Md Azree Othuman Mydin and Abdul Naser Abdul Ghani</i>	
1502: FROUDE NUMBER VARIANCE WITH RESPECT TO THE HYDRODYNAMIC RESPONSE OF A NON-STATIC VEHICLE ON A LOW-LYING FLOODED ROADWAY	35
<i>Syed Muzzamil Hussain Shah, Zahiraniza Mustaffa, Shabir Hussain Khahro, Khamaruzaman Wan Yusof, Ebrahim Hamid Hussein Al-Qadami, Aminuddin Ab Ghani and Fang Yenn Teo</i>	
ELECTRICAL, COMPUTER AND COMMUNICATIONS ENGINEERING	
1276: ROBUST TUNING OF POWER SYSTEM STABILIZER PARAMETERS USING THE MODIFIED HARMONIC SEARCH ALGORITHM... ..	47
<i>Hiba Zuhair Abdul Kareem, Husam Hasan Mohammed and Ameer Aqeel Mohammed</i>	
1396: PASSIVELY Q-SWITCHED YTTERBIUM-DOPED FIBER LASER EMPLOYING SAMARIUM OXIDE AS SATURABLE ABSORBER	58
<i>Khairul Nizam Rusdi, Afiq Arif Aminuddin Jafry, Nur Farhanah Zulkipli, Farina Saffa Mohamad Samsamnun, Mohamad Badrol Hisyam Mahyuddin, Sulaiman Wadi Harun, Mohd Shahnan Zainal Abidin and Norazlina Saidin</i>	
1495: AUTOMATIC FACIAL REDNESS DETECTION ON FACE SKIN IMAGE	68
<i>Izzati Muhimmah, Nurul Fatikah Muchlis and Arrie Kurniawardhani</i>	
1532: IMPLEMENTATION OF A MACHINE LEARNING ALGORITHM FOR SENTIMENT ANALYSIS OF INDONESIA'S 2019 PRESIDENTIAL ELECTION.....	78
<i>Ghulam Asrofi Buntoro, Rizal Arifin, Gus Nanang Syaifuddiin, Ali Selamat, Ondrej Krejcar, Herrera-Viedma and Hamido Fujita</i>	
1596: MONITORING AND CONTROL SYSTEM WITH A CLIENT-SERVER MODEL BASED ON INTERNET OF THINGS (IoT)	93
<i>Sri Ratna Sulistiyanti1, F.X. Arinto Setyawan, Sri Purwiyanti, Helmy Fitriawan and Adam Rabbani Adnan</i>	
1622: PREDICTING TRUST IN A SOCIAL NETWORK BASED ON STRUCTURAL SIMILARITIES USING A MULTI-LAYERED PERCEPTRON NEURAL NETWORK.....	103
<i>Amir Hossein Danesh and Hossein Shirgahi</i>	
ENGINEERING MATHEMATICS AND APPLIED SCIENCE	
1389: FVS-TECHNOLOGY - INTELLECTUAL SEARCH TOOLS.....	118
<i>Bahodir Muminov Boltayevich and Ulugbek Bekmurodov Bakhrom Ugli</i>	
1398: SOLUTION OF THE REVERSE FLOW REACTOR MODEL USING HOMOTOPY ANALYSIS METHOD	129
<i>Suharsono, Sri Wulandari, Aang Nuryaman, Mustofa Usman, Wamiliana and Jamal Ibrahim Daoud</i>	
1413: RELIABLE ITERATIVE METHODS FOR SOLVING 1D, 2D AND 3D FISHER'S EQUATION	138
<i>Othman Mahdi Salih and Majeed Ahmed. AL-Jawary</i>	
1497: ENERGY AND STRUCTURE STATES OF LOW-LYING BANDS IN ¹⁵⁶ Gd.....	167
<i>Pazlitdin Nuritdinovich Usmanov and Elmurod Kuchkarboyevich Yusupov</i>	
1520: MODEL DEVELOPMENT OF RIDE SPLITTING SERVICE WITH RESOURCE SHARING SCHEME ON RIDE SOURCING (ONLINE TAXI) SERVICES IN JAKARTA	175
<i>Helen Burhan, Sutanto soehodho and Nary</i>	
1569: THE HARMONIC COMPOSITION OF CURRENT IN ZERO-WORKING WIRE WITH NON-LINEAR LOAD.....	191
<i>Igor V. Yudaev, Evgeny V. Rud, Mikhail A. Yundin, Tamara Z. Ponomarenko and Aleksandra M. Isupova</i>	

MATERIALS AND MANUFACTURING ENGINEERING

1364: CHARACTERISATION AND MELT SPINNING OF POLY (LACTIC ACID)/POLY (ETHYLENE GLYCOL) BLENDS.....	201
<i>Nur Atiqah Mohd Akhir, Maizatunisa Othman, Yose Fachmi Buys and Sharifah Imihezri Syed Shahrudin</i>	
1426: GRAPHENE OXIDE MICROCAPSULES (GOMs) WITH LINSEED OIL CORE VIA PICKERING EMULSION METHOD: EFFECT OF DISPERSE SPEED.....	203
<i>Nurul Nadiah Sahir, Noor Azlina Hassan, Norita Hassan and Norhasnidawani Johari</i>	
1478: INVESTIGATION ON THE MECHANICAL, THERMAL, BIO-DEGRADATION AND BIO-COMPATIBILITY PROPERTIES OF POLY (LACTIC ACID) / POLY (ETHYLENE GLYCOL) BLEND.....	223
<i>Zohreh Zarinkolah, Hamed Bagheri, Saman Hosseinkhani and Maryam Nikkhah</i>	
1544: PREPARATION OF CAO-BASED PELLET USING RICE HUSK ASH VIA GRANULATION METHOD FOR POTENTIAL CO ₂ CAPTURE	234
<i>Farah Diana Mohd Daud, Muhammad Mirza Mohamad Azir, Mudrikah Sofia Mahmud, Norshahida Sarifuddin and Hafizah Hanim Mohd Zaki</i>	
1548: PREPARATION OF THE ELECTROSPUN POLYVINYLIDENE FLUORIDE / POLYVINYL ALCOHOL SCAFFOLD AS A POTENTIAL TISSUE REPLACEMENT	245
<i>Mohd Syahir Anwar Hamzah, Nurul Amira Ab Razak, Celine Ng, Akmal Hafiszi Abdul Azize, Jumadi Abdul Sukor, Soon Chin Fhon, Saiful Izwan Abd Raza and Nadirul Hasraf Mat Nayan</i>	
1587: THE DURABILITY OF HYGRO-IMMERSION AGED CELLULOSE FIBRE REINFORCED POLYMER LAYERED SILICATE NANOCOMPOSITES	259
<i>C. S. Suhas Kowshik, Nanjangud Mohan, Nithesh Naik, Manjunath Shettar, Ritesh Bhat and Shivaksh Rohatgi</i>	

MECHATRONICS AND AUTOMATION ENGINEERING

1403: ADAPTIVE DEVELOPMENT OF SVSF FOR A FEATURE-BASED SLAM ALGORITHM USING MAXIMUM LIKELIHOOD ESTIMATION AND EXPECTATION MAXIMIZATION	269
<i>Heru Suwoyo, Yingzhong Tian, Wenbin Wang, Long Li, Andi Adriansyah, Fengfeng Xi and Guangjie Yuan</i>	
1415: SYSTEM OF AUTOMATIC CONTROL OF THE LEVEL OF STEAM POWER GENERATORS ON THE BASIS OF THE REGULATION CIRCUIT WITH SMOOTHING OF THE SIGNAL.....	287
<i>Siddikov Isamiddin Xakimovich and Umurzakova Dilnoza Maxamadjonovna</i>	
1480: ASSIST AS NEEDED CONTROL STRATEGY FOR UPPER LIMB REHABILITATION ROBOT IN EATING ACTIVITY	298
<i>Norsinnira Zainul Azlan and Nurul Syuhadah Lukman</i>	

MECHANICAL AND AEROSPACE ENGINEERING

1538: IMPROVED CONSTRAINT HANDLING APPROACH FOR PREDICTIVE FUNCTIONAL CONTROL USING AN IMPLIED CLOSED-LOOP PREDICTION	323
<i>Muhammad Abdullah, John Anthony Rossiter and Alia Farhana Abdul Ghaffar</i>	

A NOVEL DIMENSIONALITY REDUCTION APPROACH TO IMPROVE MICROARRAY DATA CLASSIFICATION

MOHAMMED HAMIM^{1*}, ISMAIL EL MOUDDEN², MOUNIR OUZIR³,
HICHAM MOUTACHAOUK¹ AND MUSTAPHA HAIN¹

¹*12SI2E Laboratory, ENSAM- Casablanca, University Hassan II,
Casablanca, Morocco*

²*EVMS-Sentara Healthcare Analytics and Delivery Science Institute,
Eastern Virginia Medical School, Norfolk, VA, USA*

³*Group of Research in Physiology and Physiopathology, Department of Biology,
Faculty of Science, University Mohammed V, Rabat, Morocco*

*Corresponding author: mohamed.hamim@gmail.com

(Received: 12th April 2020; Accepted: 30th September 2020; Published on-line: 4th January 2021)

ABSTRACT: Cancer tumor prediction and diagnosis at an early stage has become a necessity in cancer research, as it provides an increase in the treatment success chances. Recently, DNA microarray technology became a powerful tool for cancer identification, that can analyze the expression level of a different and huge number of genes simultaneously. In microarray data, the large genes number versus a few records may affect the prediction performance. In order to handle this "curse of dimensionality" constraint of microarray dataset while improving the cancer identification performance, a dimensional reduction phase is necessary. In this paper, we proposed a framework that combines dimensional reduction methods and machine learning algorithms in order to achieve the best cancer prediction performance using different microarray datasets. In the dimensional reduction phase, a combination of feature selection and feature extraction techniques was proposed. Pearson and Ant Colony Optimization was used to select the most important genes. Principal Component Analysis and Kernel Principal Component Analysis were used to linearly and non-linearly transform the selected genes to a new reduced space. In the cancer identification phase, we proposed four algorithms C5.0, Logistic Regression, Artificial Neural Network, and Support Vector Machine. Experimental results demonstrated that the framework performs effectively and competitively compared to state-of-the-art methods.

ABSTRAK: Ramalan tumor kanser dan diagnosis pada peringkat awal telah menjadi keperluan dalam kajian kanser, kerana ia membuka peluang peningkatan kejayaan dalam rawatan. Kebelakangan ini, teknologi mikrotatasusunan DNA menjadi alat berkuasa bagi mengenal pasti kanser, di mana ia mampu menganalisa level ekspresi yang pelbagai dan gen-gen yang banyak secara serentak. Dalam data mikrotatasusunan, gen-gen yang banyak ini bakal menentukan ramalan prestasi berbanding analisa melalui rekod-rekod yang sebilangan. Fasa pengurangan dimensi adalah perlu bagi mengawal kakangan "penentuan kedimensian" dataset mikrotatasusunan, sementara itu ia memantapkan lagi keberkesanan kenal pasti kanser. Kajian ini mencadangkan rangka kombinasi kaedah pengurangan dimensi dan algoritma pembelajaran mesin bagi mencapai prestasi ramalan kanser terbaik dengan menggunakan pelbagai dataset mikrotatasusunan. Dalam fasa pengurangan dimensi, kombinasi pemilihan ciri dan teknik pengekstrakan ciri telah dicadangkan, Pengoptimuman Pearson dan Koloni Semut bagi memilih gen yang paling penting, Analisis Komponen Prinsipal dan Analisis Komponen Prinsipal Kernel, bagi menukar gen terpilih yang linear dan tak linear kepada ruang baru yang dikurangkan. Dalam

menentukan fasa mengenal pasti kanser, kajian ini mencadangkan empat algoritma iaitu C5.0, Regresi Logistik, Rangkaian Neural Buatan dan Mesin Vektor Sokongan. Dapatan kajian menunjukkan rangka ini adalah berkesan dan kompetitif berbanding kaedah semasa.

KEYWORDS: *gene selection; metaheuristic-ant colony optimization; feature extraction; pattern recognition; microarray data analysis*

1. INTRODUCTION

According to a recent publication by the World Health Organization (WHO) in 2018, cancer is considered the second most lethal factor for human beings. Knowing that early diagnosis is a mandatory and a crucial step in cancer treatment, the chance to get an appropriate treatment may require further measurements to increase the accuracy of cancer diagnosis combined with other clinical tests. With the development of machine learning techniques and microarray technology, the DNA analysis microarray data brings a great opportunity in cancer diagnosis. However, the presence of a large number of irrelevant or redundant genes (features) in gene expression data may increase the search space size, which makes pattern detection more difficult and makes it complex to capture the necessary rules for classification [1]. To overcome this "curse of dimensionality", a dimensional reduction process is strongly recommended. Dimensional reduction refers to a process that removes redundant and noisy features from the data, thus maximizing prediction performance. Dimensional reduction can be divided into feature selection (FS) and feature extraction (FE). FE methods create a subset of new features by combinations of existing features. The new features are low-dimensional features with the same or better performance in terms of prediction accuracy. In the literature, some proposed FE methods for cancer classification using gene expression data include Principal Component Analysis (PCA) [2] and kernel PCA [3]. On the other hand, the FS process focuses simply on the relevant features in the dataset by removing any redundant, irrelevant, or noisy features, which leads to better learning performance. The frequently used FS methods are divided into filter and wrapper. In the filter approach, features are scored based on statistical criteria such as Pearson correlation coefficients (P) [4]. In the wrapper approach [5], FS is combined with classification algorithms. Examples of wrapper algorithms include Ant Colony Optimization algorithm (ACO), Genetic Algorithm (GA), and others. When the number of features becomes very large, the filter methods are usually chosen due to their computational efficiency and simplicity [6]. In this paper, in addition to the Pearson correlation-based filter, a hybrid approach of feature selection has also been proposed that takes advantage of filter and wrapper methods. The proposed hybrid approach combines correlation-based feature selection with the ACO algorithm.

In this study, our aim is to improve the performance of cancer tumor modeling using a framework that combines FS and FE as dimension reduction methods with machine learning algorithms.

2. RELATED WORKS

The importance of classifying cancer patients into high or low risk groups has led to study the application of machine learning methods. Different strategies exist focusing on modifying the data for better fitting in a specific machine learning method; among them, we have dimensionality reduction, FS, and FE [7]. Several DNA microarray experiments have marked the power of datamining methods over clinical criteria for cancer diagnosis [8,9]. These studies accentuate the improvement of prediction performance based on gene

expression data by combining dimensional reduction techniques with machine learning algorithms.

To improve prostate cancer performance modeling and mining, Hicham and al. have proposed a new framework combining feature selection using Pearson and feature extraction using PCA in conjunction with machine learning algorithms. The most important result achieved in this study is obtained by the Pearson-PCA-C5.0 model with 94.05% classification accuracy and five selected features [10]. Kar et al. proposed a combination of filter method based on t-test and wrapper method based on particle swarm optimization (PSO) to find the most relevant genes in the SRBCT microarray dataset. The study achieved 100% accuracy for 14 selected genes [11].

Atiyeh and Mohammad implemented an innovative feature selection approach Based on Cooperative Game Theory and Qualitative Mutual Information (QMT). The classification accuracy on 11 microarray datasets, namely Leukemia1, SRBCT, Lung, and prostate cancer, shows that the proposed approach improves both accuracy and stability compared to other methods [12]. Chandra proposed an efficient feature selection technique that removes the drawbacks of [13], by taking into account the redundancy between features. the research study shows that the classification accuracy form using the proposed algorithm Inter Feature Effective range overlap (IFERO), for many cancers, is much superior compared to other feature selection algorithms. The proposed technique has been applied to 8 benchmark cancer datasets [14].

Shun Guo et al. formulated the feature selection problem as an optimization one based on a newly defined linear discriminant analysis criterion. The experiment was applied to 10 publicly available microarray datasets, and the results show that the proposed gene selection is an effective method for improving the accuracy of tumor classification [15].

The present paper aims to improve the classification performance for four benchmark cancer datasets. For this purpose and in order to handle the curse of dimensionality problem of the Microarray dataset, we propose a framework that combines FS and FE methods in conjunction with machine-learning algorithms.

3. MATERIALS AND METHODS

Figure 1 summarizes the main steps of our proposed framework, which is based on feature selection using Filter and Hybrid approaches, FE using linear and non-linear PCA, and cancer identification (classification) using Logistic Regression (LR), C5.0 Decision Tree algorithm, Support-Vector Machines SVM, and Artificial Neural Network (ANN). The main structure of the proposed Framework is described in Algorithm 1.

3.1 Feature Selection Methods

The feature selection or gene selection in the context of microarray data analysis is a useful technique that can reduce dimensionality by removing any redundant, irrelevant or noisy genes, which can lead to improve the classification performance and reduce the cost of computation [16]. As shown in Fig. 2, the feature selection process can be reformulated as follows: given an original set, $X = (X_1, X_1, \dots, X_p)$, of p features, find the subset which consists of k features (where $k \ll p$), such that the most informative features are selected.

The proposed framework in the present paper implements two feature selection techniques, the filter method based on statistic tools and the hybrid method that combines the filter approach with ACO.

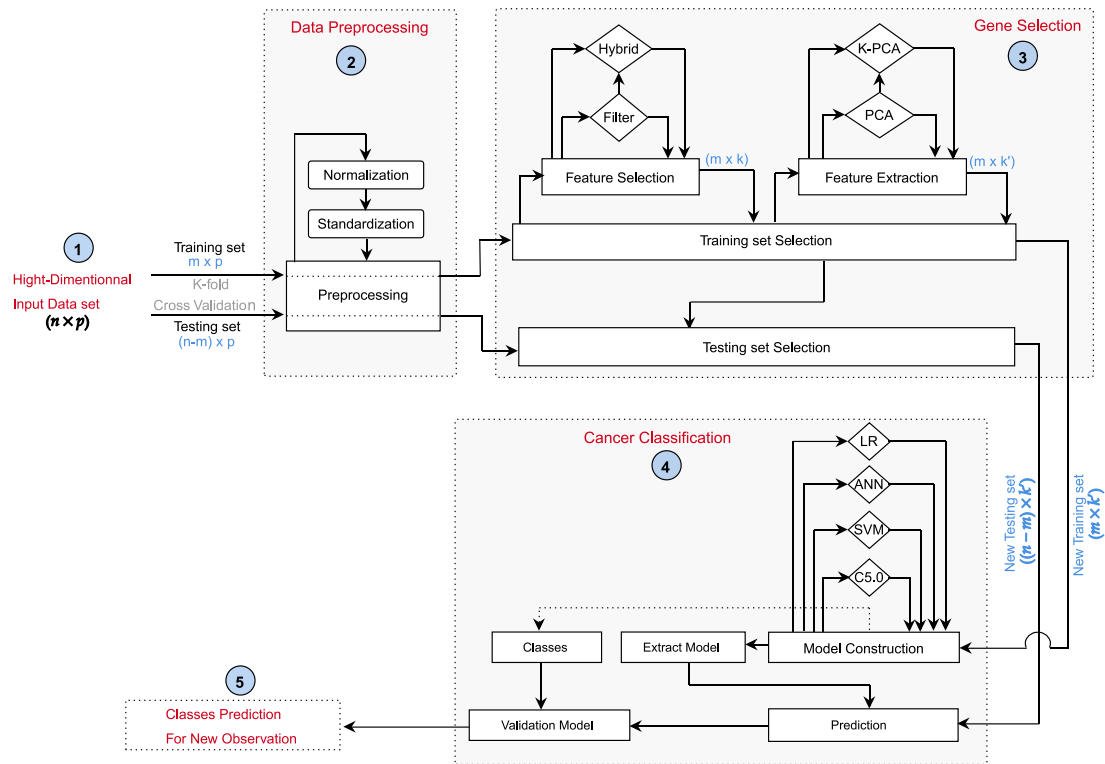


Fig. 1: Our proposed Framework.

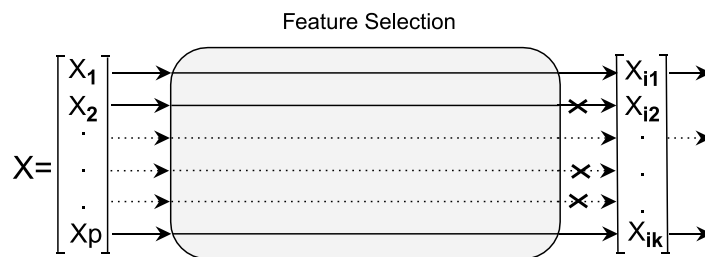


Fig. 2: Feature Selection process.

3.1.1 Filter Method using Pearson's Correlation Coefficient

Because they act independently of any classification process, filters are considered to be faster than the wrapper approach. This is because this model is frequently used when it comes to working with a large number of features [17]. To measure feature relevance using filter methods, some statistical techniques are applied for each feature, such as Pearson's correlation coefficient, Spearman's rank correlation, Pearson's Chi-square, Cramer's v, ...

In the present paper, Pearson's correlation in Eq. (1), denoted by r , was applied to recognize features (X) showing a strong linear relationship with the target (Y).

Algorithm 1: Framework

```

/* Function to preprocess data */
Function DataPreprocessing (Training_set, Testing_set);
    Training_set, Testing_set ← Log_Transformation ( Training_set, Testing_set ); // Equation (15)
    Training_set, Testing_set ← Standardization ( Training_set, Testing_set ); // Equation (16)
    return Training_set, Testing_set

/* This function returns an new subset of k genes from the original set */
Function FeatureSelection (Method, Training_set, Testing_set);
    if Method = Filter then
        Subset_train ← Select relevant genes from Training_set using Pearson correlation based Filter method. ; // Equations (1, 2)
    else if Method = Hybrid then
        Subset_train ← Select relevant genes from Training_set using PACO based Hybrid method. ; // Algorithm (2)
    Subset_test ← Select from Testing_set the same genes selected from Training_set.
    Return Subset_train, Subset_test

/* This function transforms an input set to a new set of k' predictors */
Function FeatureExtraction (Method, Training_set, Testing_set);
    if Method = PCA then
        Construct a projection matrix using Principal Component Analysis. ; // Algorithm (3)
    else if Method = KPCA then
        Construct a projection matrix using kernel Principal Component Analysis. ; // Algorithm (4)
    Subspace_train, Subspace_test ← Use the projection matrix to transform the Training_set and Testing_set into a k'-dimensional feature subspaces.
    Return Subspace_train, Subspace_test

Function Classification (Training_set, Testing_set);
    List_Classifiers = [SVM, LR, C5.0, ANN] /* iterate over all classifiers */
    for each Classifier in List_Classifiers do
        Model ← Train classifier on the Training_set
        Test the Model on the Testing_set
        Calculate average performance (Accuracy and AUC).
    Return All obtained Models with their average performances

/* Main program */
Input :-A p-dimensional DNA microarray dataset D = [y, x1, x2, ..., xp]n×1, n is the number of patterns, x is the feature vector, y is the target vector and p is the number of features
Output : List of generated models with average performance and running time for each one.
1 Split dataset D into K-folds using Stratified K-fold cross-validation technique.
2 for each fold in D do
3     D_test ← fold
4     D_train ← remaining (K-1)-folds
5     /* Step aims at separately preprocessing the Training and Testing sets */
6     D_train, D_test ← DataPreprocessing (D_train, D_test).
7     /* Step aims at generating all models based on pristine data */
8     Pristine_Models ← Classification (D_train, D_test)
9     Pristine_PCA_Models ← Classification (FeatureExtraction (PCA, D_train, D_test))
10    Pristine_KPCA_Models ← Classification (FeatureExtraction (KPCA, D_train, D_test))
11    /* Generate all models based on selected genes using Pearson correlation based filter method */
12    SubF_train, SubF_test ← FeatureSelection (Filter, D_train, D_test)
13    Pearson_Models ← Classification (SubF_train, SubF_test)
14    Pearson_PCA_Models ← Classification (FeatureExtraction (PCA, SubF_train, SubF_test))
15    Pearson_KPCA_Models ← Classification (FeatureExtraction (KPCA, SubF_train, SubF_test))
16    /* Generate all models based on selected genes using PACO based Hybrid approach */
17    SubH_train, SubH_test ← FeatureSelection (Hybrid, D_train, D_test)
18    PACO_Models ← Classification (SubH_train, SubH_test)
19    PACO_PCA_Models ← Classification (FeatureExtraction (PCA, SubH_train, SubH_test))
20    PACO_KPCA_Models ← Classification (FeatureExtraction (KPCA, SubH_train, SubH_test))
21 Return all generated models

```

$$r_{(X,Y)} = \frac{\sum_{i=1}^N (x_i - \bar{X})(y_i - \bar{Y})}{\sqrt{\sum_{i=1}^N (x_i - \bar{X})^2} \sqrt{\sum_{i=1}^N (y_i - \bar{Y})^2}} \quad (1)$$

Where N is the total number of samples in the training set. \bar{X} , \bar{Y} are, respectively, the overall mean of the X and the Y. x_i and y_i are, respectively, the i-th observation in X and Y. The $r_{(X,Y)}$ always lies between ± 1 , where 1 indicates a perfect relationship between X and Y, and the 0 indicates no relationship between them.

Then, the relevance value of each feature X is measured as $(1 - p_{\text{value}}) \times 100\%$, where p_{value} based on the t-statistic with $df = N - 2$ degree of freedom is computed using the Eq. (2).

$$p_{\text{value}} = \text{Probability}(T(df) > t) \quad (2)$$

With $t = r\sqrt{df/(1-r^2)}$, and T(df) is a random variable that follows a Student's t-distribution with df.

In this study, all features (genes) in the training set with relevance greater than 95% were selected.

3.1.2 Ant Colony Optimization Hybrid Approach

Hybrid methods attempt to combine the straightness of two feature selection methods. The most frequently used combination is the filter with a wrapper approach [17]. The present framework proposes a new hybrid technique (Fig. 3) that combines Pearson's correlation and Ant Colony Optimization (PACO). The filter step in the framework consists of reducing the number of genes by removing non-informative genes in the original training set, and then the number of pre-selected genes is given to the ACO to select the optimal subset in the original training set.

Proposed by Marco Dorigo [18], ACO is a nature-inspired metaheuristic approach. The idea behind ACO is to represent the search space of a problem in the form of a graph, then the solution of the problem is to find the optimal path in this graph using artificial ants. As in real ant colonies, each ant deposits the pheromone trail with the same rate on the components of the graph that it chooses to cross. The chosen path to cross by an ant is usually based on the accumulated pheromone trail. Thus, the accumulated pheromone is considered to be an indicator of the quality of the chosen path, which can attract ants in the next iterations to the corresponding areas in the search space [19].

The ACO has been a powerful tool in many optimization problems [20-22], and for many reasons, it was recently used as a powerful tool for gene selection [23-25]. In feature selection using ACO, each node in the graph is viewed as a feature (gene), and edges between nodes (features) represent the choice of the next node to be selected. Thus, searching the optimal subset of features is to find the optimal path in the graph until such a stopping criterion is satisfied. The problem of feature selection using PACO can be reformulated as follows: given an original training set $X = (X_1, X_1, \dots, X_p)$, of p features, find the subset that consists of k features (where $k \ll p$), such that a maximum number of iterations is reached.

According Fig. 3, before starting any iteration, the number of genes in the optimal subset to select is initialized using a Pearson correlation-based filter, and the amount of pheromone in the search space is initialized to a constant value. Then, at the start of each iteration t , each ant k starts in a randomly selected feature. To select (to visit) the next feature (nodes) from unselected ones, each ant must respect the probabilistic "transition rule" [19] using the Eq. (3).

$$P_{ij}^k(t) = \begin{cases} \frac{\tau_{ij}^\alpha(t) \cdot \eta_{ij}^\beta(t)}{\sum_{l \in S_i^k} (\tau_{il}^\alpha(t) \cdot \eta_{il}^\beta(t))}, & \forall j \in S_i^k \\ 0, & otherwise \end{cases} \quad (3)$$

Where:

S_i^k : features set that have not been visited yet.

$\tau_{ij}(t)$: the amount of pheromone trail between feature i and j .

$\eta_{ij}(t)$: the heuristic desirability of choosing feature j when the ant k at feature i .

$\alpha \geq 0$: adjustable parameters deciding the relative influence of pheromone.

$\beta \geq 1$: adjustable parameters controlling the influence of η_{ij} .

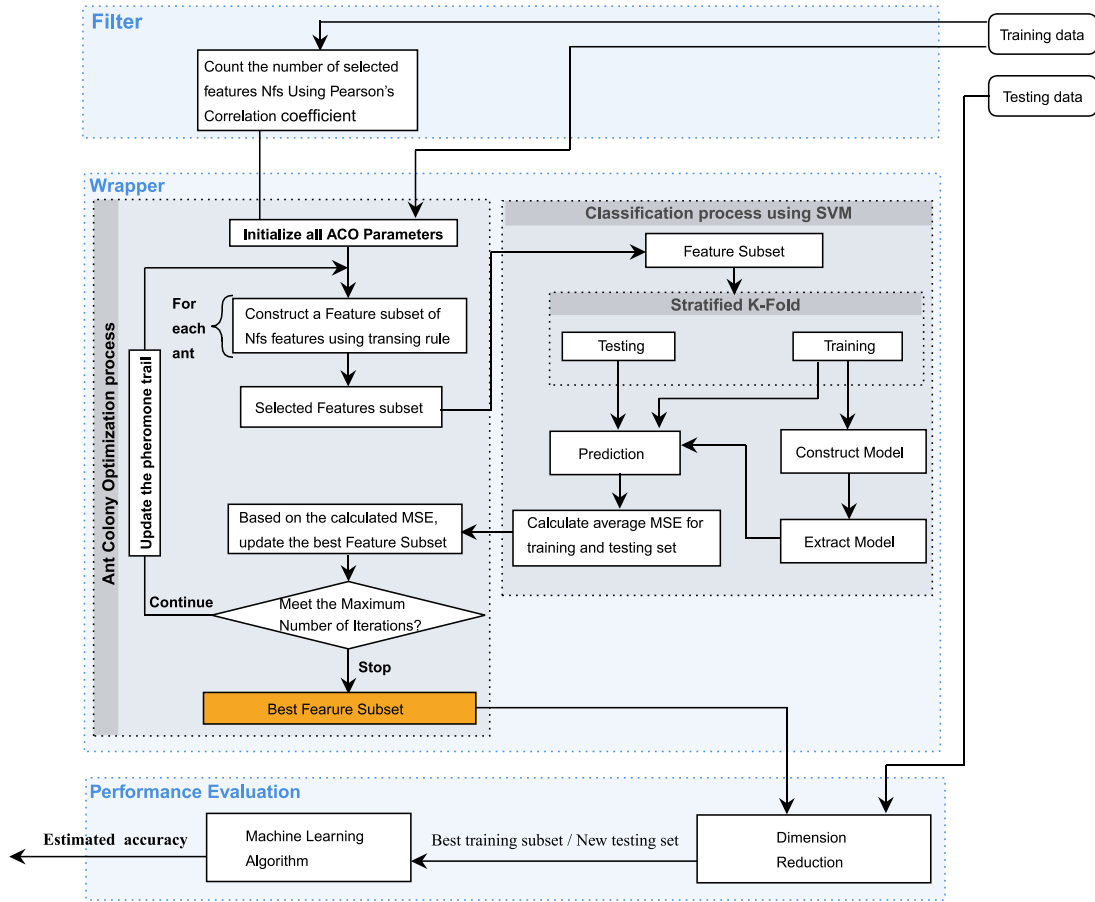


Fig. 3: Ant Colony Optimization hybrid approach.

The constructed subset S^k by the k -th ant is then evaluated using an SVM classifier, and the estimated Mean Square Error MSE_k of the classification results will decide if the current subset is the best one. The MSE is computed by applying a stratified 5 – fold Cross Validation method. The constructed subset is split into five-folds, and at each time, one of the five folds is used for the test, and the remaining folds form the training data. Then the average MSE for the five trials is calculated using the Eq. (4).

$$MSE = \frac{1}{K} \sum_{i=1}^K \frac{1}{2} (MSE_i^{Train} + MSE_i^{Test}) \quad (4)$$

The subset giving the lowest MSE is known as the best one related to the best ant and denoted by S_{best} . At the end of each iteration, the amount of pheromone in the search space is updated according to the Eq. (5) [19].

$$\tau_{ij}(t + 1) = \rho \cdot \tau_{ij}(t) + \sum_{k=1}^m \Delta\tau_{ij}^k \quad (5)$$

With : $\Delta\tau_{ij}^k = \begin{cases} \frac{Q}{MSE_k} & \text{if the edge}(i,j) \text{ is part of } S^k \\ 0 & \text{otherwise} \end{cases}$

Where:

m : is the number of ants.

S^k : represents the constructed subset corresponding to the ant k.

ρ : denotes the pheromone evaporation coefficient.

Q : a constant multiplier that defines the amount of pheromones that should put each ant.

MSE_k : denote the Mean Square Error corresponding to the constructed subset by the ant k.

The overall pseudocode of the proposed PACO gene selection approach is illustrated in Algorithm 2.

Algorithm 2: PACO algorithm

Input : $X = (X_1, X_2, \dots, X_p)$:is the training set, where p is the total number of features
 Nfs : the number of features to select
 m : define the number of ants
 $Nits$: number of iterations that algorithm repeated
Output: S_{best} : the best set of selected features from X

- 1 -Initialize the pheromone trails τ and heuristic desirability η for each edge in the search space.
- 2 -Initialize system parameters $(\alpha, \beta, \sigma, \rho, Q)$
- 3 **for** $i \leftarrow 1$ to $Nits$ **do**
- 4 **for** $k \leftarrow 1$ to m **do**
- 5 -Randomly select the first feature from the original set X
- 6 -Select the remaining $(Nfs - 1)$ features according to Equation (3)
- 7 -Evaluate the constructed subset S using SVM classifier
- 8 -If S has the best Mean Square Error (MSE), store the corresponding ant as the best one
- 9 **end**
- 10 -Update the pheromone trail according to Equation (5)
- 11 **end**
- 12 **Return** S_{best} the best constructed subsets corresponding to the best ant

3.2 Feature Extraction Methods

Feature extraction (FE) is the process of transforming original data with a large number of features into a reduced representation of a set of features. As shown in Fig. 4, the FE is achieved by transforming $X = (X_1, X_1, \dots, X_p)$, of p features to a new set of k predictor variables called components (where $k \ll p$).

Among linear and nonlinear methods, PCA and Kernel PCA are the most commonly used FE techniques for dimensionality reduction. In this paper, we attempt to use FE methods combined with FS ones in order to handle the curse of dimensionality of cancer datasets.

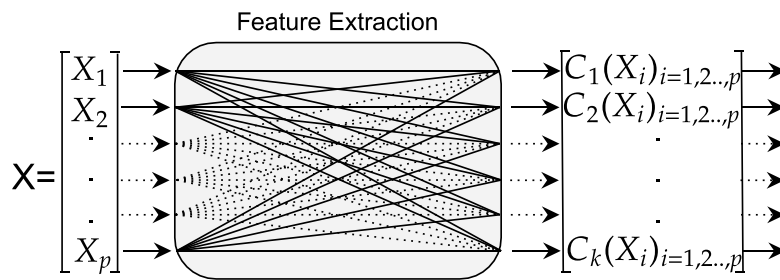


Fig. 4: Feature Extraction process.

3.2.1 Principal Components Analysis (PCA)

PCA is a classical dimension-reduction technique used to reduce large sets of variables (features) into new small ones without much loss of information from the large sets [26]. Mathematically, PCA attempts to transform a number of linearly correlated variables into a smaller number of new ones called components. In other words, PCA aims to find a linear subspace of lower dimensionality than the large variable space, where the new linear

subspace has the largest variance (has the most of the information in the large space). FE using PCA can be reformulated as follows:

Given a p -dimensional training set: $[x_1, x_2, \dots, x_p]_{n \times 1}$, Where: p denotes the number of features and n the number of patterns. We want to find Ψ , the matrix of new components where the number of principal components that should be retained is decided using the percentage of total variance explained. The pseudocode of the PCA method is illustrated in Algorithm 3.

Algorithm 3: PCA algorithm

Input : -A p -dimensional training set $X = [x_1, x_2, \dots, x_p]_{n \times 1}$, n is the number of patterns, x is the feature vector and p is the number of features
Output: ψ the matrix of principal components

- 1 Compute the mean $\bar{x} \leftarrow \frac{1}{n} \sum_{i=1}^n x_i$
- 2 compute the standard deviation $s_x \leftarrow \sqrt{\frac{1}{n} \sum_{i=1}^n (x_i - \bar{x})^2}$
- 3 Compute Z the standardized matrix : $z_i \leftarrow \frac{x_i - \bar{x}}{s_x}$
- 4 Compute the Correlation matrix $R \leftarrow \frac{1}{n} Z Z^T$, T is the matrix transposition
- 5 Compute eigenvalues λ_i and eigenvectors u_i of matrix R , $R u_i \leftarrow \lambda_i u_i$ where $i \in (1, 2, \dots, p)$
- 6 Arrange all eigenvalues (λ_i) in descending order
- 7 keep the d (where $d \ll p$) eigenvalues showing $\alpha \times 100\%$ of the variance $\frac{\sum_{i=1}^d \lambda_i}{\sum_{i=1}^p \lambda_i} \geq \alpha$
- 8 For each u_i where $i \in (1, \dots, d)$ compute $\psi_i \leftarrow Z u_i$
- 9 **Return** Ψ the matrix of principal components

3.2.2 kernel-PCA

While PCA is a dimension reduction technique that assumed to find linear transformation to represent the data in a lower dimension, kernel-PCA is used when we deal with complex structure data where linear subspace is not very useful [27]. In this paper, the kernel-PCA is used as an alternative to PCA when there is no linear correlation between features, which can affect classification accuracy.

Introduced as a nonlinear generalization of standard PCA [27], in the kernel PCA, the original input matrix $X_1, X_2, \dots, X_p \in R^n$ is mapped into a new feature space $\Phi(X_1), \Phi(X_2), \dots, \Phi(X_p) \in F$ and then the standard PCA is performed using this new feature space. However, computing $\Phi(X)$ explicitly before extracting the principal components is extremely costly [28]. The best practice is to directly construct a kernel matrix using X instead of computing $\Phi(X)$ explicitly [29]; thus, the mapping $\Phi(X)$ is implicitly specified by the kernel function. The most commonly used kernel function is the Radial Basis Function kernel (RBF) in Eq. (6)

$$k(x_i, x_j) = \exp(-\gamma \|x_i - x_j\|^2) \quad (6)$$

Where:

$\|x_i - x_j\|^2$: denotes the squared Euclidean distance

$\gamma > 0$: a parameter that sets the spread of the kernel

d : the degree of the kernel.

If the new feature space is not centered, a centering transformation can be applied directly to the kernel matrix using Eq. (7) [30].

$$K_c = K - K I_{1/n} - I_{1/n} K + I_{1/n} K I_{1/n} \quad (7)$$

Where $I_{1/n}$ is the $n \times n$ matrix with all elements equal to $1/n$ and n is the number of patterns.

The overall pseudocode of the Kernel Principal Components Analysis method is illustrated in Algorithm 4.

Algorithm 4: KPCA algorithm

Input :-A p-diemsional data set $X = \{x_1, x_2, \dots, x_n\}_{n \times p}$ n is the number of patterns, x is the feature vector and p is the number of features
 -Number of principal components d

Output: ψ the matrix of principal components

- 1 Compute $K_{(p \times p)}$ the kernel matrix using the Equation (6)
- 2 Centring transformation of K using the Equation (7)
- 3 $U \leftarrow \text{TopEigenValues}(K, d)$
- 4 $\lambda \leftarrow \text{TopEigenVectors}(K, d)$
- 5 for $i \leftarrow 1$ to n do
- 6 for $k \leftarrow 1$ to d do
- 7 $[\psi]_{k,i} \leftarrow \frac{1}{\sqrt{\lambda_k}} \sum_{t=1}^n K(x_i, x_t) U_{t,k}$
- 8 end
- 9 end
- 10 **Return** ψ

4. CANCER IDENTIFICATION AND CLASSIFICATION METHODS

4.1 C5.0 Decision Tree

C5.0 is a new decision tree algorithm developed from C4.5 by [31], which has proven its high detection accuracy in many research fields [32-34]. Compared to C4.5, C5.0 can handle different types of data, deal with missing values and support boosting to improve classifier accuracy [35]. In C5.0 algorithm, samples are split into sub-samples by using a recursive method based on information gain ratios. Each sub-sample received from the first split will be split again. The split process is repeated until there is no more split that makes a difference in terms of information gain ratios. At the end of the process, any split which doesn't have a significant contribution to the model is rejected [36].

4.2 Support Vector Machine

The Support Vector Machine (SVM) is a binary classifier algorithm that has been successfully applied in many pattern recognition areas. In linear classification, SVM constructs a classification hyper-plane that separates the data into two sets by maximizing the margins and minimizing the classification error. The hyper-plane is constructed in the middle of the maximum margin. Thus, samples above the hyper-plane are classified as positives. Otherwise, they are classified as negatives (Fig. 5). The classification function is given with Eq. (8) [37].

$$y = \text{sign}(\sum_{i=1}^n w_i x_i + b) \quad (8)$$

Where y denotes the class label, w and b are the parameters of the hyper-plane, and sign denotes the sign function.

However, in a real classification problem, datasets are often linearly non-separable. Therefore, Eq. (8) will allow some of the samples to be on the wrong side of the hyper-plane. To overcome this problem of non-linearity, a nonlinear transformation of the input vectors into a new feature space is performed, and then a linear separation is performed using this new feature space [37]. To perform a nonlinear SVM, the product (x, y) is replaced by a kernel function (Eq. (9)).

$$y = \text{sign}(\sum_{i=1}^n \alpha_i y_i k(x_i, x) + b) \quad (9)$$

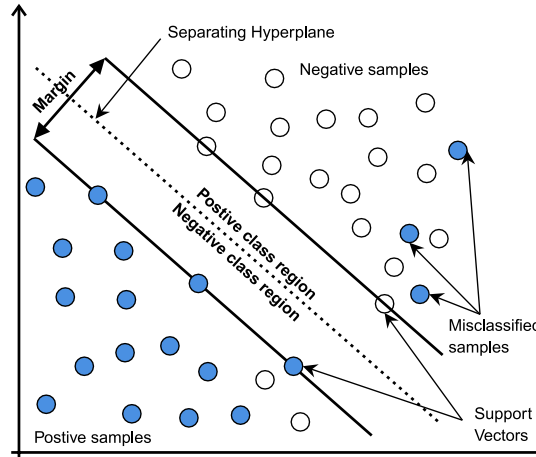


Fig. 5: Support Vector Machines diagram

In this paper a Gaussian kernel (Eq. (6)) was used to deal with the problem of non-linearity.

4.3 Artificial Neural Network

Introduced by [38], the Artificial neural network (ANN) is a form of distributed computation inspired by networks of human biological neurons. As shown in Fig. 6(a), An ANN consists of a set of interconnected artificial neurons that are organized in a minimum of three layers: the input layer, hidden layer, and output layer. All nodes (neurons) in each layer of the network are connected to the nodes of the next layer with no connection back, and all the connections are defined by weight values denoted by w . In the input layer, all nodes get information from the outside and pass it to the nodes of the next layer weighted by w . If we take a look at one of the hidden or output neurons (Fig. 6 (b)), we find that each node computes the weighting sum of all the N neurons of the previous layer and passes it through an activation function [39]. Equation (10) represents the equation for a given neuron.

$$z_j = f\left(\sum_{i=1}^N w_{ij}x_i + bj\right) \quad (10)$$

A Common choice for the activation function is non-linear functions such as the logistic sigmoid function given by the Eq. (11).

$$f(x) = \frac{1}{1+e^{-x}} \quad \text{with} \quad 0 \leq f(x) \leq 1 \quad (11)$$

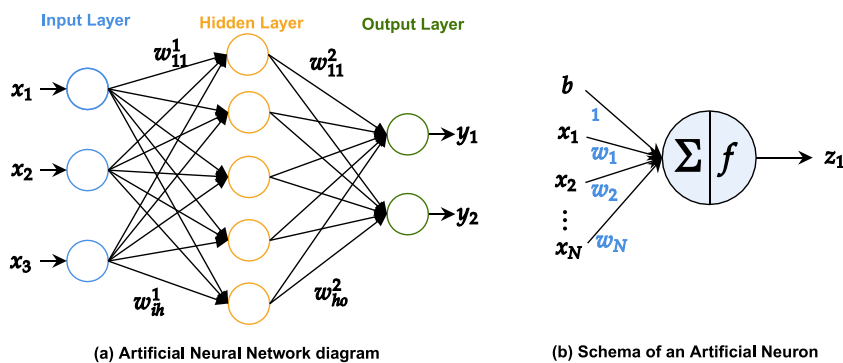


Fig. 6: Artificial Neural Network diagram.

4.4 Logistic Regression

As an extension of the linear regression algorithm for classification problems, Logistic Regression aims to find the best fitting model, which squeezes the output of a linear equation between 0 and 1 using the logistic function (Eq. (11)). In linear regression, the relationship between output and features is modeled using a linear equation (Eq. (12)). However, in a classification problem, it is strongly recommended to have probabilities between 0 and 1, which can force the outcome to be only between 0 and 1 (Eq. (13)).

$$y = b_0 + b_1x_1 + b_2x_2 + \dots + b_nx_n \quad (12)$$

$$f(x) = \frac{1}{1 + e^{-(b_0 + b_1x_1 + b_2x_2 + \dots + b_nx_n)}} \quad (13)$$

4.5 Performance Evaluation

The datamining process has several ways to check the performance of any classification model. The quality of any classification model is built from the confusion matrix (Table 1), which summarizes the comparison between predicted and observed classes for all observations.

Table 1: Confusion matrix

		Predicted classes	
		True	False
Observed classes	True	True positives (TP)	True negatives (TN)
	False	False positives (FP)	False negatives (FN)

Different types of evaluation measure are available, and the most commonly used in practice is the classification accuracy (Eq. (14)), which evaluates the classification performance by the percentage of correct predictions.

$$Accuracy = \frac{TP+TN}{TP+TN+FP+FN} \quad (14)$$

Another common evaluation metric used in Machine Learning is the receiver operating characteristic (ROC) curve which is created by plotting the True Positive Rate ($TPR = TP/(TP + FN)$) against the False Positive Rate ($FPR = FP/(FP + TN)$). The Area Under the ROC Curve (AUC) provides a good idea about model performance. The model that gives 100% of correct predictions has an AUC of 1, while the model that gives 100% of wrong predictions has an AUC of 0.

In the present paper, both accuracy and ROC curve were used to evaluate the performance of each generated model.

5. EXPERIMENTAL RESULTS

5.1 Dataset Description

In order to evaluate the ability of our framework to adapt to different situations, experiments are achieved on several public high-dimensional microarray datasets with different properties (number of genes, number of patterns, and the number of classes). Description of the datasets used in the present work is provided in Table 2.

Table 2: Microarray Datasets Characteristics

Dataset	Description	Genes	Patterns	Classes	Missing Values	Ref.
Prostate	Is the development of cancer in the prostate, a gland in the male reproductive system	10509	102	2	No	[40]
Leukemia1	It is one of the most common childhood cancers that affect leukocytes, but it most often occurs in older adults.	5327	72	3	No	[41]
SRBCT	Small-round-blue-cell tumors are four different childhood tumors; Ewing's family of tumors (EWS), neuroblastoma (NB), non-Hodgkin lymphoma and rhabdomyosarcoma (RMS)	2308	83	4	No	[42]
Lung	It is a malignant tumor caused by uncontrolled cell growth in lung tissues	12600	203	5	No	[43]

5.2 Partitioning

In order to avoid the overestimating prediction, a stratified 5 – *fold* cross-validation technique was employed. Using this technique, samples are split into five equal folds (subset) of samples. One of the five folds is used as a testing step, and the remaining four folds are put together to form the training data. This process is repeated five times. The stratification process was used to ensure that all folds are made by preserving the same percentage of samples for each class.

5.3 Data Preprocessing

Before supplying the datasets to our analysis system, it was necessary to perform data preprocessing, as it is an important step in the data analysis process. In the present paper, gene expression datasets were preprocessed using the standard procedure, which includes log transformation and standardization.

a) Data Transformation

The main motivation for using the log transformation is due to the asymmetric distribution of the derived expression levels [44], which can affect the identification of expression Patterns, and prospective Classification in Human Cancer Genomes [45].

In the present work, before transforming our data (training or testing set) using Eq. (15), a test of normality using Shapiro-Wilk [46,47] is used to evaluate whether the distribution of the data agrees with normal distribution. The calculated P-value of the Shapiro–Wilk test for each gene shows a strong significance, which indicates a deviation from the normal distribution for most of the gene expressions.

$$X = \text{Log}_{10}(X - 1 + \text{Min}(X)) \quad (15)$$

b) Data Standardization

Gene expression levels for each gene were standardized using the Eq. (16). The result is that expression levels for each feature have a mean 0 and variance 1.

$$X = \frac{x - \bar{X}}{\sigma} \quad (16)$$

Where: \bar{X} is the overall mean of the feature X and σ , its standard deviation.

5.4 Experimental Settings

a) System Configuration

Using parallel processing, our proposed framework was implemented in Python 3.7 language. All of the experiments were carried out using an Intel Xeon E5-2637 v2 3.5 GHz PC with 64 GB of RAM.

b) Parameters Settings

The parameters used in our Framework are shown in Table 3:

Table 3: Parameters settings used in our proposed Framework

Parameter	Value
PACO parameters	
Number of ants	10
Number of selected features	Initialized using the filter method
α	1
β	5
Q	100
ρ	0.5
SVM Kernel	RBF
PCA parameters	
α	0.8
Kernel-PCA parameters	
d	Initialized using standard PCA
Kernel	RBF
ANN classifier parameters	
The number of hidden nodes	Calculated by using Geometric-Pyramid-Rule [48]
The number of hidden layers	1
Activation function	Logistic
Solver (optimization algorithm)	adam
Max iterations	1000
SVM classifier parameters	
Kernel	RBF

6. RESULTS AND DISCUSSION

Table 4, which is also presented as graphs in Fig. 7, shows the overall performance of dimension reduction techniques and their respective classification algorithms used in the four public microarray datasets described in Table 2. 36 different models were generated for each microarray dataset. The quality of each model is measured by the number of selected genes k , the dimension of the new subspace k' generated by using the FE process, the running time t (the running time reported here includes both the dimension reduction and classification stages), and the cancer prediction performance which represents the average accuracy of the training and testing sets. The results of each dataset are as follows:

For the SRBCT dataset, Table 4 and Fig. 7 show that the shrinkage models P-PCA-SVM, P-PCA-ANN, and P-PCA-LR provide an excellent accuracy of **100%**. The power of these models resides in the fact that the number of genes was reduced twice. The first reduction was obtained using Pearson correlation-based feature selection (Line 9 in Algorithm 1), the dimension of dataset passed from $p = 2308$ (the original number of genes in the dataset as reported in Table. 2) to a new subset of $k = 727$ while selecting only the

more representative genes with relevance greater than 95%. Then, the new k-dimension subset was transformed to a linear subspace using PCA where only the first $k' = 22$ predictors (components) that explain approximately 80% of the total variation of genes subset (the cumulative variance equal to 80%) were retained. The same results were achieved by P-KPCA-SVM, P-KPCA-ANN, and P-KPCA-LR models with the nonlinear transformation (KPCA) for the feature extraction method. The classification rate was close to **100%** for most shrinkage models using the PACO-based feature selection method with a more significant response time increase. Fortunately, there is almost no significant accuracy loss for the rest of the generated models.

Table 4: Performance measurement using our Framework on the four datasets

Feature Selection Feature Extraction		Model	Datasets																																					
			SRBCT					Lung					Prostate					Leukemia1																						
			p	k	k'	t(s)	Accuracy (%)	p	k	k'	t(s)	Accuracy (%)	p	k	k'	t(s)	Accuracy (%)	p	k	k'	t(s)	Accuracy (%)																		
Pristine	Pristine	SVM	2308	2308	1	100	12600	2	95.42	10509	1	93.17	5327	1	91.46	5327	1	100	5327	13	100																			
		LR																				2308	1	100	12600	12	98.75	10509	1	97.62	5327	1	100							
		ANN																				2308	6	100	12600	60	98.75	10509	27	97.62	5327	13	100							
		C50																				3	1	96.45	4	21	96.74	2	6	94	2	4	95.57							
	PCA	PCA-SVM																				24	1	100	53	2	95.61	15	1	85.79	30	1	93.61							
		PCA-LR																				24	1	100	53	2	97.13	15	1	88.29	30	1	100							
		PCA-ANN																				24	1	100	53	2	97.44	17	1	93.39	30	1	100							
		PCA-C50																				6	1	92.6	8	1	96.03	4	1	88.78	5	1	89.77							
		KPCA																				KPCA-SVM	24	1	100	53	1	92.36	15	1	85.79	30	1	92.46						
																						KPCA-LR	24	1	96.3	54	1	80.44	15	1	85.18	28	1	80.53						
																						KPCA-ANN	24	1	92.6	53	2	81.82	16	1	53.05	30	1	86.7						
																						KPCA-C50	5	1	89.26	11	1	87.52	6	1	90.67	6	1	84.91						
Pearson	Pearson	P-SVM	2308	727	727	1	100	4566	4566	6	96	2824	2824	3	97	1120	1120	4	100	985	985	3	100																	
		P-LR																						727	727	1	100	4534	4534	13	97.5	2640	2640	6	97.5	985	985	3	100	
		P-ANN																						727	727	3	100	4534	4534	15	98.75	2640	2640	8	97.5	985	985	5	100	
		P-C50																						727	4	2	96.3	4679	4	10	96.74	2824	2	5	91.01	988	3	3	96.67	
	PCA	P-PCA-SVM																						727	22	1	100	4264	59	4	97.5	2824	17	3	95.15	1035	26	2	100	
		P-PCA-LR																						727	22	1	100	4534	57	8	97.5	1801	18	4	94.62	1035	26	2	100	
		P-PCA-ANN																						727	22	2	100	4446	59	7	98.75	2824	17	4	94	1035	26	3	100	
		P-PCA-C50																						756	5	1	96.45	4566	7	6	92.67	2824	6	3	97	1035	3	2	100	
		KPCA																						P-KPCA-SVM	727	22	1	100	4566	60	5	95.72	2640	17	5	95.06	985	28	3	100
																								P-KPCA-LR	727	22	1	99.24	4446	59	6	84.79	1801	18	4	93.39	1035	26	2	88.07
																								P-KPCA-ANN	756	22	2	99.23	4566	60	6	79.8	1801	18	4	90.39	1035	26	3	92.46
																								P-KPCA-C50	756	3	1	93.68	4534	9	7	92.19	2640	4	5	91.34	1041	3	2	93.33
PACO	PACO	PACO-SVM	2308	727	727	214	100	4566	4566	4502	95.42	2640	2640	3298	93.17	1120	1120	1081	92.31	985	985	1290	100																	
		PACO-LR																						727	727	214	100	4534	4534	4705	98.75	1801	1801	3591	97.62	985	985	1290	100	
		PACO-ANN																						727	727	215	100	4534	4534	4709	99	2640	2640	3301	97.5	985	985	1291	100	
		PACO-C50																						750	4	156	96.13	4446	4	6366	96.27	1801	4	3591	95.24	1035	3	1163	100	
	PCA	PACO-PCA-SVM																						727	23	214	100	4264	52	6241	95.61	2640	15	3298	90.12	1035	28	1163	95.79	
		PACO-PCA-LR																						727	23	214	100	4264	52	6241	97.13	1801	17	3591	91.53	985	30	1289	100	
		PACO-PCA-ANN																						727	23	215	100	4566	52	4503	97.56	2824	16	3620	92.15	988	30	1157	96.67	
		PACO-PCA-C50																						750	5	156	92.26	4264	8	6241	96.52	1801	6	3591	88.62	985	3	1289	91.13	
		KPCA																						PACO-KPCA-SVM	727	23	214	100	4264	52	6240	94.63	2640	15	3298	87.62	1120	30	1081	96.15
																								PACO-KPCA-LR	727	23	214	96.3	4446	54	6362	80.75	3879	16	3456	87.68	988	30	1157	80.53
																								PACO-KPCA-ANN	756	23	192	97.22	4264	52	6241	84.26	2824	16	3620	55.82	985	30	1290	89.29
																								PACO-KPCA-C50	847	6	158	90	4446	11	6362	87.22	3879	5	3456	93.17	1120	5	1081	87.61

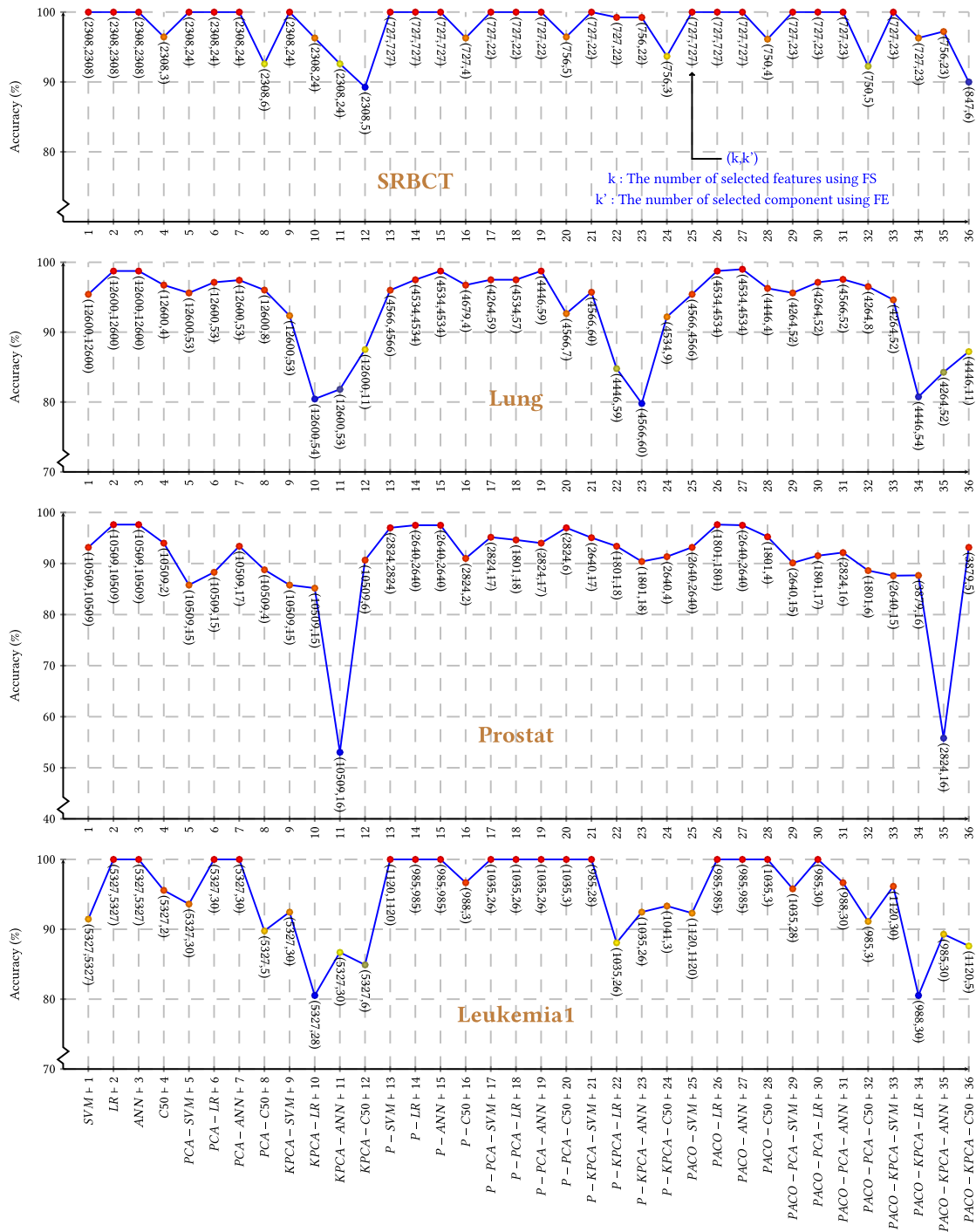


Fig. 7: Performance measurement using our Framework on the four datasets.

For the Lung dataset, The PACO-ANN model achieved the highest classification performance of 99% over the entire set of generated models while using only 36% of genes ($k = 4534$ most significant genes) from the original pre-processed dataset by using PACO-based feature selection (Line 13 in Algorithm 1). As there is no feature extraction process in this model, the selected subset of k genes PACO-based was used as an input layer for the ANN classifier, thus $k = k' = 4534$. In contrast, this model took about 4709 seconds, which is considered to be a significant response time compared to the other generated models.

For the Prostate dataset, the best performance was achieved by the PACO-LR model since the average classification accuracy of LR (Logistic Regression algorithm) reached 97.62% when involving only $k = 1801$ genes from $p = 10509$ by using the PACO feature selection method. The same average accuracy was achieved (97.62%) when applying LR and ANN on the p original genes without any dimensionality reduction process.

For the Leukemia1 dataset, with the different values of k and k' , almost all generated models produced high average classification performance close to 100%.

The power of our framework resides in the fact that it proposes a large number of models that combine different dimensionality reduction techniques with the classification process. The major aim behind this combination is to use a bare minimum of dimensions while maximizing the classification performance. Regarding Table 5, the most interesting result concerned the Leukemia1 dataset since the best model, P-PCA-C5.0, achieved an excellent accuracy of 100% with only $k' = 3$ selected dimensions and a response time of 2 seconds, which is much better than what was reported in [11-12], [14-15]. The classification accuracy of 100% was obtained by computing the percentage of correct predictions from the confusion matrix (c) shown in Fig. 9. The strongest point of the P-PCA-C5.0 model resides in the fact that the original number of genes $p = 5327$ was reduced three times to arrive at $k' = 3$ dimensions. The first reduction was obtained by selecting only the $k = 1035$ most relevant genes by using Pearson correlation-based feature selection. Then, using the PCA based FE, the new subset of k genes was converted into a new subspace of 26 dimensions (components), which in turn reduced into $k' = 3$ dimensions by using the innate feature selection capacity of C5.0 algorithm [49,50]. The quality of the P-PCA-C5.0 model in terms of classifications performance was validated by the area under the ROC curve (AUC). As we can notice from ROC curves (g) and (h) drawn in Fig. 8, the average AUC of testing and training set shows a maximum value of $AUC = 1$ which can confirm the quality of our favorite model. With a significant increase of consumed time, PACO-C5.0 model achieved exactly the same results (in terms of classification accuracy and dimension reduction degree), except that the $k' = 3$ in this model represents the numbers of genes instead of dimensions (components) obtained by P-PCA-C5.0.

Table 5: Table summarizing our favorite models for each gene expression dataset

Dataset	Model	p	k	k'	Accuracy (%)	$AUC = \frac{AUC_{Train} + AUC_{Test}}{2}$	t(s)
SRBCT	C5.0	2308	2308	3	96.45	0.98	1
Lung	P-C5.0	12600	4679	4	96.74	0.985	10
Prostate	C5.0	10509	10509	2	94	0.935	6
Leukemia1	P-PCA-C5.0	5327	1035	3	100	1	2
	PACO-C5.0	5327	1035	3	100	1	1163

For the Prostate dataset, the power of the C5.0 algorithm in terms of FS and classification performance was enough to achieve the best result compared to the other generated models. As we can notice from confusion matrix (d) in Fig. 9, 4 out of 102 samples are incorrectly classified by the C5.0 model, resulting an average accuracy of

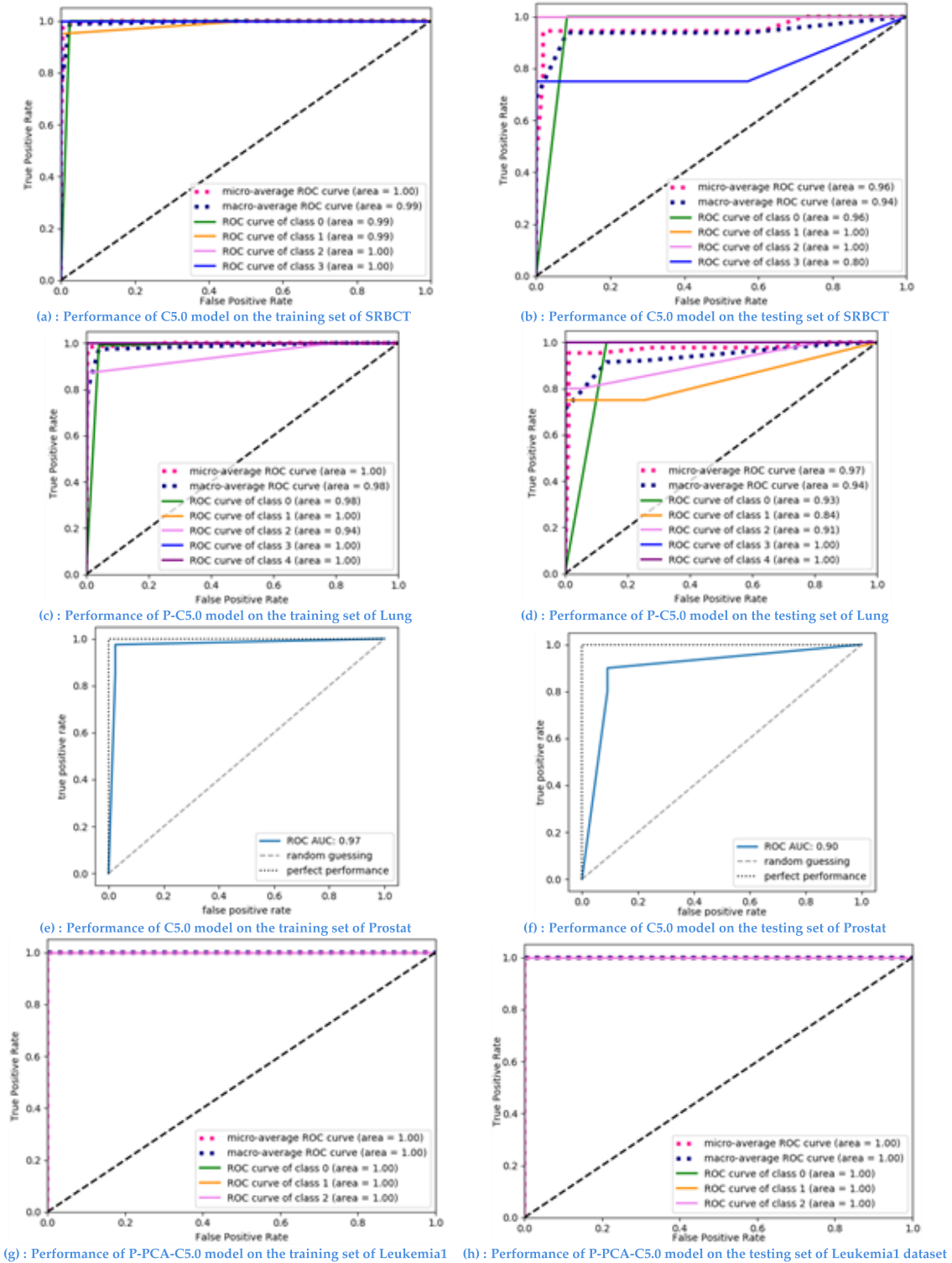


Fig. 8: ROC curves showing the performance of our favorite model on the training and testing sets of each dataset.

94% with only $k' = 2$ genes such as reported in Table 5, which is better than what is reported in [10]. The average AUC of 0.935 obtained from the ROC curves (e) and (f) confirms the quality of our model in terms of classification performance.

For the Lung dataset, as we can notice from Table 5, the **P-C5.0** model achieved a classification accuracy of 96.74% (calculated from confusion matrix (b) in Fig. 9) by involving only 4 genes. This model benefitted from both Pearson correlation-based feature selection to reduce the number of genes from $p = 12600$ to $= 4679$, and from the innate power of C5.0 to reduce a second time the number of genes from k to $k' = 4$. The average AUC of 0.99 could validate the choice of our model.

For the SRBCT dataset, our favorite model, C5.0, achieved almost the same accuracy on the Prostate dataset using only $k' = 3$ genes from $p = 2308$.

According to the results reported in Table 4 and Table 5, our framework could improve both the accuracy and degree of dimensionality reduction compared with state-of-the-art methods.

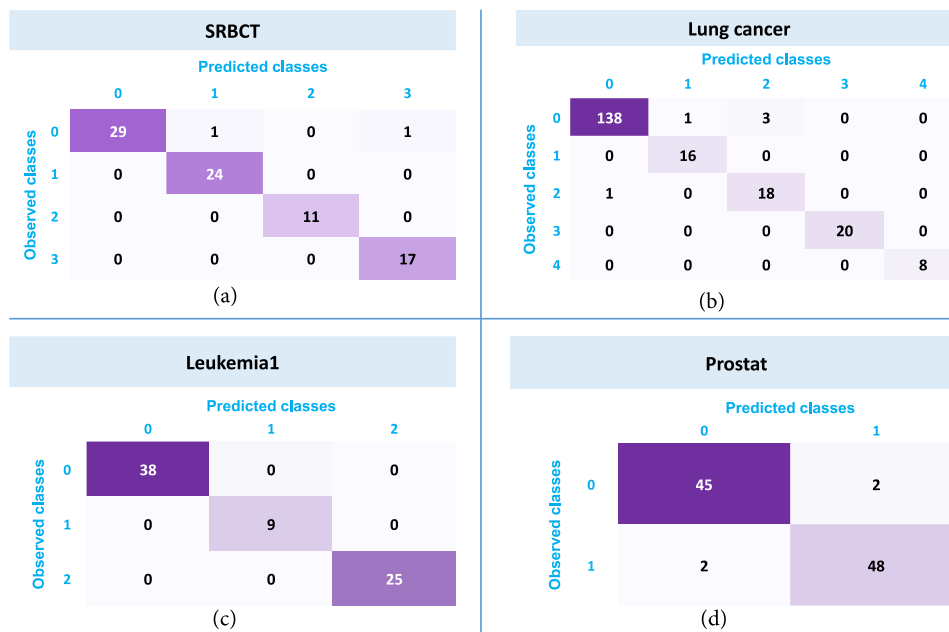


Fig. 9: Confusion Matrix of our favorite models for each dataset. (a) C5.0 model for SRBCT dataset; P-C5.0 model for Lung cancer dataset; (c) P-PCA-C5.0 and PACO-C5.0 models for Leukemia1 dataset; (d) P-PCA-C5.0 and PACO-C5.0 models for Prostate dataset.

7. CONCLUSIONS AND FUTURE WORK

Genes expression data analysis is challenging the conventional prediction techniques, since limited labeled samples versus a large number of genes may significantly affect the classification performance. To overcome this issue, a new generic approach combining dimensional reduction techniques with machine learning algorithms was proposed. The main objective behind this approach is to improve prediction performance for microarray datasets while involving a bare minimum number of predictors. The dimensional reduction process used in this paper is a combination of FS and FE techniques. The FS using Pearson correlation or PACO aims at selecting the most relevant genes, while FE using PCA or kernel-PCA aims at transforming the original genes space into a new linear or non-linear subspace. Dimensional reduction techniques were combined with four classifiers SVM, ANN, LR, and C5.0. We conducted the experiments on four public microarray gene expression data sets, SRBCT, leukemia1, lung, and Prostate cancer. Experimental results

show that the number of genes was efficiently reduced to reach two genes, with a high classification accuracy that reached up to 100% (Table 5), making our framework very effectively competitive with the reference approaches. Moreover, our experiment confirms that our coupling of dimensionality reduction with classification makes our framework powerful in terms of its ability to adapt with different kinds of microarray datasets.

Our future work includes experimentation of our proposed approach on new gene expression datasets, and study of new data mining techniques that can enhance our framework in many different aspects in the aim of identifying, with high performance, previously unknown cancer-related genes, which may guide further cancer research.

REFERENCES

- [1] Gheyas, I., & Smith, L. (2010). Feature subset selection in large dimensionality domains. *Pattern Recognition*, 43, 5–13.
- [2] Abdi, H., & Williams, L. J. (2010). Principal component analysis. *Wiley Interdisciplinary Reviews: Computational Statistics*, 2(4), 433–459.
- [3] Liu, Z., Chen, D., & Bensmail, H. (2005). Gene Expression Data Classification With Kernel Principal Component Analysis. *Journal of Biomedicine and Biotechnology*, 2005, 155–159.
- [4] Biesiada, J., & Wlodzislaw, D. (2007). Feature Selection for High-Dimensional Data—A Pearson Redundancy Based Filter. In *Advances in Soft Computing* (Vol. 45, pp. 242–249).
- [5] Kohavi, R., & John, G. H. (1997). Wrappers for feature subset selection. *Artificial Intelligence*, 97(1), 273–324.
- [6] Yu, L., & Liu, H. (2003). Feature Selection for High-Dimensional Data: A Fast Correlation-Based Filter Solution. *Proceedings, Twentieth International Conference on Machine Learning*, 2, 856–863.
- [7] Kourou, K., Exarchos, T. P., Exarchos, K. P., Karamouzis, M. V., & Fotiadis, D. I. (2015). Machine learning applications in cancer prognosis and prediction. *Computational and Structural Biotechnology Journal*, 13, 8–17.
- [8] Sayed, S., Nassef, M., Badr, A., & Farag, I. (2019). A Nested Genetic Algorithm for feature selection in high-dimensional cancer Microarray datasets. *Expert Systems with Applications*, 121, 233–243.
- [9] Ghosh, M., Begum, S., Sarkar, R., Chakraborty, D., & Maulik, U. (2019). Recursive Memetic Algorithm for gene selection in microarray data. *Expert Systems with Applications*, 116, 172–185.
- [10] Moutachaouik, H., & El Moudden, I. (2018). Mining Prostate Cancer Behavior Using Parsimonious Factors and Shrinkage Methods.
- [11] Kar, S., Sharma, K. D., & Maitra, M. (2016). A particle swarm optimization based gene identification technique for classification of cancer subgroups. *2016 2nd International Conference on Control, Instrumentation, Energy Communication (CIEC)*, 130–134. <https://doi.org/10.1109/CIEC.2016.7513800>
- [12] Mortazavi, A., & Hossein Moattar, M. (2016). Robust Feature Selection from Microarray Data Based on Cooperative Game Theory and Qualitative Mutual Information. *Advances in Bioinformatics*, 2016, 1–16. <https://doi.org/10.1155/2016/1058305>
- [13] Chandra, B., & Gupta, M. (2011). An efficient statistical feature selection approach for classification of gene expression data. *Journal of Biomedical Informatics*, 44, 529–535. <https://doi.org/10.1016/j.jbi.2011.01.001>
- [14] Chandra, B. (2018). An efficient feature selection technique for gene expression data. 1–6. <https://doi.org/10.1109/CIBCB.2018.8404977>
- [15] Guo, S., Guo, D., Chen, L., & Jiang, Q. (2016). A Centroid-based Gene Selection Method for Microarray Data Classification. *Journal of Theoretical Biology*, 400. <https://doi.org/10.1016/j.jtbi.2016.03.034>

- [16] Chu, C., Hsu, A.-L., Chou, K.-H., Bandettini, P., & Lin, C. (2012). Does feature selection improve classification accuracy? Impact of sample size and feature selection on classification using anatomical magnetic resonance images. *NeuroImage*, 60(1), 59–70.
- [17] Ang, J., Mirzal, A., Haron, H., & Hamed, H. (2016). Supervised, Unsupervised, and Semi-Supervised Feature Selection: A Review on Gene Selection. *IEEE/ACM Transactions on Computational Biology and Bioinformatics*, 13(05), 971–989.
<https://doi.org/10.1109/TCBB.2015.2478454>
- [18] Dorigo, Marco. (1992). *Optimization, Learning and Natural Algorithms* [PhD Thesis]. Politecnico di Milano.
- [19] Bullnheimer, B., Hartl, R., & Strauss, C. (1999). A New Rank Based Version of the Ant System—A Computational Study. *Central European Journal of Operations Research*, 7, 25–38.
- [20] Dorigo, M., Maniezzo, V., & Coloni, A. (1996). Ant system: Optimization by a colony of cooperating agents. *IEEE Transactions on Systems, Man, and Cybernetics, Part B (Cybernetics)*, 26(1), 29–41.
- [21] Parpinelli, R. S., Lopes, H. S., & Freitas, A. A. (2002). Data mining with an ant colony optimization algorithm. *IEEE Transactions on Evolutionary Computation*, 6(4), 321–332.
- [22] Di Caro, G., & Dorigo, M. (1998). AntNet: Distributed Stigmergetic Control for Communications Networks. *J. Artif. Int. Res.*, 9(1), 317–365.
- [23] Aldryan, D. P., Adiwijaya, & Annisa, A. (2018). Cancer Detection Based on Microarray Data Classification with Ant Colony Optimization and Modified Backpropagation Conjugate Gradient Polak-Ribière. 2018 International Conference on Computer, Control, Informatics and Its Applications (IC3INA), 13–16. <https://doi.org/10.1109/IC3INA.2018.8629506>
- [24] Wichaidit, S., Wardkean, P., Chaiwong, K., & Wettayaprasit, W. (2012). New hybrid adaptive Ant Colony Optimizaion and Self-Organizing Map for DNA microarray group finding. 2012 IEEE International Conference on Computer Science and Automation Engineering (CSAE), 3, 444–447.
- [25] Yu-Min Chiang, Huei-Min Chiang, & Shang-Yi Lin. (2008). The application of ant colony optimization for gene selection in microarray-based cancer classification. 2008 International Conference on Machine Learning and Cybernetics, 7, 4001–4006.
- [26] Jolliffe, I. T., & Cadima, J. (2016). Principal component analysis: A review and recent developments. *Phil. Trans. R. Soc. A*, 374(2065), 20150202.
- [27] Schölkopf, B., & Smola, A. J. (2001). Smola, A.: *Learning with Kernels—Support Vector Machines, Regularization, Optimization and Beyond*. MIT Press, Cambridge, MA. In *Journal of The American Statistical Association—J AMER STATIST ASSN* (Vol. 98).
- [28] Wang, Q. (2012). Kernel Principal Component Analysis and its Applications in Face Recognition and Active Shape Models.
- [29] Weinberger, K., Sha, F., & K. Saul, L. (2004). Learning a kernel matrix for nonlinear dimensionality reduction. <https://doi.org/10.1145/1015330.1015345>
- [30] Bishop, C. M. (2006). *Pattern recognition and machine learning*. Springer.
- [31] R, Q. J. (2007). C5. <http://rulequest.com>
- [32] Bujlow, T., Riaz, T., & Pedersen, J. M. (2012). A method for classification of network traffic based on C5.0 Machine Learning Algorithm. 2012 International Conference on Computing, Networking and Communications (ICNC), 237–241.
<https://doi.org/10.1109/ICCNC.2012.6167418>
- [33] Ranjbar, S., Aghamohammadi, M., & Haghjoo, F. (2016). Determining Wide Area Damping Control Signal (WADCS) based on C5.0 classifier.
- [34] Agaoglu, M. (2016). Predicting Instructor Performance Using Data Mining Techniques in Higher Education. *IEEE Access*, 4, 1–1. <https://doi.org/10.1109/ACCESS.2016.2568756>
- [35] Rathinasamy, R., & Raj, L. (2019). Comparative Analysis of C4.5 and C5.0 Algorithms on Crop Pest Data. *International Journal of Innovative Research in Computer and Communication Engineering*, 5, 2017.
- [36] Elsalamony, H., & Elsayad, A. (2013). Bank Direct Marketing Based on Neural Network. *International Journal of Engineering and Advanced Technology*, 2, 392–400.

- [37] Marjanović, M., Kovačević, M., Bajat, B., & Voženílek, V. (2011). Landslide susceptibility assessment using SVM machine learning algorithm. *Engineering Geology - ENG GEOL*, 123, 225–234.
- [38] McCulloch, W. S., & Pitts, W. H. (1988). A logical calculus of the ideas immanent in nervous activity. *Bulletin of Mathematical Biology*, 52, 99–115.
- [39] Cachim, P. (2011). Using artificial neural networks for calculation of temperatures in timber under fire loading. *Construction and Building Materials - CONSTR BUILD MATER*, 25, 4175–4180. <https://doi.org/10.1016/j.conbuildmat.2011.04.054>
- [40] Singh, D., Febbo, P., Ross, K., G Jackson, D., Manola, J., Ladd, C., Tamayo, P., A Renshaw, A., V D'Amico, A., P Richie, J., S Lander, E., Loda, M., Kantoff, P., R Golub, T., & Sellers, W. (2002). Gene Expression Correlates of Clinical Prostate Cancer Behavior. *Cancer Cell*, 1, 203–209. [https://doi.org/10.1016/S1535-6108\(02\)00030-2](https://doi.org/10.1016/S1535-6108(02)00030-2)
- [41] Golub, T. R., Slonim, D. K., Tamayo, P., Huard, C., Gaasenbeek, M., Mesirov, J. P., Coller, H., Loh, M., Downing, J. R., Caligiuri, M., D Bloomfield, C., & S Lander, E. (1999). Molecular classification of cancer: Class discovery and class prediction by gene monitoring. *Science (New York, N.Y.)*, 286, 531–537.
- [42] Westermann, F., Wei, J. S., Ringner, M., Saal, L., Berthold, F., Schwab, M., Peterson, C., Meltzer, P., & Khan, J. (2002). Classification and diagnostic prediction of cancers using gene expression profiling and artificial neural networks. *GBM Annual Fall Meeting Halle 2002, 2002*. https://doi.org/10.1240/sav_gbm_2002_h_000061
- [43] J Gordon, G., Jensen, R., Hsiao, L.-L., R Gullans, S., Blumenstock, J., Ramaswamy, S., G Richards, W., Sugarbaker, D., & Bueno, R. (2002). Translation of Microarray data into clinically relevant cancer diagnostic tests using gene expression ratios in lung cancer and mesothelioma. *Cancer Research*, 62, 4963–4967.
- [44] Li, W., Suh, Y. J., & Zhang, J. (2006). Does Logarithm Transformation of Microarray Data Affect Ranking Order of Differentially Expressed Genes? *Conference Proceedings : ... Annual International Conference of the IEEE Engineering in Medicine and Biology Society. IEEE Engineering in Medicine and Biology Society. Conference, Suppl*, 6593–6596. <https://doi.org/10.1109/IEMBS.2006.260896>
- [45] Marko, N., & Weil, R. (2012). Non-Gaussian Distributions Affect Identification of Expression Patterns, Functional Annotation, and Prospective Classification in Human Cancer Genomes. *PloS One*, 7, e46935. <https://doi.org/10.1371/journal.pone.0046935>
- [46] Shapiro, S. S., & Wilk, M. B. (1965). An Analysis of Variance Test for Normality (Complete Samples). *Biometrika*, 52(3/4), 591–611.
- [47] Royston, J. P. (1982). An Extension of Shapiro and Wilk's W Test for Normality to Large Samples. *Applied Statistics*, 31(2), 115. <https://doi.org/10.2307/2347973>.
- [48] Masters, T. (1993). *Practical Neural Network Recipes in C++*. Academic Press Professional, Inc.
- [49] Deng, L., Yan, Y., & Wang, C. (2015). Improved POLSAR Image Classification by the Use of Multi-Feature Combination. *Remote Sensing*, 7, 4157–4177.
- [50] McIver, D. K., & Friedl, M. A. (2002). Using Prior Probabilities in Decision-Tree Classification of Remotely Sensed Data. *Remote Sensing of Environment*, 81, 253–261.

INFLUENCE OF FIBREGLASS MESH ON PHYSICAL PROPERTIES OF LIGHTWEIGHT FOAMCRETE

ANISAH MAT SERUDIN, MD AZREE OTHUMAN MYDIN*
AND ABDUL NASER ABDUL GHANI

*School of Housing, Building and Planning, Universiti Sains Malaysia,
11800, Penang, Malaysia*

*Corresponding author: azree@usm.my

(Received: 12th April 2020; Accepted: 27th September 2020; Published on-line: 4th January 2021)

ABSTRACT: This research project was designed to investigate the influence of fibremesh on the durability properties of lightweight foamcrete (LFC). The fibremesh, categorized as a synthetic fibre (man-made fibre), was used for this study. It poses a continuous fibre with warp and weft structure that was used as confinement material in this investigation where four different weights per area (g/m^2) of the fibremesh were observed namely, 110 g, 130 g, 145 g, and 160 g. Three experimental tests were involved in this preliminary study: porosity, water absorption, and drying shrinkage test. All the specimens were confined with 1-layer fibremesh at a constant density of $1100\text{kg}/\text{m}^3$ of LFC and the result was compared with the control (unconfined LFC). The $160\text{ g}/\text{m}^2$ of fibremesh significantly improved the physical properties of LFC where 13.8%, 20%, and 57.4% enhancement was obtained for the porosity, water absorption, and drying shrinkage result, respectively.

ABSTRAK: Projek penyelidikan ini dijalankan bagi menyiasat kesan penggunaan jejaring sabut pada sifat ketahanan konkrit ringan berbuisa (LFC). Jejaring sabut yang digunakan dalam kajian ini adalah jejaring gentian kaca tahan-alkali yang dikategorikan sebagai serat sintetik yang juga dikenali sebagai fabrik tekstil. Ia mempunyai serat yang panjang dan bersambung dengan struktur yang lekuk dan renda yang digunakan sebagai penambahbaikan bagi konkrit ringan berbuisa. Terdapat empat berat jejaring sabut yang diuji iaitu 110 g, 130 g, 145 g, dan 160 g. Tiga jenis eksperimen bagi kajian awal ini iaitu keliangan, penyerapan air, dan pengecutan pengeringan. Semua spesimen dibalut dengan 1 lapisan jejaring sabut pada $1100\text{kg}/\text{m}^3$ LFC dan data yang diperolehi dibandingkan dengan spesimen yang tidak dibalut dengan gentian kaca berjejaring. Jejaring sabut $160\text{ g}/\text{m}^2$ meningkatkan sifat fizikal konkrit ringan berbuisa di mana 13.8%, 20%, dan 57.4% peningkatan diperolehi bagi keliangan, penyerapan air, dan pengecutan pengeringan, masing-masing.

KEYWORDS: *foamed concrete; property; fibremesh; confinement*

1. INTRODUCTION

From ancient times, concrete has been well known as the most popular material utilized in the worldwide construction industry. It is used in construction work to fulfil the high demand for housing, high-rise building, infrastructure, etc. This is because concrete is resistant to deterioration compared to wood, and it is also easier to build in several forms. Presently, the application of an air cell system becomes one of the preferable technologies to be used in a construction project due to its benefits. It is getting more attention since it has the ability to reduce the size of the foundation and structural dead load due to its low

density, thus minimizing operating costs and labour use [1,2]. It is also acknowledged as a sustainable building material [3,4]. High flowability concrete, namely, lightweight foamcrete (LFC) has a varied range of density and can be constructed to any desired application such as wall panels, slabs, or other load-bearing building elements, lightweight concrete block, void filling, etc. [5].

The density of LFC typically ranges between 300 kg/m^3 to 1600 kg/m^3 [6] which is 20% and up to 85% of its volume filled with air-void. These air-voids were created by the introduction of foam into the cement slurry or mortar causing its unit weight (density) to be lower than that of normal concrete where the density ranges between 2240 kg/m^3 and 2400 kg/m^3 [7]. However, when a high volume of foam is added into the mortar, more air-voids will be created in the mortar slurry, thereby inducing a higher porosity, water absorption, and shrinkage in the LFC. According to Shabbar et al. [8], 60 to 90% of LFC volume is pore space where the pore size and microstructure influenced its physical properties. Kurpińska and Ferenc [9] also reported that the high percentage of porosity in LFC is due to the void contents of the composite being higher, while Hilal et al. [10] clarified that the higher percentage of porosity is obtained at the lower density of LFC. Besides, Thakrele [11] also mentioned that water absorption is higher because of the higher air content in the LFC. In addition, the major drawbacks of this LFC material are the high drying shrinkage behaviour, which is 4 to 10 times higher than normal weight concrete [12]. Rai and Kumar [13] verified that this happened due to the no coarse aggregate used in the mixture that resulted in the high drying shrinkage obtained, which will lead to the low strength characteristic of LFC. Many researchers have done the study of enhancement of the properties of LFC by the inclusion of short fibres such as sisal fibres [14], kenaf fibres [15-17], oil palm fibres [15,18], polypropylene fibres [15,16], and AR-glass and steel fibres [15]. However, some of the materials have a negative impact on the long-term performance of LFC such as deterioration of natural fibre [19], and corrosion of the reinforcing steel [20]. Thus, in this research, authors have explored the potentiality of continuous fibres, namely, fibremesh, as an enhancement to the properties of LFC, this has not being practiced yet in such types of concrete. In this research, the authors examined the influence of different weight per area (g/m^2) of fibremesh-confined LFC to improve its porosity, water absorption, and drying shrinkage performance since it is correlated to the mechanical properties of the composite. The fibremesh used in this research is alkali-resistant (AR) fibremesh with four different weights per area (g/m^2) which were 110 g, 130 g, 145 g, and 160 g. This type of fibremesh is more flexible, easy to handle, cheaper, and has higher performance compared to others (carbon, aramid, etc.).

2. MATERIAL PREPARATION

To prepare the LFC mix, four (4) common materials were utilized in the production: cement, sand, water, and stable foam. Furthermore, four different weights per area (g/m^2) of fibremesh were utilized in this study, namely, 110 g, 130 g, 145 g, and 160 g. All the results obtained from respective LFC specimens confined with 1-layer of the different weights per area of fibremesh were compared to the control specimens (LFC without any reinforcement). For this particular research, Ordinary Portland Cement (OPC) was used which is in accordance with the specifications of Type 1 Portland Cement in ASTM C150-04 [21]. Sand particle size utilized in this research is less than 1.18mm diameter with the specific gravity of 2.74 and fineness modulus of 1.35. The grading limits are according to ASTM C778-06 [22]. Fine aggregate is suitable for producing the LFC since the coarse aggregate caused the existence of bigger pores and created an inconsistent mix that affected the LFC properties. The presence of water is necessary to mix the cement and fine

aggregate to form the cement slurry through chemical reaction which will lead to the hardened of mortar paste. Tap water (free from any harmful substance) was used which complied with the standard stated in ASTM C1602-C05 [23]. Foam was added to control and obtain a desirable density for the LFC. In this study, a protein-based foaming agent, namely, NORAITE PA-1 was used to produce a stable foam. 1kg of foaming agent was diluted into 30 L of water.

3. MIX PROPORTION AND EXPERIMENTAL SETUP

3.1 Mix Design

Based on the previous research, there are many factors that influence the behaviour of LFC such as the density of LFC, the water to cement ratio, the binder to cement ratio, the type of filler, the type of foaming agent, the inclusion of fibre, etc. Thus, to obtain comparable results, the mix design of LFC was fixed, as shown in Table 1. Besides, the density of LFC was the major factor that would affect the performance of LFC, so that in this research it was maintained at 1100 kg/m³. Since the application of LFC can be categorized into structural, semi structural, and non-structural, the intermediate application is more suitable to be chosen for preliminary study.

Table 1: Mix design of LFC mixes confined with fibremesh

Sample	Weights per area of fibremesh [g/m ²]	Mix density of LFC [kg/m ³]	Mix ratio of LFC		Mix proportions of LFC, kg/m ³		
			Cement/sand	Water/cement	Cement	Sand	Water
Control	-	1100	1:1.5	0.45	410.79	616.18	184.86
110 g	110	1100	1:1.5	0.45	410.79	616.18	184.86
130 g	130	1100	1:1.5	0.45	410.79	616.18	184.86
145 g	145	1100	1:1.5	0.45	410.79	616.18	184.86
160 g	160	1100	1:1.5	0.45	410.79	616.18	184.86

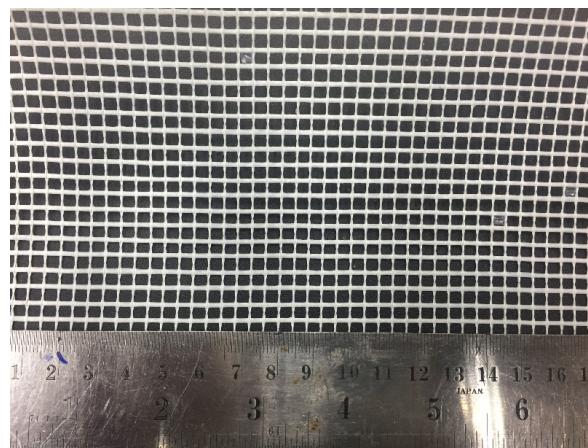


Fig. 1: Physical features of the fibremesh.

As mentioned by [24], 0.45 of water to cement ratio produced an LFC with a reasonable workability. Thus in this research, it was fixed at 0.45. The filler to cement ratio was fixed to 1:1.5 as demonstrated in previous study [15-16, 18, 25-28]. Furthermore, four different weights of fibremesh, namely, 110 g, 130 g, 145 g, and 160 g per area (g/m²) were used in this observation. The data obtained from this research would

be useful for the construction sector or other researchers that are interested in the application of fibremesh in LFC since it has not been documented yet. Figure 1 shows the physical features of the fibremesh and its physical properties is detailed in Table 2.

Table 2: Physical properties of fibremesh

Properties	Weight of woven fiberglass mesh (g/m ²)			
	110	130	145	160
Mesh size	4.0 x 5.0 mm	4.0 x 5.0 mm	4.0 x 5.0 mm	4.0 x 5.0 mm
Colour	White	White	White	White
Coating type	Alkali resistant	Alkali resistant	Alkali resistant	Alkali resistant
Mass (g/m ²)	110±3	130±3	145±3	160±3
Ignition point	391°C (735.8°F)	394°C (741.2°F)	398°C (784.4°F)	404°C (759.2°F)
Melt point	154°C (309.2°F)	156°C (312.8°F)	158°C (316.4°F)	160°C (320.0°F)
Tensile strength (MPa)	1195	1250	1325	1407
Elongation at break (%)	4.15%	3.75%	3.41%	3.07%
Compliance	ASTM C1116-02	ASTM C1116-02	ASTM C1116-02	ASTM C1116-02
Quality assured facility	ISO 9001:2008	ISO 9001:2008	ISO 9001:2008	ISO 9001:2008

3.2 Water Absorption Test

The water absorption test was determined as prescribed in BS 1881-122 [29]. Cylindrical-shaped specimens (75 mm Ø x 100 mm h) were used in this study. At the aging day of the test, 3 specimens were unwrapped and oven-dried for 72 hours. Then, the weights of the cooled oven-dried specimens were recorded as W_d , and they were fully submerged in a water tank for 30 minutes (refer Fig. 2). Next, a dry cloth was used to remove any excess water present on the test specimens and their weight was recorded in a saturated condition W_s . The water absorption was expressed in percentage, W_a , and calculated using Equation (1). The average of these 3 specimens was taken as the final result for the water absorption test.

$$\text{Water absorption (\%), } W_a = \left(\frac{W_s - W_d}{W_d} \right) \times 100\% \quad (1)$$

Where, W_s = Saturated surface dry weight
 W_d = Oven-dried weight



Fig. 2 :Water absorption test. (a) LFC specimens were fully submerged in a water tank, (b) Side view of LFC specimen.

3.3 Porosity Test

The porosity test was conducted based on the method described in RILEM [30]. This test was determined by the immersion method into a vacuum desiccator and tested on day 28. The purpose of this test was to determine the percentage of air-voids in the LFC specimens confined with different weights per area (g/m^2) of fibremesh. As mentioned by previous researchers, LFC (without any reinforcement) possesses a high porosity compared to the LFC specimens with reinforcement. Thus, the confinement of fibremesh in the LFC will decrease the percentage of porosity contained. Therefore, 3 specimens of LFC, with a diameter of 45 mm and height of 50 mm, were placed in an oven to remove moisture for 72 hours or until no changes in weight were recorded. Then, the specimens were cooled and their weights recorded as W_{dry} . The specimens were fully immersed in the vacuum chamber for 72 hours or up until no visible bubbles appeared. The weights of the specimens in water ($W_{s,w}$) and in air ($W_{s,a}$) were recorded. Figure 3 shows the setup of the vacuum desiccator for the test, while Eq. (2) was used to measure the percentage of porosity in LFC. The average value of the 3 specimens was recorded as the final result for the total porosity test.

$$\text{Total porosity (\%)} = \left(\frac{W_{s,a} - W_{dry}}{W_{s,a} - W_{s,w}} \right) \times 100\% \quad (2)$$

Where, $W_{s,a}$ = weight of saturated sample in air
 W_{dry} = weight of oven-dried sample
 $W_{s,w}$ = weight of the saturated sample in water



Fig. 3: Porosity test.

3.4 Shrinkage Test

Drying shrinkage test was measured via Mitutoyo brand digital indicator with 298 mm of reference bar and it was performed according to ASTM C157/C157M [31], where 3 prism specimens with size of 75 x 75 x 285 mm were installed with a pair of steel screws and cap nuts. After demoulding, LFC specimens were placed in the length comparator, as seen in Fig. 4, and rotated anti-clockwise to obtain the data. The readings were taken and recorded as, (Li) . Li is the corrected initial comparator reading. Then, the steps were repeated for the next testing ages, which were at days 1, 3, 7, 14, 21, 28, and 56. These readings were recorded as Lx , where x represents the test at the subsequent ages. The drying shrinkage was calculated using Eq. (3), where the corrected comparator

reading was equal to the specimen comparator reading minus the reference bar comparator reading.

$$\text{Drying shrinkage, (mm)} = \left(\frac{L_x - L_i}{285} \right) \times 100\% \quad (3)$$

Where, L_x = corrected comparator reading
 L_i = corrected initial comparator reading
 x = day test



Fig. 4: Setup for drying shrinkage test.

4. RESULTS AND DISCUSSION

4.1 Porosity

The porosity test was conducted using the vacuum saturation approach in accordance to RILEM. As verified by Hilal et al. [10], this method provides the most appropriate means of accurately assessing the porosity of LFC compared to mercury intrusion porosimetry (MIP) and apparent porosity techniques. This is because the MIP method only determines the entrained pores with diameters of less than 400 μm , while the apparent porosity approach is unsuitable as the contribution of water absorption is only applied for the capillary pores, which depend on the paste content, and the entrained pores (air-voids) do not take part in this test as they are not interlocked [10]. As shown in Fig. 5, the control specimen showed the highest porosity when compared with the other specimens, which had been confined with different weights per area (g/m^2) of fibremesh. The porosity decreased as the weight per area (g/m^2) of the fibremesh increased. As illustrated in Table 3, the porosity decreased from 5.7% to 13.8% when the LFC specimens were confined with 110 g/m^2 to 160 g/m^2 of fibremesh, respectively. This was due to the confinement effect of the fibremesh which had reduced the rate of the water penetrated into the air void

of LFC on the same day the measurements were taken. The presence of the fibremesh impeded the water movement into the paste phase of the LFC. This explained the reason for the control specimen having a higher porosity compared to all the other specimens. Besides, from the previous studies, no research has yet been done to investigate the porosity of LFC confined by fibremesh. In this experimental investigation, it was observed that the LFC that was confined with fibremesh showed the same decreasing pattern for porosity as with the inclusion of fibres (short fibres such as sisal, kenaf, oil palm, polypropylene, steel, etc.). For instance, based on a study conducted by Zamzani [27], the inclusion of 0.1% to 0.6% of *Cocos nucifera* Linn. (CNF) fibre by volume fraction in LFC (1450 kg/m^3) was able to decrease the porosity from 3% to 13% at day-28 compared to the control. This result was approximately similar to the result obtained in the current research, where the confinement of LFC with 110 g/m^2 to 160 g/m^2 improved the porosity by 5.7% to 13.8% compared to the control, which was without any confinement. Therefore, the confinement of the LFC specimens with 160 g/m^2 of fibremesh showed the best result as it reduced the porosity up to 13.8%, as obtained in this research.

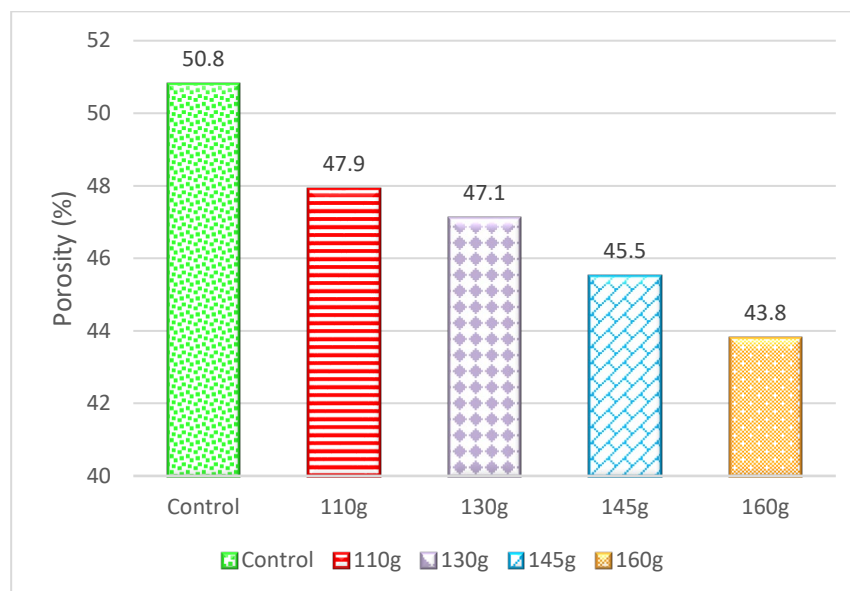


Fig. 5: Porosity of LFC specimens confined with different weights per area (g/m^2) of fibremesh at day-28.

Table 3 Percentage decrease in porosity for confined LFC specimens compared to the control specimen

Specimen	Percentage decrease (%)
110 g	5.7
130 g	10.4
145 g	13.4
160 g	13.8

4.2 Water Absorption

Water absorption occurs as a result of capillary pores in the LFC cement paste [32]. Figure 6 shows the water absorption capacity of the LFC specimens confined with different weights per area of fibremesh and of the control specimen as a reference sample. Overall, the control specimen possessed a relatively high-water absorption capacity

compared to the specimens confined with fibremesh. Theoretically, the water absorption happened due to the process whereby the concrete absorbed or drew water into its pores and capillaries [33]. It could be seen that the higher weight per area of fibremesh contributed to a greater reduction in the water absorption capacity of all the specimens that were tested in this research. As shown in Table 4, the water absorption capacity of the specimens confined with 110, 130, 145, and 160 g/m² of fibremesh decreased by 6.5%, 7.6%, 14.1% and 20.0%, respectively when compared to the control specimen. The reduction in the water absorption capacity of the LFC specimens was due to the enclosed fibremesh array that managed to prevent the penetration of water into the cement matrix. Besides, fibremesh possesses a hydrophobic characteristic where it provides an alternative solution for inhibiting the diffusion of water molecules into a cement matrix, which is contrary with the behaviour of natural fibres that tended to attract water due to their hydrophilic nature [17]. Thus, this investigation proved that the 160 g/m² of fibremesh led to a reduction in the water absorption properties of LFC.

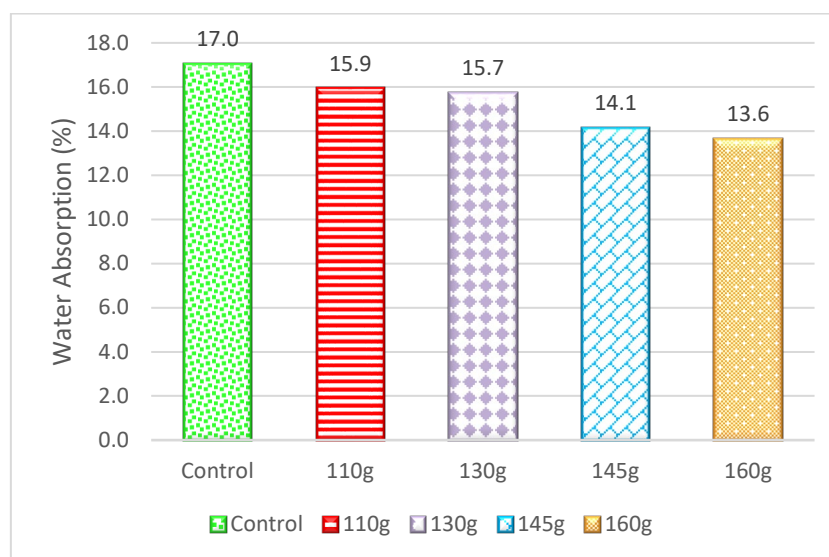


Fig. 6: Water absorption capacity of LFC specimens confined with different weights per area (g/m²) of fibremesh at day-28.

Table 4: Percentage decrease in water absorption capacity for confined specimens compared to the control specimen

Specimen	Percentage decrease (%)
110 g	6.5
130 g	7.6
145 g	14.1
160 g	20.0

4.3 Drying Shrinkage

Amran et al. [1] claimed that the drying shrinkage in LFC is ten times higher compared to normal weight concrete because of the absence of coarse aggregates. According to Cheah et al. [32], drying shrinkage occurs in a cement matrix due to the evaporation of internal free water from the concrete or mortar in the hardened state to the surrounding environment. Based on the test results shown in Fig. 7, the control specimen exhibited a

higher drying shrinkage compared to the other specimens. This was because the confinement of fibremesh reduced the drying shrinkage behaviour in LFC specimens as the fibremesh was able to maintain the water content and delay the evaporation of the internal moisture, hence lessening the drying shrinkage behaviour. Falliano et al. [34] also proved that unreinforced specimens exhibit a shrinkage that decreases with increasing dry density. Besides, Namsone et al. [35] also stated that the addition of fibre can reduce the risk of shrinkage and stabilize the fresh mix. There was a significant improvement in the drying shrinkage behaviour of the LFC specimens confined with fibremesh, as displayed in Table 5. When the LFC specimen was confined with 110 g/m² of fibremesh, the drying shrinkage behaviour was enhanced by 34.4% compared to the control specimen. The improvement of the drying shrinkage behaviour rose as the weight per area of the fibremesh increased. Consequently, 160 g/m² of fibremesh showed the best drying shrinkage prevention, where the drying shrinkage was reduced up to 57.4% compared to the control specimen.

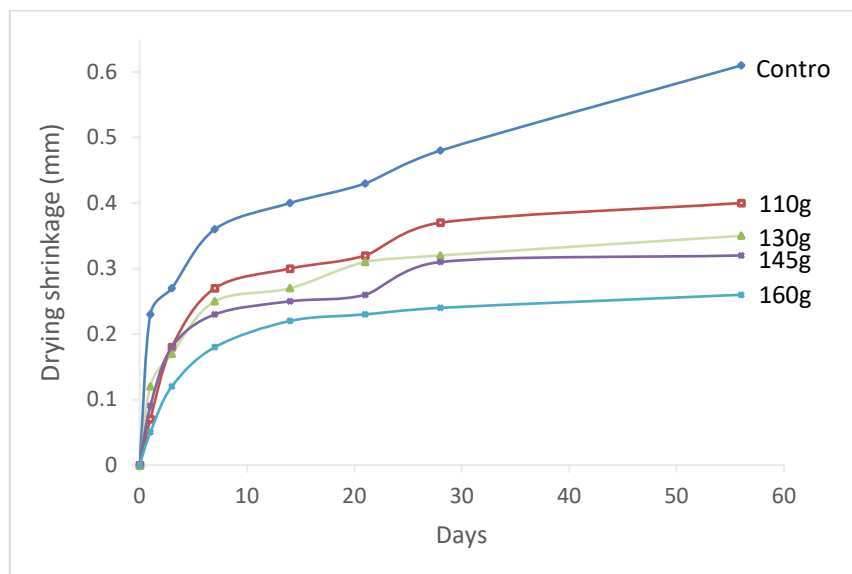


Fig. 7: Drying shrinkage of LFC specimens confined with different weight per area (g/m²) of fibremesh.

Table 5: Percentage decrease of drying shrinkage for confined specimens compared to the control specimen.

Specimen	Percentage decrease (%)
110 g	34.4
130 g	42.6
145 g	47.5
160 g	57.4

5. CONCLUSION

In this preliminary study, the influence of fibremesh on the physical properties of LFC with a density of 1100 kg/m³ was investigated. Based on the results obtained, the following conclusions can be drawn:

- Overall, the confinement of fibremesh significantly enhanced the physical properties of LFC.

- Obviously shown in the three experiment tests (porosity, water absorption, and drying shrinkage), the confinement of 160 g of fibremesh resulted in improvement of the physical properties of LFC.
- It is proven that the weight per area of fibremesh influenced the physical properties of LFC.
- As recommendation for future study, authors suggest to investigate the effect of different types of textile fibres such as carbon, aramid, basalt, etc., to be utilized as confinement material for LFC since it is not covered in this research. They also suggested cost effectiveness analysis between the mentioned textile fabrics to examine which materials give greater benefits to the construction sector.

ACKNOWLEDGEMENT

The authors would like to thank Universiti Sains Malaysia for their funding of this research through the Bridging Grant: Grant No: 304/PPBGN/6316230.

REFERENCES

- [1] Amran YHM, Farzadnia N, Ali AAA. (2015). Properties and applications of foamed concrete; A review. *Construction and Building Materials*, 101: 990-1005. <https://doi.org/10.1016/j.conbuildmat.2015.10.112>
- [2] Fu Y, Wang X, Wang L, Li Y. (2020). Foam Concrete : A State-of-the-Art and State-of-the-Practice Review. *Advances in Materials Science and Engineering*. <https://doi.org/10.1155/2020/6153602>
- [3] Moon AS, Varghese V, Waghmare SS. (2015). Foam Concrete as A Green Building Material. *International Journal for Research in Emerging Science and Technology*, 2(9): 25-32.
- [4] Siram KKB, Raj KA. (2013). Concrete + Green = Foam Concrete. *International Journal of Civil Engineering and Technology (IJCIET)*, 2(2): 1-24.
- [5] Sari KAM, Sani ARM. (2017). Applications of Foamed Lightweight Concrete. *MATEC Web of Conferences*, 97: 1-5. <https://doi.org/10.1051/mateconf/20179701097>
- [6] Jalal MD, Tanveer A, Jagdeesh K, Ahmed F. (2017). Foam concrete. *International Journal of Civil Engineering Research*, 8(1): 1-14. Retrieved from https://www.ripublication.com/ijcer17/ijcerv8n1_01.pdf
- [7] Hedjazi S. (2019). Compressive Strength of Lightweight Concrete. In *IntechOpen*:1-18. <https://doi.org/10.5772/intechopen.88057>
- [8] Shabbar R, Nedwell P, Wu Z. (2018). Porosity and Water Absorption of Aerated Concrete with Varying Aluminium Powder Content. *International Journal of Engineering and Technology*, 10(3): 234-238. <https://doi.org/10.7763/ijet.2018.v10.1065>
- [9] Kurpińska M, Ferenc T. (2017). Effect of porosity on physical properties of lightweight cement composite with foamed glass aggregate. *ITM Web of Conferences*, 15: 06005. <https://doi.org/10.1051/itmconf/20171506005>
- [10] Hilal AA, Thom NH, Dawson AR. (2014). Pore structure and permeation characteristics of foamed concrete. *Journal of Advanced Concrete Technology*, 12: 535-544. <https://doi.org/10.3151/jact.12.535>
- [11] Thakrele MH. (2014). Experimental study on foam concrete. *International Journal of Civil, Structural, Environmental and Infrastructure Engineering Research and Development*, 4(1): 145-158.
- [12] Elrahman MA, El Madawy ME, Chung SY, Sikora P, Stephan D. (2019). Preparation and characterization of ultra-lightweight foamed concrete incorporating lightweight aggregates. *Applied Sciences (Switzerland)*, 9(7): 1-12. <https://doi.org/10.3390/app9071447>
- [13] Rai A, Kumar M (2017). Experimental Study on Compressive and Split Tensile Strength of Foamed Concrete Using Stone Dust. *International Research Journal of Engineering and*

- Technology(IRJET), 4(5): 1377-1382. Retrieved from <https://www.irjet.net/archives/V4/i5/IRJET-V4I5269.pdf>
- [14] Dhanunjaya G, Dadapeer ABS, Rafi DM. (2018). An Experimental Study on the Durability Properties of Foam Concrete with Addition of Natural Fibers. *International Journal of Scientific Research in Science and Technology*, 4(2): 529-536.
- [15] Awang H, Ahmad MH. (2014). Durability Properties of Foamed Concrete with Fiber Inclusion. *International Journal of Civil, Structural, Construction and Architectural Engineering*, 8(3): 273-276.
- [16] Hanizam A, Mohammed A, Ahmad MH. (2015). Influence of Kenaf and Polypropylene Fibres on Mechanical and Durability Properties of Fibre Reinforced Lightweight Foamed Concrete. *Journal of Engineering Science and Technology*, 10(4): 496-508. <https://doi.org/10.4028/www.scientific.net/AMR.626.404>
- [17] Mahzabin MS, Hock LJ, Hossain MS, Kang LS. (2018). The influence of addition of treated kenaf fibre in the production and properties of fibre reinforced foamed composite. *Construction and Building Materials*, 178: 518-528.
- [18] Musa M. (2019). Investigation of Durability, Thermal and Mechanical Properties of Oil Palm Empty Fruit Bunch (EFB) Fibre Strengthen Lightweight Foamed Mortar (LFM). Master thesis. Universiti Sains Malaysia.
- [19] Bentur A, Mindess S. (2007). Fibre Reinforced Cementitious Composites. In A. Bentur & S. Mindess (Eds.), *Taylor & Francis (2nd Edition)*. [https://doi.org/10.1016/0010-4361\(79\)90446-4](https://doi.org/10.1016/0010-4361(79)90446-4)
- [20] Memon IA, Jhatial AA, Sohu S, Lakhari MT, Hussain Z. (2018). Influence of Fibre Length on the Behaviour of Polypropylene Fibre Reinforced Cement Concrete. *Civil Engineering Journal*, 4(9): 2124-2131. <https://doi.org/10.28991/cej-03091144>
- [21] ASTM C150-04 (2004). Standard Specification for Portland Cement C150-04. *Annual Book of ASTM Standards*, 4(2): 1-8.
- [22] ASTM C778-06 (2006). Standard Specification for Standard Sand C778-06. *Annual Book of ASTM Standards*. Retrieved from <http://www.who.int/csr/don/03-june-2016-oropouche-peru/en/>
- [23] ASTM C1602-C05 (2006). Standard Specification for Mixing Water Used in Production of Hydraulic Cement Concrete C1602. *Annual Book of ASTM Standards*.
- [24] Talaei S, Jafari M, Tarfan S, Hashemlou H. (2014). The Effect of Ratio of Aggregate to Cement Paste Volume on Structural Lightweight Concrete Strength , Viscosity , Density and Cost. *Research Journal of Environmental and Earth Sciences*, 6(9): 443-450.
- [25] Coker EB, Sadiku S, Aguwa JI, Abdullahi M. (2016). Study of the Strength Characteristics of Protein-Based Lightweight Foamed Concrete With Cement Partially Replaced With Rice Husk Ash. *Nigerian Journal of Technology*, 35(4): 699-706. <https://doi.org/10.4314/njt.v35i4.2>
- [26] Suhaili SS, Mydin MAO. (2020). Potential of stalk and spikelets of empty fruit bunch fibres on mechanical properties of lightweight foamed concrete. *International Journal of Scientific and Technology Research*, 9(3): 3199-3204.
- [27] Zamzani NM. (2019). Characterization of durability and engineering properties of *Cocos nucifera* Linn Fibre (CNF) reinforced foamcrete and its performance at elevated temperatures. Master thesis. Universiti Sains Malaysia.
- [28] Zulkarnain F. (2011). Strength and Durability Properties of Lightweight Foamed Concrete For Housing Construction. Master thesis. Universiti Sains Malaysia.
- [29] BS 1881-122 (2011). Testing Concrete Part 122 Method for determination of water absorption BS1881-122. *British Standard Institution*. <https://doi.org/10.1017/CBO9781107415324.004>
- [30] RILEM (1984). Absorption of water by concrete by immersion under vacuum. In RILEM (Ed.), *RILEM Recommendations for the Testing and Use of Constructions Materials*: 36-37. <https://doi.org/doi:10.1617/2351580117.018>
- [31] ASTM C157/C157M (2005). Standard Test Method for Length Change of Hardened Hydraulic-Cement Mortar and Concrete. *Annual Book of ASTM Standards*: 1-10.

-
- [32] Cheah CB, Lim JS, Ramli MB. (2019). The mechanical strength and durability properties of ternary blended cementitious composites containing granite quarry dust (GQD) as natural sand replacement. *Construction and Building Materials*, 197(November 2018): 291-306.
<https://doi.org/10.1016/j.conbuildmat.2018.11.194>
- [33] Jung CT, Kwong T H, Boon KH. (2018). Water absorption and drying shrinkage of recycled foamed aggregate concrete. *Malaysian Journal of Civil Engineering*, 30(3): 482-492.
- [34] Falliano D, De Domenico D, Ricciardi G, Gugliandolo E. (2019). Compressive and flexural strength of fiber-reinforced foamed concrete: Effect of fiber content, curing conditions and dry density. *Construction and Building Materials*, 198: 479-493.
<https://doi.org/10.1016/j.conbuildmat.2018.11.197>
- [35] Namsone E, Korjakins A, Sahmenko G, Sinka M. (2017). The environmental impacts of foamed concrete production and exploitation. *IOP Conference Series: Materials Science and Engineering*, 251(1). <https://doi.org/10.1088/1757-899X/251/1/012029>

FROUDE NUMBER VARIANCE WITH RESPECT TO THE HYDRODYNAMIC RESPONSE OF A NON- STATIC VEHICLE ON A LOW-LYING FLOODED ROADWAY

SYED MUZZAMIL HUSSAIN SHAH^{1*}, ZAHIRANIZA MUSTAFFA²,
SHABIR HUSSAIN KHAHRO³, KHAMARUZAMAN WAN YUSOF², EBRAHIM HAMID
HUSSEIN AL-QADAMI², AMINUDDIN AB GHANI⁴ AND FANG YENN TEO⁵

¹Civil Engineering Department,

Sir Syed University of Engineering and Technology, Karachi, Pakistan

²Department of Civil and Environmental Engineering,

Universiti Teknologi PETRONAS, Seri Iskandar, Malaysia

³College of Engineering, Prince Sultan University, Riyadh, Saudi Arabia

⁴River Engineering and Urban Drainage Research Centre (REDAC),

Universiti Sains Malaysia, Seri Ampangan, Malaysia

⁵Faculty of Science and Engineering, University of Nottingham, Semenyih, Malaysia

*Corresponding author: drmuzzamil@ssuet.edu.pk

(Received: 7th June 2020; Accepted: 27th September 2020; Published on-line: 4th January 2021)

ABSTRACT: In terms of stability, the response of static cars in floodwaters has been widely investigated. However, the hydrodynamics of a non-static vehicle exposed to such events are less explored. Herein the study ponders the assessment of the hydrodynamic forces experienced by a non-static vehicle attempting to cross a low-lying flooded street. With that regards, a Perodua Viva was modeled (1:10) and tested in the Hydraulics Laboratory under partial submergence and sub-critical flows, fulfilling the similarity laws. Since the Froude number could best analyze the flow conditions, the behavior of the hydrodynamic forces and the Froude number have been the focus of this investigation. From the study of outcomes, an inverse relation of the Froude number with respect to the buoyancy force, along with positive trends relating to drag, frictional, and rolling resistance, were noticed.

ABSTRAK: Dari segi kestabilan, tindak balas kereta statik dalam air banjir telah banyak dikaji. Walau bagaimanapun, hidrodinamik kenderaan tidak statik yang terdedah kepada kejadian seperti itu kurang diterokai. Kajian ini menilai daya hidrodinamik kenderaan tidak statik yang cuba melintas jalan raya yang banjir. Sehubungan itu, sebuah Perodua Viva dimodelkan (1:10) dan diuji dalam Makmal Hidraulik di bawah perendaman separa dan didedahkan kepada aliran sub-kritikal, seperti ketika kejadian. Manakala nombor Froude adalah terbaik dalam menganalisa keadaan aliran air. Oleh itu, tindak balas daya hidrodinamik dan nombor Froude menjadi fokus penyelidikan ini. Dapatan kajian menunjukkan kaitan terbalik nombor Froude pada daya apungan, sedangkan tren positif yang berkaitan dengan daya tarik, geseran dan rintangan guling diperhatikan.

KEYWORDS: *hydrodynamic forces; Froude number; non-static vehicle; partial submergence; subcritical flow*

1. INTRODUCTION

Communities have been menaced by floods for ages. Flood occurrence not only imposes losses to infrastructure and property but it also claims thousands of lives and leaves millions homeless [1]. During flooding, the transportation system is directly damaged due to its considerable size [2,3]. Though flooding events can be predicted well before their occurrence, people, including motorists, perish in floodwaters. This at times ends up in the form of vehicle instability that leads to vehicle-related fatalities [4]. It is therefore necessary to investigate the hydrodynamic response of flooded vehicles to ideally reduce the possible disastrous consequences and encourage researchers to continue examining the causes of vulnerability [5,6].

A vehicle, when exposed to floodwaters, undergoes several instability modes mainly due the impact of several hydrodynamic forces. Such impact on a static vehicle (perpendicular to incoming flow direction) was first studied by [7]. A similar approach was then undertaken on a static car parked parallel to the direction of incoming flow under partial submergence [8]. Both studies concluded and proposed values of friction coefficient for static cars keeping in view the condition of road surface and vehicle tires. Later, a theoretical formula was proposed to assess the incipient velocity required to cause a vehicle to become unstable during a flooding event [9]. Since 1993, no studies were performed on the vehicle hydrodynamics. However, in recent years, the stability criterion of modern vehicles (static) have been studied by various authors. This includes the work of [10-18]. From the available data, both experimental and numerical, it appeared that nearly all investigations (1967-2017) pertaining to vehicle behaviour in floodwater are solely devoted to static (parked) cars.

Herein this paper attempts to inquire the hydrodynamic behaviour of a non-static vehicle for the very first time. The experimental investigation was conducted to observe the instability thresholds of a non-static car at varying hydraulic variables. These data points were later used to theoretically assess the varying hydrodynamic forces by means of a simple numerical framework. Lastly, the relationship of hydrodynamic forces with respect to varying Froude numbers has been discussed.

2. LABORATORY EXPERIMENTAL SETUP

Academic research in the field of vehicle chassis dynamics are usually very costly and pertain to safety issues concerning prototype testing. Such studies are limited to scaled models [19]. In the current study, experimental investigations were carried out on a non-static model vehicle (1:10, Perodua Viva) that ensured all laws of similitude. The description of the vehicle both prototype and model including dimensions and weight are shown in Table 1.

Table 1: Vehicle specifications

Vehicle	Scale	Length [mm]	Width [mm]	Height [mm]	Kerb Weight (g)
Perodua	Prototype	3575	1475	1530	800000
Viva	Model (1:10)	357.5	147.5	153.0	880

Experimental runs with the non-static model were performed at the Hydraulics Laboratory, Universiti Teknologi PETRONAS (UTP), Malaysia. Herein a maximum grade of 5% (2.86°) was considered to analyze the behavior of a non-static vehicle in floodwaters on a low-lying roadway condition [20] with an area of $4 \times 1.5 \text{ m}^2$. The variables measured

during the experimental runs involved water depth (y) through point gauge, flow velocity (v) by means of velocity meter, and the time taken by the non-static vehicle to cross the flooded roadway. A laser beam was also used to detect vehicle movement in floodwaters. The velocity and water depth measurements were observed at one vehicle length upstream of the flooded vehicle [11] from a moveable hanging bridge. The details of the study area are shown in Fig. 1.

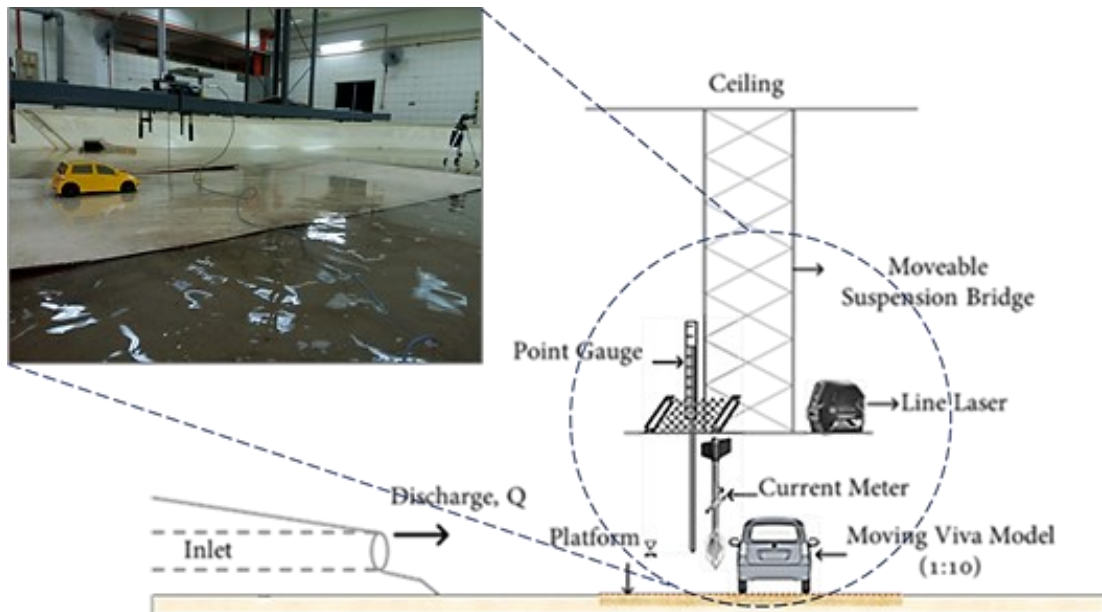


Fig. 1: Description of experimental area [21].

3. FLOATING DEPTH AND LIMITING THRESHOLDS

This section highlights the assessment of thresholds and floating conditions of a non-static car attempting to cross a low-lying flooded street. In this regard, the response of the car towards varying hydraulic variables has been presented. Since the study scope was limited to partial submergence, the water depths tested were between 0.041 m to 0.098 m, whereas to ensure sub-critical flow conditions, the observed range for flow velocities were between 0.17 m/s to 0.53 m/s, respectively. The range of Froude and Reynolds numbers attained from the empirical investigations are shown in Table 2.

At depths ≥ 0.055 m, a mode of floating instability was witnessed due to the buoyancy force that took effect at high water depths to acquire sufficient submerged volume to cause floating instability failure. On the other hand, below critical depth (the threshold at or above which floating instability occurred mainly due to the vertical push caused by the hydrodynamic forces i.e., buoyancy and lift forces), a mode of sliding instability was observed at low flow velocities mainly due to slope inclination which reduced the frictional strength between the ground surface and the tires. Herein, the laws of similitude were ensured, thus the buoyancy depth that could lead to the floating instability failure and the limiting velocity \times depth ($v \cdot y$) functions required to cause sliding failure for the prototype are highlighted in Fig. 2.

Table 2: Flow state and Reynolds number

No.	Velocity (m/s)	Depth (m)	Froude Number	Reynolds Number
1.	0.40	0.047	0.59	18800
2.	0.36	0.051	0.51	18360
3.	0.30	0.058	0.40	17400
4.	0.27	0.063	0.34	17010
5.	0.28	0.064	0.35	17920
6.	0.23	0.078	0.26	17940
7.	0.53	0.041	0.84	21730
8.	0.31	0.055	0.42	17050
9.	0.29	0.058	0.38	16820
10.	0.28	0.064	0.35	17920
11.	0.26	0.068	0.32	17680
12.	0.24	0.074	0.28	17760
13.	0.23	0.079	0.26	18170
14.	0.41	0.045	0.62	18450
15.	0.27	0.064	0.34	17280
16.	0.26	0.070	0.31	18200
17.	0.23	0.078	0.26	17940
18.	0.23	0.081	0.26	18630
19.	0.39	0.047	0.57	18330
20.	0.29	0.059	0.38	17110
21.	0.28	0.065	0.35	18200
22.	0.24	0.077	0.28	18480
23.	0.22	0.083	0.24	18260
24.	0.20	0.089	0.21	17800
25.	0.29	0.057	0.39	16530
26.	0.29	0.060	0.38	17400
27.	0.26	0.071	0.31	18460
28.	0.24	0.078	0.27	18720
29.	0.20	0.087	0.22	17400
30.	0.32	0.055	0.44	17600
31.	0.28	0.061	0.36	17080
32.	0.26	0.072	0.31	18720
33.	0.24	0.079	0.27	18960
34.	0.20	0.088	0.22	17600
35.	0.38	0.051	0.54	19380
36.	0.29	0.061	0.38	17690
37.	0.25	0.073	0.30	18250
38.	0.21	0.085	0.23	17850
39.	0.20	0.089	0.21	17800
40.	0.19	0.091	0.20	17290
41.	0.41	0.046	0.61	18860
42.	0.30	0.058	0.40	17400
43.	0.28	0.066	0.35	18480
44.	0.26	0.072	0.31	18720
45.	0.21	0.085	0.23	17850
46.	0.19	0.093	0.20	17670
47.	0.25	0.068	0.31	17000
48.	0.24	0.077	0.28	18480
49.	0.20	0.088	0.22	17600
50.	0.19	0.094	0.20	17860
51.	0.17	0.098	0.17	16660

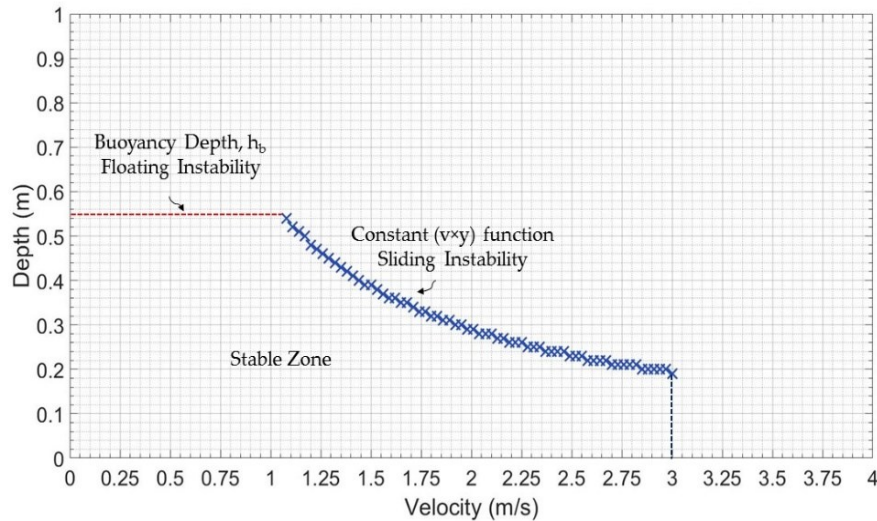


Fig. 2: Limit functions and buoyancy depth for Perodua Viva (1:1) at mild inclinations.

4. THEORETICAL ASSESSMENT OF HYDRODYNAMIC FORCES

The hydraulic variables were assessed at the point of maximum inclination. For assessing the buoyancy force, the submerged volume (V) was estimated at the given water depths. Due to the complexity of the slope inclination, the submerged fractions of the vehicle were theoretically determined through AutoCAD, Solidworks, and ANSYS (Fluent).

The description of drag force has been addressed in detail in earlier studies [5, 22] and [23]. Therefore, in the current section the focus was more on the drag influence assisted by the weight component parallel to the inclined plane. At inclinations, the gravitational force has transverse components. Under dry conditions, the parallel component supports the drag force that causes vehicle sliding. However, under wet conditions, when the flow is sub-critical, this force component becomes $mg_x = (W - F_B) \sin\theta$. Thus, the resultant drag at slopes can be expressed as $F_D = 1/2 \rho C_D A_D V^2 + (W - F_B) \sin\theta$. Herein, the value of drag coefficient C_D remained unchanged and was set to a constant value as the minimum value of Reynolds number was found to be in the order of 16000 [11].

On slopes, the friction force further reduces due to the transverse components of the gravitational force. Therefore, for such conditions, the coefficient of friction was experimentally determined (wet surface) by means of the spring-balance method. The value of the friction coefficient (μ_{FR}) opposite to the direction of incoming flow was noticed to be 0.19, whereas the value of the rolling coefficient (μ_{RO}) in the direction of vehicle movement was noticed to be 0.048.

5. RESULTS AND DISCUSSION

Free surface flows are governed by gravity forces, whereas Reynolds number effects (viscous drag) are most likely to become more significant at lower a Reynolds number [24]. Therefore, in this section, an attempt has been made to study the relation of varying hydrodynamic forces with respect to the Froude number.

5.1 Buoyancy Force (F_B) and Froude Number

At first, the impact of the buoyancy force computed at varying Froude numbers has been discussed as shown in Fig. 3.

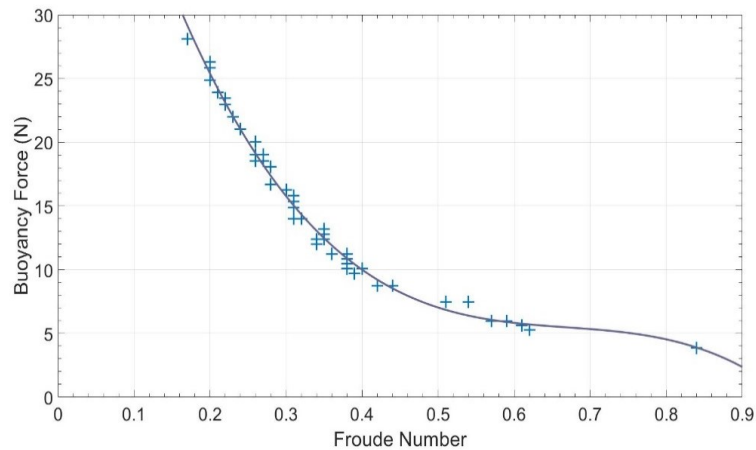


Fig. 3: Buoyancy force computed at varying Froude numbers.

Recall that the buoyancy force relates to the submerged volume that varies with the water depth. Therefore, at each increment in the floodwater level, a decline in the Froude number was seen. For example, when the Froude number reached a low value, i.e., 0.18, the impact of the buoyancy force almost approached 28 N, whereas its impact was insignificant at the highest Froude number, i.e., 0.84. Therefore, from the above graph, it can be figured that there would always be an opposite relation between Froude number and the buoyancy force. Overall, it was noticed that due to subcritical flow conditions, the influence of water depth remained dominant for the majority of the data points.

5.2 Drag Force (F_D) and Froude Number

The impact of drag force on non-static vehicles varies based on two conditions, namely (i) the incoming flow direction and (ii) the direction of vehicle movement. For the given circumstances where a vehicle slowly progresses perpendicular to the incoming flow, the drag usually acts at two sides, i.e., vehicle's side end (D_1) and its frontal area (D_2). Pertaining to drag influence at D_1 , it was noticed that its impact did not necessarily increase with respect to the increment in water depth which mainly occurred due to variation in the hydraulic variables. However, at D_2 , the drag force relied solely on the water depth due to constant velocity of the flow. That is why the impact of drag in this particular direction increased with an increment in the water level.

Under this section, the behavior of drag with respect to the Froude number has been discussed. It is important to highlight that in order to cause floating failure, the influence of buoyancy and lift forces is usually considered. Herein, the investigation noticed that under the conditions where Froude number < 1 , the impact of the lift force was disregarded [17, 25]. Furthermore, for determining the sliding instability, the horizontal pushing force, which comprises drag, friction, and driving force, was taken into account. The impact of the horizontal pushing force is always dominant below critical water depth. However, under this section, the impact of the drag force (D_1) for all data points has been highlighted, as shown in Fig. 4. Later, only those data points that were below critical water depth have been discussed, as shown in Fig. 5.

From the graph, it can be inferred that with an increase in the Froude number, the magnitude of the drag force slightly increased, mainly due to the flow velocity which was more dominant below the buoyancy depth. However, upon comparing the drag influence at vehicle's side with respect to Froude number, it can be seen that when the Froude number reached 0.83, the drag force was noticed to be 0.75 N, whereas at the lowest Froude number,

i.e., 0.51, the drag impact was almost 0.58 N. Thus, a positive relation between the two was witnessed. Similarly, the impact of drag force (D_2) for all data points has been highlighted, as shown in Figure 6. Later, only those data points that were below critical water depth have been discussed, as shown in Fig. 7.

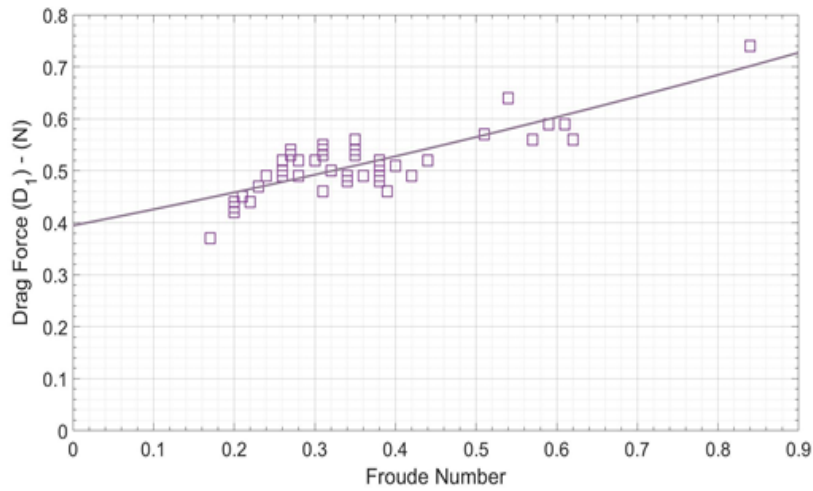


Fig. 4: Drag force (D_1) computation at varying Froude numbers (all data points).

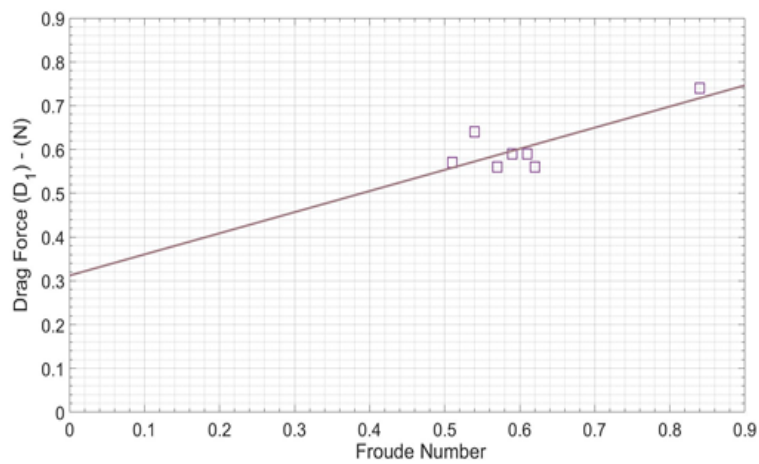


Fig. 5: Drag force (D_1) computation at varying Froude numbers (data points below critical water depth).

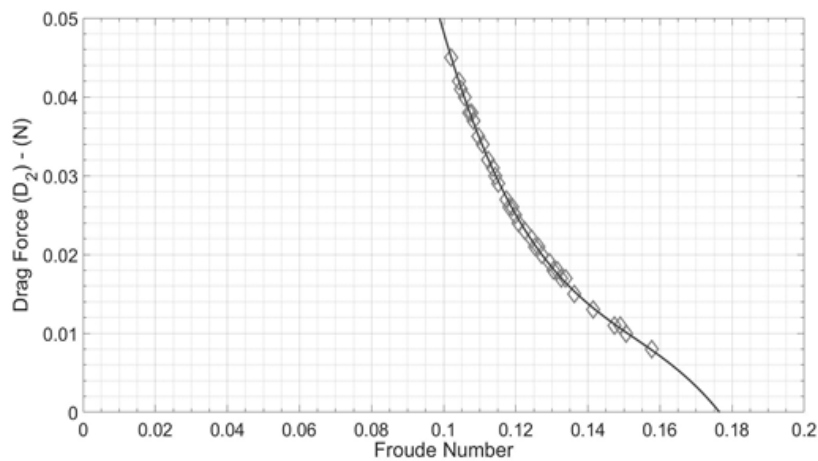


Fig. 6: Drag force (D_2) computed at varying Froude numbers (all data points).

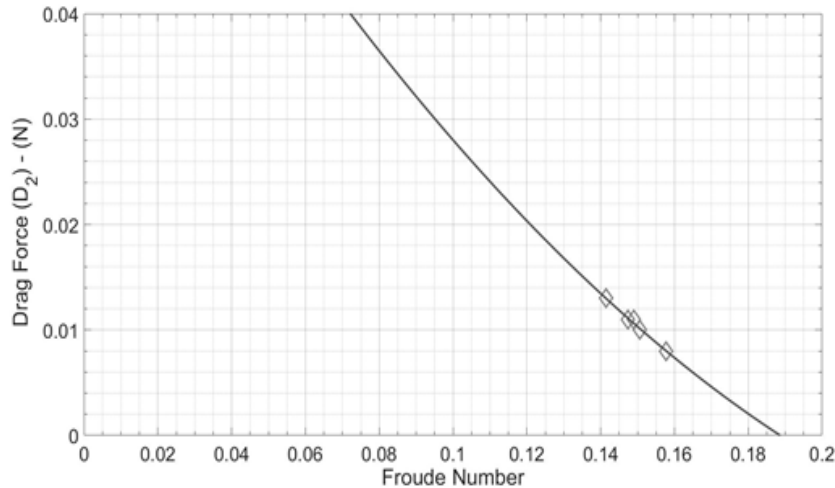


Fig. 7. Drag force (D_2) computed at varying Froude numbers (data points below critical water depth).

From the above figures, it can be observed that the magnitude of the drag force at the vehicle's front end decreased as the Froude number increased. It should be taken into account that in this particular direction, the flow velocity was found to be very low and constant throughout. Further, the impact of the drag force mainly relied on the floodwater depth. The reason for the nominal impact at the vehicle's front area could be due to two possible reasons, namely (i) low and constant flow velocity in the opposite direction of vehicle movement and (ii) smaller area available to the drag force to take effect. For instance, when the Froude reached 0.158, the drag impact was found to be 0.008 N, whereas at the highest Froude number, i.e., 0.142, the drag impact was found to be 0.012 N. Thus, a negative relation between the two was witnessed.

5.3 Friction Force (F_R and F_{RO}) and Froude Number

Recall that for the estimation of the friction force, the net vehicle weight, which can be estimated by deducting the vertical pushing force, i.e., buoyancy and lift forces, from the vehicle weight in dry conditions, is required. However, due to the subcritical state of the flow, the net vehicle weight was assessed by deducting the buoyancy force only. As highlighted earlier, the impact of friction force is dominant below critical water depth. Thus, for the sake of comparison, the variation of frictional resistance (F_R) in the direction of incoming flow with respect to the Froude number on the low-lying roadway for all data points and below critical water depth is highlighted in Fig. 8 and Fig. 9, respectively. Similarly, the variation of rolling resistance (F_{RO}) due to the tires' movement with respect to the Froude number on the low-lying roadway for all data points and below critical water depth, is highlighted in Fig. 10 and Fig. 11, respectively.

The friction force, F_R is the resistive force between the vehicle tires and the ground. To cause floating instability, the buoyancy impact was found to be more dominant when it reached the critical depth. Below critical depth, it was noticed to be slightly less effective but since an increment in the water depth reduces the vehicle weight, the frictional stability between the tires and the ground was reduced, as shown in Fig. 12(a). Therefore, it can be said that at low Froude numbers, the frictional stability is reduced and vice versa. Moreover, the weight components at an inclination affect the vehicle weight and so does the instability modes, as shown in Fig. 12(b).

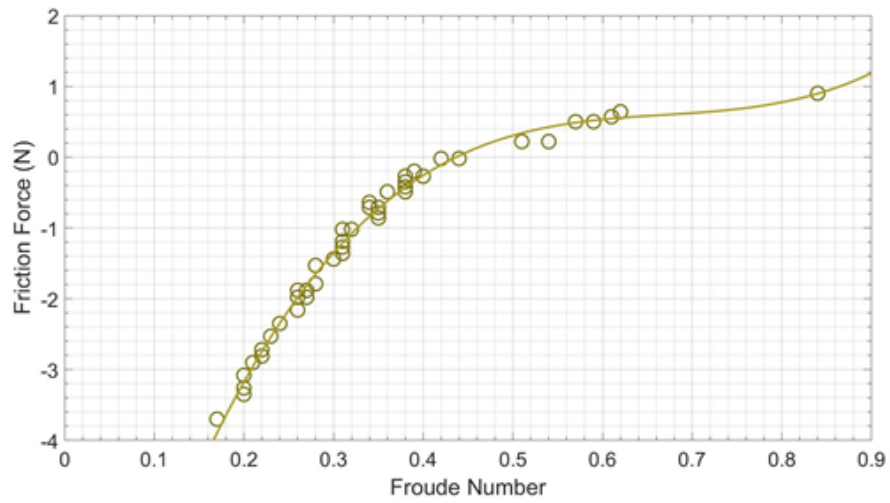


Fig. 8: Friction force (F_R) computation at varying Froude numbers (all data points).

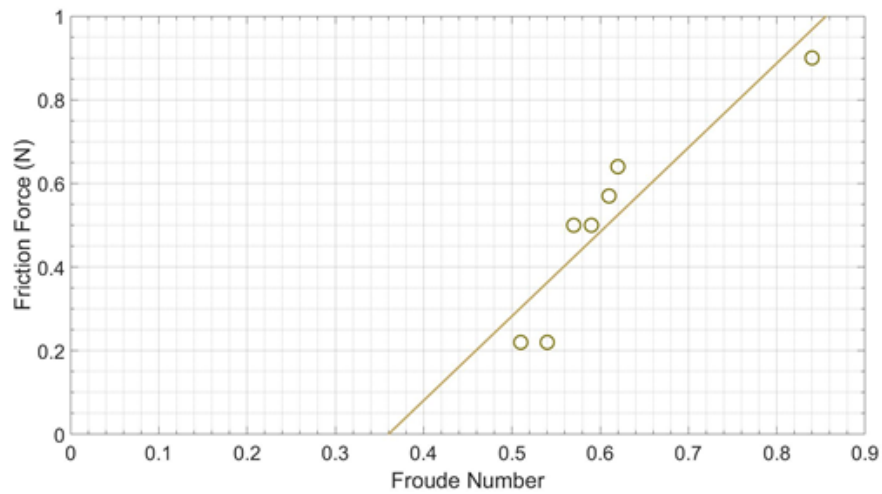


Fig. 9: Friction force (F_R) computation at varying Froude numbers (data points below critical water depth).

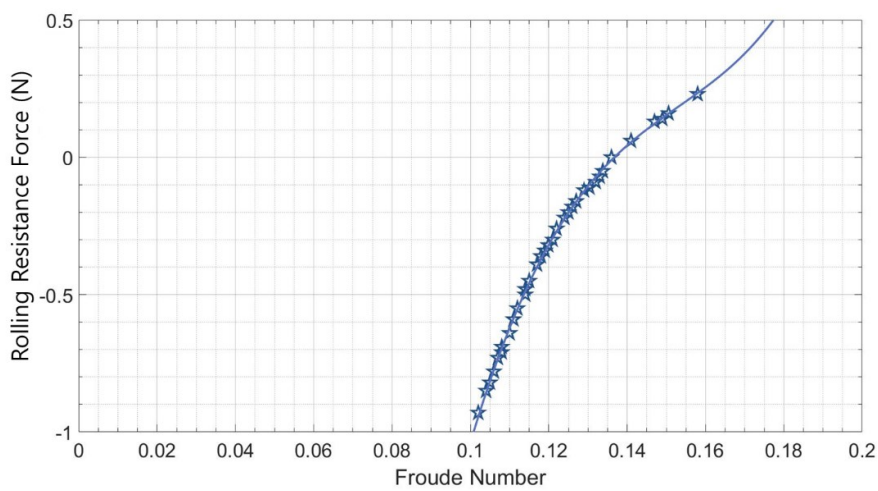


Fig. 10: Friction force (F_{RO}) computation at varying Froude numbers (all data points).

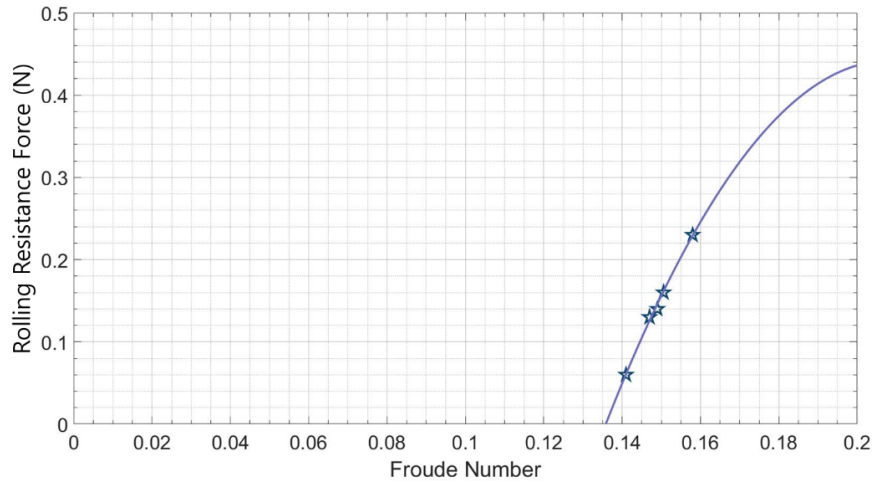


Fig. 11: Friction force (F_{RO}) computation at varying Froude numbers (data points below critical water depth).

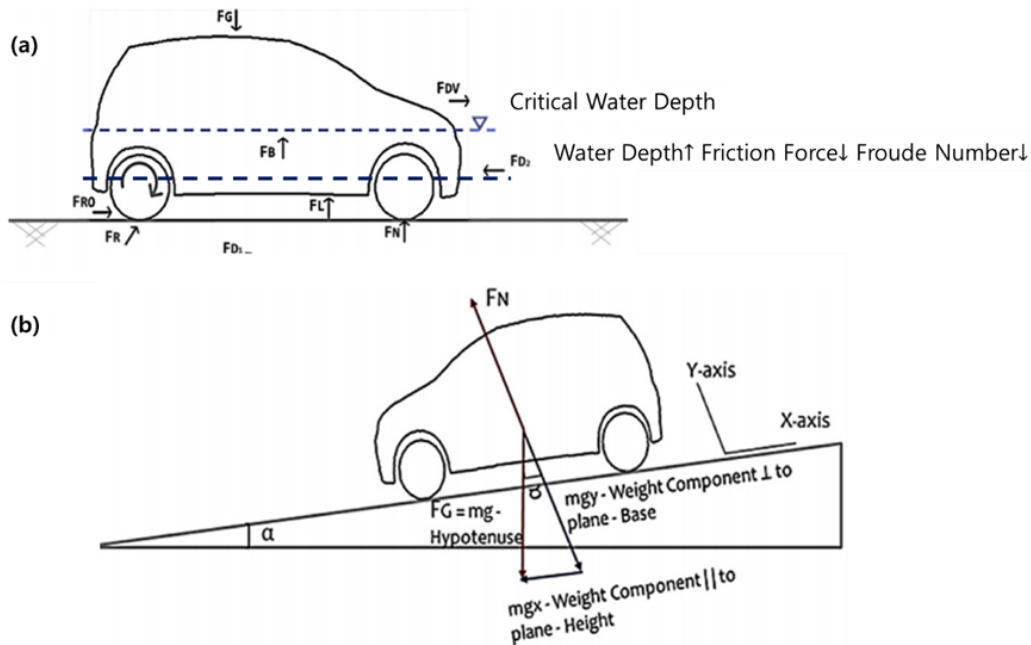


Fig. 12: (a) Hydrodynamic forces on a non-stationary vehicle in floodwaters highlighting the relation between buoyancy and friction forces and (b) Weight components distribution when the ground slope is at an angle [21].

The tires grip with the ground decreases as the water level increases around the vehicle. This further reduces the Froude number. Thus, a positive relation between the two was noticed. At high Froude number, the impact of buoyancy force was low due to low water depths. Therefore, the contact of the vehicle with the ground was strong which increased the frictional resistance. On the other side, when the value of the Froude number was low, the impact of the buoyancy force was high due to high water depths. Thus, the vehicle weight in water was reduced which loosened the frictional resistance between the tires and the ground surface. Concerning the frictional force (F_R), at the lowest Froude number, i.e., 0.51, the frictional resistance was found to be minimal, i.e., 0.20, whereas at the highest Froude number, the frictional resistance was comparatively very large. Similarly, the

influence of rolling resistance (F_{RO}) due to tires' rotation followed a similar pattern. For example, at the lowest Froude number, i.e., 0.14, the rolling resistance was found to be minimal, whereas it reached a larger value when the Froude number reached 0.16.

6. CONCLUSIONS

Among the major findings, it's been noticed that: (i) the influence of buoyancy force solely depends on the submerged volume, which varies with the water level whereas the Froude number is inversely proportional to it. Thus, an inverse relation between the two was noticed, (ii) the flow velocity was more dominant below the critical depth, thus the intensity of drag force (at D_1) slightly increased as the Froude number was increased. On the other hand, at D_2 , an inverse variation between the two was found and lastly, (iii) the vehicle weight reduced at higher water depths, which decreased the frictional stability of the car with the ground. Thus, it can be said that the frictional stability of a vehicle is reduced at low Froude numbers.

REFERENCES

- [1] Diakakis M, Deligiannakis G. (2017) Flood Fatalities in Greece: 1970–2010. *Journal of Flood Risk Management*, 10(1): 115-123.
- [2] Starita S, Scaparra MP, O'Hanley JR. (2017) A Dynamic Model for Road Protection Against Flooding. *Journal of the Operational Research Society*, 68(1): 74-88.
- [3] Ahmed MA, Haynes K, Taylor M. (2020) Vehicle-related Flood Fatalities in Australia, 2001–2017. *Journal of Flood Risk Management*, 13:e12616.
- [4] Hamilton K, Peden AE, Keech JJ, Hagger MS. (2018) Driving through Floodwater: Exploring Driver Decisions through the Lived Experience. *International Journal of Disaster Risk Reduction*, 34: 346-355.
- [5] Shah SMH, Mustaffa Z, Martinez-Gomariz E, Kim DK, Yusof KW. (2019) Criterion of Vehicle Instability in Floodwaters: Past, Present and Future. *International Journal of River Basin Management*, 0(0): 1-23.
- [6] Teo FY, Falconer RA, Lin B, Xia J. (2012) Investigations of Hazard Risks Relating to Vehicles Moving In Flood. *Journal of Water Resources Planning and Management*, 1(1): 52-66.
- [7] Bonham AJ, Hattersley RT. (1967) Low Level Causeways. Water Research Laboratory, Report no. 100. University of New South Wales, Australia.
- [8] Gordon A, Stone P. (1973) Car Stability on Road Floodways. Car stability on Road Floodways. National Capital Development Commission, Report no. 73/12. Water Research Laboratory, University of New South Wales, Australia.
- [9] Keller RJ, Mitsch B. (1993) Safety Aspects of the Design of Roadways as Floodways. Urban Water Research Association of Australia.
- [10] Teo FY. (2010) Study of the Hydrodynamic Processes of Rivers and Floodplains with Obstructions. Thesis (PhD). Available from: <https://orca.cf.ac.uk/54161/1/U517543.pdf>.
- [11] Xia J, Teo FY, Lin B, Falconer RA. (2010) Formula of Incipient Velocity for Flooded Vehicles. *Natural Hazards*, 58(1): 1-14.
- [12] Shu C, Xia J, Falconer RA, Lin B. (2011) Incipient Velocity for Partially Submerged Vehicles in Floodwaters. *Journal of Hydraulic Research*, 49(6): 709-717.
- [13] Oshikawa H, Oshima T, Komatsu T. (2011) Study on the Risk for Vehicular Traffic in a Flood Situation. *Advances in River Engineering*, 17: 461-466.
- [14] Toda K, Ishigaki T, Ozaki T. (2013) Experimental Study on Floating Cars in Flood Water. *International Conference on Flood Resilience: Experiences in Asia and Europe*.
- [15] Xia J, Falconer RA, Xia X, Wang Y. (2013) Criterion of Vehicle Stability in Floodwaters based on Theoretical and Experimental Studies. *Natural hazards*, 70(2): 1619-1630.
- [16] Xia J, Falconer RA, Wang Y, Xia X. (2014) New Criterion for the Stability of a Human Body in Floodwaters. *Journal of Hydraulic Research*, 52(1): 93-104.

- [17] Martínez-Gomariz E, Gómez M, Russo B, Djordjević S. (2017) A New Experiments-based Methodology to Define the Stability Threshold for any Vehicle Exposed to Flooding. *Urban Water Journal*, 14(9): 930-939.
- [18] Teo FY, Xia J, Falconer RA, Lin B. (2012) Experimental Studies on the Interaction between Vehicles and Floodplain Flows. *International Journal of River Basin Management*, 10(2): 149-160.
- [19] McMahon TA, Bonner JT. (1983) *On Size and Life*. Scientific American Library.
- [20] Romney M (2006). *Horizontal and Vertical Alignment*. Massachusetts Highway Department Design Guide Project Development & Design Guide.
- [21] Shah SMH, Mustaffa Z, Martínez-Gomariz E, Yusof KW, Al-Qadami EHH. (2019) Hazard Risks Pertaining to Partially Submerged Non-Stationary Vehicle on Low-Lying Roadways under Subcritical Flows. *Results in Engineering*, 3 (2019) 100032: 1-7.
- [22] Shah SMH, Mustaffa Z, Martínez-Gomariz E, Yusof KW. (2020) Hydrodynamic Effect on Non-Stationary Vehicles at Varying Froude Numbers under Subcritical Flows on Flat Roadways. *Journal of Flood Risk Management*, 13: e12657.
- [23] Shah SMH, Mustaffa Z, Martínez-Gomariz E, Yusof KW, Al-Qadami EHH (2019). A Review of Safety Guidelines for Vehicles in Floodwaters. *International Journal of River Basin Management*, 0(0): 1-17.
- [24] Liu HK, Albertson ML. (1959) Significance and Applications of Froude and Reynolds Numbers as Criteria for Similitude. Report no. CR59HKL20, Colorado State University, Fort Collins, Colorado.
- [25] Shah SMH, Mustaffa Z, Yusof KW, Nor MFM. (2018) Influence of Forces on Vehicle's Instability in Floodwaters. *Ain Shams Engineering Journal*, 9(4): 3245-3258.

ROBUST TUNING OF POWER SYSTEM STABILIZER PARAMETERS USING THE MODIFIED HARMONIC SEARCH ALGORITHM

HIBA ZUHAIR ABDUL KAREEM¹, HUSAM HASAN MOHAMMED^{1*},
AND AMEER AQEEL MOHAMMED²

¹Department of Electronic Technologies,

²Department of Computer Systems,

Babylon Technical Institute,

Al-Furat Al-Awsat Technical University, 51015, Babylon, Iraq

*Corresponding author: husam171984@gmail.com

(Received: 24th October 2019; Accepted: 18th March 2020; Published on-line: 4th January 2021)

ABSTRACT: Power System Stabilizer is used to improve power system low frequency oscillations during small disturbances. In large scale power systems involving a large number of generators, PSSs parameter tuning is very difficult because of the oscillatory modes' low damping ratios. So, the PSS tuning procedure is a complicated process to respond to operation condition changes in the power system. Some studies have been implemented on PSS tuning procedures, but the Harmony Search algorithm is a new approach in the PSS tuning procedure. In power system dynamic studies at the first step system total status is considered and then the existed conditions are extended to the all generators and equipment. Generators' PSS parameter tuning is usually implemented based on a dominant operation point in which the damping ratio of the oscillation modes is maximized. In fact the PSSs are installed in the system to improve the small signal stability in the system. So, a detailed model of the system and its contents are required to understand the dynamic behaviours of the system. In this study, the first step was to linearize differential equations of the system around the operation point. Then, an approach based on the modified Harmony Search algorithm was proposed to tune the PSS parameters.

ABSTRAK: Penstabil Sistem Kuasa digunakan bagi meningkatkan sistem kuasa ayunan frekuensi rendah semasa gangguan kecil. Dalam sistem kuasa berskala besar yang melibatkan sebilangan besar penjana, penalaan parameter PSS adalah sangat sukar kerana nisbah corak ayunan redaman yang rendah. Maka, langkah penalaan PSS adalah satu aliran rumit bagi mengubah keadaan operasi sistem kuasa. Beberapa kajian telah dilaksanakan pada prosedur penalaan PSS, tetapi algoritma Harmony Search merupakan pendekatan baru dalam prosedur penalaan PSS. Dalam kajian sistem kuasa dinamik ini, langkah pertama adalah dengan memastikan status total sistem dan keadaan sedia ada diperluaskan kepada semua penjana dan peralatan. Parameter penalaan generator PSS biasa dilaksanakan berdasarkan titik operasi yang dominan di mana nisbah corak ayunan redaman dimaksimumkan. Malah PSS dipasang di dalam sistem bagi meningkatkan kestabilan isyarat kecil dalam sistem. Oleh itu, model terperinci sistem dan kandungannya diperlukan bagi mengenal pasti perihai sistem dinamik. Kajian ini, dimulai dengan melinear sistem persamaan pembezaan pada titik operasi. Kemudian, pendekatan berdasarkan algoritma Harmony Search yang diubah suai telah dicadangkan bagi penalaan parameter PSS.

KEYWORDS: power system stabilizer (PSS); power system; harmonic search algorithm

1. INTRODUCTION

Small-signal fluctuation stability is a major issue for power system security and reliability. These fluctuations affect the power system's natural damping [1]. PSS, if well-tuned, will have the ability to function properly in the system [2]. Although these stabilizers have a simple and robust structure, their configuration, even with computer simulation or field testing, involves a highly skilled process for system parameters [3]. These parameters are not readily available and may, during normal operation of the power system, change the values of the parameters [4]. These parameters cannot be measured directly so they should be well estimated [5]. Recently, several heuristic search algorithms have been proposed for tuning, PSS parameters, such as tab search [6] evolutionary programming [7], and Particle Swarm Optimization (PSO) [8] were suggested to evaluate the PSS Parameters. However, these methods failed to determine precise parameters when the system has a specific objective function with a large-scale number of parameters.

2. PROBLEM FORMULATION

The power system can be described using a set of first-order nonlinear differential equations[8]:

$$\dot{X} = f(x, u) \quad (1)$$

Where \dot{X} or x is the state variables vector, and u is the vector of input variables. The linearized models of a power system can be used to design the power system stabilizers. Therefore, the state equation of the power system with stabilizers can be written as [9]:

$$\Delta\dot{X} = A\Delta X + BU \quad (2)$$

$$\Delta y = C\Delta X + D\Delta U \quad (3)$$

where Δ represents small changes, X is the state vector of order n , y is the output vector of order m , U is the input vector of order r , A is a square matrix of states of size n , B represents a control matrix with size $n \times r$, C refers to the output matrix with size $m \times n$, D is the leading matrix with the size $m \times r$.

A traditional lead-lag compensator PSS is utilized in this study. The transfer function of the PSS is described by the following equation [10]:

$$V_i = K_i \frac{sT_\omega}{1+sT_\omega} \frac{(1+sT_{1i})}{(1+sT_2)} \frac{(1+sT_{3i})}{(1+sT_4)} \Delta\omega_i \quad (4)$$

where V_i is the output signal for PSS at i th machine, K_i The stabilizer gain, T_ω represents the time constant, $\Delta\omega_i$ speed deviation of i th machine from the synchronous speed.

3. OBJECTIVE FUNCTIONS

The Objective functions are formulated by tuning the PSS parameter and there are three different objective functions that have been used in many studies to set parameters, which will be discussed below:

a) The damping factor can be considered as the first objective as follows [11]:

$$\left(\max_{1 \leq q \leq n_q} \sigma_q \right)_y \quad (5)$$

$$\left(\max_{1 \leq q \leq n_q} \sigma_q - \sigma_0 \right)_y \quad (6)$$

$$\left(\max_{1 \leq q \leq n_q} \sigma_q - \sigma_0 \right)_1 + \left(\max_{1 \leq q \leq n_q} \sigma_q - \sigma_0 \right)_2 + \dots + \left(\max_{1 \leq q \leq n_q} \sigma_q - \sigma_0 \right)_{ny} \quad (7)$$

$$MinF1 = \sum_{y=1}^{ny} \left(\max_{1 \leq q \leq n_q} \sigma_q - \sigma_0 \right)_y \quad (8)$$

where, ny are the all operating statuses of the test system, n_q denotes the number of eigenvalues under ny , σ_q is the damping factor, σ_0 is damping factor constant. When the $F1$ (σ_q is defined as Damping factor) is less than or equal to zero, the response for the maximum damping factor ($\max_{1 \leq q \leq n_q}$) is less than or exactly equal to the expected value σ_0 , [12].

b) The damping ratio can be considered as the second objective as follows [13]:

$$MinF2 = \sum_{y=1}^{ny} \left(\zeta_0 - \min_{1 \leq q \leq n_q} \zeta_q \right)_y \quad (9)$$

where ζ_0 represents the predicted damping ratio constant, and ζ_q represents the damping ratio. When $F2$ is less than or equal to zero, the response is the minimum damping ratio(s) ($\min_{1 \leq q \leq n_q} \zeta_q$) are more than or exactly the value of ζ_0 [14].

c) The damping ratio and damping factor can be considered as the third objective as follows [15]:

$$MinF3 = \sum_{y=1}^{ny} \left(\max_{1 \leq q \leq n_q} \sigma_q - \sigma_0 \right)_y + \alpha \sum_{y=1}^{ny} \left(\zeta_0 - \min_{1 \leq q \leq n_q} \zeta_q \right)_y \quad (10)$$

where α is the weight for combining both damping ratio and damping factor.

4. PROPOSED OBJECTIVE FUNCTION

The objective functions F1, F2, and F3 produce high frequency or low frequency, which may reduce the life of system devices [16]. Therefore, we can overcome the disadvantages mentioned earlier through the following equation [17]:

$$X = \frac{-(\sigma - \sigma_0)}{\sqrt{(\sigma - \sigma_0)^2 + \omega^2}} \times 100\% \quad (11)$$

$$MinF4 = \sum_{y=1}^{ny} \left(X_0 - \min_{1 \leq q \leq n_q} X_q \right)_y \quad (12)$$

where
 X: the constant value for the prospective damping scale
 X_q: the damping scale for the qth eigenvalue

The following equations present the constraints of the PSS parameter design model [18]:

$$\left\{ \begin{array}{l} K_{min} \leq K \leq K_{max} \\ T_{1min} \leq T_1 \leq T_{1max} \\ T_{2min} \leq T_2 \leq T_{2max} \\ T_{3min} \leq T_3 \leq T_{3max} \\ T_{4min} \leq T_4 \leq T_{4max} \end{array} \right\} \quad (13)$$

5. THE PROPOSED ALGORITHM

Harmonic Search Algorithm is one of the simplest and most up-to-date methods, which is the process of finding the optimal solution to the problem. This method was used for the first time in 2001 [19]. Harmony search is inspired by the process of jazz musicians to find the optimal solution. In this algorithm, each solution is called a harmonic and is represented by a vector (N). This algorithm contains the following steps [20]:

a) Primary generation (Initial initialization)

In the first step, the optimization problem is indicated by the relationship. Also, at this step, the Harmony Memory size (HMS) is calculated.

$$Min: \{f(x) | x \in X\} \quad (14)$$

$$Subject\ to : g(x) \geq 0 \quad h(x) = 0 \quad (15)$$

where: $f(x)$ is the objective function, $h(x)$ and $g(x)$ are the functions of equal and unequal constraints respectively. Also in this step, the HS algorithm parameters are specified. These parameters are [21] :

- 1) Harmony Memory Size (HMS), or the number of solution vectors in the harmony memory.
- 2) Harmony Memory Considering Rate (HMCR), $HMCR \in [0,1]$.
- 3) Pitch Adjusting Rate (PAR) $\in [0,1]$.
- 4) Stopping criterion or number of improvisations (NI)

b) Primary Harmonic Memory Determination

At this step, the Harmony matrix (HM) is created from a large number of solution vectors that are created randomly[22].

$$HM = \begin{bmatrix} x_1^1 & x_2^1 & \dots & x_{N-1}^1 & x_N^1 \\ x_1^2 & x_2^2 & \dots & x_{N-1}^2 & x_N^2 \\ \vdots & \vdots & \vdots & \vdots & \vdots \\ x_1^{HMS-1} & x_2^{HMS-1} & \dots & x_{N-1}^{HMS-1} & x_N^{HMS-1} \\ x_1^{HMS} & x_2^{HMS} & \dots & x_{N-1}^{HMS} & x_N^{HMS} \end{bmatrix} \quad (16)$$

c) New harmonic production based on improvisation

d) A new harmonic vector $x'(x'_1, x'_2, \dots, x'_N)$ is produced based on three rules that it describes as improvised:

- 1) Harmony Memory Considering Rate (HMCR)

- 2) sound regulation
- 3) random selection
- e) Updating Harmony Memory: If the new harmonic vector is better than the worst harmonic vector based on the selected target function, the new harmony is placed inside and the worst harmonic is left out of the set.
- f) Check the stopping criterion: when the termination criterion is satisfied, the calculations are completed, otherwise, steps 3 and 4 are repeated.

6. MODIFIED HARMONY SEARCH (MHS)

The disadvantages of the HS method are the use of PAR and Bandwidth, BW, constant values, which makes it difficult to set up these parameters. Another disadvantage of the HS is that the number of repetitions for which the algorithm needs to find the optimal solution is not appropriate [23]. If PAR is small and BW is large, the algorithm's performance is weak hence increased NI improvements are required to find that optimal solution Fig. 1.

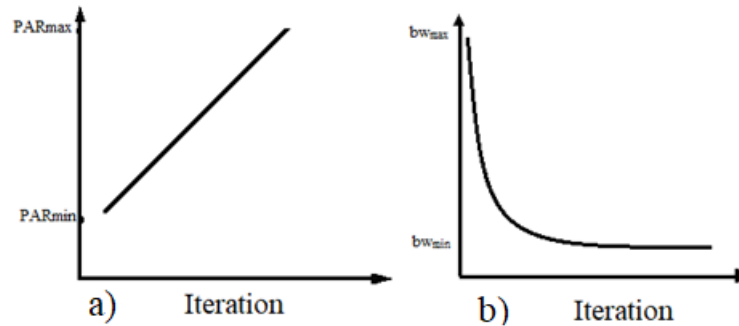


Fig. 1: a) change of PAR with iteration number,
 b) change of BW with iteration number 3-or 4.

The initial iteration of the HS has large BW and small PAR , which leads to increase the entire solution space of the search algorithm. These values are appropriate for subsequent replies in order to locally search. MHS is similar to HS, with a little difference in that PAR and BW parameter values are dynamically generated in each individual iteration according to the following relationships [24]:

$$PAR(gn) = PAR_{min} + \frac{PAR_{max} - PAR_{min}}{NI} \times t \quad (17)$$

where,

PAR(t) = Pitch Adjusting Rate for each iteration

PAR_{min} = Minimum Pitch Adjusting Rate

PAR_{max} = Maximum Pitch Adjusting Rate

NI = Number of solution vector Iteration

t = Iteration Number

$$bw(t) = bw_{max} \times e^{\left[\frac{1n \left[\frac{bw_{min}}{bw_{max}} \right] \times t}{N1} \right]} \quad (18)$$

where,

$bw(t)$ = Bandwidth for each iteration

bw_{min} = Minimum bandwidth

bw_{max} = Maximum bandwidth

7. PSS DESIGN AND SIMULATION RESULTS

In this study, the MHS algorithm is used to obtain the optimal design of the PSS parameters for the system of four generators shown in Fig. 2 [25] and compare results with other techniques (Harmony Search, Classic Approach).

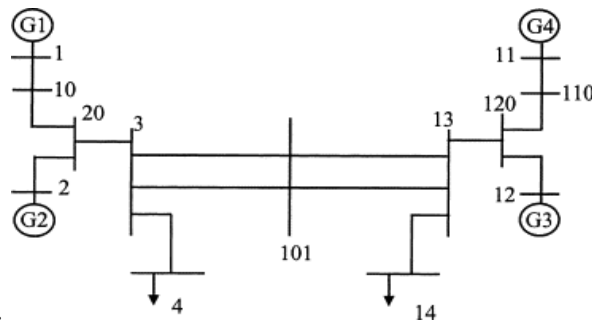


Fig. 2: Single-line diagram of the 4-generator system.

7.1 Case 1: The Stability of Four-Generators Without PSS

In this case, the system was tested after the fault at bus-3 without PSS to demonstrate the effect of PSS on the stability of this system. According to Table 1, the system is unstable. From Figures 3 and 4, it is observed that the rate of voltage changes and oscillation of the generator's speed are very high and the system is practically unstable.

Table 1: The Four-Generator data without PSS

Generators	Eigenvalues	Frequencies	Damping Ratios
1,2,3,4	$\pm 3.994j$	0.6354	-0.0134
3,4	$\pm 7.274j$	1.1577	0.0668
1,2	$\pm 7.323j$	1.655	0.0658

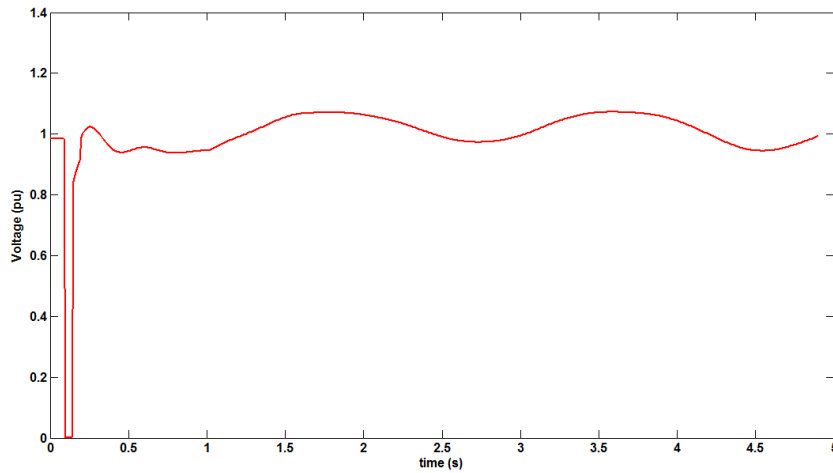


Fig. 3: The bus voltage changes after the fault at bus-3 without PSS

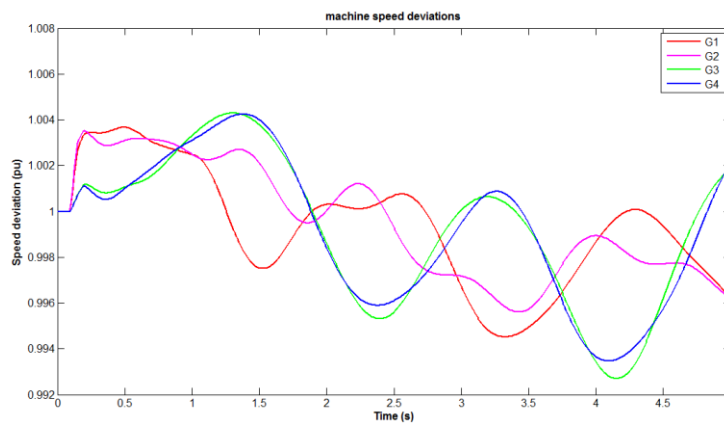


Fig. 4: Generator speed changes after the fault at bus-3 without PSS.

7.2 Case 2: The Stability of Four-Generators with PSS Based On (MHS)

In this case, PSS is installed on each generator which will guarantee stability of the system and restrain unwanted oscillations. Thus, the PSS parameter is set based on the (MHS) algorithm. The results of the modified harmonic search for the parameters are presented in Table 2. From Fig. 5 and Fig. 6 it is clear that the oscillations due to disturbances are completely repressed and the dynamic state of the system improved. All this happened only after installation of the PSS. Figure 7 explains the convergence of the objective function with MHSA and HSA. From this figure, it is clear that MHSA shows superior performance over HSA. The proposed method obtained the solution after 210 iterations while the HSA reached the solution after 300 iterations. This speed in finding the optimal solution is very important in the stability of the system.

Table 2: Optimal Designed Parameters of MHS

Generator	T ₄	T ₃	T ₂	T ₁	T _w	K
1	0.01	0.08	0.01	0.07	10	100
2	0.02	0.1	0.02	0.09	10	127
3	0.01	0.1	0.01	0.1	10	148
4	0.02	0.08	0.02	0.12	10	95

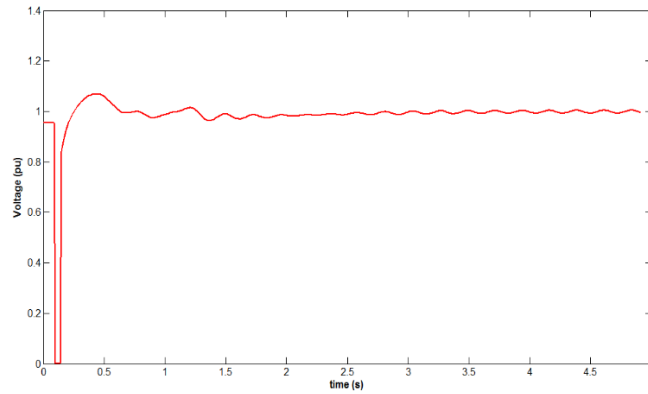


Fig. 5: Voltage changes on the bus number 3 with PSS.

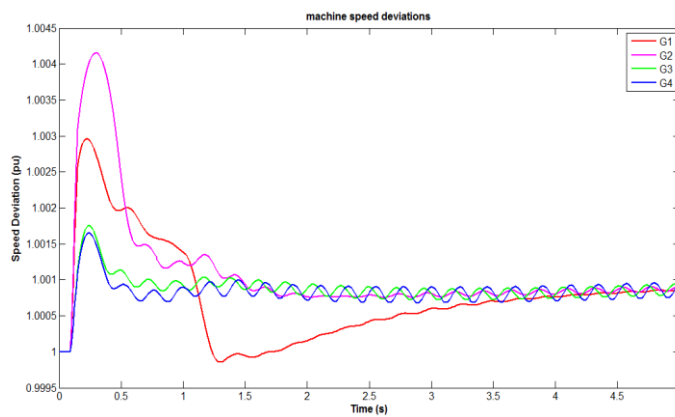


Fig. 6: Generator speed changes after the fault at bus 3 with PSS.

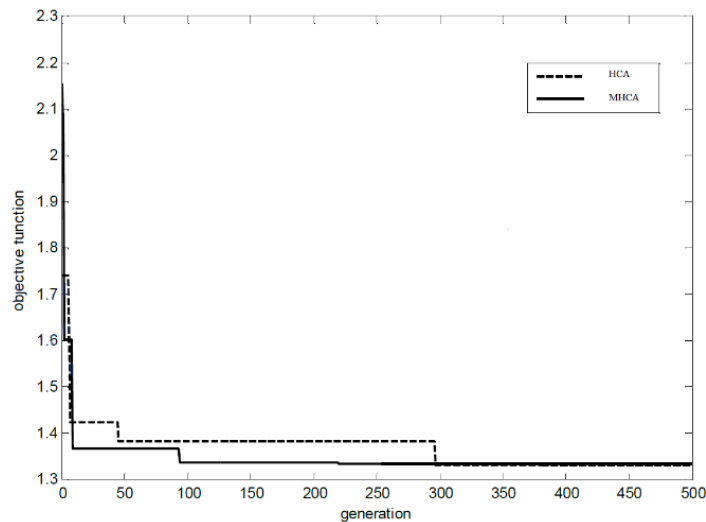


Fig. 7: Convergence characteristics of HSA and MHSA techniques.

Furthermore the above results are compared with those presented in [26] for the 4-generator system. In this reference, the parameters were obtained using the sensitivity analysis method. Table (3) shows the results of the special system values with stabilizer in the two studies. From Fig. 8-9 and Table 3, it is very clear that the performance of the PSS

designed using MHS is far better compared to the PSS designed using Sensitivity Approach (TSA) and Harmony Search.

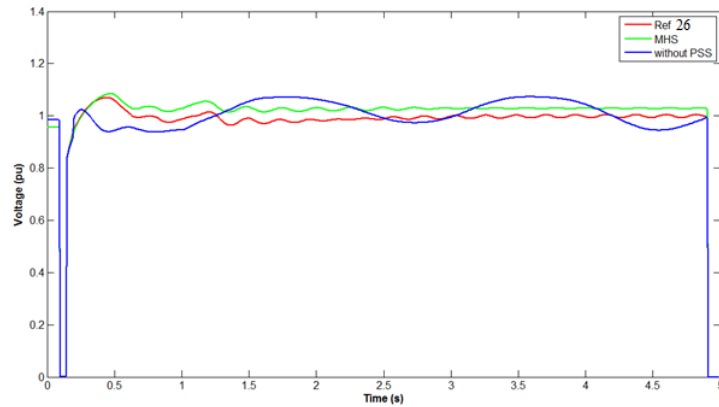


Fig. 8: Voltage changes at bus 3 after fault in the three-phase system.

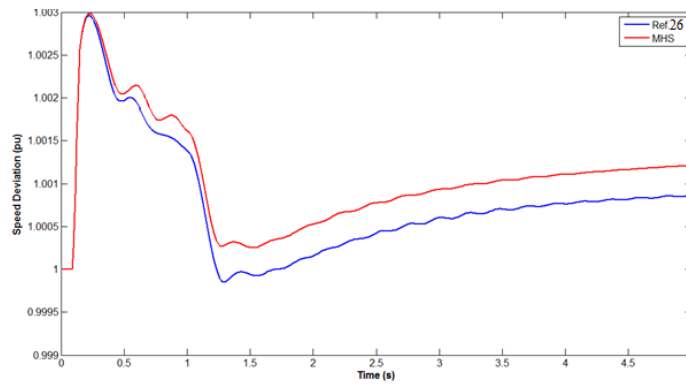


Fig. 9: the changes of the first generator speed.

Table 3: Eigenvalues of the System 4 Generators for Modified Harmony Search Method and Trajectory Sensitivity Approach

Generators	Eigenvalues	Frequencies	Damping Ratios
MHS	$-2.138 \pm j5.738$	0.856	0.397
	$-2.714 \pm j6.736$	0.891	0.391
	$-1.130 \pm j4.214$	0.637	0.268
Trajectory Sensitivity Approach (TSA)[26]	$-1.938 \pm j5.738$	0.913	0.319
	$-2.165 \pm j5.936$	0.945	0.343
	$-0.530 \pm j3.504$	0.558	0.149

8. CONCLUSION

Transient and small-signal stability are critical in power system operation and control studies due to their impact on consumers. Thus power system stabilizers could be used to solve this issue. A modified harmonic search algorithm was proposed to tune the PSS parameters to overcome the drawbacks of the previously suggested algorithms. The MHS results show that adjusted stabilizers have improved performance. The proposed method was applied to a system of four generators. The MHS algorithm results were compared

with the results of the sensitivity analysis method, which was previously suggested for this purpose. The comparison indicates the superiority of this algorithm to obtain the optimal parameters to set the stabilizer.

REFERENCES

- [1] Elazim SMA, Ali ES. (2016) Optimal power system stabilizers design via cuckoo search algorithm. *International Journal of Electrical Power & Energy Systems*.75:99-107.
- [2] Chitara D, Niazi KR, Swarnkar A, Gupta N. (2018) Cuckoo search optimization algorithm for designing of a multimachine power system stabilizer. *IEEE Transactions on Industry Applications*.54(4):3056-3065.
- [3] Chaib L, Choucha A, Arif S. (2017) Optimal design and tuning of novel fractional order PID power system stabilizer using a new metaheuristic Bat algorithm. *Ain Shams Engineering Journal*.8(2):113-125.
- [4] Radmehr M, Mohammadjafari M, GhadiSahebi MR. (2018) LOC-PSS Design for Improved Power System Stabilizer. *Journal of Applied Dynamic Systems and Control*.1(1):47-54.
- [5] Ray PK, Paital SR, Mohanty A, Eddy FYS, Gooi HB. (2018) A robust power system stabilizer for enhancement of stability in power system using adaptive fuzzy sliding mode control. *Applied Soft Computing*.73:471-481.
- [6] Ali ES. (2014) Optimization of power system stabilizers using BAT search algorithm. *International Journal of Electrical Power & Energy Systems*.61:683-690.
- [7] Pattanaik JK, Basu M, Dash DP. (2019) Dynamic economic dispatch: a comparative study for differential evolution, particle swarm optimization, evolutionary programming, genetic algorithm, and simulated annealing. *Journal of Electrical Systems and Information Technology*.6(1):1.
- [8] Sambariya DK, Prasad R. (2015) Optimal tuning of fuzzy logic power system stabilizer using harmony search algorithm. *International Journal of Fuzzy Systems*.17(3):457-470.
- [9] Kumar A. (2015) Power system stabilizers design for multimachine power systems using local measurements. *IEEE Transactions on Power Systems*.31(3):2163-2171.
- [10] Bouchama Z, Essounbouli N, Harmas MN, Hamzaoui A, Saoudi K. (2016) Reaching phase free adaptive fuzzy synergetic power system stabilizer. *International Journal of Electrical Power & Energy Systems*.77:43-49.
- [11] Islam NN, Hannan MA, Shareef H, Mohamed A. (2017) An application of backtracking search algorithm in designing power system stabilizers for large multi-machine system. *Neurocomputing*.237:175-184.
- [12] Ke D, Chung CY. (2016) Design of probabilistically-robust wide-area power system stabilizers to suppress inter-area oscillations of wind integrated power systems. *IEEE Transactions on Power Systems*.31(6):4297-4309.
- [13] Soliman HM, Yousef HA. (2015) Saturated robust power system stabilizers. *International Journal of Electrical Power & Energy Systems*.73:608-614.
- [14] Yaghooti A, Buygi MO, Shanechi MHM. (2015) Designing coordinated power system stabilizers: A reference model based controller design. *IEEE Transactions on Power Systems*.31(4):2914-2924.
- [15] Farah A, Guesmi T, Abdallah HH, Ouali A. (2016) A novel chaotic teaching-learning-based optimization algorithm for multi-machine power system stabilizers design problem. *International Journal of Electrical Power & Energy Systems*.77:197-209.
- [16] Soliman M. (2015) Robust non-fragile power system stabilizer. *International Journal of Electrical Power & Energy Systems*.64:626-634.
- [17] Rahmatian M, Seyedtabaai S. (2019) Multi-machine optimal power system stabilizers design based on system stability and nonlinearity indices using Hyper-Spherical Search method. *International Journal of Electrical Power & Energy Systems*.105:729-740.
- [18] Peres W, Júnior ICS, Passos Filho JA. (2018) Gradient based hybrid metaheuristics for robust tuning of power system stabilizers. *International Journal of Electrical Power &*

- Energy Systems.95:47-72.
- [19] Wang G-G, Gandomi AH, Zhao X, Chu HCE. (2016) Hybridizing harmony search algorithm with cuckoo search for global numerical optimization. *Soft Computing*.20(1):273-285.
- [20] Gao K-Z, Suganthan PN, Pan Q-K, Chua TJ, Cai TX, Chong C-S. (2016) Discrete harmony search algorithm for flexible job shop scheduling problem with multiple objectives. *Journal of Intelligent Manufacturing*.27(2):363-374.
- [21] Rezaie H, Kazemi-Rahbar MH, Vahidi B, Rastegar H. (2019)Solution of combined economic and emission dispatch problem using a novel chaotic improved harmony search algorithm. *Journal of Computational Design and Engineering*.6(3):447-467.
- [22] Wang L, Hu H, Liu R, Zhou X. (2019) An improved differential harmony search algorithm for function optimization problems. *Soft Computing*.23(13):4827-4852.
- [23] J. Yi, L. Gao, X. Li, and J. Gao, ‘An efficient modified harmony search algorithm with intersect mutation operator and cellular local search for continuous function optimization problems’, *Applied Intelligence*, vol. 44, no. 3, pp. 725–753, 2016.
- [24] Yi J, Gao L, Li X, Gao J.(2016) An efficient modified harmony search algorithm with intersect mutation operator and cellular local search for continuous function optimization problems. *Applied Intelligence*.44(3):725-753.
- [25] C. Canizares et al., ‘Benchmark models for the analysis and control of small-signal oscillatory dynamics in power systems’, *IEEE Transactions on Power Systems*, vol. 32, no. 1, pp. 715–722, 2016.
- [26] Yuan SQ, Fang DZ. (2009) Robust PSS parameters design using a trajectory sensitivity approach. *IEEE Transactions on Power Systems*.24(2):1011-1018.

PASSIVELY Q-SWITCHED YTTERBIUM-DOPED FIBER LASER EMPLOYING SAMARIUM OXIDE AS SATURABLE ABSORBER

KHAIRUL NIZAM RUSDI¹, AFIQ ARIF AMINUDDIN JAFRY², NUR FARHANAH ZULKIPLI³, FARINA SAFFA MOHAMAD SAMSAMNUN³, MOHAMAD BADROL HISYAM MAHYUDDIN³, SULAIMAN WADI HARUN³, MOHD SHAHNAN ZAINAL ABIDIN¹ AND NORAZLINA SAIDIN¹

¹Department of Electrical and Computer Engineering,
International Islamic University Malaysia, Jalan Gombak, 53100 Kuala Lumpur, Malaysia

²Department of Physics, Faculty of Science, Universiti Teknologi Malaysia,
81310 Skudai, Johor, Malaysia

³Photonics Engineering Laboratory, Department of Electrical Engineering,
Faculty of Engineering, University of Malaya, 50603 Kuala Lumpur, Malaysia

*Corresponding author: norazlina@iium.edu.my

(Received: 13th March 2020; Accepted: 13th August 2020; Published on-line: 4th January 2021)

ABSTRACT: The rapid developments in transition metal dichalcogenide materials as saturable absorbers (SAs) have been reported to be efficient materials for generating Q-switched fiber lasers. In this paper, we report on the use of samarium oxide (Sm_2O_3) saturable absorber (SA) for 1-micron Q-switched fiber laser generation. The Sm_2O_3 thin film SA was constructed in-house through which the Sm_2O_3 powder was mixed and stirred in polyvinyl alcohol (PVA) solution. It was then integrated into the ytterbium-doped fiber laser (YDFL) ring cavity, hence producing a sequence of Q-switched pulsed lasers at 1062.49 nm wavelength. The stable pulse train appeared from 69.97 to 111.1 kHz between the applied pump power of 57 mW to 96 mW. The signal-to-noise ratio (SNR) of 38.56 dB was recorded at the 57 mW pump power, whereas the pulse energy raised until 15.21 nJ at 96 mW. These results showed that the Sm_2O_3 could be a favourable SA material to initiate Q-switched ytterbium-doped pulsed fiber laser.

ABSTRAK: Perkembangan pesat dalam bahan logam peralihan *dichalcogenide* sebagai bahan penyerap boleh larut (SAs) telah dilaporkan sebagai kaedah yang berkesan bagi menjana laser fiber *Q-switched*. Kajian ini menggunakan *samarium* oksida (Sm_2O_3) *saturable absorber* (SA) bagi menjana laser gentian *Q-switched 1-Micron*. Filem nipis Sm_2O_3 SA telah dihasilkan melalui campuran serbuk Sm_2O_3 ke dalam cecair polivinil alkohol (PVA) dalam persekitaran makmal. Kemudian, ia diintegrasikan ke dalam rongga gelang laser gentian *dop-ytterbium* (YDFL), lalu menghasilkan denyut laser *Q-switched* stabil pada jarak gelombang 1062.49 nm. Denyutan stabil muncul dari 69.97 kepada 111.1 kHz pada kuasa pam yang dikenakan antara 57 mW hingga 96 mW. Nisbah isyarat-hingar (SNR) pada 38.56 dB telah direkodkan pada pam kuasa 57 mW, sementara denyut tenaga ditingkatkan kepada 15.21 nJ pada 96 mW. Keputusan menunjukkan Sm_2O_3 merupakan bahan SA penggalak yang memuaskan bagi menjana denyut laser gentian *dop-ytterbium Q-switched*.

KEYWORDS: *Q-switched; Sm_2O_3 saturable absorber; Samarium oxide; Ytterbium-doped fiber pulsed laser*

1. INTRODUCTION

A Q-switched laser operating in the 1 to 2 μm region have gained research attention due to their vast applications in material fabrication, radar transmission, corrective eye surgery, remote sensing and biomedicine [1-5]. Generation of Q-switched lasers takes place once the losses inside the resonator surpass the gain in active medium, therefore bringing the quality factor to a low level. The losses are often introduced by acousto- or electro-optic active modulation that require externally driven components such as shutters, mirrors, and chopper wheels. These components are necessary as a voltage-controlled modulator to control the intracavity losses [6, 7]. Although the frequencies of these active modulation techniques for pulsed laser generation are reliable and adjustable, they however acquired disadvantages; e.g being bulky and costly [8]. On the other hand, the passive method introduces simpler techniques and low fabrication costs. Normally, a material-based saturable absorber (SA) is preferred for fabricating a real SA. Its simpler implementation is such that the fabricated SA can be placed within the laser cavity for pulse generation. This simpler technique might stimulate the research on new SA materials for generating a pulsed fiber laser.

Studies on two-dimensional (2D) materials found that they have strong optical saturable absorption as is the case with carbon nanotubes (CNT) and graphene which are used as saturable absorbers (SA) that function as the nanotube film thickness. Transition metal dichalcogenides (TMDs) for instance; molybdenum diselenide (MoSe_2), tungsten diselenide (WSe_2), molybdenum disulfide (MoS_2) and tungsten disulfide (WS_2) have shown a good nonlinear absorption ability [9-11]. In view of the fact that layered TMDs have a bandgap in the perceptible frequency range, they developed a strong saturable absorption at visible wavelengths. With bandgap modification for laser generation through mechanical exfoliation, the few-layers of TMDs are turned into atomically thin layers. This then makes them compatible with pulsed initiation in the near-infrared region [12, 13]. Likewise, black phosphorus (BPs) was also proposed to initiate Q-switching and mode-locked operation [14,15]. An orthorhombic structure of BPs exhibits excellent chemical stability with the absence of high heat supply, and wide optical tunability in the near-infrared region [16]. However, according to [17] BPs are highly sensitive to their environment, especially water, which can disrupt its stability as an effective SA for all-fiber laser configurations. Hisyam et al. [15] reported a stable generation of mode-locked ytterbium-doped fiber lasers (YDFL) using BP layers as a SA, subsequently producing stable mode-locked pulses centered at 1085.58 nm with a repetition rate and pulse energy of 13.5 MHz and 5.93 nJ, respectively. Besides, Luo et al. [18] also reported on generating all-fiber pulsed lasers at visible-wavelengths using 2D materials based on layered TMDs (WS_2 , MoS_2 and MoSe_2) as a SA. The work successfully generated a visible-wavelength passive Q-switching laser at 635 nm with a repetition rate of 232 to 512 kHz, and pulse width and pulse energy of ~ 200 ns and 28.7 nJ, respectively. Of all reported 2D material-based SAs for pulsed fiber laser generation, very few reported a Q-switched laser generation for the 1-micron region that utilize TMD materials.

Use of ytterbium (Yb) ions for 1 μm laser generation is widely known for its wide spectral coverage in short-band wavelengths from 0.98 to 1.2 μm [19, 20]. Ytterbium-doped fiber possesses a low quantum defect due to its 2-level energy diagram and is therefore capable of providing high optical efficiencies and producing very low thermal load [21]. Apart from that, aluminosilicate glass containing Yb ions has broader emission with wavelengths longer than 1070 nm. It will be more susceptible to obtain lasing in the longwave spectral region allowing the glass to achieve a high level of inversion population which is needed to make the YDF transparent [20]. Therefore, most reported works for high-

power YDFs operated in 1060 to 1090 nm for the low absorption of Yb ions [22-24]. This distinct optical characteristic of YDF and the wide application in the wavelength region has attracted much attention for researchers to focus on YDF. The Q-switching generation in the 1-micron region using TMD materials as a Q-switcher is not widely reported. Apart from exhibiting excellent choice for Q-switching generation, most of the TMDs present complex fabrication procedures, low damage threshold, low modulation depth, and wavelength-dependent emission ability. Thus, the search for a new material as SA in the all-fiber laser cavity is ultimately relevant. Previously, rare-earth oxide (REO) had also been manipulated as SA in near-infrared pulsed laser generation (1-2 μm) [25, 26]. Das et al. [27] demonstrated Samarium-doped fiber as SA for ytterbium-doped fiber lasers which successfully generated pulses in the 1 μm range. With a fast response time of 5 ns, Samarium oxide (Sm_2O_3) has excellent nonlinear absorption ability of 33% in a 1.5 μm regime [28, 29]. Its thin film is reported to have high chemical and thermal stability, making it efficient for pulsed laser generation due to its ability to withstand high power illumination from laser pumps [30]. The excellent performance of Sm_2O_3 thin film suggests its capability to initiate pulses in the near-infrared region as a new SA. In view of this, we demonstrated the Sm_2O_3 thin film as SA in YDFL generating Q-switched with a pulse width as short as 4.9 to 2.86 μs corresponding to a repetition rate of 69.97 to 111.1 kHz. To the best of our knowledge, this work marks among the earliest demonstrations employing Sm_2O_3 as SA for Q-switching operation of ytterbium doped fiber laser. We hope that this work will open up other insights into research on 2D material photonics.

2. FABRICATION METHOD

Samarium oxide (Sm_2O_3) PVA films were synthesized by mixing the Sm_2O_3 powder into a polyvinyl alcohol (PVA) solution [29]. Initially, 120 ml of distilled water was used to dissolve 1 g of PVA powder. This was done for 30 minutes on a magnetic mixer with speed and temperature of 300 rpm and 100 $^\circ\text{C}$, respectively, until the PVA powder completely dissolved and became a solution. Next, 50 mg of Sm_2O_3 grain was immersed into 50 ml of the prepared PVA solution and stirred by magnetic stirrer at a speed of 300 rpm for 12 hours. Finally, the Sm_2O_3 -PVA solution was sonicated for 1 hour using an ultrasonic bath. Upon completion, it was dispensed onto a petri dish and left to dry for 48 hours or more at room temperature, until it completely became a thin film. The synthesized Sm_2O_3 PVA film was characterized using the Field Emission Scanning Electron Microscope (FESEM), X-ray diffraction (XRD), linear absorption profile and nonlinear absorption profile. Figure 1(a) shows the XRD analysis of Sm_2O_3 film.

Figure 1(a) shows the diffraction peaks observed at 29.11° , 40.79° , and 50.27° . They can be assigned at (4 0 1), (-5 1 1), and (0 2 0) planes of Sm_2O_3 . The high and strong peak patterns of Sm_2O_3 film XRD proves the successful implant of the Sm_2O_3 film onto the PVA polymer. Figure 1(b) shows a homogenous distribution of Sm_2O_3 particles and PVA solution observed by FESEM image. Figure 1(c) shows the absorption loss of about 6 dB near to 1040 nm, indicating the mode-locking process mainly corresponding to Sm_2O_3 . The nonlinear absorption profile of the Sm_2O_3 can be seen via the balanced twin-detector measurement as shown in Fig. 1(d). The point reference shows flat output transmission, while the Sm_2O_3 thin film SA shows the result of nonlinear transmission which fitted accordingly. The transmissions at various input intensities were recorded. The Sm_2O_3 thin film SA had a modulation depth of 33%, saturable intensity of 25 MW/cm^2 and a non-saturable absorption of 65%. The EDX data in Fig. 1(e) shows the element of samarium is 64.00% (Wt) and 15.51% (At), oxygen (O) and carbon (C) from PVA film is 32.68% (Wt) and 74.43% (At), 3.31% (Wt) and 10.06% (At), respectively. This data can confirm and

prove the presence of the samarium element in this PVA film. Such characteristics of the SA reveals the ability of Sm_2O_3 to act as good saturable absorber.

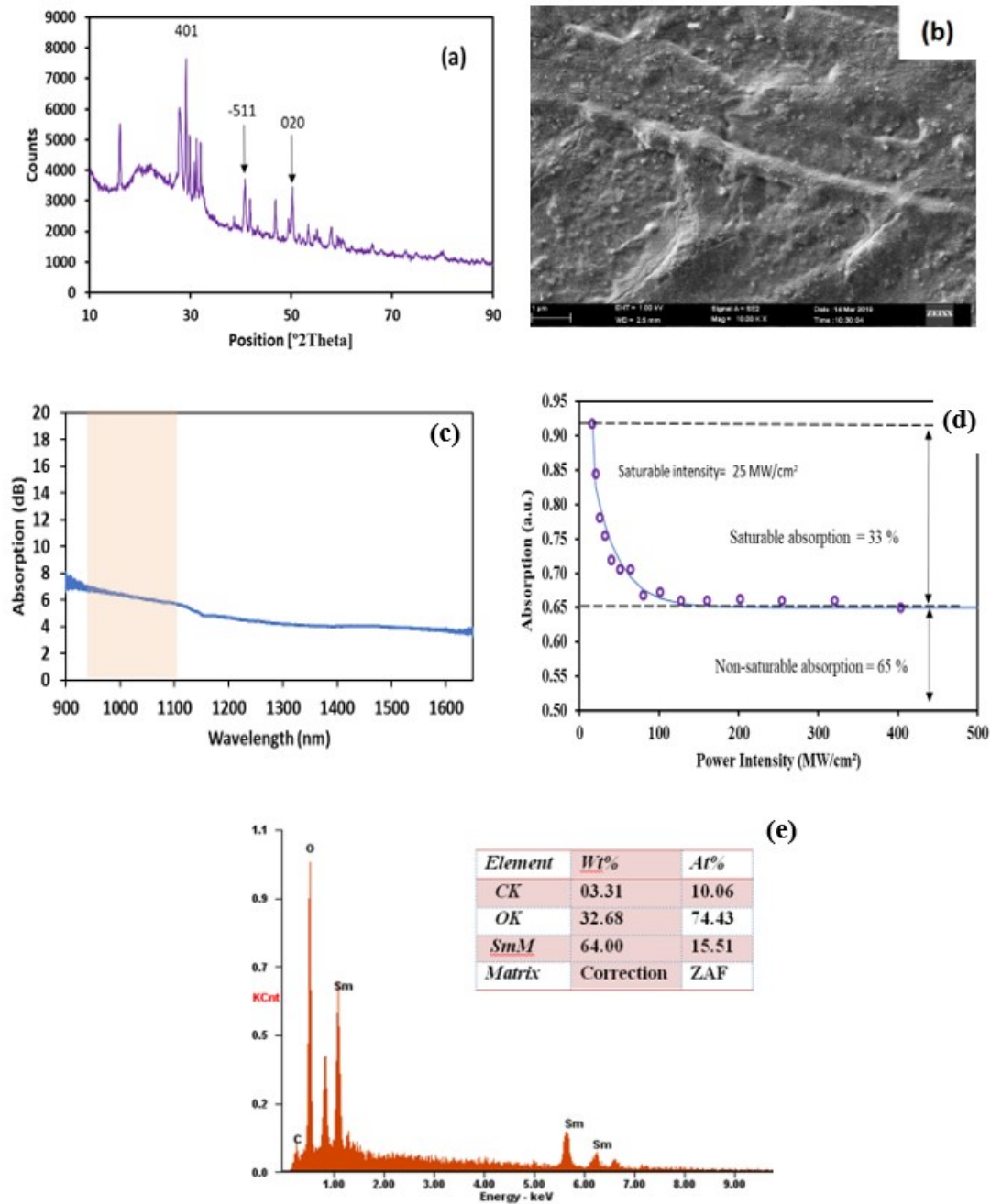


Fig. 1: Characterization of Sm_2O_3 PVA film as SA (a) XRD (b) FESEM (c) Linear absorption profile (d) Nonlinear absorption profile (e) Energy dispersive X-ray.

3. EXPERIMENTAL DEMONSTRATION

In order to perform a pulsed laser, the homemade Sm_2O_3 SA thin film was integrated in the all-fiber ring cavity laser setup. As shown in Fig. 2, the thin film SA that was placed between fiber ferrule was capped together using a fiber connector. Each end of the connector was spliced to 90/10 coupler and wavelength division multiplexing (WDM). The 90/10 coupler was used to allow 90% of the power to oscillate back in the resonator. The feedback power hit the SA when the amplified spontaneous emission gain oscillated in the resonator.

The 1064 nm wavelength division multiplexor (WDM) was spliced to the other end of the connector to form the resonator for oscillation. The 980/1064 nm WDM was used in the setup to compliment the 980nm laser diode and ~1064 nm wavelength laser that were built up from ytterbium-doped fiber (YDF) as a gain medium (2m), respectively. The isolator was placed after the YDF to prevent any unwanted signal feedback. The whole length of the YDFL cavity was approximately 9.5 m. The feedback process occurs continuously, hence accumulates the energy fed into the gain medium (YDF). When the resonator losses decrease until reaching saturation energy of the gain medium, the fiber laser will start to perform. In this experiment, an optical spectrum analyzer (Anritsu MS9710C, 0.6 - 1.75 μm) and optical power meter (PM100D THORLABS) were used to record the spectrum and power, respectively from the 10% output of the coupler. The photodetector (DET01CFC THORLABS InGaAs Biased Detector) was attached to it to record the time and frequency domain of Q-switched pulsed using an oscilloscope (GDS-3352 350 MHz 5GS/s) and radio frequency (RF) spectrum (Anritsu, 9 kHz - 7.8 GHz).

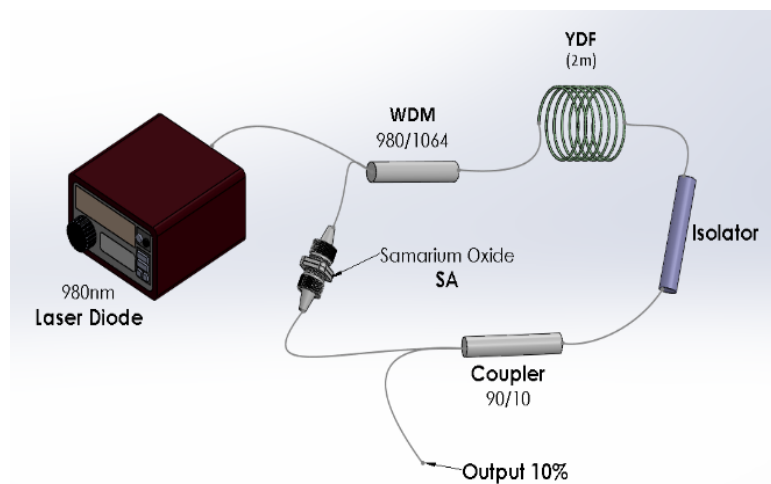


Fig. 2: The schematic for the Q-switched ytterbium laser setup incorporating Sm_2O_3 based saturable absorber (SA).

4. RESULTS AND DISCUSSION

By using homemade Sm_2O_3 SA, the stable Q-switching operation was obtained, as shown in figure 3. The generated Q-switched pulses exhibit a pulse duration between 4.9 to 2.86 μs . The pulse pattern and its characteristic display the normal features of Q-switched fiber lasers. Unlike a mode-locked laser, in Q-switching pulses, longer or shorter pulse duration is hard to determine with the modulation depth. However, it was suggested that the pulse width can be scaled down by preparing a SA with a higher modulation depth in a mode-locked case or having a short total cavity length. The inset of Fig. 3 shows a stable pulse to pulse spectral range of 14.4 μs which translates into a repetition rate of ~69.97 kHz, recorded when the pump power is 57 mW (at threshold). The pulse repetition rate shown in Fig. 4(a) rises from 69.97 to 111.1 kHz, while pulse width declines and becomes narrower, in the range of 4.9-2.86 μs , as opposed to the repetition rate. Both outputs were plotted as a function of pump power ranging from 57 to 96 mW. In case of Q-switching operation, the increase in pump power would cause the repetition rate to increase. Higher pump power will increase the amplifier gain for YDF thereby contributing to the saturation of SA. The pulse energy was calculated given 8.96 nJ using an equation of

$$Q [J] = \frac{P_0}{f_r}$$

where P_0 is the average output power and f_r is the repetition rate.

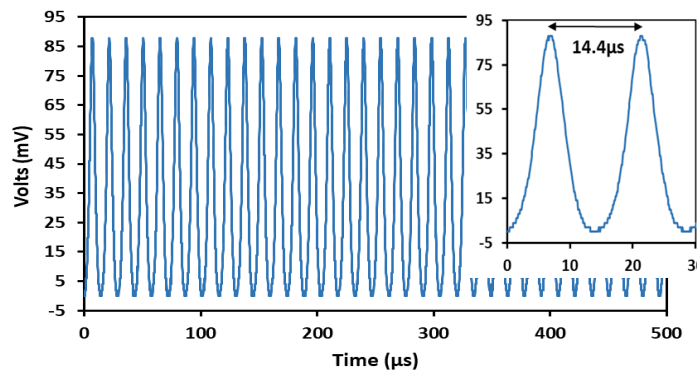
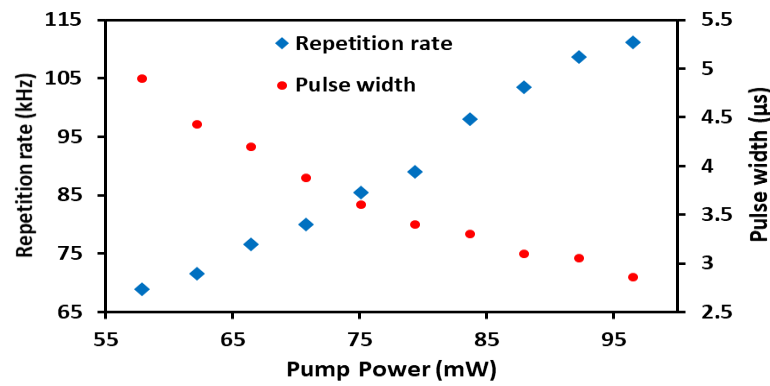
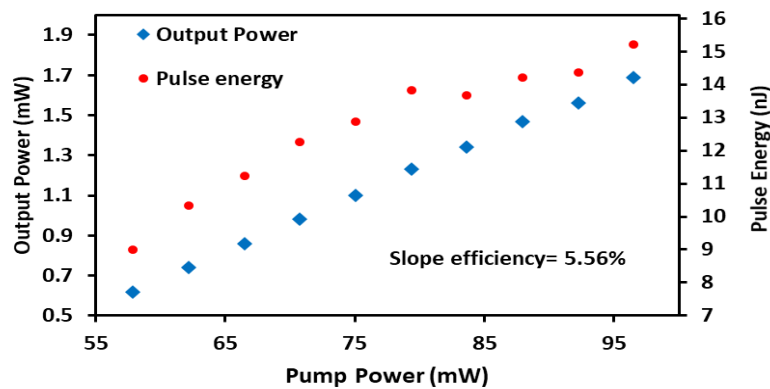


Fig. 3: The measured oscilloscope trace for the Q-switched laser at 69.97 kHz. The inset shows the free spectral range for successive pulses.



(a)



(b)

Fig. 4: Q-switched performance in terms of (a) pulse width repetition rate, (b) pulse energy and output power, versus pump power.

Stable passively Q-switched operation was successfully obtained when the pump power was tuned in the range of 57–96 mW, resulting in the output power from 0.62 to 1.69 mW, as can be seen in Fig. 4(b). The laser efficiency calculated from the output power versus pump power was 5.56% whereas the pulse energy trend was increasing from 8.96–15.21 nJ.

Figure 5 and its inset exhibit the output laser power spectrum with and without the Sm_2O_3 thin film, respectively. The central wavelength was positioned at 1062.49 nm, similar to the one observed in the Q-switched laser (with Sm_2O_3) exhibiting FWHM of ~ 0.1 nm. The threshold power of the continuous wave (CW) was recorded to be 43 mW and the Q-switched laser could be observed via oscilloscope at the pump power of 57 mW after further increment. The pulsed laser was successfully detected for 10 consecutive readings and sustained up to 96 mW. However, the Q-switched pulsed laser showed instability and the pulses diminished when the pump power was increased further. In order to check whether our Sm_2O_3 SA was able to withstand higher power, the pump power was increased to the maximum allowable threshold, which is 200 mW. As we tuned back the power to 96 mW, the Q-switched pulses were observed as before. Therefore, it is confirmed that the high pump power did not cost the perseverance of our homemade Sm_2O_3 thin film SA. The excellent properties from our Sm_2O_3 SA and high bandgap energy of 4.33 eV [30] contribute to the realization of Q-switched fiber laser in the 1-micron region. Nonetheless, if the non-saturable losses could be reduced, the fiber laser performance might be improved.

Figure 6 recorded the relative RF spectrum analyzer when the pump power was 57 mW within 750 kHz span measured using a 1 kHz resolution bandwidth (RBW) and 300 Hz video bandwidth (VBD). The signal-to-noise (SNR) ratio of 38.56 dB was observed at the fundamental RF peak when the repetition rate was 69.97 kHz. This result indicates a stable Q-switching operation. The harmonics in the RF spectrum decrease linearly before disappearing at the ninth harmonic. In this work, we also verified the generation of Q-switching operation by taking out the connector that contains the SA. When the pump power was turned on up to 200 mW, no pulse was observed, however, when the SA was restored, the Q-switched pulses were detected. Hence, our Q-switched pulse is confirmed due to our homemade Sm_2O_3 SA.

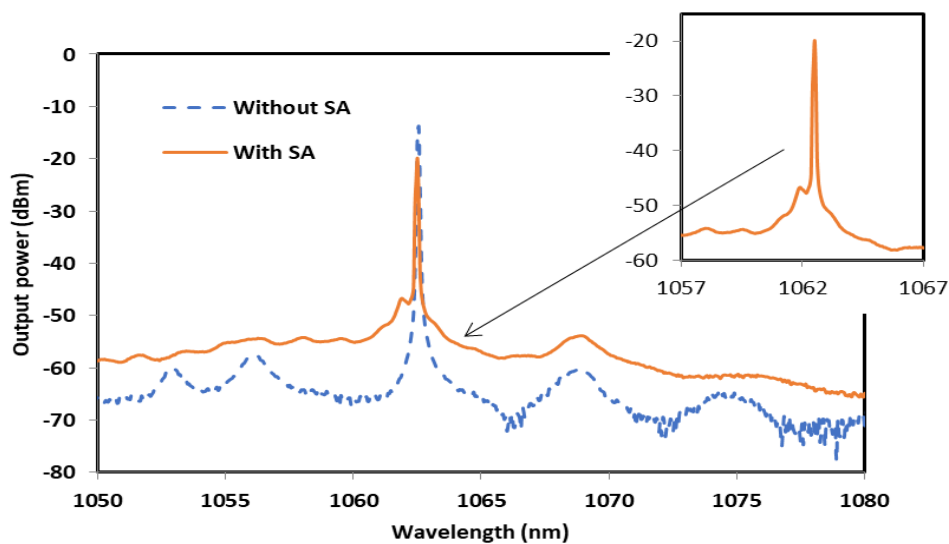


Fig. 5: Spectrum of CW laser (without SA) and Q-switched laser (with SA).

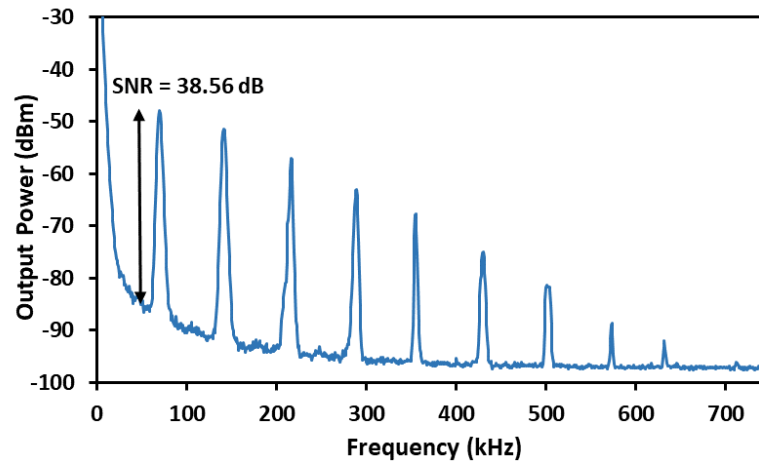


Fig. 6: Q-switched YDFL RF spectrum when the pump power is 57 mW.

5. CONCLUSION

This work successfully demonstrated a new 2D material, Sm_2O_3 as a SA to generate passive Q-switching operation for YDFL. The Sm_2O_3 based SA was embedded with a PVA solution to form the Sm_2O_3 thin film. A piece of Sm_2O_3 SA was attached between connectors and placed in the YDFL resonator. The Q-switching operation was observed at a 1062.49 nm wavelength and the pulsed fiber laser was initiated at 57 mW. The pulse width and repetition rate were obtained in the range of 4.9-2.86 μs and 69.97-111.1 kHz, respectively. The pulse energy was calculated as a change in output power over repetition rate, therefore giving the acceptable pulse energy ranging from 8.96 to 15.21 nJ. A stable pulse generation was confirmed by a high SNR of 38.56 dB. Our results suggest that the excellent properties of Sm_2O_3 has led to the pulsed fiber laser generation in the 1-micron region. The outcome of this research may promote other related research and applications in the area of material cutting and manufacturing processes.

ACKNOWLEDGEMENT

This work was supported by the Ministry of Higher Education (MOHE), Malaysia under the Fundamental Research Grant Scheme (FRGS), grant no. [FRGS/1/2018/TK04/UIAM/03/1].

REFERENCES

- [1] Raimondi MT, Eaton SM, Nava MM, Laganà M, Cerullo G, Osellame R, (2012). Two-photon laser polymerization: from fundamentals to biomedical application in tissue engineering and regenerative medicine. *Journal of Applied Biomaterials & Functional Materials*, 10(1): 56-66.
- [2] Shih PT, Chen J, Lin CT, Jiang WJ, Huang HS, Peng PC, Chi S, (2009). Optical millimeter-wave signal generation via frequency 12-tupling. *Journal of Lightwave Technology*, 28(1): 71-78.
- [3] Hodge C, McAlinden C, Lawless M, Chan C, Sutton G, Martin A (2015). Intraocular lens power calculation following laser refractive surgery. *Eye and Vision*, 2(1): 7.
- [4] Masket S, Masket SE. (2006). Simple regression formula for intraocular lens power adjustment in eyes requiring cataract surgery after excimer laser photoablation. *Journal of Cataract & Refractive Surgery*, 32(3): 430-434.
- [5] Walsh BM, Lee HR, Barnes NP. (2016). Mid infrared lasers for remote sensing applications. *Journal of Luminescence*, 169: 400-405.

- [6] Al-Masoodi AH, Ahmed MH, Latiff AA, Azzuhri SR, Arof H, Harun SW. (2017). Passively mode-locked ytterbium-doped fiber laser operation with few layer MoS₂ PVA saturable absorber. *Optik*, 145: 543-548.
- [7] Kuznetsov AG, Podivilov EV, Babin SA. (2015). Actively Q-switched Raman fiber laser. *Laser Physics Letters*, 12(3): 035102.
- [8] Keller U (2003). Recent developments in compact ultrafast lasers. *Nature*, 424(6950): 831-838.
- [9] Hu P, Liu F, Huang Y, Liu Y, Han K, Zhang F, Liu X. (2019). Passively Q-switched ytterbium-doped fiber laser operating at 1120 nm by molybdenum disulfide saturable absorber. *Optik*, 189: 97-102.
- [10] Liu W, Liu M, Han H, Fang S, Teng H, Lei M, Wei Z. (2018). Nonlinear optical properties of WSe₂ and MoSe₂ films and their applications in passively Q-switched erbium doped fiber lasers. *Photonics Research*, 6(10): C15-C21.
- [11] Wang QH, Kalantar-Zadeh K, Kis A, Coleman JN, Strano MS. (2012). Electronics and optoelectronics of two-dimensional transition metal dichalcogenides. *Nature Nanotechnology*, 7(11): 699.
- [12] Aiub EJ, Steinberg D, de Souza EA, Saito LA. (2017). 200-fs mode-locked Erbium-doped fiber laser by using mechanically exfoliated MoS₂ saturable absorber onto D-shaped optical fiber. *Optics Express*, 25(9): 10546-10552.
- [13] Khazaeinezhad R, Kassani SH, Jeong H, Yeom DI, Oh K. (2015). Femtosecond soliton pulse generation using evanescent field interaction through Tungsten disulfide (WS₂) film. *Journal of Lightwave Technology*, 33(17): 3550-3557.
- [14] Al-Masoodi AH, Yasin M, Ahmed MH, Latiff AA, Arof H, Harun SW. (2017). Mode-locked ytterbium-doped fiber laser using mechanically exfoliated black phosphorus as saturable absorber. *Optik*, 147: 52-58.
- [15] Hisyam MB, Rusdi MF, Latiff AA, Harun SW. (2016). Generation of mode-locked ytterbium doped fiber ring laser using few-layer black phosphorus as a saturable absorber. *IEEE Journal of Selected Topics in Quantum Electronics*, 23(1): 39-43.
- [16] Li S, Yin Y, Lewis E, Garrell G, Wang P. (2019). A twelve-wavelength Thulium-doped fibre laser based on a microfibre coil resonator incorporating black phosphorus. *Optics Communications*, 437: 342-345.
- [17] Island JO, Steele GA, van der Zant HS, Castellanos-Gomez A. (2015). Environmental instability of few-layer black phosphorus. *2D Materials*, 2(1): 011002.
- [18] Luo Z, Wu D, Xu B, Xu H, Cai Z, Peng J, Weng J, Xu S, Zhu C, Wang F, Sun Z. (2016). Two-dimensional material-based saturable absorbers: towards compact visible-wavelength all-fiber pulsed lasers. *Nanoscale*, 8(2): 1066-1072.
- [19] Pask HM, Carman RJ, Hanna DC, Tropper AC, Mackechnie CJ, Barber PR, Dawes JM. (1995). Ytterbium-doped silica fiber lasers: versatile sources for the 1-1.2/spl mu/m region. *IEEE Journal of Selected Topics in Quantum Electronics*, 1(1): 2-13.
- [20] Kurkov AS. (2006). Oscillation spectral range of Yb-doped fiber lasers. *Laser Physics Letters*, 4(2): 93.
- [21] Paschotta R, Nilsson J, Tropper AC, Hanna DC. (1997). Ytterbium-doped fiber amplifiers. *IEEE Journal of Quantum Electronics*, 33(7): 1049-1056.
- [22] Yu H, Wang X, Tao R, Zhou P, Chen J. (2014). 1.5 kW, near-diffraction-limited, high-efficiency, single-end-pumped all-fiber-integrated laser oscillator. *Applied Optics*, 53(34): 8055-8059.
- [23] Yan P, Yin S, He J, Fu C, Wang Y, Gong M. (2011). 1.1-kW ytterbium monolithic fiber laser with assembled end-pump scheme to couple high brightness single emitters. *IEEE Photonics Technology Letters*, 23(11): 697-699.
- [24] Jeong YE, Sahu JK, Payne DN, Nilsson J. (2004). Ytterbium-doped large-core fiber laser with 1.36 kW continuous-wave output power. *Optics express*, 12(25):6088-6092.
- [25] Muhammad AR, Haris H, Arof H, Tan SJ, Ahmad MT, Harun SW. (2018). All-fibre Q-switching YDFL operation with bismuth-doped fibre as saturable absorber. *Journal of Modern Optics*, 65(8): 946-950.

- [26] Zhang H, Lu SB, Zheng J, Du J, Wen SC, Tang DY, Loh KP. (2014). Molybdenum disulfide (MoS₂) as a broadband saturable absorber for ultra-fast photonics. *Optics express*, 22(6):7249-7260.
- [27] Das G, Chaboyer ZJ, Navratil JE, Drainville RA. (2015). Passively Q-switched Yb-and Sm-doped fiber laser at 1064 nm. *Optics Communications*, 334:258-264.
- [28] Preda CE, Ravet G, Mégret P. (2012). Experimental demonstration of a passive all-fiber Q-switched erbium-and samarium-doped laser. *Optics letters*, 37(4):629-631.
- [29] Zulkipli NF, Batumalay M, Samsamnun FS, Mahyuddin MB, Hanafi E, Izam TF, Khudus MI, Harun SW. (2019). Nanosecond Pulses Generation with Samarium Oxide Film Saturable Absorber. *Chinese Physics Letters*, 36(7):074203.
- [30] Dakhel AA. (2004). Dielectric and optical properties of samarium oxide thin films. *Journal of Alloys and Compounds*, 365(1-2):233-239.

AUTOMATIC FACIAL REDNESS DETECTION ON FACE SKIN IMAGE

IZZATI MUHIMMAH*, NURUL FATIKAH MUCHLIS
AND ARRIE KURNIAWARDHANI

Department of Informatics, Universitas Islam Indonesia, Yogyakarta, Indonesia

**Corresponding author: izzati@uii.ac.id*

(Received: 1st June 2020; Accepted: 2nd September 2020; Published on-line: 4th January 2021)

ABSTRACT: One facial skin problem is redness. On site examination currently relies on examination through direct observations conducted by doctors and the patient's medical history. However, some patients are reluctant to consult with a doctor because of shame or prohibitive costs. This study attempts to utilize digital image processing algorithms to analyze the patient's facial skin condition automatically, especially redness detection in the face image. The method used for detecting red objects on face skin for this research is Redness method. The output of the Redness method will be optimized by feature selection based on area, mean intensity of the RGB color space, and mean intensity of the Hue Intensity. The dataset used in this research consists of 35 facial images. The sensitivity, specificity, and accuracy are used to measure the detection performance. The performance achieved 54%, 99.1%, and 96.2% for sensitivity, specificity, and accuracy, respectively, according to dermatologists. Meanwhile, according to PT. AVO personnel, the performance achieved 67.4%, 99.1%, and 97.7%, for sensitivity, specificity, and accuracy, respectively. Based on the result, the system is good enough to detect redness in facial images.

ABSTRAK: Salah satu masalah kulit wajah adalah kemerahan muka. Pemeriksaan di lokasi kini bergantung pada pemeriksaan melalui pemerhatian langsung yang dilakukan oleh doktor dan sejarah perubatan pesakit. Namun, sebilangan pesakit enggan berunding dengan doktor kerana rasa malu atau kos yang terhad. Kajian ini cuba membuat sistem pengesanan kemerahan wajah yang dapat menganalisis keadaan wajah, terutama kemerahan, melalui gambar kulit wajah. Kaedah yang digunakan untuk mengesan objek merah pada kulit wajah bagi penyelidikan ini adalah kaedah Kemerahan. Keluaran kaedah Kemerahan akan dioptimumkan dengan pemilihan ciri berdasarkan luas, intensiti min RGB, dan intensiti min Hue Intensity. Set data yang digunakan dalam penyelidikan ini terdiri daripada 35 gambar wajah. Nilai pengesanan yang digunakan adalah kepekaan, kekhususan, dan ketepatan. Hasil yang diperoleh berdasarkan pakar dermatologi masing-masing adalah 54%, 99.1%, dan 96.2% untuk kepekaan, kekhususan, dan ketepatan. Sementara itu, PT. Selain itu, menurut kakitangan AVO 67.4%, 99.1%, dan 97.7%, bagi kepekaan, kekhususan, dan ketepatan, masing-masing. Berdasarkan dapatan kajian ini, sistem ini cukup baik bagi mengesan kemerahan pada gambar wajah.

KEYWORDS: *digital image processing; face skin; redness; redness method*

1. INTRODUCTION

Most people experience problems with their facial skin, such as redness [1]. Redness is one of the topics that are often discussed in either health and beauty articles or online consultation of health sites. To examine skin problems, we usually see the doctor for on-site

examination [2]. However, several patients are reluctant to consult with doctors for reasons such as fear and shame. As a result, they decide to treat their skin problem by themselves, commonly known as self-care. However, self-care can sometimes make the redness worse.

Examining facial skin redness using digital image processing is one solution [3-5]. One of the studies that has been conducted is assessment of Rosacea [4-5]. Rosacea is a skin redness problem [6]. Sainthillier et al. quantified the extent and intensity of the Rosacea using image processing and a neural network. The input images used in their study were localized in a specific area, namely the cheekbone area [4]. Furthermore, the investigator selected the zones affected by Rosacea on the image as well as the zones without signal (nonrosacea artefacts, e.g., white background). Those images were taken using a video-capillaroscope with a 50× magnification. Ledoux et al. utilized a perceptual color hit-or-miss transform for detecting Rosacea in skin image [5]. Input images used in their study were of a specific area of skin that contained Rosacea. Novin and Aarabi conducted research for skin redness analysis and pigmented skin lesions analysis [7]. This research analyzed body skin redness and the results were presented in the form of augmented reality on a smartphone. This research uses RGB color space to detect skin. Skin detection using this color space will also detect background objects that have a skin-like color and consider them to be skin as well. RGB color space is also used in the equation to find red regions in the skin. Pixels that have a red color above the threshold were set as part of the reddish object. In redness estimation a slider was provided to get a user defined threshold value.

This study attempts to utilize digital image processing algorithms to analyze the patient's facial skin condition automatically, especially redness detection. A facial redness detection is needed as early detection of skin redness conditions. It can help patients to analyze their facial skin abnormalities. In addition, in the future, the facial redness detection is expected to provide an overview of skincare products that are suitable for facial conditions.

2. METHODS AND DATA

2.1 Data

This research used secondary data obtained from the internet randomly and from beauty product companies (PT. AVO Innovation Technology). Data collected are human face images that have redness in their facial skin without certain race boundaries. The characteristics of the image used are color image, face position facing forward, and evenly distributed lighting. The dataset on this research is 35 images, two as training data and 32 as test data. The collected images are jpg, jpeg, png formats.

2.2 Redness Face Skin

Redness on skin can be caused by increase of hemoglobin saturation, increase in the diameter of the actual skin capillaries, or a combination of these factors [8]. Redness sometimes makes facial skin feel warm or gives a burning sensation. Redness can make a person feel unconfident with their own appearance. Redness on skin can occur due to inflammation, skin irritation, allergies, and bacteria [9].

2.3 Redness Method

Redness Method is feature extraction algorithm to calculate the redness value of each pixel. Eq. (1) is used to determine the redness value of each pixel [7].

$$Redness = \max \left\{ 0, \frac{2R - (G+B)}{R} \right\}^2 \quad (1)$$

where R = Red intensity in corresponding pixel; G = Green intensity in corresponding pixel; and B = Blue intensity in corresponding pixel.

2.4 K-means Clustering

Clustering is a method for dividing a set of data into groups. The clustering-based segmentation used in this research is K-Means. K in K-mean is the total number of clusters, which is randomly determined. K-means clustering will assign a data to a particular cluster according to the distance between the data and the centroid of the K cluster. Data will be assigned to a cluster whose centroid has the shortest distance to the data among the other cluster centroids [10].

2.5 Gaussian Filtering

Gaussian filtering is a pre-processing technique in digital image processing. This filter is usually used when an image has a lot of noise. Gaussian filtering reduces the noise by smoothing the image using the Gaussian principle [11]. Images smoothed using Gaussian filtering will usually change to a blurry image. A blurry image helps during the segmentation process because the intensity value of a pixel has a more uniform intensity value compared to its neighbors.

2.6 Canny Method

Canny method also known as Canny Edge Detection is a method in digital image processing to detect the edges of objects. Canny Edge Detection uses two thresholds so that it is possible to detect strong and weak edges [12]. Edges in digital image processing are found by representing a series of intensities in the image to a graph. If there are curves on the graph, this shows that there is a drastic change in the intensity of an image. This drastic change in intensity is marked as an edge.

2.7 Validation

The validation applied in this research is a Confusion Matrix with a Single Decision Threshold Method. This validation will compare the detection results performed by the system (predictive value) to the results of the diagnosis by the expert (actual value). According to Owens and Sox [13], sensitivity is used to measure the percentage of positive data that is correctly identified (both experts and systems detect the same redness object). Specificity is used to measure the percentage of negative data that is correctly identified (the system does not detect non-redness objects from candidates as redness objects). Accuracy is used to measure the percentage of the system's precision level in classifying data correctly (data that is predicted correctly by the system is divided by the total number of test data). The Confusion Matrix table can be seen in Table I.

Table 1: Confusion matrices

		Expert	
		True	False
System	True	TP	FP
	False	FN	TN

Based on the values of True Positive (TP), False Positive (FP), True Negative (TN), and False Negative (FN) we can get the values of sensitivity, specificity, and accuracy.

Following is the calculation for sensitivity, specificity, and accuracy which can be seen in Eq. (2), Eq. (3), and Eq. (4), respectively.

$$\text{Sensitivity} = \frac{TP}{TP+FN} \quad (2)$$

$$\text{Specificity} = \frac{TN}{TN+FP} \quad (3)$$

$$\text{Accuracy} = \frac{TP+TN}{TP+TN+FP+FN} \quad (4)$$

2.8 Methodology

The design of this research uses the flowchart seen in Fig. 1. The flowchart consists of four main processes. The input of the system is an RGB face image (Original Image) and the output of the system is a face image with a redness object that has been marked (Marked Image). The process consists of pre-processing (image resizing), separating face skin from the background (skin segmentation), redness object detection (feature extraction), and redness marking.

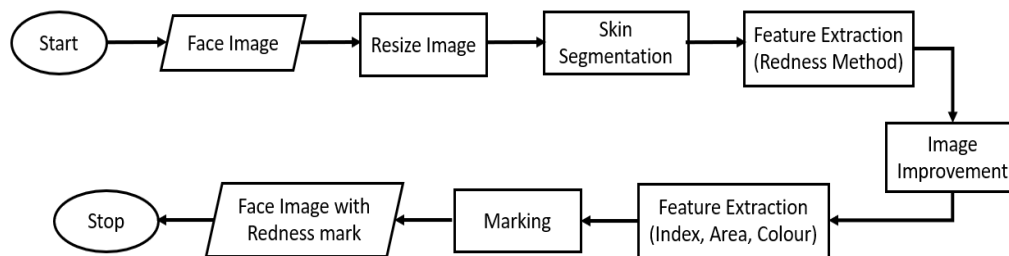


Fig. 1: Flowchart of Facial Redness Detection.

First, the input image is resized (Resized Image) when its number of rows or columns exceeds 500 pixels. If the number of rows exceeds 500 pixels and is longer than the columns, the row size will be reduced to 480 pixels and the column size will be adjusted. Conversely, if the column size exceeds the row size, then the column size will be reduced to 480 pixels and the row size will be adjusted. This process is needed because the dataset used is randomly obtained from the internet so the image size can vary.

Second, skin segmentation is the process of separating skin and non-skin objects. This skin segmentation assists the redness detection process to prevent the system from detecting any redness objects that are not in the skin area. This segmentation process separates skin and non-skin objects by clustering using K-Means in the HSV color space.

The Resized Image from the Resize image process is converted to the HSV color space (HSV Image). After being converted, HSV image is segmented according to a threshold value (Segmented HSV Image). The threshold values are less than and equal to 25 for the Hue layer and between 0.15 to 0.9 for the Saturation layer. Next, the Segmented HSV Image is clustered using K-Means clustering. The number of K for K-means clustering is 3, representing skin, non-skin, and background. Skin objects that will be taken from the results of K-means clustering are the cluster that has the highest number of members (Skin Image). This is done by assuming that the skin object has the broadest area in the face image.

Third, the Redness objects in the Skin Image are sought by identifying their characteristics. The Redness method [7] is utilized to calculate the redness value of each pixel in the Skin Image. The Redness method works on RGB images. First, the RGB value of each pixel in Skin Image is obtained. The redness value of each pixel is computed using

Eq. (1). Furthermore, the median of those redness values of all pixels in an image is determined as the threshold. Each pixel that has a value lower than the median will be omitted and each pixel that has a value greater than the median will be retained as a redness object candidate. An image with a redness object candidate is obtained (Redness Candidate Image), but there is noise in that image. A Gaussian filter with standard deviation value is 0.5 is applied in that Redness Candidate Image to get a smoother image and to reduce the noise (Gauss Image).

A Gaussian Image still has non-redness objects, so the object elimination process is needed. First, non-redness objects are eliminated according to pixel value in the Gaussian Image and Redness Image. If the pixel value in the Gaussian Image is equal to 76 (indicating the Redness object in a grayscale image), the pixel value in the Redness Image is retained. Otherwise, the pixel value in the Redness Image is changed to 0 (Gaussian Redness 1 Image). Second, the pixel values in the Gaussian Redness 1 Image that are lower than 1 are retained. Otherwise, the pixel value in the Gaussian Redness 1 Image is changed to 0 (Gaussian Redness 2 Image). Third, objects in the Gaussian Redness 2 Image that have an area wider than 90 are retained. Otherwise, the object is eliminated (Area Image). Fourth, non-redness objects are eliminated by a threshold value according to the RGB color value in the Original Image. The lower threshold value for Red intensity is Mean intensity value in the Red layer subtracted by the multiplication of the standard deviation of the intensity value in the Red layer by 1.32. Whereas the upper threshold value for Red intensity is Mean intensity value in the Red layer added to the multiplication of the standard deviation of the intensity value in the Red layer by 1.32. The same thing is done to find the lower and upper thresholds in the Blue and Green layers. If the redness object candidate in Area Image has an average intensity of RGB color in those range thresholds, the redness object candidate will be retained. Otherwise, it will be eliminated (RGB Eliminated Image). Fifth, non-redness objects are eliminated by a threshold value according to Hue color value in the Original Image. The lower threshold value for Hue intensity is Mean intensity value in the Hue layer subtracted by the multiplication of the standard deviation of the intensity value in the Hue layer by 1.16. Whereas the upper threshold value for Hue intensity is the Mean intensity value in the Hue layer added to the multiplication of the standard deviation of the intensity value in the Hue layer by 0.5. If the redness object candidate in the RGB Eliminated Image has an average intensity of hue color in those range thresholds, the redness object candidate will be retained. Otherwise, the object is eliminated (Hue Eliminated Image).

The last process is redness object marking using the Canny method. This process marks the redness objects obtained from the Hue Eliminated Image. First, the edge pixels of each redness object in Hue Eliminated Image are detected using the Canny method. In the Original Image, the intensity value of those edge pixels will be changed to red.

3. RESULTS AND DISCUSSION

All processes that have been designed in Fig. 1 were implemented into program code using MATLAB software. The first process is image resizing. The output of this process is the image that looks similar to the original image, but the size of the image is different. The maximum size, 500x500 pixels, is determined based on the training process that gives the best performance for this study. In addition, image size that exceeds 500x500 pixels will take a longer time for computation.

The HSV color space is used in the skin segmentation process because it can distinguish between brown, red, or other tones in the skin image. In addition, HSV is purest form of color based on wavelength that can truly describe the human colors. Images with non-black

and non-white skin color use hue values and saturation for the segmentation processes [14]. This research only uses the hue and saturation layers according to the data set used in this study. The parameter values of HSV are according to [15].

K-Means clustering is a process to group the results of the HSV segmentation into three clusters. In the skin segmentation process, there are still background objects in the image that are categorized as skin, so this process is needed. This clustering separates skin, non-skin, and background objects. The system will use the intensity value as a reference to group each pixel. The result of K-Means clustering can be seen in Fig. 2(a)-(c). The cluster that has the highest number of members, Fig. 2(a), is chosen. The cluster that has the highest number of members is chosen because face skin is the largest area in the image. Unfortunately, Fig. 2(a) has many holes. To close those holes, a region filling algorithm is applied. The result of skin segmentation can be seen in Fig. 2(d). The face skin can be segmented except the eyebrow. In the redness detection, this is not an issue because this study looks for the redness object that has red color characteristics.

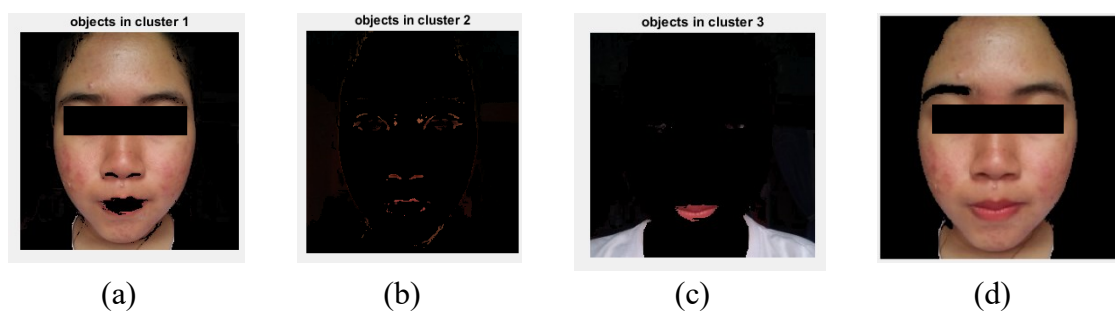


Fig. 2: K-Means Clustering Segmentation.

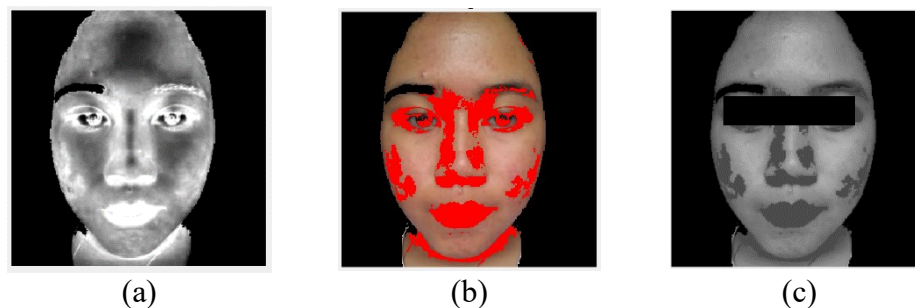


Fig. 3: Redness object detection (a) Redness method (b) Redness Pixel (c) Gaussian Filtering.

Next, the result of redness object detection with the Redness method can be seen in Fig. 3(a) and 3(b). This method identifies the redness pixel using dynamic parameters according to the RGB value of each pixel. It is different from using manual color segmentation which requires the researcher to search the redness range of each image. Gaussian Filtering is needed to eliminate scattered noise by smoothing the images. This filter can eliminate noise with results that look similar to the original image. Noise is eliminated without removing redness objects. The result of image improvement with Gaussian Filtering is shown in Fig. 3(c).

However, in Fig. 3(c) non-redness pixels are still marked, as in the eyes, nose, and lips. So, to eliminate non-redness pixels, another extraction is conducted. Non-redness objects eliminated based on pixel value in Gauss Image and Redness Image. Area, mean intensity

RGB, and Hue mean intensity of each object are calculated. The results of those processes are shown in Fig. 4(a)-4(d), respectively.

The result of the previous elimination process is able to eliminate several non-redness objects in the lips. A threshold of 90 for area is selected according to the smallest area of redness objects in the training data. The non-redness objects that are eliminated are quite numerous, with only the large objects left in the nose and neck. When using RGB intensity, the system can eliminate non-redness object in the neck. While using Hue intensity can eliminate the non-redness objects in the nose.

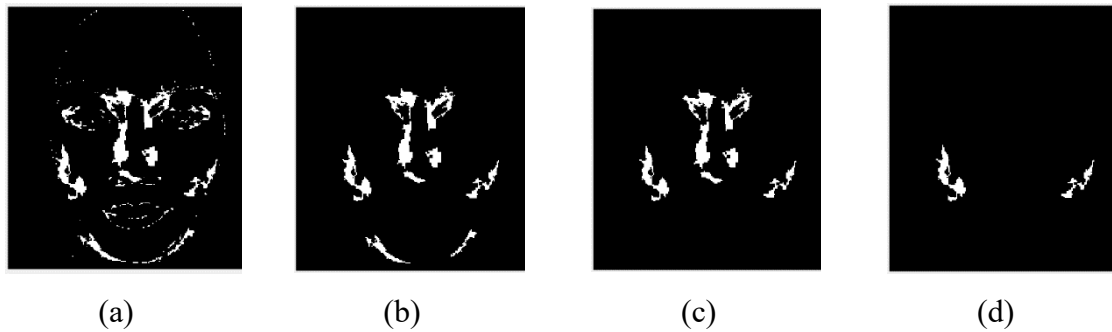


Fig. 4: Feature Extraction (a) by Index (b) by Area (a) by RGB color space (b) by Hue intensity.



Fig. 5: Redness object Marking.

The marking process aims to make it easier for users to find the redness object location in face image. The result of marking process can be seen in Fig. 5. The system interface for this study is shown in Fig. 6. The interface of this system consists of three panels. The first panel has an “Insert Image” button and the third panel has a “See Result” button to see the detection results.

The algorithm is validated using a confusion matrix that evaluates 33 test images. The validation process compares the results given by system to the expert’s diagnostic. The experts are a dermatologist from the Faculty of Medicine in Universitas Islam Indonesia and personnel of PT.AVO Innovation Technology. The validation results that compare to the dermatologist get low sensitivity value namely 54% but the specificity and accuracy values can achieve 99.1% and 96.2%. The validation results that compare to PT.AVO Skin Innovation Technology personnel reach similar results. The sensitivity, specificity, and accuracy values are 67.4%, 99.1%, and 97.7%, respectively.

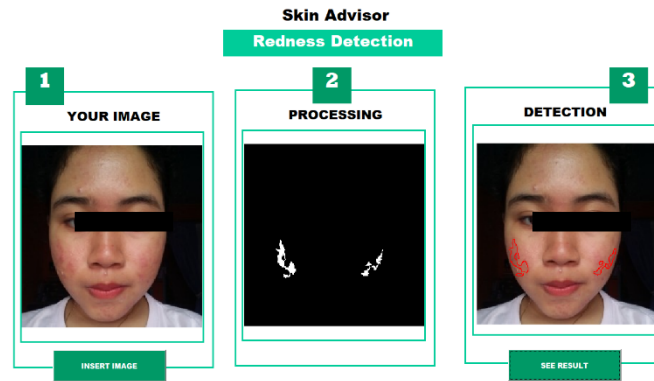


Fig. 6: Interface for Redness Object Detection.

Sensitivity that can only reach around 60% indicates that the detection of the redness object has not yet been optimal. To find the cause of detection failure, the researcher compared the results of the redness marking by the system and the assessment of the expert. In this study there are three causes of failure, namely poor image quality, uneven lighting, and overly wide range of redness color objects. The resolution of the image in Fig. 7(a) is only 250x250 pixels and the lighting is unevenly distributed. In the segmentation process, several parts of skin pixels are categorized into cluster backgrounds. It makes the redness objects unable to be detected in the following step. In Fig. 7(a) the redness objects are diagnosed by experts while in Fig. 7(b) the redness objects are detected by the system.

In Fig. 7(d) there are several redness objects that are not detected by the system, whereas they are diagnosed by experts in Fig. 7(c). On the other side, there are also some non-redness objects that were detected as redness objects by the system. Those redness objects cannot be selected by the system because of the range of mean intensity. Hue colors on the redness object are between 0.01 to 0.17. Meanwhile the range of mean intensity of the Hue colors of non-redness objects are between 0.02 to 0.05. So, there are non-redness objects detected as objects, namely eyebrows, lips, and neck. In addition, there are also undetectable redness objects, such as in the left cheekbone because it has a value of 0.4. However, if the Hue color range is increased, it can make the system detect non-redness parts as an object.



Fig. 7. Redness object detection; (a) by expert (b) by System (c) by expert (d) by System.

4. CONCLUSION

This paper tries to make a facial redness detection system that can analyze facial conditions, especially redness, through facial skin images. The system is expected to help patients for early detection of skin redness conditions to make it easier to select appropriate

facial care products and health care. The redness detection process begins by detecting facial skin in facial images. Furthermore, the redness area will be identified on the facial skin object obtained in the previous process. The method used for detecting red objects on face skin for this research is the Redness method. The output of the Redness method will be optimized by feature selection based on area, mean intensity of RGB, and mean intensity of Hue Intensity. The validation value used is sensitivity, specificity, and accuracy based on experts, namely a dermatologist and PT.AVO Innovation Technology personnel. The results obtained based on the dermatologist is 54%, 99.1%, and 96.2% for sensitivity, specificity, accuracy, respectively. Meanwhile, the results from PT.AVO personnel are 67.4%, 99.1%, and 97.7%, for sensitivity, specificity, accuracy, respectively. The cause of the sensitivity only reaching around 60% are poor image quality, uneven lighting, and an overly-wide range of colors for each object.

ACKNOWLEDGEMENT

The authors are grateful to the Informatics Department, Universitas Islam Indonesia for the financial support granted to cover the publication fee of this research article and to PT.AVO Innovation Technology personnel for image dataset support.

REFERENCES

- [1] Weller H, Mann M, Hunter H. (2015) *Cosmetic dermatology: Weller H, Mann M, Hunter H. Clinical dermatology. 5th edition. Chichester, Wiley-Blackwell; pp. 323-333.*
- [2] Fernando E. (2015) *Prototype Content Based Image Retrieval Untuk Deteksi Penyakit Kulit Dengan Metode Edge Detection (Studi Kasus : Klinik Penyakit Kulit RSU. Mataher Jambi-Indonesia) (Content Based Image Retrieval Prototype for Detection of Skin Diseases by Edge Detection Method (Case Study: Skin Disease Clinic, General Hospital, Mataher Jambi-Indonesia)). Jurnal IPTEKS Harapan, 2: 214-223.*
- [3] Herbin M, Venot A, Devaux J, Piette C. (1990). *Colour quantitation through image processing in dermatology. IEEE transactions on medical imaging, 9(3):262-269.*
- [4] Sainthillier JM, Mac S, Humbert P. (2007) *Assessment of rosacea by image processing and neural network. Expert Review of Dermatology, 2(3): 277-282.*
<https://doi.org/10.1586/17469872.2.3.277>
- [5] Ledoux A, Richard N, Capelle-Laizé AS, Fernandez-Maloigne C. (2015) *Perceptual color hit-or-miss transform: application to dermatological image processing. Signal, Image and Video Processing, 9(5): 1081-1091.*
- [6] Gessert CE, Bamford JT. (2003) *Measuring the severity of rosacea: a review. International journal of dermatology, 42(6): 444-448.* <https://doi.org/10.1046/j.1365-4362.2003.01780.x>
- [7] Novin IA, Aarabi P. (2014, October) *Skin lens: Skin assessment video filters. In 2014 IEEE International Conference on Systems, Man, and Cybernetics (SMC); pp. 1033-1038.*
<https://doi.org/10.1109/SMC.2014.6974049>
- [8] Franks AG. (1993) *Cutaneous manifestations of disorders of the cardiovascular and pulmonary systems: Dermatology in general medicine. 4th edition. New York, McGraw-Hill; pp. 2063-104.*
- [9] Fadhilah AN, Fatimah DDS, Damiri DJ. (2012) *Perancangan Aplikasi Sistem Pakar Penyakit Kulit Pada Anak Dengan Metode Expert System Development Life Cycle (Designing Expert System Application for Skin Diseases in Children with Expert System Development Life Cycle Method). Jurnal Algoritma, 9(1): 112-118.*
- [10] Zaitoun NM, Aqel M. (2015) *Survey on image segmentation techniques. Procedia Computer Science, 65: 797-806.*
- [11] Al-Najdawi N, Biltawi M, Tedmori S. (2015) *Mammogram image visual enhancement, mass segmentation and classification. Applied Soft Computing, 35: 175-185.*

- [12] Chavan A, Bendale D, Shimpi R, Vikhar P. (2016) Object detection and recognition in images. *International Journal of Computing and Technology*, 3(3):148-151.
- [13] Owens DK, Sox HC. (2014) Biomedical decision making probabilistic clinical reasoning. In *Biomedical Informatics*, Springer, London; pp. 67-107.
- [14] Shaik KB, Ganesan P, Kalist V, Sathish BS, Jenitha JMM. (2015) Comparative study of skin color detection and segmentation in HSV and YCbCr color space. *Procedia Computer Science*, 57: 41-48.
- [15] Mujahidi, S. (2012) Aplikasi perhitungan jumlah orang dalam satu foto (Application for calculating the number of people in one photo). Thesis. Universitas Islam Indonesia, Department of Informatics.

IMPLEMENTATION OF A MACHINE LEARNING ALGORITHM FOR SENTIMENT ANALYSIS OF INDONESIA'S 2019 PRESIDENTIAL ELECTION

GHULAM ASROFI BUNTORO^{1*}, RIZAL ARIFIN¹, GUS NANANG SYAIFUDDIN¹, ALI SELAMAT^{2,3}, ONDREJ KREJCAR³, HERRERA-VIEDMA⁴ AND HAMIDO FUJITA⁵,

¹Faculty of Engineering, Universitas Muhammadiyah Ponorogo, Indonesia

²Malaysia-Japan International Institute of Technology, Universiti Teknologi Malaysia

³Faculty of Informatics and Management, University of Hradec Kralove, Czech Republic

⁴Andalusian Research Institute DaSCI "Data Science and Computational Intelligence", University of Granada, Spain

⁵Faculty of Software and Information Science, Iwate Prefectural University, Iwate, Japan

*Corresponding author: ghulam@umpo.ac.id

(Received: 3rd July 2020; Accepted: 1st October 2020; Published on-line: 4th January 2021)

ABSTRACT: In 2019, citizens of Indonesia participated in the democratic process of electing a new president, vice president, and various legislative candidates for the country. The 2019 Indonesian presidential election was very tense in terms of the candidates' campaigns in cyberspace, especially on social media sites such as Facebook, Twitter, Instagram, Google+, Tumblr, LinkedIn, etc. The Indonesian people used social media platforms to express their positive, neutral, and also negative opinions on the respective presidential candidates. The campaigning of respective social media users on their choice of candidates for regents, governors, and legislative positions up to presidential candidates was conducted via the Internet and online media. Therefore, the aim of this paper is to conduct sentiment analysis on the candidates in the 2019 Indonesia presidential election based on Twitter datasets. The study used datasets on the opinions expressed by the Indonesian people available on Twitter with the hashtags (#) containing "Jokowi and Prabowo." We conducted data pre-processing using a selection of comments, data cleansing, text parsing, sentence normalization and tokenization based on the given text in the Indonesian language, determination of class attributes, and, finally, we classified the Twitter posts with the hashtags (#) using Naïve Bayes Classifier (NBC) and a Support Vector Machine (SVM) to achieve an optimal and maximum optimization accuracy. The study provides benefits in terms of helping the community to research opinions on Twitter that contain positive, neutral, or negative sentiments. Sentiment Analysis on the candidates in the 2019 Indonesian presidential election on Twitter using non-conventional processes resulted in cost, time, and effort savings. This research proved that the combination of the SVM machine learning algorithm and alphabetic tokenization produced the highest accuracy value of 79.02%. While the lowest accuracy value in this study was obtained with a combination of the NBC machine learning algorithm and N-gram tokenization with an accuracy value of 44.94%.

ABSTRAK: Pada tahun 2019 rakyat Indonesia telah terlibat dalam proses demokrasi memilih presiden baru, wakil presiden, dan berbagai calon legislatif negara. Pemilihan presiden Indonesia 2019 sangat tegang dalam kempen calon di ruang siber, terutama di laman media sosial seperti Facebook, Twitter, Instagram, Google+, Tumblr, LinkedIn, dll. Rakyat Indonesia menggunakan platform media sosial bagi menyatakan pendapat positif, berkecuali, dan juga negatif terhadap calon presiden masing-masing. Kempen pencalonan menteri, gabenor, dan perundangan hingga pencalonan presiden dilakukan melalui media internet dan atas talian. Oleh itu, kajian ini dilakukan bagi menilai sentimen terhadap calon

pemilihan presiden Indonesia 2019 berdasarkan kumpulan data Twitter. Kajian ini menggunakan kumpulan data yang diungkapkan oleh rakyat Indonesia yang terdapat di Twitter dengan hashtag (#) yang mengandung "Jokowi dan Prabowo." Proses data dibuat menggunakan pilihan komentar, pembersihan data, penguraian teks, normalisasi kalimat, dan tokenisasi teks dalam bahasa Indonesia, penentuan atribut kelas, dan akhirnya, pengklasifikasian catatan Twitter dengan hashtag (#) menggunakan Klasifikasi Naïve Bayes (NBC) dan Mesin Vektor Sokongan (SVM) bagi mencapai ketepatan optimum dan maksimum. Kajian ini memberikan faedah dari segi membantu masyarakat meneliti pendapat di Twitter yang mengandung sentimen positif, neutral, atau negatif. Analisis Sentimen terhadap calon dalam pemilihan presiden Indonesia 2019 di Twitter menggunakan proses bukan konvensional menghasilkan penjimatan kos, waktu, dan usaha. Penyelidikan ini membuktikan bahawa gabungan algoritma pembelajaran mesin SVM dan tokenisasi abjad menghasilkan nilai ketepatan tertinggi iaitu 79.02%. Manakala nilai ketepatan terendah dalam kajian ini diperolehi dengan kombinasi algoritma pembelajaran mesin NBC dan tokenisasi N-gram dengan nilai ketepatan 44.94%.

KEYWORDS: *sentiment analysis; president; Indonesia; naïve Bayes classifier; support vector machine*

1. INTRODUCTION

The turmoil resulting from organizing the 2019 Indonesian general election, notably the presidential election, has been felt since last year. This has applied not only in the real world but also in cyberspace, mainly on social media sites such as Twitter, Instagram, Facebook, etc., which people used to discuss their potential presidential candidates. The stages of the general election and presidential election in 2019 were announced by the Indonesian General Elections Commission (KPU). The names of the presidential candidates had been widely discussed on social media as far back as the candidate registration phase in early 2019 by the Indonesian KPU [1]. The virtual world is a world that is so free and difficult to control, where everyone is free to speak or give their opinion on their respective candidates. The opinions expressed by the public may be positive, neutral, or even negative.

The world of information has developed so fast that there is now a significant amount of online media, from news information to social media or friendships, with social media including Facebook, Twitter, Path, Instagram, Google+, and many more. Twitter has a total of 330 million active users to date, while around 500 million tweets are made worldwide every day. There are around 100 million active daily users of Twitter around the world [2].

Social media is not only used as a means of friendship or for making friends but also for activities such as the promotion of merchandise or sale and purchase, up to political party promos or campaigns for regent, presidential, and legislative candidates. The team charged with ensuring a candidate for president or regional head, for example, will justify any means of campaigning for their candidate, as evidenced by the presence of many Black Campaigns during the campaign period [3], especially on social media against a candidate. Today's campaign or imaging is not only done in the real world but also in the virtual world. Social media, especially Twitter, is now one of the most effective and efficient campaign venues.

Sentiment analysis continues to be used as part of opinion mining research. It is the process of understanding, extracting, and processing textual data automatically to obtain the sentiment information contained in an opinion sentence [4].

In this study, sentiment analysis was conducted with the aim of viewing and retrieving information pertaining to the opinions expressed by people in the Indonesian language on Twitter with regard to the candidates in the 2019 Indonesian presidential election, whether

those opinions were in the category of positive, neutral, or negative. To test the accuracy of the sentiment analysis in this study, we used two machine learning algorithms, namely Naïve Bayes Classifier (NBC) and Support Vector Machine (SVM) and 7 tokenizations including an Alphabetic Tokenizer, Character N-gram Tokenizer, Unigram, Bigram, Trigram, N-gram, and Word Tokenizer. The result will enable us to see the accuracy of the machine learning methods NBC and SVM[5] and 7 tokenizations including the Alphabet Tokenizer, Character N-gram Tokenizer, Character Tokenizer, Unigram, Bigram, Trigram, N-gram, and Word Tokenizer for sentiment analysis of the 2019 Indonesian presidential candidates.

2. RELATED WORK

Sentiment analysis research used machine learning to classify Turkish political news [6]. This research classified the sentiment toward Turkish political news and determined whether the sentiment expressed was positive or negative. The different features of Turkish political news were extracted with the machine learning algorithms of Naïve Bayes Classifier (NBC), Maximum Entropy (ME), and SVM to produce a classification model.

Sentiment analysis was used to group texts according to their positive or negative orientation [7]. This paper explains the experimental results that apply SVMs to conduct benchmarking with standard datasets to train sentiment analysis classifiers. N-grams and different weighting schemes were used to extract the most classic features. This study also explores the Chi-Square weight feature to select informative features for the classification method. The results of this experimental analysis reveal that using the Chi-Square feature selection can significantly enhance classification accuracy.

The main challenge for law enforcement in recent years has been the automatic detection of abusive language in online media [8]. First, we have developed a deep learning architecture that uses word frequency vectorization to implement the features above. Second, we have proposed a method that, because it does not use pre-trained word embedding, is an independent language. Third, we have conducted a comprehensive evaluation of our model using public datasets from labelled tweets and open-source implementations built using Keras. The paper presents an ensemble classifier for detecting hate speech in short texts, such as opinion tweets used as corpus datasets [9]. Our classification uses deep learning and combines a set of features related to user behaviour characteristics, such as the tendency to send rough messages as input to a combination of machine learning algorithms [10,11].

Sentiment analysis research was carried out using a hybrid approach [12] with its research methods, including mining association rules, parsing dependencies, and Sentiwordnet applied to solve this aspect-based sentiment analysis problem [13]. The performance of the research was evaluated using negative and racial domains and other benchmarks to evaluate the accuracy of aspect-based sentiment classification.

3. PROPOSED METHODOLOGY

3.1 Tweet Data Collection

Crawling [14] carried out tweet data collection with R Programming using R-Studio from Twitter. The data taken comprised only tweets in Indonesian, which consisted of 5,000 tweets containing the Jokowi keywords and 5000 tweets containing the Prabowo keywords, to give a total of 10,000 tweets. The data were taken randomly from ordinary users of Twitter (Fig. 1).

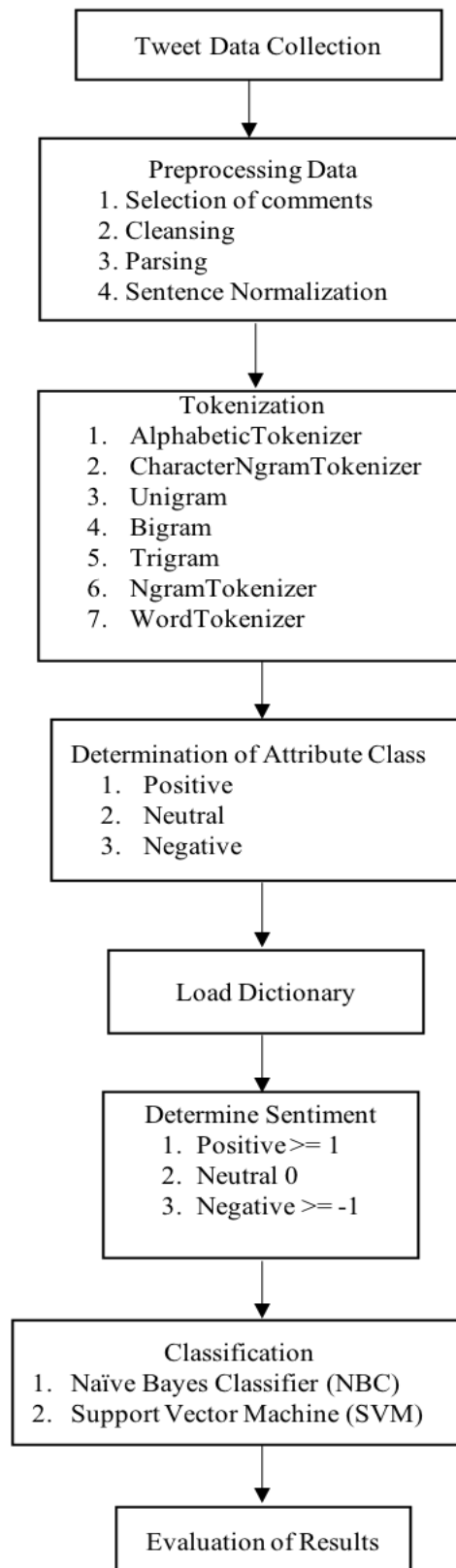


Fig. 1: Proposed method of Twitter sentiment analysis.

Figure 2 shows the coding of R Language [15] that was used to crawl the data from Twitter. The tweet data on Jokowi comprised 5,000 tweets, which, along with examples of original tweets, featured lots of noise characterized by the presence of symbols and links.

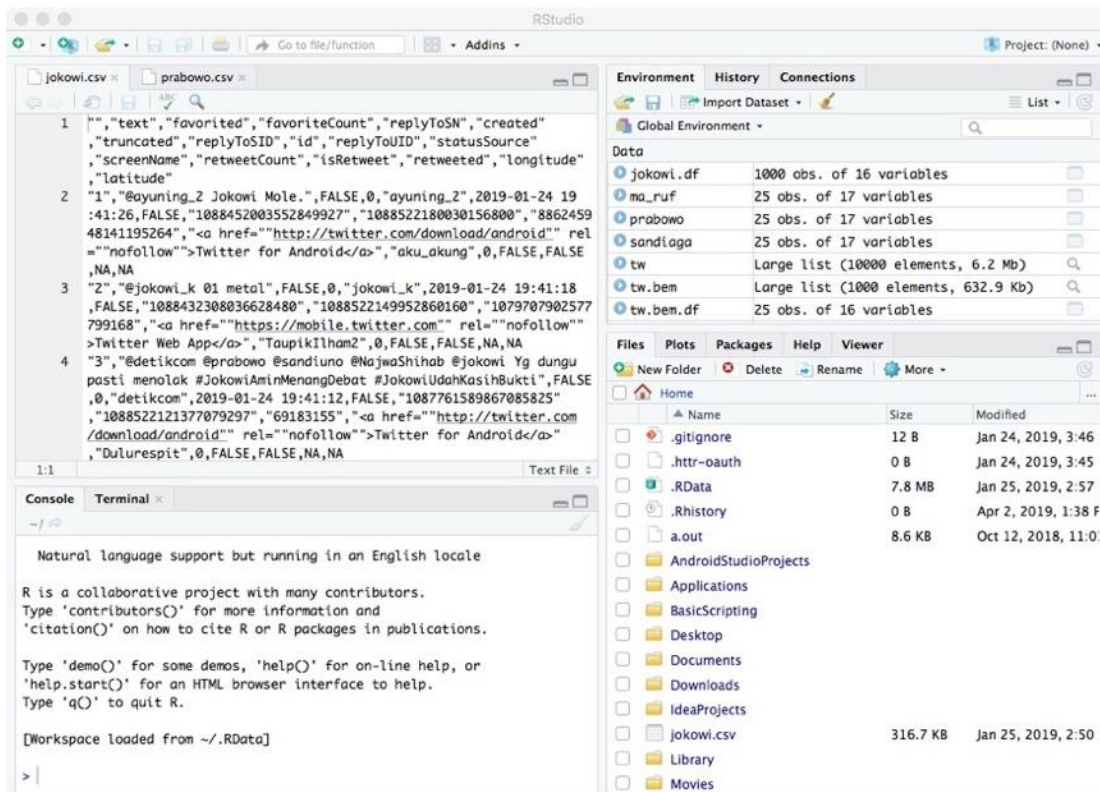


Fig. 2: Crawling tweets of opinions about Jokowi from Twitter at R-Studio.

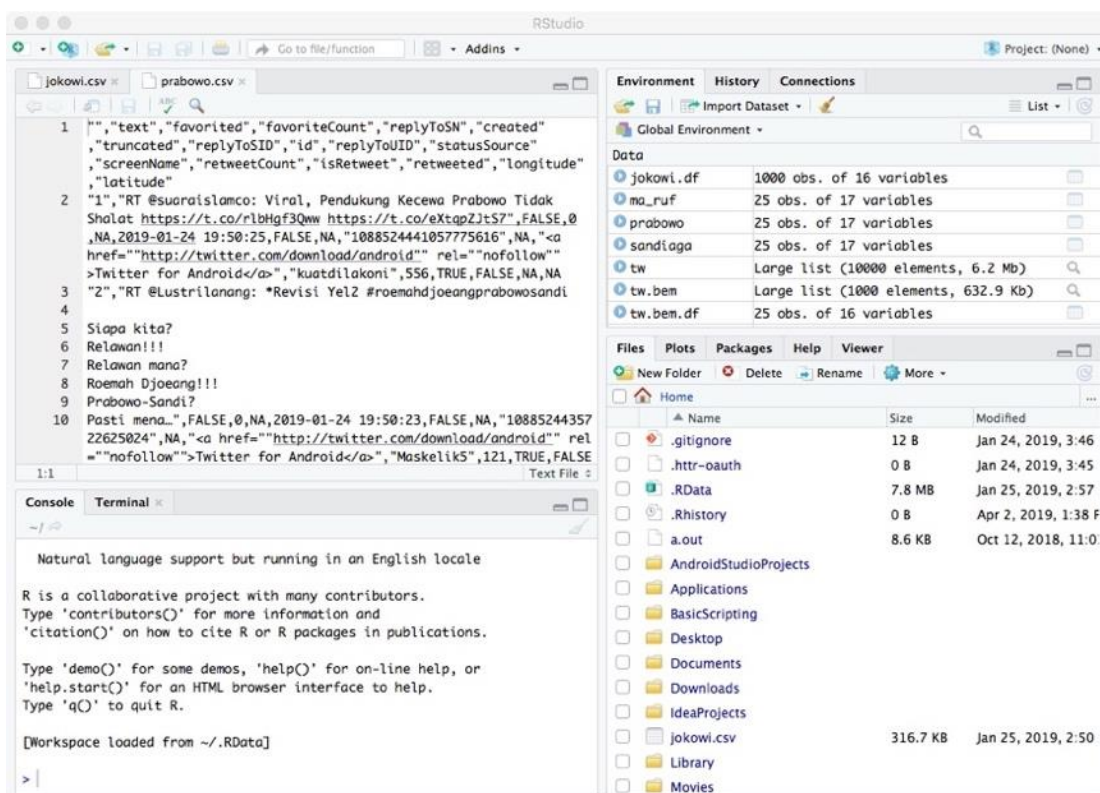


Fig. 3: Crawling tweets of opinion about Prabowo from Twitter at R-Studio.

Figure 3 contains a coding of the R Language for crawling data from Twitter. Also seen is the number of data tweets taken about Prabowo, which numbered 5,000. The left-hand panes in Figures 2 and 3 also contain examples of tweets in their original form and lots of noise from Twitter with the presence of symbols and links.

3.2 Data Pre-Processing

The data pre-processing stage [16] in this study consisted of 4 steps, which are described as follows:

A. Selection of Comments

At this stage, comments were selected that contained the keywords of hashtags (#) Jokowi and Prabowo; any data that did not contain both were deleted. When crawling all comments with the hashtag, both will be taken even if they appear in the same sentence. Then, during this process, the same comment will be deleted, even if it comes from a different Twitter account, in order to find unique tweet data.

B. Cleansing

This process aimed to clean up any comments from Twitter that were still dirty and contained a lot of noise. The opinion sentences obtained from Twitter usually contained a certain level of noise, i.e., random errors or variants in measured variables; therefore, we had to eliminate and clean the noise. The items omitted were usually HTML characters, symbols, emoticon icons, hashtags (#), usernames (@username), URL addresses (<http://websitename.com>), and email addresses (name@websitename.com).

C. Parsing

The third data pre-processing step in this study was parsing [17]. The aim was to break the document into a string of words and then analyse the collection of words by separating them and determining the syntactic structure of each word.

D. Sentence Normalization

The aim of this step was to normalize the sentences taken from Twitter; for example, a sentence containing the words Gaul or Alay [18] would be normalized so that the sentence or language of Gaul and Alay could be recognized as a language following KBBI (The Great Dictionary of the Indonesian Language) [19]. The normalization of sentences involved the following processes:

- Stretch punctuation and symbols other than the alphabet

Stretching punctuation involves inserting distance around the punctuation associated with words that come after or before. The aim is to avoid any punctuation and/or symbols other than those in the alphabet becoming one with the words during the tokenization process.

- Change to all lowercase letters
- Normalization of words. The rules in the normalization process are shown in Table 1.
- Eliminate repeated letters

When happy or upset, someone may write opinions based on their emotions; often, when expressing this in written form, they will repeat the same letter. For example: "kereeen" to express pleasure. Repeated words like "kereeen" will be normalized to "cool".

Table 1: Rules for normalizing words

Normal / slang	Normal
Suffix -ny	Suffix -nya
Suffix -nk	Suffix -ng
Suffix -x	Suffix -nya
Suffix -z	Suffix -s
Suffix -dh	Suffix -t
Repeat words: sama2	Repeat words: sama-sama
Spelling: oe	Alphabet: u
Spelling: dj	Alphabet: j

3.3 Tokenization

After normalizing the sentence, it was then broken down into tokens [20] using a delimiter or space bar. The tokens used in this study are:

- Alphabetic Tokenizer: These tokens are formed only from adjacent alphabetical sequences, for example: aku, anak, asli, baik, bagus, cara, cinta, demi, engkau, enak, film
- Character N-gram Tokenizer: This tokenizer divides the token into a one-word character; for example: pe, mi, lu, pe, mi, li, han, u, mum
- Unigram: This tokenizer divides the sentence into a token, with each token consisting of only one word; for example, "Pemilu".
- Bigram: This tokenizer divides the sentence into a token, with each token consisting of two words; for example: "Pemilihan Umum".
- Trigram: This tokenizer divides the sentence into a token, with each token consisting of three words; for example, "Pemilihan Umum Indonesia".
- N-gram Tokenizer: This tokenizer divides the string into n-grams with the minimum and maximum number of grams as specified; for example, "pemilihan, pemilihan umum, pemilihan umum Indonesia, aku, aku anak, aku anak indonesia"
- Word Tokenizer: This tokenizer divides tokens from the basic words; for example, "aku, akun, akuntansi, alam, alami, alamiah"

3.4 Determination of Class Attribute

After pre-processing, the next stage in this research is to determine the class attribute. The class attribute used here is sentiment class; in this study, there are 3 class attributes [21], namely positive, neutral, and negative. The use of 3 class attributes provides a more detailed and accurate classification of public opinion toward a particular object.

3.5 Load Dictionary

Following the class attribute determination, the next step is to apply the Lexicon-based method [22]. The dictionary used in this study comprises positive words (positive keywords), negative words (negative keywords), and negation words (negation keywords).

The following is a sample dictionary and its contents:

- Positive keywords; for example, "amanah, ahli, jujur, adil, keren".
- Negative keywords; for example, "apatis, benci, dosa, jahat, buruk".
- Negation keywords; for example, "lebih, kurang, tidak, bukan".
- Dictionary of slang conversion to KBBA; for example, "cyg = sayang, lbh = lebih, krn = karena, jd = jadi, spt = seperti, ciyus = serius".

3.6 Determination of Sentiment

This is the process used for determining the sentiment (Positive, Neutral, or Negative) in Twitter data once the processing has been performed. The sentiment determining process used in this study consisted of the Lexicon-based or Dictionary-based method with Python Programming. In this study, we are using the Positive and Negative Dictionary. The polarity score of an opinion word (p) will be 1 if the word is in the positive dictionary, meaning the word is positive. A word that is in neither the positive nor negative dictionary is worth 0, meaning it is neutral, while a word in the negative dictionary is worth -1, meaning it is negative [23]. The method for determining sentiment uses the sum formula n, namely the opinion polarity score of the word, plus p, that is the opinion commenting on the feature (f).

After determining which words in a Twitter opinion sentence are positive, neutral, or negative, the weight of the values contained in the sentence is then calculated by totalling the value of each opinion word. If the number of opinion words in the sentence is ≥ 1 , then the sentiment value of the opinion sentence is positive; if the opinion value of the sentence is 0, then the sentiment value of the opinion sentence is neutral, and if the opinion word value in the sentence is ≥ -1 , then the sentiment value of the opinion sentence is negative. The determination of sentiment can be seen in Table 2.

Table 2: Determination of Sentiment

Sentiment	Value
Positive	≥ 1
Neutral	0
Negative	≥ -1

3.7 Classification Processes

Following the process for determining sentiment and having established the sentiment value of each opinion sentence using Python Programming, the next step is the sentiment classification process. The classification process uses the WEKA 3.8.3 Machine Learning tool [24], and the machine learning algorithms used in this study are NBC and SVM. In the classification process, the data were tested using the 10-fold cross-validation method [25]. The method works by dividing the dataset into two, namely 10 parts with 9/10 parts used as training data and 1/10 parts used as testing data. The iteration process in the method can be run 10 times with a variety of training data and data testing using a combination of 10 parts of data.

3.8 Evaluation of Results

The stages of evaluation in the study will examine the performance of Accuracy, Precision, and Recall from the experiments that have been carried out. The results evaluation process is conducted using a Confusion Matrix [26] featuring as its indicators a true positive rate (TP rate), true negative rate (TN rate), false positive rate (FP rate), and false negative rate (FN rate). The TP rate is the percentage of the positive class that is successfully classified as a positive class, while the TN rate is the percentage of the negative class that is successfully classified as a negative class. The FP rate is a negative class that is classified as a positive class, and the FN rate is a positive class that is classified as a negative class.

Table 3: Confusion Matrix

		Predicted		
		Positive (A)	Neutral (B)	Negative (C)
Actual	Positive (A)	AA	AB	AB
	Neutral (B)	BA	BB	BC
	Negative (C)	CA	CB	CC

Testing	Twitter Dataset									
1	█									
2		█								
3			█							
4				█						
5					█					
6						█				
7							█			
8								█		
9									█	
10										█

Fig. 4: Illustration of 10-fold cross-validation.

4. EXPERIMENT AND RESULTS

In this study, the dataset was derived from tweets of public opinion on the Indonesian 2019 presidential candidates. The data were taken using the crawling method [27] with R Programming using R-Studio from Twitter social media. The data taken were only tweets in Indonesian, with the details of 5000 tweets containing Jokowi’s keywords and 5,000 tweets containing Prabowo’s keywords, giving a total of 10,000 tweets. The tweet data were taken randomly from both ordinary users and from the news media online on Twitter.

Following the data pre-processing, tokenization, and class attribute determination steps, the dataset used for this study contained opinion sentences from Twitter classified into their respective sentiment classes (Positive, Neutral, or Negative) with Python Programming. The number of datasets is not the same as the amount of data taken because, during the data pre-processing, the same opinion sentence will be deleted to search for unique data, whereas when the data are being crawled, all opinion sentences will be taken even though the sentence is the same. Table 4 contains the results of the determination of the sentiment class using the Lexicon-based method [28] in Python Programming with three attribute classes, namely positive, neutral, and negative.

Table 4: Results of Determination of Sentiment Classes

Sentiment	Total
Positive	2688
Neutral	4666
Negative	2646

After determining the sentiment value of each opinion sentence, the opinion sentences are formed into a dataset using the Attribute-Relation File Format (ARFF) [29] as the input for classifying data with WEKA. The tweet data were then classified or tested for accuracy using the NBC machine learning algorithms and SVM with WEKA version 3.8.3 software.

This study uses the 10-fold cross-validation method for the process of classifying or testing tweet data. In this process, the data are divided into 10 parts with 9/10 parts used for the training process and 1/10 parts used for the testing process. Iteration takes place 10 times with variations in training and testing data using a combination of 10 parts of data. Table 5 displays a comparison of the results from the NBC machine learning algorithm with SVM.

Table 5: Comparison of Classification Results *

<i>Naïve Bayes Classifier (NBC)</i>					
Tokenizer	Accuracy (%)	Precision (%)	Recall (%)	TP Rate (%)	TN Rate (%)
Alphabetic	49.94	52.5	49.9	51.4	50.5
Character N-gram	51.81	54.4	51.8	53.7	51.7
Unigram	50.11	52.6	50.1	53.3	48.4
Bigram	50.51	61.2	50.5	79.7	25.3
Trigram	55.98	68.5	56	21	20.3
N-gram	44.94	51.6	44.9	64.2	46
Word	50.11	52.6	50.1	53.3	48.4
<i>Support Vector Machine (SVM)</i>					
Tokenizer	Accuracy (%)	Precision (%)	Recall (%)	TP Rate (%)	TN Rate (%)
Alphabetic	79.02	79	79	73.8	70.3
Character N-gram	58.47	59.20	58.50	55.70	64.40
Unigram	78.9	78.9	78.9	73.2	70.8
Bigram	69.21	72.1	69.2	51.5	48
Trigram	61.21	71.7	61.2	30.1	31
N-gram	77.82	77.8	77.8	72.6	69.4
Word	78.9	78.9	78.9	73.2	70.8

*The Precision and Recall values are the average values of positive class values and negative classes

The information in Table 5 enables a comparison of the accuracy, precision, recall, TP rate, and TN rate values for each trial carried out with the NBC machine learning algorithm and SVM. The columns contain the tokenization data used in this study while the rows contain the accuracy, precision, recall, TP rate, and TN rate values for each trial conducted. The process from data pre-processing to the determination of the sentiment class produced the dataset of this research, which was then used as the input in the classification process. The classification process was carried out with WEKA Machine Learning using the NBC machine learning algorithm and SVM. The classification test process with 7 tokenizations produced values for accuracy, precision, recall, TP rate, and TN rate for each trial.

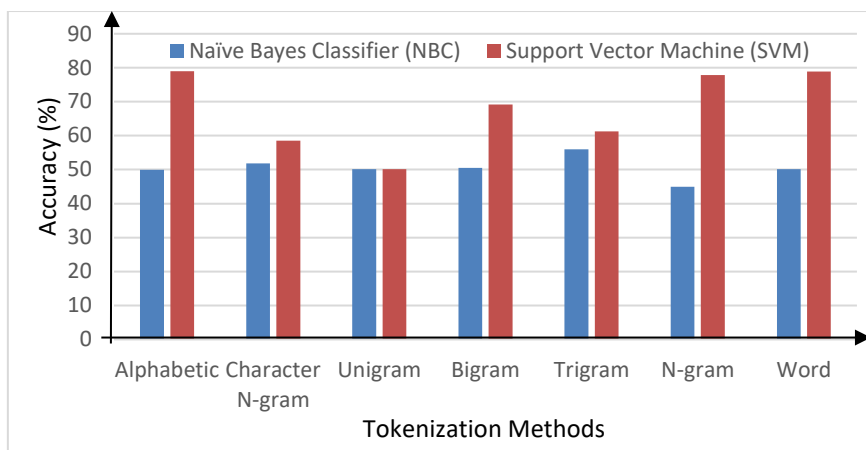


Fig. 5: Accuracy level of different machine learning algorithms and tokenization methods. The blue and orange charts correspond to the Naïve Bayes Classifier (NBC) and Support Vector Machine (SVM), respectively.

From Fig. 5, we can see that accuracy was tested in this study with two machine learning algorithms, namely NBC and SVM, and the 7 tokenizations of Alphabetic Tokenizer, Character N-gram Tokenizer, Unigram, Bigram, Trigram, N-gram, and Word Tokenizer. Accuracy was one of the main parameters in the assessment of the sentiment analysis model used in this study. The formula for the value of accuracy was the amount of data that were successfully classified according to the class of sentiment for the entire amount of data classified. Therefore, the greater the amount of data that were correctly classified according to the sentiment class, the higher the accuracy value. The highest accuracy value was obtained with respect to the combination of the SVM and Alphabetic Tokenization machine learning algorithms, which had an accuracy value of 79.02%. In this study, machine learning methods such as the SVM algorithm produced the highest accuracy because they work by recognizing word patterns. This machine learning algorithm is capable of easily recognizing and memorizing word patterns for a certain sentiment class in an opinion sentence. Yet while it is easy to classify sentiment data correctly using these methods, alphabetic tokenization can improve accuracy by breaking a sentence into words, which enables the easy classification of sentences with sentiments. The lowest accuracy value in this study was obtained for the NBC machine learning algorithm with N-gram tokenization, which yielded an accuracy value of 44.94%.

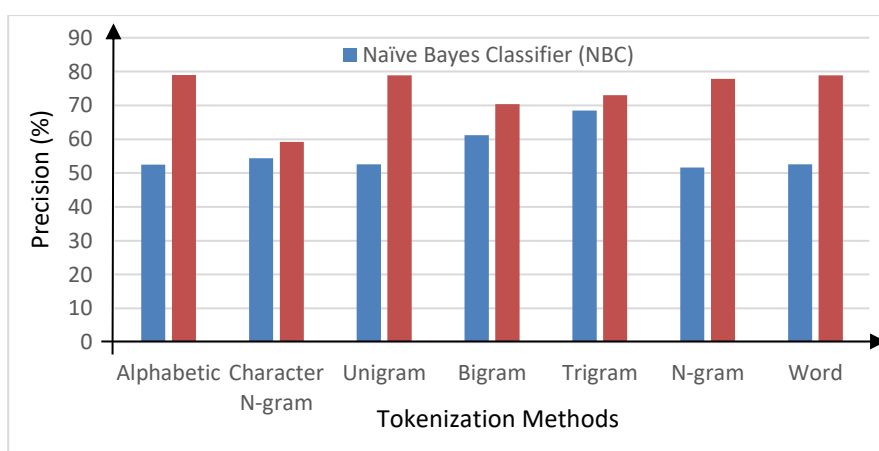


Fig. 6: Precision level of different machine learning algorithms and tokenization methods. The blue and orange charts correspond to the Naïve Bayes Classifier (NBC) and Support Vector Machine (SVM), respectively.

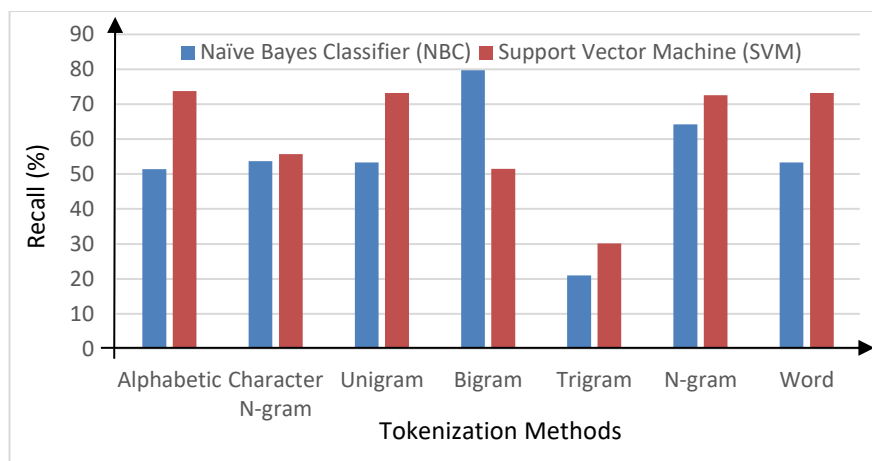


Fig. 7: Recall level of different machine learning algorithms and tokenization methods. The blue and orange charts correspond to the Naïve Bayes Classifier (NBC) and Support Vector Machine (SVM), respectively.

Figure 6 shows that the highest Precision value of 79% was obtained by the SVM machine learning algorithm with alphabetic tokenization, while the lowest precision value of 55.1% came from the NBC machine learning algorithm with N-gram tokenization. In the Figure 7, we can see that highest Recall value of 79% was obtained with the SVM machine learning algorithm and alphabetic tokenization, while the lowest Recall value of 51.6% was obtained with the NBC machine learning algorithm with N-gram tokenization. The high precision values were obtained because the precision value formula was based on the number of positive classes that were correctly classified as a positive class divided by the total data classified as a positive class, whereas the recall value formula consisted of the number of positive classes that were correctly classified as positive classes divided by the number of actual positive classes.

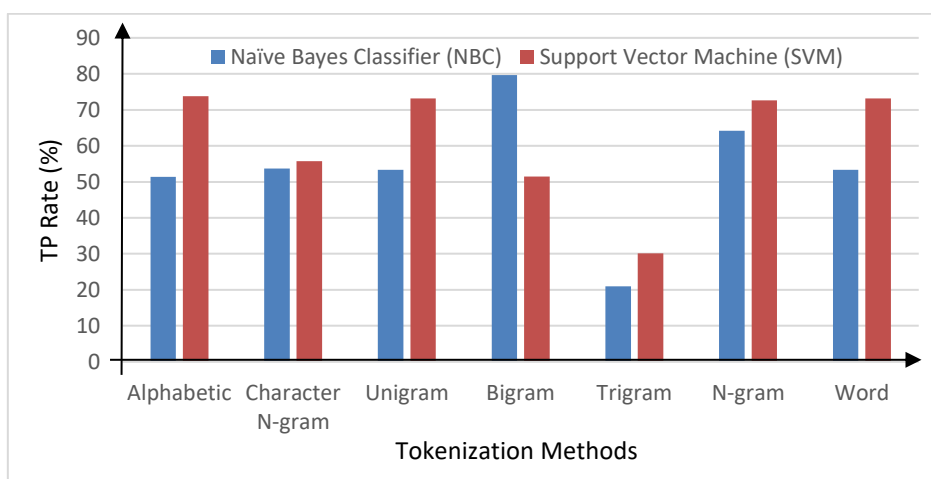


Fig. 8: TP Rate level of different machine learning algorithms and tokenization methods. The blue and orange charts correspond to the Naïve Bayes Classifier (NBC) and Support Vector Machine (SVM), respectively.

Figure 8 displays the highest and lowest TP Rate obtained using the NBC machine learning algorithm. The TP Rate is a value denoting the amount of positive tweet data that were correctly classified according to the sentiment class, which in this case was positive. In contrast, the highest and lowest TN values were obtained using the SVM machine learning algorithm as shown in Fig. 9. The TN Rate indicates the value of negative tweet

data that were correctly classified according to the sentiment class, which in this case was negative.

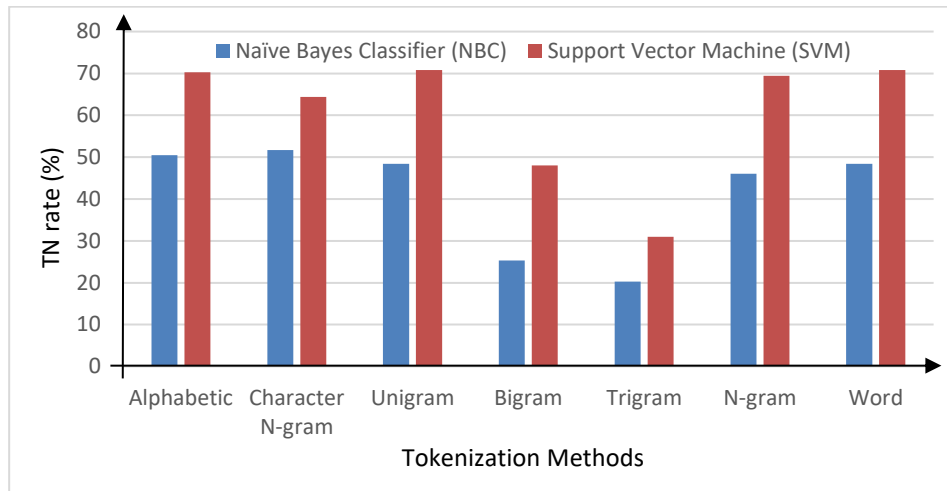


Fig. 9: TN Rate level of different machine learning algorithms and tokenization methods. The blue and orange charts correspond to the Naïve Bayes Classifier (NBC) and Support Vector Machine (SVM), respectively.

From the research carried out, it can be seen that the model constructed delivered the greatest accuracy when using a combination of the SVM machine learning algorithm and N-gram tokenization, while the lowest accuracy value was obtained when testing using a combination of the NBC machine learning algorithm with Trigram tokenization. The accuracy results produced were quite good; however, the model still made a number of mistakes when the classification process of the dataset with the distribution of sentiments was not as balanced as this study intended. The use of datasets with imbalanced distribution will lead to the incorrect classification of minority class data as majority class data [30], which results in a large value difference because most classifiers manage to correctly classify the majority class compared to the minor class [31].

5. CONCLUSIONS

From the series of studies conducted, we can conclude that the Sentiment Analysis model built was suitable for use in determining the sentiment of public opinion on Twitter with respect to the 2019 Indonesian presidential candidates. The study aimed to test and determine which machine learning algorithms were suitable for the classification of public opinion on Twitter, and also to test 7 suitable tokenizations and produce high accuracy when combined with the Naïve Bayes Classifier (NBC) and Support Vector Machine (SVM) machine learning algorithms. The sentiment analysis revealed that there was much negative public sentiment on Twitter aimed at the 2019 Indonesian presidential candidates. The greatest accuracy value was obtained when using a combination of the SVM machine learning algorithm and alphabetic tokenization, which yielded an accuracy value of 79.02%. The lowest accuracy value in this study was obtained for the NBC machine learning algorithm with N-gram tokenization, which had an accuracy value of 44.94%. This study has therefore demonstrated that the SVM machine learning algorithm produces higher accuracy compared to the NBC machine learning algorithm. It is suggested that further research should endeavour to use more data and real-time data from both Twitter and other social media sites such as Facebook and YouTube.

ACKNOWLEDGEMENTS

This research was funded by Universiti Teknologi Malaysia (UTM) under Research University Grant Vot-20H04, Malaysia Research University Network (MRUN) Vot 4L876, and the Fundamental Research Grant Scheme (FRGS) Vot 5F073 supported under the Ministry of Education Malaysia. The work is partially supported by the SPEV project, University of Hradec Kralove, FIM, Czech Republic (ID: 2103-2019), “Smart Solutions in Ubiquitous Computing Environments” and by the project of excellence 2019/2205, Faculty of Informatics and Management, University of Hradec Kralove. Partial funding by Universitas Muhammadiyah Ponorogo through the Institute for Research and Public Services (LPPM) under the contract no. 115/VI.4/PN/2018 is also acknowledged. We are also grateful for the support of Ph.D. students Sebastien Mambou and Michal Dobrovolny in consultations regarding application aspects.

REFERENCES

- [1] KPU - Portal Publikasi Pemilihan Umum 2019. Available: <https://infopemilu.kpu.go.id/>.
- [2] Instagram by the Numbers: Stats, Demographics & Fun Facts, Omnicore Agency, 2020. Available: <https://www.omnicoreagency.com/instagram-statistics/>.
- [3] Januru L. (2016) Analisis Wacana Black Campaign (Kampanye Hitam) Pada PILPRES Tahun 2014 di Media Kompas, Jawa Pos Dan Kedaulatan Rakyat, *Natapraja*, 4(2): 181-194.
- [4] Indurkha N, Damerau FJ. (2010) *Handbook of Natural Language Processing*, 2nd ed. Chapman & Hall/CRC.
- [5] Wagh B, N RW. (2016) Sentimental Analysis on Twitter Data using Naive Bayes, *IJARCCCE*, 5(12): 316-319.
- [6] Yuret D, Türe F. (2006) Learning morphological disambiguation rules for Turkish, *Proceedings of the Human Language Technology Conference of the North American Chapter of the ACL*, pages 328–334.
- [7] Zainuddin N, Selamat A. (2014) Sentiment analysis using Support Vector Machine, in *I4CT 2014 - 1st International Conference on Computer, Communications, and Control Technology*, *Proceedings*, pages. 333–337.
- [8] Pitsilis GK, Ramampiaro H, Langseth H. (2018) Effective hate-speech detection in Twitter data using recurrent neural networks, *Appl. Intell.*, 48(12): 4730-4742.
- [9] Pak A, Paroubek P. (2010) Twitter as a corpus for sentiment analysis and opinion mining, *Proc. 7th Int. Conf. Lang. Resour. Eval. Lr. 2010*, pages. 1320–1326.
- [10] Kolchyna, O., Souza, T.T., Treleaven, P., Aste, T. (2015). *Twitter Sentiment Analysis: Lexicon Method, Machine Learning Method and Their Combination*. arXiv: *Computation and Language*.
- [11] Nezhad ZB, Deihimi MA. (2019) A combined deep learning model for Persian Sentiment Analysis, *IIUM Eng. J.*, 20(1): 129-139.
- [12] Zainuddin N., Selamat A., Ibrahim R. (2016) Improving Twitter Aspect-Based Sentiment Analysis Using Hybrid Approach. In: Nguyen N.T., Trawiński B., Fujita H., Hong TP. (eds) *Intelligent Information and Database Systems. ACIIDS 2016. Lecture Notes in Computer Science*, vol 9621. Springer, Berlin, Heidelberg.
- [13] Zainuddin, N., Selamat, A., Ibrahim, R. (2018) Hybrid sentiment classification on twitter aspect-based sentiment analysis. *Appl Intell* 48, 1218–1232.
- [14] Purohit NS, Angadi AB, Bhat M, Gull KC. (2015) Crawling through web to extract the data from Social networking site-Twitter, 2015 Natl. Conf. Parallel Comput. Technol. PARCOMPTECH 2015.
- [15] R: What is R?. Available: <https://www.r-project.org/about.html>.
- [16] Sammut C. (2011) Genetic and Evolutionary Algorithms. In: Sammut C., Webb G.I. (eds) *Encyclopedia of Machine Learning*. Springer, Boston, MA.
- [17] Utomo FS, Suryana N, Azmi MS. (2020) Stemming impact analysis on Indonesian Quran translation and their exegesis classification for ontology instances. *IIUM Eng. J.*, 21(1): 33-

- 50.
- [18] Lutfiatun A, Novitasari A, Helfiyana A. (2018) Bahasa Alay Pada Chating Di Medsos Remaja Millenial (Bahasa Alay Vs Remaja Millenial), Prosiding SENASBASA (Seminar Nasional Bahasa dan Sastra), pages. 34–41.
 - [19] KBBI Daring. Available: <https://kbbi.kemdikbud.go.id/>
 - [20] Weka_tokenizers: R/Weka Tokenizers in RWeka: R/Weka Interface. Available: https://rdrr.io/cran/RWeka/man/Weka_tokenizers.html.
 - [21] Jabreel M, Moreno A. (2019) A Deep Learning-Based Approach for Multi-Label Emotion Classification in Tweets, *Appl. Sci.*, 9(6).
 - [22] Musto C, Semeraro G, Polignano M. (2014) A comparison of lexicon-based approaches for sentiment analysis of microblog, *CEUR Workshop Proc.*, 1314: 59-68.
 - [23] Buntoro GA. (2017) Analisis Sentimen Calon Gubernur DKI Jakarta 2017 Di Twitter, *Integer J. Maret*, 1(1): 32-41.
 - [24] Machine Learning Group - Department of Computer Science: University of Waikato. Available: <https://www.cs.waikato.ac.nz/research/research-groups/machine-learning-group>
 - [25] Wiley M, Wiley JF. (2019) *Advanced R statistical programming and data models: Analysis, machine learning, and visualization*. Apress Media LLC.
 - [26] Confusion Matrix for Your Multi-Class Machine Learning Model. Available: <https://towardsdatascience.com/confusion-matrix-for-your-multi-class-machine-learning-model-ff9aa3bf7826>.
 - [27] Hernandez-Suarez A, Sanchez-Perez G, Toscano-Medina K, Martinez-Hernandez V, Sanchez V, Perez-Meana H. (2018) A Web Scraping Methodology for Bypassing Twitter API Restrictions, pp. 1-7.
 - [28] Haniewicz K, Rutkowski W, Adamczyk M, Kaczmarek M. (2013) Towards the Lexicon-Based Sentiment Analysis of Polish Texts: Polarity Lexicon.
 - [29] Attribute-Relation File Format (ARFF). Available: <https://www.cs.waikato.ac.nz/~ml/weka/arff.html>.
 - [30] Handling imbalanced datasets in machine learning - Towards Data Science. Available: <https://towardsdatascience.com/handling-imbalanced-datasets-in-machine-learning-7a0e84220f28>.
 - [31] Longadge R, Dongre S. (2013) Class Imbalance Problem in Data Mining Review, *Int. J. Comput. Sci. Netw.*, vol. 2, no 1.

MONITORING AND CONTROL SYSTEM WITH A CLIENT-SERVER MODEL BASED ON INTERNET OF THINGS (IOT)

SRI RATNA SULISTIYANTI, F.X. ARINTO SETYAWAN*,
SRI PURWIYANTI, HELMY FITRIAWAN AND ADAM RABBANI ADNAN

¹Department of Electrical Engineering, Faculty of Engineering,
Universitas Lampung, Bandar Lampung, Indonesia

*Corresponding author: fx.arinto@eng.unila.ac.id

(Received: 25th August 2020; Accepted: 25th September 2020; Published on-line: 4th January 2021)

ABSTRACT: Safety and comfort are needs for all human beings. Meanwhile, the crime rate is increasing. Therefore, a remote monitoring and control system is needed. This research offers a home monitoring and control system with a client-server model using NodeMCUESP-12E. The equipment design can be used to monitor the condition of the house through sensors installed in each room. Home monitoring includes motion detection using a motion sensor, detection of the condition of the house door using a magnetic sensor, and remote door locking using a solenoid. The system can be operated offline or online using an Android smart phone. The communication model used for client-server over the transport layer protocol is User Datagram Protocol (UDP), so the server can communicate simultaneously on two clients. The fastest average response time is 0.653 seconds. The communication model between a server and a cloud uses Transmission Control Protocol (TCP) so that the data sent or received by the server through the internet is more reliable. The cloud used is Firebase which has real-time database facilities and historical data. When online, sensor response time average is the fastest on an android at 3.898 seconds, response time control is the fastest average on a client at 7.157 seconds and the control response time average is the fastest on an android at 9.495 seconds.

ABSTRAK: Keselamatan dan kesejahteraan merupakan keperluan penting untuk manusia. Sementara itu kadar jenayah pula kian meningkat. Oleh itu, kita perlu pemantauan jarak jauh dan sistem kawalan. Kajian ini merupakan sistem kawalan dan pemantauan rumah dengan model pelanggan-pelayan menggunakan NodeMCUESP-12E. Peralatan yang dibina boleh digunakan bagi mengawasi keadaan rumah melalui sensor yang dipasang dalam setiap bilik. Pemantauan rumah adalah termasuk pengesanan gerakan menggunakan sensor gerakan, pengesanan keadaan pintu rumah menggunakan sensor magnet, dan pengunci pintu jarak jauh menggunakan solenoid. Sistem ini boleh digunakan secara luar atau dalam talian menggunakan telefon pintar Android. Model komunikasi yang digunakan pada pelanggan-pelayan menggunakan protokol lapisan pengangkutan adalah Protokol Datagram Pengguna (UDP), oleh itu pelayan dapat berkomunikasi secara terus dengan dua pelanggan pada purata masa respon terlaju sebanyak 0.653 saat. Model komunikasi antara pelayan dan awan adalah menggunakan Protokol Kawalan Penghantaran (TCP), dengan harapan data dapat dihantar dan diterima oleh pelayan melalui internet dengan lebih kebolehpercayaan. Awan yang digunakan adalah Firebase yang mempunyai kelengkapan pengkalan data waktu nyata dan data sejarah. Melalui keadaan dalam talian, purata masa sensor bertindak balas adalah paling laju pada Android sebanyak 3.898 saat, purata kelajuan kawalan masa bertindak balas pada pelanggan adalah 7.157 saat dan purata masa kawalan tindak balas adalah paling laju pada Android sebanyak 9.495 saat.

KEYWORDS: *IoT; client-server; control; monitoring; android; NodeMCU ESP-12E*

1. INTRODUCTION

Home is where we live to meet daily needs. Along with the development of current times, many are using electronic systems inside their houses or buildings. Home security technologies in use today are often web-based, so home security monitoring only occurs when the owner opens the web address. Homeowners do not know the condition of their house directly, so that when there is a danger, unwanted events cannot be prevented in a timely manner.

One solution for checking security conditions and home control each time it is needed is a tool that can monitor the application via Smartphone with an internet connection using the concept of the Internet of Things (IoT) so that users can know the state of the home anytime and at any distance via the Internet. The concept of IoT is where objects can communicate with other objects or any embedded sensors connected through an Internet network [1]. One of the services used in the concept of the IoT is Firebase. Firebase is a Cloud Service Provider (CSP) and a Backend as a Service (BaaS) owned by Google which allows users to store data and read data in real time [2,3]. As a result of using these technologies, features don't need to be built from scratch and focus can shift to easily developing IoT-based applications without the need to create a cloud.

Previous research has been carried out by Nama, who designed a surveillance system over the internet using a BCM 2835 microcontroller and sent notifications via a short message service [4], and Despa, who designed smart monitoring of electrical quantities based on single board computer BCM2835 [5]. Other research was conducted by Nurfaif who designed a smart home using Raspberry Pi through the Global System for Mobile Communication (GSM) network [6]. Other research has also been carried out by Kodali whose home security system uses the CC3200 IT microcontroller. The system works on a single microcontroller with sensors via cables and sends notifications via telephone calls [7]. Subsequent research was carried out by Malche who designed a monitoring system via the MQTT-based internet web [8].

This research, designed to make home security maintained by monitoring the condition of a house, turning on the blower when there was LPG gas, locking the door electronically, and controlling the electric light in each room through the Android application over the Internet (online) or a local network (offline).

2. THE PROPOSED SYSTEM

This research uses firebase to facilitate the communication of mobile and Web applications. Firebase is a Cloud Service Provider offered by Google to facilitate the development of mobile and web applications. Firebase has real-time database facilities and historical data. The block diagram of the monitoring and control equipment designed through this research is shown in Fig. 1.

The client consists of some sensors, each of which is connected to NodeMCU ESP-12E. Client 1 is the MC-38 magnetic sensor and HC-SR505 motion sensor, client 2 is a HC-SR505 motion sensor, and client 3 is a HC-SR501 motion sensor and MC-06 gas sensor. Each client is connected to NodeMCU ESP-12E which then connects to a server in the form of NodeMCU SP-12E as well.

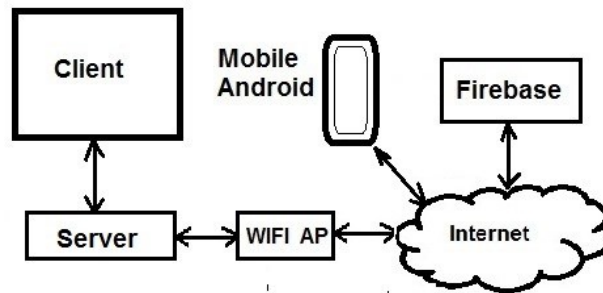


Fig. 1: Block diagram of system design.

2.1 Internet of Things

Internet of Things is a concept where certain objects have the ability to transfer data through the Internet [1]. This process does not require interaction from humans to humans or humans to a computer but can run automatically with the program. The constituent elements of IoT are artificial intelligence, sensors, connectivity, and various devices that are small in size.

Control and monitoring from very long distances can be done using IoT through the internet network. Sensors on the client side feel the phenomena that occur around them and send data to the microcontroller to be processed into information. Information from the microcontroller is then sent through the internet to the user's smartphone. Smartphone users can provide actions in the form of controlling remotely.

IOT devices can be connected to cameras installed in various locations in the city [9]. Cameras can be used for traffic monitoring, security for example, at banks, or face recognition to assist police. IOT applications in the health sector are used for remote monitoring and emergency notification systems [10]. This remote monitoring can range from monitoring blood pressure, heart rate, to sophisticated devices, namely monitoring special implants.

2.2 Firebase

Firebase is a Cloud Service Provider (CSP) and a Backend as a Service (BaaS). Firebase is the solution offered by Google to simplify mobile and Web application development [2]. This solution means that features don't need to be developed from scratch and focus can be placed on easily developing IOT-based applications without the need to create a dedicated cloud. Firebase has many SDKS that allow it to integrate with Android, iOS, Javascript, C++ to Unity.

2.3 Client-Server

Client-server is a work arrangement in accessing a server on a particular network between client and server. Data communications on the client-server are a range of interfaces that function as a place to run database applications. A client-server network is a computer network architecture where the client device will process the request for data, and the server has the task of responding in the form of data to the request [7]. The communication model of client and server network systems is shown in Fig. 2.

Client 1 used for controlling solenoid door locks in order to unlock and lock the doors, monitor motion, and monitor the condition of the door on the front porch of the House. Client 1 can be installed at the front door of the house. The goal is to be able to open and

close the door remotely and notify the homeowner if there is someone in front of the house. Client 2 is used to control the lights in the living room and monitor the movements in the House. Client 2 can be installed in the living room and used to monitor if there are people in the house.

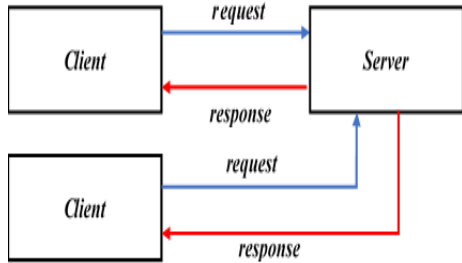


Fig. 2: Client-server network block diagram.

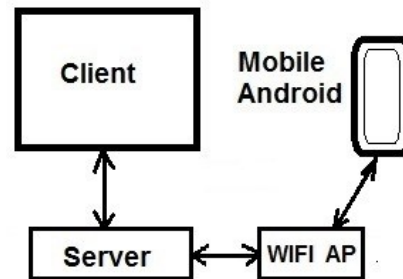


Fig. 3: Local network block diagram.

3. EXPERIMENTAL RESULTS

In this research, a comparison is made between the time response of the equipment in responding to commands when using either a local network or the Internet. The response time is determined using a stopwatch. A local network is a communication network using a Wi-Fi connection that gives commands to equipment over a maximum distance of only 10 meters. Communication or commands to equipment using the internet network can be done from anywhere with unlimited distance. Figure 3 shows a block diagram of a local network where communication is done between an Android mobile and equipment via a WiFi AP.

3.1 Client 1

Data response time on client 1 on the local network is shown in Table 1. The response time is the delay of the action that occurs on the sensor when given a command through the local network. Data is taken from five attempts with the initial conditions of both the door being closed or the door being open.

Table 1: Response time client 1 and android on the door with a magnetic sensor (MC-38) when offline

No.	Response Time of Android (seconds)	The Initial State of The Door	The Final State of The Door
1	2.24	Closed	Open
2	3.55	Closed	Open
3	2.88	Closed	Open
4	2.65	Closed	Open
5	1.65	Closed	Open
6	1.78	Open	Closed
7	2.91	Open	Closed
8	3.28	Open	Closed
9	2.69	Open	Closed
10	1.58	Open	Closed

Table 1 shows the response time for magnetic sensor (MC-38) given the state of the door with certain conditions on the local network or offline. Response time where the client sends data or sensor feedback results to the server and the server data or sensor results broadcast feedback to android WiFi AP via a network. The value of the response time average for Android is 2.521 seconds.

On the server, the data is processed in the form of JSON data type and then the sensor or result data broadcasts feedback to the WiFi AP. The Android listens to data from the server via the WiFi AP network and receives the sensor results data.

On Android applications, each client listens to data sensor results from the server via WiFi AP. The client had an arranged time span to send data or sensor feedback results to the server with a range of 1000 ms and span of time servers for broadcast data or sensor feedback results to WiFi AP i.e. 1000 ms. So, the total minimal time span required from the client to the Android application through the local network or offline is 1000 ms.

There exists a delay in response time because when the client sends to the server. If the server is not processing data at that time, such as when it is still processing data from the cloud, this creates a span of 300ms for client listening. When a server sends broadcast data to Android, Android receives data every 1000ms and processes data from the Firebase cloud conditions.

Table 2 shows Android data response time on client 1, for magnetic sensors (MC-38) given the State of the door with a particular condition on the Internet network or online. The Android response time is where the client sends data or sensor feedback results to the server and the server is writing data to the sensor or the results of the feedback to the cloud through a network of WiFi AP Firebase. The value of the response time average android is 4.373 seconds.

Table 2. Response time client 1 and android on the door with a magnetic sensor (mc-38) when online

No.	Response Time of Android (seconds)	The Initial State of The Door	The Final State of The Door
1	4.04	Closed	Open
2	5.77	Closed	Open
3	2.84	Closed	Open
4	4.54	Closed	Open
5	3.61	Closed	Open
6	5.25	Open	Closed
7	5.99	Open	Closed
8	4.76	Open	Closed
9	2.47	Open	Closed
10	4.46	Open	Closed

On the server, the data results of the sensors or feedback received from the client is processed in the form of JSON data type and, if the data changes, then the server writes the results of sensor data or feedback to the Firebase network through cloud WiFi AP.

The Android app reads sensor data from each client from the cloud Firebase. The client has an arranged time span to send data or sensor feedback results to the server with a 1000 ms range and the span of time the server to write data or sensor feedback results to the cloud through a network of WiFi AP Firebase with a 4000 ms range. So, the total minimal time span required from the client to the internet network through the android application or online is 4000 ms.

There exists a delay in response time, because when the client sends data to the server at the time of that time, the server is still processing the data from the cloud and 300ms for listening span client and when the server sends a broadcast data to Android. Android receives data every 1000 ms and processes data from the cloud conditions Firebase.

The Android data response time on client 1 for motion sensors (HC-SR505) was given to the condition of the moving objects on the local network or offline and online shown by Table 3. The response time of the android is where the client sends data or sensor feedback results to the server and the server data or sensor results broadcast feedback to android WiFi AP via a network. In this research, data retrieval is carried out 10 times when the motion sensor senses the object moving. The value of the Android response time average is 2.3 seconds for a local network and 4.753 seconds.

The Android app reads sensor data of each client from the cloud Firebase. The client has arranged a time span to send data or sensor feedback results to the server with a 1000 ms range and the span of time for the server to write data or sensor feedback results to the cloud through a network of WiFi AP Firebase is 4000 ms range. So, the total minimal time spans required from the client to the internet network through the android application or online is 4000 ms.

Table 3: Response Time Client 1 and android on the sensor motion (HC-SR505) when online

No.	Response Time of Android when offline (seconds)	Response Time of Android when online (seconds)
1	3.8	4.45
2	1.85	5.75
3	3.02	3.54
4	3.09	5.08
5	2.64	5
6	1.85	4.32
7	1.29	3.54
8	1.78	5.62
9	2.03	4.52
10	1.65	5.71

There exists a delay in response time because when the client sends data results of a sensor to the server, the server is still processing the data from the cloud and the server has a server listening span of 300 ms. When the server sends data from the cloud conditions, Firebase and Android are reading data from a cloud firebase every 1000 ms.

Table 4 shows data for the response time of Client 1 and Android, when the solenoid door lock is executed with Open and Closed conditions on the local network or offline. The client response time is faster than Android because the response time of the client is the response time span between the Android data giving instructions to the server through a Network Access Point (AP) WiFi broadcast and the server data instructions to the client via the Wi-Fi network server. While the response time on Android is the response time of a client after the process and the Android listening time. Android listening time process is a time span of listening data from the server via the WiFi AP network. The value of the average client response time is 0.653 seconds and the value of the Android response time averages is 4.108 seconds.

On the server, data and instructions from android are treated in the form of JSON data and then the instruction data is sent to the broadcast client, so the client receives the instruction data and executes it. The server has an arranged span to send data to the client with an instructions range of 500 ms. So the minimum range of client response time via local network or offline is 500 ms.

Table 4: Response Time Client 1 and android on the solenoid door lock when offline

No.	Response Time of Client (seconds)	Response Time of Android (seconds)	The Initial State of The Lamp	The Final State of The Lamp
1	0.85	4.19	Closed	Open
2	0.8	3.84	Closed	Open
3	0.6	4.47	Closed	Open
4	0.61	3.36	Closed	Open
5	0.53	3.8	Closed	Open
6	0.74	6.15	Open	Closed
7	0.6	3.95	Open	Closed
8	0.66	3.95	Open	Closed
9	0.54	3.39	Open	Closed
10	0.6	3.98	Open	Closed

On Android, the client sends data measurement results or feedback data to a server with a span that is 1000 ms, the server listening to the client is set up with a span that is 300 ms, and server processes the data of each client in the form of JSON data then Server broadcast to android apps via the AP with WiFi within 1000 ms. So the minimum range of response time from android to the server to the client and that client to the server through a local network to the Android or offline is 1500 ms.

The existence of a delay in response time is because when Android data sends instructions to a server, the server is still processing the data from the cloud, a 300ms listening client span, and the time for the server to send broadcast data to Android. The Android application receives data every 1000ms and the server processes the data to the cloud conditions Firebase. When the client next sends the feedback data to the server, the server is still processing the data from the cloud and the server has a span of 300ms for client listening. When a server sends a broadcast data to Android, Android receives data every 1000 ms.

Table 5: Response Time Client 1 and android on the solenoid door lock when online

No.	Response Time of Client (seconds)	Response Time of Android (seconds)	The Initial State of The Lamp	The Final State of The Lamp
1	7.85	14.73	Closed	Open
2	10.19	16.71	Closed	Open
3	6.8	13.79	Closed	Open
4	7.85	14.39	Closed	Open
5	6.87	12.95	Closed	Open
6	5.88	10.28	Open	Closed
7	8.24	15.03	Open	Closed
8	6.94	11.44	Open	Closed
9	8.82	12.1	Open	Closed
10	8.58	13.81	Open	Closed

Table 5 shows data of the response time of a client and Android for Client 1, when the solenoid door lock executes commands with Open and Closed conditions over the Internet network or online. The response time of the client is faster than the Android response time because the response time on the client is the response where the time span between android writes instruction data to the Firebase cloud, the server reads the Firebase cloud, and the server broadcasts the instruction data to the client via the WiFi server network. While the response time on Android is the response time after the client response time process, the

server time process writes instruction data to the Firebase cloud, and the Android time process reads the Firebase cloud. The average response time of the client is 7.802 seconds and the average response time of the android is 13.523 seconds.

3.2 Client 2

Client 2 is a controller for living room lights and monitoring of moving objects in the house. Table 6 and Table 7 shows the data for the response time of a client and Android on Client 2, when executed with the final State of a particular lamp through the local network (offline) and Internet (online).

The average client response time for the living room lights is 0.986 seconds and the average value of the Android response time is 3.719 seconds on the local or offline network. While the average client response time for a living room lamp is 7.157 seconds and the average value of Android response time is 9.495 seconds on the internet or online.

Table 6: Response Time to Client 2 and Android on the living room light when offline

No.	Response Time of Client (seconds)	Response Time of Android (seconds)	The Initial State of The Lamp	The Final State of The Lamp
1	1.19	3.44	Off	On
2	0.93	2.62	Off	On
3	0.73	2.87	Off	On
4	1.12	4.61	Off	On
5	0.79	3.1	Off	On
6	1	4.83	On	Off
7	1.19	3.26	On	Off
8	0.73	4.71	On	Off
9	1.12	4.99	On	Off
10	1.06	2.76	On	Off

Table 7: Response Time to Client 2 and Android on the living room light when online

No.	Response Time of Client (seconds)	Response Time of Android (seconds)	The Initial State of The Lamp	The Final State of The Lamp
1	8.57	11.58	Off	On
2	7.19	9.38	Off	On
3	7.46	9.56	Off	On
4	6.74	9.12	Off	On
5	6.67	8.77	Off	On
6	5.96	8.51	On	Off
7	8.82	11.07	On	Off
8	8.25	10.33	On	Off
9	5.69	8.16	On	Off
10	6.22	8.47	On	Off

Table 8 shows the Android data response time on client 2, when the motion sensor (HC-SR505) found the condition of a moving object when used on a local network and the Internet. Response time of the android on the local network is the time response when the client sends data or sensor feedback results to the server and the server data or sensor results broadcast feedback to Android WiFi AP via a network. The value of the Android response time on the local network is 1.411 seconds.

Android response time on internet network is response time where the client sends data or sensor feedback results to the server and the server is writing data to the sensor or the results of the feedback to the Firebase network through cloud WiFi AP. On the server the data results of the sensors or feedback received from the client are processed in the form of JSON data type and, if the data changes, then the server writes data the results of sensor or feedback to the cloud through a network of WiFi AP Firebase. The value of the response time averages android using the internet network is 3.898 seconds

Table 8: Response Time to Client 2 and Android on the sensor motion (HC-SR505) when offline and online

No.	Response Time of Android on local network/offline (seconds)	Response Time of Android on Internet network/online (seconds)
1	1.58	3.74
2	1.19	4.83
3	1.33	3.35
4	1.06	3.68
5	1.45	3.37
6	0.92	3.73
7	1.85	3.89
8	1.57	4.4
9	1.39	3.99
10	1.77	4

3. CONCLUSION

On the designed system, client response time for offline usage is faster than online. The offline use does not require an Internet network and is done only through WiFi AP communication with Android mobile. Online use requires an Internet network to communicate with Firebase, which takes longer. The average response time of the magnetic sensor on client 1 for offline usage is only 2.521 seconds while online usage takes 4.373 seconds. The average response time of the motion sensor on Client 1 for offline usage is only 2.3 seconds while online usage takes 4.753 seconds. The average response time of the solenoid on the client-side for offline usage is only 0.653 seconds and on Android side is 4.108 seconds while online usage takes 7.802 seconds on the client-side and 13.523 seconds on the Android-side. For lamp control on Client 2, the average response time takes 0.986 seconds on the client-side and 3.719 seconds on the Android side on offline use, while online usage takes 7.157 seconds on the client-side and 9.495 seconds on the Android side. The average response time of the motion sensor on Client 2 for offline usage is only 1.411 seconds while online usage takes 3.898 seconds.

For further research, more sensors such as gas sensors, visual sensors (cameras), temperature sensors, and voltage sensors need to be added to provide more safety for the user.

ACKNOWLEDGEMENT

Thank you to the Ministry of Research, Technology and Higher Education, Directorate General of Research and Development, Directorate of Research and Community Service for the funds provided through the PPUPIK scheme.

REFERENCES

- [1] Minerva R, Biru A and Rotondi D. (2015) Towards a definition of the Internet of Things (IoT). In Proceeding IEEE Internet Initiative: 1-86.
- [2] Moroney L. (2017) The definitive guide to firebase. A Press, California, Google.
- [3] Zuhelmi TP, Sulistiyanti SR, Setyawan FXA, Adnan AR. (2019) Smart home controlling and monitoring system using multiboard client-server internet of things (IoT). *Journal of Engineering and Scientific Research*, 1(2): 69-73.
- [4] Nama GF (2013) The design of an internet connection monitoring system at Lampung University based on a mini single board computer BCM2835. (Rancang Bangun Sistem Monitoring Sambungan Internet Universitas Lampung Berbasis Mini Single Board Computer BCM2835). In Proceeding National Seminar on Science & Technology V: 73-83.
- [5] Despa D, Kurniawan A, Komarudin M, Mardiana, Nama GF. (2015) Smart monitoring of electrical quantities based on single board computer BCM2835. In Proceeding of the 2nd International Conference on Information Technologies, Computer, and Electrical Engineering (ICITACEE 2015):315-320.
- [6] Nurfaif MB, Sulistiyanti SR, Komarudin M, Nama GF (2017) Telemetry and tele-control of electronic appliances for smart-home-system. In Proceeding International Symposium on Electronics and Smart Devices (ISESD):18-23.
- [7] Kodali RK (2016) IoT based smart security and home automation system. In Proceeding International Conference on Computing, Communication and Automation (ICCCA):1286-1289.
- [8] Malche T (2017) Internet of Things (IoT) for building Smart Home System. In Proceeding International Conference on I-SMAC Palladam-2017:65-70.
- [9] Bharati TS. (2019) Internet of Things (IoT): A Critical Review. *International Journal Of Scientific & Technology Research*, 8:227-232.
- [10] Madhavia MVDNS, Hemalathaa K, Sairamb PVS, Rajani D. (2016) Healthcare applications of the Internet of Things (IoT): A Review. *Proceedings of 3rd International Conference on Emerging Technologies in Computer Science & Engineering (ICETCSE 2016):205-213.*

PREDICTING TRUST IN A SOCIAL NETWORK BASED ON STRUCTURAL SIMILARITIES USING A MULTI-LAYERED PERCEPTRON NEURAL NETWORK

AMIR HOSSEIN DANESH¹ AND HOSSEIN SHIRGAHI^{2*}

¹Sogang University, Seoul, South Korea

²Computer Engineering Department, Islamic Azad University,
Jouybar Branch, Jouybar, Iran

*Corresponding author: hossein.shirgahi@gmail.com

(Received: 9th September 2020; Accepted: 14th October 2020; Published on-line: 4th January 2021)

ABSTRACT: Although research on social networks is progressing rapidly, the positive and negative effects of this area should be evaluated. One of the problems is that social networks are very broad and anyone can have influence on them. This matter can cause the issue of people with different beliefs. Therefore, determining the amount of trust to various resources on social networks, and especially resources for which there is no previous history on the web, is one of the main challenges in this field. In this paper, we present a method for predicting trust in a social network by structural similarities through the neural network. In this method, the web of trust data set is converted to a structural similarity data set based on the similarity of the trustors and trustees first. Then, on the created data set, a part of the data set is considered as the training data and it is trained based on the multilayer perceptron neural network and then the trained neural network is tested based on the test data. In the proposed method, the MSE value is less than 0.01, which has improved more than 0.02 compared to previous methods. Based on the obtained results, the proposed method has provided acceptable accuracy.

ABSTRAK: Walaupun kajian tentang rangkaian sosial adalah sangat pesat, kesan positif dan negatif dalam ruang lingkup ini perlu dinilai. Masalah rangkaian sosial adalah sangat luas dan sesiapa sahaja boleh terpengaruh. Perkara ini akan menyebabkan manusia dengan pelbagai isu kepercayaan. Oleh itu, menentukan nilai kepercayaan melalui pelbagai sumber dalam rangkaian sosial, terutama sumber-sumber yang tidak mempunyai sejarah lepas dalam web, adalah salah satu cabaran dalam bidang ini. Kajian ini membentangkan jangkaan kepercayaan dalam rangkaian sosial melalui persamaan struktur dengan menggunakan rangkaian neural. Kaedah ini ditentukan dengan menukar set data web kepercayaan kepada struktur set data hampir sama berdasarkan kesamaan pemegang dan pemberi amanah. Kemudian, sebilangan set data yang telah dibina ini dipertimbangkan sebagai data latihan dan ia dilatih berdasarkan rangkaian neural perseptron berbagai lapisan dan kemudian rangkaian neural yang terlatih ini diuji berdasarkan data ujian. Dalam kaedah yang dicadangkan ini, nilai MSE adalah kurang daripada 0.01, di mana telah diperbaiki kepada 0.02 lebih daripada kaedah-kaedah sebelum ini. Berdasarkan dapatan kajian, didapati kaedah yang dicadangkan ini menunjukkan ketepatan yang boleh diterima.

KEYWORDS: *social network; trust; structural similarity; web of trust; neural network*

1. INTRODUCTION

In recent years, topics such as social networks and semantic web have become the main topics of research in emerging social media. The philosophy of creating social networks is such as world wide web, in which everyone can produce information or use the information of others. So far, most of the researches that has been done in the field of semantic web and social network platform has been related to determine the standards of communication rules and facts such as XML, RDF, RDF diagram, OWL, etc., which create the necessary basis for building a social network.

It is clear we can't expect every user to know how reliable each resource is. Also, due to the objective nature of the trust, the overall values of believability cannot be determined. It must be determined to what extent each source of information can be trusted. One solution is to keep all the information high quality and with no contradicted on social network. But due to the intensity and variety of resources, this is almost impossible. As a result, assuming the variety of information quality, an efficient solution must be provided that can be considered effective.

The researchers of WWW found that a method to do this is using quality assertion in the link structure between pages [1]. Such a function is also used in social networks. Often in order to evaluate trust in social networks, web of trust is made based on users and their interactions and analysis of the above web of trust is done. The created web of trust may be used repeatedly to determine a user's trust to the other users. Remember that unlike site ranking, the result of calculations on web of trust networks is not an accumulation of each user's trust ability. Instead, each user receives a set of his personal trusts that its amount is vary greatly from person to person. Another challenge in this area is the type of assertion to the content of social networks, which can be logical or probable. If the user assertion is a logical type, each user can have agree or disagree assertion with each content. If all assertions are inconsistent about one content, that content can be believed with certainty and the assertions can be combined logically. Otherwise, probabilistic calculations can be used. Of course, the purpose is not to understand the reasons of the assertions. Rather, due to the difficulty of establishing a degree of belief in an assertion that is explicitly stated by one or more resources on the social network, the goal is finding a solution for the above problem.

The basic model is that a user's belief in an assertion should be a function of the trust to the source that provides it. If the user's belief in the source is clear, the user's belief in the person who determines the amount of trust for the source can be calculated. This is done in a variety of ways that is related to how people's beliefs are formed. If there are trusts from A to B scores at U amount and from B to C scores at V amount, then A will have a ratio of trust to C scores at T amount, which T is itself a function of U and V.

This rule can be used to measure user trust in resources and also to answer the question of how much each user can trust sources that he or she does not know directly. This law is based on the hierarchical publication of trust. Admissible methods of combining trusts that allow accurate and local calculation of derived trusts have limitations. These limitations in the composition of beliefs also cause to do only with the use of local information [2].

Consider a system consisting of n users that have m assertions in overall. Since each assertion is considered separately, we introduce the system in such a way that there seems to be only one assertion. Beliefs: Each user can affect his personal belief in assertion that ranges from 0 to 1. The high numerical value of this range indicates that the assertion is accurate and reliable. Suppose B_i represents the personal belief of the user i in the assertion.

If the user i does not have belief, we set B_i to zero. The set of personal beliefs in the assertion is shown as a B-column vector.

Trusts: User i can trust user j as T_{ij} . It ranges from 0 to 1. The high numerical value of T_{ij} shows that user i trusts user j or they have the same interests. If the trust value is not specified, we set T_{ij} to zero. Note that T_{ij} and T_{ji} do not have to be equal.

The set of personal trusts can be represented as a matrix T with $n * n$ dimensions. T_i represents the linear vector of the user i 's personal trust to the other users [3].

Integration: Web of Trust creates a structure in which we can calculate the level of belief of each user of the assertion. To distinguish it from the personal beliefs of the user (B), we call it integration beliefs.

In this article, we do not deal with the details of users' beliefs and individual assertions on the content; rather, by using the web of trust and the specific values of trust in the data set, we predict the trust for nodes that do not have a direct edge. We perform predicting trust based on different structural similarities and their combinations using a multilayer perceptron neural network in social network. In previous research, a structural similarity method is usually used. As another innovation in this article, we used the similarity of both trustor and trustee to predict trust, but in previous methods, one of these two similarities is often used.

2. PREVIOUS WORKS REVIEW

In general, there are two models of trust based on web of trust data set: the binary trust model with the probability distribution available in [4,5] and the multilevel trust model without the probability distribution [6]. Most e-commerce websites, such as eBay, Ali baba, Amazon and Yelp, have adopted a multi-level trust model. In some studies, the display of trust has been generalized in statistical distribution. In particular, reference [7] suggests a subjective logic to express distrust and to evaluate the trust probability distribution. But this method can only be used for the binary trust model. A variety of methods have been proposed to evaluate or trust propagation in different types of networks [8] and [9]. For example, in reference [9], a scoring system called Eigen Trust is created based on peers' historical functionality for peer to peer networks. However, this method is not directly applicable to assess the trust of social networks, because two people may have disparate opinions on a social network about the reliability of a person or party.

According to reference [10], for each person, a global reputation on the network is evaluated from the view of valid nodes. A Tidal Trust algorithm was proposed in reference [6], that infer and speculate trust relations using continuous scale ranking. This method collects trust data from all reference paths according to the shortest path from one source to the destination. It then uses the weighted average method to calculate the total trust value. A trust inferential model called Sunny is proposed in reference [4] to measure trust through possible sampling and to reduce the impact of longer-distance routes (usually for low-confidence estimates). A flow-based trust assessment is proposed that considers the dependence of the path using network flows, and the trust models reduce or spread trust using expanding the flow associated with each node in the reference [5].

Reference [11] uses a matrix to display direct trust relationships between users on a social network and uses the Breadth-First search algorithm to enhance users trust. A binary decision chart based method [13] is proposed to evaluate the trust between the two parties, but it is only applicable for the binary trust model in the reference [12]. In this paper, the

relationship of trust between two directly connected parts is modeled using a multifaceted trust model with probability distribution. Then, a probabilistic hybrid method based on multi-valued decision diagram (MDD)'s is presented to determine the probability distribution of different levels of trust between the two parties on the social network. The parties can be connected through multiple routes, including a direct link or several indirect links. Dependence between different paths during the creation of the MDD model has been investigated. In reference [14], the TILLIT method is proposed, which is a pattern based on a combination of trust inference and user similarity. This similarity is based on the structure of the trust diagram and user's trust behavior. This method is unlike other filter-based approaches that have used user rankings.

The trust assessment is performed based on the reputation parameters of the recommendation according to the users' profiles in the reference [3]. Its purpose is to provide a fuzzy system for evaluating trust based on users' profiles, examining the accuracy of the fuzzy system for evaluating trust, and examining the time complexity of the fuzzy system for evaluating trust in the Semantic Web. In this research, user profile data set based on semantic parameters has been used. For this purpose, they have considered their desired data set from CTI Depaul site, which includes a list of pages, user sessions, pages visited in each user session, and the time users visited the pages.

mirroring trust is used to predict trust in reference [2], which estimates the amount of trust based on the degree of similarity between the trustor and the trustee. In this paper, the parameters degree, degree quality and local density in social networks have been used to determine similarity criteria and in order to calculate the similarity of each of these parameters, a fuzzy system is used.

Shirgahi et al. [1] gained the assessment of trust in the Semantic Web and Social Network by clustering the Web of trust in their research first, after that they used distributed aggregation of indirect trust paths to predict trust for nodes that do not have direct trust. This method has an acceptable execution time.

3. MULTI-LAYERED PERCEPTRON NETWORK

Past research shows that among the various methods of the neural network, the multi-layer perceptron network (MLP) with the law of feed forward back propagation is one of the most widely used, basic, and at the same time simplest models of neural network available. Also, MLP has been evaluated a suitable method in the field of estimating unknown parameters.

The learning algorithm in these types of networks is a type of error correction algorithm, which is called error Back Propagation algorithm or back Propagation briefly. These types of networks have an input layer, one or more hidden layers, and one output layer, and the information moves only in one direction, the direction of which is forward. In fact, the information starts from the input nodes and passes through the hidden layer (s) to the output nodes. So, there is no feedback. This means that the output of each layer only affects the next layer and does not change its own one (Fig. 1). Each network cell has a nonlinear function at the output and is derived for all inputs. The structure of the neural network used in this study is the back Propagation neural network with two hidden layers and one output layer. Also, the artificial neural network model is trained using the train set and different combinations of inputs are created. Therefore, to achieve these goals, 60% of the data are used for training, 20% for testing and 20% for evaluation.

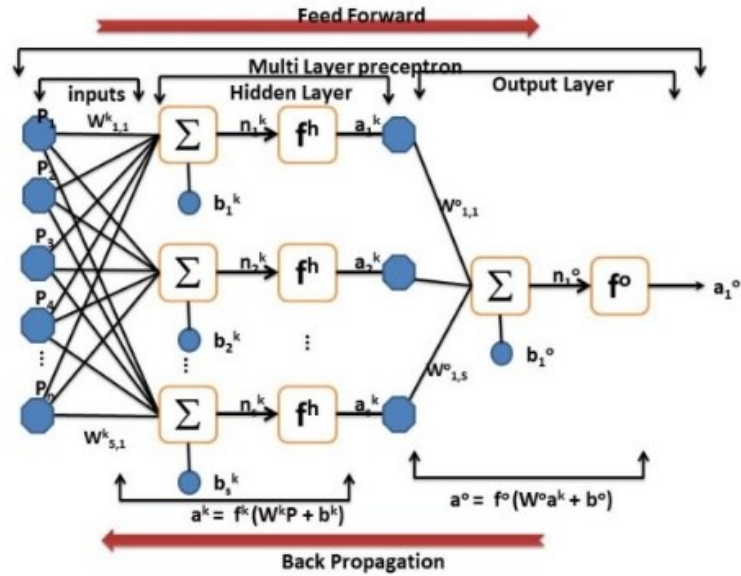


Fig. 1: View of the two-layer artificial neural network back propagation.

4. PROPOSED METHOD

In this section, the various criteria for structural similarity in the social network will be described first, then the structure of converting the social network data set to the structural similarity data set will be shown, and finally the structure of the proposed multi-layered perceptron neural network will be explained.

4.1 Structural Similarity Criteria in Social Network

In this article, to determine the structural similarity in the social network, we have used a series of structural similarities of the weighted directional graph and a series of structural parameters in the social network. Before explaining the above criteria, we first describe the structure of web of trust.

A web of trust is a weighted directional graph as Fig. 1 and the values of the weights of the nodes and edges are in the range $[0, 1]$. The nodes in this part of the study are the trustors and trustees. The weight of each node determines the global reputation of each node which is determined by Eq. 1. The weight of each edge u to v determines the value of direct trust obtained by direct interactions from u to v .

$$\text{Rep}_i = \begin{cases} 0 & N_T = 0 \\ \frac{\sum_{j \neq i, T_{ji} \neq 0} T_{ji}}{N_T} & N_T \neq 0 \end{cases} \quad (1)$$

In Eq. 1, T_{ji} is the value of direct trust from j -node to i -node and N_T is the total number of nodes that trust directly on i -node.

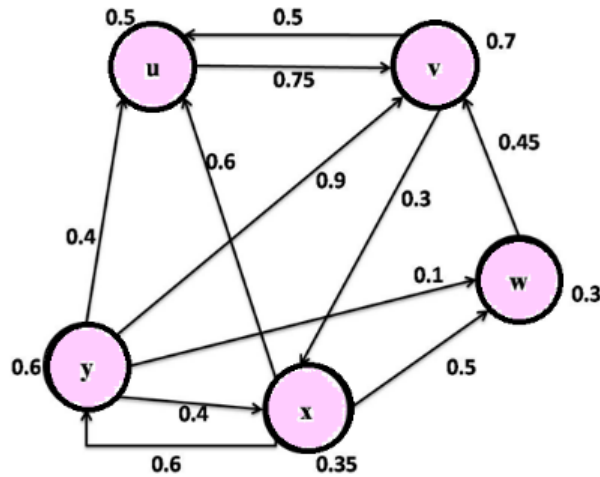


Fig. 2: An example of a web of trust network.

4.2 Graph Structural Similarities

In this paper, 5 structural similarities based on edges are used. Of course, the relationships of these similarities are weighed based on the amount of trust that exists between the nodes in the web of trust. Since the numerator of deduction of all these equations of edges based structural similarity, are according to the intersection of two u and v nodes, we define the weighted intersection of nodes according to Eq. 2.

In Eq. 2, V is a set of web of trust nodes and $|T_{ui} - T_{vi}|$ is the absolute value between T_{ui} and T_{vi} .

$$|u \cap v| = \sum_{i \in V, T_{ui} \neq 0, T_{vi} \neq 0} 1 - |T_{ui} - T_{vi}| \quad (2)$$

In this study, we weighted the structural similarities of Cosine, Dice, HDI, HPI, and Jaccard. These similarities are calculated by Eqs. (3) to (7), respectively. In these equations, $|u \cap v|$ is the weighted intersection of nodes u and v in accordance with Eq. 2 and the Rep_u and Rep_v parameters are the reputation values of nodes u and v , respectively, based on Eq. 1.

$$Sim_{Cosine}(u, v) = \frac{|u \cap v|}{\sqrt{Rep_u * Rep_v}} \quad (3)$$

$$Sim_{Dice}(u, v) = \frac{2 * |u \cap v|}{Rep_u + Rep_v} \quad (4)$$

$$Sim_{HDI}(u, v) = \frac{|u \cap v|}{\max(Rep_u, Rep_v)} \quad (5)$$

$$Sim_{HPI}(u, v) = \frac{|u \cap v|}{\min(Rep_u, Rep_v)} \quad (6)$$

$$Sim_{Jaccard}(u, v) = \frac{|u \cap v|}{Rep_u + Rep_v - |u \cap v|} \quad (7)$$

4.3 Structural Parameters in the Social Network

In web of trust networks that are used to assess trust in social networks or semantic web, different parameters are considered to compare networks and the similarity of nodes. Some of these parameters are semantic and are often used in semantic web, and others are structural parameters that are often considered in social networks to show similarities. In this part of the research, we describe some of the most important parameters of social networks that are used for the structural similarities of nodes.

Out degree:

The output degree parameter is used to determine how much a node exchanges information with other network nodes in a network. For discrete networks, the normal value of the out degree is obtained by dividing the number of output edges of a node by the maximum number of possible edges for that node (which can be the graph degree). For example, if there are five nodes in a network and one source node connects with three of the other four nodes through an edge, the out degree of the source node is 0.75.

In order to extend the out degree for weighted networks with weighted nodes, the values of these edges are weighted based on the importance of the nodes in the other heads leading to these edges. In this method, a node that is connected to other more important nodes has a higher out degree rather than a node that is connected to other nodes of the same size or less importance. In fact, in web of trust, not only the number of outgoing edges is important, but also the value of these edges and the reputation value of the destination nodes in the edges. Because the value of the edges indicates the value of direct trust between the two nodes and the value (weight) of the destination nodes and the reputation value of the destination nodes. Based on the explanations given in this study, we used Eq. 1 to determine the out degree.

$$D_{out}(i) = \frac{1}{1-Rep_i} \sum_{j \neq i} Rep_j \times T_{ij} \quad (8)$$

In Eq. 8, in addition to the reputation of destination nodes and the direct trust from the source node to the destination node, the value of the source node reputation is also effective. In Eq. 8, Rep_i is the source node reputation, Rep_j is the destination nodes reputation, T_{ij} is the value of the direct trust from i -node to j -node, and $D_{out}(i)$ is the out degree of i -node (source).

Since a node with a higher out degree can transmit more information to other nodes, so a node with a higher out degree can transmit faster or more appropriate information to other nodes compared with a node with a lower out degree. On the other hand, the out degree has no effect on the node that received the information. Therefore, we cannot expect the out degree to be effective on the time required for a node to receive information. The degree of input in many researches in web of trust is also called degree of reputation. By combining weighted nodes, the in degree can be defined based on the Eq. 9.

$$D_{in}(i) = \frac{1}{1-Rep_i} \sum_{j \neq i} Rep_j \times T_{ji} \quad (9)$$

In Eq. 9, Rep_i is the source node reputation, Rep_j is the destination nodes reputation, T_{ij} is the value of the direct trust from j -node to i -node, and $D_{in}(i)$ is the in degree of i -node (source). The input and output degrees are the same for symmetric networks, but these degrees are usually different in web of trust.

In degree:

The input degree parameter is used to determine how much a node receives information from other nodes. For discrete networks, the normalized value of the in degree is obtained by dividing the number of input edges of a node by the maximum number of possible edges for that node (which can be the degree of the graph). The advogato social network data set is a directed graph with 51332 edges and 47300 nodes. Each record has 3 attributes, respectively the trustor user, the trustee user, and the value of trust. In this article, we have created a structural similarity data set using information about the edges and structural similarities of nodes. It has 51332 records, and each record is obtained based on the structural similarity analysis of each record in the advogato social network data set.

The structural similarity data set has 13 features for each A_i record from the advogato social network data set. $A_{i,1}$ is the number of a trustor node that trusts the trustee node $A_{i,2}$ as much as $A_{i,3}$ in the i -th record of the data set.

4.4 Converting Web of Trust Data Set to a Structural Similarity Data Set

In this study, converting the web of trust data set to a structural similarity dataset is done based on graph structural similarity and structural parameters in the social web. First, look at Fig. 3. The main problem is that the trustor p -node has no previous interaction with the trustee node q . The goal is to estimate the value of p to q based on the structural similarities between nodes p and q and other nodes. We can obtain the structural similarity of the q -node with all the trustee nodes with which the p -node has previously interacted (Fig. 3a). Based on this, the trust value can be predicted to determine the structural similarities of p -node with other nodes.

In addition, we can obtain the structural similarity of p -node with all other trustor nodes that have previously interacted with q -node (Fig. 3b) and predict the trust value on this basis. In this study, we used a combination of two structural similarities between trustors and trustees. Also, the out degree of the p -node and the in degree of the trustee nodes have a large effect on the prediction of the trust. As a result, we consider both of these features.

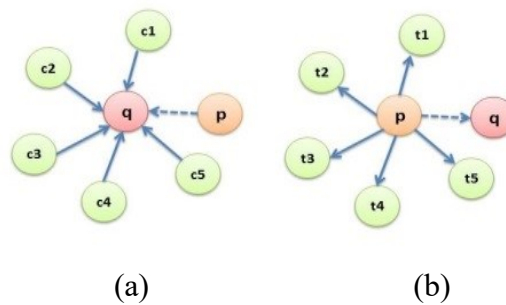


Fig. 3. Trustees Similarities and Trustors Similarities in Predicting Trust
a) Trustors Similarities, b) Trustees Similarities.

The general structure of converting web of trust data set to a structural similarity data set is shown in Fig. 4. In the social network data set, we have an $A_{n \times 3}$ matrix that n is the total number of edges and the three columns in A , respectively, are the number of trustor nodes, the number of trustee nodes, and the trust value corresponding to each trustor node to the trustee node. The structural similarity data set is a $B_{n \times 13}$ matrix, which n is the total number of edges, columns 1 to 12 are the structural similarity features, and column 13 is the trust value of the corresponding record in matrix A . Here's how to calculate the above 13 features: the first 5 features are obtained based on the structural similarity of $A_{i,1}$ and $A_{i,2}$ nodes in terms of the similarity of the trustees to them, respectively, according to the similarities of Cosine, Dice, HDI, HPI and Jaccard and the sixth feature is obtained based on the normalized out degree of $A_{i,1}$.

The features 7 to 11 are obtained based on the structural similarity of $A_{i,1}$ and $A_{i,2}$ nodes in terms of the similarity of the trustors to them, respectively, according to the similarities of Cosine, Dice, HDI, HPI and Jaccard. The twelfth attribute is based on the normalized value of $A_{i,2}$ node's in degree and the thirteenth attribute indicates the trust value, in other words $A_{i,3}$ node. Our goal of such a structural change has been to have a data set independence of the number of nodes, to have a trust value according to the different types of structural similarities between trustee and trustor nodes.

After creating the structural similarity data set, we randomly considered 70% of the data set as training data, 15% of the data as experimental data, and 15% of the data as validation data. You can see the general structure of the multilayer perceptron neural network in Fig. 5. In this structural similarity data set, the first 12 features are considered as input and the last feature is considered as output. Then, by teaching the above data set through the artificial neural network, the trust between structural similarity and trust value is obtained. Finally, the trust value for nodes that do not have a direct edge in the web of trust data set is estimated based on the trained neural network.

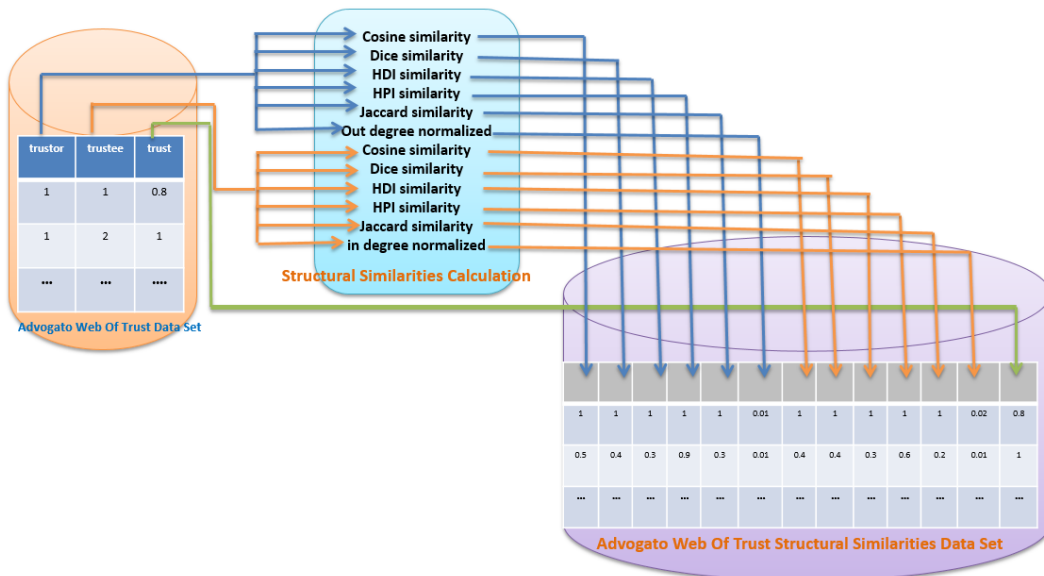


Fig. 4: Converting web of trust data set to a structural similarity data set.

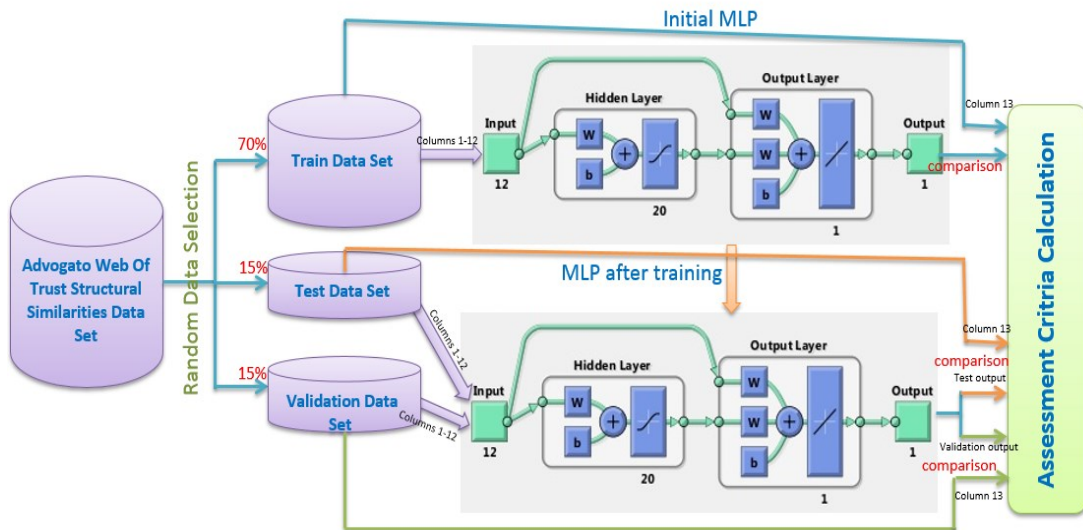


Fig. 5: General structure of multilayer perceptron neural network in the proposed method.

5. SIMULATIONS AND TESTS

The simulation of this article is done in MATLAB 2016. For this purpose, we used advogato web of trust data set, including a graph which characteristics are shown in Table 1 [15]. This data set has 51332 records; each record contains 3 columns (attributes) that

represent the trustor node, trustee node and trust value, respectively. In this data set, the trust values are positive and have one of the values 0.6, 0.8 and 1, and there are no distrust values. Clearly, if there is an edge between the two nodes, it shows that there has been a trusted interaction in the past. Therefore, trust is inferred from trustee behaviors, in other words, if the trustee's performance is appropriate, the trustor will trust it. Only if there is no direct edge between the two nodes, is it necessary to perform the trust prediction. In test operation, if there is a direct path between two nodes in web of trust, we also calculate the trust of the indirect path and compare the two values.

Table 1: Advogato web of trust data set characteristics

Characteristic	Value
Number of nodes	47300
Number of edges	51332
Graph density	0.0035
The most node degree	947
The least node degree	1

5.1 Evaluation Criteria

In this paper, the following evaluation criteria are used to evaluate the performance of the proposed method:

a) Mean squared error (MSE) and Root Mean squared error (RMSE): The mean square error of a set with n data is a method of estimating the error value, which is actually the difference between the estimated values and what is estimated.

$$MSE = \frac{1}{n} \sum_{i=1}^n (x_i - y_i)^2 \quad (10)$$

$$RMSE = \sqrt{\frac{1}{n} \sum_{i=1}^n (x_i - y_i)^2} \quad (11)$$

Where y_i is the predicted value, x_i is the measured value, $\frac{1}{n} \sum_{i=1}^n$ has done averaging operation and x_i calculates the value of square error of each data.

b) Scatter Index (SI): When the root mean square value is normalized to the measured average, it is sometimes referred to as the scatter index.

$$MSE = \frac{1}{n} \sum_{i=1}^n (x_i - y_i)^2 \quad (12)$$

c) Coefficient of Error (CE): It provides information on the accuracy of estimates of each measurement where CE_x shows the average estimation and n is the number of people.

$$CE_x = \frac{\sqrt{CE_1^2 + CE_2^2 + \dots + CE_n^2}}{n} \quad (13)$$

d) Correlation Coefficient (R): This parameter expresses the power and direction of a linear correlation between two variables and its values are in the range -1 to 1. 1 indicates a One-to-one linearity and complete correlation, and -1 indicates a negative correlation. Coefficient of determination (R^2) describes the variance between two variables with a linear fit.

$$R = \frac{\sum_{i=1}^n (x_i - \bar{x})(x_i - \bar{x})}{\sqrt{\sum_{i=1}^n (x_i - \bar{x})^2 \sum_{i=1}^n (y_i - \bar{y})^2}} \quad (14)$$

$$R^2 = \left[\frac{\sum_{i=1}^n (x_i - \bar{x})(x_i - \bar{x})}{\sqrt{\sum_{i=1}^n (x_i - \bar{x})^2 \sum_{i=1}^n (y_i - \bar{y})^2}} \right]^2 \quad (15)$$

6. SIMULATION RESULTS

We use a multi-layered Perseptron neural network for training, test and validation based on structural similarities and the Levenberg training function. The maximum number of iterations is considered to be 1000 and the desired neural network is performed 10 times for 1 to 20 neurons in the hidden layer. We obtained the average results for each of the 1 to 20 neurons of hidden layer separately. You can see the implementation results in Fig. 6 to Fig. 11.

Figure 6 shows a comparison of the MSE criterion with different number of neurons. The lowest MSE is 0 with 3 neurons in training data, the lowest MSE is 0.00000014 with 4 neurons in test data, and the lowest MSE is 0.000012 with 1 neuron in validation data. Figure 7 shows a comparison of the RMSE criteria with different number of neurons. The lowest RMSE is 0 with 3 neurons in training data, the lowest RMSE is 0.00037 with 4 neurons in test data, and the lowest RMSE is 0.0035 with 1 neuron in validation data.

Figure 8 shows a comparison of the CE criteria with different number of neurons. The maximum CE is 1 with 3 neurons in training data, the maximum CE is 0.99982 with 4 neurons in test data, and the maximum CE is 0.99959 with 1 neuron in validation data. Figure 9 shows a comparison of the SI criteria with different number of neurons. The lowest SI is 0 with 3 neurons in training data, the lowest SI is 0.04527 with 4 neurons in test data, and the lowest SI is 0.42713 with 1 neuron in validation data.

Figure 10 shows a comparison of the R criteria with different number of neurons. The maximum R is 0.998225 with 3 neurons in training data, the maximum R is 0.98209 with 4 neurons in test data, and the maximum R is 0.97939 with 1 neuron in validation data. Figure 11 shows a comparison of run time with different number of neurons, the minimum run time is 10.452 seconds with 3 neurons. Figure 12 shows a comparison of the R criterion with 20 neurons. The R is 0.98225 in training data, the R is 0.98209 in test data, and the R is 0.97939 in validation data. In general, the criterion R is 0.97939.

Since the reference [14] researched in the field of predicting of trust on the Advogato data set, so we compared the obtained results with the RMSE criteria. You can see the comparison results in Table 2.

Table 2: Comparison of the proposed method with previous work

MSE	RMSE	Method
0.000012	0.0035	Structural similarity method with MLP
0.033708	0.1836	TILLIT [14]

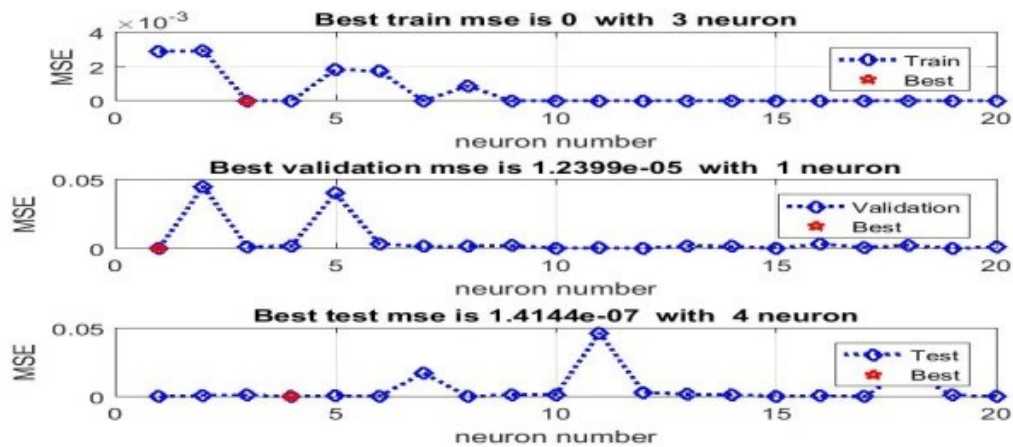


Fig. 6: Comparison of MSE criteria with a different number of neurons.

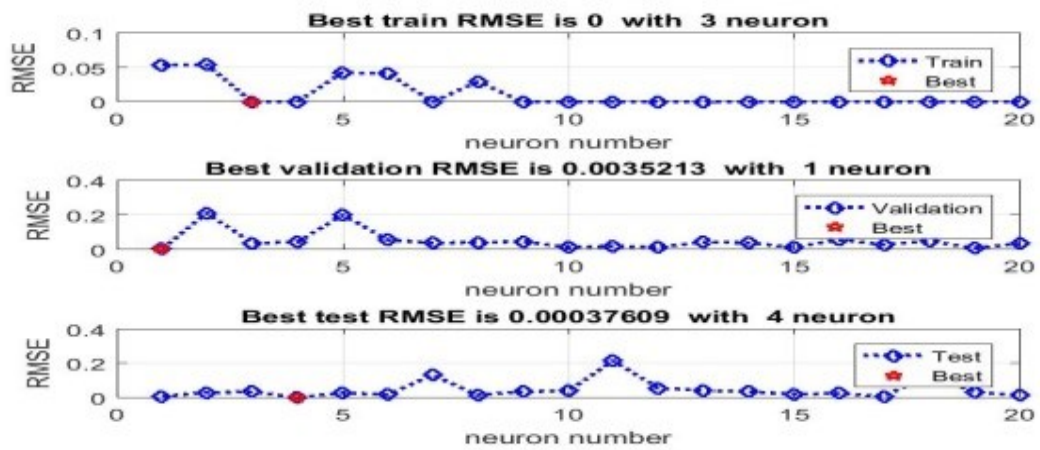


Fig. 7: Comparison of RMSE criteria with a different number of neurons.

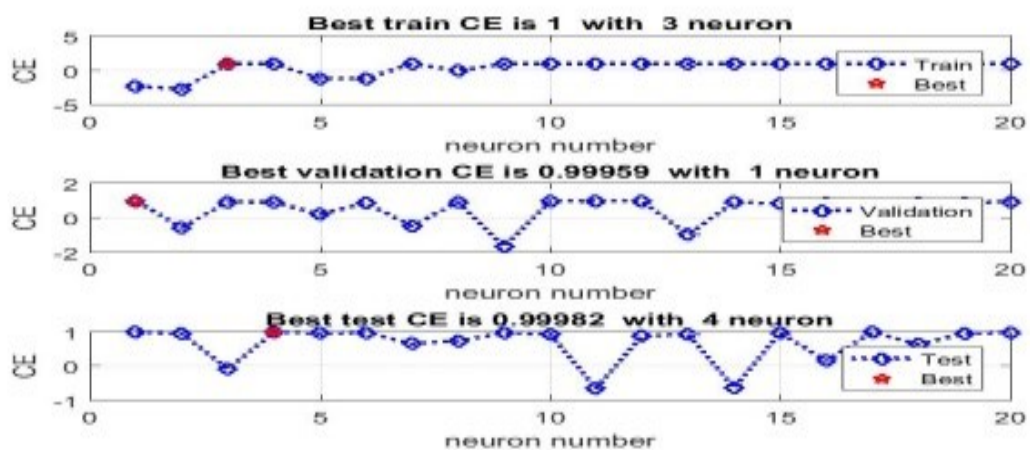


Fig. 8: Comparison of CE criteria with a different number of neurons.

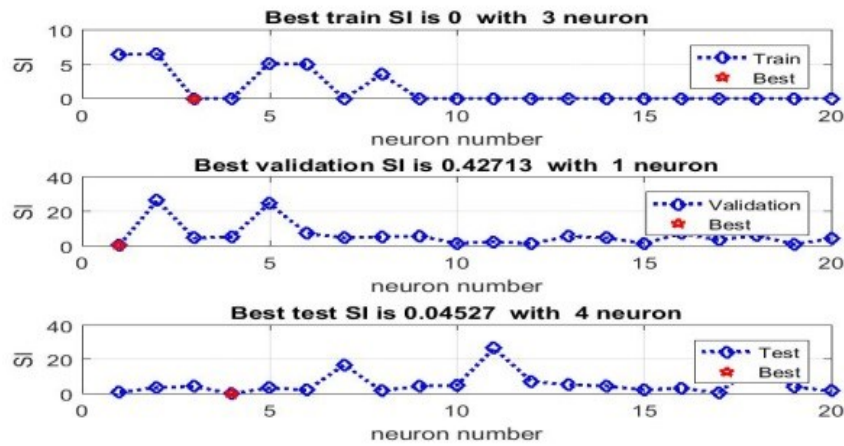


Fig. 9: Comparison of SI criteria with a different number of neurons.

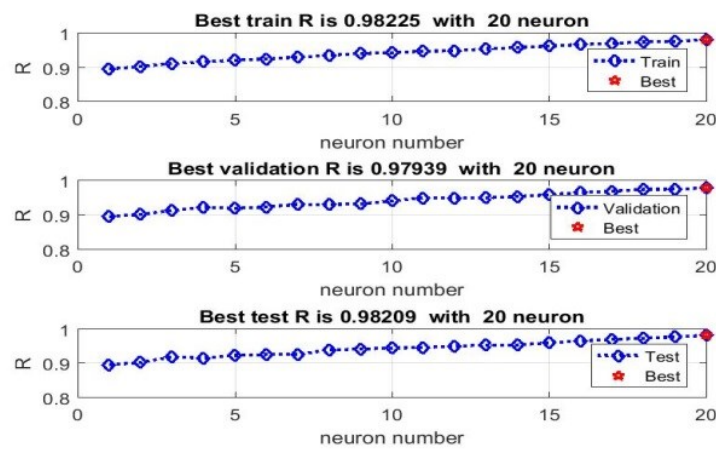


Fig. 10: Comparison of R criteria with a different number of neurons.

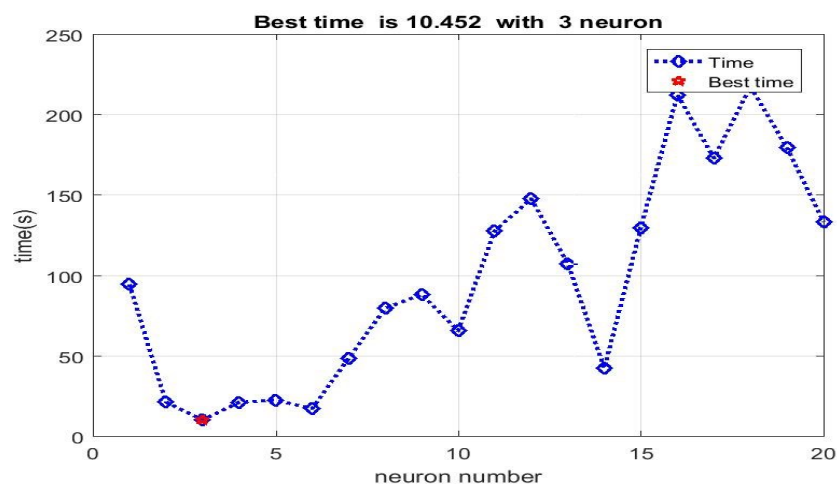


Fig. 11: Comparison of execution time with a different number of neurons.

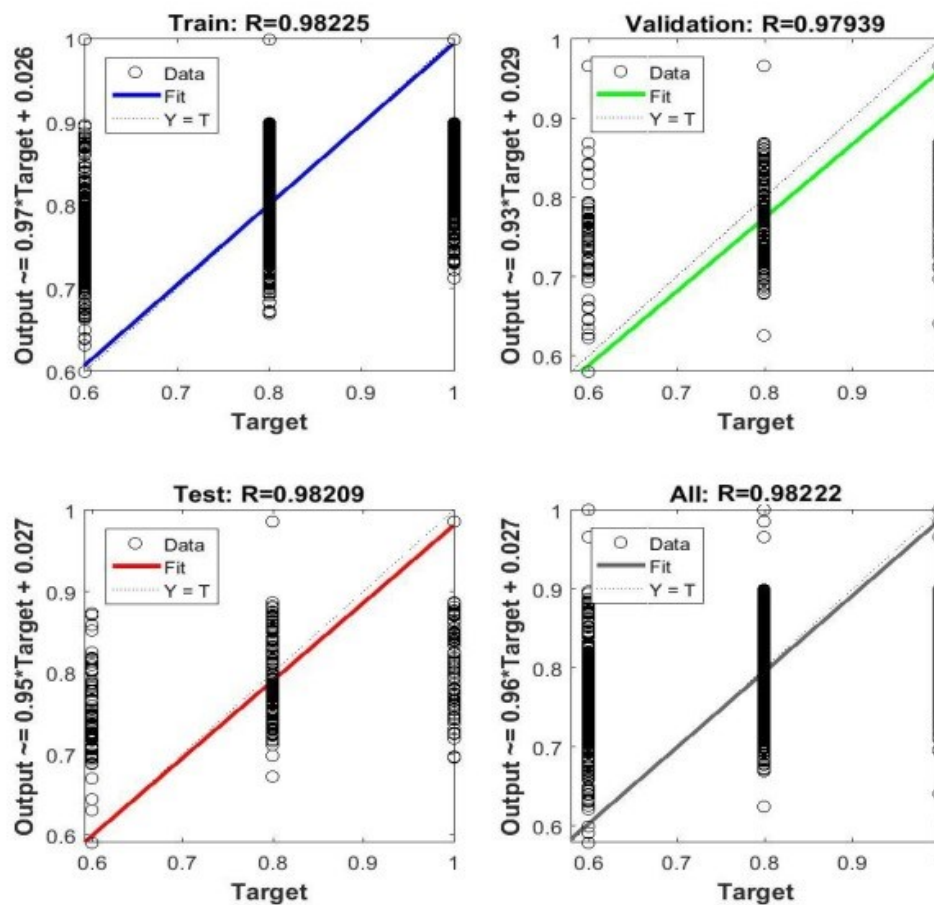


Fig. 12: Comparison of R criteria with 20 neurons in different states.

7. CONCLUSIONS AND SUGGESTIONS

In this research, after converting the web of trust data set into a structural similarity data set of trustors and trustees using a multilayer perceptron neural network, we trained the system. Then we implemented the test and validation data on the trained network. The simulation results are reported as follows:

For the validation data with 3 neurons in the hidden layer, the best MSE was 0.000012 and the best RMSE was 0.0035213. For the validation data with 1 neuron in the hidden layer, the most suitable CE was 0.99959 and the best SI was 0.42713. The best R for validation data with 20 neurons in the hidden layer has been obtained 0.97939. The proposed method has achieved good accuracy based on the results and it can be useful for predicting trust on social networks.

The proposed method is a centralized method, and on social networks with several hundred million users, predicting trust is a time consuming operation. Our suggestion for future work is that if each user identifies a set of trusted users (possibly a small set) accurately, a distributed method can be used that offers a less expensive, faster, and more scalable method. In this case, although it may be somewhat less accurate, such an approach would be more effective on the semantic web and neural network.

REFERENCES

- [1] Shirgahi H, Mohsenzadeh M, Seyyed Javadi HH. (2017) Trust estimation of the semantic web using semantic web clustering. *Journal of Experimental & Theoretical Artificial Intelligence*, 29(3): 537-556.
- [2] Shirgahi H, Mohsenzadeh M, Seyyed Javadi HH. (2018) A new method of trust mirroring estimation based on social networks parameters by fuzzy system. *International Journal of Machine Learning and Cybernetics*, 9(7): 1153-1168.
- [3] Ashtari S, Danesh M, Shirgahi H. (2019) A novel user profile-based fuzzy approach for evaluating trust in semantic web. *IIUM Engineering Journal*, 20(1): 158-176.
- [4] Kuter U, Golbeck J. (2007) A new algorithm for trust inference in social networks using probabilistic confidence models. in *Proc. AAAI, Vancouver, BC, Canada*, pp. 1377-1382.
- [5] Jiang W, Wu J, Li F, Wang G, Zheng H. (2016) Trust evaluation in online social networks using generalized network flow. *IEEE Trans. Comput.*, 65(3): 952-963.
- [6] Golbeck J. (2005) Computing and applying trust in Web-based social networks. Ph.D. dissertation, Dept. Comput. Sci., Univ. of Maryland, College Park, MD, USA.
- [7] Jøsang A, Hayward R, Pope S. (2006) Trust network analysis with subjective logic. in *Proc. ACSC, Hobart, TAS, Australia*. pp. 85-94.
- [8] Wang G, Jiang W, Wu J, Xiong Z. (2014) Fine-grained feature-based social influence evaluation in online social networks. *IEEE Trans. Parallel Distrib. Syst.*, 25(9): 2286-2296.
- [9] Kamvar SD, Schlosser MT, Garcia-Molina H. (2003) The eigentrust algorithm for reputation management in P2P networks. in *Proc. WWW, Budapest, Hungary*, pp. 640-651
- [10] Levien R, Aiken A. (1998) Attack-resistant trust metrics for public key certification. in *Proc. UNIX ATC, San Antonio, TX, USA*, pp. 229-242.
- [11] Liu G, Chen Q, Yang Q, Zhu B, Wang H, Wang W. (2017) Opinionwalk: An efficient solution to massive trust assessment in online social networks. in *Proc. INFOCOM, Atlanta, GA, USA*, pp. 1-9.
- [12] Xing L, Wang H, Wang C, Wang Y. (2012) BDD based two party trust sensitivity analysis for social networks. *Int. J. Secur. Netw.*, 7(4): 242-251.
- [13] Zaitseva E, Levashenko V, Kostolny J (2015) Application of logical differential calculus and binary decision diagram in importance analysis. *Ekspluat. Niezawodn.*, 17(3): 379-388.
- [14] Tavakolifard M, Herrmann P, Knapskog SJ. (2009) Inferring Trust Based on Similarity with TILLIT. *International Federation for Information Processing, IFIP AICT 300*, pp. 133-148.
- [15] http://www.trustlet.org/wiki/Advogato_dataset

FVS-TECHNOLOGY: INTELLECTUAL SEARCH TOOLS

**BAHODIR MUMINOV BOLTAYEVICH* AND
ULUGBEK BEKMURODOV BAKHROM UGLI**

*Fundamentals of Informatics Department
Tashkent University of Information Technologies named after Muhammad al-Khwarizmi,
Tashkent, Uzbekistan*

**Corresponding author: mbbahodir@gmail.com*

(Received: 10th March 2020; Accepted: 29th September 2020; Published on-line: 4th January 2021)

ABSTRACT: It is enough to have 3 basic stages of the modules in the SPD of a diversified corporate network: (F) - the method of submitting the request, i.e. the method of forming the expression of the information needs of the system user (S) - the function of the correspondence of the electronic resource to the request degree of compliance with the request and the found electronic resource; (V) - method of presenting electronic resources. Combining these three stages for models, methods, and software modules of the AML, is referred to as FSV technology (FSV platform, FSV Framework). FSV technology is an instrumental software platform based on a client-server architecture, integration and modification of models, and methods and algorithms of AML in the information environment of corporate networks. The following architecture has been developed for the FSV technology proposed for the search index in data retrieval systems.

ABSTRAK: Tiga peringkat asas modul adalah cukup dalam pelbagai rangkaian korporat SPD iaitu: (F) - kaedah penyerahan permintaan, kaedah membentuk ungkapan keperluan maklumat pengguna sistem (S) - fungsi surat-menyurat sumber elektronik bagi permintaan tahap pematuhan permintaan dan sumber elektronik yang dijumpai; (V) - kaedah penyampaian sumber elektronik. Gabungan tiga peringkat model, kaedah dan modul perisian AML, dipanggil teknologi FSV (platform FSV, rangka FSV). Teknologi FSV adalah platform perisian instrumen berdasarkan seni bina pelanggan-pelayan, integrasi dan pengubah suaian model, kaedah-kaedah dan algoritma AML dalam persekitaran maklumat dalam rangkaian korporat. Seni bina ini telah di bina bagi teknologi FSV yang dicadangkan bagi indeks carian dalam sistem dapatan data.

KEYWORDS: *intellectual search; FVS technology; information resource; search module; program module*

1. INTRODUCTION

In the world to meet the needs of the population in electronic resources, information is given great attention to the creation of intelligent data search systems in corporate networks of information and resource centers. Technologies of using information resources, the number of which is increasing every day, are one of the important issues of today. In this regard, including special attention is paid to improving the technology of searching and processing data based on semantic and fuzzy rules in corporate networks, database design and logical knowledge.

The world conducts research work aimed at creating data retrieval systems, database design and semantic knowledge, creating and improving software modules and algorithms

for mining, search, data storage in corporate networks. In this regard, the important tasks are the design, development of models, methods for searching and processing data, creating software for building data retrieval systems in fuzzy and stochastic information environments of corporate networks.

Modern technologies that do not replace many years of experience and highly qualified specialists, are designed to significantly improve the quality and efficiency of its work. This was discussed at the international forum held and dedicated to modern intellectual systems.

As it was noted, the modern IT industry all over the world is going through a new stage of its development. The catalyst for this process is the latest technology that can solve problems that have traditionally been considered creative. The forum discussed trends in the development of modern intellectual systems, their implementation in various sectors of the economy, the health sector.

With the independence of the republic, special attention is paid to the formation of a database of information resource centers (IRCs), on the creation of corporate information library systems, national content in raising the level of informatization of society based on intelligent management of hardware and software in information technologies. In this direction, the development of databases and software systems for logical search in data retrieval systems is included. The objectives for “... developing national content, improving the mechanisms for creating and promoting modern educational, scientific and educational information resources, multimedia products in the state language, meeting the needs of young people, ... introducing information and communication technologies ...” were defined. The implementation of this task, including the formation of electronic resources, the improvement of data mining systems, the development of a database of semantic data and knowledge in corporate information library systems, is one of the most important issues.

In the world of creating electronic resources, modeling processes and creating high-performance control systems to study the issues of intelligent search and data processing, research is carried out in a number of priority areas, including the creation of intelligent software modules based on the theory of fuzzy sets in solving problems in the fields of computer science and library, creation of methods for analyzing, searching and storing data based on models and methods of Data mining and Text mining, Big Data, development of methods and algorithms for integrating systems data retrieval, creation of algorithms, methods for processing and searching full texts, creating databases of aggregate data of corporate information library systems, creating methods and algorithms for processing requests for artificial and natural languages, creating a knowledge base, a semantic core based on the principles of SMART and SEO, developing software and data retrieval models based on local language.

Studies have shown that issues related to information retrieval, the structure and properties of data, the formation and processing of queries, the creation of a semantic core, the identification of electronic resources rating, the development of models and methods for intelligent search, the presentation and processing of data in fuzzy and stochastic information environments of corporate information biotech systems are not well understood.

The purpose of the research is the development of models, methods for searching and processing data in fuzzy and stochastic information environments, as well as the creation of software for corporate information library systems.

2. MAIN CHAPTER

Methods of forming queries, determining the rating and elements of data search in the corporate network are devoted to the questions of forming queries, determining the rating and elements of searching in fuzzy and stochastic information environments (NSNS).

A “search module” is a subsystem that, upon request, provides the most current ordered set of electronic resources, equipped with a user-friendly interface, including a database and statistical data.

The search module in the corporate network consists of two main elements that are independent of each other: an indexing element and a search element. The user sees only the capabilities of the search item and uses it. The indexing element is used to create the appropriate form for the effective presentation of information when searching for the necessary data in the data retrieval system (DPS).

Suppose that in the database are consistently given and are in the segment $V = [1, n]$, $N = \{0, 1, 2, 3, \dots\}$ with DosID identifiers with the set V , which has n electronic resources:

a) A quote (or reference) is a pair of ordinal electronic resources. $(i, j) \in V^2$. i - incoming link and j outbound link electronic resource.

In the set V between the electronic resources from all the links we form the E set, the graph directed to the links can be called reference graphs $G = (V, E)$.

b) For example, $G = (V, E)$ in this case the graph is the final set of vertices, $E = V \times V$ and $i \in V$, denote $I(i)$ the incoming set of links, and $O(i)$ the outgoing set of links denote as, then:

$$I(i) = \{e \in E \mid e = (i, j), j \in V\}, \quad O(i) = \{e \in E \mid e = (i, j), j \in V\} \quad (1)$$

c) If $O(i)$ and $I(i)$ do not exist and, then they are denoted as in this case $\{\emptyset\}$, the rating of the electronic resource $i \in V$ equals 0.

d) No electronic resource can provide its inbound links $I(i)$ and outbound links $O(i)$ to these links. The rating of incoming links I_r and outgoing links O_r is determined as follows:

$$I_r = \frac{\sum_{i=1}^{|I(i)|} Doc_r^i}{|I(i)| \sum_{count(I(i))} I(i)} \quad O_r = \frac{|O(i)|}{\sum_{count(O(i))} O(i)} \quad (2)$$

Here $count(I(i))$ - is the number of incoming, $count(O(i))$ - the number of all outgoing links.

Using the expression given above (2), we determine the method of preliminary rating of an electronic resource using (3) an expression.

$$D_r = (I_r + O_r) / 2 \quad (3)$$

Expression (2) allows the definition of electronic resources with a high rating and select a set that is recognized as relevant based on the identification of the rating of electronic resources in corporate information library systems (ICBS).

Suppose that $q = \{q_i\}$ a lot of requests and given to q_i the corresponding to a variety of electronic resources $R^i = \{r_j^i\}$, $j = 1 \dots M_d$ $j = 1 \dots N_q$. Here M_d – is the number of electronic resources viewed in the system, N_q – is the number of requests in the system. The method of logical-semantic search for a couple of queries, we will write as follows.

$$f(q_i, q_j) = \langle q_i | q_j \rangle = \frac{|R^j \cap R^i|}{|R^j|} \quad (4)$$

Here, $\langle a | b \rangle$ - denotes the relation and similarity of a with respect to b. $|R^j \cap R^i| \leq |R^j|$ - the condition must be relevant.

Rule 1: If $\langle q_i | q_j \rangle = 0$, then in this case q_i - is not semantically related to q_j , and is also considered not similar to each other.

Rule 2: If $\langle q_i | q_j \rangle = 1$, then in this case it is considered that q_i , q_j is completely semantically related and the similarity 1 is considered (q_i exactly similar).

Rule 3: If the expression (4) is equal $i = j$, then in this case $\langle q_i | q_j \rangle = 1$ it is considered semantically related, the similarity is 1 (it is exactly the same).

Rule 4: If $0 \leq \langle q_i | q_j \rangle \leq 1$, then q_i in this case, it is considered that semantically equal q_j and the similarity is calculated by the expression (4).

The method of logical-semantic search (4) for all queries, we write as follows:

$$f(q_1, q_2, \dots, q_{N_q}) = \sum_{i=1}^{N_q} \sum_{j=1}^{N_q} \langle q_i | q_j \rangle = \sum_{i=1}^{N_q} \sum_{j=1}^{N_q} \frac{|R^j \cap R^i|}{|R^j|} \quad (5)$$

here \sum is the union of the elements of the set. (5) the expression allows you to create a base of semantic knowledge in the data retrieval system (DPS).

Creating models, methods, and software for searching and processing data in fuzzy information environments, using the theory of fuzzy sets and using the linguistic variable model, defines the method for developing fuzzy queries in the data retrieval system (PDS) as follows:

- 1) (β) – defined linguistic variable;
- 2) $T(\beta)$ – we define a linguistically similar variable of a fuzzy set of terms;
- 3) X – for fuzzy sets of terms, we determine the set of values;
- 4) $G(\beta)$ – defined in the set of fuzzy terms, characterized by logical and modifier outputs;
- 5) $\mu_x - X$ defines the membership function of the set.

When designing a parametric membership function, the set $\mu_x - X$ is the linguistic variable of the corresponding object characteristic, the parametric design

β –method of the membership function is an important element in the intellectualization capabilities of the data retrieval system (PDS). μ_x – in the membership function, enter 4 parameters and give the following definition:

Proposition 5: If a, b, c, d parameters are taken from X – the set of values, then in this case the function is considered to be $\mu_x(a,b,c,d)$ the membership function of the set of values - X .

Proposition 6: In the membership function $\mu_x(a,b,c,d)$, the parameters a, b, c, d among themselves must be in ascending order. So one of the conditions $a < b$ or $b < c$ or $c < d$ must be constantly met.

Proposition 7: $T(\beta)$ – the parameters of the membership function for each term of the set of fuzzy terms corresponding to linguistic variables $T(\beta)$, at least one distinguishing parameter must be introduced.

It is recommended to use the choice of classes for the selection of membership functions corresponding to the linguistic variables of a fuzzy set in intelligent search and processing in a fuzzy information environment.

When intelligently searching for data in a fuzzy information environment of corporate information library systems, the main problem is the creation and management of the semantic core. We give the definition of a semantic core for intelligent search and data processing.

In a fuzzy information environment:

The semantic core is a set of relationships recognized as relevant, relevant in content and essence to normalized terms and electronic inquiry. Based on this definition, 3 methods have been developed for creating the semantic core of data retrieval systems in a fuzzy information environment. These include:

- Automatic construction of the semantic core as a result of search and processing.
 - Creating a semantic core by processing the citation of links, data in electronic resources.
 - Creating a semantic core with the help of expert groups. This method is carried out in version 2.
- a) Creation of a semantic core by an expert by creating queries corresponding to an electronic resource.
 - b) Expert processing of the existing semantic core, cancellation, modification, creation by it of the relationship of the request with the electronic resource, if necessary.

A model of the semantic core, based on the implementation of the control of the semantic core and 3 algorithms of methods for creating a semantic core, has been developed.

To determine the relevance of the semantic core model 4 properties have been added to the semantic core. If in property 1 there is a semantic link of the electronic resource and the query is 1, otherwise it takes the value 0, property 2 activates N - the total number of links, property 3 - m - the number of link-references.

In a fuzzy information environment for intelligent search and data processing in the development of models and rules for fuzzy search, the core of the knowledge base will form a fuzzy query q in a variety of fuzzy queries q^* (6) to form the rule condition as follows:

$$f : q \rightarrow q^* = \{q_1^*, q_2^*, \dots, q_n^*\} \quad (6)$$

in this case, $q_i^* - q_{i1}^*$ the term consists of a fuzzy pair of terms q_{i2}^* and can be defined as $\langle q_{i1}^* | q_{i2}^* \rangle$, and, $i = 1 \dots n$, $n \leq 2 \cdot |q_{i2}^*|$, $|q_{i2}^*| - q_{i2}^*$ is the number of fuzzy terms.

Conditions of the rule for the logical action "And" and q_1^* a pair of terms (6) we write as follows:

$$(q_1^* = q) \text{ and } (q_{11}^* = d) \text{ and } (q_{12}^* = t^*) \text{ and } (a_1 = \mu_{1,x_1}(q_{12}^*)) \quad (7)$$

where $(q_1^* = q) - q_1^* - q -$ is the pairing or non-pairing of the terms that make up the query, $(q_{11}^* = d)$ - the semantic relation of the electronic resource d and term, q_{11}^* , $(q_{12}^* = t^*)$ - the presence or absence in the set of fuzzy terms t^* of a database of fuzzy data q_{12}^* , $(a = \mu_x(q_{12}^*)) - (q_{11}^* = d)$, the weight a and the membership or non-membership of the values of membership functions of fuzzy terms q_{12}^* .

Using this condition (7) we write as follows.

Optimally, the fuzzy rules are based on the Mamdani method for intelligent data search in the data retrieval system.

$$\bigcup_{i=1}^n ((q_i^* = q) \text{ and } (q_{i1}^* = d) \text{ and } (q_{i2}^* = t^*) \text{ and } (a_i = \mu_{i,x_i}(q_{i2}^*))) \rightarrow R \quad (8)$$

If, on the basis of fuzzy rules, to write the set D of electronic resources in the knowledge base of rule (8), we obtain a system of fuzzy rules $D = \{d_1, d_2, \dots, d_m\}$, m - the number of electronic resources in the database.

We introduce the concept of the knowledge base kernel for the definition method, a fuzzy term and modifier, parameters corresponding to the membership functions that have been developed and are constantly updated with the help of expert experts. The algorithm for the development of the knowledge base kernel, the IDEF1x model, and relationships in the model have been developed.

For the formation of a variety of electronic resources that meet the requirements in a fuzzy information environment, IDEF0 models have been developed that describe the functional structure and functionality of category 3 related tools to create a knowledge base based on the knowledge base, semantic core, and processing fuzzy requests.

Creation and implementation of software for searching and processing data in the corporate network, is devoted to the development of technology and architecture of FSV, composite modules and models, for the effective operation of search modules in corporate information-library environments it is necessary to have several basic steps.

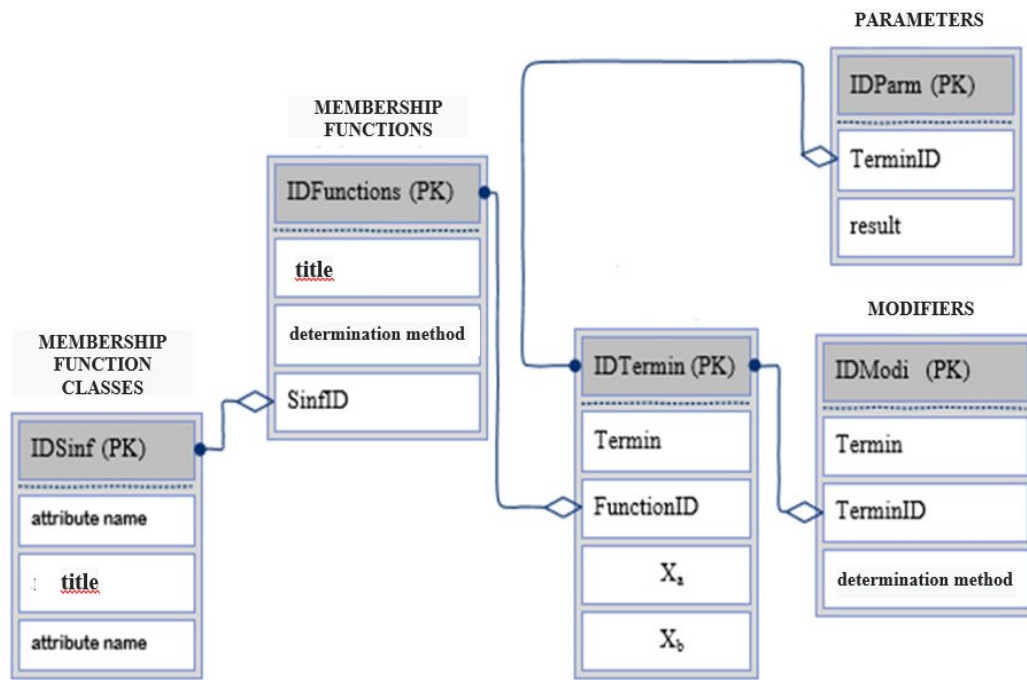


Fig. 1: IDEF1x core model knowledge base.

It is enough to have 3 basic stages of the modules of the search box in the data retrieval system of a multi-profile corporate network. These include:

1. (F) - method of presenting the request, i.e. method of forming the expression of the information needs of the user system.
2. (S) - the function of the correspondence of the electronic resource to the request, i.e. the degree of compliance with the query and the found electronic resource.
3. (V) - method of presenting electronic resources.

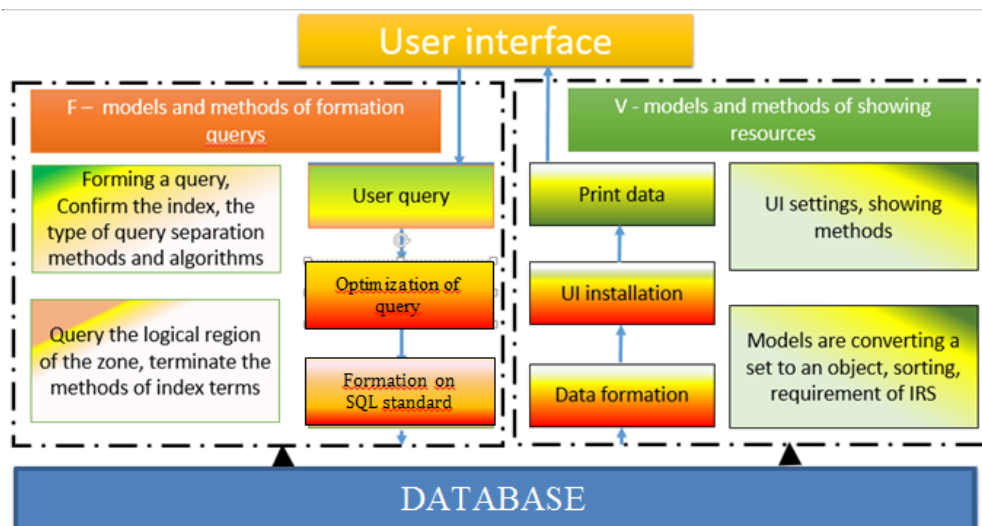


Fig. 2: Architecture of FSV technology for processing data.

Combining these three stages for models, methods and software modules of the AML, we call FSV technology (FSV platform, FSV Framework).

FSV technology is an instrumental software platform based on a client-server architecture, integration and modification of models, methods and algorithms for searching and processing data in the information environment of corporate networks.

The following architecture has been developed for the FSV technology proposed for the search index in data retrieval systems. In the development of the functional structure and IDEF models of the instrumental software module for query processing corporate networks request processing is divided into 2 stages.

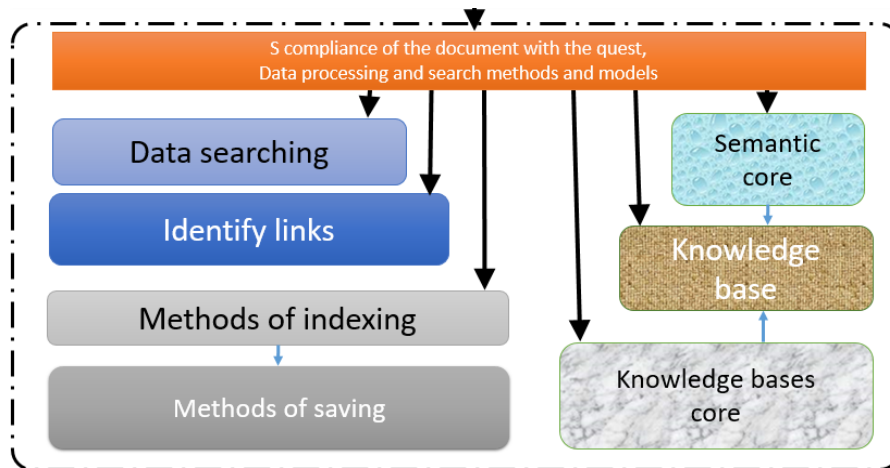


Fig. 3: Architecture of FSV technology for intellectual research.

At stage I, requests are created in natural language, based on the request processing methods, artificially created requests, based on the UI (User interface) methods. The second stage, which is a recurrent sequence, is carried out by clearing additional and auxiliary terms, determining the type of query, creating indices of logical and fuzzy terms, of the zonal field.

When creating IDEF models and functional structure of a software search and presentation software module. In the corporate network, an IDEF0 model was developed based on the methods, data retrieval system models in fuzzy and stochastic environments, traditional search, and S-ER matching process. Presentation V includes the processes of receiving a set of electronic resources, choosing a presentation method, determining the type of UI, providing constraints and filters and representing the set based on them, determining and controlling calls in the user's electronic resources.

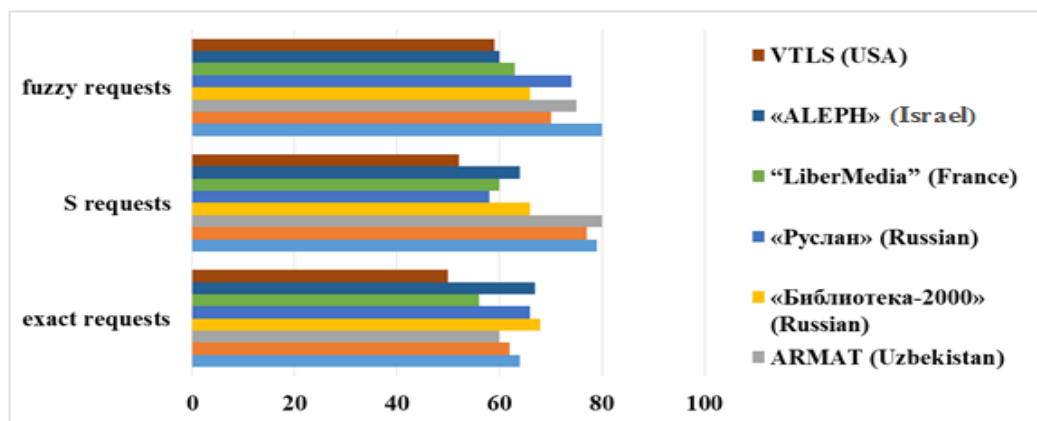


Fig. 4: Search results and data processing for the parameter "Speed".

FSV technology is integrated into such systems as: “ARMAT ++” - an automated system of information resource centers, “Mobile-Library” - mobile software on library resources, “vLibrary” - a virtual library of written cultural heritage of Turkic peoples of Central Asia of the XIX century (Kazakhstan).

For the experiment in MARC21 format, you can use the ISO2709 data exchange standard when exchanging data in corporate information library systems. Therefore, more than 50,000 titles of various electronic resources and full texts were chosen. For comparison and analysis results, such parameters as “Speed”, “Number of found data”, “Average relevance value” were selected and their results are given in the following figures (Fig. 3 and Fig. 4).

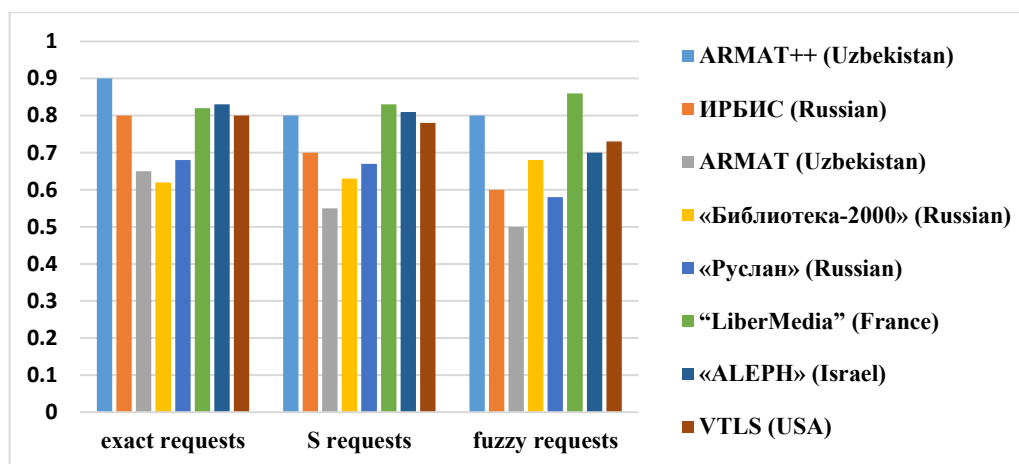


Fig. 5. Search results and data processing for the parameter "Average relevance".

The results of the experiment show that high speed provides the user with, firstly, superfluous information, secondly, it is very difficult to satisfy the information needs, i.e. need to analyze a lot of data. Although the search takes more time, but finding the necessary data indicates the effectiveness of search systems, since the analysis and limitation of redundant information saves 25%, sometimes up to 50% of the time of users.

The implementation of the results. Based on the software "ARMAT ++", created on the basis of FSV technology, models, methods of searching and processing data in fuzzy and stochastic information media:

- a method for determining a preliminary rating of an electronic resource based on references, a software module and an algorithm for designing parametric membership functions based on linguistic variables for fuzzy user requests, a software module, a method and algorithm for creating a knowledge base were introduced into the corporate networks of the main library of the Academy of Sciences (reference dated October 30 2017 No. 33-8 / 7293 of the Ministry for the Development of Information Technologies and Communications). As a result of scientific research, there were opportunities to improve the efficiency of determining electronic resources rating by 30%, using high-rating resources when presenting resources to users, improving the efficiency of processing requests in the corporate network by 15%, increasing the efficiency of collecting, searching, processing and providing data by 12%.
- a mathematical model of logical-semantic search, a software module and an algorithm for designing parametric membership functions based on a linguistic

- variable for fuzzy user requests, a model, methods, algorithms and a software module for creating a semantic core (reference from October 30, 2017 No. 33-8 / 7293 of the Ministry for the Development of Information Technologies and Communications). The results of the research allowed to increase the choice of resources that meet the requirements described in natural language by 30%, increase the efficiency of data search by 8%, reduce the number of corresponding electronic resources found by 2 times and increase accuracy by 30%.
- an information retention algorithm with a recurrent relationship, a model, an algorithm and a software module of the semantic core, a model, an algorithm and a software module for creating a knowledge base were introduced into the information resource center of the Intellectual Property Agency in accordance with Rule m Mamdani (reference dated October 30, 2017 No. 33-8 / 7293 of the Ministry of Information Technology and Communications Development). The results of the research allowed to increase the efficiency of the formation and processing of the original data by 15%, increase the efficiency of data retrieval by 12%, increase the amount of data matching the requests by processing fuzzy thermal queries by 30% and reduce the amount of unnecessary data by 50%.
 - E-Line Press Ltd. introduced a database project and IDEF-architecture architecture of FSV technology, developed to create a method and software module for determining a preliminary rating of an electronic resource based on links, a mathematical method of logical-semantic search, a data retrieval system (reference from October 30, 2017 No. 33-8 / 7293 of the Ministry for the Development of Information Technologies and Communications). The results of the study allowed to increase the efficiency of determining the accuracy of the preliminary rating of scientific resources and periodicals by 1.5 times, increase the efficiency of creating a database by 20%, increase the efficiency of data search by 5%, reduce the number of corresponding resources found by 50% and improve their accuracy in 1.3 times.

3. CONCLUSION REMARKS

As a result of the scientific and practical work “Models, methods of searching and processing data in fuzzy and stochastic information environments” the following results were obtained and the following main conclusions were made.

For the evaluation of data retrieval systems, compliance with the criteria of accuracy and integrity, reducing search time, a logical-semantic search model was developed, which increased the search efficiency by 5%. It can serve to study the issues of indexing sets of predefined ERs and queries, building their semantic links, optimizing search speed based on criteria and mathematical methods for searching and processing data in multi-disciplinary and multi-stage information resources.

The algorithm and software module for determining the relationship between the parameters of parametric membership functions, the choice of fuzzy terms corresponding to the classes of membership functions in the methods of intelligent search and data processing have been developed. Improved processing of fuzzy requests by 22%.

Developed algorithms, software module and 3 ways on creation of a semantic core for data retrieval systems in a fuzzy information environment of corporate information library systems, as well as increased the amount of data matching the query, on 10%.

IDEF0 and IDEF1x models for software modules of data retrieval systems in

corporate information library systems were developed. Serves for use in related research with the design of the functionality of the instrumental software module for analysis, text processing and the development of IDEF models, with questions of indexing, compression, information security, the choice of technical means.

The architecture, technologies FSV-software for creating a system for searching and processing data in corporate information library systems has been created. The results of introducing FSV technology into the ARMAT ++ corporate information library system make it possible to increase the effectiveness of the “Number of found data” by 7%, the Average relevance value by 10%, and the Search by 5%.

REFERENCES

- [1] Anagnostopoulos A, Andrei Z, Kunal P. (2006) Effective search engine model. In Proc. CIKM, pp 208-217.
- [2] Arlitsch K, Obrien P, Rossmann B. (2013) Managing Search Engine Optimization. Journal of Library Administration, 53(2-3): 177-188.
- [3] Azevedo C, Iacob M, Almeida J, Van S, Pires L, Guizzardi G. (2015) ArchiMate. Information Systems, 54: 235-262.
- [4] Bhat NA, Ganaie Sh. A. (2016) E-resources: Y.S. Parmar University of Horticulture and Forestry. Collection Building, 35(1): 16-21.
- [5] Brock EO. (2016) Declarative semantics of transactions in ORM. Information Systems, 60:85-94.
- [6] Cai F, Rijke M. (2016) Learning from homologous queries and semantically query auto completion. Information Processing & Management, 52(4): 628-643.
- [7] Muminov BB. (2014) Methods of information retrieval and cash algorithms. ITPA, 4-5 November, pp.194-196.
- [8] Muminov BB. (2016) The model of logical semantic searching. Proceedings of the Uzbek-Japan Symposium on Ecotechnologies, Tashkent, pp 72-77.
- [9] Newquist H. P. Data Mining: The AI Metamorphosis // Database Programming and Design. - 1996. - № 9. HP. (1996.)
- [10] Muminov BB. (2016.), Malumotlarni izlash usullari. Fan va texnologiya, Toshkent pg 276.
- [11] Muminov BB. (2016.), Data search methods. Science and Technology, Tashkent pg 276.

SOLUTION OF THE REVERSE FLOW REACTOR MODEL USING HOMOTOPY ANALYSIS METHOD

SUHARSONO¹, SRI WULANDARI¹, AANG NURYAMAN¹, MUSTOFA USMAN¹,
WAMILIANA¹ AND JAMAL IBRAHIM DAUD²

¹Department of Mathematics, FMIPA Universitas Lampung,
Jl. Prof. Dr. Soemantri Brojonegoro No. 1, Bandar Lampung 35145, Indonesia

²Department of Science in Engineering, Kulliyah of Engineering,
International Islamic University Malaysia,
Jalan Gombak, 53100 Kuala Lumpur, Malaysia

*Corresponding author: aang.nuryaman@fmipa.unila.ac.id

(Received: 13th March 2020; Accepted: 21st July 2020; Published on-line: 4th January 2021)

ABSTRACT: Methane (CH₄) is one of the most dangerous greenhouse gases in the atmosphere. A reverse flow reactor is utilized to convert CH₄ to carbon dioxide (CO₂) as a means of reducing the effect of global warming. The dynamics of its dependent variables can be stated by a set of convective-diffusion equations. In this article, we examined analytical solutions of temperature dynamics and methane conversion for a 1-D pseudo homogeneous model without refrigeration by using the homotopy analysis method. The results show that temperature and conversion of methane will go to constant when time goes to infinity.

ABSTRAK: Metana (CH₄) merupakan salah satu gas rumah hijau paling berbahaya di atmosfera. Reaktor aliran balik telah dipakai bagi menukar CH₄ kepada CO₂ bagi mengurangkan kesan pemanasan global. Dinamik pemboleh ubah bersandar ini dapat diterangkan melalui satu set persamaan konvektif-difusi. Artikel ini akan mengkaji penyelesaian analisis dinamik suhu dan penukaran metana bagi model 1-D pseudo-homogen tanpa penyejukan dengan menggunakan kaedah analisis homotopi. Hasil kajian menunjukkan bahawa suhu dan penukaran metana akan berterusan dengan masa tak terhingga.

KEYWORDS: analytical solution; 1-D pseudo homogeneous model; reverse flow reactor; homotopy analysis method

1. INTRODUCTION

There are several mathematical models in differential equation form that are difficult to solve using ordinary analytic partial differential equations. Hence, various methods have been developed to solve these equations, such as the Laplace transformation method, the perturbation method, the finite difference method, etc.

One natural phenomena that gets very intensive attention is global warming caused by greenhouse gas emissions. One of the dangerous and numerous greenhouse gases in the atmosphere is methane (CH₄). Reducing the global warming effect can be achieved by converting CH₄ into carbon dioxide (CO₂) according to the oxidation (combustion) equation:



Every one mole of oxidized CH₄ gas will release as much heat energy of 802.7 kJ. Hence, converting CH₄ gas to CO₂ gas will reduce the heating effect by 87%. The presence of fairly small amounts of methane gas in the air (0.1–1% by volume) causes the conversion of methane gas to CO₂ gas but needs a catalyst so that the reaction can take place. On the other hand, low methane temperature (around 303 K), so far from the reaction temperature, requires preheating of the feed gas.

One technology which can be used to anticipate the negative impact and characteristic of methane is the use of a reverse flow reactor (RFR) to oxidize CH₄ into CO₂. Further explanation about RFR can be seen in [1,2]. A mathematical model illustrating the dynamics of temperature and concentration on oxidation of CH₄ through RFR has been revealed by Khinast et al. [3] and van Norden [4]. In those articles, a one-dimensional (1-D) pseudo homogeneous model was used to describe the dynamic of dependent variables in a cooled-reverse flow reactor. Previous studies [5,6] used this model to investigate operating parameter sensitivities of RFR on the behavior of dependent variables for periodic feed gas by using a numerical approach. Whereas in [7,8], this model was used to construct singular perturbation problems by considering certain assumptions for steady state conditions and solved them using asymptotic methods. While for the unsteady state case, Nuryaman [9] reported an analytical solution for conversion equation that was derived from the 1-D pseudo homogeneous model which assumed that the reaction took place spontaneously at a certain reaction rate. The homotopy perturbation method was used to get its analytical solution.

In this article, we consider the 1-D pseudo homogeneous model in [4] and we assume that the reactor is in the condition without cooling such that the equations become as follows:

$$u_t = au_{xx} - bu_x + cg(u)(1 - v), \quad x \in [0,1] \quad (2)$$

$$v_t = ev_{xx} - fv_x + lg(u)(1 - v), \quad t \geq 0, \quad (3)$$

$$g(u) = \frac{1,6656 \times 10^{-5} \exp\left(\frac{25,785(u-1)}{u}\right)}{1,6656 \times 10^{-5} + \exp\left(-\frac{25,785}{u}\right)} \quad (4)$$

where $u = u(x, t)$, $v = v(x, t)$ are dimensionless variables for temperature and conversion variables. Here $a, b, c, e, f,$ and l are dimensionless parameters which values are given in Table 1, and $g(u)$ is a nonlinear function that corresponds to the rate of reaction in the RFR.

Table 1: The dimensionless parameter values of RFR [4]

No	Parameter	Values
1	a	6.9393×10^{-4}
2	b	0.1749
3	c	1.5577×10^{-6}
4	e	2.4038×10^{-3}
5	f	174.06
6	l	0.01

Based on equations (2)-(3) and under the certain assumptions, in this article, we investigate an analytical solution by applying the homotopy analysis method (HAM). In recent years, HAM can be applied for solving various linear and nonlinear systems, and homogeneous and nonhomogeneous equations [10]. The HAM is used to solve problems

using the determination of series convergence with respect to an embedded parameter [11]. In fact, the homotopy method is easier to use in solving difficult problems. Therefore, the HAM method will be applied herein solving the RFR model.

2. METHODOLOGY

The Homotopy Analysis Method (HAM) was designed firstly in 1992 by Liao [12] and was then modified in 1997 [13]. This is a semi-analytics technique for solving ordinary nonlinear problems or partial differential equations. Homotopy can be defined as a link between two different objects in mathematics that have the same characteristics in several aspects [13].

The HAM is based on concepts in topology and differential geometry to produce a series convergence of a nonlinear system. The concept of homotopy is then traced back to Jules Henri Poincare, a French mathematician. Homotopy explains a kind of deformation variation in mathematics. For example, a circle can be deformed continuously into an ellipse, and the shape of a coffee cup can be deformed continuously into a donut shape.

Suppose there are zeroth-order differential equations:

$$N_k[z_k(\omega, \tau)] = 0, \quad k = 1, 2, \dots, m \quad (5)$$

where N_k are nonlinear operators that represent the whole equations, ω and τ denote the independent variables, and $z_k(\omega, \tau)$ are unknown functions. Liao constructed the deformation equations as

$$(1 - q)L[\phi_k(\omega, \tau; q) - z_{k,0}(\omega, \tau)] = q\hbar_k N_k[\phi_k(\omega, \tau; q)] \quad (6)$$

where q is an embedding parameter, $q \in [0,1]$, \hbar_k are nonzero auxiliary functions, L is an auxiliary linear operator, $z_{k,0}(\omega, \tau)$ are initial guesses of $z_k(\omega, \tau)$, and $\phi_k(\omega, \tau; q)$ are unknown functions. One has great freedom to choose auxiliary objects such as \hbar_k and L . Obviously, when $q = 0$ and $q = 1$, ϕ_k hold:

$$\phi_k(\omega, \tau; 0) = z_{k,0}(\omega, \tau) \text{ and } \phi_k(\omega, \tau; 1) = z_k(\omega, \tau) \quad (7)$$

Thus, if q increases from 0 to 1, then the solutions $\phi_k(\omega, \tau; q)$ move from $z_{k,0}(\omega, \tau)$ to $z_k(\omega, \tau)$. $\phi_k(\omega, \tau; q)$ are then expanded in Taylor series with respect to q , and then becomes

$$\phi_k(\omega, \tau; q) = z_{k,0}(\omega, \tau) + \sum_{n=1}^{+\infty} z_{k,n}(\omega, \tau)q^n \quad (8)$$

where

$$z_{k,n} = \frac{1}{n!} \frac{\partial^n \phi_k(\omega, \tau; q)}{\partial q^n} \Big|_{q=0}. \quad (9)$$

When \hbar_k , L , $z_{k,0}(\omega, \tau)$, and $\phi_k(\omega, \tau; q)$ are properly chosen, then Equation (8) converges at $q = 1$ and

$$\phi_k(\omega, \tau; 1) = z_{k,0}(\omega, \tau) + \sum_{n=1}^{+\infty} z_{k,n}(\omega, \tau) \quad (10)$$

which has to be one of the solutions. As $\hbar_k = -1$, Equation (6) becomes

$$(1 - q)L[\phi_k(\omega, \tau; q) - z_{k,0}(\omega, \tau)] + qN_k[\phi_k(\omega, \tau; q)] = 0 \quad (11)$$

The governing equations can be deduced from the zeroth-order deformation Equation (6). Define the vectors

$$\vec{z}_{k,m} = \{z_{k,0}(\omega, \tau), z_{k,1}(\omega, \tau), \dots, z_{k,m}(\omega, \tau)\} \quad (12)$$

The n th order deformation can be found by differentiating (6) n times with respect to q and then putting $q = 0$. After that divide it by $n!$ such that

$$L[z_{k,n}(\omega, \tau) - \chi_n z_{k,n-1}(\omega, \tau)] = \hbar_k R_{k,n}(\overline{z_{i,n-1}}) \quad (13)$$

where

$$R_{k,n}(\overline{z_{k,n-1}}) = \frac{1}{(n-1)!} \frac{\partial^{n-1} N_k[\phi_k(\omega, \tau; q)]}{\partial q^{n-1}} \Big|_{q=0} \quad (14)$$

and

$$\chi_n = \begin{cases} 0, & n \leq 1 \\ 1, & n > 1 \end{cases} \quad (15)$$

Note that $z_{k,n}(\omega, \tau)$ ($n \geq 1$) are governed by (13) with boundary conditions coming from the original problem.

3. RESULT AND DISCUSSION

Consider the 1-D pseudo homogeneous model in Equations (2)-(3). By using a rescaling process and the assumption that the reaction rate takes place at certain temperature such that the nonlinear term approach to one. We obtain a dimensionless equation set that illustrates the dynamics of temperature and conversion of methane gas to methane oxidation using RFR without cooling as follows:

$$u_t - au_{xx} + bu_x + cv - c = 0 \quad (16)$$

$$v_t - ev_{xx} + fv_x + lv - l = 0 \quad (17)$$

where $u = u(x, t)$, $v = v(x, t)$ are dimensionless variables for temperature and conversion and a, b, c, e, f , and l are dimensionless parameters which values given in Table 1. In this case, initial conditions are

$$u(x, 0) = \beta, \quad \beta > 1 \quad (18)$$

where β is constant and

$$v(x, 0) = 0 \quad (19)$$

The linear operator

$$L[\varphi_k(x, t; q)] = \frac{\partial \varphi_k(x, t; q)}{\partial t}, \quad k = 1, 2 \quad (20)$$

with $L[p_k] = 0$, where p_k ($k = 1, 2$) are integral constants.

The nonlinear operator

$$N_1[\varphi_1(x, t; q)] = \frac{\partial \varphi_1(x, t; q)}{\partial t} - a \frac{\partial^2 \varphi_1(x, t; q)}{\partial x^2} + b \frac{\partial \varphi_1(x, t; q)}{\partial x} + c \varphi_2(x, t; q) - c \quad (21)$$

$$N_2[\varphi_2(x, t; q)] = \frac{\partial \varphi_2(x, t; q)}{\partial t} - e \frac{\partial^2 \varphi_2(x, t; q)}{\partial x^2} + f \frac{\partial \varphi_2(x, t; q)}{\partial x} + l \varphi_2(x, t; q) - l \quad (22)$$

Using the above definition, we construct the zeroth-order deformation equations

$$(1 - q)L[\varphi_k(x, t; q) - z_{k,0}(x, t)] = q \hbar_k N_k[\varphi_k(x, t; q)], \quad k = 1, 2$$

When $q = 0$ and $q = 1$, respectively, yields

$$\varphi_1(x, t; 0) = z_{1,0}(x, t) = u_0(x, t)$$

$$\varphi_2(x, t; 0) = z_{2,0}(x, t) = v_0(x, t)$$

$$\varphi_1(x, t; 1) = u(x, t)$$

$$\varphi_2(x, t; 1) = v(x, t)$$

After expanding $\varphi_k(x, t; q)$ in Taylor series with respect to q , it yields

$$\varphi_k(x, t; q) = z_{k,0}(x, t) + \sum_{n=1}^{+\infty} z_{k,n}(x, t)q^n$$

where

$$z_{k,n}(x, t) = \frac{1}{n!} \frac{\partial^n \varphi_i(x, t; q)}{\partial q^n} \Big|_{q=0}$$

The above series will converge at $q = 1$, so that

$$u(x, t) = z_{1,0}(x, t) + \sum_{n=1}^{+\infty} z_{1,n}(x, t)$$

$$v(x, t) = z_{2,0}(x, t) + \sum_{n=1}^{+\infty} z_{2,n}(x, t)$$

These are the solution of the nonlinear equation systems (16, 17). Now, we define the vector

$$\vec{z}_{k,m} = \{z_{k,0}(x, t), z_{k,1}(x, t), \dots, z_{k,m}(x, t)\}$$

So, the n th-order deformation equations is

$$L[z_{k,n}(x, t) - \chi_n z_{k,n-1}(x, t)] = \hbar_k R_{k,n}(\vec{z}_{k,n-1})$$

where

$$R_{1,n}(\vec{z}_{k,n-1}) = (z_{1,n-1})_t - a(z_{1,n-1})_{xx} + b(z_{1,n-1})_x + c(z_{2,n-1}) - c + cX_n$$

$$R_{2,n}(\vec{z}_{k,n-1}) = (z_{2,n-1})_t - e(z_{2,n-1})_{xx} + f(z_{2,n-1})_x + l(z_{2,n-1}) - l + lX_n$$

Now, the solution of the n th-order deformation equation for $n \geq 1$ becomes

$$z_{k,n}(x, t) = \chi_n z_{k,n-1}(x, t) + \hbar_k \int_0^t R_{k,n}(\vec{z}_{k,n-1}) d\tau + p_k$$

where the integration constants $p_k = 0$.

We, now successively have

$$z_{1,0}(x, t) = \beta$$

$$z_{1,1}(x, t) = -cht$$

$$z_{1,2}(x, t) = -cht - ch^2t - \frac{clh^2t^2}{2}$$

$$z_{1,3}(x, t) = -cht - 2ch^2t - clh^2t^2 - ch^3t - clh^3t^2 - \frac{cl^2h^3t^3}{6}$$

$$z_{1,4}(x, t) = -cht - 3ch^2t - clh^2t^2 - 3ch^3t - 3clh^3t^2 - \frac{cl^2h^3t^3}{2} - ch^4t - \frac{3clh^4t^2}{2} - \frac{cl^2h^4t^3}{2} - \frac{clh^2t^2}{2} - \frac{c[h^4t^4]}{24}$$

$$z_{1,5}(x, t) = -cht - 4ch^2t - 2clh^2t^2 - 6ch^3t - 6clh^3t^2 - cl^2h^3t^3 - 4ch^4t - 6clh^4t^2 - 2cl^2h^4t^3 - \frac{cl^3h^4t^4}{6} - ch^5t - 2clh^5t^2 - cl^2h^5t^3 - \frac{cl^3h^5t^4}{6} - \frac{cl^4h^5t^5}{120}$$

$$z_{2,0}(x, t) = 0$$

$$z_{2,1}(x, t) = -lht$$

$$z_{2,2}(x, t) = -lht - lh^2t - \frac{l^2h^2t^2}{2}$$

$$z_{2,3}(x, t) = -lht - 2lh^2t - l^2h^2t^2 - lh^3t - l^2h^3t^2 - \frac{l^3h^3t^3}{6}$$

$$z_{2,4}(x, t) = -lht - 3lh^2t - 3lh^3t - 3l^2h^3t^2 - \frac{l^3h^3t^3}{2} - lh^4t - \frac{l^3h^4t^3}{2} - \frac{3l^2h^2t^2}{2} - \frac{3l^2h^4t^2}{2} - \frac{l^4h^4t^4}{24}$$

$$z_{2,5}(x, t) = -lht - 4lh^2t - 6lh^3t - l^3h^3t^3 - 4lh^4t - 2l^3h^4t^3 - 2l^2h^2t^2 - 6l^2h^4t^2 - \frac{l^4h^4t^4}{6} - lh^5t - l^3h^5t^3 - 6l^2h^3t^2 - \frac{l^4h^5t^4}{6} - 2l^2h^5t^2 - \frac{l^5h^5t^5}{120}$$

The solutions then have the form

$$u(x, t) = z_{1,0}(x, t) + z_{1,1}(x, t) + z_{1,2}(x, t) + z_{1,3}(x, t) + z_{1,4}(x, t) + z_{1,5}(x, t) + \dots$$

$$v(x, t) = z_{2,0}(x, t) + z_{2,1}(x, t) + z_{2,2}(x, t) + z_{2,3}(x, t) + z_{2,4}(x, t) + z_{2,5}(x, t) + \dots$$

By putting $h = -1$, yields

$$u(x, t) = \beta + ct - \frac{clt^2}{2} + \frac{cl^2t^3}{6} - \frac{cl^3t^4}{24} + \frac{cl^4t^5}{120} - \dots$$

$$= \beta + ct + \frac{c}{l} \left(-\frac{l^2t^2}{2} + \frac{l^3t^3}{6} - \frac{l^4t^4}{24} + \frac{l^5t^5}{120} - \dots \right)$$

$$= \beta + ct + \frac{c}{l} (1 - lt - e^{-lt})$$

$$= \beta + ct + \frac{c}{l} - ct - \frac{ce^{-lt}}{l}$$

$$= \beta + \frac{c}{l} - \frac{ce^{-lt}}{l}$$

$$= \frac{\beta l + c - ce^{-lt}}{l}$$

$$v(x, t) = 0 + lt - \frac{l^2 t^2}{2} + \frac{l^3 t^3}{6} - \frac{l^4 t^4}{24} + \frac{l^5 t^5}{120} - \dots$$
$$= 1 - e^{-lt}$$

Using the physical data available in Table 1, the solution graph for $u(x, t)$ and $v(x, t)$, as shown in Fig. 1 and Fig. 2.

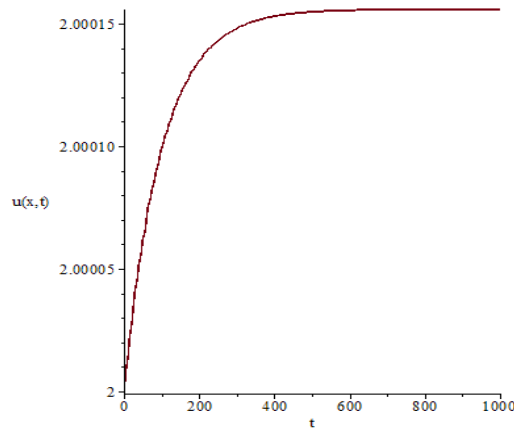


Fig. 1: The solution graph for $u(x, t)$ at certain position.

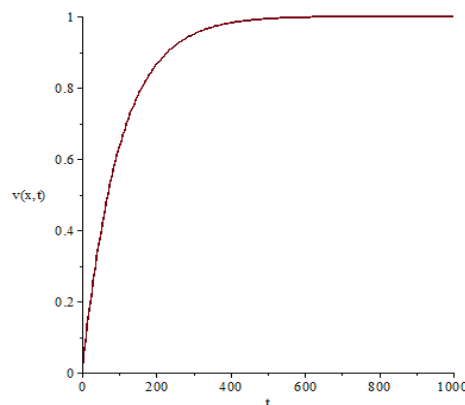


Fig. 2: The solution graph for $v(x, t)$ at certain position.

In RFR, the heat that is stored in the reactor can be used to preheat the feed. If the reaction temperature has been reached, the reactor system no longer needs a preheater for preheating the feed so that the process has high energy efficiency. This condition is illustrated by the graph $u(x, t)$. As shown in Figure 1, there is an increase in temperature within a certain time interval, after which the temperature does not increase or decrease but moves constantly. This condition has reached the steady state; thus, no preheater is needed. The $v(x, t)$ graph in Figure 2 illustrates the amount of concentration that reacts. After the concentration reacts entirely within a certain time, then the graph will move constantly. When this condition is reached, it means that the feed gas has completely reacted. Thus no more heat is released so that the temperature of the reactor becomes constant.

4. CONCLUSION

In this article, we consider the 1-D pseudo homogeneous model that describes the dynamics of temperature and conversion variables in RFR without the cooling process. Here, we consider only the feed gas flow from left to the right end of RFR. Then, we solve this

model using the homotopy analysis method. Based on the description above, it can be concluded that the solution of the dimensionless equation system describing the dynamics of temperature and conversion to methane oxidation using RFR without refrigeration is obtained as $u(x, t) = \frac{\beta l + c - ce^{-lt}}{k}$ and $v(x, t) = 1 - e^{-lt}$. The solution graph of $u(x, t)$ illustrates an increase in temperature within a certain time interval, after which the temperature does not increase or decrease but it moves constantly. This condition has reached the steady state; thus, no preheater is needed. The solution graph of $v(x, t)$ describes the amount of concentration that reacts. After the concentration reacts entirely within a certain time, then the graph will move constantly. Future studies can be extended by considering the cooling process term in the 1-D pseudohomogeneous model. In the real problem, the heat energy expended during the methane oxidation should be controlled so that reactor overheating will not occur.

ACKNOWLEDGEMENT

The authors would like to thank the reviewers for invaluable suggestions and corrections. Also, the authors would like to thank Universitas Lampung for the facilities, funding through BLU Research Grants No. 2280/UN.21/PN/2019, and support during the research.

REFERENCES

- [1] Frank-Kamenetskii DA. (1955) Diffusion and Heat Transfer in Chemical Kinetics. Princeton Univ. Press, Princeton, NJ.
- [2] Matros Yu. Sh., Bunimovich GA. (1999) Reverse-flow operation in fixed bed catalytic reactors. *Catalysis Reviews: Science & Engineering*, 38: 1-68.
- [3] Khinast J, Jeong YO, Luss D. (1999). Dependence of Cooled Reverse-Flow Reactor Dynamics on Reactor Model. *A.I.Ch.E. Journal*, 45: 299-309.
- [4] Van Noorden TL, Verduyn Lunel SMV, Blik A. (2003) The efficient computation of periodic states of cyclically operated chemical processes. *IMA Journal of Applied Mathematics*, 68: 149-166. <https://doi.org/10.1093/imamat/68.2.149>
- [5] Nuryaman A, Riyanto R, Saidi S. (2019) Dynamics of Temperature and Concentration on Oxidation Reaction using Reverse Flow Reactor with Periodic Feed Gas Like Square Wave Function: a Numerical Approach. *J. of Phys.: Conf. Ser.*, 1338: 012040. <https://doi.org/10.1088/1742-6596/1338/1/012037>
- [6] Nuryaman A, Zakaria L, Suharsono S. (2020) Parameter Sensitivity Analysis on Mathematical Model of Methane Oxidation using Reverse Flow Reactor with Periodically Perturbed Feed Gas. *JP Journal of Heat and Mass Transfer*, 19(1): 31-42. ISSN 0973-5763. <http://dx.doi.org/10.17654/HM019010031>
- [7] Nuryaman A, Gunawan AY, Sidarto AS, Budhi YW. (2012) A Singular Perturbation Problem for Steady State Conversion of Methane Oxidation in a Reverse Flow Reactor. *ITB J. Sci.*, 44(3): 275-284. DOI number 10.5614/itbj.sci.2012.44.3.7
- [8] Nuryaman A, Gunawan AY. (2017) A Singular Perturbation Problem in Steady State of Methane Combustion using Reverse Flow Reactor. *Far East Journal of Mathematical Sciences*, 102(9): 2069-2079. <http://dx.doi.org/10.17654/MS102092069>.
- [9] Nuryaman A. (2018) An Analytical Solution of 1-D Pseudo homogeneous Model for Oxidation Reaction using Homotopy Perturbation Methods. *Journal of Research in Mathematics Trend and Technology*, 1: 7-12. <https://doi.org/10.32734/jormtt.v1i1.751>
- [10] Sami Bataineh A, Noorani MSM, Hashim, I. (2008). Approximate Analytical Solutions of Systems of PDEs by Homotopy Analysis Method. *Computers and Mathematics with Applications*, 55: 2913-2923. <https://doi.org/10.1016/j.camwa.2007.11.022>

- [11] Liao SJ. (2012). Homotopy Analysis Method in Nonlinear Differential Equation. Higher Education Press, Beijing.
- [12] Liao SJ. (1992). The proposed homotopy analysis techniques for the solution of nonlinear problems, Ph.D. dissertation, Shanghai Jiao Tong University, Shanghai. (in English).
- [13] Liao SJ. (1997). An Approximate solution technique which does not depend upon small parameters (Part 2): An application in fluid dynamics. *Internat. J. Non-Linear Mech.* 32: 815-822.

RELIABLE ITERATIVE METHODS FOR SOLVING 1D, 2D AND 3D FISHER'S EQUATION

OTHMAN MAHDI SALIH, MAJEED AHMED. AL-JAWARY

*Department of Mathematics, College of Education for Pure Science Ibn Al-Haitham,
University of Baghdad, Baghdad, Iraq.*

**Corresponding author: majeed.a.w@ihcoedu.uobaghdad.edu.iq*

(Received: 23rd March 2020; Accepted: 7th October 2020; Published on-line: 4th January 2021)

ABSTRACT: In the present paper, three reliable iterative methods are given and implemented to solve the 1D, 2D and 3D Fisher's equation. Daftardar-Jafari method (DJM), Temimi-Ansari method (TAM) and Banach contraction method (BCM) are applied to get the exact and numerical solutions for Fisher's equations. The reliable iterative methods are characterized by many advantages, such as being free of derivatives, overcoming the difficulty arising when calculating the Adomian polynomial boundaries to deal with nonlinear terms in the Adomian decomposition method (ADM), does not request to calculate Lagrange multiplier as in the Variational iteration method (VIM) and there is no need to create a homotopy like in the Homotopy perturbation method (HPM), or any assumptions to deal with the nonlinear term. The obtained solutions are in recursive sequence forms which can be used to achieve the closed or approximate form of the solutions. Also, the fixed point theorem was presented to assess the convergence of the proposed methods. Several examples of 1D, 2D and 3D problems are solved either analytically or numerically, where the efficiency of the numerical solution has been verified by evaluating the absolute error and the maximum error remainder (*MER*) to show the accuracy and efficiency of the proposed methods. The results reveal that the proposed iterative methods are effective, reliable, time saver and applicable for solving the problems and can be proposed to solve other nonlinear problems. All the iterative process in this work implemented in MATHEMATICA®12.

ABSTRAK: Kajian ini berkenaan tiga kaedah berulang boleh percaya diberikan dan dilaksanakan bagi menyelesaikan 1D, 2D dan 3D persamaan Fisher. Kaedah Daftardar-Jafari (DJM), kaedah Temimi-Ansari (TAM) dan kaedah pengecutan Banach (BCM) digunakan bagi mendapatkan penyelesaian numerik dan tepat bagi persamaan Fisher. Kaedah berulang boleh percaya di kategorikan dengan pelbagai faedah, seperti bebas daripada terbitan, mengatasi masalah-masalah yang timbul apabila sempadan polinomial bagi mengurus kata tak linear dalam kaedah penguraian Adomian (ADM), tidak memerlukan kiraan pekali Lagrange sebagai kaedah berulang Variasi (VIM) dan tidak perlu bagi membuat homotopi sebagaimana dalam kaedah gangguan Homotopi (HPM), atau mana-mana anggapan bagi mengurus kata tak linear. Penyelesaian yang didapati dalam bentuk urutan berulang di mana ianya boleh digunakan bagi mencapai penyelesaian tepat atau hampiran. Juga, teorem titik tetap dibentangkan bagi menaksir kaedah bentuk hampiran. Pelbagai contoh seperti masalah 1D, 2D dan 3D diselesaikan samada secara analitik atau numerik, di mana kecekapan penyelesaian numerik telah ditentukan dengan menilai ralat mutlak dan baki ralat maksimum (*MER*) bagi menentukan ketepatan dan kecekapan kaedah yang dicadangkan. Dapatan kajian menunjukkan kaedah berulang yang dicadangkan adalah berkesan, boleh percaya, jimat masa dan boleh guna bagi menyelesaikan masalah dan boleh dicadangkan menyelesaikan masalah tak linear lain. Semua proses berulang dalam kerja ini menggunakan MATHEMATICA®12.

KEYWORDS: Fisher's equation, Iterative methods, Exact solution, Numerical solutions and Maximum error remainder.

1. INTRODUCTION

Many problems arising in engineering, science, finance, ecology, chemistry, etc., can be expressed by partial non-linear differential equations (PDEs). A non-linear PDE solution is a challenge for engineers and scientists where an analytical solution cannot be obtained. Therefore, many mathematicians have attempted to solve these problems in different ways and algorithms, for examples, ADM, VIM, HPM, homotopy analysis method (HAM), finite difference methods and some other approximate and numerical methods, see [1-6].

Fisher's equation is defined as the nonlinear reaction diffusion equation that describes the relationship between the diffusion and nonlinear multiplication of a species [7]. Fisher's equation is used in chemical kinetics and population dynamics which included problems such as nonlinear evolution of a population in a one-dimensional habitat and neutron population in a nuclear reaction and branching, the same equation occurs in neurophysiology, logistic growth models [8,9]. During the past half century, Fischer's equation was studied and a solution was found it, and the research field is still active to develop some good numerical algorithms and methods to obtain an accurate or approximate solution to it [10].

Moreover, some analytical, approximate and numerical methods were used and implemented to solve the Fisher's equation such as, finite elements and the Galerkin method [11], homotopy perturbation method [12], modified variational iteration method [13], Sinc collocation method [14]. In addition, Wazwaz and Gorguis studied the Fisher equation by using ADM [15]. In 2017, Parand and Nicarea solved Fischer's equation by using a spectral collocation method based on the Bessel functions of the first kind the Jacobian free Newton-generalized minimum residual method with adaptive preconditions[16].

In this paper, the three iterative methods DJM, TAM and BCM will be applied to solve the 1D, 2D and 3D Fisher's equations to obtain either exact or numerical solutions. The first method is the DJM suggested by Daftardar-Gejji and Jafari in 2006 [17], the second method is the TAM proposed by Temimi and Ansari in 2011 [18] and the third method is the BCM introduced by Daftardar-Gejji and Bhalekar in 2009 [19]. These iterative methods have been effectively used to solve different types of non-linear differential equations, for more details see [20-26].

This paper has been arranged as follows: In section 2, the 1D, 2D and 3D Fisher's equation mathematical formulation will be given. The basic ideas of three semi-analytical iterative methods will be presented in section 3. The convergence of the suggested techniques will be illustrated in section 4. In section 5, solving some examples of 1D, 2D and 3D Fisher's equation by using the DJM, TAM and BCM will be given. Finally, the conclusion is given in section 6.

2. THE MATHEMATICAL FORMULATION OF 1D, 2D AND 3D FISHER'S EQUATION

Fisher's equation is nonlinear partial differential equation that belongs to the class of reaction diffusion equations and has many important applications in biology, chemistry, physics and medicine as is the case in many reactions spread equations [13, 16].

In this study, the 1D Fisher's equation can be simply present in following form

$$w_t(x, t) = \alpha w_{xx}(x, t) + \beta R(w(x, t)) + u(x, t), \quad 0 \leq t \leq T, \quad a \leq x \leq b, \quad (1)$$

with the following initial conditions:

$$w(x, 0) = w_0.$$

The 2D Fisher's equation is presented in this form

$$w_t(x, y, t) = \alpha[w_{xx}(x, y, t) + w_{yy}(x, y, t)] + \beta R(w(x, y, t)) + u(x, y, t), \quad (2)$$
$$0 \leq t \leq T, \quad a \leq x, y \leq b,$$

with the following initial conditions:

$$w(x, y, 0) = w_0.$$

The 3D Fisher's equation can be expressed in this form

$$w_t(x, y, z, t) = \alpha[w_{xx}(x, y, z, t) + w_{yy}(x, y, z, t) + w_{zz}(x, y, z, t)] + \beta R(w(x, y, z, t)) + u(x, y, z, t), \quad (3)$$
$$0 \leq t \leq T, \quad a \leq x, y, z \leq b,$$

with the following initial conditions:

$$w(x, y, z, 0) = w_0,$$

where t is the time, x, y, z are the spatial coordinate, α the constant diffusion coefficient, β the reaction factor and R the nonlinear reaction term, w unknown function and u is known function represent the non- homogenous term.

3. THE BASIC CONCEPTS OF THE THREE ITERATIVE METHODS

In this section, the basic idea of the suggested three iterative methods DJM, TAM and BCM will be introduced.

3.1. The basic steps of DJM

Daftardar-Gejji and Jafari have considered the following nonlinear functional equation [17, 27]:

$$w = g + L(w) + N(w), \quad (4)$$

where L and N represent are linear and nonlinear operators, respectively, g is a known function and w is an unknown function.

We are looking for a solution wofEq. (4) and can be obtained by the following series:

$$w = \sum_{p=0}^{\infty} w_p.$$

Because L is linear operator, then

$$L\left(\sum_{p=0}^{\infty} w_p\right) = \sum_{p=0}^{\infty} L(w_p).$$

Hence, Eq. (4) can be written as

$$\sum_{p=0}^{\infty} w_p = g + \sum_{p=0}^{\infty} L(w_p) + N\left(\sum_{p=0}^{\infty} w_p\right),$$

and the N can be decomposed as bellow

$$N\left(\sum_{p=0}^{\infty} w_p\right) = N(w_0) + \sum_{i=1}^{\infty} \left\{ N\left(\sum_{p=0}^i w_p\right) - N\left(\sum_{p=0}^{i-1} w_p\right) \right\}.$$

Now, let us define the relation as below

$$J_0 = N(w_0),$$

$$J_1 = N(w_0 + w_1) - N(w_0),$$

$$J_2 = N(w_0 + w_1 + w_2) - N(w_0 + w_1),$$

⋮

$$J_i = \left\{ N\left(\sum_{p=0}^i w_p\right) - N\left(\sum_{p=0}^{i-1} w_p\right) \right\}, \quad i \geq 1.$$

From the above relation we get

$$N\left(\sum_{p=0}^{\infty} w_p\right) = J_0 + J_1 + J_2 + \dots + J_i + \dots$$

Now, we will define the inverse operator as follows

$$L^{-1}(\cdot) = \int_0^t (\cdot) d\tau, \tag{5}$$

By taking the inverse for together sides of Eq. (4), and applying the initial condition, we obtain

$$\sum_{p=0}^{\infty} w_p = f + L^{-1}\left(N\left(\sum_{p=0}^{\infty} w_p\right)\right),$$

where f represents the final formula for $L^{-1}(g)$.

Therefore, the components of the solution w are

$$w_0 = f,$$

$$w_1 = L^{-1}(J_0),$$

$$w_2 = L^{-1}(J_1),$$

$$\begin{aligned} & \vdots \\ w_{p+1} &= L^{-1}(J_p), \quad p = 0,1,2, \dots \end{aligned} \tag{6}$$

As a result, the n-term approximate solution of Eq. (4) is presented by the following form

$$\theta_n = \sum_{i=0}^n w_i. \tag{7}$$

Finally, the solution w for the nonlinear problem is given by

$$w = \sum_{p=0}^{\infty} w_p. \tag{8}$$

3.2. The basic steps of TAM

Temimi and Ansari have presented an iterative method namely (TAM) for solving nonlinear differential equations [18, 28].

To explain the basic ideas of the suggested technique, we assume the general form of partial differential equation

$$L(w) + N(w) + g = 0, \tag{9}$$

with boundary condition, $B\left(w, \frac{\partial w}{\partial x}\right) = 0$.

where L is a linear operator, N is a nonlinear operator, x, t denotes the independent variables, w is an unknown function, g is a known function and B is a boundary operator.

Now, we start by supposing that w_0 is an initial approximation of the problem w through solving the following initial equation

$$L(w_0) + g = 0, \text{with } B\left(w_0, \frac{\partial w_0}{\partial x}\right) = 0.$$

To obtain the next iteration w_1 to the solution w , we must solve the following equation

$$L(w_1) + g + N(w_0) = 0, \text{with } B\left(w_1, \frac{\partial w_1}{\partial x}\right) = 0.$$

Similarly, all iterations w_{n+1} can be obtained as

$$L(w_{n+1}) + g + N(w_n) = 0, \text{with } B\left(w_{n+1}, \frac{\partial w_{n+1}}{\partial x}\right) = 0. \tag{10}$$

Note that each of them w_n is a solution to Eq. (9). Also, by increasing the iterations, we will obtain better accuracy for the approximate solution.

So, the solution for the Eq. (9) is given by

$$w = \lim_{n \rightarrow \infty} w_n. \tag{11}$$

3.3. The basic steps of BCM

To study the basic concept of the suggested technique, we assume the general form of nonlinear functional equation, see [19]:

$$w = g + N(w), \tag{12}$$

Now, we will define successive approximations as follows

$$w_0 = g,$$

$$\begin{aligned}w_1 &= w_0 + N(w_0), \\w_2 &= w_0 + N(w_1), \\&\vdots \\w_n &= w_0 + N(w_{n-1}), \quad n = 1, 2, \dots\end{aligned}\tag{13}$$

It has been shown that the series defined by Eq. (13) is convergent [19]. Thus, the solution of Eq. (12) is given by

$$w = \lim_{n \rightarrow \infty} w_n.\tag{14}$$

4. THE CONVERGENCE OF THE PROPOSED TECHNIQUES

To show the convergence of the DJM, TAM and BCM, we are going to discuss the basic concepts and the fundamental theorems. In the DJM the convergence can be directly proved. However, in TAM and BCM, we should follow some steps as below

$$\begin{aligned}v_0 &= w_0, \\v_1 &= A[v_0], \\v_2 &= A[v_0 + v_1], \\&\vdots \\v_{n+1} &= A[v_0 + v_1 + \dots + v_n].\end{aligned}\tag{15}$$

where the operator A can be defined by the following form

$$A[v_p] = S_p - \sum_{i=0}^{p-1} v_i, \quad p = 1, 2, 3, \dots\tag{16}$$

where the term S_p is the solution appeared from the iterative methods.

Now, for the TAM as

$$L(v_p) + g + N\left(\sum_{i=0}^{p-1} v_i\right) = 0, \quad p = 1, 2, 3, \dots\tag{17}$$

For the BCM

$$v_p = v_0 + N\left(\sum_{i=0}^{p-1} v_i\right), \quad p = 1, 2, 3, \dots$$

Now, applying the same conditions that used in the iterative technique, we have

$$w = \lim_{n \rightarrow \infty} w_n = \sum_{n=0}^{\infty} v_n.$$

Hence, by using the Eqs. (15) and (16), we can get the solution by the following form

$$w = \sum_{i=0}^{\infty} v_i.\tag{18}$$

The following theorems show the convergence of the proposed methods: the DJM, BCM and TAM, more details for the theorems can be found in [29].

Theorem 4.1. Let A presented in Eq. (16), be an operator from a Hilbert space H to H . The series solution $w_n = \sum_{i=0}^n v_i$ is convergent if $\exists 0 < \lambda < 1$ when $\|A[v_0 + v_1 + \dots + v_{i+1}]\| \leq \lambda \|A[v_0 + v_1 + \dots + v_i]\|$ (such that $\|v_{i+1}\| \leq \lambda \|v_i\|$) $\forall i = 0, 1, \dots$

Theorem 4.1 is a specific case from the *Banach's fixed point theorem* which is a sufficient condition to study the convergence of the proposed iterative methods.

Theorem 4.2. If the series solution $w = \sum_{i=0}^{\infty} v_i$ convergent, then this series will consider the exact solution of the present nonlinear problem.

Theorems 4.1 and 4.2 show that the achieved solution from the DJM, TAM and BCM that is given in Eqs. (6), (10) and (13), respectively, for the nonlinear equation (Eq. (4)) is convergent to the exact solution under the given condition, $\exists 0 < \lambda < 1; \|v_{i+1}\| \leq \lambda \|v_i\| \forall i = 0, 1, 2, \dots$

In other words, we will define the following parameter as

$$\delta_i = \begin{cases} \frac{\|v_{i+1}\|}{\|v_i\|} & \text{if } \|v_i\| \neq 0 \\ 0 & \text{if } \|v_i\| = 0 \end{cases} \quad (19)$$

Then, the series solution $\sum_{i=0}^{\infty} v_i$ for the nonlinear problem converges to the exact solution w , when $0 \leq \delta_i < 1, \forall i = 0, 1, 2, \dots$. Moreover, the maximum truncation error can be calculated using the following form: $\|w - \sum_{i=0}^n v_i\| \leq \frac{1}{1-\delta} \delta^{n+1} \|v_0\|$, where $\delta = \max\{\delta_i, i = 0, 1, \dots, n\}$ as shown in theorem 4.3.

5. SOLVING THE 1D, 2D AND 3D FISHER'S EQUATION

In this section we are going to solve some examples of the 1D, 2D and 3D Fisher's equations by using the DJM, TAM and BCM.

Example 5.1. Consider the 1D Fisher's equation given in Eq. (1), when we substitute the values of $\alpha = \beta = 1$, as follows [12, 13]:

$$w_t = w_{xx} + w(1 - w), \quad (20)$$

The constant initial condition is given as, $w(x, 0) = \lambda$.

Solving example 5.1 by using the DJM

First of all, to implement the DJM for the 1D Fisher's equation, we write the operator form of the Eq. (20) as follows

$$L_t(w) = N(w), \quad (21)$$

where $L_t = \frac{\partial}{\partial t}$ and $N(w) = w_{xx} + w(1 - w)$, is the nonlinear operator for the 1D Fisher's equation.

By taking the inverse for together sides of Eq. (21) and applying the initial condition, we obtain

$$w = \lambda + L_t^{-1}N(w). \quad (22)$$

Finally, according to the DJM for Eq. (22) and by applying the recurrence relation, we achieve the components w_n as the following in a series form

$$w_0 = \lambda,$$

$$w_1 = L_t^{-1}(J_0) = L_t^{-1}N(w_0) = t\lambda - t\lambda^2,$$

$$w_2 = L_t^{-1}(J_1) = L_t^{-1}N(w_0 + w_1) - w_1,$$

$$= \frac{t^2\lambda}{2} - \frac{3t^2\lambda^2}{2} - \frac{t^3\lambda^2}{3} + t^2\lambda^3 + \frac{2t^3\lambda^3}{3} - \frac{t^3\lambda^4}{3},$$

⋮

Moreover, by using a similar way the iterations w_3 and w_4 were also calculated but for brevity is not mentioned here.

Thus, we get the following approximate solutions

$$\theta_1 = w_0 + w_1 = \lambda + (\lambda - \lambda^2)t + O[t]^5,$$

$$\theta_2 = w_0 + w_1 + w_2 = \lambda + (\lambda - \lambda^2)t + \left(\frac{\lambda}{2} - \frac{3\lambda^2}{2} + \lambda^3\right)t^2 + \frac{1}{3}(-\lambda^2 + 2\lambda^3 - \lambda^4)t^3 + O[t]^5,$$

⋮

In general, according to Eq. (7) the n -term approximate solution obtained by the DJM will be

$$\theta_n = \sum_{i=0}^n w_i = w_0 + w_1 + w_2 + w_3 + w_4 + \dots$$

Hence, according to the Eq. (8), we obtain the exact solution of Eq. (20) in a series form by sum of the above components w_i obtained from the DJM, this has the closed form obtained upon using the Taylor expansion:

$$w = \sum_{p=0}^{\infty} w_p = \frac{\lambda e^t}{1 - \lambda + \lambda e^t}.$$

Solving example 5.1 by using the TAM

To implement the TAM for the 1D Fisher's equation, we re-write the Eq. (20) in the operator form, as follows

$$L(w) = w_t, \quad N(w) = w_{xx} + w(1 - w),$$

with initial condition, $w(x, 0) = \lambda$.

We start by supposing that w_0 is an initial approximation of the problem w through solving the following initial equation

$$L_t(w_0) = 0, \text{ with } w_0(x, 0) = \lambda, \quad L_t = \frac{\partial}{\partial t}.$$

Then, we get

$$w_0 = \lambda.$$

Also, to get the next iteration, we have to solve the following problem

$$L_t(w_1) + N(w_0) = 0, \text{ with } w_1(x, 0) = \lambda.$$

Then, we get

$$w_1 = \lambda + (\lambda - \lambda^2)t + O[t]^5.$$

In the second iteration, we have to solve the following problem

$$L_t(w_2) + N(w_1) = 0, \text{ with } w_2(x, 0) = \lambda.$$

Thus, we get

$$w_2 = \lambda + (\lambda - \lambda^2)t + \left(\frac{\lambda}{2} - \frac{3\lambda^2}{2} + \lambda^3\right)t^2 + \frac{1}{3}(-\lambda^2 + 2\lambda^3 - \lambda^4)t^3 + O[t]^5.$$

⋮

Furthermore, by proceeding in this way the iterations w_3 and w_4 were also calculated but for the purpose of brevity is not mentioned here. Then, each iteration of the w_i represents an approximate solution to the Eq. (20).

Thus, According to Eq. (11) we obtain the exact solution upon using the Taylor expansion:

$$w = \lim_{n \rightarrow \infty} w_n = \frac{\lambda e^t}{1 - \lambda + \lambda e^t}. \tag{23}$$

Solving example 5.1 by using the BCM

To implement the BCM to solve the Eq. (20), by following the identical steps as used in the DJM, we obtain Eq. (22).

Also, suppose

$$g = \lambda \text{ and } N(w) = L_t^{-1}N(w),$$

where, $L_t^{-1}(\cdot) = \int_0^t (\cdot) dt$, $N(w) = w_{xx} + w(1 - w)$.

Applying the steps of the BCM, we get

$$w_0 = g = \lambda,$$

$$w_n = w_0 + N(w_{n-1}), n \in \mathbb{N}.$$

Hence,

$$w_1 = \lambda + (\lambda - \lambda^2)t + O[t]^5,$$

$$w_2 = \lambda + (\lambda - \lambda^2)t + \left(\frac{\lambda}{2} - \frac{3\lambda^2}{2} + \lambda^3\right)t^2 + \frac{1}{3}(-\lambda^2 + 2\lambda^3 - \lambda^4)t^3 + O[t]^5,$$

⋮

Moreover, by using a similar way the iterations w_3 and w_4 were also calculated but for brevity is not mentioned here.

Also, each iteration of the w_i represents an approximate solution to the Eq. (20) and so the exact solution obtained by the BCM will be the similar to exact solution obtained by the DJM and TAM.

Example 5.2. Consider the 1D Fisher's equation given in Eq. (1) as follows [30, 31]:

$$w_t = \alpha w_{xx} + \beta w(1 - w), \tag{24}$$

The initial condition is given as, $w(x, 0) = \lambda \text{Sech}[10x]^2$. The exact solution is unknown.

Solving example 5.2 by using the DJM

To implement the DJM to solve Eq.(24), we write it in the operator form, as follows

$$L_t(w(x, t)) = N(w), \tag{25}$$

where, $L_t = \frac{\partial}{\partial t}$ and $N(w) = \alpha w_{xx} + \beta w(1 - w)$, is the nonlinear operator of Eq.(24).

By taking the inverse for together sides of Eq. (25) and applying the initial condition, we obtain

$$w = \lambda \text{Sech}[10x]^2 + L_t^{-1}N(w). \tag{26}$$

Finally, according to the DJM for Eq. (26) and by applying the recurrence relation, we achieve the components w_n as the following in a series form

$$w_0 = \lambda \text{Sech}[10x]^2,$$

$$w_1 = L_t^{-1}(J_0) = L_t^{-1}N(w_0) = \frac{1}{2}\lambda(-800\alpha + \beta - 2\beta\lambda + (400\alpha + \beta)\text{Cosh}[20x])\text{Sech}[10x]^4t + O[t]^3,$$

$$w_2 = L_t^{-1}(J_1) = L_t^{-1}N(w_0 + w_1) - w_1$$

$$= \frac{1}{16}\lambda(5280000\alpha^2 + 800\alpha\beta(-3 + 20\lambda) + \beta^2(3 + 4\lambda(-3 + 4\lambda)) - 4(1040000\alpha^2 + \beta^2(-1 + 3\lambda) + 400\alpha(\beta + 6\beta\lambda))\text{Cosh}[20x] + (400\alpha + \beta)^2\text{Cosh}[40x])\text{Sech}[10x]^6t^2 + O[t]^3,$$

⋮

Also, the iterations w_3 and w_4 were calculated but for the purpose of brevity is not mentioned here.

In general, according to Eq. (7) the n -term approximate solution obtained by the DJM will be

$$w_i = \sum_{i=0}^4 w_i = w_0 + w_1 + w_2 + w_3 + w_4.$$

To prove the convergence analysis for the DJM for the Eq. (24), we have applied the process as presented in section 4. Hence, let choose the same above components obtained by the DJM, we get

$$v_0 = w_0 = \lambda \text{Sech}[10x]^2,$$

$$v_1 = w_1 = \frac{1}{2}\lambda(-800\alpha + \beta - 2\beta\lambda + (400\alpha + \beta)\text{Cosh}[20x])\text{Sech}[10x]^4t + O[t]^3,$$

⋮

and so on, when we substitute the values of $\alpha = 0.1$, $\lambda=0.1$ and $\beta =1$ in the iterations above and we evaluate the δ_i given in Eq. (19) to check the convergent conditions of the obtained estimated solution, then, we get

$$\delta_0 = \frac{\|v_1\|}{\|v_0\|} = 0.001875362147319159 < 1,$$

$$\delta_1 = \frac{\|v_2\|}{\|v_1\|} = 0.00407630739235568 < 1,$$

$$\delta_2 = \frac{\|v_3\|}{\|v_2\|} = 0.005390541847501205 < 1,$$

$$\delta_3 = \frac{\|v_4\|}{\|v_3\|} = 0.007399148330331557 < 1.$$

The results of δ_i , for all $i \geq 0$, $0 < t < 1$ and $0 \leq x \leq 1$, are less than one. Therefore, according to the convergence condition, the approximate solution obtained by the DJM is converges.

Solving example 5.2 by using the TAM

To implement the TAM for solving the Eq. (24), we write it in the operator form, so we have the following form

$$L(w) = w_t, \quad N(w) = \alpha w_{xx} + \beta w(1 - w),$$

with initial condition, $w(x, 0) = \lambda \text{Sech}[10x]^2$.

We start by supposing that w_0 is an initial approximation of the problem w through solving the following initial equation

$$L_t(w_0) = 0, \text{ with } w_0(x, 0) = \lambda \text{Sech}[10x]^2, L_t = \frac{\partial}{\partial t}.$$

Then, we get

$$w_0 = \lambda \text{Sech}[10x]^2,$$

Also, to obtain the next iteration, we have to solve the following problem

$$L_t(w_1) + N(w_0) = 0, \text{ with } w_1(x, 0) = \lambda \text{Sech}[10x]^2.$$

Then, we get

$$w_1 = \lambda \text{Sech}[10x]^2 + \frac{1}{2} \lambda (-800\alpha + \beta - 2\beta\lambda + (400\alpha + \beta) \text{Cosh}[20x]) \text{Sech}[10x]^4 t + O[t]^3.$$

In the second iteration, we have to solve the following problem

$$L_t(w_2) + N(w_1) = 0, \text{ with } w_2(x, 0) = \lambda \text{Sech}[10x]^2.$$

Thus, we get

$$w_2 = \lambda \text{Sech}[10x]^2 + \frac{1}{2} \lambda (-800\alpha + \beta - 2\beta\lambda + (400\alpha + \beta) \text{Cosh}[20x]) \text{Sech}[10x]^4 t + \frac{1}{16} \lambda (5280000\alpha^2 + 800\alpha\beta(-3 + 20\lambda) + \beta^2(3 + 4\lambda(-3 + 4\lambda)) - 4(1040000\alpha^2 + \beta^2(-1 + 3\lambda) + 400\alpha(\beta + 6\beta\lambda)) \text{Cosh}[20x] + (400\alpha + \beta)^2 \text{Cosh}[40x]) \text{Sech}[10x]^6 t^2 + O[t]^3,$$

⋮

Also, the iterations w_3 and w_4 were calculated but for the purpose of brevity is not mentioned here.

To prove the convergence of the TAM for the Eq. (24), we have applied the procedure as presented in Eqs. (15), (16) and (17), and we evaluate the δ_i given in Eq. (19) to check the convergent conditions of the obtained estimated solution, then we get:

$$\delta_0 = \frac{\|v_1\|}{\|v_0\|} = 0.0018753621473192403 < 1,$$

$$\delta_1 = \frac{\|v_2\|}{\|v_1\|} = 0.004076307392334906 < 1,$$

$$\delta_2 = \frac{\|v_3\|}{\|v_2\|} = 0.0053905418254422 < 1,$$

$$\delta_3 = \frac{\|v_4\|}{\|v_3\|} = 0.007399147822582866 < 1.$$

The results of δ_i , for all $i \geq 0$, $0 < t < 1$ and $0 \leq x \leq 1$, are less than one. Therefore, according to the convergence condition, the approximate solution obtained by the TAM is converges.

Solving example 5.2 by using the BCM

To implement the BCM to solve the Eq. (24), by following the identical steps as used in the DJM, we obtain Eq. (26).

Also, suppose,

$$g = \lambda \text{Sech}[10x]^2 \text{ and } N(w) = L_t^{-1}N(w),$$

where, $L_t^{-1}(\cdot) = \int_0^t (\cdot) dt$, $N(w) = \alpha w_{xx} + \beta w(1 - w)$.

Applying the steps of the BCM, we get

$$w_0 = g = \lambda \text{Sech}[10x]^2,$$

$$w_n = w_0 + N(w_{n-1}), n \in \mathbb{N}.$$

Hence,

$$w_1 = \lambda \text{Sech}[10x]^2 + \frac{1}{2} \lambda (-800\alpha + \beta - 2\beta\lambda + (400\alpha + \beta) \text{Cosh}[20x]) \text{Sech}[10x]^4 t + O[t]^3,$$

$$w_2 = \lambda \text{Sech}[10x]^2 + \frac{1}{2} \lambda (-800\alpha + \beta - 2\beta\lambda + (400\alpha + \beta) \text{Cosh}[20x]) \text{Sech}[10x]^4 t + \frac{1}{16} \lambda (5280000\alpha^2 + 800\alpha\beta(-3 + 20\lambda) + \beta^2(3 + 4\lambda(-3 + 4\lambda)) - 4(1040000\alpha^2 + \beta^2(-1 + 3\lambda) + 400\alpha(\beta + 6\beta\lambda)) \text{Cosh}[20x] + (400\alpha + \beta)^2 \text{Cosh}[40x]) \text{Sech}[10x]^6 t^2 + O[t]^3.$$

⋮

Also, the iterations w_3 and w_4 were calculated but for the purpose of brevity is not mentioned here.

To prove the convergence analysis for the BAM for the Eq. (24), we have applied the similar process as presented in section 4 and then, we evaluate the δ_i given in Eq. (19) to check the convergent conditions of the obtained estimated solution, then we get

$$\delta_0 = \frac{\|v_1\|}{\|v_0\|} = 0.0018753621473191209 < 1,$$

$$\delta_1 = \frac{\|v_2\|}{\|v_1\|} = 0.004076307392346145 < 1,$$

$$\delta_2 = \frac{\|v_3\|}{\|v_2\|} = 0.005390541859136445 < 1,$$

$$\delta_3 = \frac{\|v_4\|}{\|v_3\|} = 0.0073991506075805555 < 1.$$

The results of δ_i , for all $i \geq 0$, $0 < t < 1$ and $0 \leq x \leq 1$, are less than one. Therefore, according to the convergence condition, the approximate solution obtained by the BCM is converges.

Because the exact solution of the Eq. (24) is unknown, the MER_n will be calculated as follows, $MER_n = \max_{0 \leq x \leq 1} |w_t - \alpha w_{xx} - \beta w(1 - w)|$, to test the efficiency of the approximate solutions that we obtained by the DJM, TAM, BCM, and compared them with the ADM and VIM [13, 31], for two values of the time t equal to either 0.0001 or 0.001. From Fig. 1, it can be easily recognized that the error is decreasing by increasing the number of iterations. Also, good agreement have been achieved with ADM and VIM, without required to calculate Adomian polynomials to handle the nonlinear terms in ADM, or compute Lagrange multiplier as in VIM and time saver.

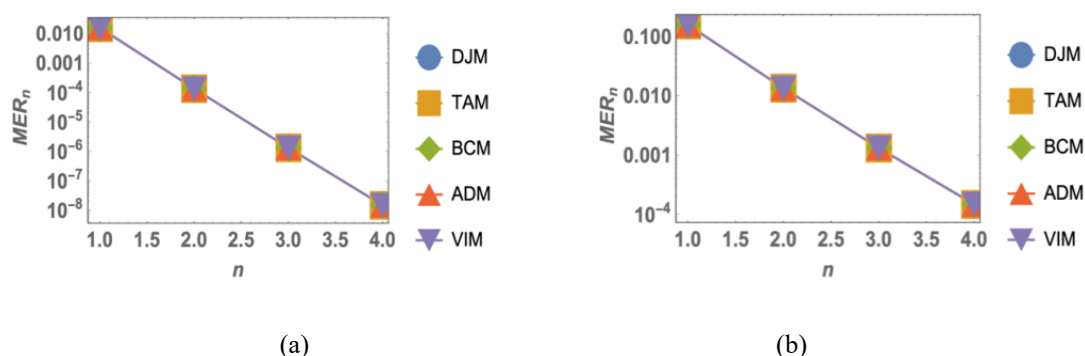


Fig. 1. The MER_n values for example 5.2 obtained by the DJM, TAM, BCM, ADM and VIM for times (a) $t = 0.0001$, (b) $t = 0.001$.

Example 5.3. Consider the 2D Fisher's equation given in Eq. (2), when we substitute the values of $\alpha = \beta = 1$, as follows [11,16]:

$$w_t = w_{xx} + w_{yy} + tw(1 - w) + u(x, y, t), \quad (27)$$

and the initial condition, $w(x, y, 0) = x^2 + y^2$.

where, $u(x, y, t) = -4 + 2t - t(1 - t^2 - x^2 - y^2)(t^2 + x^2 + y^2)$, $0 < t < 1$. The exact solution for this equation is

$$w = x^2 + y^2 + t^2.$$

Solving example 5.3 by using the DJM

To implement the DJM to solve Eq. (27), we write it in the operator form, as follows

$$L_t(w) = N(w), \quad (28)$$

where, $L_t = \frac{\partial}{\partial t}$ and $N(w) = w_{xx} + w_{yy} + tw(1 - w) + u(x, y, t)$, is the nonlinear operator for the Eq. (27).

By taking the inverse for both sides of Eq. (28), and applying the initial condition, we get

$$w = (x^2 + y^2) + L_t^{-1}N(w). \quad (29)$$

Finally, according to the DJM for Eq. (29) and by applying the recurrence relation, we achieve the components w_n as the following in a series form

$$w_0 = x^2 + y^2,$$

$$w_1 = L_t^{-1}(J_0) = L_t^{-1}N(w_0) = t^2 - \frac{t^4}{4} + \frac{t^6}{6} + \frac{t^4x^2}{2} + \frac{t^4y^2}{2},$$

$$w_2 = L_t^{-1}(J_1) = L_t^{-1}N(w_0 + w_1) - w_1$$

$$= \frac{t^4}{4} + \frac{2t^5}{5} - \frac{5t^6}{24} + \frac{t^8}{12} - \frac{19t^{10}}{480} + \frac{t^{12}}{144} - \frac{t^{14}}{504} - \frac{t^4x^2}{2} + \frac{t^6x^2}{6} - \frac{t^8x^2}{6} + \frac{t^{10}x^2}{40}$$

$$- \frac{t^{12}x^2}{72} - \frac{t^6x^4}{6} - \frac{t^{10}x^4}{40} - \frac{t^4y^2}{2} + \frac{t^6y^2}{6} - \frac{t^8y^2}{6} + \frac{t^{10}y^2}{40} - \frac{t^{12}y^2}{72} - \frac{1}{3}t^6x^2y^2$$

$$- \frac{1}{20}t^{10}x^2y^2 - \frac{t^6y^4}{6} - \frac{t^{10}y^4}{40},$$

⋮

Furthermore, by proceeding in this way the iterations w_3 and w_4 were also calculated but for the purpose of brevity is not mentioned here.

To prove the convergence analysis of the DJM for the Eq. (27), we have applied the process as presented in section 4. Hence, let choose the same above components obtained by the DJM, we get

$$v_0 = w_0 = x^2 + y^2,$$

$$v_1 = w_1 = t^2 - \frac{t^4}{4} + \frac{t^6}{6} + \frac{t^4x^2}{2} + \frac{t^4y^2}{2},$$

⋮

and so on, by using the iterations above and we evaluate the δ_i given in Eq. (19) to check the convergent conditions of the obtained approximate solution. Then, we get

$$\delta_0 = \frac{\|v_1\|}{\|v_0\|} = 0.00005000375008333333 < 1,$$

$$\delta_1 = \frac{\|v_2\|}{\|v_1\|} = 0.00007459982180570717 < 1,$$

$$\delta_2 = \frac{\|v_3\|}{\|v_2\|} = 0.005312394687736893 < 1,$$

$$\delta_3 = \frac{\|v_4\|}{\|v_3\|} = 0.00021050502578039127 < 1.$$

The results of δ_i , for all $i \geq 0$, $0 < t < 1$ and $0 \leq x, y \leq 1$, are less than one. Therefore, the approximate solution obtained by the DJM is converges.

Also, the absolute error (**Abs. errs.**) will be calculated to check the accuracy of the approximate solutions that obtained by the DJM for three values of the time $t = 0.1, 0.01$ and 0.001 , presented in Fig. 2. Moreover, Table 1 shows the absolute error values obtained by DJM for the iterations with $x = \{0, 0.2, 0.4, 0.6, 0.8, 1\}$. It can be easily recognized that the error is decreasing by increasing the number of iterations and decreasing the time.

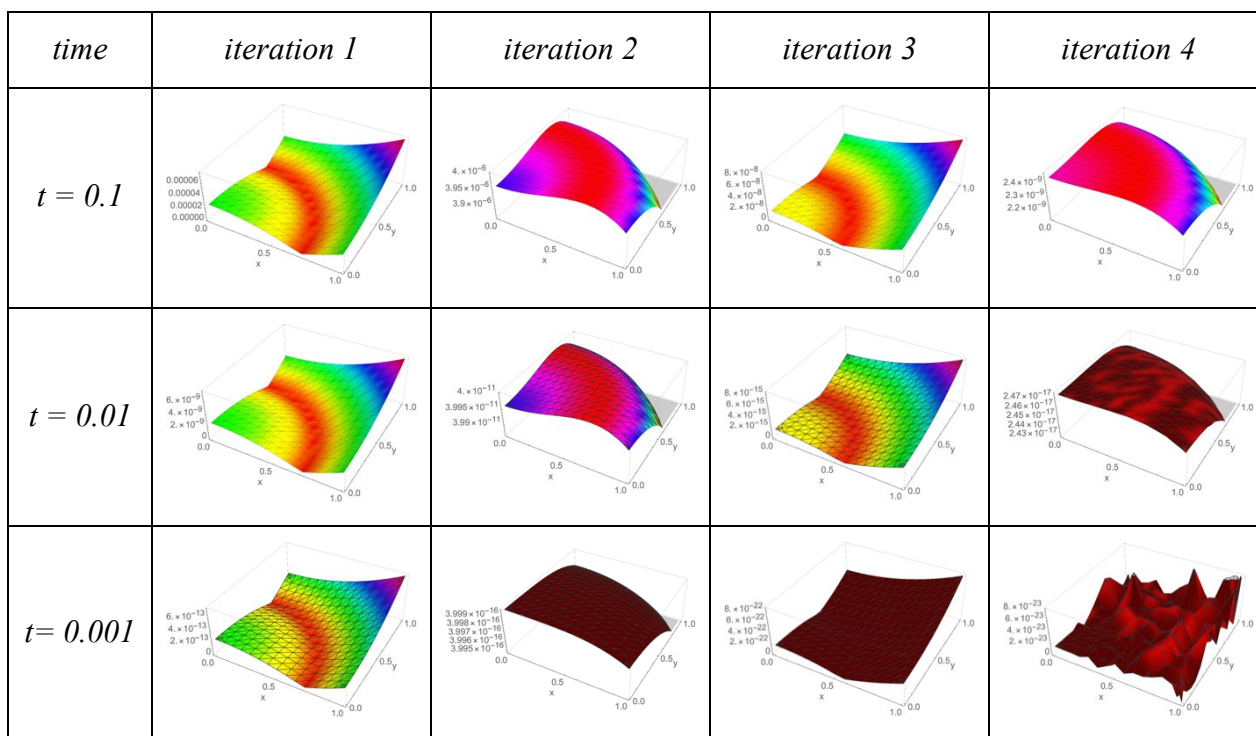


Fig. 2. The absolute error values for example 5.3 obtained by the DJM for $w_1, w_2, w_3,$ and w_4 with different values of t .

Table 1: The absolute error values for example 5.3 obtained by DJM, for four iterations with different values of t .

Time	x_i	Abs. errs. For 1 st iteration	Abs. errs. For 2 nd iteration	Abs. errs. For 3 rd iteration	Abs. errs. For 4 th iteration
$t=0.1$	0	0.0000251666666677221	0.0000039574960347114	$3.439519622754291 \times 10^{-8}$	$2.367214207006091 \times 10^{-9}$
	0.2	0.00002716666666776434	0.000003950495930156153	$3.636235764046649 \times 10^{-8}$	$2.352566504062037 \times 10^{-9}$
	0.4	0.00003316666666789095	0.000003926295568490412	$4.225011372322602 \times 10^{-8}$	$2.303341876975943 \times 10^{-9}$
	0.6	0.0000431666666668102	0.00000387529480571418	$5.200767991296621 \times 10^{-8}$	$2.203745339426222 \times 10^{-9}$
	0.8	0.00005716666666683975	0.000003781493401827455	$6.551841495654667 \times 10^{-8}$	$2.027660150299521 \times 10^{-9}$
	1	0.00007516666666687773	0.000003622491020830237	$8.255182044155353 \times 10^{-8}$	$1.739110699410879 \times 10^{-9}$
$t=0.01$	0	$2.500166636275423 \times 10^{-9}$	$3.995843050700178 \times 10^{-11}$	$3.428213061620738 \times 10^{-15}$	$2.459218564137952 \times 10^{-17}$
	0.2	$2.700166635059928 \times 10^{-9}$	$3.995150072691333 \times 10^{-11}$	$3.626173005459958 \times 10^{-15}$	$2.45742245436945 \times 10^{-17}$
	0.4	$3.300166631413446 \times 10^{-9}$	$3.992751138664317 \times 10^{-11}$	$4.219916824177479 \times 10^{-15}$	$2.451761901624386 \times 10^{-17}$
	0.6	$4.300166625335975 \times 10^{-9}$	$3.987686248617691 \times 10^{-11}$	$5.208940479372794 \times 10^{-15}$	$2.441165215801239 \times 10^{-17}$
	0.8	$5.700166616827516 \times 10^{-9}$	$3.978355402549054 \times 10^{-11}$	$6.592083907044729 \times 10^{-15}$	$2.421667439210999 \times 10^{-17}$
	1	$7.500166605888068 \times 10^{-9}$	$3.962518600455048 \times 10^{-11}$	$8.367051017590978 \times 10^{-15}$	$2.391594246117009 \times 10^{-17}$
$t=0.001$	0	$2.500446168850624 \times 10^{-13}$	$3.997917031149732 \times 10^{-16}$	$3.428519345071701 \times 10^{-22}$	$1.29344286891825 \times 10^{-23}$
	0.2	$2.700463948967092 \times 10^{-13}$	$3.997781031149732 \times 10^{-16}$	$3.626601056472554 \times 10^{-22}$	$2.982009645350879 \times 10^{-23}$
	0.4	$3.300517289316497 \times 10^{-13}$	$3.997341031149732 \times 10^{-16}$	$4.220832590662312 \times 10^{-22}$	$5.933053221032608 \times 10^{-24}$
	0.6	$4.300606189898838 \times 10^{-13}$	$3.996501031149732 \times 10^{-16}$	$5.211163547602576 \times 10^{-22}$	$2.836415786838725 \times 10^{-23}$
	0.8	$5.700730650714116 \times 10^{-13}$	$3.995101031149732 \times 10^{-16}$	$6.597477927229343 \times 10^{-22}$	$4.991046909818666 \times 10^{-23}$
	1	$7.500890671762329 \times 10^{-13}$	$3.992917031149732 \times 10^{-16}$	$8.379546129453018 \times 10^{-22}$	$3.223603558845966 \times 10^{-23}$

Solving example 5.3 by using the TAM

To implement the TAM to solve the Eq. (2), we write it in the operator form, as follows

$$L(w) = w_t, \quad N(w) = w_{xx} + w_{yy} + tw(1 - w) + u(x, y, t),$$

with initial condition, $w(x, y, 0) = x^2 + y^2$.

We start by supposing that w_0 is an initial approximation of the problem w through solving the following initial equation

$$L_t(w_0) = 0, \text{ with } w_0(x, y, 0) = x^2 + y^2, L_t = \frac{\partial}{\partial t}.$$

Then, we get

$$w_0 = x^2 + y^2.$$

Also, to get the next iteration, we have to solve the following problem

$$L_t(w_1) + N(w_0) = 0, \text{ with } w_1(x, y, 0) = x^2 + y^2.$$

Then, we get

$$w_1 = t^2 - \frac{t^4}{4} + \frac{t^6}{6} + x^2 + \frac{t^4 x^2}{2} + y^2 + \frac{t^4 y^2}{2}.$$

In the second iteration, we have to solve the following problem

$$L_t(w_2) + N(w_1) = 0, \text{ with } w_2(x, y, 0) = x^2 + y^2.$$

Thus, we get

$$w_2 = t^2 + \frac{2t^5}{5} - \frac{t^6}{24} + \frac{t^8}{12} - \frac{19t^{10}}{480} + \frac{t^{12}}{144} - \frac{t^{14}}{504} + x^2 + \frac{t^6 x^2}{6} - \frac{t^8 x^2}{6} + \frac{t^{10} x^2}{40} - \frac{t^{12} x^2}{72} - \frac{t^6 x^4}{6} - \frac{t^{10} x^4}{40} + y^2 + \frac{t^6 y^2}{6} - \frac{t^8 y^2}{6} + \frac{t^{10} y^2}{40} - \frac{t^{12} y^2}{72} - \frac{1}{3} t^6 x^2 y^2 - \frac{1}{20} t^{10} x^2 y^2 - \frac{t^6 y^4}{6} - \frac{t^{10} y^4}{40},$$

⋮

Furthermore, by proceeding in this way the iterations w_3 and w_4 were also calculated but for the purpose of brevity is not mentioned here.

To prove the convergence for the TAM for the Eq. (27), we have applied the process as given in Eqs. (15), (16) and (17), and we evaluate the δ_i given in Eq. (19) to check the convergent conditions of the obtained approximate solution. Then, we get

$$\delta_0 = \frac{\|v_1\|}{\|v_0\|} = 0.00005000375008334945 < 1,$$

$$\delta_1 = \frac{\|v_2\|}{\|v_1\|} = 0.00007459982251031754 < 1,$$

$$\delta_2 = \frac{\|v_3\|}{\|v_2\|} = 0.005312373670156887 < 1,$$

$$\delta_3 = \frac{\|v_4\|}{\|v_3\|} = 0.00020729220357214892 < 1.$$

The results of δ_i , for all $i \geq 0$, $0 < t < 1$ and $0 \leq x, y \leq 1$, are less than one. Therefore, the obtained approximate solution by the TAM is converges.

Also, the absolute error will be calculated with the same values of x , t given in solving the problem by using the DJM. It can be seen clearly in Fig. 3 and Table 2 the error is decreasing by increasing the number of iterations. Moreover, the error approximately tends to zero at the fourth iteration with $t=0.001$.

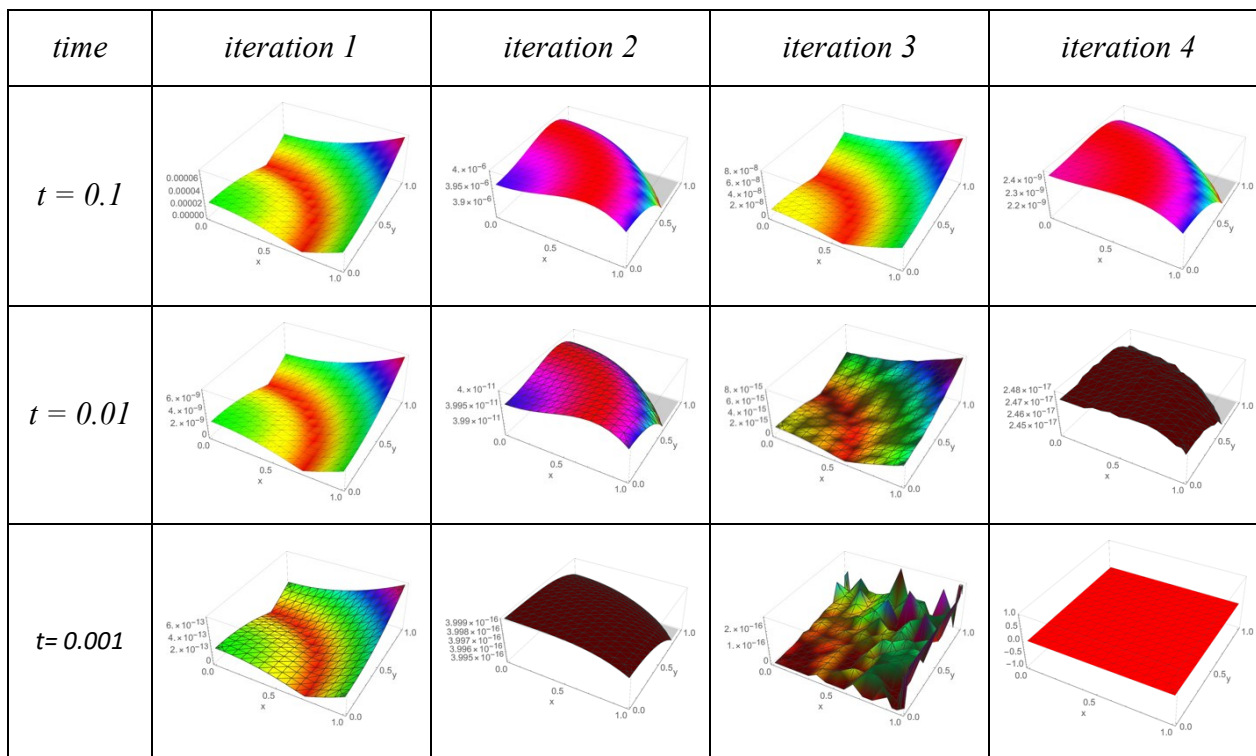


Fig. 3. The absolute error values for example 5.3 obtained by the TAM for w_1, w_2, w_3 , and w_4 with different values of t .

Table 2: The absolute error values for example 5.3 obtained by TAM, for four iterations with different values of t .

Time	x_i	Abs. errs. For 1 st iteration	Abs. errs. For 2 nd iteration	Abs. errs. For 3 rd iteration	Abs. errs. For 4 th iteration
$t=0.1$	0	0.00002516666666677221	0.0000039574960347114	$3.439519623976705 \times 10^{-8}$	$2.367214167742215 \times 10^{-9}$
	0.2	0.000027166666666776434	0.000003950495930156153	$3.636235775678065 \times 10^{-8}$	$2.352566464552952 \times 10^{-9}$
	0.4	0.000033166666666789095	0.000003926295568490412	$4.225011396297162 \times 10^{-8}$	$2.303341833237437 \times 10^{-9}$
	0.6	0.0000431666666668102	0.00000387529480571418	$5.200767994040234 \times 10^{-8}$	$2.20374528521472 \times 10^{-9}$
	0.8	0.00005716666666683975	0.000003781493401827455	$6.551841491564403 \times 10^{-8}$	$2.027660084974458 \times 10^{-9}$
	1	0.00007516666666687773	0.000003622491020830237	$8.255182026850605 \times 10^{-8}$	$1.739110619403128 \times 10^{-9}$
$t=0.01$	0	$2.500166636275423 \times 10^{-9}$	$3.995843050700178 \times 10^{-11}$	$3.341687278453353 \times 10^{-15}$	$2.465204689688915 \times 10^{-17}$
	0.2	$2.700166635059928 \times 10^{-9}$	$3.995150072691333 \times 10^{-11}$	$3.760880495917718 \times 10^{-15}$	$2.463849436973309 \times 10^{-17}$
	0.4	$3.300166631413446 \times 10^{-9}$	$3.992751138664317 \times 10^{-11}$	$4.32986979603811 \times 10^{-15}$	$2.461138931542095 \times 10^{-17}$
	0.6	$4.300166625335975 \times 10^{-9}$	$3.987686248617691 \times 10^{-11}$	$5.329070518200751 \times 10^{-15}$	$2.448941657101633 \times 10^{-17}$
	0.8	$5.700166616827516 \times 10^{-9}$	$3.978355402549054 \times 10^{-11}$	$6.439293542825908 \times 10^{-15}$	$2.434033877229957 \times 10^{-17}$
	1	$7.500166605888068 \times 10^{-9}$	$3.962518600455048 \times 10^{-11}$	$8.215650382226158 \times 10^{-15}$	$2.401507812055392 \times 10^{-17}$
$t=0.001$	x_i	Abs. errs. For 1 st iteration	Abs. errs. For 2 nd iteration	Abs. errs. For 3 rd iteration	Abs. errs. For 4 th iteration
	0	$2.500446168850624 \times 10^{-13}$	$3.997917031149732 \times 10^{-16}$	$1.39778012230615 \times 10^{-16}$	0.
	0.2	$2.700463948967092 \times 10^{-13}$	$3.997781031149732 \times 10^{-16}$	$5.551115123125783 \times 10^{-17}$	0.
	0.4	$3.300517289316497 \times 10^{-13}$	$3.997341031149732 \times 10^{-16}$	$2.775557561562891 \times 10^{-17}$	0.
	0.6	$4.300606189898838 \times 10^{-13}$	$3.996501031149732 \times 10^{-16}$	$1.665334536937734 \times 10^{-16}$	0.
	0.8	$5.700730650714116 \times 10^{-13}$	$3.995101031149732 \times 10^{-16}$	$1.110223024625156 \times 10^{-16}$	0.
1	$7.500890671762329 \times 10^{-13}$	$3.992917031149732 \times 10^{-16}$	$2.220446049250313 \times 10^{-16}$	0.	

Solving example 5.3 by using the BCM

To implement the BCM to solve the Eq. (2), by following the same steps as in the DJM, we obtain Eq. (29).

Also, suppose

$$g = x^2 + y^2, \text{ and } N(w) = L_t^{-1}N(w),$$

where, $L_t^{-1}(\cdot) = \int_0^t (\cdot) dt$, $N(w) = w_{xx} + w_{yy} + tw(1 - w) + u(x, y, t)$.

Applying the steps of the BCM, we get

$$w_0 = g = x^2 + y^2,$$

$$w_n = w_0 + N(w_{n-1}), n \in \mathbb{N}.$$

Hence,

$$w_1 = t^2 - \frac{t^4}{4} + \frac{t^6}{6} + x^2 + \frac{t^4x^2}{2} + y^2 + \frac{t^4y^2}{2},$$

$$w_2 = t^2 + \frac{2t^5}{5} - \frac{t^6}{24} + \frac{t^8}{12} - \frac{19t^{10}}{480} + \frac{t^{12}}{144} - \frac{t^{14}}{504} + x^2 + \frac{t^6x^2}{6} - \frac{t^8x^2}{6} + \frac{t^{10}x^2}{40} - \frac{t^{12}x^2}{72}$$

$$- \frac{t^6x^4}{6} - \frac{t^{10}x^4}{40} + y^2 + \frac{t^6y^2}{6} - \frac{t^8y^2}{6} + \frac{t^{10}y^2}{40} - \frac{t^{12}y^2}{72} - \frac{1}{3}t^6x^2y^2$$

$$- \frac{1}{20}t^{10}x^2y^2 - \frac{t^6y^4}{6} - \frac{t^{10}y^4}{40},$$

⋮

Furthermore, by proceeding in this way the iterations w_3 and w_4 were also calculated but for the purpose of brevity is not mentioned here.

To prove the convergence analysis of the BCM for the Eq. (27), we have applied the similar process as presented in section 4 and then, we evaluate the δ_i to check the convergent conditions of the obtained approximate solution. Thus, we get

$$\delta_0 = \frac{\|v_1\|}{\|v_0\|} = 0.00005000375008334945 < 1,$$

$$\delta_1 = \frac{\|v_2\|}{\|v_1\|} = 0.00007459982251031754 < 1,$$

$$\delta_2 = \frac{\|v_3\|}{\|v_2\|} = 0.0053123909674375296 < 1,$$

$$\delta_3 = \frac{\|v_4\|}{\|v_3\|} = 0.00020887885059192363 < 1.$$

The results of δ_i , for all $i \geq 0$, $0 < t < 1$ and $0 \leq x, y \leq 1$, are less than one. Therefore, the obtained approximate solution is converges.

Also, the absolute errors will be calculated to check out the efficiency for the approximate solutions that we found by the BCM for the same values of x, t used in the DJM

and TAM. It can be observed from Fig. 4 and Table 3 the absolute error values obtained by BCM is decreasing by increasing the number of iterations and decreasing the time.

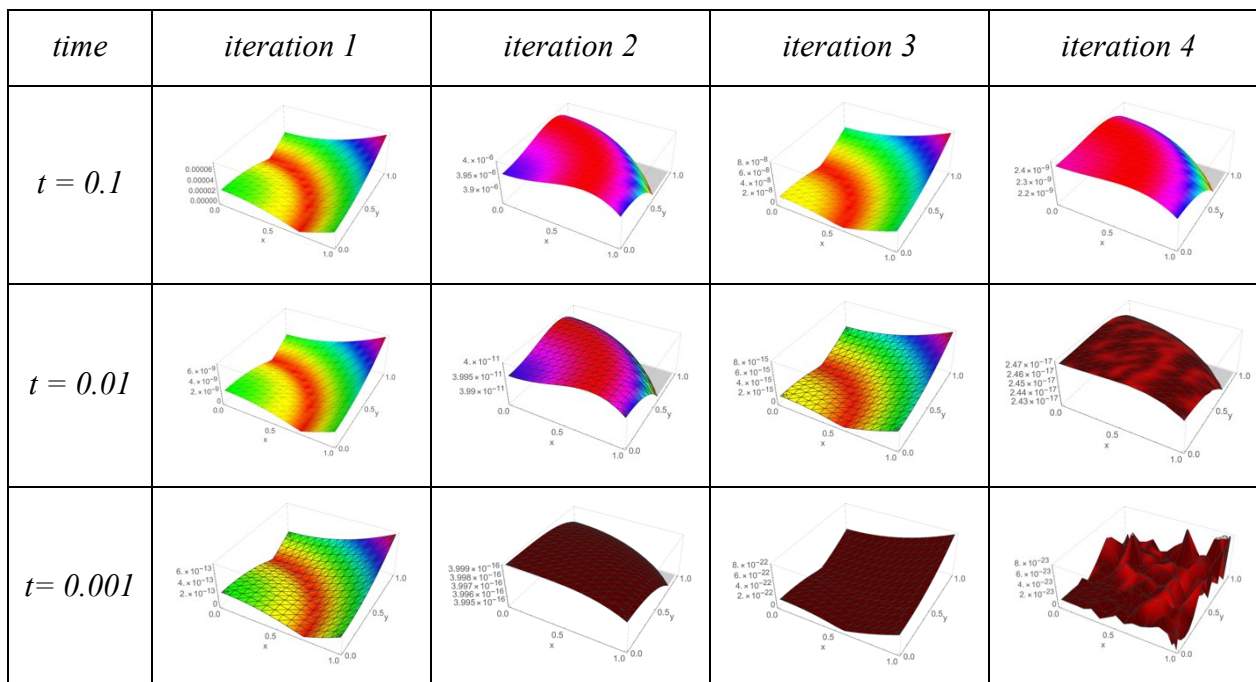


Fig. 4. The absolute error values for example 5.3 obtained by the BCM for $w_1, w_2, w_3,$ and w_4 with different values of t .

Table 3: The absolute error values for example 5.3 obtained by BCM, for four iterations with different values of t .

Time	x_i	Abs. errs. For 1 st iteration	Abs. errs. For 2 nd iteration	Abs. errs. For 3 rd iteration	Abs. errs. For 4 th iteration
$t=0.1$	0	0.00002516666666677221	0.0000039574960347114	$3.439519622754291 \times 10^{-8}$	$2.367214207006091 \times 10^{-9}$
	0.2	0.000027166666666776434	0.000003950495930156153	$3.636235764046649 \times 10^{-8}$	$2.352566504062037 \times 10^{-9}$
	0.4	0.000033166666666789095	0.000003926295568490412	$4.225011372322602 \times 10^{-8}$	$2.303341876975943 \times 10^{-9}$
	0.6	0.0000431666666668102	0.00000387529480571418	$5.200767991296621 \times 10^{-8}$	$2.203745339426222 \times 10^{-9}$
	0.8	0.00005716666666683975	0.000003781493401827455	$6.551841495654667 \times 10^{-8}$	$2.027660150299521 \times 10^{-9}$
	1	0.00007516666666687773	0.000003622491020830237	$8.255182044155353 \times 10^{-8}$	$1.739110699410879 \times 10^{-9}$
$t=0.01$	x_i	Abs. errs. For 1 st iteration	Abs. errs. For 2 nd iteration	Abs. errs. For 3 rd iteration	Abs. errs. For 4 th iteration
	0	$2.500166636275423 \times 10^{-9}$	$3.995843050700178 \times 10^{-11}$	$3.428213061620738 \times 10^{-15}$	$2.459218564137952 \times 10^{-17}$
	0.2	$2.700166635059928 \times 10^{-9}$	$3.995150072691333 \times 10^{-11}$	$3.626173005459958 \times 10^{-15}$	$2.45742245436945 \times 10^{-17}$
	0.4	$3.300166631413446 \times 10^{-9}$	$3.992751138664317 \times 10^{-11}$	$4.219916824177479 \times 10^{-15}$	$2.451761901624386 \times 10^{-17}$
	0.6	$4.300166625335975 \times 10^{-9}$	$3.987686248617691 \times 10^{-11}$	$5.208940479372794 \times 10^{-15}$	$2.441165215801239 \times 10^{-17}$
	0.8	$5.700166616827516 \times 10^{-9}$	$3.978355402549054 \times 10^{-11}$	$6.592083907044729 \times 10^{-15}$	$2.421667439210999 \times 10^{-17}$
1	$7.500166605888068 \times 10^{-9}$	$3.962518600455048 \times 10^{-11}$	$8.367051017590978 \times 10^{-15}$	$2.391594246117009 \times 10^{-17}$	
$t=0.001$	x_i	Abs. errs. For 1 st iteration	Abs. errs. For 2 nd iteration	Abs. errs. For 3 rd iteration	Abs. errs. For 4 th iteration
	0	$2.500446168850624 \times 10^{-13}$	$3.997917031149732 \times 10^{-16}$	$3.428519345071701 \times 10^{-22}$	$1.29344286891825 \times 10^{-23}$
	0.2	$2.700463948967092 \times 10^{-13}$	$3.997781031149732 \times 10^{-16}$	$3.626601056472554 \times 10^{-22}$	$2.982009645350879 \times 10^{-23}$
	0.4	$3.300517289316497 \times 10^{-13}$	$3.997341031149732 \times 10^{-16}$	$4.220832590662312 \times 10^{-22}$	$5.933053221032608 \times 10^{-24}$
	0.6	$4.300606189898838 \times 10^{-13}$	$3.996501031149732 \times 10^{-16}$	$5.211163547602576 \times 10^{-22}$	$2.836415786838725 \times 10^{-23}$
	0.8	$5.700730650714116 \times 10^{-13}$	$3.995101031149732 \times 10^{-16}$	$6.597477927229343 \times 10^{-22}$	$4.991046909818666 \times 10^{-23}$
1	$7.500890671762329 \times 10^{-13}$	$3.992917031149732 \times 10^{-16}$	$8.379546129453018 \times 10^{-22}$	$3.223603558845966 \times 10^{-23}$	

Example 5.4. Consider the 3D Fisher's equation given in Eq. (3), with $\alpha = \beta = 1$, as follows

$$w_t = w_{xx} + w_{yy} + w_{zz} + tw(1 - w) + u(x, y, z, t), \quad (30)$$

and the initial condition, $w(x, y, z, 0) = x^3 + y^3 + z^3$,

where, $u(x, y, z, t) = 3t^2 - 6x - 6y - 6z - t(1 - t^3 - x^3 - y^3 - z^3)(t^3 + x^3 + y^3 + z^3)$.
 The exact solution for this equation is

$$w = x^3 + y^3 + z^3 + t^3.$$

Solving example 5.4 by using the DJM

To implement the DJM for solving the Eq.(30), we write it in the operator form as follows

$$L_t(w(x, y, z, t)) = N(w), \tag{31}$$

where, $L_t = \frac{\partial}{\partial t}$ and $N(w) = w_{xx} + w_{yy} + w_{zz} + tw(1 - w) + u(x, y, z, t)$.

By taking the inverse for together sides of Eq. (31), and applying the initial condition, we obtain

$$w = (x^3 + y^3 + z^3) + L_t^{-1}N(w). \tag{32}$$

Finally, according to the DJM for Eq. (32) and by applying the recurrence relation, we achieve the components w_n as the following in a series form

$$w_0 = x^3 + y^3 + z^3,$$

$$w_1 = L_t^{-1}(J_0) = L_t^{-1}N(w_0) = t^3 - \frac{t^5}{5} + \frac{t^8}{8} + \frac{2t^5x^3}{5} + \frac{2t^5y^3}{5} + \frac{2t^5z^3}{5},$$

$$w_2 = L_t^{-1}(J_1) = L_t^{-1}N(w_0 + w_1) - w_1$$

$$= \frac{t^5}{5} - \frac{t^7}{35} - \frac{t^8}{8} + \frac{21t^{10}}{400} - \frac{t^{12}}{300} - \frac{t^{13}}{52} + \frac{t^{15}}{300} - \frac{t^{18}}{1152} + \frac{2t^6x}{5} - \frac{2t^5x^3}{5} + \frac{4t^7x^3}{35} - \frac{21t^{10}x^3}{200} + \frac{t^{12}x^3}{75} - \frac{t^{15}x^3}{150} - \frac{4t^7x^6}{35} - \frac{t^{12}x^6}{75} + \frac{2t^6y}{5} - \frac{2t^5y^3}{5} + \frac{4t^7y^3}{35} - \frac{21t^{10}y^3}{200} + \frac{t^{12}y^3}{75} - \frac{t^{15}y^3}{150} - \frac{8}{35}t^7x^3y^3 - \frac{2}{75}t^{12}x^3y^3 - \frac{4t^7y^6}{35} - \frac{t^{12}y^6}{75} + \frac{2t^6z}{5} - \frac{2t^5z^3}{5} + \frac{4t^7z^3}{35} - \frac{21t^{10}z^3}{200} + \frac{t^{12}z^3}{75} - \frac{t^{15}z^3}{150} - \frac{8}{35}t^7x^3z^3 - \frac{2}{75}t^{12}x^3z^3 - \frac{8}{35}t^7y^3z^3 - \frac{2}{75}t^{12}y^3z^3 - \frac{4t^7z^6}{35} - \frac{t^{12}z^6}{75},$$

⋮

By continuing in this way the iterations w_3 and w_4 were also calculated but for the purpose of brevity is not mentioned here.

To prove the convergence of the DJM for the Eq. (30), we have applied the process as presented in section 4. Hence, let choose the same above components obtained by the DJM, we get

$$v_0 = w_0 = x^3 + y^3 + z^3,$$

$$v_1 = w_1 = t^3 - \frac{t^5}{5} + \frac{t^8}{8} + \frac{2t^5x^3}{5} + \frac{2t^5y^3}{5} + \frac{2t^5z^3}{5},$$

⋮

and so on, by using the iterations above and we evaluate the δ_i given in Eq. (19) to check the convergent conditions of the obtained approximate solution, then, we get

$$\delta_0 = \frac{\|v_1\|}{\|v_0\|} = 3.333666666708334 \times 10^{-7} < 1,$$

$$\delta_1 = \frac{\|v_2\|}{\|v_1\|} = 0.00009879727563096987 < 1,$$

$$\delta_2 = \frac{\|v_3\|}{\|v_2\|} = 0.012075415524177402 < 1,$$

$$\delta_3 = \frac{\|v_4\|}{\|v_3\|} = 0.0002323087617440097 < 1.$$

The results of δ_i , for all $i \geq 0$, $0 < t < 1$ and $0 \leq x, y, z \leq 1$, are less than one. Therefore, the approximate solution obtained by the DJM is converges.

Also, the absolute errors are calculated to check out the efficiency for the approximate solutions for various values of the time $t = 0.1, 0.01$ and 0.001 , given in Fig. 5. Moreover, Table 4 shows the absolute error values obtained by DJM for the iterations with $x = \{0, 0.2, 0.4, 0.6, 0.8, 1\}$, it can be easily recognized that the error is decreasing by increasing the number of iterations and decreasing the value of time.

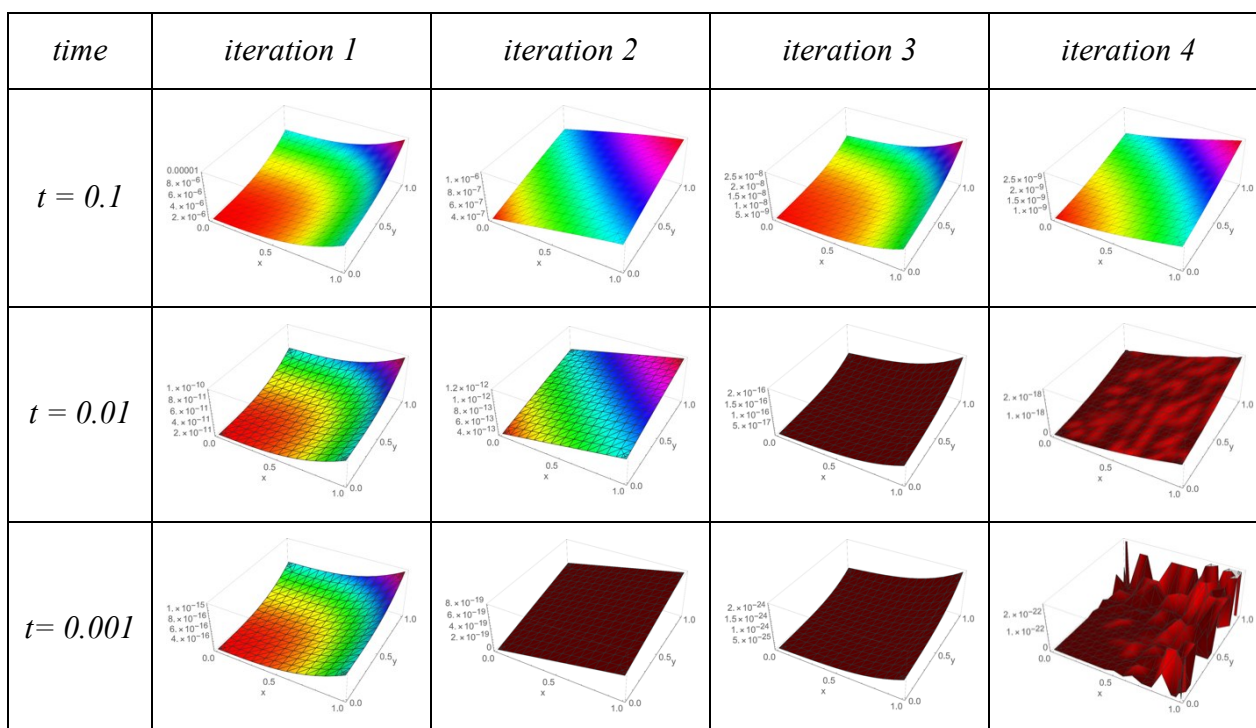


Fig. 5. The absolute error values for example 5.4 obtained by the DJM for w_1, w_2, w_3 , and w_4 with different values of t .

Table 4: The absolute error values for example 5.4 obtained by DJM, for four iterations with different values of t .

Time	x_i	Abs. errs. For 1 st iteration	Abs. errs. For 2 nd iteration	Abs. errs. For 3 rd iteration	Abs. errs. For 4 th iteration
$t=0.1$	0	0.00000600124999983187	$7.742699323627617 \times 10^{-7}$	$1.320252550675336 \times 10^{-8}$	$1.67004493323643 \times 10^{-9}$
	0.2	0.000006033249999831014	$8.539948308988224 \times 10^{-7}$	$1.406757778557003 \times 10^{-8}$	$1.837622725104753 \times 10^{-9}$
	0.4	0.000006257249999825021	$9.320281606034605 \times 10^{-7}$	$1.530290758255603 \times 10^{-8}$	$2.05549086807278 \times 10^{-9}$
	0.6	0.000006865249999808754	0.000001006328729380217	$1.746112293136207 \times 10^{-8}$	$2.314295728200713 \times 10^{-9}$
	0.8	0.000008049249999777076	0.000001073714315230005	$2.128396463294381 \times 10^{-8}$	$2.597436775633328 \times 10^{-9}$
	1	0.000010001249999724848	0.000001128545093286537	$2.767829010265537 \times 10^{-8}$	$2.872778668825741 \times 10^{-9}$
$t=0.01$	x_i	Abs. errs. For 1 st iteration	Abs. errs. For 2 nd iteration	Abs. errs. For 3 rd iteration	Abs. errs. For 4 th iteration
	0	$6.000000496442226 \times 10^{-11}$	$7.97649253302486 \times 10^{-13}$	$9.38428773337254 \times 10^{-17}$	$1.070649645329436 \times 10^{-18}$
	0.2	$6.032000499089918 \times 10^{-11}$	$8.77622012661146 \times 10^{-13}$	$1.023660726055963 \times 10^{-16}$	$1.233279971202261 \times 10^{-18}$
	0.4	$6.256000517623761 \times 10^{-11}$	$9.574272321717656 \times 10^{-13}$	$1.138474363261675 \times 10^{-16}$	$1.45012040569936 \times 10^{-18}$
	0.6	$6.864000567929908 \times 10^{-11}$	$1.036862409700589 \times 10^{-12}$	$1.331019827670317 \times 10^{-16}$	$1.707618421664664 \times 10^{-18}$
	0.8	$8.048000665894506 \times 10^{-11}$	$1.115610940256718 \times 10^{-12}$	$1.669606053641445 \times 10^{-16}$	$2.087089182034583 \times 10^{-18}$
1	$1.000000082740371 \times 10^{-10}$	$1.193110458849249 \times 10^{-12}$	$2.242460647913282 \times 10^{-16}$	$2.493664996716629 \times 10^{-18}$	
$t=0.001$	x_i	Abs. errs. For 1 st iteration	Abs. errs. For 2 nd iteration	Abs. errs. For 3 rd iteration	Abs. errs. For 4 th iteration
	0	$6.661338147750939 \times 10^{-16}$	$3.998857142857143 \times 10^{-19}$	$9.392000002026451 \times 10^{-25}$	$1.48331235938098 \times 10^{-48}$
	0.2	$6.696865284538944 \times 10^{-16}$	$4.798838784 \times 10^{-19}$	$1.024444335758498 \times 10^{-24}$	$2.117582368135751 \times 10^{-22}$
	0.4	$6.9455524205498 \times 10^{-16}$	$5.598706176 \times 10^{-19}$	$1.139348554054155 \times 10^{-24}$	$2.117582368135751 \times 10^{-22}$
	0.6	$7.620570841027075 \times 10^{-16}$	$6.398310107428573 \times 10^{-19}$	$1.332174526510562 \times 10^{-24}$	$2.117582368135751 \times 10^{-22}$
	0.8	$8.93507490218326 \times 10^{-16}$	$7.197387264 \times 10^{-19}$	$1.67146743228809 \times 10^{-24}$	$2.117582368135751 \times 10^{-22}$
1	$1.110223024625156 \times 10^{-15}$	$7.995428571428572 \times 10^{-19}$	$2.246031746364245 \times 10^{-24}$	$3.004975599994815 \times 10^{-47}$	

Solving example 5.4 by using the TAM

To implement the TAM for Eq.(30), we write it in the operator form, as follows

$$L(w) = w_t, \quad N(w) = w_{xx} + w_{yy} + w_{zz} + tw(1 - w) + u(x, y, z, t),$$

with initial condition,

$$w(x, y, z, 0) = x^3 + y^3 + z^3.$$

We start by assuming that w_0 is an initial approximation of the problem w through solving the following initial equation

$$L_t(w_0) = 0, \quad \text{with } w_0(x, y, z, 0) = x^3 + y^3 + z^3, \quad L_t = \frac{\partial}{\partial t}.$$

Then, we get

$$w_0 = x^3 + y^3 + z^3.$$

Also, to obtain the next iteration, we have to solve the following problem

$$L_t(w_1) + N(w_0) = 0, \quad \text{with } w_1(x, y, z, 0) = x^3 + y^3 + z^3.$$

Then, we get

$$w_1 = t^3 - \frac{t^5}{5} + \frac{t^8}{8} + x^3 + \frac{2t^5x^3}{5} + y^3 + \frac{2t^5y^3}{5} + z^3 + \frac{2t^5z^3}{5}.$$

In the second iteration, we have to solve the following problem

$$L_t(w_2) + N(w_1) = 0, \quad \text{with } w_2(x, y, z, 0) = x^3 + y^3 + z^3.$$

Thus, we get

$$\begin{aligned}
 w_2 = t^3 &- \frac{t^7}{35} + \frac{21t^{10}}{400} - \frac{t^{12}}{300} - \frac{t^{13}}{52} + \frac{t^{15}}{300} - \frac{t^{18}}{1152} + \frac{2t^6x}{5} + x^3 + \frac{4t^7x^3}{35} - \frac{21t^{10}x^3}{200} \\
 &+ \frac{t^{12}x^3}{75} - \frac{t^{15}x^3}{150} - \frac{4t^7x^6}{35} - \frac{t^{12}x^6}{75} + \frac{2t^6y}{5} + y^3 + \frac{4t^7y^3}{35} - \frac{21t^{10}y^3}{200} + \frac{t^{12}y^3}{75} \\
 &- \frac{t^{15}y^3}{150} - \frac{8}{35}t^7x^3y^3 - \frac{2}{75}t^{12}x^3y^3 - \frac{4t^7y^6}{35} - \frac{t^{12}y^6}{75} + \frac{2t^6z}{5} + z^3 + \frac{4t^7z^3}{35} \\
 &- \frac{21t^{10}z^3}{200} + \frac{t^{12}z^3}{75} - \frac{t^{15}z^3}{150} - \frac{8}{35}t^7x^3z^3 - \frac{2}{75}t^{12}x^3z^3 - \frac{8}{35}t^7y^3z^3 \\
 &- \frac{2}{75}t^{12}y^3z^3 - \frac{4t^7z^6}{35} - \frac{t^{12}z^6}{75}.
 \end{aligned}$$

⋮

and by continuing in this way the iterations w_3 and w_4 were also calculated but for the purpose of brevity is not mentioned here.

To prove the convergence for the TAM for the Eq. (30), we have applied the process as given in Eqs. (15), (16) and (17), and we evaluate the δ_i given in Eq. (19) to check the convergent conditions of the obtained approximate solution.

Then, we get

$$\delta_0 = \frac{\|v_1\|}{\|v_0\|} = 3.333666667160173 \times 10^{-7} < 1,$$

$$\delta_1 = \frac{\|v_2\|}{\|v_1\|} = 0.00009879757291895636 < 1,$$

$$\delta_2 = \frac{\|v_3\|}{\|v_2\|} = 0.012067708416467766 < 1,$$

$$\delta_3 = \frac{\|v_4\|}{\|v_3\|} = 0. < 1.$$

The results of δ_i , for all $i \geq 0$, $0 < t < 1$ and $0 \leq x, y, z \leq 1$, are less than one. Therefore, a convergent approximate solution is obtained. Also, the absolute errors are evaluated in similar cases done for the DJM. Fig. 6 and Table 5 show the absolute error values obtained by TAM, it can be easily recognized that the error is decreasing by increasing the number of iterations and decreasing the time.

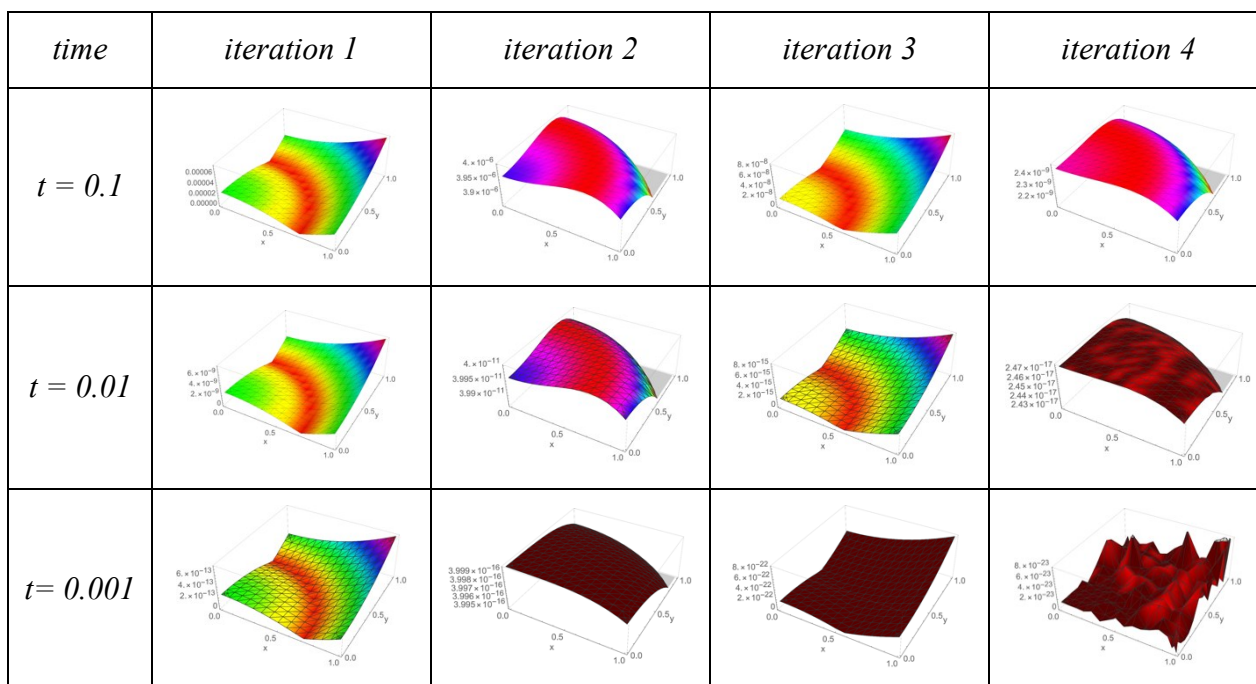


Fig. 6. The absolute error values for example 5.4 obtained by the TAM for w_1, w_2, w_3 , and w_4 with different values of t .

Table 5: The absolute error values for example 5.4 obtained by TAM, for four iterations with different values of t .

Time	x_i	Abs. errs. For 1 st iteration	Abs. errs. For 2 nd iteration	Abs. errs. For 3 rd iteration	Abs. errs. For 4 th iteration
$t=0.1$	0	0.00000600124999983187	$7.742699323627617 \times 10^{-7}$	$1.320252529524168 \times 10^{-8}$	$1.670044996390784 \times 10^{-9}$
	0.2	0.000006033249999831014	$8.539948308988224 \times 10^{-7}$	$1.406757776933886 \times 10^{-8}$	$1.837622790263129 \times 10^{-9}$
	0.4	0.000006257249999825021	$9.320281606034605 \times 10^{-7}$	$1.530290782980614 \times 10^{-8}$	$2.055490934144838 \times 10^{-9}$
	0.6	0.000006865249999808754	0.000001006328729380217	$1.746112321399096 \times 10^{-8}$	$2.314295792548229 \times 10^{-9}$
	0.8	0.000008049249999777076	0.000001073714315230005	$2.128396436873458 \times 10^{-8}$	$2.597436836145397 \times 10^{-9}$
	1	0.000010001249999724848	0.000001128545093286537	$2.767828988226028 \times 10^{-8}$	$2.872778724757538 \times 10^{-9}$
$t=0.01$	0	$6.000000496442226 \times 10^{-11}$	$7.97649253302486 \times 10^{-13}$	$2.220446049250313 \times 10^{-16}$	$8.050561119707455 \times 10^{-17}$
	0.2	$6.032000499089918 \times 10^{-11}$	$8.77622012661146 \times 10^{-13}$	$2.220446049250313 \times 10^{-16}$	$8.033323999230829 \times 10^{-17}$
	0.4	$6.256000517623761 \times 10^{-11}$	$9.574272321717656 \times 10^{-13}$	$2.220446049250313 \times 10^{-16}$	$8.010475285478645 \times 10^{-17}$
	0.6	$6.864000567929908 \times 10^{-11}$	$1.036862409700589 \times 10^{-12}$	$4.440892098500626 \times 10^{-16}$	$7.982205560864032 \times 10^{-17}$
	0.8	$8.048000665894506 \times 10^{-11}$	$1.115610940256718 \times 10^{-12}$	0.	$7.948578352858036 \times 10^{-17}$
	1	$1.000000082740371 \times 10^{-10}$	$1.193110458849249 \times 10^{-12}$	0.	$7.909974826286921 \times 10^{-17}$
$t=0.001$	0	$6.661338147750939 \times 10^{-16}$	$3.998857142857143 \times 10^{-19}$	0.	$8.274037093680878 \times 10^{-17}$
	0.2	$6.696865284538944 \times 10^{-16}$	$4.798838784 \times 10^{-19}$	0.	$8.274037093680878 \times 10^{-17}$
	0.4	$6.9455524205498 \times 10^{-16}$	$5.598706176 \times 10^{-19}$	0.	$8.274037093680878 \times 10^{-17}$
	0.6	$7.620570841027075 \times 10^{-16}$	$6.398310107428573 \times 10^{-19}$	0.	$8.274037093680878 \times 10^{-17}$
	0.8	$8.93507490218326 \times 10^{-16}$	$7.197387264 \times 10^{-19}$	0.	$8.274037093680878 \times 10^{-17}$
	1	$1.110223024625156 \times 10^{-15}$	$7.995428571428572 \times 10^{-19}$	0.	$8.274037093680878 \times 10^{-17}$

Solving example 5.4 by using the BCM

To implement the BCM to solve the Eq. (30), we followed similar steps as given for the DJM, we obtain Eq. (32).

Also, suppose

$$g = x^3 + y^3 + z^3, \text{ and } N(w) = L_t^{-1}N(w),$$

Where,

$$L_t^{-1}(\cdot) = \int_0^t (\cdot) dt, N(w) = w_{xx} + w_{yy} + w_{zz} + tw(1 - w) + u(x, y, z, t).$$

Applying the steps of the BCM, we get

$$w_0 = g = x^3 + y^3 + z^3,$$

$$w_n = w_0 + N(w_{n-1}), n \in \mathbb{N}.$$

Hence,

$$w_1 = t^3 - \frac{t^5}{5} + \frac{t^8}{8} + x^3 + \frac{2t^5x^3}{5} + y^3 + \frac{2t^5y^3}{5} + z^3 + \frac{2t^5z^3}{5},$$

$$w_2 = t^3 - \frac{t^7}{35} + \frac{21t^{10}}{400} - \frac{t^{12}}{300} - \frac{t^{13}}{52} + \frac{t^{15}}{300} - \frac{t^{18}}{1152} + \frac{2t^6x}{5} + x^3 + \frac{4t^7x^3}{35} - \frac{21t^{10}x^3}{200} + \frac{t^{12}x^3}{75} - \frac{t^{15}x^3}{150} - \frac{4t^7x^6}{35} - \frac{t^{12}x^6}{75} + \frac{2t^6y}{5} + y^3 + \frac{4t^7y^3}{35} - \frac{21t^{10}y^3}{200} + \frac{t^{12}y^3}{75} - \frac{t^{15}y^3}{150} - \frac{8}{35}t^7x^3y^3 - \frac{2}{75}t^{12}x^3y^3 - \frac{4t^7y^6}{35} - \frac{t^{12}y^6}{75} + \frac{2t^6z}{5} + z^3 + \frac{4t^7z^3}{35} - \frac{21t^{10}z^3}{200} + \frac{t^{12}z^3}{75} - \frac{t^{15}z^3}{150} - \frac{8}{35}t^7x^3z^3 - \frac{2}{75}t^{12}x^3z^3 - \frac{8}{35}t^7y^3z^3 - \frac{2}{75}t^{12}y^3z^3 - \frac{4t^7z^6}{35} - \frac{t^{12}z^6}{75},$$

$$\vdots$$

and the iterations w_3 and w_4 were also calculated but for the purpose of brevity is not mentioned here.

To prove the convergence of the BCM for the Eq. (30), we have applied the similar procedure as presented in section 4 and then, we evaluate the δ_i to check the convergent conditions of the obtained approximate solution.

Then, we get

$$\delta_0 = \frac{\|v_1\|}{\|v_0\|} = 3.333666667160173 \times 10^{-7} < 1,$$

$$\delta_1 = \frac{\|v_2\|}{\|v_1\|} = 0.00009879757291895636 < 1,$$

$$\delta_2 = \frac{\|v_3\|}{\|v_2\|} = 0.012071065747678055 < 1,$$

$$\delta_3 = \frac{\|v_4\|}{\|v_3\|} = 0.00012935399757212153 < 1.$$

The results of δ_i , for all $i \geq 0$, $0 < t < 1$ and $0 \leq x, y, z \leq 1$, are less than one. Therefore, the obtained approximate solution by the BCM is converges.

Fig. 7 and Table 6 show the absolute error values obtained by BCM, it can be easily recognized that the error is decreasing by increasing the number of iterations and decreasing the time.

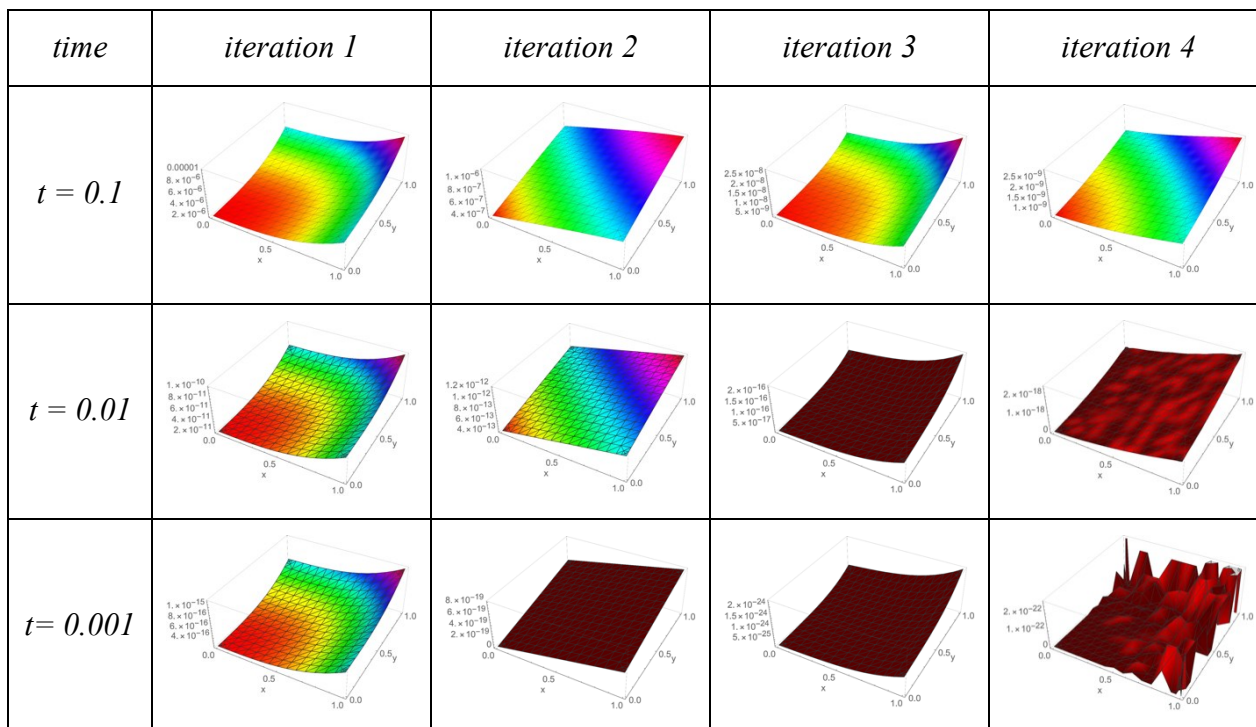


Fig. 7. The absolute error values for example 5.4 obtained by the BCM for $w_1, w_2, w_3,$ and w_4 with different values of t .

Table 6: The absolute error values for example 5.4 obtained by BCM, for four iterations with different values of t .

Time	x_i	Abs. errs. For 1 st iteration	Abs. errs. For 2 nd iteration	Abs. errs. For 3 rd iteration	Abs. errs. For 4 th iteration
$t=0.1$	0	0.00000600124999983187	$7.742699323627617 \times 10^{-7}$	$1.320252550675336 \times 10^{-8}$	$1.67004493323643 \times 10^{-9}$
	0.2	0.000006033249999831014	$8.539948308988224 \times 10^{-7}$	$1.406757778557003 \times 10^{-8}$	$1.837622725104753 \times 10^{-9}$
	0.4	0.000006257249999825021	$9.320281606034605 \times 10^{-7}$	$1.530290758255603 \times 10^{-8}$	$2.05549086807278 \times 10^{-9}$
	0.6	0.000006865249999808754	0.000001006328729380217	$1.746112293136207 \times 10^{-8}$	$2.314295728200713 \times 10^{-9}$
	0.8	0.000008049249999777076	0.000001073714315230005	$2.128396463294381 \times 10^{-8}$	$2.597436775633328 \times 10^{-9}$
	1	0.000010001249999724848	0.000001128545093286537	$2.767829010265537 \times 10^{-8}$	$2.872778668825741 \times 10^{-9}$
$t=0.01$	0	$6.000000496442226 \times 10^{-11}$	$7.97649253302486 \times 10^{-13}$	$9.38428773337254 \times 10^{-17}$	$1.070649645329436 \times 10^{-18}$
	0.2	$6.032000499089918 \times 10^{-11}$	$8.77622012661146 \times 10^{-13}$	$1.023660726055963 \times 10^{-16}$	$1.233279971202261 \times 10^{-18}$
	0.4	$6.256000517623761 \times 10^{-11}$	$9.574272321717656 \times 10^{-13}$	$1.138474363261675 \times 10^{-16}$	$1.45012040569936 \times 10^{-18}$
	0.6	$6.864000567929908 \times 10^{-11}$	$1.036862409700589 \times 10^{-12}$	$1.331019827670317 \times 10^{-16}$	$1.707618421664664 \times 10^{-18}$
	0.8	$8.048000665894506 \times 10^{-11}$	$1.115610940256718 \times 10^{-12}$	$1.669606053641445 \times 10^{-16}$	$2.087089182034583 \times 10^{-18}$
	1	$1.000000082740371 \times 10^{-10}$	$1.193110458849249 \times 10^{-12}$	$2.242460647913282 \times 10^{-16}$	$2.493664996716629 \times 10^{-18}$
$t=0.001$	0	$6.661338147750939 \times 10^{-16}$	$3.998857142857143 \times 10^{-19}$	$9.392000002026451 \times 10^{-25}$	$1.48331235938098 \times 10^{-48}$
	0.2	$6.696865284538944 \times 10^{-16}$	$4.798838784 \times 10^{-19}$	$1.024444335758498 \times 10^{-24}$	$2.117582368135751 \times 10^{-22}$
	0.4	$6.9455524205498 \times 10^{-16}$	$5.598706176 \times 10^{-19}$	$1.139348554054155 \times 10^{-24}$	$2.117582368135751 \times 10^{-22}$
	0.6	$7.620570841027075 \times 10^{-16}$	$6.398310107428573 \times 10^{-19}$	$1.332174526510562 \times 10^{-24}$	$2.117582368135751 \times 10^{-22}$
	0.8	$8.93507490218326 \times 10^{-16}$	$7.197387264 \times 10^{-19}$	$1.67146743228809 \times 10^{-24}$	$2.117582368135751 \times 10^{-22}$
	1	$1.110223024625156 \times 10^{-15}$	$7.995428571428572 \times 10^{-19}$	$2.246031746364245 \times 10^{-24}$	$3.004975599994815 \times 10^{-47}$

6. CONCLUSION

In this paper, we presented and applied three iterative methods to solve the nonlinear 1D, 2D and 3D Fisher's equation. These methods can be applied without restriction conditions for nonlinear equations unlike VIM and ADM; where they required furthermore calculations like Adomian polynomials to handle the nonlinear terms in the ADM and calculate Lagrange multiplier as in the VIM which required additional time during the calculation process. It can be concluded, that the absolute error values and the maximum error remainder decreased when increased the iterations and decreased the time. Also, it has been noticed after solving 1D, 2D and 3D problems the TAM provided highest accuracy and required less time in comparison to the DJM and BCM. Moreover, the proposed methods: DJM, TAM, and BCM are accurate, reliable and applicable to solve the nonlinear problems. However, the limitation of the proposed methods that by increasing the interval of x and t , the accuracy deteriorates and the error is increasing. Since these approaches lead to an expansion of the solution, where we increase the interval of x and t , in fact we go farther from the initial point. Thus, the accuracy of the proposed methods diminishes as in Taylor expansion.

REFERENCES

- [1] Akyildiz FT, Siginer DA, Vajravelu K, Van Gorder RA. (2010) Analytical and numerical results for the Swift–Hohenberg equation. *Applied Mathematics and Computation*, 216(1):221-226.
- [2] Al-Jawary MA. (2017) A semi-analytical iterative method for solving nonlinear thin film flow problems. *Chaos, Solitons & Fractals*, 99:52-56.
- [3] Al-Jawary MA, Azeez MM, Radhi GH. (2018) Analytical and numerical solutions for the nonlinear Burgers and advection–diffusion equations by using a semi-analytical iterative method. *Computers & Mathematics with Applications*, 76(1):155-171.
- [4] Sahib AAA, Hasan SQ. (2014) Convergence of the Generalized Homotopy Perturbation Method for Solving Fractional Order Integro-Differential Equations. *Baghdad Science Journal*, 11(4):1637-1648.
- [5] Al-Hawasy JAA, Al-Rawdanee EH. (2019) Numerical Solution for Classical Optimal Control Problem Governing by Hyperbolic Partial Differential Equation via Galerkin Finite Element-Implicit method with Gradient Projection Method. *Ibn AL-Haitham Journal For Pure and Applied Science*, 32(2):71-80.
- [6] Gorial II. (2011) Finite Difference Method for Two-Dimensional Fractional Partial Differential Equation with parameter. *Ibn AL-Haitham Journal For Pure and Applied Science*, 24(2).
- [7] Mittal RC, Arora G. (2010) Efficient numerical solution of Fisher's equation by using B-spline method. *International Journal of Computer Mathematics*, 87(13):3039-3051.
- [8] Matinfar M, Ghanbari M. (2009) The application of the modified variational iteration method on the generalized Fisher's equation. *Journal of Applied Mathematics and Computing*, 31(1-2):165-175.
- [9] Verma A, Jiware R, Koksai ME. (2014) Analytic and numerical solutions of nonlinear diffusion equations via symmetry reductions. *Advances in Difference Equations*, 2014(1):229.
- [10] Tyson JJ, Brazhnik PK. (2000) On traveling wave solutions of Fisher's equation in two spatial dimensions. *SIAM Journal on Applied Mathematics*, 60(2):371-391.

-
- [11] Roessler J, Hüßner H. (1997) Numerical solution of the 1+ 2 dimensional Fisher's equation by finite elements and the Galerkin method. *Mathematical and Computer Modelling*, 25(3):57-67.
- [12] Ağırseven D, Öziş T. (2010) An analytical study for Fisher type equations by using homotopy perturbation method. *Computers & Mathematics with Applications*, 60(3):602-609.
- [13] Rehman YU, Yaqub M, Ul-Hassan QM, Ayub K, Siddiqa A. (2017) Solving Fisher's Equation by Using Modified Variational Iteration Method. *American Journal of Engineering, Technology and Society*, 4(5):74.
- [14] Al-Khaled K. (2001) Numerical study of Fisher's reaction–diffusion equation by the Sinc collocation method. *Journal of Computational and Applied Mathematics*, 137(2):245-255.
- [15] Wazwaz AM, Gorguis A. (2004) An analytic study of Fisher's equation by using Adomian decomposition method. *Applied Mathematics and Computation*, 154(3):609-620.
- [16] Parand K, Nikarya M. (2017) A numerical method to solve the 1D and the 2D reaction diffusion equation based on Bessel functions and Jacobian free Newton-Krylov subspace methods. *The European Physical Journal Plus*, 132(11):496.
- [17] Daftardar-Gejji V, Jafari H. (2006) An iterative method for solving nonlinear functional equations. *Journal of Mathematical Analysis and Applications*, 316(2):753-763.
- [18] Temimi H, Ansari AR. (2011) A semi-analytical iterative technique for solving nonlinear problems. *Computers & Mathematics with Applications*, 61(2):203-210.
- [19] Daftardar-Gejji V, Bhalekar S. (2009) Solving nonlinear functional equation using Banach contraction principle. *Far East Journal of Applied Mathematics*, 34(3):303-314.
- [20] Al-Jawary MA, Adwan MI, Radhi GH. (2018) Three iterative methods for solving second order nonlinear ODEs arising in physics. *Journal of King Saud University-Science*, 23(1):312-323.
- [21] AL-Jawary MA, Radhi GH, Ravnik J. (2018) Daftardar-Jafari method for solving nonlinear thin film flow problem. *Arab Journal of Basic and Applied Sciences*, 25(1):20-27.
- [22] Al-Jawary MA, Raham RK. (2017) A semi-analytical iterative technique for solving chemistry problems. *Journal of King Saud University-Science*, 29(3):320-332.
- [23] Al-Jawary MA, Radhi GH, Ravnik J. (2017) Semi-analytical method for solving Fokker-Planck's equations. *Journal of the Association of Arab Universities for Basic and Applied Sciences*, 24:254-262.
- [24] AL-Jawary MA. (2016) An efficient iterative method for solving the Fokker–Planck equation. *Results in Physics*, 6:985–991.
- [25] Abdul Nabi AJ, AL-Jawary MA. (2018) Analytical and Numerical Solutions for the Linear and Nonlinear 1D, 2D and 3D Telegraph Equations. *Journal of Advanced Research in Dynamical and Control Systems*, 10(10-Special):2090-2105.
- [26] Mitlif RJ. (2014) New Iterative Method for Solving Nonlinear Equations. *Baghdad Science Journal*, 11(4):1649-1654.
- [27] Daftardar-Gejji V, Bhalekar S. (2010) Solving fractional boundary value problems with Dirichlet boundary conditions using a new iterative method. *Computers & Mathematics with Applications*, 59(5):1801-1809.
- [28] Temimi H, Ansari AR. (2011) A new iterative technique for solving nonlinear second order multi-point boundary value problems. *Applied Mathematics and Computation*, 218(4):1457-1466.
- [29] Odibat ZM. (2010) A study on the convergence of variational iteration method. *Mathematical and Computer Modelling*, 51(9-10):1181-1192.
-

- [30] Mittal RC, Kumar S. (2006) Numerical study of Fisher's equation by wavelet Galerkin method. *International Journal of Computer Mathematics*, 83(3):287-298.
- [31] Mavoungou T, Cherruault Y. (1994) Numerical study of Fisher's equation by Adomian's method. *Mathematical and computer modelling*, 19(1):89-95.

ENERGY AND STRUCTURE STATES OF LOW-LYING BANDS IN ^{156}Gd

PAZLITDIN NURITDINOVICH USMANOV* AND
ELMUROD KUCHKARBOYEVICH YUSUPOV

*Department of Physics, Namangan Engineering and Technology Institute,
160115 Namangan, Uzbekistan*

*Corresponding author: usmanov1956.56@mail.ru

(Received: 3rd June 2020; Accepted: 3rd September 2020; Published on-line: 4th January 2021)

ABSTRACT: The experimental results of the literary and electronic nuclear database for ^{156}Gd were summarized and analyzed. Inertial parameters of rotating core were determined using the Harris method. The theoretical values of energy and wave functions were calculated within the framework of a phenomenological model that takes into account Coriolis mixing of state rotational bands. The calculated energy values were compared with existing experimental data, which were in good agreement.

ABSTRAK: Hasil dapatan kajian melalui eksperimen pangkalan data nuklear dan elektronik bagi ^{156}Gd diringkaskan dan dianalisis. Parameter inersia putaran berputar ditentukan menggunakan kaedah Harris. Nilai teori fungsi tenaga dan gelombang dikira dalam kerangka model fenomenologi yang mengambil kira campuran Coriolis pada band putaran keadaan. Nilai pengiraan tenaga dibandingkan dengan data eksperimen memberikan persetujuan yang baik.

KEYWORDS: *nuclei; energy; states; rotational bands; phenomenological model*

1. INTRODUCTION

The gadolinium isotope with a mass $A=156$ is one of the most studied nuclei. The main reason is the large cross section (n, γ) - reaction in ^{156}Gd , which provides big opportunities for studying the emission spectra in this reaction. Full results on this nucleus are given in references [1,2]. Several other nuclear processes supplement information on the levels and rotation bands in ^{156}Gd . In the reaction of $(\alpha, 2n)$ data were obtained on the states of rotational bands with $K^\pi = 0_1^+ - \text{to } I = 26^+$, $K^\pi = 0_2^+ - \text{to } I = 14^+$, $K^\pi = 0_3^+ - \text{to } I = 10^+$, $K^\pi = 0_4^+ - \text{to } I = 6^+$, $K^\pi = 0_5^+ - \text{to } I = 4^+$, $K^\pi = 2_1^+ - \text{to } I = 15^+$ and $K^\pi = 2_2^+ - \text{to } I = 4^+$.

A wealth of experimental information was obtained as a result of studying the reaction $(n, n'\gamma)$ [3]. Based on the totality of the experimental data, one can think that for ^{156}Gd all or almost all levels were found up to excitation energy of 2 MeV. In ^{156}Gd five rotational bands with $K^\pi = 0^+$ are known. Therefore, systematic study of the properties of these levels is very important to search the corresponding levels in the neighboring nuclei.

^{156}Gd and ^{158}Gd are the first nuclei in which a new type of excitation was discovered – collective states with $I^\pi = 1^+$ [4]. At present, there have been several collective states experimentally observed in ^{156}Gd with $I^\pi = 1^+$. Their excitation energies and reduced probabilities $B(M1) \uparrow$ are determined [5].

Nonadiabaticity is observed in the energies and especially in the electromagnetic characteristics of the excited states of rotational bands with $K^\pi = 0^+$ and $K^\pi = 2^+$ of these nuclei [6-9]. In the present work, to explain these nonadiabatics, we use a phenomenological model that takes into account Coriolis mixing of low-lying rotational bands [10, 11]. The energy levels and wave functions of the rotational band states are calculated. The nonadiabatics observed in the energies and wave functions of rotational states are discussed.

More details of the phenomenological model used are given in Ref. [10] and this model was also successfully applied to study the mixing of state bands of both positive and negative parity in [11-14].

2. DESCRIPTION OF THE MODEL

According to the phenomenological model of the nucleus [10], the Hamilton operator has the following appearance:

$$H = H_{\text{rot}}(I^2) + H_{K,K'} \quad (1)$$

$$H_{K,K'} = \omega_K \delta_{K,K'} - \omega_{\text{rot}}(I) \langle K | \hat{j}_x | K' \rangle \chi(I, K) \delta_{K,K'\pm 1} \quad (2)$$

$\omega_{\text{rot}}(I) = dE_{\text{rot}}(I)/dI$ – angular frequency of rotation of the core; ω_K – the head energies of the rotational bands; $\langle K | \hat{j}_x | K' \rangle$ – matrix element of Coriolis interaction between the states of rotational bands; $\chi(I, K)$ – the coefficients are as follows:

$$\chi(I, 0) = 1, \quad \chi(I, 1) = \left| 1 - \frac{2}{I(I+1)} \right|^{1/2}.$$

The Eigen wave function of the Hamilton operator (1) has the following appearance:

$$|IMK\rangle = \sqrt{\frac{2I+1}{16\pi^2}} \left\{ \sqrt{2} \Psi_{\text{gr}, K}^I D_{M,0}^I(\theta) + \sum_{K'} \frac{\Psi_{K',K}^I}{\sqrt{1+\delta_{K',0}}} \left[D_{M,K'}^I(\theta) b_{K'}^+ + (-1)^{I+K} D_{M,-K'}^I(\theta) b_{-K'}^+ \right] \right\} |0\rangle, \quad (3)$$

here $D_{M,K'}^I(\theta)$ are generalized spherical functions; $|0\rangle$ is the vacuum for the b_K^+ operators (in other words, the ground state of the nucleus in the intrinsic reference system); $\Psi_{K,K'}^I$ are the amplitudes of mixing states of different bands with the same angular momentum I due to the Coriolis interaction.

Eigen energies and wave functions of the rotational states are determined by diagonalization of the Hamiltonian operator (2):

$$H_{K,K'}^\sigma \Psi_{K,n}^I = \varepsilon_n^I \Psi_{K,n}^I \quad (4)$$

The total energies of the states can be found by the following formula:

$$E_K(I) = E_{\text{rot}}(I) + \varepsilon_K(I) \quad (5)$$

There are different methods for determining the energy of the core rotational motion of the nucleus, for example, Harris proposed to determine the following two-parameter formula [15]:

$$\sqrt{I(I+1)} = \mathfrak{I}_0 \omega_{\text{rot}}(I) + \mathfrak{I}_1 \omega_{\text{rot}}^3(I) \quad (6)$$

$$E_{\text{rot}}(I) = \frac{1}{2} \mathfrak{I}_0 \omega_{\text{rot}}^2(I) + \frac{3}{4} \mathfrak{I}_1 \omega_{\text{rot}}^4(I),$$

here \mathfrak{I}_0 and \mathfrak{I}_1 – inertia parameters of the rotational core.

3. CALCULATION AND RESULTS

According to Bohr–Mottelson and Bengtsson–Frauendorf, at small values of the spin of the nucleus, the rotational energy of the nucleus corresponds to the ground rotational states energy [16,17]. Therefore, the inertial parameters of the core were determined by the Harris method using the experimental energy states of ground band up to spin $I \leq 8$.

Table 1: Values of the model parameters used in calculating level energies

\mathfrak{I}_0	\mathfrak{I}_1	ω_{2_1}	ω_{2_2}	$\langle 0_1 \hat{j}_x 1_v^+ \rangle$	$\langle 0_2 \hat{j}_x 1_v^+ \rangle$	$\langle 0_3 \hat{j}_x 1_v^+ \rangle$	$\langle 0_4 \hat{j}_x 1_v^+ \rangle$	$\langle 0_5 \hat{j}_x 1_v^+ \rangle$	$\langle 2_1^+ \hat{j}_x 1_v^+ \rangle$	$\langle 2_2^+ \hat{j}_x 1_v^+ \rangle$
33.3	169.47	1.076	1.739	0.416	0.45	0.25	0.91	0.42	0.40	0.1

NOTE: \mathfrak{I}_0 (\hbar^2/MeV), \mathfrak{I}_1 (\hbar^4/MeV^3) are the inertial parameters of the rotating core (Harris parameters), $\omega_{2_{1,2}}$ (MeV) are energies of the $K^\pi = 2_{1,2}^+$ band heads, and $\langle K | \hat{j}_x | K' \rangle$ (MeV) are the matrix elements of the Coriolis interaction.

Figure 1 shows the values of the moment of inertia obtained by the Harris method, which are compared with the effective values obtained using the following formula

$$\mathfrak{I}_{\text{eff}}(I) = \frac{\sqrt{I(I+1)}}{\omega_{\text{rot}}(I)}, \text{ here } \omega_{\text{rot}}(I) = \frac{E^{\text{rot}}(I+1) - E^{\text{rot}}(I-1)}{2} \quad (7)$$

It can be seen from the comparison that there is a difference between them at high values of angular rotation frequency. I.e. at the large values of the total angular momentum I , deviations from the adiabatic theory are observed in the energies of the ground band. Such nonadiabaticity is more pronounced in the energies of the vibration bands with $K^\pi = 0^+$ and $K^\pi = 2^+$. To determine the causes of nonadiabaticity in the energies of the states of low-lying rotational bands, we use the phenomenological model presented above.

The energy of the rotational motion of the nucleus, for the bands included in the basis of the Hamiltonian operator (1), is considered the same and its values are determined by formula (6). The rotational motion at low frequencies is not related to its internal structure, i.e., the rotation of the nucleus does not affect the Hamiltonian basic model (1). Ground, five beta band ($K^\pi = 0^+$), two gamma $K^\pi = 2^+$ and fifteen $K^\pi = 1_v^+$ rotational bands are introduced in the Hamiltonian model. The Schrödinger equation of size (23X23) was solved.

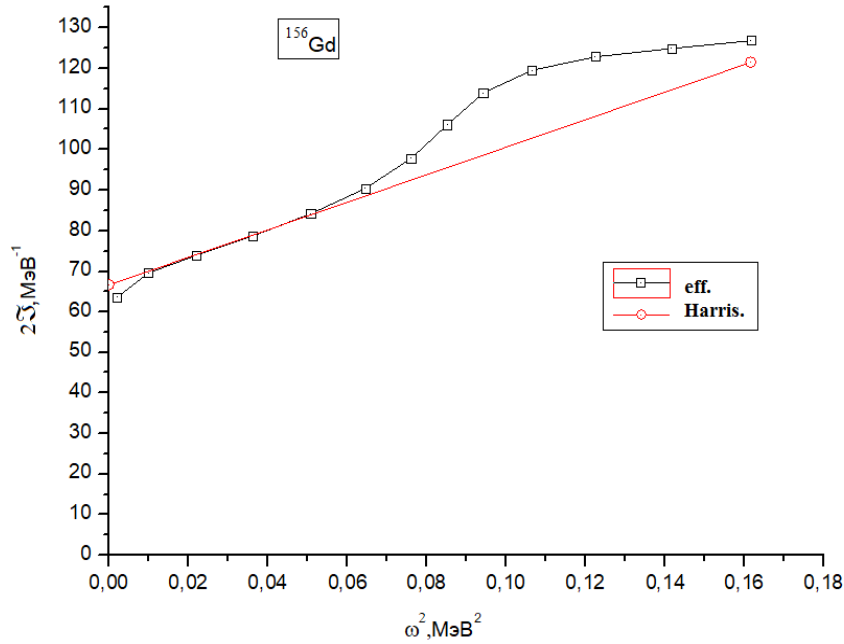


Fig. 1: Comparison of the values of the moments of inertia determined by the effective and Harris method.

The parameters of the model are determined in the following sequence:

1. For the head energies ω_K of the ground ($K^\pi = 0_1^+$) and $K^\pi = 0_n^+$ bands are using the experimental values $E_{K_n}^{\text{exp.}}(I=0)$ because the head energies of these bands $I=0$ (in this case $\omega_{\text{rot}}(0) = 0$) and these states are not mixed by the Coriolis forces;
2. The head energies ω_{1_v} of the $K^\pi = 1_v^+$ bands found using their experimental values $\omega_{1_v} = E_{1_v}^{\text{exp.}}(I=1) - E_{\text{rot}}(I=1)$;
3. The head energies $\omega_{2_1}, \omega_{2_2}$ of the $K^\pi = 2^+$ bands and $\langle 2_{1,2} | \hat{j}_x | 1_v^+ \rangle$ are free parameters, their values were obtained by the least squares method, from the condition of better agreement of the theoretical energy of states with odd spins $K^\pi = 2_1^+$ and $K^\pi = 2_2^+$ rotational bands with the experimental data;
4. The parameters $\langle 0_n | \hat{j}_x | 1_v^+ \rangle$ describing the Coriolis interaction of the states of the $K^\pi = 0_n$, and $K^\pi = 1_v^+$ bands are determined from the good agreement of the calculated theoretical energies of the states with even spins of the ground (0_1), $K^\pi = 0_2^+, 0_3^+, 0_4^+, 0_5^+$ and $K^\pi = 2_{1,2}^+$ of bands with experimental values.

The selected numerical values of the model parameters are given in Table 1. Figure 2 shows the calculated energy values in the framework of the model which are compared with experimental results.

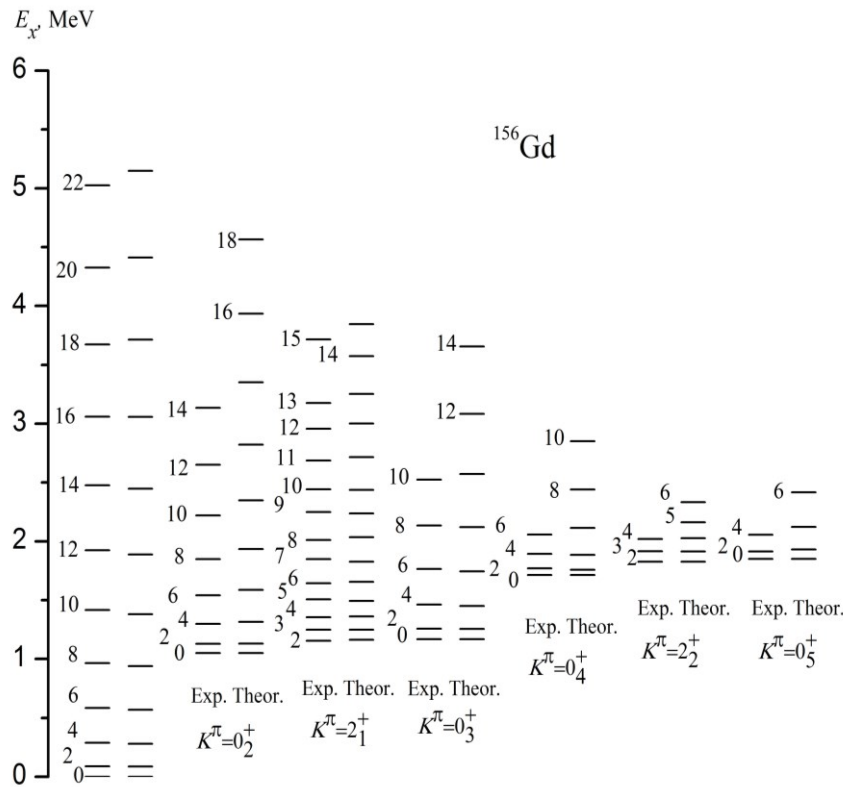


Fig. 2: Comparison of theoretical and experimental energy values.

The results of the comparison show that at small values of spin, the compatibility between them is good, and the difference increases with increasing spin. This difference suggests that additional effects must be taken into account when studying the properties of high-spin states. For example, it may be necessary to take into account the effect of the rotational motion of the nucleus on the intrinsic energy when the rotation of the nucleus is high.

The wave functions of the states $K^\pi = 0_2^+$, $K^\pi = 0_3^+$, $K^\pi = 0_4^+$ and $K^\pi = 2_1^+$ bands obtained by solving the Schrödinger equation (2) are present in tables 2, 3, 4 and 5 respectively. The Hamiltonian basis includes 15 bands with $K^\pi = 1_\nu^+$, but the table shows one component of $K^\pi = 1_1^+$. The components $\psi_{1_\nu K}^I$ of the other $K^\pi = 1_\nu^+$ bands are determined using the following formula

$$\psi_{1_\nu K}^I = \psi_{1_1 K}^I \frac{\omega_{1_1} - \omega_K}{\omega_{1_\nu} - \omega_K} \quad (8)$$

In Table 2, it can be seen that in the band with $K^\pi = 0_2^+$, the other components $\psi_{K0_2}^I$ of the mixed bands increase with increasing spin I . This picture can be observed in other rotation bands. This result, which is due to Coriolis interaction, is the main cause of the nonadiabatics manifested in the energy and electromagnetic characteristics of the excited states.

Table 2: The amplitude of the mixing of the base states $\Psi_{K0_2^+}^I$ for $K^\pi = 0_2^+$ band

		K						
I	gr	0₂⁺	0₃⁺	0₄⁺	0₅⁺	1₁⁺	2₁⁺	2₂⁺
2	-0.0052	0.9927	0.0261	0.0176	0.0068	0.0279	0.0927	0.0011
4	-0.0183	0.9516	0.0808	0.0599	0.0231	0.0555	0.2534	0.0043
6	-0.0385	0.8926	0.1404	0.1186	0.0460	0.0829	0.3496	0.0087
8	-0.0638	0.8353	0.1872	0.1815	0.0708	0.1068	0.3890	0.0135
10	-0.0922	0.7835	0.2177	0.2395	0.0942	0.1260	0.3988	0.0179
12	-0.1222	0.7378	0.2352	0.2884	0.1143	0.1404	0.3951	0.0216
14	-0.1529	0.6983	0.2440	0.3274	0.1306	0.1506	0.3859	0.0246
16	-0.1836	0.6645	0.2476	0.3577	0.1436	0.1576	0.3750	0.0270
18	-0.2141	0.6355	0.2482	0.3808	0.1537	0.1621	0.3639	0.0288
20	-0.2444	0.6106	0.2469	0.3984	0.1615	0.1649	0.3533	0.0302

Table 3: The amplitude of the mixing of the base states $\Psi_{K0_3^+}^I$ for $K^\pi = 0_3^+$ band

		K						
I	gr	0₂⁺	0₃⁺	0₄⁺	0₅⁺	1₁⁺	2₁⁺	2₂⁺
2	-0.0025	-0.0275	0.9986	0.0118	0.0044	0.0161	-0.0183	0.0007
4	-0.0072	-0.0794	0.9923	0.0330	0.0122	0.0260	-0.0618	0.0023
6	-0.0120	-0.1374	0.9795	0.0549	0.0204	0.0319	-0.1110	0.0040
8	-0.0162	-0.1895	0.9625	0.0732	0.0272	0.0347	-0.1562	0.0054
10	-0.0194	-0.2321	0.9446	0.0872	0.0324	0.0356	-0.1938	0.0064
12	-0.0218	-0.2655	0.9278	0.0974	0.0362	0.0356	-0.2238	0.0072
14	-0.0236	-0.2916	0.9129	0.1050	0.0391	0.0350	-0.2476	0.0078
16	-0.0250	-0.3121	0.9001	0.1107	0.0412	0.0342	-0.2666	0.0082
18	-0.0260	-0.3285	0.8890	0.1151	0.0429	0.0333	-0.2819	0.0086
20	-0.0269	-0.3419	0.8795	0.1186	0.0442	0.0324	-0.2944	0.0088

Table 4: The amplitude of the mixing of the base states $\Psi_{K0_4^+}^I$ for $K^\pi = 0_4^+$ band

		K						
I	gr	0₂⁺	0₃⁺	0₄⁺	0₅⁺	1₁⁺	2₁⁺	2₂⁺
2	-0.0119	-0.0347	-0.0239	0.9486	0.1105	0.1673	-0.0186	0.0396
4	-0.0302	-0.0952	-0.0675	0.8892	0.1910	0.2087	-0.0596	0.0546
6	-0.0471	-0.1625	-0.1199	0.8468	0.2258	0.2115	-0.1055	0.0569
8	-0.0604	-0.2265	-0.1744	0.8123	0.2393	0.2019	-0.1497	0.0566
10	-0.0698	-0.2812	-0.2257	0.7809	0.2427	0.1886	-0.1881	0.0554
12	-0.0760	-0.3249	-0.2708	0.7521	0.2414	0.1748	-0.2192	0.0539
14	-0.0798	-0.3584	-0.3090	0.7262	0.2379	0.1620	-0.2436	0.0524
16	-0.0822	-0.3838	-0.3408	0.7035	0.2337	0.1507	-0.2623	0.0510
18	-0.0836	-0.4030	-0.3671	0.6839	0.2294	0.1409	-0.2767	0.0497
20	-0.0844	-0.4177	-0.3890	0.6670	0.2254	0.1324	-0.2879	0.0486

Table 5: The amplitude of the mixing of the base states $\Psi_{K2_1^+}^I$ for $K^\pi = 2_1^+$ band

I	gr	K						
		0_2^+	0_3^+	0_4^+	0_5^+	1_1^+	2_1^+	2_2^+
2	0.0021	0.0954	-0.0144	-0.0076	-0.0029	-0.0116	-0.9949	-0.0005
3	-	-	-	-	-	-0.0209	-0.9987	-0.0013
4	0.0052	0.2667	-0.0352	-0.0191	-0.0073	-0.0168	-0.9620	-0.0014
5	-	-	-	-	-	-0.0328	-0.9967	-0.0032
6	0.0070	0.3819	-0.0460	-0.0253	-0.0096	-0.0164	-0.9217	-0.0019
7	-	-	-	-	-	-0.0424	-0.9945	-0.0053
8	0.0078	0.4465	-0.0510	-0.0283	-0.0108	-0.0149	-0.8920	-0.0021
9	-	-	-	-	-	-0.0504	-0.9921	-0.0076
10	0.0082	0.4841	-0.0536	-0.0298	-0.0114	-0.0136	-0.8721	-0.0022
11	-	-	-	-	-	-0.0572	-0.9898	-0.0097
12	0.0085	0.5078	-0.0551	-0.0307	-0.0117	-0.0124	-0.8585	-0.0023
13	-	-	-	-	-	-0.0630	-0.9875	-0.0119
14	0.0087	0.5237	-0.0560	-0.0313	-0.0119	-0.0115	-0.8489	-0.0023
15	-	-	-	-	-	-0.0682	-0.9854	-0.0139
16	0.0088	0.5350	-0.0566	-0.0317	-0.0121	-0.0108	-0.8418	-0.0024
17	-	-	-	-	-	-0.0727	-0.9833	-0.0158
18	0.0089	0.5435	-0.0571	-0.0320	-0.0122	-0.0102	-0.8363	-0.0024
19	-	-	-	-	-	-0.0768	-0.9812	-0.0177
20	0.0089	0.5500	-0.0574	-0.0322	-0.0123	-0.0097	-0.8321	-0.0024
2	0.0021	0.0954	-0.0144	-0.0076	-0.0029	-0.0116	-0.9949	-0.0005

4. CONCLUSION

Theoretical calculations were carried out for ^{156}Gd nucleus in the framework of the phenomenological model taking into account Coriolis mixing of low-lying rotation bands with positive parity.

Nonadiabaticities observed in the energies is explained by the Coriolis mixing of low excited rotational states. To describe all the adiabatic rotational bands, the same moments of inertia have been used. The energy spectra of the positive parity states have been calculated. The results of calculation of energy spectra for ground ($K^\pi = 0_1^+$), $K^\pi = 0_2^+$, $K^\pi = 0_3^+$, $K^\pi = 0_4^+$, $K^\pi = 0_5^+$, $K^\pi = 2_1^+$, and $K^\pi = 2_2^+$ band states is compared with the existing experimental data correspondingly and their compatibility is given. The mixing effects of the lower bands have been shown to be significant even at small spins.

In the high spin states of ground band, the difference between the theory and experiment was observed. This may be due to the fact that for large values of the angular frequency of rotation of the nucleus, it is necessary to take into account the effects of rotation on intrinsic energy.

The wave function of states of the rotational bands is calculated. The regularities of the change in the state components of the mixing bands are studied depending on the total angular momentum.

ACKNOWLEDGEMENT

This work has been financial supported by the Committee for the Coordination of the Development of the Science and Technology under the Cabinet of Ministers of the Republic of Uzbekistan, Fundamental Grant “OT-F2-75” (2017-2021).

REFERENCES

- [1] Reich CW. (2012) Nuclear Data Sheets for A=156. 113: 2537-2840.
- [2] Backlin A, Hedin G, Folgelberg B, et al. (1982) Levels in ^{156}Gd studied in the (n, γ) reaction. Nucl. Phys. A, 380: 189-260.
- [3] Berzin YY, Guseva TV, Tamberg YY. (1983) Investigation of ^{156}Gd in the reaction (n, γ) Izv. Akad. Nauk Lat. SSR, Ser. Fiz. Tekh. Nauk. 1: 9-12.
- [4] Bohle D, Richter A, Steffan W, et al. (1984) New magnetic dipole excitation mode studied in the heavy deformed nucleus ^{156}Gd by inelastic electron scattering. Phys. Lett. B 137: 27-31.
- [5] Pitz HH, Berg UEP, Heil RD, Knaissl U, Stock R. et al. (1989) Systematic study of low-lying dipole excitations in $^{156,158,160}\text{Gd}$ by photon scattering. Nucl. Phys. A, 492: 411-425.
- [6] Demidov A. M, Govor L. I, Kurkin V. A, Mikhailov I. V. (2009) Deexcitation of $K^\pi = 0_2^+, 0_3^+$, and 2_1^+ levels by $M1$ transitions in nonspherical even-even nuclei. Phys. At. Nucl. 72(2): 201-208.
- [7] Demidov AM, Govor LI, Kurkin VA, Mikhailov IV. (2009) Confrontation of Nucleus Deformation and Multipole Mixture Parameters in $(2^+0_n - 2^+0_1)$ Transitions with Rotational Band Structure for $K^\pi = 0_2^+$ and $K^\pi = 0_3^+$. Phys. At. Nucl., 72(2): 209-213.
- [8] Aprahamian A, Leshner SR, Stratman A. (2017) First Excited 0^+ States in Deformed Nuclei. Bulg. J. Phys. 44: 372--379.
- [9] Aprahamian A, de Haan RC, Leshner SR, et al. (2018) Lifetime measurements in ^{156}Gd . Phys. Rev. C., 98:034303.
- [10] Usmanov P. N, Mikhailov I. N. (1997) Effects of nonadiabaticity of collective motion in even-even deformed nuclei. Phys. Part. Nucl. 28(4): 348-373.
- [11] Usmanov PN, Okhunov AA, Salikhbaev US, Vdovin AI. (2010) Analysis of Electromagnetic Transitions in Nuclei $^{176,178}\text{Hf}$. Phys. Part. Nucl. Letters. 7(3):185–191.
- [12] Usmanov PN, Adam I, Salikhbaev US, Solnyshkin AA. (2010) Theoretical Analysis of Experimental Data on ^{160}Dy That were Obtained in Studying Beta Decay. Phys. At. Nucl. 73(12): 1990-1996.
- [13] Usmanov PN, Vdovin AI, Solnyshkin AA, Salikhbaev US. (2014) Properties of Octupole - Vibrational Bands in the ^{160}Dy Nucleus. Phys. At. Nucl. 77(11): 1343-1349.
- [14] Usmanov PN, Vdovin AI, Yusupov EK, Salikhbaev US. (2019) Phenomenological Analysis of Characteristics of Rotational Bands in $^{158,160}\text{Gd}$ Isotopes. Phys. Part. Nucl. Letters. 19(6): 706-712.
- [15] Harris SM. (1965) Higher Order Corrections to the Cranking Model Phys. Rev. B 138(3): 509-513.
- [16] Bohr A, Mottelson B. (1977) Nuclear Structure, Vol. 1,2. New York: Benjamin
- [17] Bengtsson R, Frauendorf S. (1979) An interpretation of backbending in terms of the crossing of the ground state band with an aligned two-quasiparticle spectra band. Nucl. Phys., A 314: 27-36.

MODEL DEVELOPMENT OF RIDE SPLITTING SERVICE WITH RESOURCE SHARING SCHEME ON RIDE SOURCING (ONLINE TAXI) SERVICES IN JAKARTA

HELEN BURHAN^{1*}, SUTANTO SOEHODHO², NAHRY¹

¹Department of Mathematics, Universitas Indonesia, Depok, Indonesia

²Department of Civil Engineering, Universitas Indonesia, Depok, Indonesia

*Corresponding author: helen.burhan@sci.ui.ac.id

(Received: 21st June 2020; Accepted: 24th October 2020; Published on-line: 4th January 2021)

ABSTRACT: This study aims to solve the increasing number of vehicles for ride-sourcing or online taxi service on the road and the operational issues in those services by developing an optimization model of ride-splitting services in the online taxi with a resource sharing (sharing platform) scheme. Ride-splitting service is a ride-sourcing service where one vehicle can serve two or more request customers at a similar time. Meanwhile, the resource-sharing scheme interlinks drivers from different platforms in providing services to the customers. That is, a driver from platform X can serve customers from platform Y and vice versa, with a predetermined profit sharing. We formulate the optimization problem as a new modified weighted bipartite matching and solve the problem using a greedy heuristic method. Based on the simulation, the proposed model can generate higher overall profit for all vehicles serving passengers, use fewer vehicles, and lower passengers' waiting time.

ABSTRAK: Kajian ini bertujuan menyelesaikan jumlah penambahan kendaraan angkutan-berpusat atau servis taksi dalam talian di atas jalan raya dan isu operasi dalam perkhidmatan dengan membangunkan model pengoptimuman pada servis angkutan-pecahan bagi taksi dalam talian dengan skim perkongsian sumber (platform bersama). Servis angkutan-pecahan adalah servis angkutan-berpusat di mana satu kenderaan menyediakan perkhidmatan kepada dua atau lebih permintaan pengguna pada satu-satu masa. Manakala, perkongsian sumber menghubungkan pemandu dengan platform berlainan dalam menyediakan servis untuk penumpang. Iaitu, pemandu platform X boleh mengangkut penumpang platform Y dan sebaliknya, dengan menentukan terlebih dahulu keuntungan bersama. Kajian ini diformulasi dengan pengoptimuman masalah sebagai perubahan terbaru dalam menilai kesesuaian kedua-dua pihak dan menyelesaikan masalah menggunakan kaedah heuristik rakus. Berdasarkan simulasi ini, model yang dicadangkan dapat menghasilkan keuntungan keseluruhan lebih tinggi bagi semua kenderaan perkhidmatan, dengan mengurangkan jumlah kenderaan dan masa menunggu penumpang.

KEYWORDS: *Ride Sourcing (Online Taxi) Services, Ride Splitting Service, Resource Sharing Scheme, Modified Weighted Bipartite Matching, Greedy Heuristic Method.*

1. INTRODUCTION

In line with the increasing usage of ride-sourcing service, which is more commonly known as online taxi, new problems stemming from the increasing usage of the service are also arising. One of those problems is the increased number of private vehicles on the road. This is due to the attractive idea of online taxi as a new business potential, so that idle private vehicles are now utilized as the online taxi fleet, some business owners even buy new cars purposely to be

rented for online taxi services [1]. The increased usage of private vehicles for the online taxi services is not in accordance with the initial purpose of ride-sourcing service, which was initially a ride-sharing concept that was designed to minimize the usage of private vehicles in order to reduce traffic [2, 3]. On the other hand, one of the many services offered by the online taxi provider is ride-splitting, a service that is unfortunately still underused. Ride-splitting service is a ride-sourcing service that is in line with the actual concept of ride sharing, where one vehicle (single driver) can serve two or more riders (multi-riders) at a similar time [4].

Currently, there are two big companies providing online taxi services in Jakarta whose operational services are not yet optimized. This can be concluded from the long waiting time for customers to be picked up, which is sometimes a lot longer than the estimate time shown on the app; and also from the surge pricing system, where the fare will be higher than the standard fare when the demand for services is high and the vehicle availability is low, the surge pricing system is deemed as non-transparent so that it can disadvantage consumers [5]. In the previous research, Burhan et.al [6] developed an optimized model of pure ride-sourcing service (single driver - single rider) with a resource sharing scheme to tackle the operational problems. Therefore, this study aims to solve the increasing number of vehicles for online taxi on the road and the operational issues in online taxi services, by developing an optimization model of ride-splitting services in online taxi with a resource sharing (sharing platform) scheme.

To optimize the ride-splitting service with resource sharing scheme, an optimized route is sought to pick up and drop off two or more customer requests (in this research is limited to only two requests) from the nearby or adjacent area at the similar travel time. The resource sharing scheme here is the same one as defined by Burhan et.al [6], which is interlinking drivers from different operators (platforms) in providing services to the customers, where a driver from platform X can serve customers from platform Y and vice versa, with a predetermined profit sharing. The mathematical model in optimizing issues in this study will be using a new modified weighted bipartite matching problem, while the solving method will be using greedy heuristic method.

The rest of the paper is organized as follows. Section 2 presents a literature review, while section 3 describes the problem formulation, and section 4 describes the solution method, section 5 present the computational experiment, and finally, section 6 concludes and illustrates future research directions.

2. LITERATURE REVIEW

Ride-sourcing service, which is more commonly known as online taxi, is a public transportation service using private owned vehicles as fleet to serve customers as taxi service using technology of smartphones, GPS and GIS [2,3]. Based on the type of service offered, the service can be grouped into two types [4], pure ride-sourcing (single driver, single rider) and ride splitting (single driver, multi riders). In pure ride sourcing, a driver of personal vehicle is connected to one request customer, and in the ride-splitting service, a driver is connected to two or more request customers in which customers can choose to split (share) a ride and fare. Based on that classification, ride- splitting is the appropriate form of ride-sourcing based on the ride-sharing concept for single driver - multi rider, so that the problem of optimizing the ride-splitting service is the optimization problem in finding the vehicle route to pick up and drop off passengers [7].

The optimization problem in finding the vehicle route to pick up and and drop off passengers on ride-splitting service is similar to dynamic pick up and delivery problem with time windows [8]. Generally, the pick up and delivery problems with time windows is one

variant of vehicle routing problem which aims to find the optimal vehicle route to deliver and pick up a number of customers in an interval of time (time windows), taking into account a number of constraints such as vehicle capacity and some other precedent constraints, with minimum costs [9]. The dynamic term here refers to the requests which gradually revealed throughout the day, so that vehicle routes are constructed in real-time [10].

Several previous studies that discussed the problem of optimizing ride-sharing services for the case of a single driver-multi rider, some of which are, Hosni et al. [11] use mixed integer programming to model the problem of maximize profit for shared taxi problem and present a Lagrangian decomposition approach as well as two heuristics to solve the problem, Wang et.al [12] use binary integer programming to model the problem of minimize cost and travel time for a pickup and delivery problem with the use of HOV lanes and use Tabu search heuristic to solve the problem, Santos and Xavier [13] use mixed integer programming to model the problem of maximize the number of served requests and minimize the cost for the ride-sharing problem and solved the problem by a greedy randomized adaptive search procedure, Mahmoudi and Zhou [14] propose a new time discretized multi-commodity network flow model for ride-sharing problem within state space-time network to minimize cost and using a forward dynamic programming solution algorithm and Lagrangian approach to solve the problem. While Bei and Zhang [15] use a three-dimensional matching problem to minimize cost for the ride-sharing problem and use a two-phase greedy approach to solve the problem. To the best of our knowledge, the previous studies have never been including maximizing profit and minimizing waiting time in the objective function simultaneously and explicitly. Therefore, in this study, we will use a new modified weighted bipartite graph problem to formulate the optimization problem of ride splitting service to maximize the driver's profit while minimizing passenger's waiting time.

In the meantime, researches relating to the operational problems in ride-sourcing services are discussing more of the surge pricing problems; because surge pricing is considered as lack transparency and is harmful to the consumer [16-18]. However, since the price for ride service cannot be unlimited, there is usually a reasonable or legitimate range of prices in practice. Such a constrained surge pricing strategy fails to balance demand and supply in certain cases, e.g., even adopting the maximum allowed price cannot reduce the demand to an affordable level during peak hours [19]. Therefore, this study is developing a resource sharing scheme based on research conducted by Burhan, H, et.al [6] to solve the surge pricing problems in ride-sourcing services.

3. PROBLEM FORMULATION

In ride-splitting service with resource sharing scheme, customer from platform X can be served by vehicle from platform Y, and the other way around, with a profit sharing between platforms that is predetermined beforehand. With the predetermined scheme, characteristics of the ride-splitting service with the resource sharing scheme in this paper, are as follows:

- Customer will get less waiting time
- Driver will get more profit due to less operational cost by picking up customer from the different platform, whose pick-up location is closer to the driver's position, rather than picking up customer from the same platform but whose pick-up location is quite far from the driver's position.
- Matching rate between driver and passenger/customer is also increasing, because the probability is bigger for the customer whose pick-up time and location is similar to the driver, as opposed to when compared to the possibility from only the same platform.

Assume, there are two different operators (platforms) providing ride-splitting services, where it can be enlarged to n platforms and a homogenous fleet of vehicles with the same capacities. The request from a customer in this study arrives dynamically, thus the customer's requests and available vehicles will be grouped first, based on a period of time, and then the optimization process to assign vehicle and passengers is done statically per period. The period length is based on an acceptable time limit of a customer to wait for a decision to be picked up and time for the optimization process. The first period starts at the time, at which the first request from a customer arrived.

In the optimization process, initially, we must pair potential vehicles which feasible to serve a request customer by generating the first weighted bipartite graph. Then, we will get a set of feasible vehicle and the first customer pairs. In this study, the ride splitting service is limited to serving only two request customers in one trip. Thus, next stage is to generate a second weighted bipartite graph to pair a vehicle and the first customer with a potential second request customer. The objective of the optimization problem is to maximize the total profit earned by drivers (vehicles) while minimizing the total passenger's waiting time. Then, we model the problem using a new modified weighted bipartite matching. The final stage, use a greedy heuristic method to solve the problem.

Next, we present the process of generating first weighted bipartite graph as the first stage for the optimization process.

3.1. First Weighted Bipartite Graph

Let k and r be the number indexes for platform which requested by customer, where $k, r = 1, 2$ and τ be the period for optimization process. Let P_{kl}^τ be the l -th passenger of platform k in period τ and V_{rs}^τ be the s -th available vehicle of platform r in period τ . Then:

- P_k^τ be a set of customers who request vehicle from platform k in period τ , where: $P_k^\tau = \{P_{kl}^\tau | \text{the } l\text{-th passenger of platform } k \text{ in period } \tau; l = 1, 2, \dots, n_k\}$, for $k = 1, 2$ and P^τ be the set of customers who request vehicle in period τ .
- V_r^τ be a set of available vehicles from platform r in period τ , where: $V_r^\tau = \{V_{rs}^\tau | \text{the } s\text{-th vehicle of platform } r \text{ in period } \tau; s = 1, 2, \dots, m_r\}$, for $r = 1, 2$ and V^τ be the set of available vehicles in period τ .

Note that P^{τ_i} consists of all new customer requests in period τ_i and all assigned passengers in the previous period τ_{i-1} , but still not get a passenger pair to share a ride, for $i = 2, 3, \dots$. Likewise, V^{τ_i} consists of all newly available vehicles in period τ_i and all available vehicles which still eligible to serve a customer from the previous period τ_{i-1} , for $i = 2, 3, \dots$

Each passenger P_{kl}^τ is associated with time at which customer request a vehicle $t_{request_P_{kl}^\tau}$, origin or pick up location $o_{P_{kl}^\tau}$, destination or drop off location $d_{P_{kl}^\tau}$, an earliest departure time $e_{dept_P_{kl}^\tau}$, a latest departure time $l_{dept_P_{kl}^\tau}$, and the number of passenger $q_{P_{kl}^\tau}$. Also, passenger P_{kl}^τ must arrive at destination at least on $e_{arr_P_{kl}^\tau}$, and not after $l_{arr_P_{kl}^\tau}$, and cannot ride a vehicle more than $t_{maxride_P_{kl}^\tau}$. While, each available vehicle V_{rs}^τ is associated with origin or current location $i_{V_{rs}^\tau}$, time to leave from or arrive at location on $time_{i_{V_{rs}^\tau}}^{V_{rs}^\tau}$, maximum capacity $Q_{V_{rs}^\tau}$, and vehicle's occupation $V_{rs}^\tau\text{-occ}$.

Let $G_1^\tau = (N_1^\tau, E_1^\tau)$ be the first weighted bipartite graph for optimization process, where N_1^τ be the set of nodes of G_1^τ and E_1^τ be the set of edges of G_1^τ .

Defined $N_1^\tau = V^\tau \cup P^\tau$ be a bipartite node set of all request customers and available vehicles in period τ . For each passenger P_{kl}^τ in P^τ , the distance $D_{i_{V_{rs}^\tau} o_{P_{kl}^\tau}}$ and the travel time $TT_{i_{V_{rs}^\tau} o_{P_{kl}^\tau}}$ be

a distance and a travel time of shortest path from origin $o_{P_{kl}^\tau}$ to destination $d_{P_{kl}^\tau}$. For each vehicle V_{rs}^τ in V^τ , the distance $D_{i_{V_{rs}^\tau} o_{P_{kl}^\tau}}$ and the travel time $TT_{i_{V_{rs}^\tau} o_{P_{kl}^\tau}}$ be a distance and a travel time of shortest path from vehicle's origin (current) location $i_{V_{rs}^\tau}$ to passenger's origin $o_{P_{kl}^\tau}$.

For each passenger P_{kl}^τ , earliest and latest departure time, earliest and latest arrival time, and maximum ride time are determined with the following formula:

$$e_{dept_{P_{kl}^\tau}} := t_{request_{P_{kl}^\tau}} + \lambda_{early} \quad (1)$$

$$l_{dept_{P_{kl}^\tau}} := e_{dept_{P_{kl}^\tau}} + \lambda_{late} \quad (2)$$

$$e_{arr_{P_{kl}^\tau}} := time_{i_{V_{rs}^\tau}^{V_{rs}^\tau}} + \left((1 + \varepsilon) TT_{i_{V_{rs}^\tau} o_{P_{kl}^\tau}} \right) + t_{service_{-P_{kl}^\tau}}^{V_{rs}^\tau} + TT_{od_{P_{kl}^\tau}} \quad (3)$$

$$l_{arr_{P_{kl}^\tau}} := e_{arr_{P_{kl}^\tau}} + \lambda_{late} \quad (4)$$

$$t_{maxride_{P_{kl}^\tau}} := \left((1 + \mu) TT_{od_{P_{kl}^\tau}} \right) \quad (5)$$

where λ_{early} be a level of service for early departure time; λ_{late} be a level of service for early departure or arrival time; $t_{service_{-P_{kl}^\tau}}^{V_{rs}^\tau}$ be time for passenger to get into (get off from) a vehicle; $(1 + \varepsilon)$ and $(1 + \mu)$ be multiplier factor for tolerance time deviation, with $0 < \varepsilon, \mu < 1$.

Vehicle V_{rs}^τ is feasible to serve a passenger P_{kl}^τ , if the following criteria are met.

1) Time Constraints:

a) Vehicle must arrive at passenger's origin on departure time windows:

$$e_{dept_{P_{kl}^\tau}} \leq time_{i_{V_{rs}^\tau}^{V_{rs}^\tau}} + \left((1 + \varepsilon) TT_{i_{V_{rs}^\tau} o_{P_{kl}^\tau}} \right) \leq l_{dept_{P_{kl}^\tau}} \quad (6)$$

b) Vehicle must arrive at passenger's destination on arrival time windows:

$$e_{arr_{P_{kl}^\tau}} \leq time_{i_{V_{rs}^\tau}^{V_{rs}^\tau}} + \left((1 + \varepsilon) TT_{i_{V_{rs}^\tau} o_{P_{kl}^\tau}} \right) + t_{service_{-P_{kl}^\tau}}^{V_{rs}^\tau} + TT_{od_{P_{kl}^\tau}} \leq l_{arr_{P_{kl}^\tau}} \quad (7)$$

2) Capacity Constraint:

The number of passengers in each request must be less than or equal to available vehicle's capacity:

$$q_{P_{kl}^\tau} \leq Q_{V_{rs}^\tau} \quad (8)$$

Let P_{kl}^τ in P^τ and V_{rs}^τ in V^τ . Defined an edge in E_1^τ be a pair of $(V_{rs}^\tau, P_{kl}^\tau)$, where vehicle V_{rs}^τ is met the feasible criterion in (6) – (8) to serve passenger P_{kl}^τ . Then, $E_1^\tau = \{(V_{rs}^\tau, P_{kl}^\tau) | P_{kl}^\tau \text{ and } V_{rs}^\tau \text{ are feasible match; } V_{rs}^\tau \in V^\tau, P_{kl}^\tau \in P^\tau\}$. The weight of each edge $(V_{rs}^\tau, P_{kl}^\tau)$ in E_1^τ is defined as the fare that has to be paid by passenger P_{kl}^τ served by vehicle V_{rs}^τ , where the fare is calculated by using the following formula:

$$F^{P_{kl}^\tau} = Tariff_k \times D_{od_{P_{kl}^\tau}} \quad (9)$$

where $Tariff_k$ is tariff of platform k for ride splitting service per 1 distance unit.

Next, mathematical model for the optimization problem of ride splitting service with resource sharing scheme will be presented. Before that, we generate a second weighted bipartite graph.

3.2. New Modified Weighted Bipartite Matching Problem

Let $G_2^\tau = (N_2^\tau, E_2^\tau)$ be the second weighted bipartite graph for optimization process, where N_2^τ be the set of nodes of G_2^τ and E_2^τ be the set of edges of G_2^τ .

Let $N_2^\tau = V^\tau P^\tau \cup DV^\tau P^\tau$, be a bipartite set of nodes of graph G_2^τ . For $V_{rs}^\tau \in V^\tau$ and $P_{kl}^\tau \in P^\tau$, defined $V_{rs}^\tau P_{kl}^\tau$ be a node in $V^\tau P^\tau$ if only if $(V_{rs}^\tau, P_{kl}^\tau)$ is an edge in E_1^τ . Thus, $V^\tau P^\tau = \{V_{rs}^\tau P_{kl}^\tau | (V_{rs}^\tau, P_{kl}^\tau) \text{ is an edge in } E_1^\tau; V_{rs}^\tau \in V^\tau, P_{kl}^\tau \in P^\tau\}$ and $DV^\tau P^\tau$ is a duplication set of $V^\tau P^\tau$ where $DV^\tau P^\tau = \{V_{r's'}^\tau P_{k'l'}^\tau | \text{if } V_{rs}^\tau P_{kl}^\tau \in V^\tau P^\tau\}$.

Let $V_{rs}^\tau P_{kl}^\tau$ be a node in $V^\tau P^\tau$ and $V_{r's'}^\tau P_{k'l'}^\tau$ be a node in $DV^\tau P^\tau$, defined, an edge in E_2^τ be a pair of $(V_{rs}^\tau P_{kl}^\tau, V_{r's'}^\tau P_{k'l'}^\tau)$, where $r = r', s = s'$ and V_{rs}^τ is feasible to serve customers P_{kl}^τ and $P_{k'l'}^\tau$. Note that, in the edge $(V_{rs}^\tau P_{kl}^\tau, V_{r's'}^\tau P_{k'l'}^\tau)$, V_{rs}^τ and $V_{r's'}^\tau$ have to be the same vehicles. Thus, $E_2^\tau = \{(V_{rs}^\tau P_{kl}^\tau, V_{r's'}^\tau P_{k'l'}^\tau) | r = r', s = s' \text{ and } V_{rs}^\tau \text{ is feasible match with } P_{kl}^\tau \text{ and } P_{k'l'}^\tau\}$;

$V_{rs}^\tau P_{kl}^\tau \in V^\tau P^\tau, V_{r's'}^\tau P_{k'l'}^\tau \in DV^\tau P^\tau\}$.

Route of vehicle V_{rs}^τ to pick up and drop off customers P_{kl}^τ and $P_{k'l'}^\tau$, $Route_{V_{rs}^\tau - P_{kl}^\tau - P_{k'l'}^\tau}$ is defined as the shortest path from vehicle's current location $i_{V_{rs}^\tau}$ to the first passenger's origin $o_{P_{kl}^\tau}$, then to the second passenger's origin $o_{P_{k'l'}^\tau}$ and next to passenger's destination $d_{P_{kl}^\tau}$ or $d_{P_{k'l'}^\tau}$ for which one is the closest. Then, $Route_{V_{rs}^\tau - P_{kl}^\tau - P_{k'l'}^\tau}$ is the shortest path between route $i_{V_{rs}^\tau} - o_{P_{kl}^\tau} - o_{P_{k'l'}^\tau} - d_{P_{kl}^\tau} - d_{P_{k'l'}^\tau}$ and route $i_{V_{rs}^\tau} - o_{P_{kl}^\tau} - o_{P_{k'l'}^\tau} - d_{P_{k'l'}^\tau} - d_{P_{kl}^\tau}$. $Distance_{V_{rs}^\tau - P_{kl}^\tau - P_{k'l'}^\tau}$ and $TT_{V_{rs}^\tau - P_{kl}^\tau - P_{k'l'}^\tau}$ are defined as the distance and the travel time of $Route_{V_{rs}^\tau - P_{kl}^\tau - P_{k'l'}^\tau}$.

Vehicle V_{rs}^τ is feasible to serve customers P_{kl}^τ and $P_{k'l'}^\tau$, if the following criteria are met:

1) Time feasibility:

a) Vehicle must arrive at passenger's origin on passenger's departure time windows:

- For first passenger, P_{kl}^τ :

$$e_{deprt_{P_{kl}^\tau}} \leq WT_{V_{rs}^\tau}^{P_{kl}^\tau} \leq l_{deprt_{P_{kl}^\tau}} \quad (10)$$

where $WT_{V_{rs}^\tau}^{P_{kl}^\tau}$ is passenger P_{kl}^τ 's waiting time to be picked up by vehicle V_{rs}^τ ,

$$\text{with } WT_{V_{rs}^\tau}^{P_{kl}^\tau} = time_{i_{V_{rs}^\tau}}^{V_{rs}^\tau} + ((1 + \epsilon) TT_{i_{V_{rs}^\tau} o_{P_{kl}^\tau}}) \quad (11)$$

- For second passenger, $P_{k'l'}^\tau$:

$$e_{deprt_{P_{k'l'}^\tau}} \leq WT_{V_{rs}^\tau}^{P_{k'l'}^\tau} \leq l_{deprt_{P_{k'l'}^\tau}} \quad (12)$$

where $WT_{V_{rs}^\tau}^{P_{k'l'}^\tau}$ is passenger $P_{k'l'}^\tau$'s waiting time to be picked up by vehicle V_{rs}^τ ,

$$\text{with } WT_{V_{rs}^\tau}^{P_{k'l'}^\tau} = WT_{V_{rs}^\tau}^{P_{kl}^\tau} + t_{service_{P_{k'l'}^\tau}}^{V_{rs}^\tau} + TT_{o_{P_{kl}^\tau} o_{P_{k'l'}^\tau}} \quad (13)$$

b) Vehicle must arrive at passenger's destination on passenger's arrival time windows:

If $Route_{V_{rs}^\tau - P_{kl}^\tau - P_{k'l'}^\tau}$ is $i_{V_{rs}^\tau} - o_{P_{kl}^\tau} - o_{P_{k'l'}^\tau} - d_{P_{kl}^\tau} - d_{P_{k'l'}^\tau}$, then:

- For first passenger, P_{kl}^τ :

$$e_{arr_{P_{kl}^\tau}} \leq WT_{V_{rs}^\tau}^{P_{k'l'}^\tau} + t_{service_{P_{k'l'}^\tau}}^{V_{rs}^\tau} + TT_{o_{P_{k'l'}^\tau} d_{P_{kl}^\tau}} \leq l_{arr_{P_{kl}^\tau}} \quad (14)$$

- For second passenger, $P_{k'l'}^\tau$:

$$e_{arr_{P_{k'l'}^\tau}} \leq t_{service_{P_{kl}^\tau}}^{V_{rs}^\tau} + TT_l \leq l_{arr_{P_{k'l'}^\tau}} \quad (15)$$

$$\text{where } TT_l = TT_{i_{V_{rs}^\tau} - o_{P_{kl}^\tau} - o_{P_{k'l'}^\tau} - d_{P_{kl}^\tau} - d_{P_{k'l'}^\tau}} \quad (16)$$

Else if $Route_{V_{rs}^\tau - P_{kl}^\tau - P_{k'l'}^\tau}$ is $i_{V_{rs}^\tau} - o_{P_{kl}^\tau} - o_{P_{k'l'}^\tau} - d_{P_{k'l'}^\tau} - d_{P_{kl}^\tau}$, then:

- For first passenger, P_{kl}^τ :

$$e_{arr_P_{kl}^\tau} \leq WT_{V_{rs}^\tau}^{P_{k'l'}^\tau} + t_{service_P_{k'l'}^\tau}^{V_{rs}^\tau} + TT_{o_{P_{k'l'}^\tau} d_{P_{k'l'}^\tau}} \leq l_{arr_P_{k'l'}^\tau} \quad (17)$$

- For second passenger, P_{kl}^τ :

$$e_{arr_P_{kl}^\tau} \leq t_{service_P_{kl}^\tau}^{V_{rs}^\tau} + TT_{II} \leq l_{arr_P_{kl}^\tau} \quad (18)$$

$$\text{where } TT_{II} = TT_{i_{V_{rs}^\tau} - o_{P_{kl}^\tau} - o_{P_{k'l'}^\tau} - d_{P_{k'l'}^\tau} - d_{P_{kl}^\tau}} \quad (19)$$

- c) The time spent by a customer in a vehicle cannot exceed a given value (maximum ride time) :

If **Route** $_{V_{rs}^\tau - P_{kl}^\tau - P_{k'l'}^\tau} = i_{V_{rs}^\tau} - o_{P_{kl}^\tau} - o_{P_{k'l'}^\tau} - d_{P_{kl}^\tau} - d_{P_{k'l'}^\tau}$, then:

- For passenger P_{kl}^τ :

$$TT_{o_{P_{kl}^\tau} o_{P_{k'l'}^\tau}} + t_{service_P_{k'l'}^\tau}^{V_{rs}^\tau} + TT_{o_{P_{k'l'}^\tau} d_{P_{kl}^\tau}} \leq t_{maxride} P_{kl}^\tau \quad (20)$$

- For passenger $P_{k'l'}^\tau$:

$$TT_{o_{P_{k'l'}^\tau} d_{P_{kl}^\tau}} + t_{service_P_{kl}^\tau}^{V_{rs}^\tau} + TT_{d_{P_{kl}^\tau} d_{P_{k'l'}^\tau}} \leq t_{maxride} P_{k'l'}^\tau \quad (21)$$

Else if **Route** $_{V_{rs}^\tau - P_{kl}^\tau - P_{k'l'}^\tau}$ is $i_{V_{rs}^\tau} - o_{P_{kl}^\tau} - o_{P_{k'l'}^\tau} - d_{P_{k'l'}^\tau} - d_{P_{kl}^\tau}$, then:

- For passenger P_{kl}^τ :

$$TT_{o_{P_{kl}^\tau} o_{P_{k'l'}^\tau}} + \left(2 \times t_{service_P_{k'l'}^\tau}^{V_{rs}^\tau} \right) + TT_{o_{P_{k'l'}^\tau} d_{P_{k'l'}^\tau}} + TT_{d_{P_{k'l'}^\tau} d_{P_{kl}^\tau}} \leq t_{maxride} P_{kl}^\tau \quad (22)$$

- For passenger $P_{k'l'}^\tau$:

$$TT_{o_{P_{k'l'}^\tau} - d_{P_{k'l'}^\tau}} \leq t_{maxride} P_{k'l'}^\tau \quad (23)$$

- 2) Capacity feasibility:

The number of passengers in each request must be less than or equal to available vehicle's capacity:

$$q_{P_{kl}^\tau} + q_{P_{k'l'}^\tau} \leq Q_{V_{rs}^\tau} \quad (24)$$

Next, we define model of the optimization problem of ride splitting service with resource sharing scheme on graph $G_2^\tau = (N_2^\tau, E_2^\tau)$, and we use the following decision variables:

$$x_{P_{kl}^\tau, P_{k'l'}^\tau}^{V_{rs}^\tau} = \begin{cases} 1, & \text{if passengers } P_{kl}^\tau \text{ and } P_{k'l'}^\tau \text{ served by vehicle } V_{rs}^\tau \\ 0, & \text{otherwise} \end{cases}$$

$$z_{V_{rs}^\tau}^{P_{kl}^\tau} = \begin{cases} 1, & \text{if vehicle } V_{rs}^\tau \text{ serves passenger } P_{kl}^\tau \\ 0, & \text{otherwise} \end{cases}$$

$$w_{V_{rs}^\tau}^{P_{kl}^\tau} = \begin{cases} 1, & \text{if platform index } k = r \\ \alpha, & \text{otherwise} \end{cases}$$

α is profit sharing multiplier, where $0 < \alpha < 1$

$$V_{rs_occ}^\tau = \begin{cases} 2, & \text{if } x_{P_{kl}^\tau, P_{k'l'}^\tau}^{V_{rs}^\tau} = 1 \text{ and } P_{kl}^\tau \neq P_{k'l'}^\tau \\ 1, & \text{if } x_{P_{kl}^\tau, P_{k'l'}^\tau}^{V_{rs}^\tau} = 1 \text{ and } P_{kl}^\tau = P_{k'l'}^\tau \\ 0, & \text{else} \end{cases}$$

$$Q_{V_{rs}^\tau} = \begin{cases} 4, & \text{if } V_{rs_occ}^\tau = 0 \\ 4 - q_{P_{kl}^\tau}, & \text{if } V_{rs_occ}^\tau = 1 \\ 0, & \text{else} \end{cases}$$

For each feasible match $(V_{rs}^{\tau} P_{kl}^{\tau}, V_{r's'}^{\tau} P_{k'l'}^{\tau})$ in E_2^{τ} , calculate:

1) The operational cost of **Route** $_{V_{rs}^{\tau} P_{kl}^{\tau} - P_{k'l'}^{\tau}}$:

$$op.cost_{P_{kl}^{\tau} - P_{k'l'}^{\tau}}^{V_{rs}^{\tau}} = c_{V_{rs}^{\tau}} \times Distance_{V_{rs}^{\tau} P_{kl}^{\tau} - P_{k'l'}^{\tau}} \quad (25)$$

where $c_{V_{rs}^{\tau}}$ is vehicle V_{rs}^{τ} 's operational cost per one distance unit

2) The profit of **Route** $_{V_{rs}^{\tau} P_{kl}^{\tau} - P_{k'l'}^{\tau}}$:

$$profit_{P_{kl}^{\tau} - P_{k'l'}^{\tau}}^{V_{rs}^{\tau}} = \left(w_{V_{rs}^{\tau} P_{kl}^{\tau}}^{P_{kl}^{\tau}} z_{V_{rs}^{\tau} P_{kl}^{\tau}}^{P_{kl}^{\tau}} F^{P_{kl}^{\tau}} \right) + \left(w_{V_{rs}^{\tau} P_{k'l'}^{\tau}}^{P_{k'l'}^{\tau}} z_{V_{rs}^{\tau} P_{k'l'}^{\tau}}^{P_{k'l'}^{\tau}} F^{P_{k'l'}^{\tau}} \right) - op.cost_{P_{kl}^{\tau} - P_{k'l'}^{\tau}}^{V_{rs}^{\tau}} \quad (26)$$

3) The total waiting time of passenger for a ride on **Route** $_{V_{rs}^{\tau} P_{kl}^{\tau} - P_{k'l'}^{\tau}}$:

$$WT_{P_{kl}^{\tau} - P_{k'l'}^{\tau}}^{V_{rs}^{\tau}} = WT_{V_{rs}^{\tau} P_{kl}^{\tau}}^{P_{kl}^{\tau}} + WT_{V_{rs}^{\tau} P_{k'l'}^{\tau}}^{P_{k'l'}^{\tau}} \quad (27)$$

4) The money value of total passenger's waiting time:

$$\overline{WT}_{P_{kl}^{\tau} - P_{k'l'}^{\tau}}^{V_{rs}^{\tau}} = \overline{wt}_{money} \times WT_{P_{kl}^{\tau} - P_{k'l'}^{\tau}}^{V_{rs}^{\tau}} \quad (28)$$

where \overline{wt}_{money} is money value of passenger's waiting time per one time unit

5) The weight of edge $(V_{rs}^{\tau} P_{kl}^{\tau}, V_{r's'}^{\tau} P_{k'l'}^{\tau})$:

$$Wg_{P_{kl}^{\tau} - P_{k'l'}^{\tau}}^{V_{rs}^{\tau}} = \frac{profit_{P_{kl}^{\tau} - P_{k'l'}^{\tau}}^{V_{rs}^{\tau}}}{\overline{WT}_{P_{kl}^{\tau} - P_{k'l'}^{\tau}}^{V_{rs}^{\tau}}} \quad (29)$$

The weight $Wg_{P_{kl}^{\tau} - P_{k'l'}^{\tau}}^{V_{rs}^{\tau}}$ is defined as a ratio between the profit gained by a vehicle and the money value of total passenger's waiting time.

The mathematical model for the problem is:

$$Max \sum_{((V_{rs}^{\tau}, P_{kl}^{\tau}), (V_{r's'}^{\tau}, P_{k'l'}^{\tau})) \in E_2^{\tau}} \overline{Wg}_{P_{kl}^{\tau} - P_{k'l'}^{\tau}}^{V_{rs}^{\tau}} x_{P_{kl}^{\tau} - P_{k'l'}^{\tau}}^{V_{rs}^{\tau}} \quad (30)$$

Subject to:

$$\sum_{V_{rs}^{\tau} \in V^{\tau}, P_{kl}^{\tau} \in P^{\tau}: ((V_{rs}^{\tau}, P_{kl}^{\tau}), (V_{r's'}^{\tau}, P_{k'l'}^{\tau})) \in E_2^{\tau}} x_{P_{kl}^{\tau} - P_{k'l'}^{\tau}}^{V_{rs}^{\tau}} + \sum_{V_{rs}^{\tau} \in V^{\tau}, P_{ab}^{\tau} \in P^{\tau}: ((V_{rs}^{\tau}, P_{ab}^{\tau}), (V_{r's'}^{\tau}, P_{a'b'}^{\tau})) \in E_2^{\tau}} x_{P_{ab}^{\tau} - P_{a'b'}^{\tau}}^{V_{rs}^{\tau}} \leq 1,$$

$$\forall P_{kl}^{\tau}, P_{k'l'}^{\tau}, P_{ab}^{\tau}, P_{a'b'}^{\tau} \in P^{\tau}, \text{ for } k = a', l = b' \quad (31)$$

$$\sum_{P_{kl}^{\tau}, P_{k'l'}^{\tau} \in P^{\tau}: ((V_{rs}^{\tau}, P_{kl}^{\tau}), (V_{r's'}^{\tau}, P_{k'l'}^{\tau})) \in E_2^{\tau}} x_{P_{kl}^{\tau} - P_{k'l'}^{\tau}}^{V_{rs}^{\tau}} \leq 1, \quad \forall V_{rs}^{\tau} \in V^{\tau} \quad (32)$$

$$x_{P_{kl}^{\tau} - P_{k'l'}^{\tau}}^{V_{rs}^{\tau}} \in \{0, 1\}, \quad \forall P_{kl}^{\tau}, P_{k'l'}^{\tau} \in P^{\tau}; \forall V_{rs}^{\tau} \in V^{\tau} \quad (33)$$

The objective function (30) maximizes the total weight. Constraints (31) ensures each passenger at most in one feasible match, and (32) ensures each vehicle at most in one feasible match. Finally, constraints (33) enforce the binary condition.

In the next section, we will present the solution algorithm to solve the optimization problem in each period.

4. SOLUTION METHODOLOGY

The optimization problem will be solved in three stages. At first, algorithm 1 is performed to obtain a set of feasible pair of a vehicle and the first customer by generating the first weighted

bipartite graph. Algorithm 2 in the second stage is performed to obtain the set of feasible pair of a vehicle and two request customers by generating second modified weighted bipartite graph. Finally, algorithm 3 is performed to obtain the optimal assignment of vehicle and passenger pair.

Procedure to generate first weighted bipartite graph is presented in the following algorithm.

Algorithm 1. Generating first weighted bipartite graph

Step 1: Node construction. Initially, there is no node in graph G_1^t . Let t be time at which the first request from a customer arrived. Set period $\tau = \tau_1$, where the first period $\tau_1 = [t, t + \delta - Opt_T)$, δ be an acceptable time limit for a customer waiting for a decision to be picked up; and Opt_T be time to do assignment optimization. For the next period, set $\tau_i = [t + (i - 1)\delta - Opt_T, t + i * \delta - Opt_T)$, for $i = 2, 3, \dots$. In this study we set $\delta = 60''$ and $Opt_T = 10''$. Create a set P^τ consisting of all request customers with request time $t_{request_P_{kl}^\tau}$ in period τ_i and all assigned customers in the previous period τ_{i-1} who still not get a customer pair to share a ride in ride splitting service.

Create a set V^τ consisting of all available vehicle in period τ_i including all vehicle which still only assigned to one request customer in the previous period τ_{i-1} .

Then set $N_1^\tau = V^\tau \cup P^\tau$, be the set of nodes of graph G_1^τ .

Step 2: Shortest path, distance and travel time determination. For each customer in P^τ and each vehicle in V^τ , determine shortest path passenger's origin-destination to get $route_{od_{P_{kl}^\tau}}$ and from vehicle's current location to passenger's origin to get $route_{i_{V_{rs}^\tau} o_{P_{kl}^\tau}}$. Then, calculate the distance $D_{od_{P_{kl}^\tau}}$ and $D_{i_{V_{rs}^\tau} o_{P_{kl}^\tau}}$, travel time $TT_{od_{P_{kl}^\tau}}$ and $TT_{i_{V_{rs}^\tau} o_{P_{kl}^\tau}}$.

Step 3: Departure time windows, arrival time windows, and max ride time calculation. For each customer in P^τ , calculate earliest and latest departure time, earliest and latest arrival time and maximum ride time using equation (1)-(5). In this study we set $\epsilon, \mu = 0.2$, $\lambda_{early} = 5'$, $\lambda_{late} = 15'$ and $t_{service_P_{kl}^\tau}^{V_{rs}^\tau} = 1'$.

Step 4: Feasible match determination and edge construction. For each vehicle in V^τ and for each customer in P^τ , determine whether a vehicle is feasible to serve a customer by using feasible criterion (6)-(8). Then node V_{rs}^τ in V^τ is adjacent to node P_{kl}^τ in P^τ , or $(V_{rs}^\tau, P_{kl}^\tau)$ is an edge in E_1^τ if and only if vehicle V_{rs}^τ is met the feasible criterion in (6) – (8) to serve customer P_{kl}^τ . Then $E_1^\tau = \{(V_{rs}^\tau, P_{kl}^\tau) | P_{kl}^\tau \text{ and } V_{rs}^\tau \text{ are feasible match; } V_{rs}^\tau \in V^\tau, P_{kl}^\tau \in P^\tau\}$.

Step 5: Weight calculation. For each edge in E_1^τ calculate its weight, where the weight is the fare that has to be paid by passenger P_{kl}^τ if served by vehicle V_{rs}^τ , using equation (9).

Step 6: Output. From step 1 to step 5, set graph $G_1^\tau = (N_1^\tau, E_1^\tau)$.

The next stage is to performed Algorithm 2 with the following procedure.

Algorithm 2. Generating The Second Weighted Bipartite Graph

Step 1: Node construction. Initially, there is no node in graph G_2^t .

Let N_1^τ and E_1^τ be the set of nodes and the set of edges of G_1^τ from algorithm 1

For $V_{rs}^\tau \in V^\tau$ and $P_{kl}^\tau \in P^\tau$, create a set $V^\tau P^\tau$ consisting all pairs of $V_{rs}^\tau P_{kl}^\tau$, where $(V_{rs}^\tau, P_{kl}^\tau)$ is an edge in E_1^τ . Create a set $DV^\tau P^\tau$, a duplication set of $V^\tau P^\tau$.

That is $DV^\tau P^\tau = \{V_{rs}^\tau, P_{kl}^\tau | \text{if } V_{rs}^\tau P_{kl}^\tau \in V^\tau P^\tau\}$.

Then set $N_2^\tau = V^\tau P^\tau \cup DV^\tau P^\tau$ be a bipartite set of nodes of graph G_2^τ .

- Step 2:** Vehicle route, distance and travel time determination. For each pair of nodes $V_{rs}^{\tau}P_{kl}^{\tau}$ in $V^{\tau}P^{\tau}$ and $V_{r's'}^{\tau}P_{k'l'}^{\tau}$ in $DV^{\tau}P^{\tau}$, with $r = r'$ and $s = s'$, determine shortest path from vehicle's current location to the first passenger's origin, then to the second passenger's origin and next to the closest passenger's destination to get $Route_{V_{rs}^{\tau}P_{kl}^{\tau}-P_{k'l'}^{\tau}}$. Then, $Route_{V_{rs}^{\tau}P_{kl}^{\tau}-P_{k'l'}^{\tau}}$ is the shortest path between route $i_{V_{rs}^{\tau}} - o_{P_{kl}^{\tau}} - o_{P_{k'l'}^{\tau}} - d_{P_{kl}^{\tau}} - d_{P_{k'l'}^{\tau}}$ and route $i_{V_{r's'}^{\tau}} - o_{P_{kl}^{\tau}} - o_{P_{k'l'}^{\tau}} - d_{P_{k'l'}^{\tau}} - d_{P_{kl}^{\tau}}$. Next, calculate the distance: $Distance_{V_{rs}^{\tau}P_{kl}^{\tau}-P_{k'l'}^{\tau}}$ and travel time: $TT_{V_{rs}^{\tau}P_{kl}^{\tau}-P_{k'l'}^{\tau}}$.
- Step 3:** Feasible match determination and edge construction. For nodes $V_{rs}^{\tau}P_{kl}^{\tau}$ in $V^{\tau}P^{\tau}$ and $V_{r's'}^{\tau}P_{k'l'}^{\tau}$ in $DV^{\tau}P^{\tau}$, with $r = r'$ and $s = s'$, check if the vehicle V_{rs}^{τ} is feasible to serve customers P_{kl}^{τ} and $P_{k'l'}^{\tau}$ by using feasible criterion in (10)-(24), then node $V_{rs}^{\tau}P_{kl}^{\tau}$ is adjacent to node $V_{r's'}^{\tau}P_{k'l'}^{\tau}$, or $(V_{rs}^{\tau}P_{kl}^{\tau}, V_{r's'}^{\tau}P_{k'l'}^{\tau})$ is an edge in E_2^{τ} .
- Step 4:** Weight calculation. For each edge in E_2^{τ} , calculate vehicle's operational cost and profit gained, passenger's total waiting time and its money value, and the edge weight using formula (25)-(29).
- Step 5:** Output. From step 1-step 4, set graph $G_2^{\tau} = (N_2^{\tau}, E_2^{\tau})$.

Finally, performed The Greedy Heuristic Algorithm based on [20] to solve the mathematical model (30)-(33) for the optimization problem.

Algorithm 3. The Greedy Heuristic Algorithm

- Step 1:** Select the edge in graph G_2^{τ} with the largest weight and add it to the matching. Let the edge with the largest weight in E_2^{τ} is $(V_{rs}^{\tau}P_{kl}^{\tau}, V_{r's'}^{\tau}P_{k'l'}^{\tau})$, then set the vehicle V_{rs}^{τ} serves customers P_{kl}^{τ} and $P_{k'l'}^{\tau}$. Update the vehicle V_{rs}^{τ} 's occupation: $V_{rs}^{\tau}occ$ and capacity: $Q_{V_{rs}^{\tau}}$.
- Step 2:** Delete the endpoints of the edge selected in step 1, all nodes related to vehicles V_{rs}^{τ} and $V_{r's'}^{\tau}$, customers P_{kl}^{τ} and $P_{k'l'}^{\tau}$, and all edges incident to these nodes. If the graph contains at least two nodes, return to step 1; otherwise stop.

5. COMPUTATIONAL EXPERIMENTS

To test the model and its solution methodology, in this paper we use two periods of time, which consists of six request customers and six available vehicles and three values for parameter α (profit sharing multiplier factor) as comparison, those are 85%,90% and 95%. The consideration to use three α values is based on the willingness of the driver (and the operator) to share profit with the initial operator requested by the customer and to keep being profitable for the serving driver (operator). All experiments in this study is coded with Python 3.7.

In the meantime, the number of operators (platforms) providing online taxi services used is two platforms, while the tariff for the ride-splitting service charged to each passenger from each platform is using three cases as a comparison. Those cases are the equal tariff, 5% and 10% difference in tariff. Table 1 describes the fare charged by platform 1 and 2 for all cases. In the first case, the fare charged by platform 1 and 2 is 2\$/ distance unit. At the second case, the difference in tariff between platform 1 and 2 is 5%, whereas the fare charged by platform 1 to the customer in ride-splitting service is 2\$ /distance unit, while in platform 2, it is 2.1\$ /distance unit. While in the last case, the difference in tariff between platform 1 and 2 is 10%, whereas the fare charged by platform 1 to the customer in ride-splitting service is 2\$ /distance unit while in platform 2, it is 2.2\$ /distance unit. With the three fare difference cases, it will be seen that the resource sharing scheme used with a certain limit value of profit share, can still be profitable for the driver (and operator) even though there is a difference for the

cheaper fare paid by the customer. Next, the optimization of the ride-splitting service with the resource sharing scheme compared to the optimization without using the scheme, by taking the value of $w_{V_{rs}}^{P_{kl}} = 1$

Table 1. Fare charged by Platform 1 and 2

Case	Fare of Platform 1 per distance unit	Fare of Platform 2 per distance unit
For Equal tariff	2\$	2\$
For 5% difference	2\$	2.1\$
For 10% difference	2\$	2.2\$

Gradually, there come four request customers in the first period and two request customers in the second period, where there are four available vehicles in the first period and two new available vehicles in the second period.

Let figure 1 illustrates example of a road transportation network where the passenger's origin and vehicle location are located in the first period. Assume that one distance unit can be traveled in one time unit. The weight of each link describes the distance between two different nodes, for example the distance between node 1 and 4 is 16 distance unit.

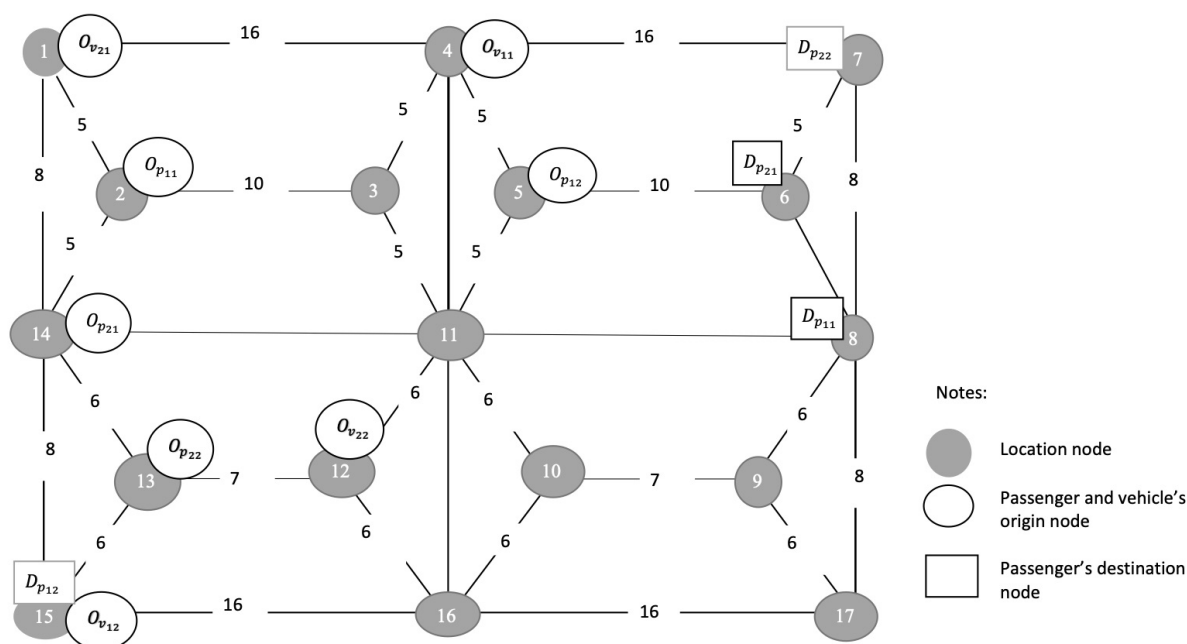


Fig.1 Illustration of Road Transportation Network in The First Period

Let the first period start at 7^{00} and end at 7^{01} , and the list of customer requests given in the table 2. From table 2, in the first period, there are four customers: P_{11}, P_{21}, P_{12} and P_{22} which request ride splitting services. Let P_{11} be the first customer which request a service (vehicle) from platform 1, P_{21} be the first customer which request a service from platform 2. The origin (pick up) location of P_{11} is at node 2, meanwhile the origin of P_{21} is at node 14. The destination (drop off) location of P_{11} is at node 8 and P_{21} is at node 6. The number of passengers per request of customer P_{11} is 1 passenger, which has to be picked up between $7^{01} - 7^{16}$, meanwhile a request of customer P_{21} consists of 2 passengers, which has to be picked up between $7^{01} - 7^{16}$.

Table 2. List of Customer Requests in The First Period

customer	$t_{request-P_{kl}}$	$o_{P_{kl}}$	$d_{P_{kl}}$	$e_{dept-P_{kl}}$	$l_{dept-P_{kl}}$	$q_{P_{kl}}$
P_{11}	7^{00}	2	8	7^{01}	7^{16}	1
P_{12}	7^{00}	5	15	7^{01}	7^{16}	2
P_{21}	7^{00}	14	6	7^{01}	7^{16}	2
P_{22}	7^{00}	13	7	7^{01}	7^{16}	1

There are four available vehicles in the first period, which are vehicle V_{11} and V_{12} from platform 1, and vehicle V_{21} and V_{22} from platform 2. Data of available vehicle's locations and capacities between 7^{00} - 7^{01} is given by table 3.

Table 3. Data of Available Vehicles in The First Period

vehicle	$i_{V_{rs}}$	$t_{i_{V_{rs}}}^{V_{rs}}$	$Q_{V_{rs}}$
V_{11}	4	7^{00}	4
V_{21}	1	7^{00}	4
V_{12}	15	7^{00}	4
V_{22}	12	7^{00}	4

Let $c_{V_{rs}}$, the vehicle cost per distance unit, is 1\$ and \overline{wt}_{money} , the money value of passenger's waiting time, is 1\$ per minute. Using the solution method in section 4 with three fare difference cases, the optimum assignment result in the first period is described on table 4 and the profit gained by driver is described in figure 2.

Table 4. The Optimum Assignment Result in Period 1

	Ride Splitting with resource sharing scheme, for $\alpha = 85\%, 90\%$ and 95%	Ride Splitting without resource sharing scheme
Assignment Result in Period 1	V_{21} is serving P_{11} and P_{21} V_{22} is serving P_{22} V_{11} is serving P_{12} V_{12} is not yet serving any customer	V_{22} is serving P_{21} and P_{22} V_{12} is serving P_{11} V_{11} is serving P_{12} . V_{21} is not yet serving any customer
Total vehicle used	3	3
Total passenger's waiting time	17 minutes	31 minutes

It can be seen from table 4, total passenger's waiting time to be picked up by a vehicle for the ride splitting service with sharing platform scheme in the first period is 17 minutes, while in the ride splitting service without sharing platform scheme is 31 time unit.

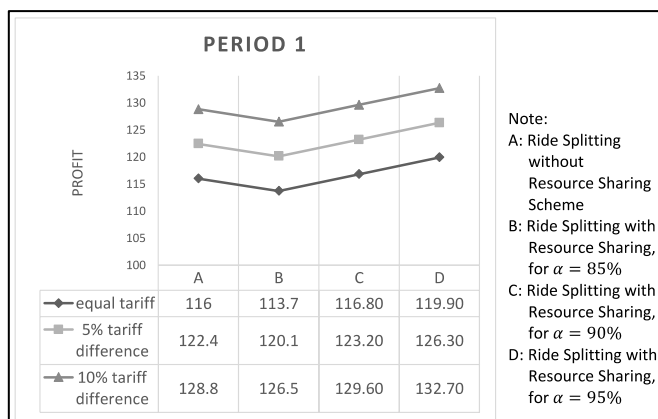


Fig.2 Profit gained comparison in the first period

Based on figure 2, the profit gained by ride splitting service without sharing platform scheme (A) for equal tariff case is 116\$, while ride splitting service with sharing platform scheme for $\alpha = 85\%$ (B), $\alpha = 90\%$ (C) and $\alpha = 95\%$ (D) are 113,7\$, 116,8\$ and 119,9\$ respectively. It can be seen that profit gained by ride splitting service with sharing platform scheme using $\alpha = 90\%$ (C) and 95% (D) for all fare difference cases are higher than ride splitting service without sharing platform scheme (A). While, ride splitting service with sharing platform scheme using $\alpha = 85\%$ (B) for all fare difference cases is gaining profit lower than ride splitting service without sharing platform scheme (A). Based on the simulation, the parameter value for profit sharing platform scheme will result in higher profit than without sharing platform scheme when the value is greater than or equal to 0.9 ($\alpha = 90\%$).

In the second period, there are two new customer requests, summarized in the following table 5.

Table 5. List of Customer Requests in Second Period

customer	$t_{request_P_{kl}}$	$o_{P_{kl}}$	$d_{P_{kl}}$	$e_{dept_P_{kl}}$	$l_{dept_P_{kl}}$	$q_{P_{kl}}$
P_{13}	7^{01}	16	7	7^{02}	7^{17}	1
P_{23}	7^{01}	11	15	7^{02}	7^{17}	2

Meanwhile, available vehicles in the second period is summarized in table 6, where there are three vehicles originating from the first period and two new vehicles from the second period. Based on the assignment result in the first period, vehicle V_{11} is serving passenger P_{12} , so that available seat left is only 2, while vehicle V_{22} is serving passenger P_{22} , so that vehicle capacity left is only 3 seats.

Table 6. Data of Available Vehicles in The Second Period

vehicle	$i_{V_{rs}}$	$t_{i_{V_{rs}}}^{V_{rs}}$	$Q_{V_{rs}}$
V_{11}	4	7^{00}	2
V_{12}	15	7^{00}	4
V_{22}	12	7^{00}	3
V_{13}	3	7^{01}	4
V_{23}	10	7^{01}	4

Using the solution method in section 4, the optimum assignment results in the first and second period is described on table 7 and profit gained comparison for three fare difference cases is described in figure 3.

Table 7. The Optimum Assignment Results in Two Periods

	Ride Splitting with resource sharing scheme, for $\alpha = 85\%$, 90% or 95%	Ride Splitting without resource sharing scheme
Assignment Result in Period 1 and 2	V_{21} is serving P_{11} and P_{21} V_{22} is serving P_{22} V_{11} is serving P_{12} and P_{23} V_{23} is serving P_{13} V_{12} and V_{13} are not yet serving any customer	V_{22} is serving P_{21} and P_{22} V_{12} is serving P_{11} V_{11} is serving P_{12} V_{13} is serving P_{13} V_{23} is serving P_{23} V_{21} is not yet serving any customer
Total vehicle used	4 (or 66,7% of vehicle availability)	5 (or 83,3% of vehicle availability)
Total passenger's waiting time	33 minutes	50 minutes

From table 7, it can be seen that total passenger's waiting time for ride splitting service with sharing platform scheme case is only 33 minutes, lower than without sharing platform scheme case, which is 50 minutes, and so is the total vehicle used, the ride splitting service with the scheme only use 66,7% of available vehicles, while the ride splitting service without the scheme use 83,3% of available vehicles.

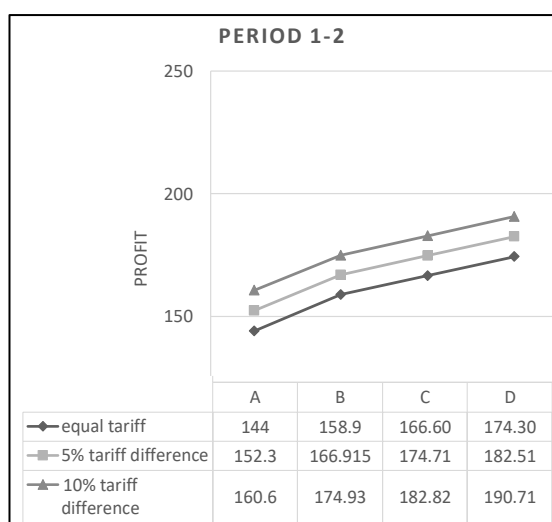


Fig.3 Total Profit Gained Comparison For Total Two Periods

Based on figure 3, total profit gained by ride splitting service without sharing platform scheme (A) for equal tariff case is 144\$, while ride splitting service with sharing platform scheme for $\alpha = 85\%$ (B), $\alpha = 90\%$ (C) and $\alpha = 95\%$ (D) are 158,9\$, 166,6\$ and 174,3\$ respectively. It can be seen that profit gained by ride splitting service with sharing platform scheme using $\alpha = 85\%$ (B), 90%(C) and 95% (D) for all fare difference cases are higher than ride splitting service without sharing platform scheme (A).

6. CONCLUSIONS

Based on the experiment, it can be concluded that the optimization of ride-splitting service with resource-sharing scheme can reduce the vehicle used for online taxi services. Moreover, it can generate higher overall profit for all vehicles serving passenger, and the parameter value

for profit sharing platform scheme is better greater than or equal to 0,9 ($\alpha = 90\%$). Meanwhile, total passenger's waiting time to be picked up by a vehicle for ride splitting service with sharing platform scheme case is lower than without sharing platform scheme case.

This study is still using small instance as an experiment to prove that the optimization of ride-splitting service with resource-sharing scheme is possible to be utilized, so that for the next research, bigger data usage is required

ACKNOWLEDGEMENT

The authors would like to thank to Kemenristek Dikti and LPDP for scholarship in order the completion of doctoral studies at Universitas Indonesia.

REFERENCES

- [1] Burhan, H., Soehodho, S., and Nahry. (2017). Review on the Development of Ride Sharing System using Online Transportation Service in Jakarta. Proceeding of 6th IEEE International Conference on Advanced Logistics and Transport, pp.173-178.
- [2] Anderson, D. N.,(2014). "Not Just A Taxi"? For-Profit Ridesharing, Driver Strategies, and VMT. *Transportation* 41, pp.1099–1117. <http://dx.doi.org/10.1007/s11116-014-9531-8>.
- [3] Rayle, L., Dai, D., Chan, N., Cervero, R., and Shaheen, S. (2015). Just a better taxi? A survey-based comparison of taxis, transit, and ridesourcing services in San Francisco. *Transp. Policy*, pp.168–178.
- [4] Shaheen, S., Cohen, a., and Zohdy, I. (2016). *Shared Mobility: Current Practices and Guiding Principles*. U.S. Department of Transportation, Federal Highway Administration. Report No. FHWA-HOP-16-022.
- [5] Chen, L., Mislove, A., and Wilson, C. (2015). Peeking Beneath the Hood of Uber. In *Proc. of the ACM Conference on Internet Measurement Conference*, ACM.
- [6] Burhan, H., Soehodho, S., and Nahry. (2019). A Resource Sharing (Sharing Platform) Scheme on Online Taxi Services. *MATEC Web of Conferences*, vol. 270, art.no.03010.
- [7] Agatz, N.A.H., Erera, A.L., Savelsbergh, M.W.P., and Wang, X. (2012). Optimization for dynamic ride-sharing: a review. *European Journal of Operational Research*, vol.223 (2), pp.295–303.
- [8] Lu, Q., and Dessouky, M. (2006). A new insertion-based construction heuristic for solving the pickup and delivery problem with hard time windows. *European Journal of Operational Research*, vol.175 (2), pp.672–687.
- [9] Dumas, Y., Desrosiers, J., and Soumis, F. (1991). The pickup and delivery problem with time windows. *European Journal of Operations Research*, vol.54, pp.7–22.
- [10] Toth, P. and Vigo, D. (2002). *The Vehicle Routing Problem*. Siam, Philadelphia <http://dx.doi.org/10.1137/1.9780898718515>.
- [11] Hosni, H., Naoum-Sawaya, J., and Artail, H. (2014). The shared-taxi problem: Formulation and solution methods. *Transp. Res. Part B: Methodol.* 70, pp. 303–318.
- [12] Wang, X., Dessouky, M., and Ordóñez, F. (2015). A pickup and delivery problem for ridesharing considering congestion. *Transp. Lett.: Int. J. Transp. Res.*,1942787515Y-000000002.
- [13] Santos, D.O., and Xavier, E.C. (2015). Taxi and Ride Sharing: A Dynamic Dial-a-Ride Problem with Money as an Incentive. *Expert Systems with Applications*, vol. 42, pp.6728–6737.
- [14] Mahmoudi, M., and Zhou, X. (2017). Finding optimal solutions for vehicle routing problem with pickup and delivery services with time windows: a dynamic programming approach based on state-space-time network representations. *Transport. Res. Part B: Methodol.* Vol.89, pp.19–42.
- [15] Bei, X., and Zhang, S. (2018). Algorithms for trip-vehicle assignment in ride-sharing. In: *Proceedings of the 32nd AAAI Conference on Artificial Intelligence*, pp. 3–9.

- [16] Banerjee, S., Johari, R., and Riquelme, C. (2015). Pricing in ride-share platforms: A queueing-theoretic approach. Working Paper. Available at SSRN: <https://ssrn.com/abstract=2568258> or <http://dx.doi.org/10.2139/ssrn.2568258>.
- [17] Chen, Y., and Hu, M. (2017). Pricing and Matching with Forward-Looking Buyers and Sellers. Working Paper. Available at SSRN: <https://ssrn.com/abstract=2859864> or <http://dx.doi.org/10.2139/ssrn.2859864>.
- [18] Zha, L., Yin, Y., and Xu, Z. (2018). Geometric matching and spatial pricing in ride-sourcing markets. *Transportation Research Part C: Emerging Technologies*, Vol.92, pp.58-75.
- [19] Yang, H., Shao, C., Wang, H., and Ye, J. (2018). Integrated Reward Scheme and Surge Pricing in a Ride Sourcing Market. Report, June 18, 2018. Available at SSRN: <https://ssrn.com/abstract=3198081> or <http://dx.doi.org/10.2139/ssrn.3198081>.
- [20] Evans, J.R., and Minieka, E. (1992). *Optimization algorithms for networks and graphs*, 2nd edition Revised. New York.

THE HARMONIC COMPOSITION OF CURRENT IN ZERO-WORKING WIRE WITH NON-LINEAR LOAD

IGOR V. YUDAEV^{1*}, EVGENY V. RUD², MIKHAIL A. YUNDIN³,
TAMARA Z. PONOMARENKO² AND ALEKSANDRA M. ISUPOVA³

¹*Department of Thermal Engineering and Information Management System,
Azov-Black Sea Engineering Institute of Don State Agrarian University,
Zernograd, Russian Federation*

²*ICPE “Energy Institute for Advanced Studies of the PJSC “Kubanenergo”,
Krasnodar, Russian Federation*

³*Department of Electric Power and Electrical Engineering,
Azov-Black Sea Engineering Institute of Don State Agrarian University,
Zernograd, Russian Federation*

*Corresponding author: yudaev5303@ubogazici.in

(Received: 4th August 2020; Accepted: 14th October 2020; Published on-line: 4th January 2021)

ABSTRACT: The purpose of this study was experimental investigations and a study of the nature of the change in the main harmonic components of the current in the neutral working wire of a three-phase four-wire network with a voltage of 0.38 kV. The study of the amplitude-phase-frequency characteristics of currents flowing in an electric network with a predominant non-linear load is one of the most urgent tasks, the solution of which will increase the efficiency of electric power transmission and eliminate the negative consequences due to the current flow in a zero-working wire in the network at 0.38 kV. To study the effect of load changes on the amplitude-phase-frequency characteristics of currents in the linear and zero working wires at the input of the load node, measurements were carried out by certified electrical measuring instruments namely, the “Resource-UF2M” and “Hioki 3196”. With these devices, the phase voltages at the input to the load node were measured. The analysis of the results obtained for the load node whose power was formed mainly by a lighting system with fluorescent and LED lamps and a system of office electrical receivers (computers, copiers, printers, scanners, etc.) was performed. It can be concluded that a current comparable to the currents of the linear wires of the network flows from the load node with the predominant nonlinear power receivers through the zero-working wire. At the same time, in the zero-working wire of the network, the third harmonic current prevails over the main frequency currents.

ABSTRAK: Tujuan kajian ini adalah penyelidikan eksperimental dan kajian mengenai sifat perubahan komponen harmonik utama arus dalam wayar kerja neutral rangkaian empat wayar tiga fasa dengan voltan 0.38 kV. Kajian mengenai ciri-ciri frekuensi-amplitud-fasa arus yang mengalir dalam rangkaian elektrik dengan beban bukan linear yang dominan adalah salah satu tugas yang paling mendesak, penyelesaiannya akan meningkatkan kecekapan penghantaran tenaga elektrik dan menghilangkan akibat negatif yang disebabkan ke arus semasa dalam wayar sifar bekerja di rangkaian pada 0.38 kV. Untuk mengkaji kesan perubahan beban pada ciri frekuensi-fasa frekuensi arus dalam wayar linier dan sifar pada input nod beban, pengukuran dilakukan oleh alat pengukur elektrik yang disahkan iaitu, "Resource-UF2M" dan "Hioki 3196". Dengan peranti ini, voltan fasa pada input ke simpul beban diukur. Analisis hasil yang diperoleh untuk simpul beban yang kekuatannya dibentuk terutama oleh sistem pencahayaan dengan lampu pendarfluor dan LED dan sistem penerima elektrik pejabat (komputer, mesin fotokopi, pencetak, pengimbas, dll.). Dapat disimpulkan bahawa arus yang setanding dengan arus

wayar linier rangkaian mengalir dari nod beban dengan penerima kuasa bukan linier yang dominan melalui wayar sifar. Pada masa yang sama, dalam wayar sifar rangkaian, arus harmonik ketiga berlaku berbanding arus frekuensi utama.

KEYWORDS: *three-phase four-wire network; zero working wire of the network; harmonic currents; non-symmetry; non-linear power receiver*

1. INTRODUCTION

The main reasons for current appearance in the zero-working wire of a three-phase four-wire network are the asymmetry of the loads in the phases and presence of nonlinear power receivers. When flowing through a zero-working wire, the components of the currents of higher harmonics and asymmetries cause additional losses of voltage and electricity; reduction in the service life of cable lines; increase the resistance of grounding devices of electrical installations; and interference in low-voltage communication lines [1-6].

The study of the amplitude-phase-frequency characteristics of currents flowing in an electric network with a predominant non-linear load is one of the most urgent tasks, the solution of which will increase the efficiency of electric power transmission and eliminate the negative consequences due to the current flow in a zero-working wire in the network at 0.38 kV [7].

Since the spectral composition of currents in real electric networks is influenced by a large number of simultaneously influencing factors (the composition of power receivers in the load node, their connection diagram, switching frequency, etc.), the study of the harmonic composition of currents of the most common typical consumers is of practical interest. The power of the load node under study was formed mainly by a lighting system with fluorescent and LED lamps and a system of office electrical receivers (computers, copiers, printers, scanners, etc.) [8].

To study the effect of load changes on the amplitude-phase-frequency characteristics of currents in linear and zero working wires at the input of the load node, measurements were carried out by certified electrical measuring instruments [9]. The “Resource-UF2M” and “Hioki 3196” devices controlled currents in linear and zero working (“Hioki 3196”) wires. At the same time, the same devices measured the phase voltages at the input to the load node.

2. CHARACTERISTICS OF THE DISTORTION COEFFICIENT OF THE SINE CURVE IN ACCORDANCE WITH DAILY CHANGES

The change in the total active power at the input of the load node during the day is shown in Fig. 1. The range of changes in the total active power is large – from 5 kW at night up to 68 kW during the day. The greatest loads were during daylight hours from 7:30 to 17:00 hours. The minimum value of the total active power, as seen in Fig. 1, was recorded in the morning (from 5:00 to 7:00 hours), and the maximum – in the daytime from 12:00 to 13:32 hours. As can be seen from Fig. 1, the power consumption of the load node occurred according to a two-stage schedule.

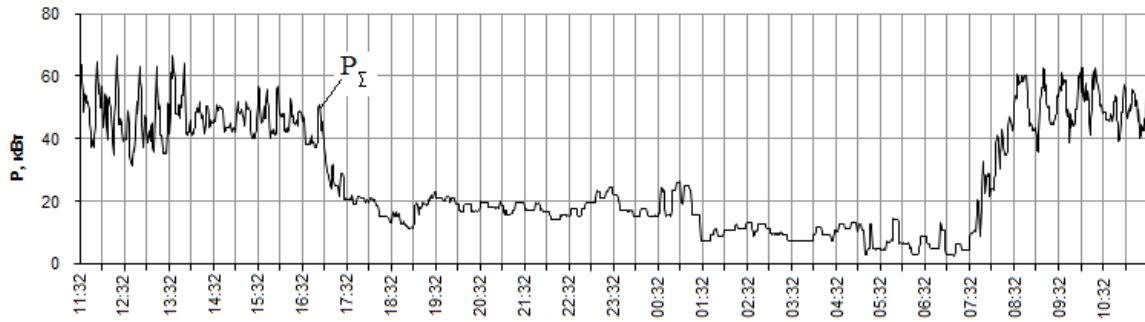


Fig. 1: Schedule of changes in total active power at the input of the load node.

Moreover, the change in active capacities during the day is very asymmetric in the network phases (Fig. 2). The active power P_1 of the first phase L1 during the day turned out to be the smallest most of the time. Separate bursts of active power P_1 of phase L1 were clearly observed in the period from 5:00 to 6:00 hours, when the load was the greatest. Most of the day, the greatest load fell on the L3 phase with an active power of P_3 . Only in the period from 14:00 to 16:32 hours the active power of P_2 exceeded P_3 .

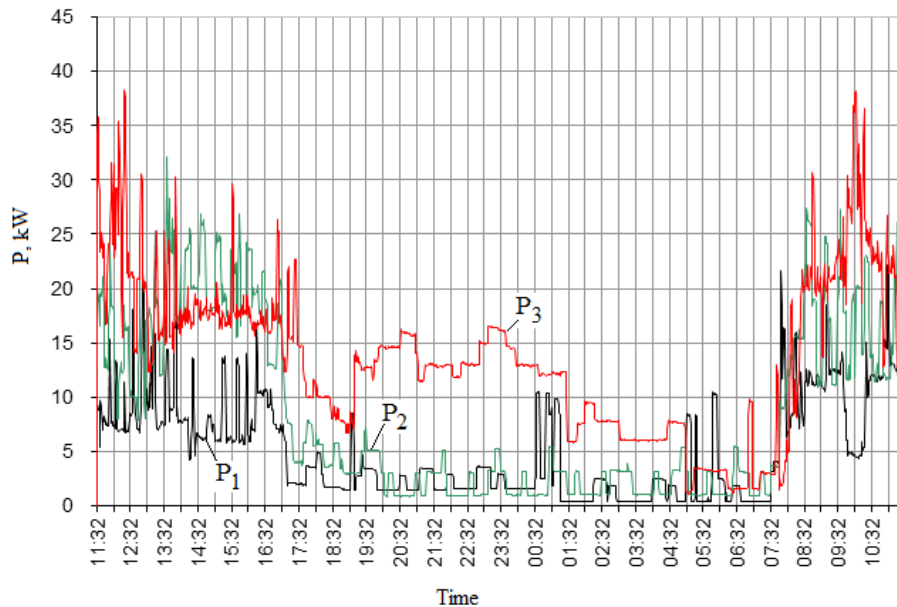


Fig. 2: Daily graphs of changes in active powers for the phases of the network 0.38 kV at the input of the load node.

Due to the asymmetric load of the phases, the voltage asymmetry coefficients in the zero and reverse sequences of the fundamental frequency were significant (Fig. 3). So, for example, the voltage asymmetry coefficient in the zero sequence of the fundamental frequency (K_{0U}) did not fall during the day, even with a minimum (below 2%) load. During periods of greatest power consumption (from 8:00 to 17:00 hours), the voltage unbalance coefficient in the zero sequence of the fundamental frequency often exceeded 5%.

The voltage asymmetry coefficient in the reverse sequence of the fundamental frequency (K_{2U}) during the day had lower values. Moreover, it turned out to be more stable than the coefficient K_{0U} . The range of variation of K_{2U} ranged from 2% to 4%. The results of these studies, as well as an analysis of literature [10-15] indicate that the active use of switching power supplies in electrical appliances leads to an increase in harmonic distortions of voltages and currents in the electrical network. Moreover, the distortion coefficients of

the sinusoidality of the voltages have lower values than the distortion coefficients of the sinusoidality of the load currents.

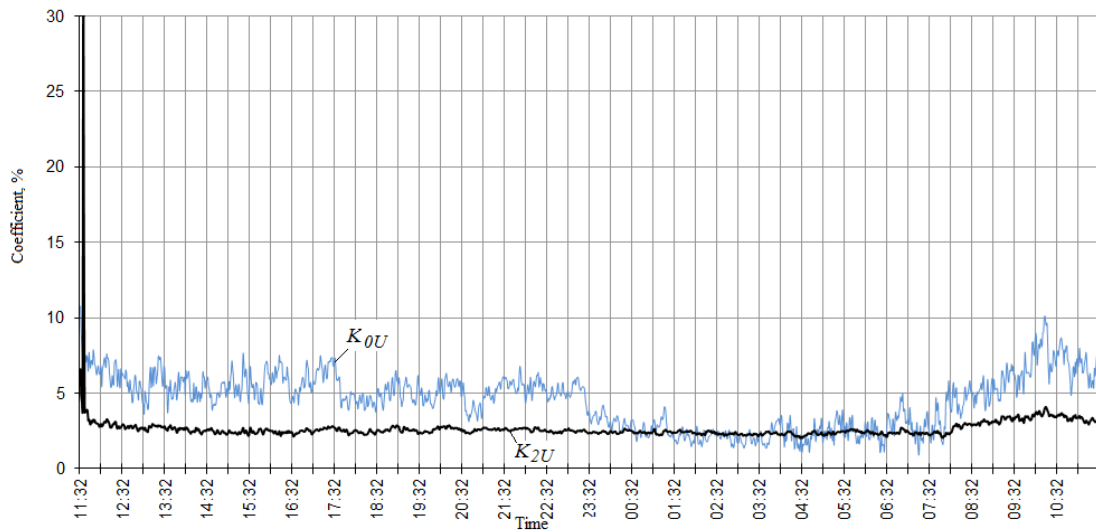


Fig. 3: Diagrams of daily changes in the voltage asymmetry coefficients in the zero and reverse sequence at the input of the load node with the prevailing non-linear power receivers.

Figure 4 shows graphs of daily changes in the distortion coefficients of the sinusoidality of the voltage curves in the phases of the network at the input of the load node 0.38 kV. It should be noted that in none of the phases at the input of the load node, the distortion coefficient of the sinusoidality of the voltage curves did not exceed the minimum allowable value – 8%.

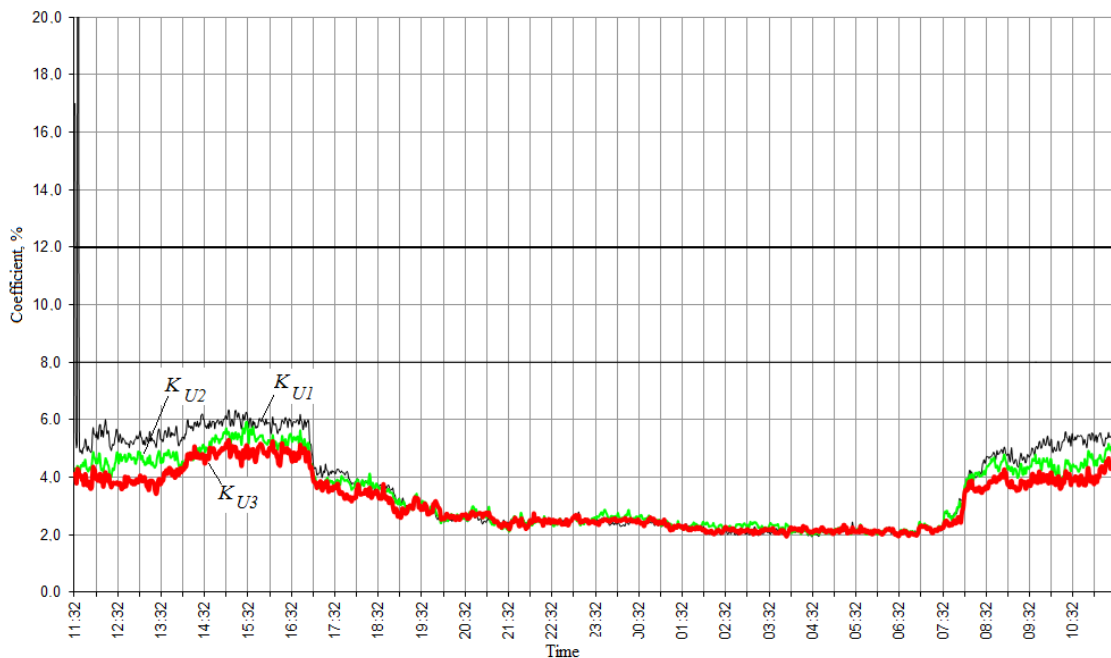


Fig. 4: Diagrams of daily changes in the distortion coefficients of the sinusoidality of the phase voltage curves at the input of the load node with predominant non-linear power receivers.

During periods of maximum load (from 8:00 to 17:00 hours), the distortion coefficient of the sinusoidality of the voltage curve in the first phase K_{UI} was the largest, more than 6% (see Fig. 4). During load shedding, the distortion coefficients of the sinusoidality of the voltage curves in phases became the same (over 2%). The average amplitude-frequency characteristic of the most significant average daily coefficients of the 3rd, 5th, 7th, 9th and 11th voltage harmonics in the phases of the network 0.38 kV at the input to the load node (Fig. 5) clearly show that the odd harmonic voltage components prevail over even ones.

Among the odd higher voltage harmonics, the 3rd, 5th, and 9th harmonics had the largest amplitudes. It should be noted that the largest amplitudes of the 3rd and 5th voltage harmonics were recorded in the first phase, and the 9th voltage harmonic was the largest in the second phase of the network 0.38 kV (Fig. 5). The coefficients of the 3rd voltage harmonic by phase at the input to the load node varied from 4.7% to 5.5%, the coefficients of the 5th voltage harmonic, respectively, from 1.4% to 2.5%, and the coefficients of the 9th voltage harmonic, respectively, from 1.0% to 1.4% (Fig. 5).

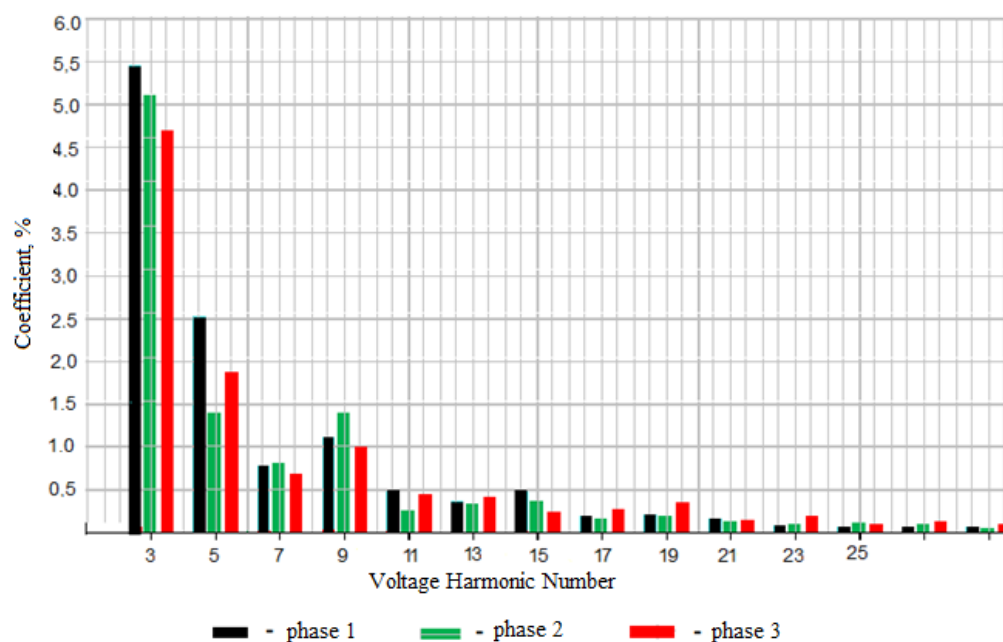


Fig. 5: Frequency response of the most significant daily average coefficients of the n -th harmonic components of the phase voltage at the input of the load node.

3. CHANGES IN CURRENT PARAMETERS AT VARIOUS LOADS OF THE POWER RECEIVER

To assess the degree of distortion of currents sinusoidality during the period of the highest loads, the waveforms of the phase currents and in the zero-working wire at the input of the load node were recorded using the “Hioki 3196” instrument (Fig. 6).

The current waveforms correspond to the time interval on the daily graph of the change in the total active power at the highest load (from 11:40 to 12:00 hours according to the schedule of Fig. 1). An analysis of the current shape in the zero-working wire $i_4(t)$ on the waveform shows (Fig. 6) that it is not substantially sinusoidal. The waveforms of currents in the linear wires of the load node $i_1(t)$, $i_2(t)$ and $i_3(t)$ are also significantly distorted by higher harmonics.

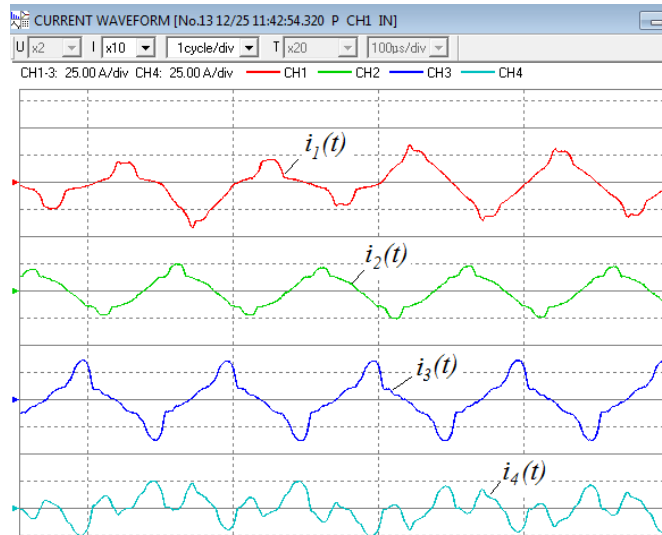


Fig. 6: A fragment of the waveforms of the phase currents and the zero-working wire at the input of the load node with the prevailing non-linear power receivers.

Using the “Hioki 3196” software package, the amplitudes and phases of the currents were determined for seven significant harmonic components not equal to zero (odd harmonics from the 1st to the 13th). For compact recordings, these transformations are presented in the form of Fig. 7, which also shows mathematical models (expressions) of instantaneous current values at the input to the load node.

In Fig. 7, the Fourier expansion is performed up to the 50th harmonic of the current. This allows us to justify the selection of the seven most significant harmonic components of the current by comparison. The sinusoidal distortion coefficients of the curves (see Fig. 7) are denoted by THD (Total Harmonic Distortions) and are called the “total current harmonic distortion coefficient”.

As can be seen from Fig. 5, the values of the sinusoidality distortion coefficients of the current curves THDI1, THDI2 and THDI3 significantly exceed the similar voltage coefficients. In the first linear wire L1 at the input of the load node, the total THDI current distortion factor for the considered time was 23.7%, in the second wire L2 – 15.98%, in the third wire L3 – 36.18%, and in the neutral wire – 138.35%, respectively.

The analysis of the harmonic composition of the current of the zero-working wire $i_4(t)$ is of interest. As can be seen from Fig. 1, in the working (mean square) current I_4 , the proportion of the main harmonic of the current is 6.77 A. The proportion of the third harmonic components of the currents flowing in the linear wires of the network 0.38 kV, in the zero working wire for the considered time point, is 8.9 A, in 5th harmonic current, respectively, 2.33 A, 7th – 0.79 A, 9th – 1.13 A, 11th – 0.51 A and 13th – 0.58 A. In this case, the total current load of the zero-working wire for the considered time was equal to 12.48 A.

With this load mode, the current values in the linear wires of the network 0.38 kV were as follows: $I_1 = 16.63$ A; $I_2 = 13.54$ A; $I_3 = 18.8$ A. That is, the current load of the zero working wire is commensurate with the load of the linear wires. Obviously, the third and ninth current harmonics make the main contribution to the increase in the current load of the zero-working wire to the values of the currents flowing in the linear wires of the network 0.38 kV.

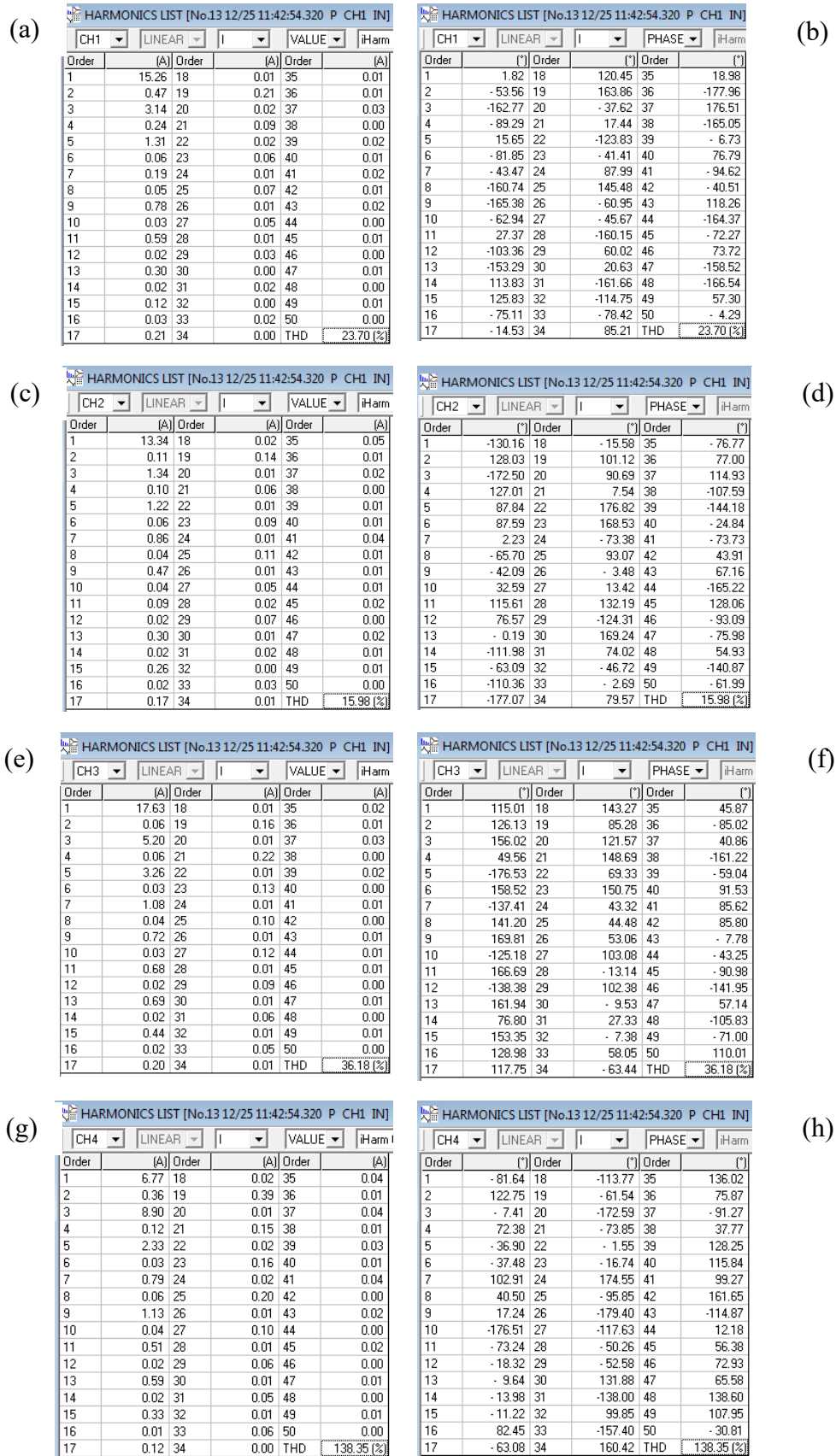


Fig. 7: Vector diagrams of currents and voltages at a frequency of 150 Hz at the input of a load node with predominant nonlinear power consumers:

$$\begin{aligned}
 \text{a), b) } - i_1(t) &= \sqrt{2} \cdot \left(\begin{aligned} &15,26 \sin(\omega t + 2^\circ) + 3,14 \sin(3\omega t - 163^\circ) + \\ &+1,31 \sin(5\omega t + 16^\circ) + 0,19 \sin(7\omega t - 44^\circ) + 0,78 \sin(9\omega t - 165^\circ) + \\ &+0,59 \sin(11\omega t + 27^\circ) + 0,30 \sin(13\omega t - 153^\circ) \end{aligned} \right) \text{A} \\
 \text{c), d) } - i_2(t) &= \sqrt{2} \cdot \left(\begin{aligned} &13,34 \sin(\omega t - 130^\circ) + 1,34 \sin(3\omega t - 173^\circ) + \\ &+1,22 \sin(5\omega t + 88^\circ) + 0,86 \sin(7\omega t + 2^\circ) + 0,47 \sin(9\omega t - 42^\circ) + \\ &+0,09 \sin(11\omega t + 116^\circ) + 0,30 \sin(13\omega t - 0^\circ) \end{aligned} \right) \text{A} \\
 \text{e), f) } - i_3(t) &= \sqrt{2} \cdot \left(\begin{aligned} &17,63 \sin(\omega t + 115^\circ) + 5,20 \sin(3\omega t + 156^\circ) + \\ &+3,26 \sin(5\omega t - 177^\circ) + 1,08 \sin(7\omega t - 137^\circ) + 0,72 \sin(9\omega t + 164^\circ) + \\ &+0,68 \sin(11\omega t + 167^\circ) + 0,69 \sin(13\omega t + 162^\circ) \end{aligned} \right) \text{A} \\
 \text{g), h) } - i_4(t) &= \sqrt{2} \cdot \left(\begin{aligned} &6,77 \sin(\omega t - 82^\circ) + 8,90 \sin(3\omega t - 7^\circ) + \\ &+2,33 \sin(5\omega t - 37^\circ) + 0,79 \sin(7\omega t + 103^\circ) + 1,13 \sin(9\omega t + 17^\circ) + \\ &+0,51 \sin(11\omega t - 73^\circ) + 0,59 \sin(13\omega t - 10^\circ) \end{aligned} \right) \text{A}
 \end{aligned}$$

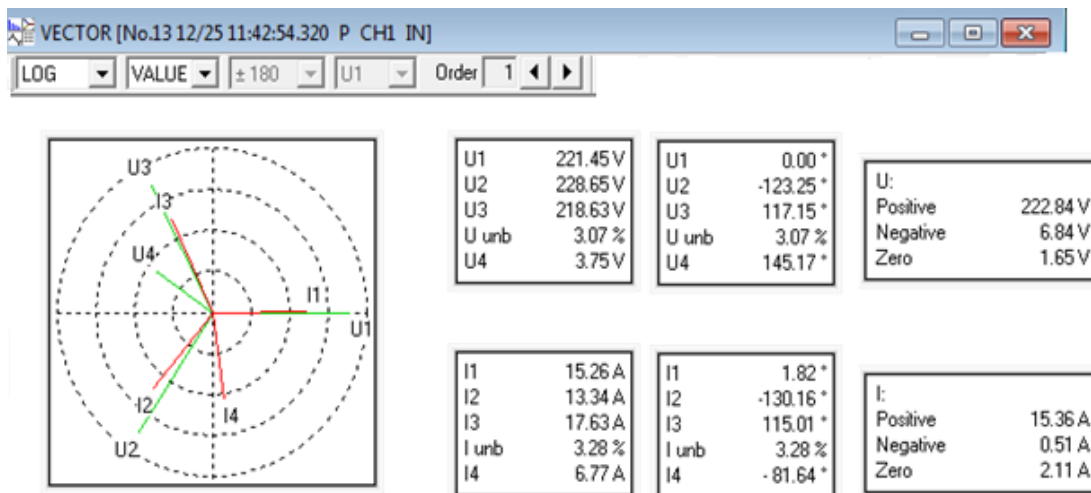


Fig. 8: Vector diagrams of currents and voltages at a frequency of 50 Hz at the input of a load node with predominant nonlinear power consumers.

Figure 8, obtained using the “HIOKI 3196” instrument software, shows the logical vector diagrams of currents and voltages at the input of the load node with prevailing nonlinear power receivers at time 11:42 (see Fig. 1). Along with this, the amplitude of the third harmonic of the current $i_4(t)$ is greater than the amplitude of the fundamental harmonic.

In addition to the current values of voltage and current, the phase shifts of each value are also indicated here. For the first harmonic (frequency 50 Hz) the components of the direct (Positive), reverse (Negative) and zero (Zero) sequences of voltages and currents are given. With these components, real three-phase voltage and current systems can be balanced to a symmetrical system. Similar characteristics for the considered time and frequency of 150 Hz are presented in Fig. 9.

A distinctive feature of the vector diagrams of voltages and currents of the third harmonic (Fig. 9) is the lack of common mode between the vectors of different phases. Along with the lack of phase matching of vectors, they are also characterized by inequality in magnitude. So, for example, the effective current of the third harmonic in the first phase is 3.14 A, in the second phase is 1.34 A, and in the third phase is 5.2 A (see Fig. 1). This is

explained by the nature of the formation of these currents in the load node in case of accidental switching on of various power consumers under different voltages.

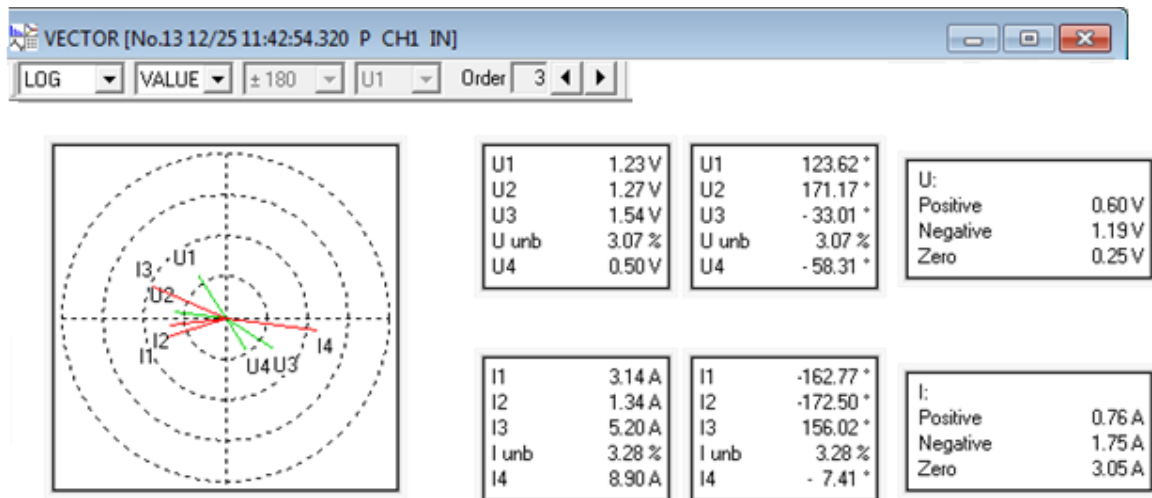


Fig. 9: Vector diagrams of currents and voltages at a frequency of 150 Hz at the input of a load node with predominant nonlinear power consumers.

4. CONCLUSIONS

The research contribution of this work lies in the fact that an experimental study was carried out, the nature of the change in the fundamental harmonic components of the current in the zero-working wire of a three-phase four-wire network with a voltage of 0.38 kV was studied. The results obtained during the work will increase the efficiency of electric power transmission and eliminate the negative consequences due to the current flow in a zero-working wire in the network 0.38 kV.

The analysis of the research results shows that in the presence of non-linear power receivers, the current in the zero-working wire of a three-phase four-wire network is comparable with the currents in linear wires. So, in the maximum load mode, with the current value of the zero working wire current 12.48 A, the currents of the linear wires were $I_1 = 16.63$ A, $I_2 = 13.54$ A, and $I_3 = 18.8$ A, respectively.

Based on the obtained results of the study, it can be argued that the currents of the third harmonic component, which dominate in the neutral working wire of the network 0.38 kV, are not in-phase in the linear wires. The results obtained are of great practical importance when designing technical means that provide current unloading of the zero-working wire of the network 0.38 kV and, ultimately, reduce energy losses during transmission.

REFERENCES

- [1] Grigoriev OA, Petukhov VS, Sokolov VA, Krasilov IA. (2003) On the impact of electronic equipment on power networks. Computer Press, 1. Retrieved from <http://www.compress.ru/article.aspx?id=9553&iid=404>.
- [2] Om PM, Abdul GSh, Neeraj G. (2015) A critical review of detection and classification of power quality events. *Renewable & Sustainable Energy Reviews*, 41: 495-505.
- [3] Daus YV, Yudaev IV, Taranov MA, Voronin SM, Gazalov VS. (2019) Reducing the costs for consumed electricity through the solar energy utilization. *International Journal of Energy Economics and Policy*, 9(2): 19-23.

- [4] Ded AV. (2017) To the problem of the current state of the levels of indices of asymmetry of voltages and currents in networks of 0.4 kV. *Omsk Scientific Herald*, 2(152): 63-65.
- [5] Kosoukhov FD, Vasiliev NV, Kuznetsova ES. (2017) New scientific directions in energy saving in three-phase transformers and four-wire lines with asymmetric, non-linear and reactive loads. *News of St. Petersburg State Agrarian University*, 2(47): 300-309.
- [6] Belitsky AA, Shklyarsky YE. (2018) Estimation of additional power losses in networks with non-linear and asymmetric load. *Bulletin of Tula State University. Technical Science*, 7: 86-93.
- [7] Wang T, Meskin M, Su X, Grinberg I, Wang Z. (2019) Optimal inverter based distributed generation units control strategy to improve voltage profiles in unbalanced distribution networks. *IET Generation, Transmission and Distribution*, 13(21): 4910-4921.
- [8] Zeng XJ, Zhai HF, Wang MX, Yang M, Wang MQ. (2019) A system optimization method for mitigating three-phase imbalance in distribution network. *International Journal of Electrical Power & Energy Systems*, 113: 618-633.
- [9] Zhang B, Wang L, Han X, Meng R, Ren C, Wang Q. (2018) Source current control strategy of active power filters for unbalanced load compensation in three-phase four-wire distribution networks. *Journal of Power Electronics*, 18(5): 1545-1554.
- [10] Deokar SA, Waghmare LM. (2011) Analysis of distribution transformer performance un-der non-linear balanced load conditions and it's remedial. *International Journal of Technology and Advanced Engineering*, 1(2): 152-161.
- [11] Corasaniti VF, Barbieri MB, Arnera PL, Valla MI. (2006) Characteristics of the loads in medium voltage networks from the point of view using active filters. In: *IEEE PES Transmission and Distribution Conference and Exposition: Latin America* (pp. 1-7). 16-19 August, in Caracas, Venezuela. Piscataway: Institute of Electrical and Electronics Engineers.
- [12] Barutskov I.B., Vdovenko S.A., Tsygankov E.V. (2011) Harmonic distortion during operation of frequency converters. *Chief Power Engineer*, 6: 5-13.
- [13] Om PM, Abdul GSh. (2016) Topological aspects of power quality improvement techniques: A comprehensive overview. *Renewable and Sustainable Energy Reviews*, 58: 1129-1142.
- [14] Bodart M, Denejer A, Keppens A, Rikart UR, Rojzin B. (2010) Characteristics of compact fluorescent lamps with integrated ballasts and their comparison with incandescent lamps. *Lighting Engineering*, 2: 18-24.
- [15] Suslov KV, Stepanov VS, Solonina NN. (2013) Effect of high harmonics on electricity consumers in distribution networks. *Proceedings of the 2013 International Symposium on Electromagnetic Compatibility (EMC Europe 2013)*: 841-845.

CHARACTERIZATION AND MELT SPINNING OF POLY (LACTIC ACID)/POLY (ETHYLENE GLYCOL) BLENDS

NUR ATIQAH MOHD AKHIR¹, MAIZATULNISA OTHMAN¹
YOSE FACHMI BUYS², NORHASHIMAH SHAFFIAR¹, DZUN NORAINI JIMAT¹ AND
SHARIFAH IMIHEZRI SYED SHAHARUDDIN^{1*}

¹Department of Mechanical Engineering,
Kulliyah of Engineering,

International Islamic University Malaysia,
Jalan Gombak, 53100 Kuala Lumpur, Malaysia

²Department of Mechanical Engineering, Faculty of Engineering,
University of Malaya, 50603 Kuala Lumpur, Malaysia

*Corresponding author: shaimihezri@iium.edu.my

(Received: 15th February 2020; Accepted: 14th June 2020; Published on-line: 4th January 2021)

ABSTRACT: In this study, melt blended compositions of pure PLA with additions of polyethylene glycol (PEG) up to 30 wt% were prepared. Fourier-transform infrared spectroscopy (FTIR), differential scanning calorimeter (DSC), and thermogravimetric analysis (TGA) were used to investigate the properties of PLA/PEG blends, such as structural, thermal, and morphological properties. The results showed that further increments of PEG cause the -OH group of PLA/PEG blends to show a broad peak, indicating that there is hydrogen bonding interaction between PEG and PLA chains. DSC result revealed that the addition of PEG decreases the glass transition temperature from 57 °C to 46 °C and crystallization temperature from 107 °C to 87 °C. Such trends suggest enhanced chain mobility of PLA chains. TGA thermograms showed that further additions of PEG into PLA resulted in a consistent shift to lower temperature and decrease in thermal stability. Optical microscopy (OM) and scanning electron microscopy (SEM) observations of the melt spun PLA/PEG microfibers revealed that the diameter of the microfibers averaged between 15 to 80 microns.

ABSTRAK: Kajian ini menganalisa komposisi adunan lebur PLA asli bersama tambahan polietilena glikol (PEG) sebanyak 30%. Penjelmaan Fourier spektroskopi inframerah (FTIR), kalorimeter pengimbasan pembezaan (DSC) dan analisis termogravimetri (TGA) telah digunakan bagi mengkaji sifat-sifat adunan PLA/PEG, seperti struktur, terma dan sifat-sifat morfologi. Keputusan menunjukkan penambahan PEG seterusnya menyebabkan kumpulan -OH campuran PLA/PEG memberikan puncak yang lebar, ini menunjukkan ada interaksi ikatan hidrogen antara rangkaian PEG dan PLA. Keputusan DSC menunjukkan penambahan PEG mengurangkan perubahan gelas dari 57 °C kepada 46 °C dan suhu kristalisasi dari 107 °C kepada 87 °C. Trend ini mencadangkan peningkatan pergerakan rangkaian pada rangkaian PLA. Termogram TGA menunjukkan dengan penambahan berterusan PEG ke dalam PLA menghasilkan penurunan konsisten pada suhu dan pengurangan kestabilan haba. Pemerhatian mikroskop optik (OM) dan mikroskopi elektron penskanan (SEM) mikrofiber spun lebur PLA/PEG menunjukkan purata diameter mikrofiber ini antara 15 ke 80 mikron.

KEYWORDS: *microfiber; poly lactic acid (PLA); polyethylene glycol (PEG); melt spinning*

1. INTRODUCTION

The advancement of biodegradable polymers, particularly aliphatic polyester, has attracted curiosity and a great deal of interest among researchers due to their potentials as high performance biomedical and environment-friendly material [1,2]. Examples of aliphatic polyester are poly (lactic acid) (PLA), poly(glycolic acid) (PGA), and poly(caprolactone) (PCL) [3]. In recent years, PLA has received considerable attention due to biodegradability and biocompatibility properties [4]. PLA is one of the renewable resources that are rich in starch such as beetroots, corn, and potato [5] and allowed by the US Food and Drug Administration (FDA) for internal consumption [6,7].

PLA is a suitable candidate to be utilized for biomedical applications since the degradation product of PLA is non-toxic [8]. PLA possesses excellent mechanical properties and good physical properties such as high strength, thermoplasticity, and great processability [2,9]. There are various processing methods such as extrusion, injection molding, blow molding, thermoforming, and fiber spinning that PLA can go through to produce the desirable end product; solid shape, film, or fiber [13,14]. However, pure PLA has a stiff chain back-bone that restricts its plasticity [12] and causes low deformation at break and high modulus [13]. The stiffness of PLA can be improved by blending with other biocompatible plasticizers [14].

Plasticizer is used to increase flexibility and processability of matrix material [15]. Common examples of plasticizer are polyethylene glycol (PEG), polycaprolactone PCL, acetyl triethyl citrate and partial fatty acid esters [16]. In this study, polyethylene glycol (PEG) is used to improve PLA properties since it is non-toxic, miscible and biodegradable [17]. Phuphuak et al. [18] and Pillin et al. [19] stated that plasticizing PLA with PEG facilitates the chain mobility of PLA which results with improved ductility and drawability of the blends. Thus, these PLA/PEG blends can be melt spun into microfiber and potentially be used in biomedical application such as for wound dressings and sutures.

One of the manufacturing processes used to produce fibers is the melt spinning method. The melt spinning method does not require the use of solvents during the drawing process [20], is low in cost, and allows for continuous production of fiber [21]. The polymer material is melted into viscous liquid through the heater at the spinneret and then rapidly solidifies upon extrusion. In this paper, PLA and PEG were mixed at different compositions via melt blending method and were melt spun into microfiber.

2. MATERIALS AND METHODS

2.1 Materials

A pellet form of Poly (lactic acid) was purchased from Nature Works LLC (USA) grade 3052D Natureworks Ingeo TM Biopolymer. Polyethylene glycol flake was purchased from Merck (Darmstadt, Germany).

2.2 Preparation of PLA/PEG Blends

The PLA pellets were placed in a drying oven at 50 °C for an hour to remove moisture before being melt blended with PEG. The PLA/PEG compositions and their sample code are described in Table 1.

PLA, PEG, and PLA/PEG blends were mixed in an internal mixer (Haake PolyLab Rheomix) for 10 minutes at 170 °C mixing temperature with speed of 50 rpm. PLA, PEG, and PLA/PEG melt blended were then crushed using a crusher machine (HITOP, M SY-20)

into smaller pieces. The crushed PLA, PEG, and PLA/PEG blends acquired were then again dried in an oven for minimum an hour at temperature 50 °C to reduce the moisture contents.

Table 1: Composition of PLA/PEG blends sample used in this study

Sample	Ratio (wt %)	
	PLA	PEG
Pure PLA	100	0
95/5 PLA/PEG	95	5
90/10 PLA/PEG	90	10
85/15 PLA/PEG	85	15
80/20 PLA/PEG	80	20
75/25 PLA/PEG	75	25
70/30 PLA/PEG	70	30
Pure PEG	0	100

2.3 Characterization of Melt Blended Compositions

2.3.1 Thermal property

a) Differential Scanning Calorimetry (DSC)

The thermal property test was conducted using a Sapphire DSC (Perkin Elmer Instruments, USA). The DSC was conducted for 2 samples for each composition that were measured in the range of 5–10 mg. Thermograms were obtained when the samples were heated at a temperature of 25 °C – 200 °C at a rate of 10 °C/min in a nitrogen environment. The glass transition temperature (T_g), crystallization temperature (T_c), melting temperature (T_m), melting enthalpy (ΔH_m), and crystallization enthalpy (ΔH_c) of the studied compositions were investigated. The crystallinity degree were also obtained based on Equation 1,

$$X_c (\%) = ((\Delta H_m - \Delta H_c) / \Delta H_o - W) \times 100 \% \quad \text{Equation (1)}$$

Where; ΔH_m = melting enthalpy of the PLA

ΔH_c = crystallization enthalpy of the PLA

ΔH_o = melting enthalpy of 100% crystalline PLA homopolymer 93.6 J/g [21]

W = wt % of PLA

b) Thermal Gravimetric Analysis (TGA)

TGA was conducted using a Simultaneous Thermal Analyzer (STA7300) (Hitachi High Technologies, USA) to determine the thermal property of the PLA, PEG, and PLA/PEG blends. The test was carried out under air atmosphere, heated at room temperature to 600 °C and a rate of 5 °C/min. The initial degradation temperature (T_i) and the final degradation temperature (T_f) were noted and investigated.

2.3.2 Structural Property

Fourier-Transform Infrared Spectroscopy (FTIR) was carried out using an FTIR spectroscopy Spectrum 100 (Perkin Elmer, USA) to characterize the presence and intensity of the functional groups of the studied compositions. The analysis was conducted in the range of 600 cm^{-1} to 4000 cm^{-1} with a resolution of 4 cm^{-1} and a scanning frequency of 16 per sample.

2.4 Melt Spinning and Characterization of PLA/PEG Microfiber

Microfibers of PLA/PEG were drawn using an in-house built melt spinning tower. The microfibers were spun at a spinning temperature of 150 °C – 160 °C and at a spinning speed of 430 rpm. An Olympus Microscope (BX41M, UK) was used to observe the diameter of the melt spun microfibers with a magnification of 20x. The fiber cross-sections were observed using a Scanning Electron Microscope (JEOL JSM-IT 100, Japan). The fiber samples were cut and placed on a double-sided carbon adhesive stub and coated with palladium using a Polaron SC7620.

3. RESULTS AND DISCUSSION

3.1 Fourier-Transform Infrared (FTIR) Analysis

Figure 1 shows the (FTIR) peaks of the PLA, PEG, and PLA/PEG blends. Table 2 represents the peak assignments and wave numbers for the samples.

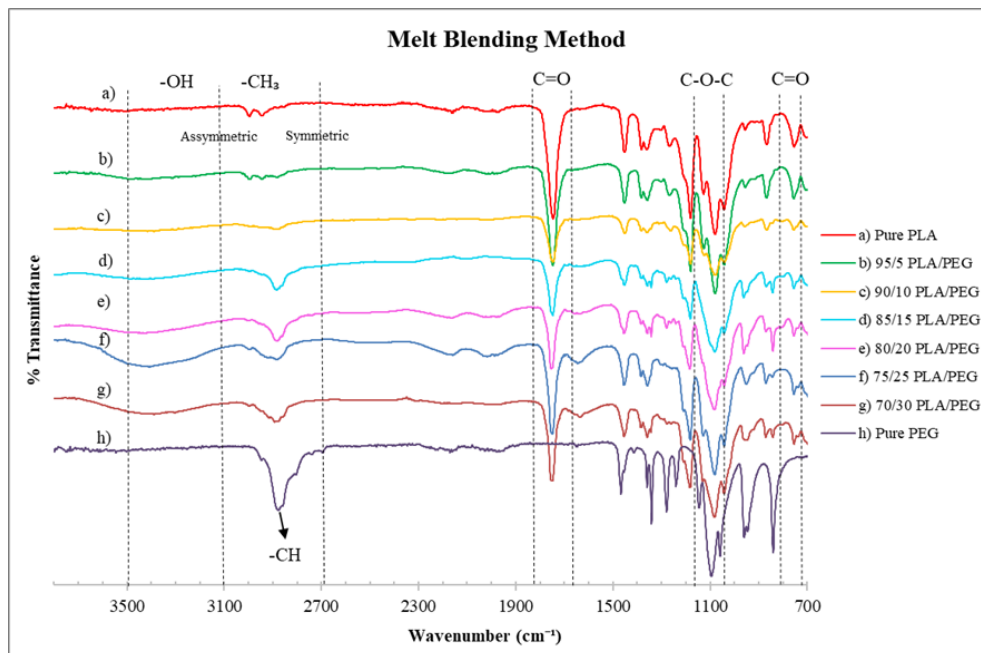


Fig. 1: FTIR spectra of various PLA/PEG blends used in this study.

Table 2: FTIR spectra of various PLA/PEG blends used in this study.

Peak Assignment	Samples wavenumber (cm ⁻¹)				
	-OH	-CH ₃ asymmetric	-CH ₃ symmetric	C=O	C-O-C
Pure PLA	3503	2995	2942	1746; 754	1076
95/5 PLA/PEG	3426	2993	2943	1747; 754	1078
90/10 PLA/PEG	3388	N/A	2881	1747; 756	1078
85/15 PLA/PEG	3427	N/A	2884	1747; 755	1077
80/20 PLA/PEG	3440	N/A	2883	1754; 755	1077
75/25 PLA/PEG	3409	N/A	2886	1749; 755	1080
70/30 PLA/PEG	3388	N/A	2892	1754; 754	1084
Pure PEG	3466	-CH stretching; 2879		N/A	1095

The PLA backbone structure consists of the carbon chain of the carbonyl group (C=O) while PEG structural arrangement is made of C-O-C bonds. The IR spectra of the carbonyl group (C=O) of PLA appears at the frequency region of 754-756 cm^{-1} and 1746-1754 cm^{-1} . Meanwhile, for PEG, the C-O-C group appears at the frequency of 1095 cm^{-1} . The PLA showed peaks of the asymmetrical CH_3 and symmetrical CH_3 at 2995 cm^{-1} and 2942 cm^{-1} , respectively.

It was observed that as the incorporation of PEG increases above 10 wt %, the stretching for asymmetrical CH_3 became invisible (refer Table 2). The FTIR graph showed a strong methylene/methyl band (CH_2/CH_3) at 1470 cm^{-1} and a weak methyl band (1380 cm^{-1}), plus a band between 725-720 cm^{-1} (methylene rocking vibration). The presence of these bands indicates the existence of linear aliphatic structure in the form of long chains. This is attributed to the crystallinity and the formation of a backbone structure with a high amount of regularity in the PLA/PEG blends [22].

The spectra showed only one significant peak of the C-H stretching band. The peak that correlates to C-H stretching became more intense as the amount of PEG wt% increased. The PLA and PEG were melt blended at a temperature of 170 °C and a study by Sarasua et al. [23] suggested that such melt blending process may have resulted in a stronger C-H interaction. The presence of OH functional groups in the PLA structure was confirmed by the presence of a broad peak at 3422 cm^{-1} .

The C-H stretch vibrations for methyl ($-\text{CH}_3$) and methyne ($-\text{CH}$) in PLA and PEG structure, respectively confirm that both compounds are organic-based compounds that contain at least one aliphatic fragment or center. It can be seen that with further increments of PEG wt%, the incorporation of PEG increases, and the -OH group of PLA/PEG blends showed an increasingly broader peak. Thus, it is proposed that interaction of the hydrogen bonds between the two polymers [24,25] have occurred in the PLA/PEG blends. Similar observations were also deduced by Chieng et al. [9]. The author suggested [9] that the hydrogen bonding may have occurred due to intermolecular interaction between the oxygen that is fixed to the carbonyl (C=O) in PLA structure and the hydroxyl ($-\text{OH}$) terminal group present in the PEG molecular structure.

3.2.1 Differential Scanning Calorimetry (DSC) Analysis

The thermogram characteristics are shown in Figure 2 and information on glass-transition temperatures (T_g), crystallization temperatures (T_c), and melting temperatures (T_m) are tabulated and presented in Table 2.

Table 2: The thermal properties of various PLA/PEG compositions used in this study based on DSC analysis.

Sample	T_g (°C)	T_c (°C)	H_c (J/g)	T_m (°C)	H_m (J/g)	X_c (%)
Pure PLA	57.3 ± 0.3	107.6 ± 0.7	31.5	155.3 ± 0.1	32.6	1.2
95/5 PLA/PEG	46.3 ± 0.1	84.1 ± 0.1	21.8	152.8 ± 0.2	29.5	8.7
90/10 PLA/PEG	44.9 ± 0.8	87.4 ± 0.1	21.2	151.5 ± 0.8	36.2	17.9
85/15 PLA/PEG	40.1 ± 1.9	87.1 ± 0.2	16.5	152.7 ± 0.7	38.5	27.7
80/20 PLA/PEG	40.5 ± 0.5	87.4 ± 1.0	13.9	151.8 ± 0.0	33.9	34.2
75/25 PLA/PEG	38.5 ± 0.4	86.7 ± 0.4	1.3	151.5 ± 0.2	34.4	47.1
70/30 PLA/PEG	37.0 ± 0.0	83.3 ± 0.3	3.7	151.6 ± 0.3	32.3	45.8
Pure PEG	-	-	-	67.6	175.9	-

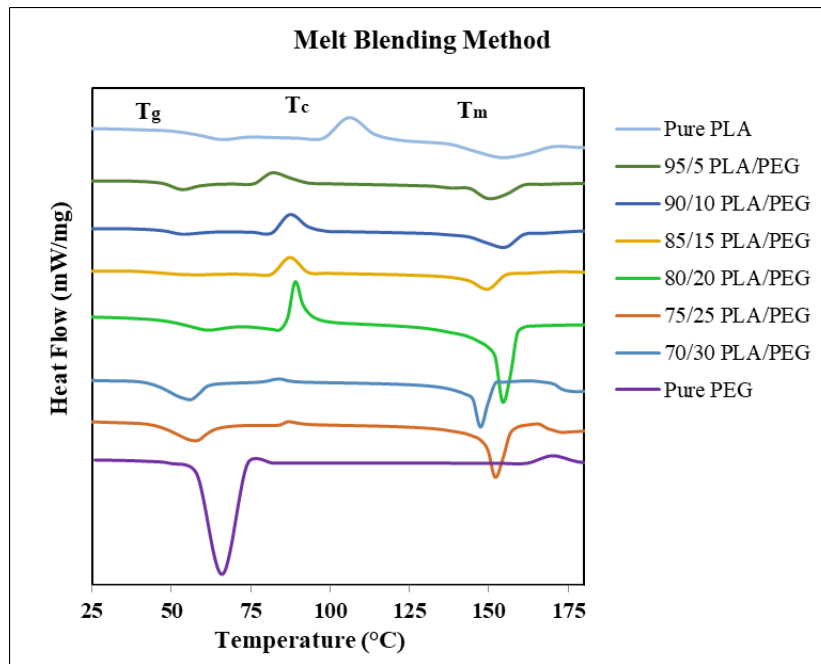


Fig. 2: Characteristics of DSC thermograms of various PLA/PEG compositions used in this study.

The T_g , T_c and T_m values of pure PLA are observed at 57 °C, 107 °C, and 155 °C, respectively. As PEG is added to PLA, the resultant PLA/PEG blends exhibited a trend of decreasing T_g values compared to pure PLA. The decreasing T_g trend with further PEG additions indicates enhanced chain mobility of PLA backbones [2,15,26]. Furthermore, PEG is formed based on a chain structure that allows greater degree of flexibility compared to the chain structure of PLA [16]. Thus, the PEG chains may be able to occupy the intermolecular spaces between PLA polymer chains to form hydrogen bonding [17,27]. The FTIR result (Figure 1) also showed a strong intensity correlated to hydroxyl bonding with further increments of PEG wt %. The decreasing T_g trend was also consistent with the studies by Hashim et al. [27] and Pivsa et al. [2].

The improved mobility of the blends with PEG addition facilitates the crystallization event to occur at lower temperatures. Moreover, Table 2 shows that the blend's crystallinity (X_c) increases as the concentration of PEG increases up to 25 wt % indicating that a good plasticization effect from PEG. However, as PEG was added at 30 wt %, the crystallinity of the PLA/PEG blend slightly decreased to 1.3%. A comparable trend of decreasing crystallinity degrees was also obtained by Li et al. [17] and was proposed due to the separation of the PEG phase in the blend. It is observed that the further increments of PEG into PLA decrease the melting temperature by 3-4 °C. A similar T_m trend was also observed by Chieng et al. [28].

3.2.2 Thermogravimetric Analysis (TGA)

The TGA was performed to identify the thermal properties of the studied compositions. Table 3 shows relevant data of the TGA thermogram for initial degradation temperature (T_i) and final degradation temperature (T_f) of these blends. The TGA thermograms of PLA, PEG, and PLA/PEG blends in the range of 40 °C to 450 °C are shown in Figure 3. It was observed that the studied compositions experienced a single weight-loss behavior. The T_i of pure PLA occurred at 323 °C. It is known that PLA has hydroxyl end groups in the main chain of its molecular structure. According to Song [29] and Maiza [26], hydroxyl end

groups will be critically affected during thermal degradation due to chain-scission which leads to decreasing thermal stability of PLA.

Table 3: The T_i and T_f obtained from TGA for various PLA/PEG compositions in this study

Sample	T_i (°C)	T_f (°C)
Pure PLA	323.3	384.1
95/5 PLA/PEG	315.3	378.6
90/10 PLA/PEG	308.5	374.4
85/15 PLA/PEG	305.1	392.4
80/20 PLA/PEG	306	383.3
75/25 PLA/PEG	304.6	419.2
70/30 PLA/PEG	301	433.6
Pure PEG	230	510

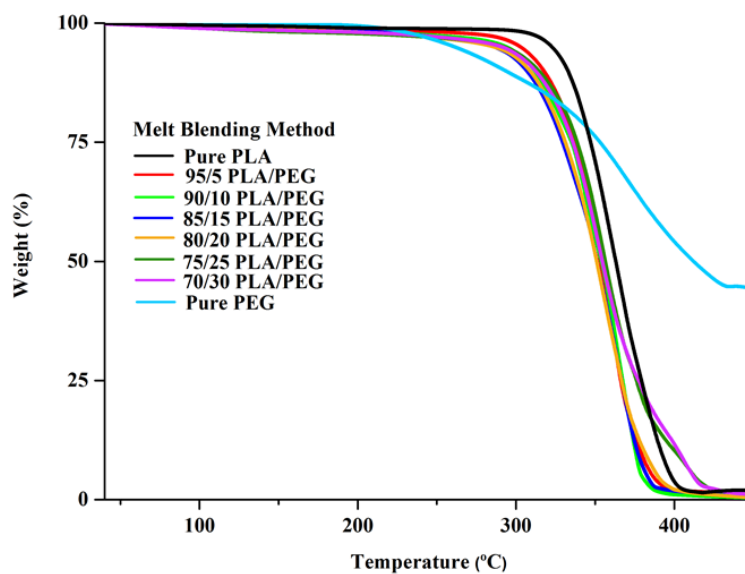


Fig. 3: TGA thermograms for various PLA/PEG compositions used in this study.

Pure PEG only experiences a weight loss of 60% as the temperature reaches 400°C and T_f at 510 °C. Comparable study by Zhang et al. [12] reported that PEG with different (high and low) molecular weight affects the thermal stability of a polymer blend and concluded that high molecular weight of PEG requires extra energy to undergo chain scission due to the longer chain thus indicates higher thermal stability. Septevani & Bhakri [30] and Silverajah et al. [31] proposed that the long polymer chain of PEG functioned as a surface protector of the polymer blends. The presence of the protective layer impedes the permeability of volatile degradation products out from the blend and slows down the degradation of the blend.

Further increments of PEG wt% into PLA resulted with a trend of decreasing T_i temperatures. Other studies have also observed similar trend [12,16]. According to Chieng et al. [28], PEG chains scatter themselves around PLA chains and break the polymer-polymer interactions that led to a decrease in thermal stability. It is necessary to identify the temperature region where thermal degradation will commence to avoid decrease in physical and mechanical properties at the melt spinning temperature for the studied compositions [31].

3.3 PLA/PEG Fibers

3.3.1 Morphological Study

The surface morphologies and diameter of melt spun fibers are depicted in the optical microscope (OM) micrographs at 20x magnifications in Fig. 4. Table 4 shows the average fiber diameter for the PLA and PLA/PEG fibers.

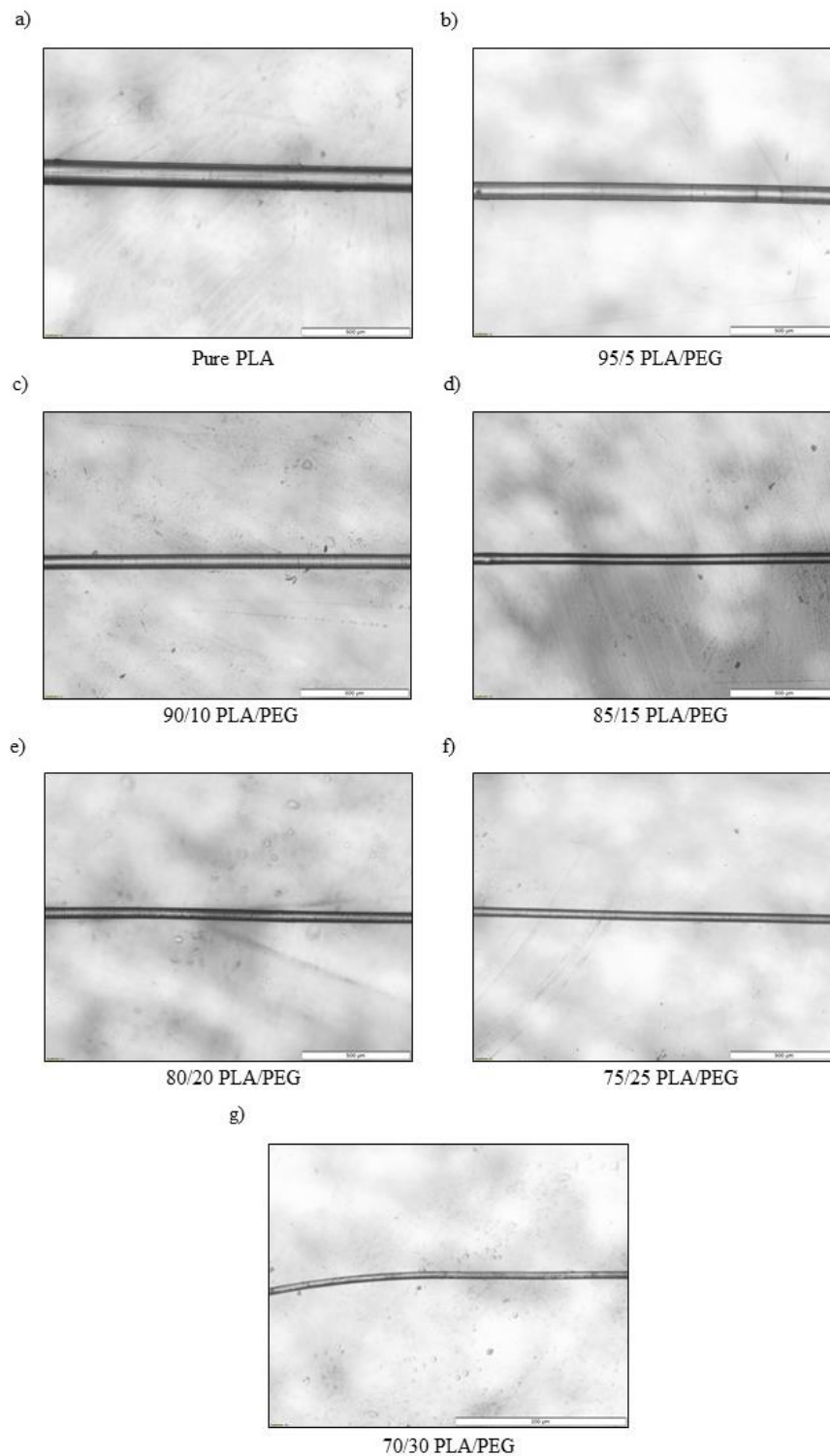


Fig. 4: OM micrographs of the melt spun microfiber for various PLA/PEG compositions used in this study.

It can be observed from Table 4 that the increase of PEG wt % led to a trend of decreasing fiber diameter from 112 μm to 15 μm . It was therefore deduced that the increase in chain mobility (as evidenced in DSC result) further reduced the viscosity of the PLA/PEG blends at the melt-spinning temperature of 150 $^{\circ}\text{C}$ – 160 $^{\circ}\text{C}$. This, in turn, exerted an increase in the degree of flexibility and workability [32] which enables much thinner fibers to be drawn. The OM images (Figure 4) revealed that the melt spinning process produces clear, bead-free, and uniform PLA and PLA/PEG microfibers. The surface and cross-section morphologies of PLA/PEG fibers are depicted in scanning electron microscopy (SEM) micrographs at 500x magnifications in Fig. 5.

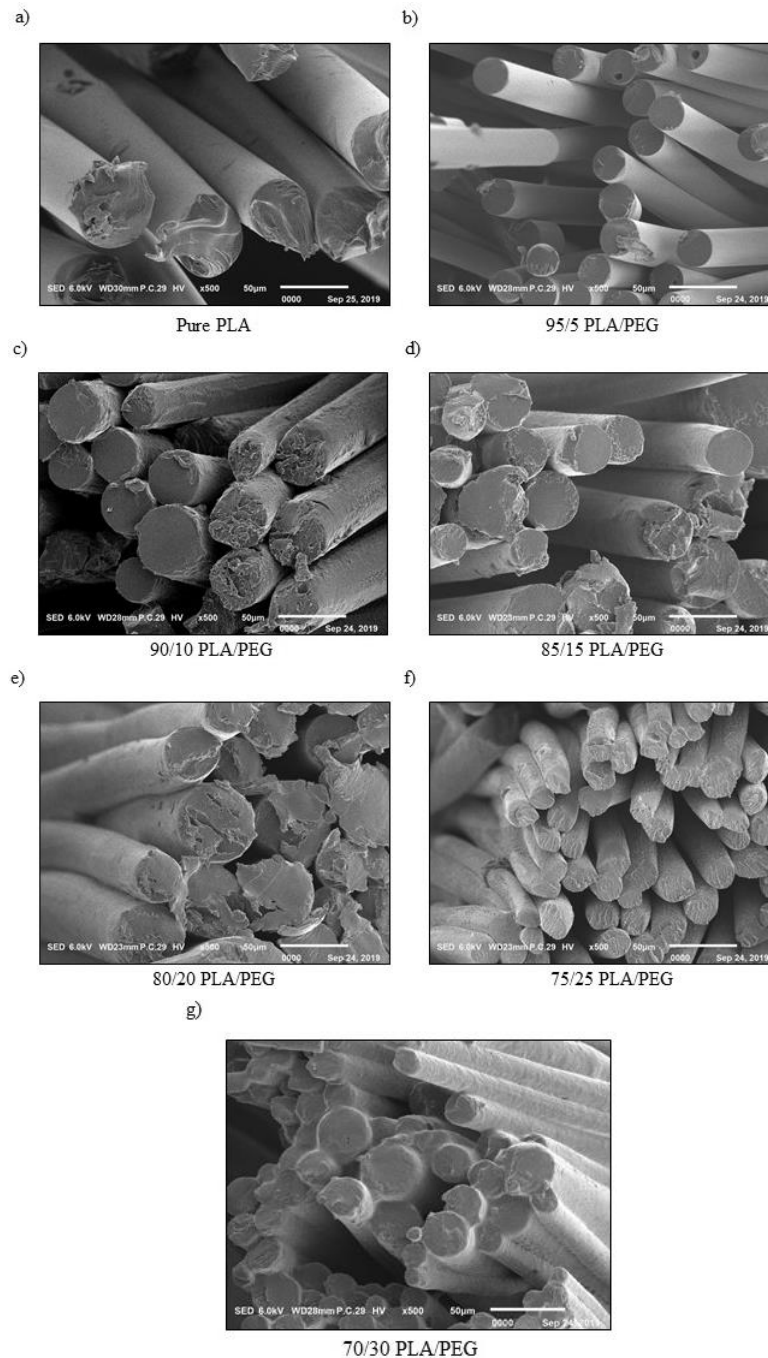


Fig. 5: SEM micrographs at 500x magnification of the melt spun microfiber for various PLA/PEG compositions used in this study.

Table 4: Measured diameter obtained via OM for the melt spun PLA/PEG microfiber

Sample	Fiber diameter (μm)
Pure PLA	112
95/5 PLA/PEG	80
90/10 PLA/PEG	67
85/15 PLA/PEG	60
80/20 PLA/PEG	48
75/25 PLA/PEG	38
70/30 PLA/PEG	15

The SEM micrographs of melt spun PLA and PLA/PEG fibers at spinning temperature 150 °C – 160 °C revealed that all the fibers produced were circular cross-section in shape. PLA fiber has a smooth, uniform morphology, and larger fiber diameter than PLA/PEG fibers. With increasing PEG wt%, it was revealed that the surface of the fiber transitions from smooth to slightly rough. Such rough surface condition is proposed due to thermally induced phase separation of PLA and PEG. Mohamed [33] and Buttaro et al. [34] explained that the tendency for phase separation increases during melt spinning due to its processing conditions such as the distance from the spinneret to take-up wheels and the spinning temperature. Similar surface condition was also noted by Clarkson et al. [35] on microfiber produced via melt spinning method.

4. CONCLUSION

In this study, the effect of PEG addition was structurally and thermally characterized via FTIR, DSC, TGA, and SEM. FTIR results suggest that the intermolecular reaction occurring between hydrogen and oxygen and the carbonyl (C=O) in the PLA structure reacts with hydroxyl (–OH) terminal group in the PEG molecular structure. Such interactions were indicated by the increasing broad peak of –OH group as PEG composition in PLA/PEG blend increased. The crystallinity degrees of PLA/PEG blends showed increasing trend up to 25 wt % PEG indicating a good plasticization effect from PEG. TGA results revealed that the addition of PEG into PLA lowers the T_i and T_f of PLA/PEG. This is attributed to the poor thermal stability of PEG. The melt spinning method was then used to successfully produce bead-free and uniform PLA/PEG microfibers. The mechanical performance of these melt drawn fibers will be investigated in the next phase of this study.

ACKNOWLEDGMENT

This work was fully supported by the International Islamic University Malaysia, IIUM (RIGS17-052-0627). The authors would like to express their deepest gratitude to facilities and technical assistance provided by the International Institute for Halal Research and Training (INHART), IIUM.

REFERENCES

- [1] Farah TMN, Nadia AA. (2014) Study the mechanical and thermal properties of biodegradable polylactic acid/poly ethylene glycol nanocomposites. *International Journal of Application or Innovation in Engineering & Management*, 3(1): 459-464.
- [2] Weraporn P, Kazunori F, Keiichiro N, Yuji A, Hitomi A, Hideki Y. (2016) The effect of poly (ethylene glycol) as plasticizer in blends of poly (lactic acid) and poly (butylene succinate). *Journal of Applied Polymer Science*, 133(8): 1-10.

- [3] Mariya S, Olya S, Nevena M, Iliya R, George A. (2007) Preparation of PLLA/PEG Nanofibers by Electrospinning and Potential Applications. *Journal of Bioactive and Compatible Polymers*, 22(1): 62-76.
- [4] Gupta AP, Vimal K. (2007) New emerging trends in synthetic biodegradable polymers - Polylactide: A critique. *European Polymer Journal*, 43(10): 4053-4074.
- [5] Ching WL, Chun HY, Yueh SC, Tsung CH, Jia HL and Wen HH. (2008) Manufacturing and Properties of PLA Absorbable Surgical Suture. *Textile Research Journal* 78(11): 958-965.
- [6] Yangling C, Shaobo D, Paul C, Roger R. (2009) Polylactic acid (PLA) synthesis and modifications: A review. *Frontiers of Chemistry in China*, 4(3): 259-264.
- [7] Cynthia DCE, Ricardo JA, Jarbas MR, Roberto FSF and Ricardo GS. (2012) Synthesis and Characterization of Poly(D, L-Lactide-co-Glycolide) Copolymer. *Journal of Biomaterials and Nanobiotechnology*, 3: 208-225.
- [8] Lin X, Bo W, Guang Y and Mario G. (2006) Poly(Lactic Acid)-Based Biomaterials: Synthesis, Modification and Applications. In *Biomedical Science, Engineering and Technology*. Edited by Prof. Dhanjoo N. Ghista. InTech; pp 248-282.
- [9] Buong WC, Nor AI, Wan MZWN, Mohd ZH. (2014) Poly(lactic acid)/poly(ethylene glycol) polymer nanocomposites: Effects of graphene nanoplatelets. *Polymers*, 6(1): 93-104.
- [10] Jong-Whan R, Amar KM, Sher PS, Perry KWG. (2006) Effect of the processing methods on the performance of polylactide films: Thermocompression versus solvent casting. *Journal of Applied Polymer Science*, 101(6): 3736-3742.
- [11] Muhammad AAS, Wan AWAR, Rohah AM. (2014) Effect of different solvents on the thermal, IR spectroscopy and morphological properties of solution casted PLA / starch films. *Malaysian Journal of Fundamental and Applied Sciences*, 10(1): 33-36.
- [12] Jianming Z, Shiwei W, Yuhui Q, Qian L. (2016) Effect of morphology designing on the structure and properties of PLA/PEG/ABS blends. *Colloid and Polymer Science*. 294(11):1779–1787.
- [13] Hu Y, Rogunova M, Topolkaev V, Hiltner A, Baer E. (2003) Aging of poly(lactide)/poly(ethylene glycol) blends. Part 1. Poly(lactide) with low stereoregularity. *Polymer*, 44(19): 5701-5710.
- [14] Aswini KM, Smita M, Sanjay KN. (2014) Properties and characterization of biodegradable poly (lactic acid) (PLA)/poly(ethylene glycol) (PEG) and PLA/PEG/organoclay. *J. Thermoplast. Compos. Mater.*, 29(4): 443-463.
- [15] Savitha S, Girija B, Ravichandran K. (2018) Effect of Polyethylene glycol on Mechanical, Thermal, and Morphological Properties of Talc Reinforced Poly(lactic acid) Composites. *Materials Today: Proceedings*, 5(1): 1591-1598.
- [16] Saddys RL, Bernabe LR, Monica AP, Florence PS. (2012) Poly(ethylene glycol) as a compatibilizer and plasticizer of poly(lactic acid)/clay nanocomposites. *High Performance Polymers*, 24(4): 254-261.
- [17] Feng JL, Shui DZ, Ji ZL, Jun ZW. (2015) Effect of polyethylene glycol on the crystallization and impact properties of polylactide-based blends. *Polymer Advanced Technologies*, 26: 465-475.
- [18] Yupin P, Yong M, Philippe Z, Suwabun C. (2013) Balancing crystalline and amorphous domains in PLA through star-structured polylactides with dual plasticizer / nucleating agent functionality. *Polymer*, 54:7058-7070.
- [19] Isabelle P, Nicolas M, Yves G. (2006) Thermo-mechanical characterization of plasticized PLA: Is the miscibility the only significant factor? *Polymer*, 47(13): 4676-4682.
- [20] Nor AI, Wan MZWN, Maizatunisa O, Khalina A, Kamarul AH. (2010) Poly (Lactic Acid) (PLA)-reinforced kenaf bast fiber composites: The effect of triacetin. *Journal of Reinforced Plastics and Composites*, 29(7): 1099-1111.
- [21] Gupta VB, Kothari VK. *Manufactured Fibre Technology*, First Edit. Chapman & Hall, 1997.
- [22] Kurniawan Y, Yohanes AP, Setyo P, Bruce AW, Hadi KP, Titi CS. (2016) Infrared and Raman studies on polylactide acid and polyethylene glycol-400 blend. *AIP Conference Proceedings*. 1725, 020101.
- [23] Jose-Ramon S, Nerea LR, Alberto LA, Emilio M. (2005) Stereoselective crystallization and specific interactions in polylactides. *Macromolecules*, 38(20): 8362-8371.

- [24] Yong J, Xin-Yao Y, Tao L, Mei-Yun Z, Jin-Huia L, Xing-Jiu H. (2013) PEG aggregation templated porous ZnO nanostructure: Room temperature solution synthesis, pore formation mechanism, and their photoluminescence properties. *CrystEngComm.*, 15(18): 3647-3653.
- [25] Decai L, Yang J, Shanshan L, Xiaojing L, Jiyou G, Qifeng C, Yanhua Z. (2018) Preparation of plasticized poly (lactic acid) and its influence on the properties of composite materials. *PLoS One*, 13(3): 1-15.
- [26] Mounira M, Mohamed TB, Guilhem Q, Valerie MN. (2015) Biobased additive plasticizing Polylactic acid (PLA). *Polimeros*, 25(6): 581-590.
- [27] Norazlina H, Kamala R, Santhoshini S, Kamal Yusoh. (2015) Effect of Processing Method on Thermal Behavior in PLA/PEG Melt Blending. *Advanced Materials Research*, 1134: 185-190.
- [28] Buong WC, Nor AI, Wan MZWN, Mohd ZH. (2013) Plasticized Poly (lactic acid) with Low Molecular Weight Poly (ethylene glycol): Mechanical, Thermal and Morphology Properties. *Journal of Applied Polymer Science*, 130(6): 4576-4580.
- [29] Yan PS, De YW, Xiu LW, Ling L, Yu ZW. (2011) A method for simultaneously improving the flame retardancy and toughness of PLA. *Polymer advanced technologies*, 22(12):2 295-2301.
- [30] Athanasia AS, Samsul BI. (2017) Plasticization of poly (lactic acid) using different molecular weight of poly (ethylene glycol). In *Proceedings of the 3rd International Symposium on Applied Chemistry: 23–24 October 2017; Jakarta, Indonesia. Volume 1904. Issue 1.*
- [31] Giita S, Nor AI, Norhazlin Z, Wan MZWY and Hazimah AH. (2012) Mechanical, thermal and morphological properties of poly(lactic acid)/epoxidized palm olein blend. *Molecules*. 17(10): 11729–11747.
- [32] Melissa GAV, Mariana AS, Lucielen OS, Marisa MB. (2011) Natural-based plasticizers and biopolymer films: A review. *European Polymer Journal*. 47(3):254–263.
- [33] Khayet M. (2015) Melt Spinning. *Encyclopedia of Membranes*.
- [34] Larissa. MB, Erin D, Margaret WF. (2014) Phase separation to create hydrophilic yet non-water soluble PLA/PLA-b-PEG fibers via electrospinning. *Journal of Applied Polymer Science*, 131(19): 1-7.
- [35] Caitlyn MC, Sami MEAA, Reaz C, Shoumya NS, James S, Gregory S, Volkan O, Jeffrey PY. (2019) Melt Spinning of Cellulose Nano fibril/Polylactic Acid (CNF/PLA) Composite Fibers for High Stiffness. *Applied Polymer Material*, 1:160-168.

GRAPHENE OXIDE MICROCAPSULES (GOMs) WITH LINSEED OIL CORE VIA PICKERING EMULSION METHOD: EFFECT OF DISPERSE SPEED

NURUL NADIAH SAHIR¹, NOOR AZLINA HASSAN^{1*}, NORITA HASSAN¹
AND NORHASNIDAWANI JOHARI²

¹*Department of Manufacturing and Materials Engineering,
International Islamic University Malaysia,
Jalan Gombak, 53100 Kuala Lumpur, Malaysia*

²*Department of Mechanical Precision Engineering,
Malaysia-Japan International Institute of Technology,
UTM, 54100 Kuala Lumpur, Malaysia*

*Corresponding author: noorazlina_hassan@iium.edu.my

(Received: 25th March 2020; Accepted: 3rd September 2020; Published on-line: 4th January 2021)

ABSTRACT: Graphene oxide microcapsules (GOMs) have been prepared through Pickering emulsion method by varying the disperse speed to study its effect on the GOM's size. The GOMs were characterized through phase separation observation, polarized optical microscope (POM), and particle size analyser (PSA). Phase separation observation showed more viscous and cloudy emulsion was produced when the disperse speed was increased. After 24 hours, only 800 rpm emulsion did not show any phase separation. POM characterization depicted that increasing the emulsification energy led to the finer emulsion with the 1200 rpm sample showing the smallest microcapsule size of around 8 μm . However, PSA analysis suggested that although the disperse speed controls the GOMs size, the amount of GO in the emulsion plays an important role for the microcapsule to maintain its stability. Emulsion produced at 800 rpm possesses satisfactory stability with GOMs diameter of 11.15 μm . The result also suggested that graphene oxide encapsulated linseed oil may act as a promising candidate for healing microcapsules in a self-healing coating system.

ABSTRAK: Mikrokapsul graphene oksida (GOMs) telah dihasilkan melalui kaedah emulsifikasi Pickering dengan memvariasikan tenaga pengemulsi untuk mengkaji kesannya terhadap saiz GOMs. GOMs dicirikan melalui pemerhatian pemisahan fasa, mikroskop optik polarisasi (POM) dan penganalisis saiz zarah (PSA). Pemerhatian pemisahan fasa menunjukkan emulsi yang lebih likat dan keruh dihasilkan apabila kelajuan pengemulsi meningkat. Selepas 24 jam, hanya emulsi 800 rpm tidak menunjukkan pemisahan fasa. Pencirian POM meunjukkan bahawa peningkatan tenaga pengemulsi menghasilkan emulsi yang lebih halus dengan sampel 1200 rpm menunjukkan saiz mikrokapsul terkecil, sekitar 8 μm . Walau bagaimanapun, analisis PSA mencadangkan bahawa walaupun kelajuan pengemulsi mengawal saiz GOMs, jumlah GO dalam emulsi memainkan peranan penting untuk mengekalkan kestabilan mikrokapsul. Emulsi yang dihasilkan pada 800 rpm mempunyai kestabilan yang memuaskan dengan purata saiz GOMs sekitar 11.15 μm . Berdasarkan dapatan kajian, graphene oksida yang terkandung minyak biji rami boleh menjadi salah satu mikrokapsul penyembuh dalam sistem cat auto-semboh.

KEYWORDS: *graphene oxide; Pickering emulsion; linseed oil; microcapsules*

1. INTRODUCTION

Graphene oxide (GO), is the most important derivative of graphene. GO is a two-dimensional material that consists of partially broken sp^2 -bonded carbon networks. Phenol, hydroxyl and epoxide groups occupy the basal planes of the sheet and carboxylic acid groups attached to the edges make the GO sheet possess the amphiphilic property and be readily dispersed in water or any solvent [1]. Although the thickness of the GO sheet is only in nanometers, its excellent impermeability indicates GO possesses a superior barrier property [2]. Many researchers utilize this advantage by incorporating the GO sheets into a protective coating for metals, polymer membranes for gas barrier films, and water treatment applications [3-5]. Di et al. found that GO incorporated coating exhibits good anti-corrosion properties by delaying the migration of corrosive species to the underlying substrate, while Ammar et al. reported that the gas barrier property of GO infused polymer increased dramatically [6,7].

GO has also been utilized in liquid crystals (LC) for various applications such as supercapacitors, sensors, optical-switching devices, and also graphene oxide-based foam and aerogel for sound absorbers [8-11]. Graphene oxide liquid crystals (GOLCs), a highly anisotropic fluid consist of the long-range crystal-like ordering of GO. This latest class of 2D nanomaterials possesses colloidal liquid crystallinity contributed by their intrinsic disc-like shape anisotropy [12]. As reported by Abedin et al., water is the most reported media for GOLC due to the extensive hydrogen bonding [13]. The colloidal system containing 2D GO sheets can be effectively aligned by external shear force because of their self-alignment ability in nematic phases. Jalili et al. suggested that this behaviour makes the GOLC suitable to synthesize macroscopic objects such as fibers, film, membranes, and foams [14].

This paper reports on the utilization of GOLCs to encapsulate the healing agent as the potential candidate for a healing agent reservoir in a self-healing coating. The graphene oxide microcapsules (GOMs) were synthesized through the Pickering emulsion method. Pickering emulsion is an emulsion of any type, whether oil-in-water (O/W) or water-in-oil (W/O) stabilized by solid particles [15]. The interesting differences between the Pickering emulsions compared to the classical emulsion are the absence of surfactant, superior stability, and low toxicity [16]. By employing GO as the stabilizer in the Pickering emulsion system, it is possible to tailor microscopic capsules due to its surface flexibility and strong van der Waals force between individual GO sheets [17]. The excellent barrier properties of GO sheets also make them suitable candidates to store the healing agent in self-healing coatings where the impermeability to diffusion is needed [18].

The core material for the GOMs, linseed oil (LO), is the most popular seed extract for corrosion inhibition and was also reported as a hydrophobic agent [19]. It is a type of drying oil that undergoes oxidative polymerization if it is exposed to the atmosphere [20]. Linseed oil has been encapsulated within various materials including poly(urea) formaldehyde (PUF), ethylcellulose and poly(methyl methacrylate) for self-healing coating application [21-23]. In this research, GOMs is produced by using only GO sheets and linseed oil with the help of high shear stirring. The disperse speed is varied to study their effect on the microcapsule's size. The optimum shear speed for the fabrication of GOMs is proposed for their application in water-based self-healing coating for future works.

2. MATERIALS AND METHOD

GOMs were synthesized through the Pickering emulsion method as discussed by Li et al. [24]. The disperse speed (rpm) is the parameter that affects the microcapsule's size. Briefly, GOMs were prepared by adding 0.37g linseed oil (Sigma Aldrich, 0.93 g/ml) into

the 5 ml graphene oxide solution (Hummer method, Graphene SupermarketTM, 3.7 mg/ml) followed by mixing it with an overhead stirrer for 10 minutes. The disperse speed (rpm) was varied (400, 800, 1200, 1600, 2000, and 2400 rpm) while maintaining the same amount of GO concentration. The emulsion formed is then transferred to 7 ml polyethylene vials.

The resultant emulsions were characterized through phase separation observation and polarized optical microscope (POM) (model: LEXT OLS4100). The emulsions formed were viscous and not suitable for optical microscope characterization. To capture the image clearly, the emulsions were diluted with deionized water with a dilution factor of 3. Then, they were dropped onto the surface of a glass slide and characterized immediately. The GOMs size is recorded based on the POM images. The coefficient of variation, C_v of the GOMs was calculated by using the Eq. (1) below:

$$\text{Coefficient of Variation } (C_v) = \frac{\text{standard deviation}}{\text{mean size of GOMs}} \quad (1)$$

Droplet size distribution for oil-in-water emulsions was analyzed by Particle size analyzer (PSA) (model: Malvern Zetasizer Nano). The refractive index is set to 1.4795 (linseed oil).

3. RESULTS AND DISCUSSION

3.1 Phase Separation Observation

To study the effect of emulsification energy on the properties of the emulsions formed, the disperse speed was varied from 400 to 2400 rpm. Figure 1 shows the digital images of the emulsions right after the synthesis. Emulsion in Fig. 1(b) to 1(f) showed a successful emulsification process based on the cloudy appearance. Emulsion tends to appear cloudy because the light is scattered off the phase interphases between the oil and water components [25]. The visible cloudiness is also an indication that the GOMs produced are in micron-ranges [26]. As reported by Kim et al. GO sheets can stabilize the linseed oil in water as they could behave like a colloidal surfactant [27].

By increasing the mixing speed, the emulsion is observed to be more viscous. This is also another indication that the size of the GOMs is reduced and the amount of the GOMs is increased, which in turn increases the interfacial area. An early study by Thompson et al. found that the increase in the interfacial area led to an increase in interfacial viscosity effects and also an increase in hydrodynamic interactions [28]. Gohtani & Yoshii also reported the same phenomenon where the emulsion diameter was found to significantly affect the emulsion viscosity, in which the viscosity increased as the emulsion diameter decreased [29].

Emulsions as shown in Fig. 1(a), stirred with low rpm, showed not all solid particles and oil participate in the emulsification process. This can be proven by the formation of two different phases with the oil phase occupying the upper part of the mixture. The dark brown colour of the lower water phase shows that there is a large amount of GO left in the water. The emulsification energy supplied for emulsion (a) is not sufficient enough to fully emulsify the linseed oil. As the disperse speed increased, the colour of the emulsion becomes lighter, as depicted by the colour bar in Fig. 1.

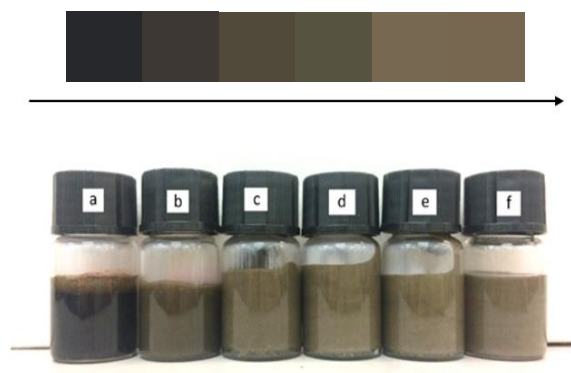


Fig. 1: Digital image of the emulsions formed with different rotational shear speed a) 400 rpm, b) 800 rpm, c) 1200 rpm, d) 1600 rpm, e) 2000 rpm, and f) 2400 rpm.

Based on Fig. 2, the emulsion prepared at 800 rpm is the only sample that showed no phase separation layer, while destabilization occurred to the rest of the emulsion. The bottom part was occupied by the continuous phase, while the top region or the creaming part was rich with the GOMs. It was postulated that the destabilization happened due to an insufficient amount of GO sheets to stabilize the GOMs.

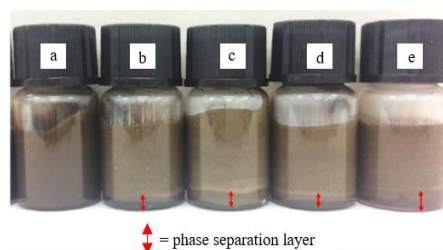


Fig. 2: Digital images of emulsions containing GOMs prepared with varied disperse speed monitored after 24 hours, a) 800 rpm, b) 1200 rpm, c) 1600 rpm, d) 2000 rpm, and e) 2400 rpm.

3.2 Polarized Optical Microscope (POM) Analysis

POM characterization was done directly after the emulsification process. The images in Fig. 3 showed that GOMs were present in all samples, based on the existence of bright shining halos around the emulsion droplets. Under normal light, the milky emulsion was difficult to observe. Therefore polarized light was needed. The presence of shining halos around the oil droplets suggested the GO sheets assembled themselves at the liquid-liquid interface. The distinct shining halos observed indicate the emulsion was isotropic except for the bright GO shells. The birefringence has a cross-shape that originates from the presence of oil droplets in the anisotropic colloidal structure [30]. Note that emulsions formed without GO do not behave in this way due to the fact that they are optically isotropic, which means they cannot emit the liquid crystal behaviour [31]. The liquid crystal structure is formed when GO align themselves around the oil droplets and these molecularly ordered GO sheets are what gave off the birefringence property, which is a typical fingerprint of liquid crystals [32]. Therefore, it shows that GOMs were successfully obtained.

GO sheets tend to localize between the liquid-liquid interface to minimize the interfacial energy between two immiscible liquids (linseed oil and water). The high surface area of the

GO sheets enables them to wrap around the linseed oil droplets. The wettability of GO also made this possible. The wettability test done by Panda et al. showed that GO obtained through Hummer method possess the contact angle (θ_w) of less than 90° , which is around 46.5° [33]. The test involves the measuring of the contact angle between the GO film and water. This indicates that GO is partially hydrophilic and prone to stabilize oil-in-water (O/W) emulsion due to its particle surface resides more in water than in oil. This is in line with our experimental results. GOMs are readily dispersed in water, implying the formation of an O/W emulsion system with linseed oil droplets as the dispersed phase and GO solution making up the continuous phase.

Figure 3 also showed the images of GOMs with uneven size distribution and as the shear speed was increased, finer and more even microcapsule sizes were produced. The average size and coefficient of variation (C_v) for each emulsion listed in Table 1 also supported the finding. As the speed increased, the value of C_v decreased, indicating a low variation of droplets diameter [34]. This is in good agreement with Chevalier & Bolzinger suggesting that in Pickering emulsion, a high energy emulsification process can break the oil into small droplets resulting in finer emulsions [35].

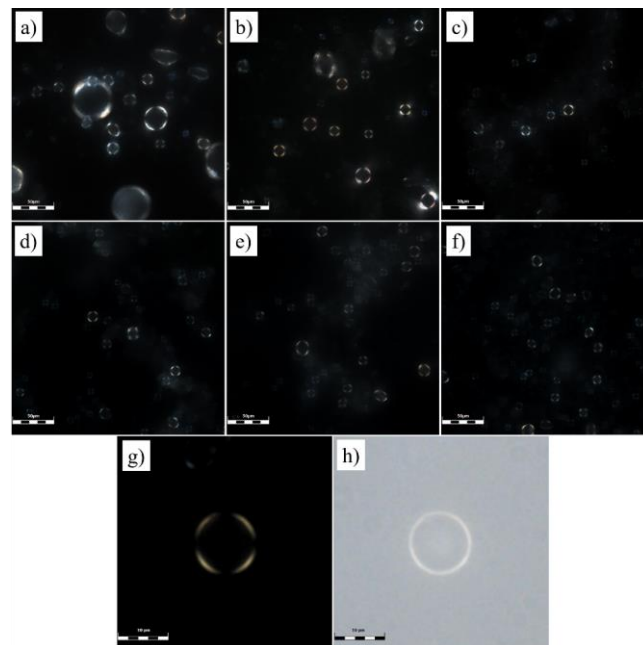


Fig. 3: Image of the emulsion under a polarized optical microscope, a) 400 rpm, b) 800 rpm, c) 1200 rpm, d) 1600 rpm, e) 2000 rpm, f) 2400 rpm, g) single GOM under polarized light and h) single GOM under optical microscope.

Table 1: Average size and C_v value for each emulsion

Disperse Speed [rpm]	Average Size [μm]	Coefficient of Variation [C_v]
400	20.36	0.73
800	11.15	0.34
1200	8.57	0.31
1600	8.33	0.26
2000	8.02	0.29
2400	8.11	0.24

To further understand the GOMs formation, Fig. 4 depicts the schematic representation of the preparation process and encapsulation mechanism. An overhead stirrer breaks the oil

into small droplets (Fig. 4b) followed by the stabilization of the oil droplets by hydrophilic GO sheets that assembled themselves at the oil-liquid interface (Fig. 4c). Figure 4(d) showed the desired final product that was called graphene oxide encapsulated linseed oil, or graphene oxide Pickering emulsion or GOMs.

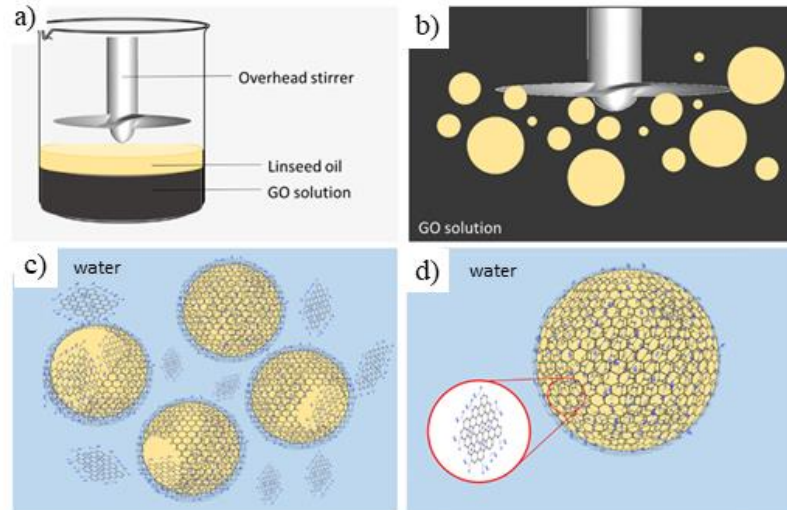


Fig. 4: Encapsulation process, a) Emulsion preparation, b) Breaking of linseed oil into small droplets by the propeller, c) GO sheets assembled themselves around the linseed oil droplets, d) stabilized Pickering emulsion (GOMs).

It needs to be noted that a small microcapsule with an even size distribution is more favourable to be used in self-healing coatings. The incorporation of the bigger container into the coating can disrupt the barrier properties and reduce the coating resistance [36]. Although increasing the shear speed does decrease the microcapsule's size, there is no significant size reduction observed for the GOMs when the disperse was higher than 1200 rpm. This might be due to the oil droplets reaching their maximum limit to further break down into smaller droplets and a limited amount of GO sheets to stabilize them.

3.3 Particle Size Analyzer (PSA) Analysis

Figure 5 displays the size distribution for all emulsions. As the size of the GOMs did not change much when they were prepared at 1200 rpm and above, only four emulsions were characterized. In contrast with POM results, the result obtained from particle size analyzer showed a different trend where the droplet size increased as the disperse speed was increased. The PSA result showed GOMs prepared with the disperse speed of 400 rpm exhibits the smallest size compared to others but its POM result displayed the emulsion is only partially stabilized. It should be noted that the sample taken for PSA characterization is from the continuous phase and not from the creaming part.

The PSA characterization was done after 24 hours which allowed the emulsions to settle down. This phenomenon explains why the increasing trend happened. The oil droplets were able to maintain their size for a while but after a few hours, they started to coalesce due to lack of stabilizing moieties. Increasing the shear speed breaks the oil into small droplets, resulting in the increasing amount of droplets present in the continuous phase. This will also cause the surface area of the droplets to increase, thus, requiring more GO particles to wrap the linseed oil droplet and form a stable emulsion. This result is also supported by the phase separation observation discussed in section 3.1 previously. It is worth mentioning that other stabilizers or surfactants could be added to hold the GOMs structure to maintain their sizes

prior to the PSA characterization. However, POM analysis may give more accurate and reliable results as the GOMs used in this study only utilized GO sheets as a stabilizer.

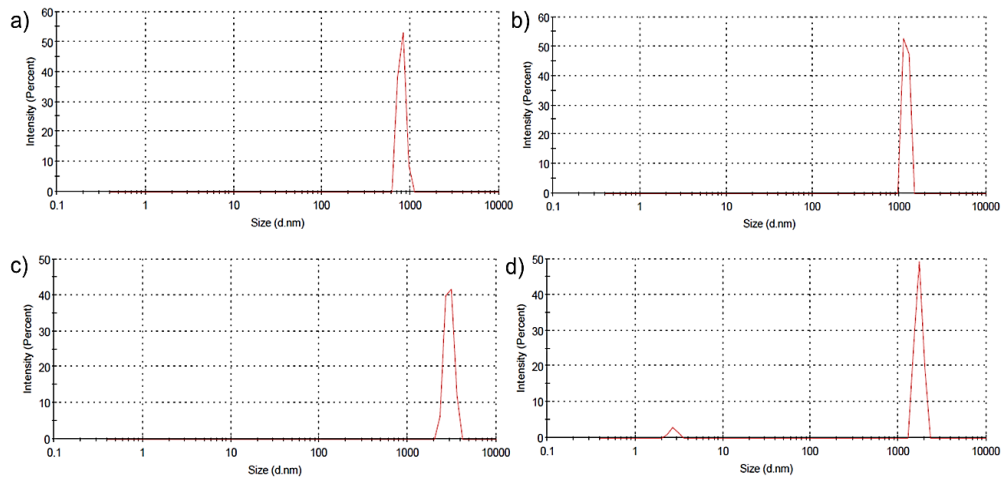


Fig. 5: The droplet size distribution of GOMs, a) 400 rpm, b) 800 rpm, c) 1200 rpm and d) 1600 rpm.

This finding implied that the disperse speed and stabilizing moieties go hand in hand and controlling only one parameter is not enough to produce stable GOMs. Studies done by Tsabet & Fradette also supported the above-mentioned observations. They suggested that by increasing the energy will promote droplet generation and produce a larger interface, and the amount of stabilizing particles also need to be increased to cover and stabilize the interface [37].

Figure 6 displays the GOMs size comparison obtained through POM and PSA. There are some discrepancies between POM and PSA results as the POM measures the GOMs diameter which includes the GO shell thickness, while PSA measures only the linseed oil droplet's diameter. Nevertheless, the increasing size pattern that comes from the PSA analysis needs to be taken into account and cannot be ignored. By comparing POM and PSA analysis, 800 rpm is the preferable speed for the preparation of GOMs with satisfied microcapsule size. This was further supported by the phase separation observation discussed in section 3.1, where only GOMs prepared at 800 rpm maintained its stability.

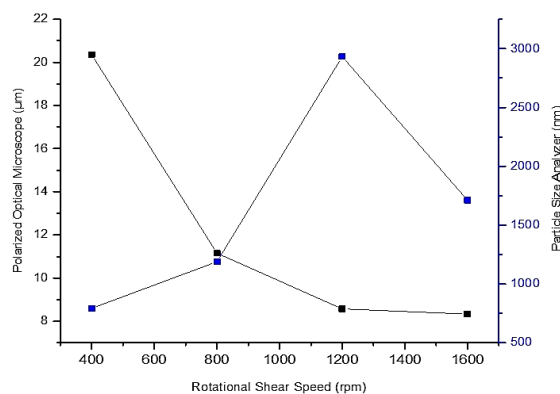


Fig. 6: Average size distribution based on POM images and PSA of the emulsions.

4. CONCLUSION

GOMs were successfully produced through the Pickering emulsion method. The POM analysis showed the disperse speed affects the size of the produced GOMs, where insufficient emulsification energy led to a partially stabilized emulsion. However, PSA analysis suggests the GO-HMs size depends on both disperse speed and the amount of stabilizing moieties. Controlling only one parameter is not sufficient to produce fine and stable emulsions. Although POM images showed that the disperse speed of 1200 rpm produced the smallest diameter of GOMs (around 8 μm), considering the PSA pattern and phase separation observations, 800 rpm is chosen as the ideal processing speed to produce GOMs with satisfactory size (11.15 μm) and stability. Linseed oil is effectively wrapped-up by GO in the oil-in-water emulsion system based on the presence of shining halos around the oil droplets. This finding also showed GO is capable to encapsulate healing agents and may be a suitable candidate for microcapsules to be used in waterborne self-healing coating.

ACKNOWLEDGEMENT

This work was funded by RIGS17-107-0682 and FRGS19-058-0666 research grants. The authors would like to acknowledge the Kuliyyah of Engineering, International Islamic University Malaysia (IIUM), Ministry of Higher Education (MOHE), Malaysia and every party involved both directly and indirectly in this work.

REFERENCES

- [1] Shao, JJ, Lv W, Yang QH. (2014) Self-assembly of graphene oxide at interfaces. *Advanced Materials*, 26(32): 5586-5612.
- [2] Wu J, Huang G, Li H, Wu S, Liu Y, Zheng J. (2013) Enhanced mechanical and gas barrier properties of rubber nanocomposites with surface functionalized graphene oxide at low content. *Polymer*, 54(7): 1930-1937.
- [3] Ramezanzadeh B, Niroumandrad S, Ahmadi A, Mahdavian M, Moghadam MM. (2016) Enhancement of barrier and corrosion protection performance of an epoxy coating through wet transfer of amino functionalized graphene oxide. *Corrosion Science*, 103: 283-304.
- [4] Bandyopadhyay P, Park WB, Layek RK, Uddin ME, Kim NH, Kim HG, Lee JH. (2016) Hexylamine functionalized reduced graphene oxide/polyurethane nanocomposite-coated nylon for enhanced hydrogen gas barrier film. *Journal of Membrane Science*, 500: 106-114.
- [5] Wang J, Zhang P, Liang B, Liu Y, Xu T, Wang L, Cao B, Pan K. (2016). Graphene oxide as an effective barrier on a porous nanofibrous membrane for water treatment. *ACS Applied Materials & Interfaces*, 8(9): 6211-6218.
- [6] Di H, Yu Z, Ma Y, Li F, Lv L, Pan Y, Lin Y, Liu Y, He Y. (2016) Graphene oxide decorated with Fe_3O_4 nanoparticles with advanced anticorrosive properties of epoxy coatings. *Journal of the Taiwan Institute of Chemical Engineers*, 64: 244-251.
- [7] Ammar A, Al-Enizi AM, AlMaadeed MA, Karim A. (2016) Influence of graphene oxide on mechanical, morphological, barrier, and electrical properties of polymer membranes. *Arabian Journal of Chemistry*, 9(2): 274-286.
- [8] Wang B, Liu J, Zhao Y, Li Y, Xian W, Amjadipour M, MacLeod J, Motta N. (2016) Role of graphene oxide liquid crystals in hydrothermal reduction and supercapacitor performance. *ACS Applied Materials & Interfaces*, 8(34): 22316-22323.
- [9] Choi SJ, Yu H, Jang JS, Kim MH, Kim SJ, Jeong HS, Kim ID. (2018) Nitrogen-Doped Single Graphene Fiber with Platinum Water Dissociation Catalyst for Wearable Humidity Sensor. *Small*, 14(13): 1703934.
- [10] Shen TZ, Hong SH, Song JK. (2014) Electro-optical switching of graphene oxide liquid crystals with an extremely large Kerr coefficient. *Nature Materials*, 13(4): 394-399.

- [11] Oh JH, Kim J, Lee H, Kang Y, Oh IK. (2018) Directionally antagonistic graphene oxide-polyurethane hybrid aerogel as a sound absorber. *ACS Applied Materials & Interfaces*, 10(26): 22650-22660.
- [12] Narayan R, Kim JE, Kim JY, Lee KE, Kim SO. (2016) Graphene oxide liquid crystals: discovery, evolution and applications. *Advanced Materials*, 28(16): 3045-3068.
- [13] Abedin MJ, Gamot, TD, Martin ST, Ali M, Hassan KI, Mirshekarloo MS, Majumder M. (2019) Graphene Oxide Liquid Crystal Domains: Quantification and Role in Tailoring Viscoelastic Behavior. *ACS Nano*, 13(8): 8957-8969.
- [14] Jalili R, Aboutalebi SH, Esrafilzadeh D, Konstantinov K, Moulton SE, Razal JM, Wallace GG. (2013) Organic solvent-based graphene oxide liquid crystals: A facile route toward the next generation of self-assembled layer-by-layer multifunctional 3D architectures. *ACS Nano*, 7(5): 3981-3990.
- [15] Chevalier Y, Bolzinger MA, Briançon S. (2015) Pickering emulsions for controlled drug delivery to the skin. In *Percutaneous Penetration Enhancers Chemical Methods in Penetration Enhancement* (pp. 267-281). Springer, Berlin, Heidelberg.
- [16] Wu J, Ma GH. (2016) Recent studies of Pickering emulsions: particles make the difference. *Small*, 12(34): 4633-4648.
- [17] Teo GH, Ng YH, Zetterlund PB, Thickett SC. (2015) Factors influencing the preparation of hollow polymer-graphene oxide microcapsules via Pickering miniemulsion polymerization. *Polymer*, 63: 1-9.
- [18] Ullah H, Azizli, KA, Man ZB, Ismail MBC, Khan MI. (2016) The potential of microencapsulated self-healing materials for microcracks recovery in self-healing composite systems: A review. *Polymer Reviews*, 56(3): 429-485.
- [19] Montemor MF. (Ed.) (2015). *Smart composite coatings and membranes: Transport, structural, environmental and energy applications*. Elsevier.
- [20] Hughes AE, Mol JM, Zheludkevich ML, Buchheit RG. (2016) Active protective coatings. *Active Protective Coatings: New-Generation Coatings for Metals*, Springer Series in Materials Science, vol. 233. ISBN 978-94-017-7538-0. Springer Science+ Business Media Dordrecht.
- [21] Çömlekçi GK, Ulutan S. (2019) Acquired self-healing ability of an epoxy coating through microcapsules having linseed oil and its alkyd. *Progress in Organic Coatings*, 129: 292-299.
- [22] Abbaspoor S, Ashrafi A, Abolfarsi R. (2019) Development of self-healing coatings based on ethyl cellulose micro/nano-capsules. *Surface Engineering*, 35(3): 273-280.
- [23] Navarchian AH, Najafipoor N, Ahangaran F. (2019) Surface-modified poly (methyl methacrylate) microcapsules containing linseed oil for application in self-healing epoxy-based coatings. *Progress in Organic Coatings*, 132: 288-297.
- [24] Li J, Feng Q, Cui J, Yuan Q, Qiu H, Gao S, Yang J. (2017) Self-assembled graphene oxide microcapsules in Pickering emulsions for self-healing waterborne polyurethane coatings. *Composites Science and Technology*, 151: 282-290.
- [25] Afshar Ghotli R, Raman AA, Ibrahim S, Baroutian S. (2013) Liquid-liquid mixing in stirred vessels: A review. *Chemical Engineering Communications*, 200(5): 595-627.
- [26] Yamashita Y, Miyahara R, Sakamoto K. (2017) *Emulsion and emulsification technology in Cosmetic Science and Technology* (1st edition), Elsevier, pp 489-506.
- [27] Kim J, Cote LJ, Kim F, Yuan W, Shull KR, Huang J. (2010) Graphene oxide sheets at interfaces. *Journal of the American Chemical Society*, 132(23): 8180-8186.
- [28] Thompson DG, Taylor AS, Graham DE. (1985) Emulsification and demulsification related to crude oil production. *Colloids and Surfaces*, 15: 175-189.
- [29] Gohtani S, Yoshii H. (2018) Microstructure, composition, and their relationship with emulsion stability. In *Food Microstructure and Its Relationship with Quality and Stability* (pp. 97-122). Woodhead Publishing.
- [30] Lapointe CP, Mason TG, Smalyukh, II. (2009) Shape-controlled colloidal interactions in nematic liquid crystals. *Science*, 326(5956): 1083-1086.
- [31] Wan W, Zhao Z, Hughes TC, Qian B, Peng S, Hao X, Qiu J. (2015) Graphene oxide liquid crystal Pickering emulsions and their assemblies. *Carbon*, 85: 16-23.

- [32] Andrienko, D. (2018) Introduction to liquid crystals. *Journal of Molecular Liquids*, 267: 520-541.
- [33] Panda D, Nandi A, Datta SK, Saha H, Majumdar S. (2016) Selective detection of carbon monoxide (CO) gas by reduced graphene oxide (rGO) at room temperature. *RSC advances*, 6(53): 47337-47348.
- [34] Low LE, Wong SK, Tang SY, Chew CL, De Silva HA, Lee JMV, Hoo CH, Kenrick K. (2019) Production of highly uniform Pickering emulsions by novel high-intensity ultrasonic tubular reactor (HUTR). *Ultrasonics sonochemistry*, 54: 121-128.
- [35] Chevalier Y, Bolzinger MA. (2013) Emulsions stabilized with solid nanoparticles: Pickering emulsions. *Colloids and Surfaces A: Physicochemical and Engineering Aspects*, 439: 23-34.
- [36] Borisova D, Akçakayırın D, Schenderlein M, Möhwald H, Shchukin DG. (2013) Nanocontainer-Based Anticorrosive Coatings: Effect of the Container Size on the Self-Healing Performance. *Advanced Functional Materials*, 23(30): 3799-3812.
- [37] Tsabet E, Fradette L. (2015) Effect of processing parameters on the production of Pickering emulsions. *Industrial & Engineering Chemistry Research*, 54(7): 2227-2236.

INVESTIGATION ON THE MECHANICAL, THERMAL, BIO-DEGRADATION, AND BIO-COMPATIBILITY PROPERTIES OF POLY (LACTIC ACID) / POLY (ETHYLENE GLYCOL) BLEND

ZOHREH ZARINKOLAH¹, HAMED BAGHERI^{*1}, SAMAN HOSSEINKHANI²,
AND MARYAM NIKKHAH²

¹Faculty of Interdisciplinary Science and Technology,

²Faculty of Biological Sciences,
Tarbiat Modares University, Tehran, Iran

*Corresponding author: hbagheri@modares.ac.ir

(Received: 19th May 2020; Accepted: 29th July 2020; Published on-line: 4th January 2021)

ABSTRACT: Absorbable sutures are widely used in surgery. In addition to acceptable mechanical properties, the surgical sutures should exhibit favorable degradability properties. In this research, the mechanical and thermal properties, hydrophilicity, biodegradability, pH changes, and drug release profile of polylactic acid (PLA) and polyethylene glycol (PEG) alloy were examined to fabricate absorbable sutures. The test results for the mechanical properties showed that the strength of the PLA/PEG alloy decreased with increasing PEG content, leading to an increase in elongation. The differential thermal analysis indicated that the resulting material was above its glass transition temperature (T_g) at ambient temperature and was thus flexible enough. According to the degradation test results, the alloys were degraded similar to the commercial sample. Furthermore, the pH measurements revealed that the degradation of the alloy had no significant effect on the pH of the environment. Bupivacaine hydrochloride was incorporated into a certain amount of PLA and PEG, and the drug release rate was then measured. The sample provided a suitable substrate for burst release. Moreover, the cytotoxicity test was carried out to evaluate the biocompatibility properties of the PLA/PEG alloy and it was found that this alloy is biocompatible and the biocompatibility of the material decreases with increasing drug loading.

ABSTRAK: Suture boleh serap telah digunakan dalam pembedahan secara meluas. Tambahan kepada sifat-sifat mekanikal ini, suture pembedahan perlu memiliki ciri-ciri keboleharuan yang dikehendaki. Dalam kajian ini, sifat-sifat mekanikal dan terma, kehidrofilikan, keboleharuan, perubahan pH, dan profil penguraian ubat asid polilaktik (PLA) dan aloi polietilena glikol (PEG) telah dikaji bagi mencipta suture boleh serap. Hasil kajian mendapati sifat-sifat mekanikal menunjukkan kekuatan PLA/PEG aloi berkurangan dengan penambahan level PEG, menyebabkan bertambahnya pemanjangan. Analisis pembezaan terma menunjukkan hasil bahan adalah melepasi suhu perubahan gelas (T_g) pada suhu sekitar dan oleh itu sangat lentur. Berdasarkan hasil kajian degradasi, aloi ini telah digradasi seperti sampel komersial. Tambahan lagi, ukuran pH menunjukkan degradasi aloi ini tidak menunjukkan kesan langsung pada pH persekitaran. Bupivacaine hidroklorida dimasukkan ke dalam PLA dan PEG, dan kadar ubat dibebaskan kemudiannya diukur. Sampel substrat yang bersesuaian disediakan bagi pelepas letus. Tambahan, ujian Kesitotoksikan telah dijalankan bagi menilai ciri-ciri keserasian-bio aloi PLA/PEG dan didapati aloi ini serasi-bio dan keserasian-bio bahan berkurangan dengan penambahan beban ubat.

KEYWORDS: *surgical suture; drug release; PLA / PEG; bupivacaine hydrochloride; blend*

1. INTRODUCTION

Surgical sutures are one of the most common types of biomaterials. Natural or synthetic sutures are used to ligate blood vessels or to hold tissues together [1][2]; hence, they can potentially be suitable for the delivery of a pain reliever in the surgical site to reduce the patient's drug dose and potential side effects. A wide range of biopolymers have been used in various medical applications, including drug delivery. Currently, most studies in this field focus on modern controlled drug delivery systems [3].

Sutures have been used as a platforms for the release of antimicrobial drugs such as triclosan-coated sutures [4], which, due to drug resistance, were replaced with silver nanoparticles such as silver solution-soaked multifilament absorbable PLGA sutures [5][6]. To release analgesics such as ibuprofen, the drug was loaded on PLGA sheets and was physically connected to commercially available Vicryl sutures [7]. Natural compounds such as plant extracts, which are rich in phenolic compounds, have received much attention in wound healing applications [5].

A new material with desirable properties can be produced by blending various polymers. A wide range of properties can be obtained using this method to reach a specific goal in a relatively short period at a lower cost, compared to polymerization processes [8][9]. The properties of such systems can be improved using appropriate chemical and physical compatibility techniques as well as methods reducing tensile space in the molten state and increasing phase dispersion and adhesion [10]. In this study, drug-loaded sutures were prepared by mechanical blending of polylactic acid (PLA) and polyethylene glycol (PEG) with bupivacaine HCl as a strong local anesthetic drug having a long-lasting effect [11].

Given that mechanical blending is a simple, cost-effective, and large-scale production method, and PLA is much cheaper than polymers used in the surgical suture industry, the desired properties can be achieved by combining PLA with other polymers. This composition has not yet been used for surgical sutures. The drug loaded on the resulting material is another novelty of the present study.

2. MATERIALS AND METHODS

2.1 Materials

Polylactic acid (PLA) was purchased from Hisun PLA---REVODE190 (L130); polyethylene glycol (PEG) with Mw (6000) was purchased from Merck Company; Bupivacaine hydrochloride was also purchased from Aburaihian Pharmaceutical Co Ltd. Synthetic absorbable sutures (MONOCRYL®) were kindly donated from ETICON.

2.2 Preparation of Blends

Four samples were prepared by blending a mixture of two polymers PLA / PEG with 5, 10, 15, 20 wt.% PEG and 60 g weight [12-14]. The material was dried in an oven at 35 °C for 10 hours. Each sample was homogeneous as a result of mixing in an internal mixer manufactured by Brabender Germany Model W50 at 180 °C and 80 rpm for a 15-minute duration. For mechanical and biological tests, the samples were prepared in sheets with 1-mm diameter by hot press machine made by Toyo seiki model WCH (2002) at 190 °C and pressure of 50 kPa for 5 minutes. The sample was then pressurized to 27 kPa for 5 minutes by cold press.

2.3 Preparation of Drug-containing Samples

Solvent casting sampling was performed on the PLA/PEG sample with 15 wt% PEG and bupivacaine hydrochloride with 5, 10, and 15 wt% of the drug. The polymer mixture was dissolved in dichloromethane at 10 wt.%. Then the weight concentrations of the drug were added to 10 wt% PLA/PEG polymer mixture [15]. The homogeneous solution was poured into a mold. After 72 hours, the solvent evaporation and the sample containing the drug were prepared.

2.4 Mechanical Testing

Prototyping was performed according to ASTM D882 with length, width, and thickness of 110, 20, and 1 mm, respectively. The test was performed by GT7010-D2E, manufactured by GOTECH Taiwan, at a speed of 5 mm/min, with a 50 mm interval between the jaws. The test was performed on 4 samples with 5, 10, 15, and 20 wt% PEG and 3 specimens were taken to determine data point.

2.5 Thermal Analysis

To carry out this test in accordance with ISO 11357, the DSC 200 F3, manufactured by NETZSCH, was set up at a temperature of 25 °C to 220 °C and a rate of 5 °C/min.

2.6 Biodegradability Test

To perform this test in accordance with ISO 13781, the samples were prepared in strips of approximately 10 × 20 × 5 mm and placed in 50 ml of PBS buffer with a pH of about 7.4 at 37 °C.

The weight loss of the sample was examined over seven months at two-week intervals. At the specified time intervals, the samples were extracted from the buffer solution, washed twice with distilled water, and incubated at a temperature of 45 °C for 5 hours. They were then dried and weighed by scales.

2.7 Measuring pH Changes

The samples were prepared as 10 × 20 × 5 mm strips and placed in 50 ml of phosphate buffer saline (PBS) at pH 7.4 and 37 °C. The pH changes in the solution containing the samples were performed at a time interval of 7 months and two-week intervals. At the end of the experiment, the pH value was measured by pH meter device (made by Sana model SANA SL-901), and then, was replaced with freshly-made PBS solution every time.

2.8 Contact Angle Test

The contact angle was measured with a drop of water (4 µl) using a system equipped with a drop-shot CCD camera and a drop-angle contact angle measurement software at the desired level.

2.9 *In-vitro* Release Study

To measure the release rate, 10 mg of PLA/PEG polymeric sample containing 15 wt% PEG and bupivacaine hydrochloride with 5, 10, and 15 wt% were prepared and dissolved in 50 ml of phosphate buffered saline (PBS) with a pH of approximately 7.4 at 37 °C by incubator shakers LIEBHERR models manufactured by Tintometer Germany at 180 rpm. After 0, 0.5, 1, 4, 8, and 24 hours for 14 days, 2 ml of the extract was daily replaced with 2 ml of PBS buffer. The extract absorption rate was measured by using uv spectroscopy manufactured by Biochrom U.K. Model WPA to determine the concentration of the drug.

2.10 Cytotoxicity Test

The MTT cytotoxicity test method examined the samples containing drug to measure cell viability in the presence of various concentrations of the drug. The test was performed on the MEF (CF-1) and HEK-293 cell lines (donated by Tarbiat Modarres University).

3. RESULTS AND DISCUSSION

3.1 Tensile test

As shown in Fig. 1, the stress is reduced in the samples containing 5, 10, 15, and 20 wt% PEG. A comparison between the PLA/PEG and pure PLA strain rates in Fig. 2 shows that the strain is significantly influenced by increased PEG level due to a decrease in PLA level. This finding is reasonable since the PLA/PEG melt is expected to have interstitial properties.

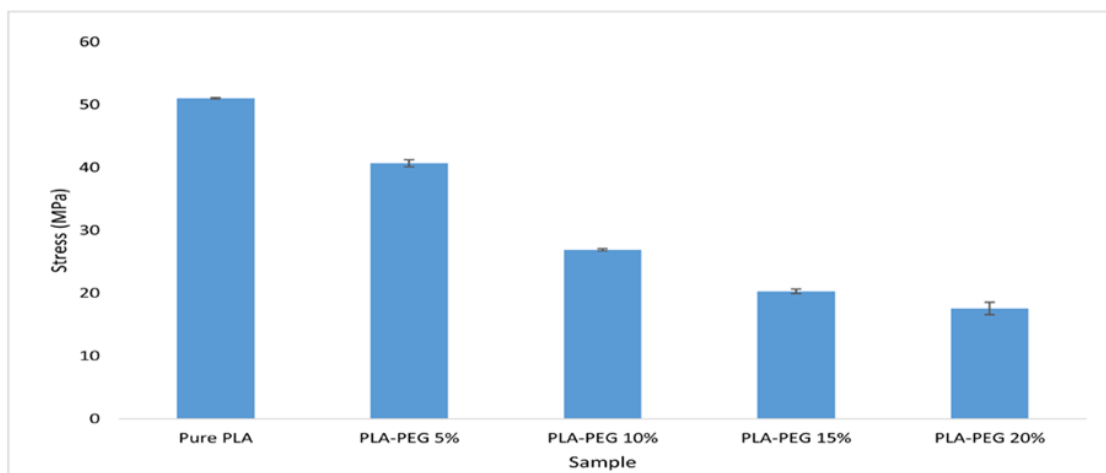


Fig. 1: Tensile strength properties as a function of increasing (%) PEG.

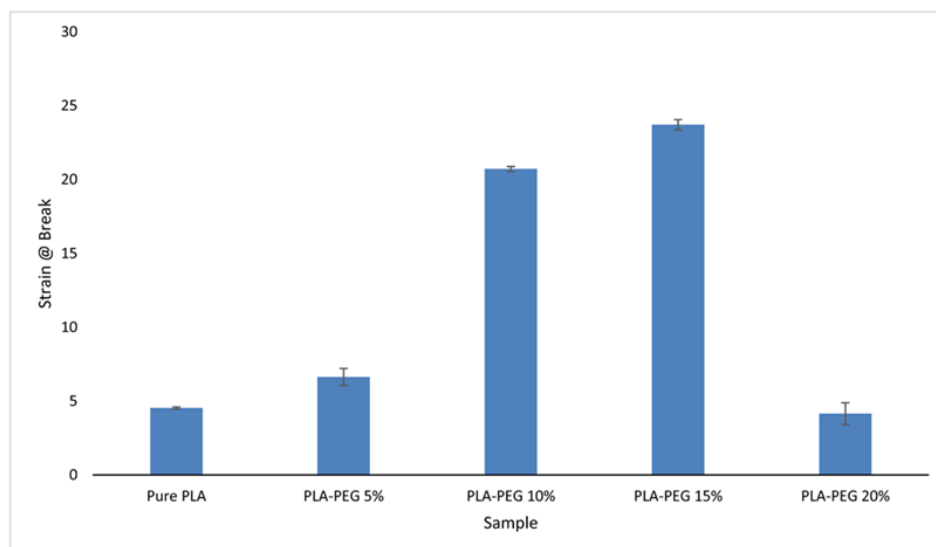


Fig. 2: Elongation properties as a function of increasing (%) PEG.

The stress and strain rates in PLA/PEG20% were not similar to the ones observed for the other samples such that the strain rate decreased with an increase in the PEG level.

According to Pillin et al. two substances are miscible to a certain extent under blending conditions. Therefore, the observed behavior can be caused by the immiscibility of PLA and PEG in this composition [16].

In this study, blending process aimed at obtaining a composition with desirable properties to fabricate absorbable sutures; therefore, the final blend should have a proper strain to better control and handle the resulting sutures. On the other hand, strength is a significant factor in the preparation of sutures with desirable properties [1,17]. The main point was to find a composition with the maximum elongation against the lowest strength reduction. According to the results of the tensile test and considering the abovementioned criterion, the PLA/PEG sample with 15 wt% PEG had the lowest strength reduction with maximum elongation.

3.2 Differential Thermal Analysis

Figure 3 shows the differential thermal analysis curve for five samples. As it can be observed, the peaks in the diagram represent the phase changes of the material.

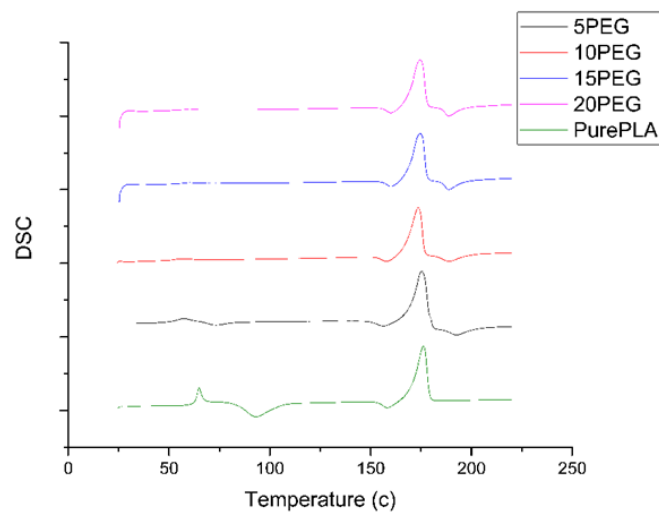


Fig. 3: DSC curves of PLA / PEG samples.

According to Table 1, the amount of the absorbed heat decreased with an increase in the PEG level. Given that the glass transition temperature (T_g) of PEG is 63 °C [18], the less heat absorbed for the phase change was due to an increase in the PEG level. On the other hand, PLA and PEG are miscible, and the glass transition temperature of the polymeric alloy is expected to be decreased with the increase in the PEG level. Considering the low glass transition temperature of PEG, the reduction in T_g of the alloy is reasonable and indicates the plasticizing effect of PEG as a plasticizer. The decrease in the T_g peak reveals that the resulting material is softened at ambient temperature. The plasticizing effect of PEG is also proven in the tensile test. On the other hand, the peak T_m has also decreased due to the decrease in the PLA level, and also by calculating the area under the curve of this peak (Table1), it proves that the volume of heat received in the whole material has decreased.

Table 1: Thermal properties of PLA-PEG blends derived from DSC curve

sample	Pure PLA	PLA/PEG 5%	PLA/PEG 10%	PLA/PEG 15%	PLA/PEG 20%
ΔH (J/g)	7.936	6.306	5.796	5.435	4.121

3.3 Degradation Test

Figure 4 presents the rate of weight loss for all the samples. All samples experienced a weight loss, compared to pure PLA so that the weight loss increased with an increase in the PEG level. A comparison of the graphs revealed that the degradability properties of PLA were improved as a result of it being mixed with PEG. The degradability rate of the commercially available MONOCRYL Poliglecaprone 25 sutures was also measured for further comparison. In this regard, pure PLA revealed no weight loss within 36 weeks, and this might be due to the crystalline structure of PLA [19]. The PLA/PEG sample containing 15 wt% PEG showed a weight loss close to that of the commercial sutures. However, the weight loss of the commercial sutures was measured during a 4-week period, although there was no possibility to measure the weight because of the appearance of the sample. Given the semi-crystalline structure of PLA, the penetration of buffer or any other liquid into PLA mass is difficult [19].

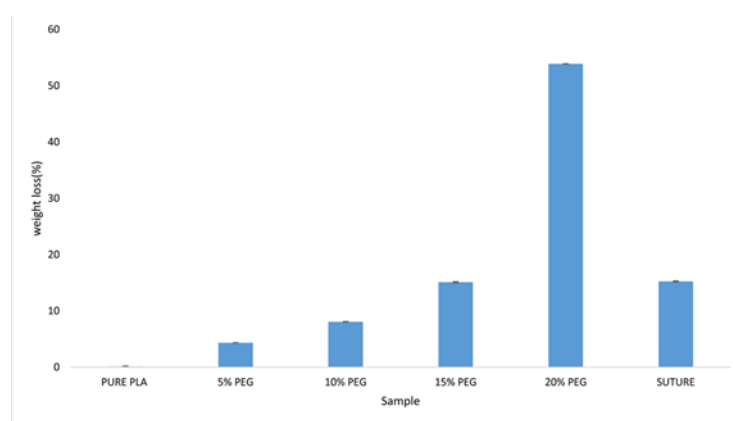


Fig. 4: Loss of mass of the of PLA / PEG specimens as a function of (%) PEG.

With the increase in the amount of PEG added to PLA, the buffer penetration into the polymeric mass improved due to the nature of PEG. This led to the failure of the polymeric backbone, and the weak points in the material then caused cracking. Given that wound healing requires a reduction in the strength of sutures and the gradual removal of sutures, the failure at the surface would reduce strength and eventually facilitate the removal of sutures. The micrographs of the degradation test are shown in Fig. 5.

3.4 pH Changes

Figure 6 presents pH changes during the degradation of the PLA/PEG samples. Accordingly, the pH measured to the initial pH increased maximum 3 to 4%. Given that the pH of the body is about 7.4, and the maximum change was 0.2 units, the prepared samples did not change the pH in the body.

3.5 Contact Angle Test

Table 2 lists the contact angle of a water droplet on the surface of pure PLA and PLA/PEG blends containing 5, 10, 15 and 20 wt% PEG. A smaller contact angle indicates a more hydrophilic nature of the material. In this study, the contact angle decreased with increasing PEG in the resulting blend, implying the effect of hydrophilic properties of PEG.



Fig. 5: Micrograph of samples after 34th week of degradation test.

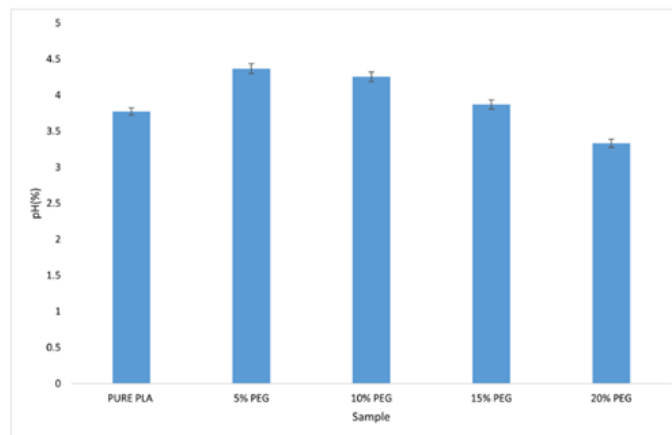


Fig. 6: Variations in pH of the degradation media as a function of (%) PEG.

Table 2: Water Contact angle measurement on surface of PLA / PEG samples

sample	Pure PLA	PLA/PEG 5%	PLA/PEG 10%	PLA/PEG 15%	PLA/PEG 20%
(Degree) contact angle	62	57	46	30	21

This in turn affected the properties of the blend so that the resulting material became more hydrophilic. Since the absorbable sutures should be hydrophilic to be effectively degraded, the resulting blend was thus suitable for the desired application. As a result, PLA properties were modified in this way. The effect of PEG hydrophilic nature was also observed in the degradation test. The micrograph of the contact angle of the samples is shown in Fig. 7.

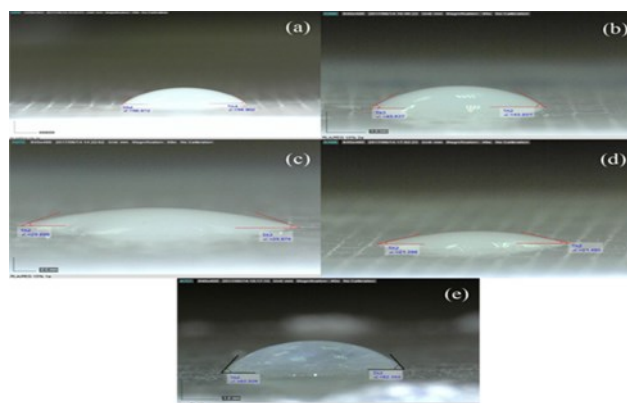


Fig. 7: Water contact angle image of PLA/PEG samples, (a) PLA/PEG 5%, (b) PLA/PEG 10%, (c) PLA/PEG 15%, (d) PLA/PEG 20%, (e) PLA.

3.6 Drug Release Profile

Figure 8 shows the drug release profiles for 312 hours (13 days). The highest drug release rate occurred during 1-4 h and then a declining trend was observed. In other words, the sample provides a suitable substrate for rapid drug release in the wound site. Since this study aimed at achieving sutures with desired properties for rapid drug release in the first hours of injury at the closure site of a trauma or a scar, all the three samples can be used for this purpose. The concentration of the released drug was increased with an increase in drug loading. This means that the prepared material would be a suitable substrate for the controlled drug release at a required rate.

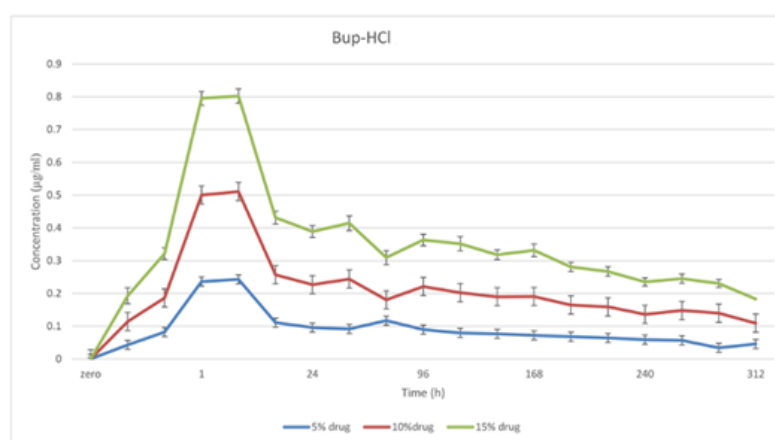


Fig. 8: Modeled *in vivo* release profiles of bupivacaine hydrochloride of PLA/PEG samples.

3.7 Cytotoxicity Test

Figure 9 shows the viability of MEF (CF-1) cell line in the control sample and in the extract containing bupivacaine hydrochloride. As it can be observed, the viability decreased with an increase in the drug percentage [20,21]. Figure 10 shows the viability of HEK-293 cell line in the bupivacaine hydrochloride extract. In this test, the viability of cells decreased with an increase in the drug concentration, as compared to the control sample [20,21].

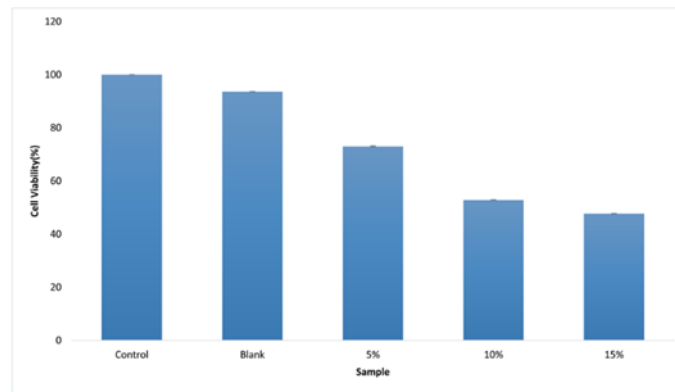


Fig. 9: Percentage of cell viability on the series of the diluted extracted solution of (MEF (CF-1)) in 24 hours in the vicinity of the samples containing drug.

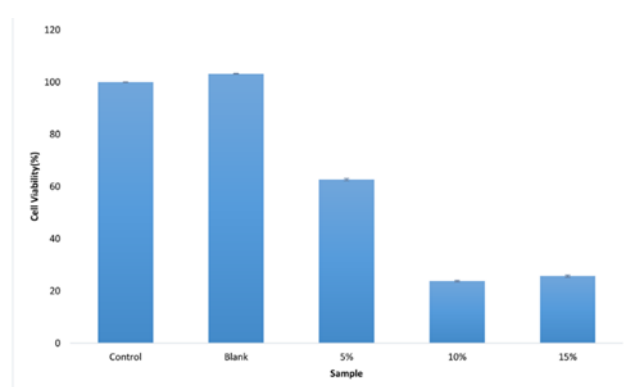


Fig. 10: Percentage of cell viability on the series of the diluted extracted solution of (HEK-293 in 24 hours in the vicinity of the samples containing drug.

According to the results of this study as well as statistical calculations, the difference in cell viability percentage is significant and in the vicinity of the cell with the material extract, has led to cell death. As can be seen in Fig. 9 and Fig. 10, the rate of cell death increased with increasing percentage of drug loaded in the polymer alloy. In the two types of cell lines used, the survival rate of cells is different, which is due to the difference in tolerance of different cell lines. Thus, the HEK-293 cell line had a lower drug tolerance compared to the cell line (MEF (CF-1)).

4. CONCLUSION

Poly(lactic acid) (PLA) and poly(ethylene glycol) (PEG) were mechanically blended to obtain interstitial properties. Poly(lactic acid) is a rigid brittle polymer with a high mechanical strength. PLA is rigid at ambient temperature and is almost hydrophobic. Poly(ethylene glycol) is a hydrophilic polymer with a low melting point and high degradation rate. These two polymeric materials are miscible, whose blending results in interstitial properties. The resulting polymeric material is flexible and more hydrophilic than the poly(lactic acid) and exhibits a higher strength than poly(ethylene glycol). According to the tensile test results, increasing the PEG level caused a decrease in strength but an increase in elongation. In this study, blending aimed at obtaining a composition with desirable properties to produce absorbable sutures. Accordingly, the final blend should have a proper strain for better control and mobility of the resulting sutures. On the other hand, strength is a critical factor in the preparation of sutures with desirable properties. The main point is to find a

composition with the maximum elongation against the lowest strength reduction. According to the results of the tensile test and considering the abovementioned criterion, PLA/PEG sample with 15 wt% PEG had the lowest strength reduction with maximum elongation.

The results of the degradation test indicated that increasing the PEG level led to greater penetration of fluids in the polymeric mass, resulting in an increase in the degradation rate. In this study, a PLA/PEG sample containing 15 wt% PEG showed a weight loss close to that of commercial sutures. It is worth mentioning that the difference in the weights of samples was not significant during the study period, and the material was degraded with no significant weight loss.

According to the contact angle test results, the hydrophilic properties of the resulting polymeric material increased with an increase in the PEG level. Due to the fact that absorbable sutures should be hydrophilic to be effectively degraded, the resulting material would be suitable for the desired application. As a result, PLA properties were modified in this way.

The drug release profiles revealed that the maximum drug release occurred during 1-4 h, and then a declining trend was observed. With an increase in drug loading, the drug concentration also increased, suggesting that the polymeric material would be a suitable substrate for controlled drug release at a required rate.

According to the results of cytotoxicity test on the drug-containing samples, the cell death rate increased with an increase in the amount of drug loaded in the polymeric blend. The cell viability was different in two types of cell lines due to the differences in the tolerance of the cell lines.

REFERENCES

- [1] Pillai CKS, Sharma CP. (2010) Absorbable polymeric surgical sutures: Chemistry, production, properties, biodegradability, and performance. *Journal of Biomaterials Applications*. 25(4): 291-366. <http://jba.sagepub.com/content/25/4/291>
- [2] Tajirian AL, Goldberg DJ. (2010) A review of sutures and other skin closure materials. *Journal of Cosmetic Laser Therapy*, 12(6): 296-302. <https://doi.org/10.3109/14764172.2010.538413>
- [3] Ratner BD, Hoffman AS, Schoen FJ, Lemons JE. (1997) *Biomaterials Science, An Introduction to Materials in Medicine Book (3rd Edition)* 2013. Edited by Ratner BD, Hoffman AS, Schoen FJ, Lemons JE.
- [4] Joseph B, George A, Gopi S, Kalarikkal N, Thomas S. (2017) Polymer sutures for simultaneous wound healing and drug delivery – A review,” *International Journal of Pharmaceutics*, 524(1): 454-466, <https://doi.org/10.1016/j.ijpharm.2017.03.041>
- [5] Gallo AL, Paladini F, Romano A, Verri T, Quattrini A, Sannino A, Pollini M. (2016) Efficacy of silver coated surgical sutures on bacterial contamination, cellular response and wound healing. *Materials Science and Engineering*, C69: 884-893. <https://doi.org/10.1016/j.msec.2016.07.074>
- [6] Hu W, Huang ZM, Liu XY. (2010) Development of braided drug-loaded nanofiber sutures. *Nanotechnology*, 21(31): 315104 (11pp)
- [7] Lee JE, Park S, Park M, Kim MH, Park CG, Lee S.H, Choi SY, Kim BH, Park HJ, Park JH, Heo CY, Choy YB. (2013) Surgical suture assembled with polymeric drug-delivery sheet for sustained, local pain relief. *Acta Biomaterialia*, 9(9): 8318-8327. <https://doi.org/10.1016/j.actbio.2013.06.003>
- [8] Yu L, Dean K, Li L. (2006) Polymer blends and composites from renewable resources. *Progress Polymer Science*, 31: 576-602. <https://doi.org/10.1016/j.progpolymsci.2006.03.002>
- [9] Lai W, Liao W, Lin T. (2004) The effect of end groups of PEG on the crystallization behaviors of binary crystalline polymer blends PEG / PLLA. *Polymer*, 45: 3073–3080.

- [10] Pracella M. (2017) Blends and Alloys. Modification of properties, Elsevier Inc. 155-184
- [11] Terry D. (1990) Analytical Profiles of Drug Substances Wilson Sterling Research & Group Rensselaer, 19: 59-94
- [12] Mohapatra AK, Mohanty S, Nayak SK. (2013) Effect of PEG on PLA / PEG Blend and Its Nanocomposites: A Study of Thermo-Mechanical and Morphological Characterization. <https://doi.org/10.1002/pc.22660>
- [13] Ozdemir E, Hacaloglu J. (2017) Characterizations of PLA-PEG Blends Involving Organically Modified Montmorillonite. Journal of Analytical and Applied Pyrolysis 127: 343-349.
- [14] Bramfeldt H, Sarazin P, Vermette P. (2008) Blends as a strategy towards tailored hydrolytic degradation of poly (ϵ -caprolactone-co-D,L-lactide)-poly(ethylene glycol)-poly(ϵ -caprolactone-co-D,L-lactide) co-polymers. Polymer Degradation and Stability, 93(4): 877-882.
- [15] Weldon CB, Tsui JH, Shankarappa SA, Nguyen VT, Ma M, Anderson DG, Kohane DS. (2012) Electrospun drug-eluting sutures for local anesthesia. Journal of Controlled Release, 161(3): 903-909, <https://doi.org/10.1016/j.jconrel.2012.05.021>
- [16] Pillin I, Montrelay N, Grohens Y. (2006) Thermo-mechanical characterization of plasticized PLA: Is the miscibility the only significant factor? Polymer, 47: 4676-4682.
- [17] Patel KA, Thomas WEG. (2008) Sutures, ligatures and staples. Surgery 26(2): 48-53.
- [18] Wang X, Michael A, Van Den Mooter G. (2004) Study of the phase behavior of polyethylene glycol 6000 – itraconazole solid dispersions using DSC. International Journal of Pharmaceutics (272): 181-187.
- [19] Davachi SM, Kaffashi B, Torabinejad B, Zamanian A. (2016) *In-vitro* investigation and hydrolytic degradation of antibacterial nanocomposites based on PLLA / triclosan / nano-hydroxyapatite. Polymer, 83:101-110. <https://doi.org/10.1016/j.polymer.2015.12.015>
- [20] Wang D, Vo NV, Sowa GA, Hartman RA, Ngo K, Choe SR, Witt WT, Dong Q, Lee JY, Niedernhofer LJ, Kang JD. (2011) Bupivacaine decreases cell viability and matrix protein synthesis in an intervertebral disc organ model system. The Spine Journal, 11(2): 139-146, <https://doi.org/10.1016/j.spinee.2010.11.017>
- [21] Quero L, Klawitter M, Nerlich AG, Leonardi M, Boos N, Wuertz K. (2011) Bupivacaine-the deadly friend of intervertebral disc cells? The Spine Journal, 11(1): 46-53. <https://doi.org/10.1016/j.spinee.2010.11.001>

PREPARATION OF CaO-BASED PELLET USING RICE HUSK ASH VIA GRANULATION METHOD FOR POTENTIAL CO₂ CAPTURE

FARAH DIANA MOHD DAUD^{1*}, MUHAMMAD MIRZA MOHAMAD AZIR¹,
MUDRIKAH SOFIA MAHMUD¹, NORSHAHIDA SARIFUDDIN,
HAFIZAH HANIM MOHD ZAKI

¹*Department of Manufacturing and Materials Engineering, Kulliyah of Engineering, International Islamic University Malaysia, P.O. Box 10, 50728 Kuala Lumpur, Malaysia*

**Corresponding author: farah_diana@iium.edu.my*

(Received: 11th July 2020; Accepted: 18th November 2020; Published on-line: 4th January 2021)

ABSTRACT: CO₂ capturing has become very significant option to reduce the emission of CO₂ in the atmosphere and hence, minimizing environmental issues. Among solid CO₂ sorbent, calcium oxide (CaO) is an attractive regenerable sorbent for CO₂ capturing because of their reactivity and high CO₂ absorption capacity. CaO alone suffers from rapid decay of CO₂ adsorption during multiple carbonation/calcination reaction cycles. The stability of CaO sorbents during cyclic runs can be achieved via the incorporation of additive support materials. The silica (SiO₂) from natural sources such as rice husk is the best candidate to be used as an additive in the sorbents. However, the CaO-based sorbent in finely generated powders are prone to severe attrition problems. Therefore, this research focuses on preparation of CaO-based pellets by using rice husk ash (RHA) via granulation method. The result of the raw materials confirmed that Ca(OH)₂ have crystalline structure with finely distributed grains and RHA exhibit amorphous structure with randomly oriented size grains. Based on the XRD, it is confirmed that the insertion of RHA does not alter the phase structure of the pellets. Each ratio yield different intensity value and has formation of new peaks after sintering. Meanwhile, the microstructures of the pellets show that the pores reduced as the calcination temperature increased while the incorporation of RHA caused the pores size increased with randomly oriented shape. These findings indicate that the optimum value for the pellets is with the Ca(OH)₂:RHA ratio of 80:20 and calcination temperature of 750 °C.

ABSTRAK: Penangkapan CO₂ telah menjadi pilihan yang sangat penting untuk mengurangkan pelepasan CO₂ di atmosfer serta kesan alam sekitar. Antara penyerap CO₂ pepejal, kalsium oksida (CaO) adalah penyerapan yang menarik untuk CO₂ yang ditangkap kerana kereaktifan dan kapasiti penyerapan CO₂ yang tinggi. CaO sahaja menderita daripada pelepasan cepat penyerapan CO₂ semasa kitaran tindakbalas karbonasi / kalsinasi. Kestabilan CaO penyerap semasa berlaku kitaran boleh dicapai melalui penggabungan bahan sokongan tambahan. Silika (SiO₂) dari sumber semula jadi seperti sekam padi (RHA) adalah calon terbaik untuk digunakan sebagai aditif dalam penyerap. Walau bagaimanapun, penyerap berasaskan CaO dalam bentuk serbuk halus yang dihasilkan adalah terdedah kepada masalah pergeseran yang teruk. Oleh itu, kajian ini memberi tumpuan kepada penyediaan pelet berasaskan CaO dengan menggunakan abu sekam beras melalui kaedah granulasi. Hasil bahan mentah mengesahkan bahawa Ca(OH)₂ mempunyai struktur kristalografi dengan bijirin halus dan RHA yang mempamerkan struktur bukan kristal dengan butiran saiz berorientasikan secara rawak. Berdasarkan XRD, ia disahkan bahawa penyisipan RHA tidak mengubah struktur kristalografi pelet. Setiap nisbah menghasilkan nilai intensiti yang berbeza dan mempunyai pembentukan puncak baru selepas pensinteran. Sementara itu, mikrostruktur pelet menunjukkan bahawa pori-pori berkurangan apabila suhu kalsinasi meningkat sementara pembentukan RHA menyebabkan saiz pori meningkat dengan bentuk berorientasikan rawak. Penemuan ini menunjukkan bahawa nilai optimum bagi pelet adalah dengan nisbah Ca(OH)₂:RHA 80:20 dan suhu kalsinasi 750 °C.

KEYWORDS: CO₂ capture; CaO-based pellets; RHA; Granulation method.

1. INTRODUCTION

In Malaysia, the main contribution of CO₂ emission is from the energy sectors such as fossil fuels, natural gas, and coal power plants. The energy sectors in Malaysia contributed at about approximately 36% of the total global CO₂ emissions in 2004 and among all of the greenhouse gases, CO₂ gases responsible for 60% of greenhouse effect that cause the global warming [1]. Moreover, Malaysia plans to reduce the amount of CO₂ release by 25% reduction from all sectors and this is according to Green Technology Master Plan 2017-2030 proposed by Malaysia government [2]. Thus, planning and solution must be done in order to control and resolve the problems of CO₂ emissions and greenhouse gases effect.

One of the solutions to reduce the CO₂ gases emitted to the atmosphere is by introducing the carbon capture and storage (CCS) technology. This technology captures up to 90% of CO₂ which led to significant reduction of CO₂ level in atmosphere [3]. Among the CO₂ capture methods, CO₂ capture by adsorption into a sorbent is the most common technique used in the industry due to its better thermal properties and high amount of CO₂ adsorption [4]. The adsorbent materials are usually made from ceramic materials such as CaO, MgO, and ZrO₂. It is well known that ceramic materials possess better thermal properties, and these materials will be acceptable to be used in the elevated temperature condition.

However, the limitation of the recent CO₂ adsorbent materials is that it has low stability and reduction in reactivity in cyclic operation. Recent studies show that other additives such as SiO₂, MgO, and Al₂O₃ reinforced into the sorbents can improve the cycle loop of the CO₂ adsorption [4]. Improvement of the CO₂ adsorption is done by designing the CO₂ capture technologies in the form of pellets rather than sorbents itself and the introduction of biomass resources with the pellets is one of the advantages upon using waste and eco green materials [5]. Thus, this paper aims to study the effect of cycling loops with the pellets design when introducing other additives into the sorbents. Plus, the utilization of waste materials such as rice husk ash introduced into the pellets will be a huge impact on the economic and environmental factor.

There are many methods and techniques have been done on previous study to produce CaO-based sorbents with the addition of SiO₂ including, sol-gel, wet impregnation, bio-template via infiltration, mixing and extrusion-spheronization methods. Among all the methods mentioned above, three of the methods utilizing biomass materials, mainly from the rice husks to act as the additives inside the CaO-based sorbents while the other two methods (sol-gel and wet impregnation) used silica sources from synthetic means. Rice husk ash used as the precursor in the CaO-SiO₂ sorbent due to the high content of silica. Plus, the sources of rice husk are abundant and easy to obtain as it is being produced as the by-product in paddy field makes it the best candidate to be used in the CaO-based sorbent.

Different parameters used in the preparation of the CaO-SiO₂ sorbent play a crucial role in determining the performance of the pellet. There are several parameters needed for the investigation and different parameters usually will give different effects on the pellet whether it will improve the performance or becoming unfavourable. One of them is amount of silica sources incorporated with the CaO-based sorbents or the ratio amount between those two materials. Previous studies showed that different ratio or amount of silica added exhibits different cyclic adsorption performance. In one study, ratio of 3:7 RHA/CaO shown better stability over 50 cycles compared to 1:9 RHA/CaO even though 1:9 RHA/CaO has better carbonation conversion in early cycles [6]. Meanwhile, in the other study, 10%, 20%, 30%, 40% and 50% of RHA added into the CaO-based sorbent. Initially, the ratio of 20% RHA express the highest CO₂ adsorption compare to other ratios but it reduces significantly started

at the first cycle. Then, it is observed that 40% and 50% RHA into the CaO sorbent maintained the highest CO₂ capture over the nine cycles [7].

The main objective of this paper is to prepare CaO-based pellet with addition of RHA as the sacrificial bio-template through granulation method. The pellets were prepared according to two different ratios and undergo calcination process at 750°C. The effect of RHA addition and calcination at 750°C on the properties of CaO-based pellets were examined through the phase structure and morphological characteristics.

2. EXPERIMENTAL

2.1. Materials

Calcium hydroxide from R&M Chemical Sdn. Bhd. was selected as the calcium precursor. The rice husk ash (RHA) as the biotemplate material was obtained from MARDI Perlis.

2.2. Preparation of the RHA

Initially, RHA is oven-dried at 70°C overnight to eliminate moisture. Then, the fine powder of RHA is obtained by ball milling process at 200 rpm for 1 hour. Finally, the ball milled RHA was sieved at the size range of 50 µm to 90 µm.

2.3. Preparation of the Sorbent Pellets

Next, Ca(OH)₂ and RHA powders were weighed according to two different ratios as shown in Table 1. At first, the weighed materials were vigorously mixed in a granulator machine at 73 rpm speed for 10 minutes. Then, the mixture undergoes granulation process at the speed of 1700 rpm and simultaneously wetted by spraying 300 ml of deionized water. After the granulation process, the Ca(OH)₂-RHA pellet was obtained in spherical shape and randomly in size. Lastly, the CaO-SiO₂ pellets were obtained after calcination process in furnace at 750°C.

Table 1: Two different ratios of Ca(OH)₂ and RHA with different weight of each ratio

Ratio of Ca(OH) ₂ and RHA	Weight of Ca(OH) ₂ (g)	Weight of RHA (g)
80:20	800	200
70:30	700	300

2.4 Characterization

2.4.1 X-Ray Diffraction (XRD)

The phase structure of Ca(OH)₂, RHA and the prepared CaO-SiO₂ pellets, before and after calcination at 750°C was examined by X-Ray Diffractometer (XRD) model BRUKER D2 PHASER.

2.4.2 Scanning Electron Microscopy (SEM)

The morphological characteristic of raw materials (Ca(OH)₂ and RHA) and the prepared CaO-SiO₂ pellets at different ratio, before and after calcination process was investigated by JSM-IT100 Scanning Electron Microscopy (SEM) machine manufactured by JEOL.

3. RESULTS AND DISCUSSION

3.1. Analysis on the Raw Materials

Fig. 1(a) and 1(b) show the XRD pattern of $\text{Ca}(\text{OH})_2$ and RHA at different scale of intensity. Based on the Fig. 1(a), sharp peaks at $2\theta = 18.1^\circ$, 29.45° , 34.15° , 47.25° and 50.85° proved the crystalline structure of $\text{Ca}(\text{OH})_2$. Whereas Fig. 1(b) indicated broad peak, centered at about $2\theta = 23^\circ$ which confirms the amorphous structure of RHA. It is common that silica contain in RHA has amorphous structure, and its transformation to crytalline structure will occur when temperature is increased beyond 700°C [9].

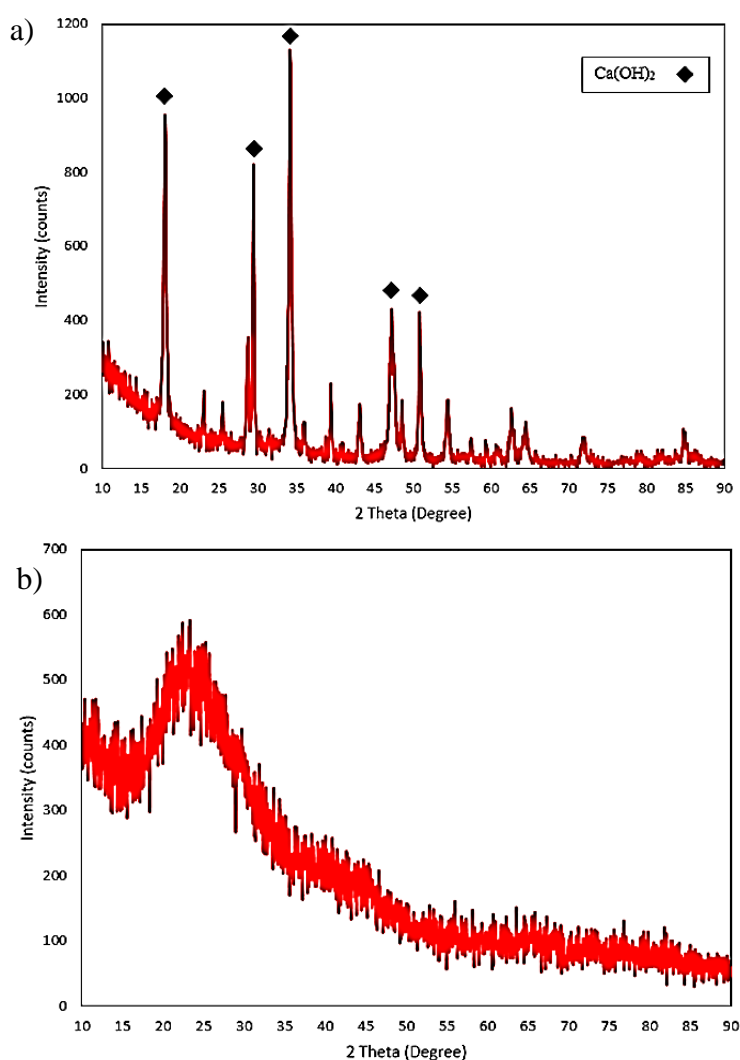


Fig.1. XRD pattern of a) $\text{Ca}(\text{OH})_2$ and b) RHA.

Fig. 2 and 3 displayed the SEM micrographs of $\text{Ca}(\text{OH})_2$ and RHA. It has been observed for $\text{Ca}(\text{OH})_2$ that it consist of finely dispersed, small size particles. Under X5000 magnification (Fig. 2(c)), the morphology of $\text{Ca}(\text{OH})_2$ revealed that the microstructure is in granular and agglomerated shape. While for RHA, the SEM images reveals the siliceous nature and with some porosity of the ashes. It was observed that RHA has agglomerated particles in various sizes and irregular structures.

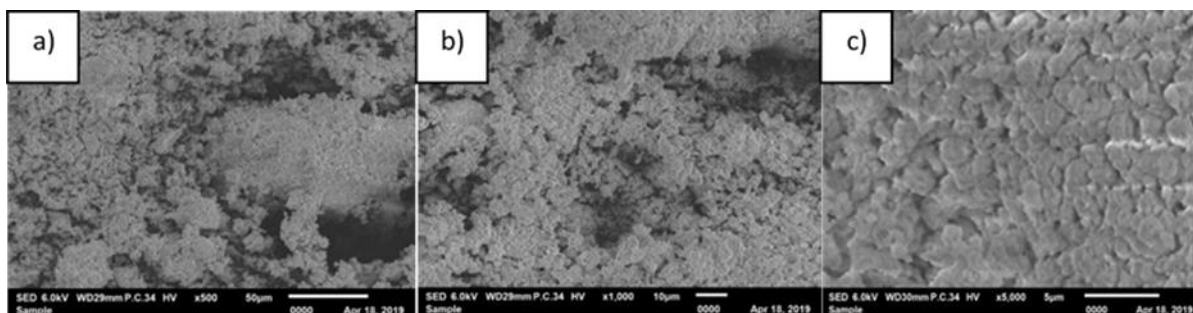


Fig. 2. SEM micrographs of $\text{Ca}(\text{OH})_2$ at magnification of a) 500X, b) 1000X and c) 5000X.

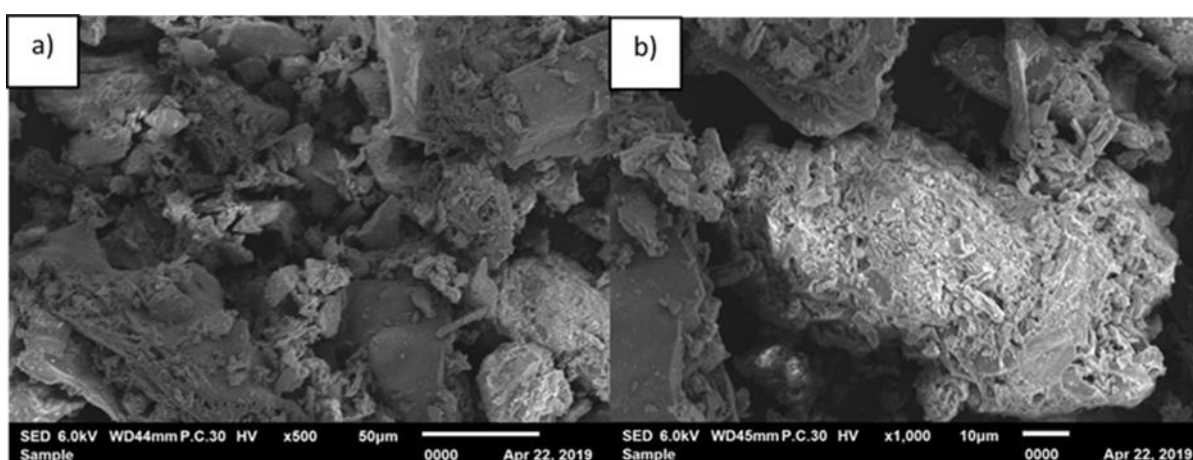


Fig 3: SEM micrographs of RHA at magnification of a) 500X and b) x1000X.

3.2. Characterization of the Sorbent Pellets

3.2.1 Average Size of the Pellets

Fig. 4 (a) and (b) show the different ratio of CaO-SiO_2 pellets obtained from the granulation process. As shown in Fig. 4 (a) and (b), the average size of particles for 80:20 and 70:30 pellets are 3.0 mm and 4.5 mm respectively.

The utilization of high speed of granulator and optimum amount of deionized water added during the granulation process resulted in small size of pellets. A small size of pellets was desired as the smaller the pellets, the higher the surface area of the pellets to covered for potential CO_2 adsorption application. However, the significant difference in the average particles size among the two ratios is presumed to occur due to the different amount of RHA, as the SiO_2 source added in CaO-SiO_2 pellets. The smaller size of pellets is obtained when lower amount of RHA added. Table 2 summarized the details of granulation process and the resulted average particles size for each ratio before undergo calcination process at 750°C .

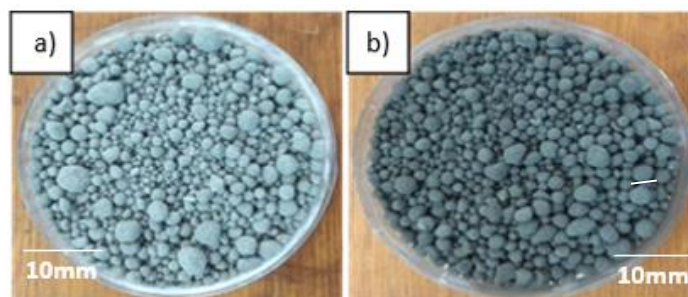


Fig. 4 .The obtained pellets from the granulation process of (a) ratio 80:20 and (b) ratio 70:30.

Table 2: Summary of the pellets obtained from two different ratios.

Ratio of Ca(OH) ₂ and RHA	Impeller and Chopper Speed (rpm)	Amount of Deionized Water (ml)	Average Size (mm)
80:20	73, 1700-1800	300	3.0
70:30	73, 1700-1800	300	4.5

Fig. 5 shows that CaO-SiO₂ pellets after the calcination process at 750°C. As can be observed in Fig. 5, all pellets have significant reduction in the size of pellet which is much smaller compared to the one before the calcination. This is probably due to the elimination of moisture from the pellets and significant reduction/shrinkage in pellets size after the calcination indicates huge amount of moisture content in each pellets.

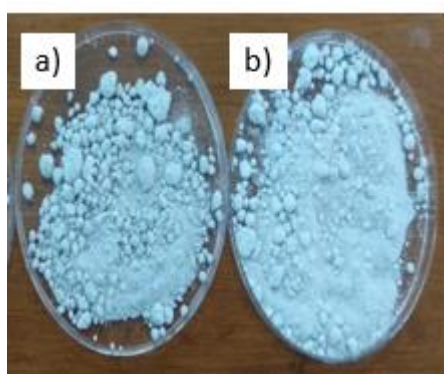


Fig. 5. Pellets after calcination of different ratio ;(a) 80:20 and (b) 70:30.

3.2.2 Different Ratio of CaO-SiO₂ Pellets Before Calcination

The phase structure of CaO-SiO₂ pellets for each ratio before the calcination process was characterized by XRD analysis, as displayed in Fig. 6 (a) and (b). The peak characteristics of Ca(OH)₂ and SiO₂ are detected in XRD pattern of all CaO-SiO₂ pellets. According to Fig. 6, it is evident that the main crystalline peaks of Ca(OH)₂ were detected at about $2\theta = 28.76^\circ$,

34.17°, 47.21° and 62.78°. However, the intensity for each peak was decreased with increasing amount of RHA added. Besides, the characteristics peak of silica also could be observed from the XRD pattern, however, the intensity of the peaks was very low due to its amorphous nature. The silica peak centered about $2\theta = 23^\circ$ was observed in both XRD spectras of pellets prepared.

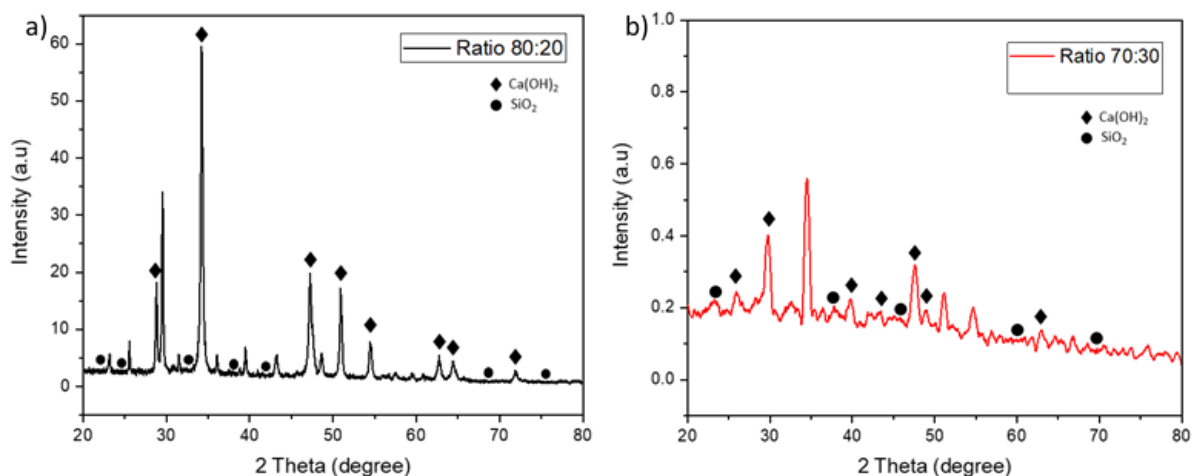


Fig. 6. XRD spectra for different ratio of CaO-SiO₂ before calcination, (a) 80: 20 and (b) 70:30

Different ratio of RHA addition in the CaO-SiO₂ pellets as the biomass sacrificial template did not disrupted the crystalline structure of the calcium precursor. This is proved by the almost similar XRD pattern obtained from the CaO-SiO₂ pellets with the XRD pattern of the raw Ca(OH)₂. Besides, the detection of similar major diffraction peaks from XRD pattern of all pellets evidenced the incorporation of sacrificial biomass template materials did not modify the crystallinity of the pellets produced [8].

The SEM micrograph of the prepared CaO-SiO₂ pellets at different ratios were shown in Fig. 7 and 8. All the micrographs illustrated that addition of RHA had significantly altered the morphology of CaO-SiO₂ pellets prepared, according to the ratio. Based on Fig. 8, 80:20 pellet shows large and irregular grains size with random distribution. Meanwhile, 70:30 pellet exhibits randomly distributed, irregular, and smaller shape of microstructures. Some small needle-like or flake structure could be observed which indicates the presence of ash or biomass material inside the pellets that have been prepared. According to the micrographs obtained, increasing amount of RHA added caused the grains size to decrease significantly which lead to the development of irregular microstructures.

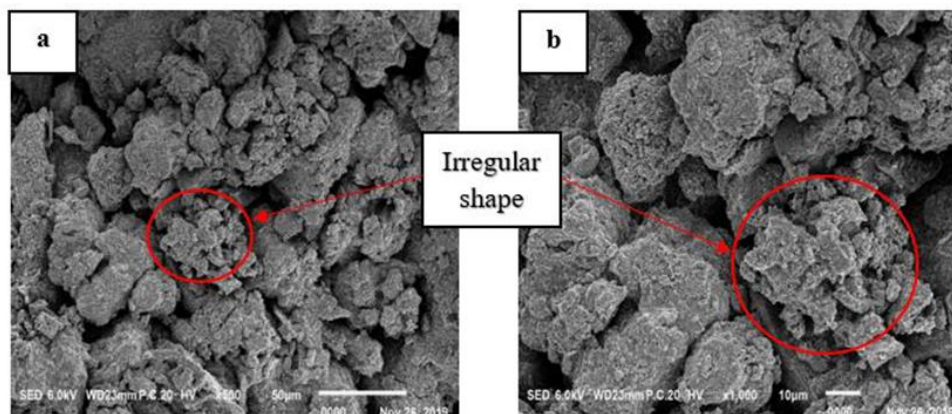


Fig.7. SEM micrographs of CaO-SiO₂ pellets ratio 70:30 before calcination at different magnification a) 500X and b) 1000X

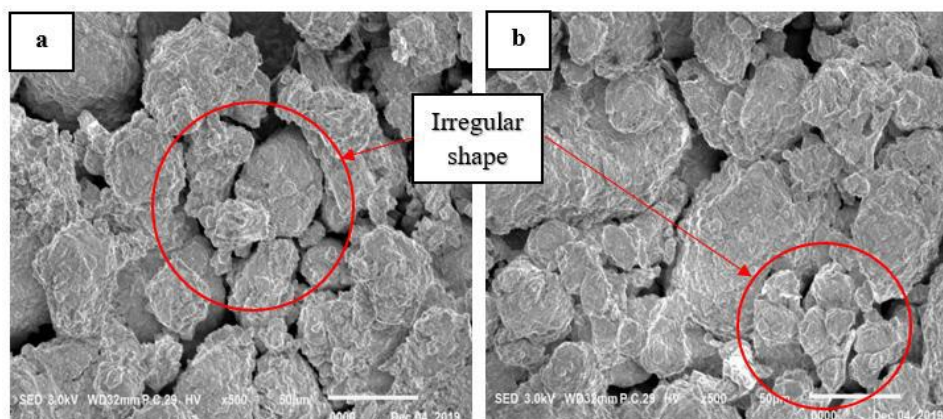


Fig.8. SEM micrographs of CaO-SiO₂ pellets ratio 80:20 before calcination at two different spots by magnification of 500X

3.2.3 Effect of Different Ratio after 750 °C Calcination

The effect of calcination at 750°C on the phase structure of CaO-SiO₂ pellets prepared is shown in Fig. 9. Sharp peaks were detected from all of the XRD pattern obtained which confirmed the existence of crystalline phase. This is due to the formation of CaO after sintering at 750°C. The CaO peaks can be observed at $2\theta = 29.76^\circ, 33.02^\circ, 39.49^\circ, 47.56^\circ, 51.91^\circ$ and 54.58° .

However, there is significant difference in intensity of peak at $2\theta = 29.76^\circ$. The highest peak intensity was observed in 70:30 pellet followed by 80:20 pellet. Supposedly, if the amount of CaO is higher compared to the silicate, the significant increment in peak intensity of CaO should be obtained whereas the silicate peaks should remain unchanged [10]. But from the XRD pattern obtained, pellet with low amount of CaO (70:30 pellet specifically) possessed the highest peak of CaO. This is presumed to occur due to the calcination process at 750°C might have altered the phase structure of silica in RHA and thus modified the XRD pattern of all pellets.

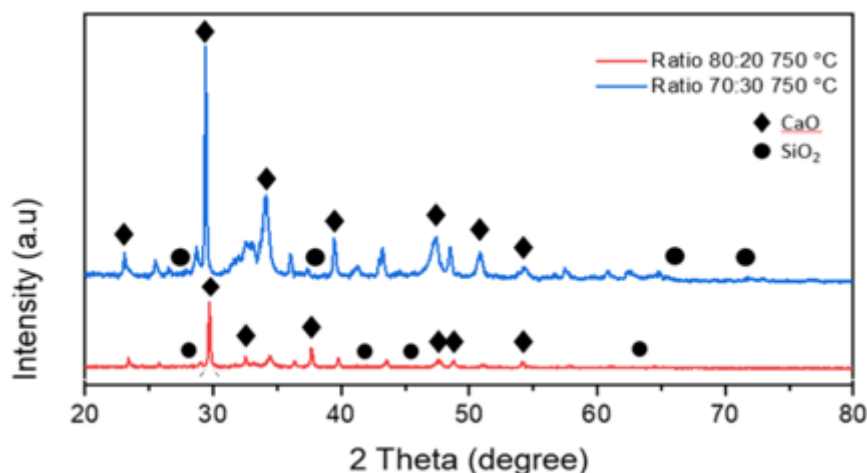


Fig.9. XRD spectra for different ratio of CaO-SiO₂ pellet calcined at 750°C

Morphology of the calcined CaO-SiO₂ pellets for each ratio are shown in Fig. 10 and 11. After calcination at 750°C, the formation of pores was observed in micrographs acquired. For 80:20 pellet, grains with random sized have been developed after sintering at 750°C with the presence of needle-like structure. The presence of needle-like structure suggests formation of a new compound resulted from the calcination of CaO-RHA which mainly composed of Ca, Si and O elements [11]. As for 70:30 pellet, the morphology consists of randomly scattered grains which is small in size as shown in Fig. 11. 70:30 pellet has irregular pores structure but not as large as compared to the pore structure in 80:20 pellet. However, 80:20 pellet shows better porosity as the pores size were larger which caused an increased in porosity. Higher amount of well-structured pores were more preferred for CO₂ capture application; in which it would contribute to an excellent performance of CO₂ adsorption.

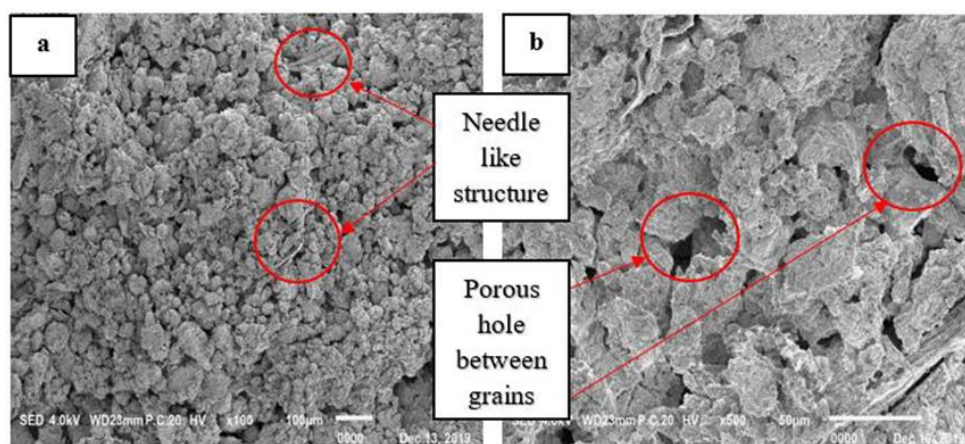


Fig.10. SEM micrographs of CaO-SiO₂ pellets ratio 80:20 after calcination at 750°C with different magnification a) 100X and b) 500X.

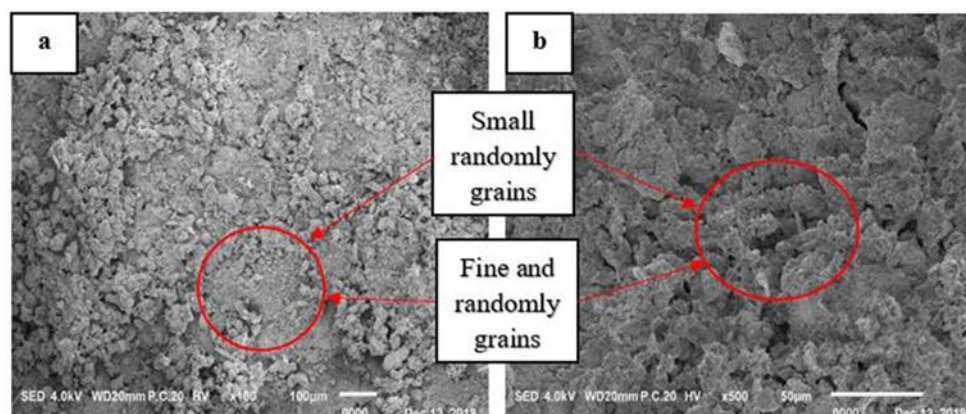


Fig.11. SEM micrographs of CaO-SiO₂ pellets ratio 70:30 after calcination at 750 °C with different magnification a) 100X and b) 500X.

4. CONCLUSION

This study presented the CaO-based pellets with addition of RHA as the sacrificial bio-temple had been successfully prepared via granulation method. The calcium precursor, Ca(OH)₂ has agglomerates and granular microstructures and RHA has an irregular and in definitive shape of microstructures. Based on the XRD analysis, the Ca(OH)₂ has crystalline structure, while RHA has amorphous structure. XRD analysis proved that the inclusion of RHA in the Ca(OH)₂ did not disrupted the crystalline structure of the samples and intensity of the peaks were reduced with increasing amount of RHA added. However, the calcination at 750°C has significantly modified the XRD pattern of all CaO-SiO₂ pellets. The sharp peaks indicated the development of crystalline CaO and different ratio has different peak intensity. The pellets with low amount of RHA has finer grain structure observed as for increased the amount of RHA caused the pores became agglomerate, increase in size and randomly distributed. To conclude, based from the characterization result it indicates that ratio 80:20 and calcination temperature of 750 °C were the optimum parameters to be used for the pellets production.

REFERENCES

- [1] Rawshan AB, Kazi S, Sharifah Mastura SA, Mokhtar J. (2015) CO₂ emissions, energy consumption, economic and population growth in Malaysia. *Renew.Sust. Energ. Rev.*, 41:594–601.
- [2] Alifah Z. (2017). Malaysia to slash another 25% of CO₂ emission by 2030. Retrieved from: <https://themalaysianreserve.com/2017/06/21/malaysia-slash-another-25-co2-emission-2030/>
- [3] Naeem MA, Armutlulu A, Kierzkowska A & Müller CR. (2017) Development of High-performance CaO-based CO₂ Sorbents Stabilized with Al₂O₃ or MgO. *Energy Procedia*, 114: 158–166.
- [4] Zhang Z, Tohid NGB, Muftah HEN. (2018) Carbon Capture. Chapter 4.5, Exergetic, Energetic Environ. Dimensions, 997-1016.
- [5] Wang J, Huang L, Yang R, Zhang Z, Wu J, Gao Y, Wang Q, O'Hare D, Zhong Z. (2014) Recent advances in solid sorbents for CO₂ capture and new development trends. *Energy. Environ. Sci.*, 7:3478–3518.

-
- [6] Monica BG, Jose, MV, Antonio P, Pedro ESJ, Luis APM. (2018) Low-cost Ca-based composites synthesized by biotemplate method for thermochemical energy storage of concentrated solar power. *Appl. Energy*, 210:108–116.
- [7] Mustakimah M, Suzana Y, Armando TQ, Tetsuya K. (2018) Utilization of rice husk to enhance calcium oxide-based sorbent prepared from waste cockle shells for cyclic CO₂ capture in high-temperature condition. *Environ. Sci. Pollut. Res.*, 26:33882-33896.
- [8] Liu, W., An, H., Qin, C., Yin, J., Wang, G., Feng, B., Xu, M. (2012) Performance Enhancement of Calcium Oxide Sorbents for Cyclic CO₂ Capture: A Review. *Energ. Fuels*, 26:275-2767.
- [9] María E, Vasilije M, Edward JA. (2016) Calcium looping sorbents for CO₂ capture. *Appl. Energy*, 180:722–742.
- [10] Sanchez-Jimenez PE, Perez-Maqueda LA, & Valverde JM. (2014) Nanosilica supported CaO: a regenerable and mechanically hard CO₂ sorbent at Ca-looping conditions. *Appl. Energy*, 118:92-99.
- [11] Li Y, Zhao C, Ren Q, Duan L, Chen H, Chen X. (2009) Effect of rice husk ash addition on CO₂ capture behavior of calcium-based sorbent during calcium looping cycle. *Full Processing Technology*, 90: 825-834.

PREPARATION OF THE ELECTROSPUN POLYVINYLIDENE FLUORIDE / POLYVINYL ALCOHOL SCAFFOLD AS A POTENTIAL TISSUE REPLACEMENT

MOHD SYAHIR ANWAR HAMZAH¹, NURUL AMIRA AB RAZAK¹, CELINE NG¹,
AKMAL HAFISZI ABDUL AZIZE¹, JUMADI ABDUL SUKOR¹, SOON CHIN FHONG²,
MOHD SAFIEE IDRIS³ AND NADIRUL HASRAF MAT NAYAN^{2*}

¹Faculty of Engineering Technology, Universiti Tun Hussein Onn Malaysia,
Pagoh Higher Education Hub, Jalan Panchor, Pagoh, Johor, 84600, Malaysia

²Microelectronics and Nanotechnology-Shamsuddin Research Centre,
Universiti Tun Hussein Onn Malaysia, Parit Raja, Johor, 86400, Malaysia

³Faculty of Technical and Vocational Education, Universiti Tun Hussein Onn
Malaysia, Parit Raja, Johor, 86400, Malaysia

*Corresponding author: nadirul@uthm.edu.my

(Received: 12th April 2020; Accepted: 30th September 2020; Published on-line: 4th January 2021)

ABSTRACT: Polyvinylidene fluoride (PVDF), a piezoelectric material, is commonly used in tissue engineering due to its potential for mimicking the electrical microenvironment of biological conditions for tissue development. In this present research, polyvinyl alcohol (PVA) was introduced into electrospun PVDF fabrication through an electrospinning process, aiming to enhance the nanofibrous membrane's biocompatibility properties by improving the hydrophilicity properties to act as an artificial tissue scaffold. The electrospun PVDF/PVA membranes are found to be optimum at a PVDF-to-PVA ratio of 90:10 due to its excellent mechanical, morphological, and hydrophilicity conductivity properties. Fourier transform infrared (FTIR) spectroscopy verified strong hydrogen bonding interaction formed between the fluorine group of PVDF with oxygen-containing in the hydroxyl group of PVA. *In-vitro* cell culture showed that the enhanced hydrophilic property of electrospun PVDF/PVA could significantly enhance the cell growth. These positive results indicated that the scaffold could be implemented as artificial tissue material for tissue engineering applications.

ABSTRAK: Polivinilidena fluorida (PVDF) adalah bahan piezoelektrik yang biasa digunakan dalam kejuruteraan tisu kerana potensinya menyerupai keadaan persekitaran mikro-elektrik biologi bagi perkembangan tisu. Dalam penyelidikan ini, polivinil alkohol (PVA) diperkenalkan ke dalam fabrikasi pintalan-elektro PVDF melalui proses pemintalan-elektro, yang bertujuan bagi mengembangkan sifat biokompatibiliti membran nanogentian dengan meningkatkan sifat hidrofilik bagi menjadi perancah tisu tiruan. Membran pintalan-elektro PVDF / PVA didapati optimum pada nisbah PVDF-ke-PVA, 90:10 kerana sifat kekonduksian, mekanikal, morfologi dan hidrofiliknya yang sangat baik. Spektroskopi transformasi inframerah Fourier (FTIR) mengesahkan interaksi ikatan hidrogen yang kuat terbentuk antara kumpulan fluoro PVDF dengan oksigen yang terkandung dalam kumpulan hidroksil PVA. Kultur sel secara *in-vitro* menunjukkan bahawa sifat hidrofilik pintalan-elektro PVDF / PVA dapat meningkatkan pertumbuhan sel secara signifikan. Hasil positif ini menunjukkan bahawa perancah ini dapat digunakan sebagai bahan tisu buatan bagi aplikasi kejuruteraan tisu.

KEYWORDS: *polyvinylidene fluoride; polyvinyl alcohol; electrospinning; tissue engineering; nanofiber scaffold*

1. INTRODUCTION

Damaged tissues or organs can lead to fatal health problems. When natural repair is impossible, doctors use tissue or organ transplantation to restore damaged biological systems' structures and functions [1–3]. Transplant demand currently exceeds availability, generating unmet clinical needs. The U.S. Department of Health and Human Services estimated that 20 people die every day waiting for transplants inaccessible due to organ or tissue scarcity. Tissue engineering has long been known as a promising alternative to donor tissues, often in short supply. Nanofiber-based scaffolds are preferred for nerve, skin, cartilage, and other soft tissue replacement applications among various scaffolds. The tissue scaffold provides a temporary matrix to promote tissue regeneration by remodeling tissue functions and promoting cell growth in artificial microarchitecture [2-4]. For clinical applications, tissue scaffold's mechanical properties should be enough to withstand internal and external forces depending on tissue and organ types. The tissue scaffold must be biocompatible with good hydrophilic characteristics and a high ratio of surface-to-volume to speed up cell seeding and nutrient diffusion through the artificial tissue structures [3].

Electrospinning is a simple technique commonly used due to its ability to be manufactured with controllable surface morphology, flexible porosity, and optimum mechanical efficiency, which is favorable for the preparation of nanofiber scaffolds [5]. Studies show that the alignment and diameter of electrospinning fibers can be modified to suit the design of a broad range of cells/tissues, favorably influencing cell formation, degradation rates, physical condition, and artificial scaffold mechanical properties [6-7]. The material selection is important because the performance of the electrospinning process depends on the polymer solution's ability to form a fine charged jet while applying a strong electric field. An electroactive material is a potential choice, especially a piezoelectric material, to recreate the electrical microenvironment of cell or tissue growth [8-9]. It can produce electrical stimulation under body movement action without an external power source. Electrical stimulation can control several cellular functions, including the reorganization of their cytoskeleton, differentiation, intracellular pathway activation, protein secretion, and gene expression [9].

Polyvinylidene fluoride (PVDF) is a piezoelectric polymer with semi-crystalline structure and could exist in different possible polymorphism phases which are α , β , γ , and δ [10]. Previous study on the electrospinning of PVDF shows that the dominant orientation crystalline structure of polar β -phase crystal along the fiber axis, which gives high electric conductivity behavior and makes it suitable for tissue engineering [11]. The major drawback of PVDF in tissue engineering is that it is not a hydrophilic polymer that can lead to low cell affinity and inflammatory effect towards the host tissue or organ. For that reason, many researchers have incorporated PVDF with hydrophilic fillers such as polyurethane (PU), trifluoroethylene (TrFE), chitosan, graphene oxide (GO), and polyhedral oligomeric silsesquioxane–epigallocatechin gallate (POSS–EGCG) conjugate to increase its water absorption ability and specific cell recognition sites without losing its mechanical integrity [12-15]. The study of modified PVDF with trifluoroethylene (TrFE) for in-vitro cell culture shows better support for Schwann cells and myelination growth than the neat PVDF scaffold alone [16]. Other studies showed success in manufacturing microporous PVDF membranes for nerve tissue engineering by covalently immobilising L-lysine on the surface of the PVDF membrane [17].

Polyvinyl alcohol (PVA) is a semicrystalline hydrophilic polymer easily soluble in water, commonly used in biomedical applications due to its biocompatibility with most tissue types, ability to absorb protein molecules, ability to follow minimum cell adhesion,

and high stability at large temperature ranges [18-19]. Other than that, the crystalline structure consists of the hydroxyl group, which makes a high degree of miscibility with other materials and serves as a cell-bind recognition site at the scaffold throughout the process of regeneration [20]. PVA structure also has a negative charge and an excellent ability to absorb cation molecules. It is also tasteless and odorless, has strong mechanical strength, high capacity to shape scaffolds, good biocompatibility, and biodegradability in human tissue and fluid [21]. Therefore, PVA can be combined with PVDF to obtain a scaffold with desired physical properties suitable for cell and tissue regeneration processes.

In this work, electrospun PVDF/PVA scaffolds were fabricated using single phase horizontal type electrospinning (illustrated in Figure 1). The electrospun samples were systematically characterized in terms of mechanical property, wettability, swelling percentage, morphological condition, conductivity performance, and FTIR spectroscopy. The in-vitro cell behavior was also examined by culturing human dermal fibroblast (HDF) cells on top of the electrospun samples before being analyzed using MTT assay and SEM micrograph. To date, no single-phase PVDF / PVA nanofiber scaffold studies using the electrospinning technique have been published.

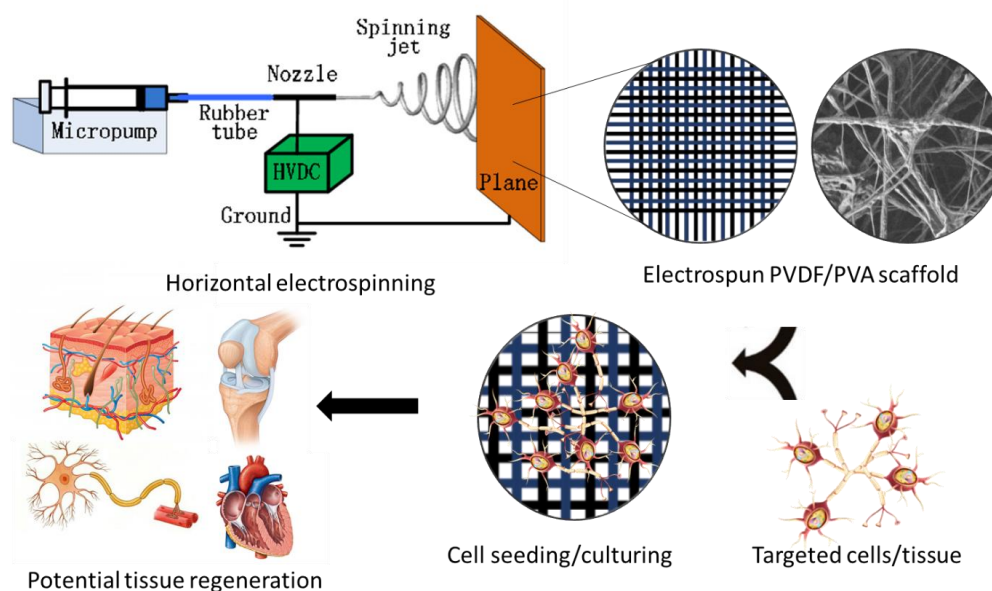


Fig. 1: Illustration of horizontal of electrospinning process and the potential application of electrospun PVDF/PVA membranes in tissue engineering.

2. MATERIALS AND METHODOLOGY

2.1 Materials

All materials used in this work are analytical grade materials. PVDF with molar weight of 534,000 g/mol and PVA with molar weight of more than 89,000 g/mol were purchased from Sigma Aldrich. Dimethyl sulfoxide (DMSO) with molar weight of 84.17 g/mol and phosphate buffered saline (PBS) were supplied by Merck.

2.2 Preparation of Electrospun PVDF/PVA

The PVDF and PVA were dissolved in 5 mL DMSO solution forming 0.15% (w/v) concentration with varied PVDF-to-PVA ratio and six electrospun PVDF/PVA nanofiber samples were prepared (Table 1). The electrospinning apparatus was set up horizontally. 5-

mL polymer solution was placed in a 5-mL plastic syringe with 23G needle size and an injection rate of 1.0 ml/h. The needle tip of the syringe was connected to a 5-kV voltage power with the tip-to-collector distance of 13 cm.

Table 1: PVDF-to-PVA ratio used in fabrication process

PVDF-to-PVA ratio	Type of sample
100:0	100PVDF/0PVA or Neat PVDF
95:5	95PVDF/5PVA
90:10	90PVDF/10PVA
85:15	85PVDF/15PVA
80:20	80PVDF/20PVA
75:25	75PVDF/25PVA

2.3 Field Emission Scanning Electron Microscope (FESEM)

The FESEM model JSM-7800F, brand JEOL was used for morphological observation of PVDF/PVA nanofiber. The nanofiber was sputter coated with gold for 30 s at 18 Ma with 100× – 10000× magnification. From the magnified image, the diameter of nanofiber was determined using ImageJ software to analyze at least 100 different fibers.

2.4 Tensile Test

Tensile test was conducted to obtain the stress–strain graph using a universal tester according to ASTM D-882 (Instron, 2018). The testing of the sample was performed at a strain rate of 10 mm/min and load strength of 5 kN at room temperature. Five replications were conducted for each sample.

2.5 Water Contact Angle (WCA)

The WCA was measured using the sessile drop method adopted from ASTM D7334 - 08, where the image of 1 µl of deionized water dropped on the surface of the samples was captured using the video contact angle system (VCA Optima, Ast Products Inc.) after 3s. Three replications were tested for each sample.

2.6 Degree of Swelling

The samples were dried in the oven at 70 °C until a constant weight was achieved to eliminate water before testing. Then, the nanofiber was immersed in 10 ml of PBS and the weight of the swollen nanofiber was recorded in the time interval of 1 day, to 5 days. Three replications were conducted for each sample. The degree of swelling for each sample was calculated using Eq. 1.

$$\text{Degree of Swelling (\%)} = \frac{w_f - w_i}{w_f} \times 100 \quad (1)$$

where, w_f represents the weight of swollen nanofiber at a predetermined time and w_i is the initial weight of the nanofiber.

2.7 Conductivity

The conductivity of PVDF/PVA nanofiber was measured using a multimeter (SANWA, Japan). The nanofiber with a thickness of 1 cm and diameter of 0.4 cm was placed between two blades that were planted on a nonconductive substrate. Three resistance measurements were taken for each specimen and the conductivity was calculated using Eq. 2.

$$\text{Conductivity} = \frac{1}{\rho} = \frac{l}{RA} \quad (2)$$

where, ρ represents the electrical resistivity through a specific area, R is the resistance given by the sample, l signifies the sample thickness used, and A is the surface area of the sample.

2.8 Fourier Transform Infrared Spectroscopy (FTIR)

FTIR spectroscopy (Perkin Elmer Frontier) was used to determine the structural and interaction characteristic of pristine PVDF and the optimum PVDF/PVA nanofibers within the wavelength from 400 to 4000 cm^{-1} . The sample of nanofiber was prepared into a size of 1 cm x 1 cm and placed in the holder and the total pressure applied was set before processing the sample.

2.9 In-vitro Culture of Human Dermal Fibroblast (HDF) Cells

In this experiment, the 5th to 10th passages of HDF cells were used and cultured in T-flasks comprising DMEM medium supplemented with 10% (v/v) fetal bovine serum (FBS), 1% (v/v) L-glutamine, and 1% (v/v) penicillin/streptomycin. The cells were incubated at 37°C with 5% CO_2 and the medium was refreshed every 3 days. The nanofibrous samples were seeded with HDF cell suspension at 1×10^4 cells/ml in 24-well culture plates. The cells were allowed to attach for at least 10 minutes and the medium was refreshed with a new culture medium before the samples were subjected to incubation periods depending on assay requirements [22].

2.10 Cytotoxicity: MTT Assay

MTT assay was performed to evaluate the cell proliferation and metabolic activity by quantifying the purple formazan crystals absorbance that represents the amount of survived cell after 24 and 48 hrs of incubation period. The nanofibrous samples were transferred into new wells and the MTT reagent was added into each well. Then, the samples were incubated for 4 hrs until formazan crystals were formed. The absorbance of the solution was measured at 570 nm using a microplate reader [22].

2.11 Scanning Electron Microscope (SEM)

The morphological characteristic of HDF cultured cells was examined using SEM after 24 hrs. The samples were washed with PBS and fixed with 2.5% glutaraldehyde at 4 °C overnight. Then, the samples were dehydrated using a series of graded alcohol and allowed to vacuum dry before being sputter coated with gold. Then, the samples were perceived using SEM (Leo Supra 50VP Field Emission SEM, Carl Zeiss, Germany) at the accelerating voltage of 15 kV.

3. RESULTS AND DISCUSSION

3.1 Morphology Characterization

Figure 2 shows the fibrous nanostructure fibers of pure PVDF and electrospun PVDF/PVA with its diameter distribution. Figure 2(a)–1(c) show that the diameter of nanofibers decreased from 210 to 161 nm as the PVA ratio achieved 10% (w/v) of PVDF polymer solution.

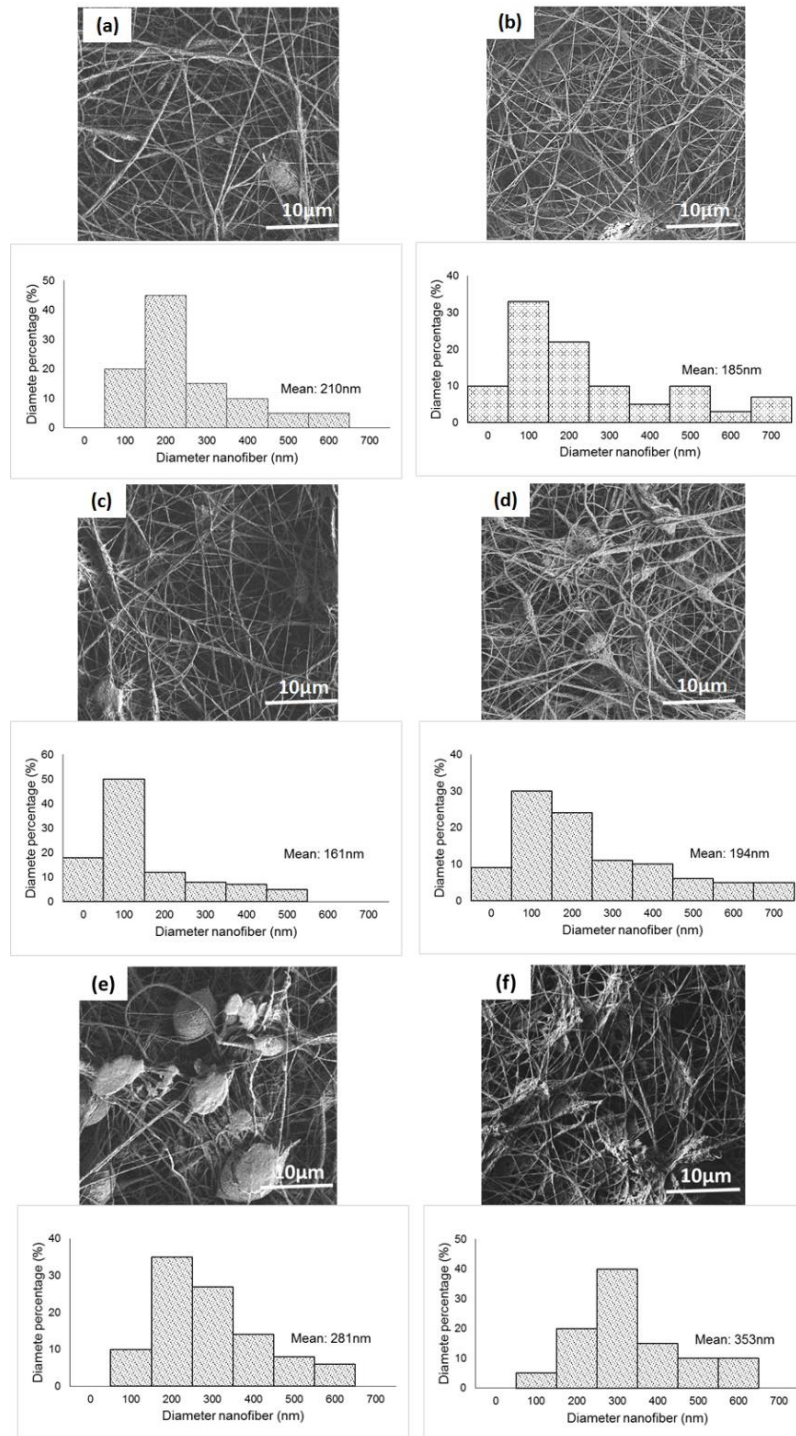


Fig. 2: FESEM micrograph and diameter distribution of electrospun samples of (a) 100PVDF/0PVA, (b) 95PVDF/5PVA, (c) 90PVDF/10PVA, (d) 85PVDF/15PVA, (e) 80PVDF/20PVA, and (f) 75PVDF/25PVA at 1.00k magnification.

The small amount of PVA inclusion has significantly effect on the viscosity of PVDF polymer solution, which leads to better dispersion resulting from sufficient jet stretching time and volatilization of solvents. However, significant morphological changes were observed as the PVA ratio increased from 15% in 85PVDF/15PVA to 25% in 75PVDF/25PVA. Further ratio alteration caused more bead-on-string formation resulting in non-homogeneous surface occurring due to low voltage that does not allow uniform stretching of polymer that is capable of promoting uniform nanofibers. Beads occur due to

incomplete solvent evaporation due to the reduction of dielectric potential resulting from the low viscosity of conductive PVDF polymer solution. In tissue engineering applications, the diameter size of the electrospun will significantly influence the fibrous surface area and volume for cell attachment, where smaller diameter can provide high density for cell cultivation [23-24]. This advantage will greatly benefit the cells or tissues that have limited capacity for endogenous regeneration and/or replacement of defective cells such as those in the brain and nervous system.

3.2 Tensile Strength Characterization

Mechanical properties of electrospun nanofiber are crucial elements in tissue engineering, especially during surgeries. An ideal electrospun nanofiber should be durable, flexible, and able to sustain high pressure when tissue begins to infiltrate into the scaffold, and increase growth [25]. The tensile properties of the tested samples are summarized in Fig. 3. The tensile strength and Young's modulus of the neat electrospun PVDF was 1.33 ± 0.7 MPa and 9.61 ± 0.2 MPa, respectively. The alteration of PVDF-to-PVA ratio from 5% to 10% increased the tensile strength and Young's modulus significantly. However, the higher inclusion of PVA (15% to 25%) drastically reduced the mechanical integrity of the electrospun nanofiber. This reduction may be caused by the loss of PVDF phases in the formulation as shown in the SEM micrograph. The higher reduction of PVDF ratio produced an unstable electrospinning process that led to the high number of beads that affect the structural integrity of the electrospun fiber's performance. Sample 90PVDF/10PVA has an optimal tensile strength of 1.72 ± 0.6 MPa and Young's modulus of 22.03 ± 0.5 MPa. Previous study reported that the tensile strength for natural soft collagenous tissues such as cartilage, cornea, nerve, and skin is around 1 to 10 MPa [3, 23]. Therefore, based on these findings, the modified electrospun nanofiber meets the requirement as a potential tissue scaffold.

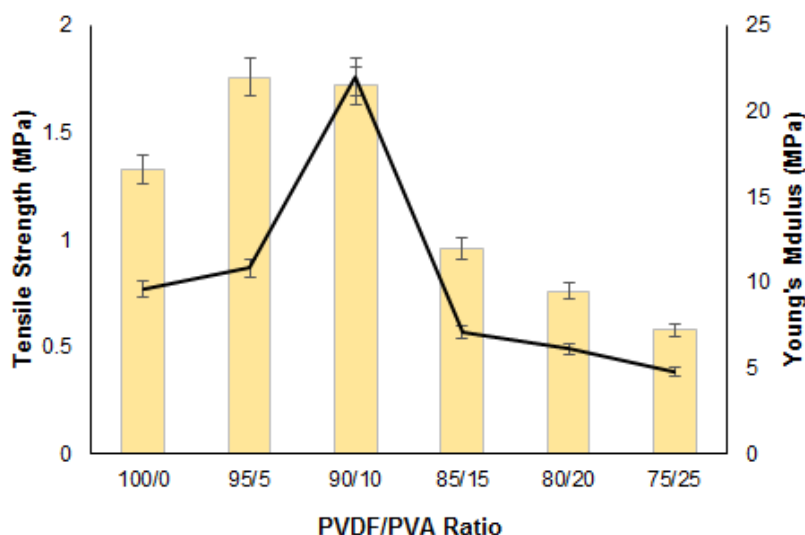


Fig. 3: The tensile strength and Young's modulus of neat PVDF and electrospun PVDF/PVA.

3.3 Water Contact Angle (WCA)

In tissue engineering, the surface of the artificial tissue scaffold is the first component that comes into contact with the biological structure, which allows the desired outcome of tissue growth if it is biocompatible. The WCA is one of the methods used to study the sample's surface performance in terms of wettability [26-27]. Figure 4 presents the WCA

and the images of water dropped on the electrospun samples. The WCA for 100PVDF/0PVA was 130.50° , indicating the super hydrophobicity of the electrospun sample surface contributed by its low surface energy and hydrophobic property. However, the addition of PVA monomer in the PVDF formulation significantly reduced the WCA in achieving the hydrophilic value of more than 90° . The PVA monomer introduced hydroxyl and carbonyl groups into the electrospun PVDF surface and changed the polarity of surfaces by increasing the specific hydrogen bond as well as the electrostatic forces with water molecules. Figure 4 (d)–(f) show that the higher increase of PVA addition slightly increased the WCA values due to the increase in bead-string formation that results in rougher surfaces compared to the PVA at 5% and 10% ratio as shown by FESEM micrograph in Figure 2 (d)–(f). Generally, higher surface roughness leads to low water drop–material contact area, which will interrupt water-fiber interface and further reduce the contact area between the artificial scaffold and biological specimen. Hence, low WCA will be favorable for tissue engineering applications because it will maximize the output outcome when the scaffold is allocated at the lesion site of tissues [26,28].

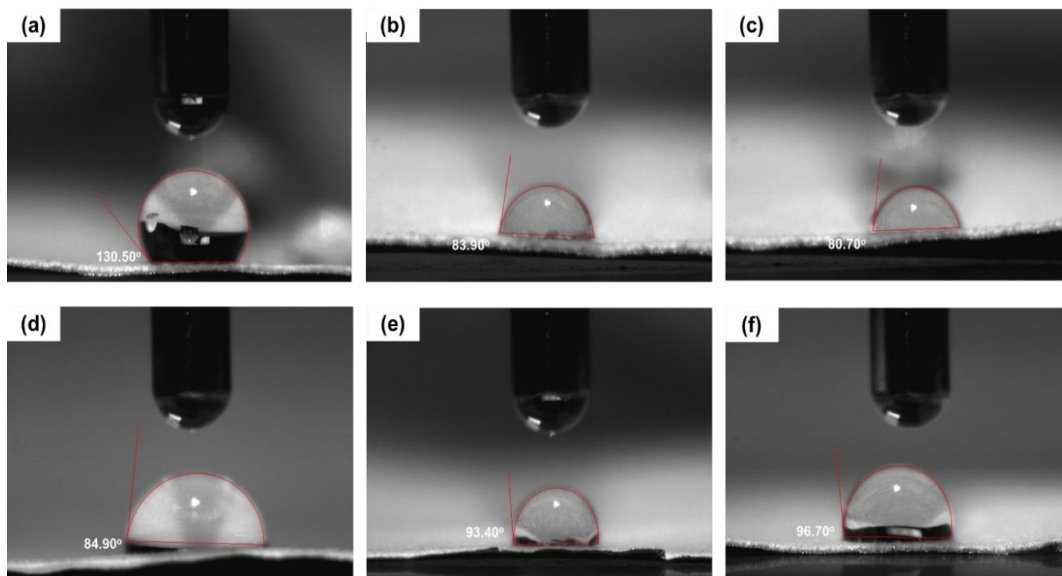


Fig. 4: Surface contact angle of (a) 100PVDF/0PVA, (b) 95PVDF/5PVA, (c) 90PVDF/10PVA, (d) 85PVDF/15PVA, (e) 80PVDF/20PVA, and (f) 75PVDF/25PVA.

3.4 Degree of Swelling

The ability of the sample to absorb water molecules plays a major role during cell growth, especially during cell seeding. It will also influence the potential of the electrospun composite to maintain its shape during the application. Figure 5 presents the degree of swelling percentage of the neat PVDF and its modification containing electrospun PVA. The results reveal that the inclusion of PVA strongly influences the swelling capacity of the electrospun nanofiber as the degree of swelling increased from $4.76\pm 1.3\%$ (for 100PVDF/0PVA) to $69.84\pm 1.5\%$ (for 90PVDF/10PVA) after 24 hrs of immersion in PBS at pH 7.4. The increase of the swelling percentage could be attributed to the fine inter- and intra-polymer reactions and the addition of hydrophilic groups in the electrospun PVDF/PVA. This observation corroborates the WCA experiment, where the presence of PVA increased the specific interaction between the electrospun surfaces as a substrate to water molecule through the hydrogen bond. Increases can also be seen after 24 hours of

immersion, showing a positive indication to sustaining the swelling activity during the healing process as it will affect the signaling mechanism of molecules and nutrients. [29].

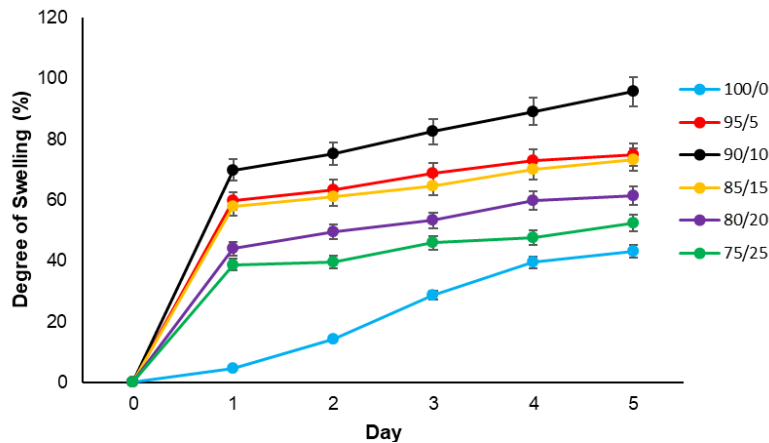


Fig. 5: Percentage of swelling for neat PVDF and electrospun PVDF/PVA.

3.5 Conductivity Analysis

The conductivity of each sample was calculated using Equation 2 and is presented in Table 2. The conductivity of the neat PVDF nanofiber was 4.023×10^{-4} S/cm. The conductivity of electrospun PVDF was contributed to by the formation of a β -phase that plays an important role in piezoelectric and pyroelectric performance [30-31]. The conductivity increased with the increasing amount of PVA until 10% inclusion at 5.991×10^{-4} S/cm. This might be due to the electrospinning process causing the dielectric polarization of the dielectric PVA monomer. It has led to the increase in intermolecular distance and the mobility of the chains, which accelerates the orientation of the modified polymer molecules into more crystalline structures. Besides, this improvement was also contributed to by the uniform dispersion and proper interaction of PVDF and PVA forming a uniform, porous, and well-fibered structure, which will act as a charge carrier (hole) motion for the conducting electrical charges [32]. However, higher inclusion reduced the conductivity due to the higher loss of PVDF monomer and increased bed-string fiber, thus causing low electrical motion carrier throughout the electrospun samples.

Table 2: The conductivity of neat PVDF and PVDF/PVA electrospuns.

PVDF/PVA Ratio	Conductivity (S/cm)
100/0	$4.023 \times 10^{-4} \pm 0.021$
95/5	$4.834 \times 10^{-4} \pm 0.013$
90/10	$5.991 \times 10^{-4} \pm 0.026$
85/15	$4.917 \times 10^{-4} \pm 0.023$
80/20	$4.123 \times 10^{-4} \pm 0.015$
75/25	$3.533 \times 10^{-4} \pm 0.016$

In general, the bioactive conductive scaffolds give huge advantages during cell attachment and proliferation where it will improve intracellular electrical signaling to sensitive cells to increase cytoplasmic content, especially for fibroblasts, neurons, myoblasts, and osteoblasts cell types [33]. Previous study reported that scaffolds with conductivity from 1.21 to 4.54×10^{-4} S/cm demonstrate excellent work in enhancing myoblasts proliferation, while scaffolds conductivity around 3.5×10^{-3} S/cm show good growth activities on cardiomyocyte and neuron cells [34]. It was also reported that the scaffolds with conductivity from 6.5×10^{-4} to 1.4×10^{-3} S/cm show good adhesion and

proliferation of cells using rabbit adipose-derived mesenchymal stem cells [35]. Accordingly, the electrospun PVDF/PVA prepared in this study might be suitable for electrically sensitive tissue applications. Among the formulations, 90PVDF/10PVA is considered to be a proper condition for further testing due to its excellent morphology, and mechanical and wettability properties.

3.6 FTIR Analysis

The chemical composition of PVDF, PVA, and PVDF-PVA blended ratio 90:10 nanofiber was characterized using the FTIR spectrum. Figure 6 (a) shows a strong peak at 1400 cm^{-1} that corresponds to the C–H antisymmetric deformation, representing typical PVDF nanofiber characteristics. Meanwhile, strong peaks at 1072 , 1174 , and 1275 cm^{-1} correspond to the vibration of C–F bond that was found in the PVDF nanofiber [36]. Figure 6 (b) shows the spectrum for PVA film. The characteristic band at peaks of 3398 and 3430 cm^{-1} indicate the interconnection between the hydrogen bond of the hydroxyl functional group (O–H) [30-31]. The interaction between PVDF and PVA is depicted in Figure 6 (c), which shows the hydrogen bond interconnection between the two materials that can be observed through the new peak at 3363 cm^{-1} , which indicates the association of PVDF fluorine groups to the hydroxyl group of PVA [37]. A new peak at 2850 cm^{-1} was found in the PVDF/PVA transmission profile which donates from the C–H bond. Other strong peaks at 1071 , 1275 , and 1400 cm^{-1} , found in the PVDF/PVA spectrum, indicate the possible stretching vibration of C–F from PVDF and C–O–C bond from PVDF/PVA [14,18,36]. Meanwhile, the vibration bands occurring at 839 and 831 cm^{-1} indicate CF_2 bending and CF_2 rocking corresponding to the α and β phases [18,38].

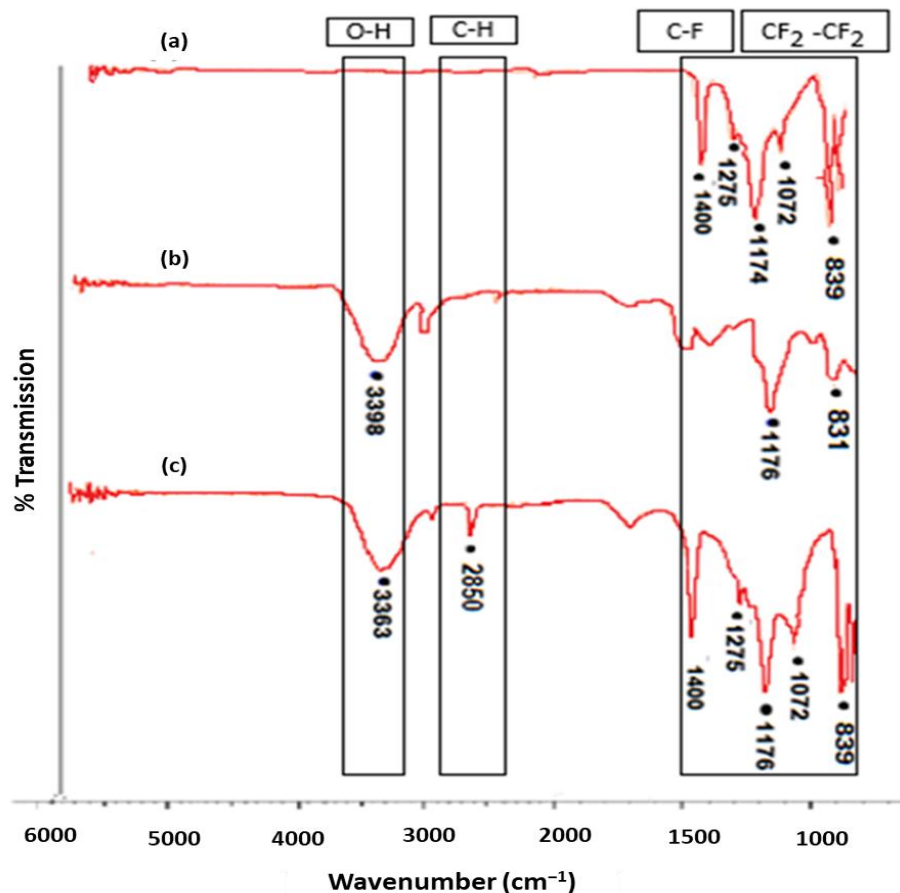


Fig. 6: FTIR spectra of electrospun (a) PVDF, (b) PVA and (c) PVDF/PVA nanofiber.

3.7 In-vitro Cytotoxicity

MTT assay was carried out to evaluate the biocompatibility of the neat PVDF and electrospun PVDF/PVA using HDF cells and compared to control negative (normal culturing) and control positive (Trixton-X). Figure 7 (a) shows that the proliferation of cells on the electrospun PVDF/PVA was higher than that of the neat electrospun PVDF, indicating that the composite polymer might have enhanced the adhesion and differentiation of HDF cells. Besides, the PVA inclusion in electrospun PVDF/PVA showed better attachment and proliferative behavior of cells after 24 hrs of seeding process compared to neat electrospun PVDF, as presented in Fig. 7 (b) and (c). The micrographs of HDF cells displayed the complete stretching morphology for both scaffold and well spreading and interaction onto electrospun PVDF/PVA surfaces compared to the neat electrospun PVDF. The addition of PVA have altered the wettability and introduced biochemical signals onto the electrospun surface, which makes it favorable for specific cells–substrate interactions [39]. Furthermore, the ability of the electrospun PVDF/PVA to absorb fluid acts as an important reason for the proliferative performance of HDF cells, because it aids in transferring metabolic products and nutrients efficiently during the cell culture.

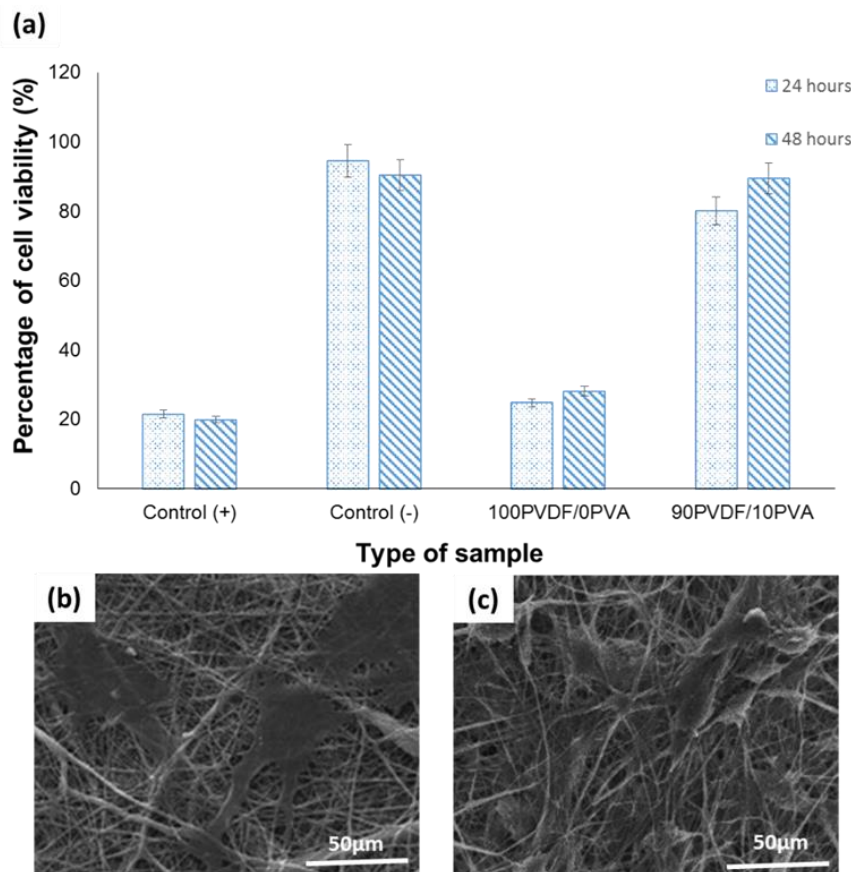


Fig. 7: (a) Percentage viability of HDF cells using MTT assay; SEM micrograph of HDF cells after 24 hrs onto electrospun (b) 100PVDF/PVA and (c) 90PVDF/10PVA at 1.5k magnification.

4. CONCLUSION

Here, nanofibrous membrane scaffolds of PVDF/PVA were developed by electrospinning with an average fiber diameter ranging from 160 to 180 nm. A PVDF-to-PVA ratio of 90:10 (90PVDF/10PVA) was found for optimal electrospun nanofiber with excellent mechanical, wettability, and electrical properties. Other studies assisted the FTIR spectra in indicating the excellent interaction between the PVDF chain and PVA monomer. PVDF/PVA has strong biocompatibility and is nontoxic to HDF cells, where the modified nanofibrous scaffold successfully assisted the process of cell differentiation and proliferation. Future work is required to reassure the impact of the nanofibrous membrane on specific targeted tissue engineering applications.

ACKNOWLEDGEMENT

This work is supported by the Universiti Tun Hussein Onn Malaysia (UTHM) through the Geran Penyelidikan Pascasiswazah (GPPS-Vot number H458) as well as Ministry of Higher Education Malaysia (KPT) through the Fundamental Research Grant Scheme FRGS/1/2019/TK10/UTHM/03/1 (FRGS-K220) and Malaysia Technical University Network Grant Scheme (MTUN-K243 and K124).

REFERENCES

- [1] Okutan N, Terzi P, Altay F. (2014) Affecting parameters on electrospinning process and characterization of electrospun gelatin nanofibers. *Food Hydrocolloids*, 39: 19-26. <https://doi.org/10.1016/j.foodhyd.2013.12.022>
- [2] Meng ZX, Xu XX, Zheng W, Zhou HM, Li L, Zheng YF, Lou X. (2011) Preparation and characterization of electrospun PLGA/gelatin nanofibers as a potential drug delivery system. *Colloids and Surfaces B: Biointerfaces*, 84(1): 97-102. <https://doi.org/10.1016/j.colsurfb.2010.12.022>
- [3] Khoo W, Koh CT, Lim SC. (2017) Synthetic and natural fibrous scaffolds for soft tissue engineering applications. *Journal of Mechanical Engineering*, 4, 223-233. Retrieved from <https://jmeche.uitm.edu.my/>
- [4] Savaşer S, Kınay ÖB, Kara BY, Cay P. (2019) Organ transplantation logistics: a case for Turkey. *OR Spectrum*, 41(2): 327-356.
- [5] Li WJ, Laurencin CT, Catterson EJ, Tuan RS, Ko FK. (2002) Electrospun nanofibrous structure: a novel scaffold for tissue engineering. *Journal of Biomedical Materials Research: An Official Journal of The Society for Biomaterials, The Japanese Society for Biomaterials, and The Australian Society for Biomaterials and the Korean Society for Biomaterials*, 60(4): 613-621. <https://doi.org/10.1002/jbm.10167>
- [6] Franco RA, Nguyen TH, Lee BT. (2011) Preparation and characterization of electrospun PCL/PLGA membranes and chitosan/gelatin hydrogels for skin bioengineering applications. *Journal of Materials Science: Materials in Medicine*, 22(10): 2207. <https://doi.org/10.1007/s10856-011-4402-8>
- [7] Hackett JM, Dang TT, Tsai EC, Cao X. (2010) Electrospun biocomposite polycaprolactone/collagen tubes as scaffolds for neural stem cell differentiation. *Materials*, 3(6): 3714-3728. <https://doi.org/10.3390/ma3063714>
- [8] Shuai C, Zeng Z, Yang Y, Qi F, Peng S, Yang W, He C, Wang G, Qian G. (2020) Graphene oxide assists polyvinylidene fluoride scaffold to reconstruct electrical microenvironment of bone tissue. *Materials & Design*, 190: 108564. <https://doi.org/10.1016/j.matdes.2020.108564>
- [9] Kitsara M, Blanquer A, Murillo G, Humblot V, Vieira SDB, Nogués C, Ibáñez E, Esteve J, Barrios L. (2019) Permanently hydrophilic, piezoelectric PVDF nanofibrous scaffolds

- promoting unaided electromechanical stimulation on osteoblasts. *Nanoscale*, 11(18): 8906-8917. <https://doi.org/10.1039/C8NR10384D>
- [10] Shao HJF, Wang H, Lin T. (2015) Effect of electrospinning parameter and polymer concentration on mechanical to electrical energy conversion of randomly oriented electrospun poly(vinylidene fluoride) nanofiber mats. *Advances*, 5(19): 14345-50. <https://doi.org/10.1039/C4RA16360E>
- [11] Ribeiro C, Correia DM, Ribeiro S, Sencadas V, Botelho G, Lanceros-Méndez S. (2015) Piezoelectric poly (vinylidene fluoride) microstructure and poling state in active tissue engineering. *Engineering in Life Sciences*, 15(4): 351-356. <https://doi.org/10.1002/elsc.201400144>
- [12] Jeong HG, Han YS, Jung KH, Kim YJ. (2019) Poly (vinylidene fluoride) composite nanofibers containing polyhedral oligomeric silsesquioxane–epigallocatechin gallate conjugate for bone tissue regeneration. *Nanomaterials*, 9(2): 184. <https://doi.org/10.3390/nano9020184>
- [13] Hamzah MSA, Azize AHA, Yusof S, Noor SM, Nayan NHM. (2019) Electrospinning and controlled release studies of polyvinylidene fluoride/pectin electrospun loaded with crocin as neuroprotective membrane prospect. *Proceedings of National Innovation & Invention Competition 2019* (pp. 335-338). Johor, Malaysia: Universiti Tun Hussein Onn Malaysia, ISBN: 978-967-2389-31-6
- [14] Park JA, Cho KY, Han CH, Nam A, Kim JH, Lee SH, Choi JW. (2019) Quaternized amphiphilic block copolymers/graphene oxide and a poly (vinyl alcohol) coating layer on graphene oxide/poly (vinylidene fluoride) electrospun nanofibers for superhydrophilic and antibacterial properties. *Scientific Reports*, 9(1): 383. <https://doi.org/10.1038/s41598-018-36479-w>
- [15] Moradi R, Karimi-Sabet J, Shariaty-Niassar M, Koochaki M. (2015) Preparation and characterization of polyvinylidene fluoride/graphene superhydrophobic fibrous films. *Polymers*, 7(8): 1444-1463. <https://doi.org/10.3390/polym7081444>
- [16] Wu S, Chen MS, Maurel P, Lee YS, Bunge MB, Arinzeh TL. (2018) Aligned fibrous PVDF-TrFE scaffolds with Schwann cells support neurite extension and myelination in vitro. *Journal of Neural Engineering*, 15(5): 056010. <https://doi.org/10.1088/1741-2552/aac77f>
- [17] Young TH, Lin UH, Lin DJ, Chang HH, Cheng LP. (2009) Immobilization of L-lysine on microporous PVDF membranes for neuron culture. *Journal of Biomaterials Science, Polymer Edition*, 20(5-6): 703-720. <https://doi.org/10.1163/156856209X426574>
- [18] Nkhwa S, Lauriaga KF, Kemal E, De, S. (2014) Poly (vinyl alcohol): physical approaches to designing biomaterials for biomedical applications. In *Conference Papers in Science* (Vol. 2014). Hindawi. <https://doi.org/10.1155/2014/403472>
- [19] Uslu I, Daştan H, Altaş A, Yayli A, Atakol O, Aksu ML. (2007) Preparation and characterization of pva/boron polymer produced by an electrospinning technique. *e-Polymers*: 7(1). DOI: <https://doi.org/10.1515/epoly.2007.7.1.1568>
- [20] Teodorescu, M., Bercea, M., & Morariu, S. (2019). Biomaterials of PVA and PVP in medical and pharmaceutical applications: Perspectives and challenges. *Biotechnology Advances*, 37(1): 109-131. <https://doi.org/10.1016/j.biotechadv.2018.11.008>
- [21] Kumar A, Han SS. (2017) PVA-based hydrogels for tissue engineering: A review. *International Journal of Polymeric Materials and Polymeric Biomaterials*, 66(4): 159-182. <https://doi.org/10.1080/00914037.2016.1190930>
- [22] Hamzah MSA, Razak SIA, Kadir MRA, Bohari SPM, Nayan NHM. (2020) Fabrication and evaluation of polylactic acid/pectin composite scaffold via freeze extraction for tissue engineering. *Journal of Polymer Engineering*, 40(5). DOI: <https://doi.org/10.1515/polyeng-2019-0377>
- [23] Hamzah MSA, Austad A, Razak SIA, Nayan NHM. (2019) Tensile and wettability properties of electrospun polycaprolactone coated with pectin/polyaniline composite for drug delivery application. *International Journal of Structural Integrity*, 10(5): 704-713. <https://doi.org/10.1108/IJSI-04-2019-0033>

- [24] Pezeshki-Modaress M, Zandi M, Rajabi S. (2018) Tailoring the gelatin/chitosan electrospun scaffold for application in skin tissue engineering: An in vitro study. *Progress in Biomaterials*, 7(3): 207-218. <https://doi.org/10.1007/s40204-018-0094-1>
- [25] Alhasssan ZA, Burezq YS, Nair R, Shehata N. (2018) Polyvinylidene difluoride piezoelectric electrospun nanofibers: Review in synthesis, fabrication, characterizations, and applications. *Journal of Nanomaterials*, 2018: 1-12. <https://doi.org/10.1155/2018/8164185>
- [26] Saudi A, Rafienia M, Zargar Kharazi A, Salehi H, Zarrabi A, Karevan M. (2019) Design and fabrication of poly (glycerol sebacate)-based fibers for neural tissue engineering: Synthesis, electrospinning, and characterization. *Polymers for Advanced Technologies*, 30(6): 1427-1440. <https://doi.org/10.1002/pat.4575>
- [27] Raffaini G, Ganazzoli F. (2007) Understanding the performance of biomaterials through molecular modeling: crossing the bridge between their intrinsic properties and the surface adsorption of proteins. *Macromolecular Bioscience*, 7(5): 552-566. <https://doi.org/10.1002/mabi.200600278>
- [28] Menzies KL, Jones L. (2010) The impact of contact angle on the biocompatibility of biomaterials. *Optometry and Vision Science*, 87(6): 387-399. <https://doi.org/10.1097/OPX.0b013e3181da863e>
- [29] Pan JF, Liu NH, Sun H, Xu F. (2014) Preparation and characterization of electrospun PLCL/poloxamer nanofibers and dextran/gelatin hydrogels for skin tissue engineering. *PLoS One*, 9(11). <https://doi.org/10.1371/journal.pone.0112885>
- [30] Rianjanu A, Winardianto B, Munir M, Kartini I, Triyana K. (2016) Electrical conductivity improvement of polyvinyl alcohol nanofiber by solvent vapour treatment. *International Journal on Advanced Science, Engineering and Information Technology*, 6(5): 675-681. <https://doi.org/10.18517/IJASEIT.6.5.1055>
- [31] Aqeel SM, Wang Z, Than L, Sreenivasulu G, Zeng X. (2015) Poly (vinylidene fluoride)/poly (acrylonitrile)-based superior hydrophobic piezoelectric solid derived by aligned carbon nanotubes in electrospinning: fabrication, phase conversion and surface energy. *RSC Advances*, 5(93): 76383-76391. <https://doi.org/10.1039/C5RA11584A>
- [32] Shahini, A., Yazdimamaghani, M., Walker, K. J., Eastman, M. A., Hatami-Marbini, H., Smith BJ, Ricci JL, Madihally SV, Vashae D, Tayebi L. (2014) 3D conductive nanocomposite scaffold for bone tissue engineering. *International Journal of Nanomedicine*, 9: 167. <https://doi.org/10.2147/IJN.S54668>
- [33] Balint R, Cassidy NJ, Cartmell SH. (2014) Conductive polymers: Towards a smart biomaterial for tissue engineering. *Acta Biomaterialia*, 10(6): 2341-2353. <https://doi.org/10.1016/j.actbio.2014.02.015>
- [34] Zhao YH, Niu CM, Shi JQ, Wang YY, Yang YM, Wang HB. (2018) Novel conductive polypyrrole/silk fibroin scaffold for neural tissue repair. *Neural Regeneration Research*, 13(8): 1455. <https://doi.org/10.4103/1673-5374.235303>
- [35] Dong R, Zhao X, Guo B, Ma PX. (2016) Self-healing conductive injectable hydrogels with antibacterial activity as cell delivery carrier for cardiac cell therapy. *ACS Applied Materials & Interfaces*, 8(27): 17138-17150. <https://doi.org/10.1021/acsami.6b04911>
- [36] Park MJ, Gonzales RR, Abdel-Wahab A, Phuntsho S, Shon HK. (2018) Hydrophilic polyvinyl alcohol coating on hydrophobic electrospun nanofiber membrane for high performance thin film composite forward osmosis membrane. *Desalination*, 426: 50-59. <https://doi.org/10.1016/j.desal.2017.10.042>
- [37] Boccaccio T, Bottino A, Capannelli G, Piaggio P. (2002) Characterization of PVDF membranes by vibrational spectroscopy. *Journal of Membrane Science*, 210(2): 315-329. [https://doi.org/10.1016/S0376-7388\(02\)00407-6](https://doi.org/10.1016/S0376-7388(02)00407-6)
- [38] Martins P, Lopes AC, Lanceros-Mendez S. (2014) Electroactive phases of poly (vinylidene fluoride): Determination, processing and applications. *Progress in Polymer Science*, 39(4): 683-706. <https://doi.org/10.1016/j.progpolymsci.2013.07.006>
- [39] Ghasemi-Mobarakeh L, Prabhakaran MP, Morshed M, Nasr-Esfahani MH, Ramakrishna S. (2008) Electrospun poly (ϵ -caprolactone)/gelatin nanofibrous scaffolds for nerve tissue engineering. *Biomaterials*, 29(34): 4532-4539. <https://doi.org/10.1016/j.biomaterials.2008.08.007>

THE DURABILITY OF HYGRO-IMMERSION AGED CELLULOSE FIBRE REINFORCED POLYMER LAYERED SILICATE NANOCOMPOSITES

C. S. SUHAS KOWSHIK¹, NANJANGUD MOHAN¹, NITHESH NAIK¹, MANJUNATH SHETTAR¹, RITESH BHAT^{1*} AND SHIVAKSH ROHATGI²

¹Department of Mechanical and Manufacturing Engineering, Manipal Institute of Technology, Manipal Academy of Higher Education, Manipal, India 576104

² Department of Propulsion Aeronautics and Space Engineering, École Centrale de Lyon, Écully, France 69134

*Corresponding author: ritesh.bhat@manipal.edu

(Received: 19th August 2020; Accepted: 21st October 2020; Published on-line: 4th January 2021)

ABSTRACT: This study aims at investigating the effect of water ageing on the durability of cellulose fibre reinforced polymer layered silicate nanocomposite. The material used comprises cellulose fibres from pinewood as reinforcement and high-density polyethylene (HDPE) coupled with nanoclay as matrix phase. The prepared material is subjected to tap water ageing for 21 days. The durability is quantified by Barcol hardness for the material and measured at an interval period of 7 days. The obtained results indicate a reduction of hardness by 5.24, 13.17, and 16.60% in 7, 14, and 21 days aged nanocomposites. Besides, the one-way ANOVA test shows that the immersion time for the composite has a significant effect on the durability of the material with an R² value of 99.96% tested at 95% confidence interval. The concluding remarks are validated using the results obtained for thickness swelling using the Fourier analysis. The work also presents a regression equation with high degree of accuracy, capable of estimating the Barcol hardness value for a given immersion time.

ABSTRAK: Kajian ini bertujuan untuk mengkaji kesan penuaan air terhadap ketahanan nanokomposit silikat berlapis polimer bertetulang serat selulosa. Bahan yang digunakan terdiri daripada serat selulosa dari kayu pina sebagai tetulang dan polietena berketumpatan tinggi (HDPE) ditambah dengan nanoclay sebagai fasa matriks. Bahan yang disediakan mengalami penuaan air paip selama 21 hari. Ketahanan diukur dengan kekerasan bahan Barcol dan diukur pada selang waktu 7 hari. Hasil yang diperoleh menunjukkan penurunan kekerasan sebanyak 4.74, 8.88 dan 18.90% dalam nanokomposit usia 7, 14 dan 21 hari. Selain itu, analisis satu arah ujian varians menunjukkan bahawa masa rendaman komposit mempunyai pengaruh yang signifikan terhadap ketahanan bahan dengan nilai R² 99.96% yang diuji pada selang keyakinan 95%. Ucapan penutup disahkan menggunakan hasil yang diperoleh untuk pembengkakan ketebalan menggunakan analisis Fourier. Karya ini juga menyajikan persamaan regresi dengan tahap ketepatan yang tinggi, yang dapat menganggarkan nilai kekerasan Barcol untuk masa rendaman tertentu.

KEYWORDS: *mechanical property; nanocomposites; natural fibres; polymers; ANOVA*

1. INTRODUCTION

The usage of modified polymer layered silicate as matrix phase, comprising a base thermoplastic resin and clay as the primary elements have been proven to improve the mechanical and thermal properties of nanocomposites. Besides, they are determined to be

lighter in weight and have excellent barrier properties compared to simple polymer composites [1].

Polyethene, polythene, or polyethylene is a known polymer that accounts for one-third of the world's total plastic production and is generally compounded with natural minerals to enhance its properties, dimensional stability, and electric insulation properties while being used in composites. The compounding of clay with polythene has been proven by researchers [2] to improve exfoliation. Improved exfoliation ought to improve the mechanical performance of the polymer layered silicate matrix nanocomposites. Amongst polyethene, high-density polyethene (HDPE) has been considered as a prime base resin for its ease of availability and recyclability compared to other counterparts.

Furthermore, the addition of clay to the HDPE intends to improve the toughness of prepared nanocomposites [3-4]. Addition of nanoclay to HDPE has been proven to reduce gas permeability while increasing mechanical properties, flame retardance, and thermal stability [5]. During the last few years, cellulose fibre reinforced polymer composites have emerged as a significant class of advanced engineering materials and have found a wide range of applications. Moreover, the cellulose fibre reinforced polymer layered silicate nanocomposite outperforms natural wood in flexural properties [6]. Thus, cellulose fibre reinforced polymer layered silicate nanocomposites with HDPE as base resin coupled with nanoclay, and cellulose fibres as reinforcements, have been a topic of interest for various researchers. For example, Delhom et al. [7] investigated the tensile strength, flame retardance, and thermal expansion of cellulose fibre reinforced polyethene layered silicate nanocomposites. Authors extracted the cellulose fibres from cotton lint and wood pulp. Three variants were studied based on the varying percentages of clay by weight (7, 10, and 15%). The results indicated nanocomposites with 7 wt.% of clay is optimum considering the thermal properties. However, considering the mechanical properties, the nanocomposites comprising 15 wt% of clay proved better as the ultimate tensile strength increased by 80%. Sheshmani et al. [8] examined the physical properties of the developed cellulose fibre reinforced polymer layered silicate nanocomposite. The authors used HDPE as base resin coupled with montmorillonite nanoclay to form the matrix with wood fibres as the reinforcement. The result indicated an improvement in the resistance offered to water uptake by the developed nanocomposite over the conventional wood-plastic composites. On a similar account, Deka and Maji [9] in their extensive experimental work, coupled the Montmorillonite nanoclay with several variants and polymers to develop different cellulose fibre reinforced nanocomposites. They investigated the post and pre-effect of the addition. The results indicated that the addition of nanoclay improved thermal stability, flame resistance, hardness, and resistance to water absorption, compared to conventional wood plastic composites.

Hossen et al. [10] investigated the mechanical and physical properties of cellulose fibre reinforced HDPE layered silicate nanocomposites, wherein the cellulose fibres used were from jute fibres. The result indicated an improvement by 8% in the tensile strength and 15% in modulus when compared to the composites without nanoclay. Eshraghi et al. [11] investigated the combined effect of ultraviolet and moisture on the mechanical and physical properties of the cellulose fibre reinforced HDPE layered silicate nanocomposites. The obtained results indicated the nanocomposites having nanoclay particles demonstrated an improvement in the tensile property as well as in the resistance to water uptake under ageing condition compared to the counterpart. Besides, the Fourier transform infrared spectroscopy indicated the lowest carboxy index in the case of cellulose fibre reinforced HDPE layered silicate nanocomposites. Hossen et al. [12] investigated the thermal behaviour of cellulose fibre reinforced HDPE layered silicate nanocomposites, wherein the cellulose fibres used

were from the jute fibres. The result indicated a decrease in thermal degradation in the developed nanocomposites when compared to the composites without nanoclay.

El-Fattah and El-Kader [13] demonstrated in their work the influence of nanoclay addition on the mechanical and water absorption properties of cellulose fibre reinforced HDPE layered silicate nanocomposites. With just 2% addition of clay, the tensile strength improved by 9.7% and resistance to water uptake enhanced by 27.5%. The research is never-exhausting and several researchers, even to this date, are working on cellulose fibre reinforced HDPE layered silicate nanocomposites. For example, Wang et al. [14] in their research work proved that the tensile properties of cellulose fibre reinforced polymer composites enhances with the addition of the nanoclay in it.

Hossen et al. [15] assessed the thermal and mechanical behaviour of chemically treated cellulose fibre reinforced HDPE composites with and without nanoclay addition. The results indicated the improvement in thermomechanical properties with the addition of nanoclay. From the literature reviewed, it is evident that the cellulose fibre reinforced HDPE layered silicate nanocomposite is a hot topic of research. Though a good amount of research has been conducted on the thermal, mechanical, physical, and microstructural characterisation of the said material, there is a requirement of checking the durability concerning the hardness change due to water immersion effect on the same. Besides, the cellulose fibres from pinewood have rarely been used and investigated concerning the cellulose fibre reinforced HDPE layered silicate nanocomposites. Thus, adding to the existing literature, the present work focuses on investigating the effect of water immersion on the durability concerning the hardness and of cellulose fibre reinforced HDPE layered silicate nanocomposites, wherein pine wood fibres are used. The results are validated by observing the thickness swelling in nanocomposites. The prepared nanocomposites are immersed in tap water for 21 days, and required responses are measured periodically at an interval of seven days. The one-way analysis of variance (ANOVA) is then used to validate the results statistically.

2. MATERIALS AND METHODS

2.1 Materials and Aging Process

The cellulose fibre reinforced polymer layered silicate is used in the presented study. High density polyethylene (HDPE) having a melt flow of 0.7 g/min at 190 °C and density of 0.962 g/cc was employed as the base resin. Finely powdered pine wood (40 mesh size) was used as the reinforcement phase. The montmorillonite nanoclay is also added to make the complete nanocomposite. The cellulose-based nanocomposite comprised 65 wt% of reinforcing pine wood powder, 20 wt.% of HDPE and 14 wt% of montmorillonite nanoclay and looked just like natural wood. The density was measured for five samples using the ASTM D2395-17 standard, and the average value was determined to be 695 kg/m³. The average maximum tensile strength of five specimens as per ASTM D638-14 standard is determined to be 18 MPa. Nine samples measuring 100 x 65 x 16 mm were prepared for ageing studies. The materials were then submerged in a tub comprising tap water and allowed to age for the required number of days (7, 14 and 21). The marking was made on the tub to prevent any confusion. Fig. 1 represents the cross-sectional view of the prepared specimen and Fig. 2 represents the arrangement of submerged material in the tub with days and batch marked on it.



Fig. 1. The cross-sectional view of the prepared specimen.



Fig. 2. Cellulose fibre reinforced HDPE layered silicate nanocomposites immersed in water for ageing.

2.2 Experimental Procedures

Hardness is defined as the resistance of any material to the local deformation caused due to the indentation of the predetermined geometry under known loading conditions [16]. Hardness is a function of ductility, elastic stiffness, plasticity, strain, strength, toughness, viscoelasticity, and the viscosity [17]. It is an important property to be studied as it acts as the base for discussing the tribological characteristics of materials [18]. Thus, the study is focused on evaluating the effect of ageing on the hardness of the material. For this purpose, the Barcol hardness test on the specimens is carried out as per the ASTM D2583-95 standard test method of testing the indentation hardness of the rigid polymer composite material using the portable Barcol impressor model 945 (meant for softer materials). The hardness of the material corresponds to the depth of penetration of the indenter. Since the specimens are heterogeneous, a minimum of 25 readings was taken on each of the specimens, and the average value was recorded as the final value. Besides, all the readings were taken at 3 mm away from the edges. The apparatus was well-calibrated initially as per the standard operating procedure, before all the testing.

Besides hardness, yet another important property of interest, particularly in cellulose-based composites, is the thickness swelling in composite due to water absorption. The thickness swelling in composites represents the stability performance of the composite materials [19], [20]. Thus, to determine the effect of ageing on thickness swelling behaviour of the nanocomposites, the thickness of the specimen was measured daily (gap of 24 h) using digital Vernier calliper 1112-150 by INSIZE to get the precise reading up to two decimal values. The materials were removed and wiped with a clean, dry cloth before measuring. Since both sides of the specimen were not coated and were completely immersed in water, the ageing can be considered as accelerated and the worst-case scenario. The thickness swelling was measured for five zones for each specimen, and the average value was considered as the final value of swollen thickness for the particular specimen.

A large number of readings were taken to eliminate the effect of the variances caused by the inhomogeneous nature of the material. ANOVA is a widely used technique for univariate data. It is a basic tool in many fields of research as it determines and quantifies the effect of experimental factors on the observed outcome of an experiment [21]. One-way ANOVA is the fundamental model that specifies the common mean value for the observations in a group [22]. Thus, once all the values were recorded, the one-way ANOVA test was conducted to determine the significance of immersion time on the hardness and thickness swelling of the developed cellulose fibre reinforced HDPE silicate layered nanocomposites. Eq. (1) was used to determine the final value of Barcol hardness (HB_f) and Eq. (2) was used to calculate the final value of swollen thickness (t_f) for each specimen, where $i = 1, 2, 3, \dots, 25$ and $j = 1, 2, \dots, 5$.

The thickness swelling is determined using Eq. (3), wherein t_0 represents the initial thickness, and t_m represents the thickness after ageing. The number of the ageing period is represented by $k = 7, 14, \text{ and } 21$ in Eq. (3).

$$HB_f = \sum_{i=1}^{25} HB_i \quad (1)$$

$$t_f = \sum_{j=1}^5 t_j \quad (2)$$

$$t_j = \frac{t_{mk} - t_0}{t_0} \quad (3)$$

3. RESULTS AND DISCUSSION

The recorded values of Barcol hardness for unaged and aged specimen are given by Table 1, Table 2, and Table 3. The average Barcol value for each specimen recorded in the table refers to the average of 25 readings measured on each one of them. Fig. 3. represents the comparison bar chart for the average values of Barcol hardness concerning unaged and aged specimens.

Table 1: Barcol hardness measurement for 7 days aged samples.

Sample No.	Average Barcol hardness for unaged material (HB ₀)	Average Barcol hardness for 7 days aged material (HB ₇)	Percentage change in Barcol hardness	Average Percentage change in Barcol hardness for 7 days aged material
1	39.75	37.58	5.41%	
2	39.81	37.64	5.28%	5.24%
3	39.75	37.75	5.03%	

Table 2: Barcol hardness measurement for 14 days aged samples.

Sample No.	Average Barcol hardness for unaged material (HB ₀)	Average Barcol hardness for 14 days aged material (HB ₁₄)	Percentage change in Barcol hardness	Average Percentage change in Barcol hardness for 14 days aged material
1	39.75	34.50	13.21%	13.17%
2	39.85	34.45	13.33%	
3	39.75	34.60	12.96%	

Table 3: Barcol hardness measurement for 21 days aged samples.

Sample No.	Average Barcol hardness for unaged material (HB ₀)	Average Barcol hardness for 21 days aged material (HB ₂₁)	Percentage change in Barcol hardness	Average Percentage change in Barcol hardness for 21 days aged material
1	39.75	33.20	16.48%	16.60%
2	39.85	33.15	16.60%	
3	39.75	33.10	16.73%	

From the results obtained, it is evident that the durability concerning the Barcol hardness of the developed cellulose fibre reinforced HDPE layered silicate nanocomposite has decreased with the increase in the immersion time. The overall Barcol hardness reduction is determined to be 5.24, 13.17, and 16.60% for 7, 14, and 21 days aged samples. While observing critically, the maximum damage is caused during the 14 days, wherein the change of hardness between 7 to 14 days is recorded approximately 8%. The hardness

reduction between the 14th and 21st day is only 3.43%. The same is evident from the bar graph shown in Fig. 3. The average Barcol hardness value of 7 days aged specimen is 37.67 HB which was reduced to 34.52 HB on the 14th day. However, the average hardness number of 21 days aged material is recorded as 33.150, which is very near to the 14th day specimen. Thus, it is a clear indication that the maximum degradation has taken place during the initial period and gradually the rate of degradation is reducing. The phenomenon that took place could be divided into two phases. Initially, the water was absorbed by the hygroscopic pine wood material to the maximum possible extent. Following the absorption, the interfacial degradation was caused and increased water absorption further.

The results could be validated by SEM and EDX analysis. Nevertheless, the present work focuses on just investigating the statistically significant effect of ageing on the hardness and thickness swelling of the developed nanocomposite and not the microstructural analysis. Thus the latter portion can be dealt with in detail by researchers in the future. However, the remarks made are validated through the observations made about the thickness swelling due to the ageing effect on the developed nanocomposite.

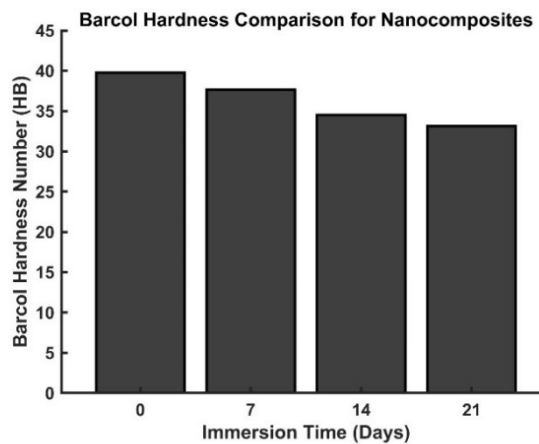


Fig. 3: Comparison of overall hardness values of Barcol hardness for aged and unaged nanocomposites.

The thickness swelling phenomenon in the developed and aged nanocomposites, measured using the digital vernier calliper, was recorded and analysed using the curve fitting tool of MATLAB R2019b. The Fourier equation represented by Eq. (4) is used to fit the curve and predict the thickness for a given period. The goodness of fit is determined to be extremely good with an R^2 value of 98.93 % and $R^2(\text{adj})$ value of 98.62 % at a 95% confidence interval.

$$f(x) = y = a_0 + a_1 \cos(xw) + b_1 \sin(xw) \quad (3)$$

The values of a_0 , a_1 , b_1 and w are calculated by the analysis as 16.06, 0.006158, 0.05883 and 1.022 respectively. Fig. 4. is the Fourier curve depicting the change in thickness concerning the increase in immersion time. There is a continuous increase in thickness, and then it retains constancy, which can be said as a Fickian behaviour of water absorption.

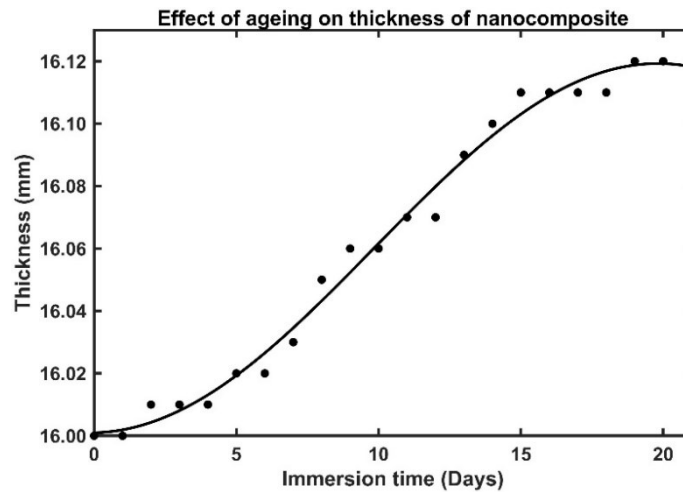


Fig. 4: Fourier curve representing the effect of ageing on the nanocomposite thickness.

The obtained results show that ageing affects the hardness of the developed nanocomposite. Now to check whether the effect is significant, an one-way analysis of variance (ANOVA) test is conducted. Tab. 4 gives the result of ANOVA concerning the hardness of nanocomposite conducted at a 95% confidence interval.

Table 4: ANOVA results for the hardness of nanocomposite.

Source	DF	Seq SS	Contribution	Adj SS	Adj MS	F-Value	P-Value
Days	3	80.9441	99.96%	80.9441	26.9814	6361.03	0.000
Error	8	0.0339	0.04%	0.0339	0.0042		
Total	11	80.9781	100.00%				

The p-value of 0.00 indicates that the effect of ageing is highly significant on the change in hardness. The error is just 0.04%. In other words, the immersion time contributes 99.6% towards the variance in the hardness of the developed composites. Thus, for the nanocomposite developed, the durability concerning the hardness can be termed as the function of immersion time and said to have a significant effect of ageing. Furthermore, the regression analysis is done with a cubic model to obtain the prediction equation relating the immersion time with the hardness value. The obtained equation is represented by Eq. (5), wherein HB represents the Barcol hardness, and the term D represents the immersion time in days. The R^2 and the (adj) R^2 values are 99.94 and 99.92%, which represent an extreme degree of fitness and accuracy for the obtained equation.

$$HB = 39.77 - 0.09700D - 0.3866D^2 + 0.001341D^3 \quad (3)$$

The cubic regression model curve representing the behaviour of hardness concerning the immersion time is represented by Fig. 5, which indicates a drop in the hardness value with the increase in the immersion time as explained with reasons earlier in the article.

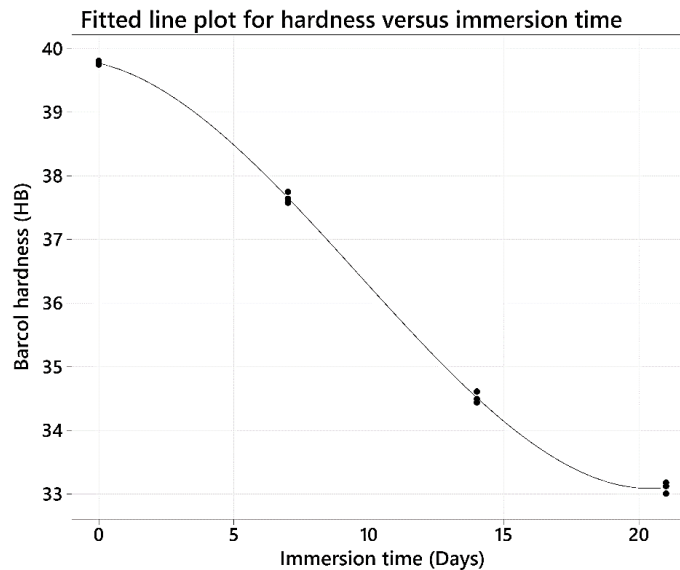


Fig. 5: Cubic regression model curve representing the effect of ageing on the hardness of nanocomposites.

4. CONCLUSION

The presented work focused on developing a cellulose fibre reinforced polymer layered silicate nanocomposite and testing the effect of ageing on its durability. The pinewood material contributed towards the required cellulose component, and high-density polyethylene (HDPE) was used as the base polymer. The montmorillonite nanoclay was also added to make the complete nanocomposite. Hardness is a property of interest for most researchers, as it is believed to be a function of a tribological characteristic of the material, and is considered as the measure of durability in the presented work. The material is studied for the ageing condition, wherein it is immersed in tap water condition for 21 days. The hardness is quantified using Barcol hardness number. The study indicates that there is a significant effect of immersion time, in other words, ageing on the hardness (durability) of the developed nanocomposites. The one-way ANOVA results conducted at a 95% confidence interval indicates that the immersion time contributes 99.6% towards the variance in the hardness of the developed composites. The phenomenon that took place is due to (i) initially, the water absorption by the hygroscopic pinewood material, followed by (ii) the interfacial degradation, causing a further increase in water absorption. The thickness swelling phenomenon observed and analysed using Fourier equation validates the conclusive remarks.

ACKNOWLEDGEMENT

We would like to thank Ms Jaya Letchumi for helping us translate the abstract from English to Bahasa Melayu as per the requirement from the journal.

REFERENCES

- [1] Bafna A, Beaucage G, Mirabella F, Mehta S. (2003) 3D hierarchical orientation in polymer-clay nanocomposite films. *Polymer*, 44(4): 1103-1115. doi: 10.1016/S0032-3861(02)00833-9.
- [2] Osman MA, Rupp JEP, Suter UW. (2005) Tensile properties of polyethylene-layered

- silicate nanocomposites. *Polymer*, 46(5): 1653-1660. doi: 10.1016/j.polymer.2004.11.112.
- [3] Tanniru M, Yuan Q, Misra RDK. (2006) On significant retention of impact strength in clay-reinforced high-density polyethylene (HDPE) nanocomposites. *Polymer*, 47(6): 2133-2146. doi: 10.1016/j.polymer.2006.01.063.
- [4] Jamal NA. (2010) A Linear Relationship between the Mechanical, Thermal and Gas Barrier Properties of MAPE Modified Rubber Toughened Nanocomposites. *IIUM Engineering Journal*, 11(2): 225-239. doi: 10.31436/iiumej.v11i2.114.
- [5] Chrissafis K, Paraskevopoulos KM, Tsiaoussis I, Bikiaris D. (2009) Comparative study of the effect of different nanoparticles on the mechanical properties, permeability, and thermal degradation mechanism of HDPE. *Journal of Applied Polymer Science*, 14(3): 1606-1618. doi: 10.1002/app.30750.
- [6] Faruk O, Matuana LM. (2008) Nanoclay reinforced HDPE as a matrix for wood-plastic composites. *Composites Science and Technology*, 68(9): 2073-2077. doi: 10.1016/j.compscitech.2008.03.004.
- [7] Delhom CD, White-Ghoorahoo LA, Pang SS. (2010) Development and characterisation of cellulose/clay nanocomposites. *Composites Part B: Engineering*, 41(6): 475-481. doi: 10.1016/j.compositesb.2009.10.007.
- [8] Sheshmani S, Ashori A, Hamzeh Y. (2010) Physical properties of polyethylene-wood fibre-clay nanocomposites. *Journal of Applied Polymer Science*, 118(6): 3255-3259. doi: 10.1002/app.32623.
- [9] Deka BK, Maji TK. (2011) Study on the properties of nanocomposite based on high density polyethylene, polypropylene, polyvinyl chloride and wood. *Composites Part A: Applied Science and Manufacturing*, 42(6): 6860-693. doi: 10.1016/j.compositesa.2011.02.009.
- [10] Hossen MF, Hamdan S, Rahman MR, Rahman MM, Liew FK, Lai JC. (2015) Effect of fibre treatment and nanoclay on the tensile properties of jute fibre reinforced polyethylene/clay nanocomposites. *Fibers and Polymers*, 16(2): 479-485. doi: 10.1007/s12221-015-0479-x.
- [11] Eshraghi A, Khademislam H, Ghasemi I. (2016) Effect of weathering on physical and mechanical properties of hybrid nanocomposite based on polyethylene, woodflour and nanoclay. *Maderas: Ciencia y Tecnologia*, 18(4): 617-626. doi: 10.4067/S0718-221X2016005000054.
- [12] Hossen MF, Hamdan S, Rahman MR, Islam MS, Liew FK, Lai JC, Rahman MM. (2017) Improved thermal properties of jute fibre-reinforced polyethylene nanocomposites. *Polymer Composites*, 38(7): 1266-1272. doi: 10.1002/pc.23691.
- [13] Abd El-Fattah A, Abd ElKader E. (2018) Influence of different clays on the mechanical, thermal, and water absorption properties of recycled high-density polyethylene/wood flour hybrid composites. *Journal of Composite Materials*, 52(9): 1215-1226. doi: 10.1177/0021998317723180.
- [14] Zhu B, Wang X, Zeng Q, Wang P, Wang Y, Liu C, Shen, C. (2019) Enhanced mechanical properties of biodegradable poly(ϵ -caprolactone)/cellulose acetate butyrate nanocomposites filled with organoclay. *Composites Communications*, 13: 70-74. doi: 10.1016/j.coco.2019.03.002.
- [15] Hossen MF, Asraf MA, E-Zahan MK, Haque MM, Zamir R, Zakaria RM. (2020) Optimisation of Nanoclay Loading on the Thermo-mechanical Behavior of Chemically Treated Jute Polyethylene Nanocomposites. *Journal of Materials Science Research and Reviews*, 5(3): 1-12.
- [16] Faraji G, Kim HS, Kashi HT. (2018) Mechanical Properties of Ultrafine-Grained and Nanostructured Metals. *Severe Plastic Deformation*. Elsevier; pp. 223–257.
- [17] Di Gianfrancesco A. (2017) Technologies for chemical analyses, microstructural and inspection investigations. *Materials for Ultra-Supercritical and Advanced Ultra-Supercritical Power Plants*. Elsevier; pp. 197–245.
- [18] Stachowiak GW, Batchelor AW, Stachowiak GB. (2004) Simulation of wear and friction. *Tribology Series*, 44: 13-23.
- [19] Adhikary KB, Pang S, Staiger MP. (2008) Long-term moisture absorption and thickness swelling behaviour of recycled thermoplastics reinforced with *Pinus radiata* sawdust. *Chemical Engineering Journal*, 142(2): 190-198. doi: 10.1016/j.cej.2007.11.024.

- [20] Atiqah A, Jawaid M, Ishak MR, Sapuan SM. (2017) Moisture Absorption and Thickness Swelling Behaviour of Sugar Palm Fibre Reinforced Thermoplastic Polyurethane. *Procedia Engineering*, 184: 581-586, 2017, doi: 10.1016/j.proeng.2017.04.142.
- [21] Hoefsloot HCJ, Vis DJ, Westerhuis JA, Smilde AK, Jansen JJ. (2009) Multiset Data Analysis: ANOVA Simultaneous Component Analysis and Related Methods. *Comprehensive Chemometrics. Volume 2*. Elsevier; pp. 453–472.
- [22] Christensen R. (2001) Analysis of Variance and Generalised Linear Models. *International Encyclopedia of the Social & Behavioral Sciences*. Elsevier; pp. 473–480.

ADAPTIVE DEVELOPMENT OF SVSF FOR A FEATURE-BASED SLAM ALGORITHM USING MAXIMUM LIKELIHOOD ESTIMATION AND EXPECTATION MAXIMIZATION

HERU SUWOYO^{1,3}, YINGZHONG TIAN^{1,2}, WENBIN WANG⁴, LONG LI^{1,2},
ANDI ADRIANSYAH^{3*}, FENGFENG XI⁵, GUANGJIE YUAN^{1,2}

¹*School of Mechatronic Engineering and Automation, Shanghai University, Shanghai, China*

²*Shanghai Key Laboratory of Intelligent Manufacturing and Robotics, Shanghai University, Shanghai, China*

³*Department of Electrical Engineering, Universitas Mercu Buana, Jakarta, Indonesia*

⁴*Mechanical and Electrical Engineering School, Shenzhen Polytechnic, Guangdong, China*

⁵*Department of Mechanical Aerospace, and Industrial Engineering, Ryerson University, Toronto, Canada*

*Corresponding author: andi@mercubuana.ac.id

(Received: 18th March 2020; Accepted: 23rd October 2020; Published on-line: 4th January 2021)

ABSTRACT: The smooth variable structure filter (SVSF) has been considered as the robust estimator. Like other filters, the SVSF needs an accurate system model and known noise statistics to approximate the posterior state. Unfortunately, the system cannot be accurately modeled, and the noise statistic is unknown in the real application. For these reasons, the performance of SVSF might be decreased or even led to divergence. Therefore, the enhancement of SVSF is required. This paper presents an Adaptive SVSF. Initially, SVSF is smoothed. To provide the ability to estimate the noise statistic, ASVSF is then derived based on maximum likelihood estimation (MLE) and expectation-maximization (EM). Additionally, the unbiased noise statistic is also approached. However, its covariance is complicatedly formulated. It might cause a negative definite symmetric matrix. Therefore, it is tuned based on the innovation covariance estimator (ICE). The ASVSF is designed to solve the online problem of Simultaneous Localization and Mapping (SLAM). Henceforth, it is termed as the ASVSF-SLAM algorithm. The proposed algorithm showed better accuracy and stability compared to the conventional algorithm in terms of root mean square error (RMSE) for both Estimated Path Coordinate (EPC) and Estimated Map Coordinate (EMC).

ABSTRAK: Penapis struktur bolehubah lembut (SVSF) telah dianggap sebagai penganggar teguh. Seperti penapis lain, SVSF memerlukan model sistem yang tepat dan statistik hingar yang diketahui bagi menganggar keadaan posterior. Malangnya, sistem tidak dapat dimodelkan dengan tepat dan statistik hingar tidak diketahui dalam aplikasi sebenar. Atas sebab-sebab ini, prestasi SVSF mungkin berkurangan, bahkan berbeza. Oleh itu, memperbaharui SVSF adalah perlu. Kajian ini adalah mengenai SVSF Mudah Suai. Pada awalnya, SVSF dilembutkan. Bagi menyediakan keupayaan anggaran statistik hingar, ASVSF dihasilkan terlebih dahulu berdasarkan anggaran kemungkinan maksimum (MLE) dan maksimum-harapan (EM). Tambahan, statistik hingar yang tidak berat sebelah juga dibuat. Walau bagaimanapun, rumusan formula kovarians ini adalah kompleks. Ini mungkin menyebabkan matriks simetri menjadi negatif. Oleh itu, ia diselaraskan berdasarkan penganggar kovarians inovasi (ICE). ASVSF dibina bagi menyelesaikan masalah dalam talian Penempatan dan Pemetaan Serentak (SLAM) dalam talian. Oleh itu, ia disebut sebagai

algoritma ASVSF-SLAM. Algoritma yang dicadangkan ini menunjukkan ketepatan dan kestabilan yang lebih baik berbanding algoritma konvensional dari segi ralat punca min kuasa dua (RMSE) bagi kedua-dua Koordinat Anggaran Laluan (EPC) dan Anggaran Koordinat Peta (EMC).

KEYWORDS: *SLAM, ASVSF, MLE, EM, ICE*

1. INTRODUCTION

It has been stated that the role of a consistent map of a complex environment can significantly help the robot to conduct the navigation task [1], [2]. However, the robot is commonly blind from this environment. Therefore, the robot should be completed to construct the map used to navigate itself and concurrently locate the position of the robot used [1] for the initial base of the mapping task. Theoretically, it is known as Simultaneous Localization and Mapping (SLAM) problem) [3]–[6]. Due to this widespread problem's challenges, the SLAM has been attracting much attention from different researchers. As the manner to fulfill the objective to estimate the robot path and static map, the estimation based on the probability principle has been frequently proposed, such as Extended Kalman Filter (EKF) [5]–[9]. The use of EKF has been limited because of the consistency issue [10].

For this reason, the Smooth Variable Structure Filter (SVSF) [10]–[13] is often chosen as the alternative filtering method of EKF. The SVSF is relatively considered a new predictor-estimator that adopts the sliding mode [13]–[15]. The switching gain is utilized as a way to reach the convergence by forcing the estimated values to always on the boundary of the truth estimates. Similar to the former implementation of EKF, which keeps the noise statistic to be invariant under the step increment, SVSF has been proven to successfully solving the feature-based online SLAM problem [16]–[19]. Fundamentally, the SVSF requires the accurate system model and known characteristic of the noise statistic. Unfortunately, these orders are often unavailable. Therefore, it still poses a risk of divergence and filter degradation quality [18], [20]. In order to cover this possibility, its conventional form needs to modify and enhance [21]–[24].

The most effective way to improve is by adaptively approximating the unknown parameters based on the offline batch estimation. Generally, it can significantly tune the gain of SVSF [7], [15], [20], [22]. The use of this approach has been proven when used as the manner to improve the EKF [7], [8], [23], [25]–[29], Unscented Kalman Filter (UKF) [18], [30]–[34], and Cubature Kalman Filter (CKF) [24], [34]–[37]. There are some types of the method can be adopted, and two of them are used in this experiment, Maximum Likelihood Estimation (MLE) [7], [18], [31], [38]–[41] and the working principle of Expectation-Maximization (EM) [7], [40]–[43]. The process of obtaining the suboptimal solution under these creations seem to unobservable. For this reason, the improved SVSF expanded based on the one-step smoothing point is involved [7], [20], [44]. It is adopted to proceed with the derivation process under MLE [15]. These processes aim produces the time-varying formulation relative to the noise statistic and its covariances. It gives the form with high complexity; thus, it is compactly reduced. However, it was not strong enough to guarantee positive definite covariance. Accordingly, the Innovation Covariance Estimation (ICE) [7], [25], [38], [45], [46] is involved. Then it is further implemented as the feature-based SLAM algorithm of a wheeled mobile robot.

The rest parts of this paper are organized as follows. Section II presents the formulation of SVSF. Section III presents the adaptive SVSF with mathematical derivation. The first solution calculated using the MLE and EM, the enhanced SVSF, the unbiased MLE-estimator, its time-

varying, and the addition of ICE. Section IV presents all the prerequisites to build the SLAM algorithm as well as presents the feature-based online SLAM algorithm referring to the proposed method. Section V presents a discussion about the results. Section VI presents the conclusion.

2. CLASSICAL SMOOTH VARIABLE STRUCTURE FILTER

Given a nonlinear Gaussian system as shown below,

$$\begin{cases} x_k = f(x_{k-1}, u_k) + \omega_{k-1} \\ z_k = h(x_k) + v_k \end{cases} \quad (1)$$

where k is the discrete time index, $x \in \mathbb{R}^n$ refers to the state vector, u is the control vector, and $z \in \mathbb{R}^m$ is the measurement vector. Meanwhile, $\omega \in \mathbb{R}^n$ is the additive noise following the process and $v \in \mathbb{R}^m$ is the additive noise of the measurement. Therefore, once $f(\cdot)$ and $h(\cdot)$ are assumed as the transition and measurement function, respectively, the characteristic noise of Eq. (1) is expressed as follows

$$\begin{cases} E[\omega_k] = q_k, Cov[\omega_k, \omega_j] = Q_k \delta_{kj} \\ E[v_k] = r_k, Cov[v_k, v_j] = R_k \delta_{kj} \\ E[\omega_k, v_j] = 0 \end{cases} \quad (2)$$

where δ is well-known as the Kronecker delta function. Meanwhile, $E[\cdot]$ is term used to indicate the expectation or mean and $Cov[\cdot, \cdot]$ is used to indicate the covariance term.

Once Eq. (1) and Eq. (2) are described, the summary of SVSF are chained as follows [12]

$$\hat{x}_{k|k-1} = f(\hat{x}_{k-1|k-1}, u_k) + q \quad (3)$$

$$P_{k|k-1} = FP_{k-1|k-1}F^T + Q \quad (4)$$

$$e_{z,k|k-1} = z_k - h(\hat{x}_{k|k-1}) - r \quad (5)$$

$$\psi = \left(\overline{\overline{|e_{z,k|k-1}|_{abs} + \gamma |e_{z,k-1|k-1}|_{abs}}} \right)^{-1} HP_{k|k-1}^{-1} H^T (HP_{k|k-1} H^T + R)^{-1} \quad (6)$$

$$sat[\psi^{-1} \overline{\overline{|e_{z,k|k-1}|}}] = \begin{cases} 1 & \psi^{-1} \overline{\overline{|e_{z,k|k-1}|}} \geq 1 \\ \psi^{-1} \overline{\overline{|e_{z,k|k-1}|}} & 1 < \psi^{-1} \overline{\overline{|e_{z,k|k-1}|}} < -1 \\ -1 & \psi^{-1} \overline{\overline{|e_{z,k|k-1}|}} \leq -1 \end{cases} \quad (7)$$

$$K_k^{SVSF} = H^+ \left\{ \overline{\overline{|e_{z,k|k-1}|_{abs} + \gamma |e_{z,k-1|k-1}|_{abs}}} \circ sat[\psi^{-1} \overline{\overline{|e_{z,k|k-1}|}}] \right\} [\psi^{-1} \overline{\overline{|e_{z,k|k-1}|}}]^{-1} \quad (8)$$

$$\hat{x}_{k|k} = \hat{x}_{k|k-1} + K_k^{SVSF} e_{z,k|k-1} \quad (9)$$

$$P_{k|k} = (I - K_k^{SVSF} H) P_{k|k-1} (I - K_k^{SVSF} H)^T + K_k^{SVSF} R_k K_k^{SVSF T} \quad (10)$$

$$e_{z,k|k} = z_k - h(\hat{x}_{k|k}) \quad (11)$$

where, P represents the state error covariance matrix, F refers to the Jacobian matrix of $f(\cdot)$ and e_z is innovation of measurement error. The sign of $\overline{\overline{\cdot}}$ refers to the diagonal term, γ refers to the constant indicating the convergence rate $0 < \gamma_{ii} \leq 1$, ψ refers to the boundary

layer width, $Q \in \mathbb{R}^{n \times n}$ correspondences to the covariance matrix of the noise statistic relative to the process and $R \in \mathbb{R}^{m \times m}$ correspondences to the covariance matrix of the noise statistic relative to the measurement and H is Jacobian matrix of the measurement. Meanwhile, the sign of \cdot^+ and \circ are used to indicate the function of the pseudo-invers and Schur matrix multiplication, respectively. The stability of SVSF and its convergence to the existence of the subspace are satisfied if the absolute error about the posterior is smaller than the prior one [11], [12], [47]–[49]. Mathematically, it can be described as follows

$$|e_{z,k-1|k-1}|_{abs} > |e_{z,k|k}|_{abs} \quad (12)$$

3. ADAPTIVE SMOOTH VARIABLE STRUCTURE FILTER

Assuming Eq. (1) contains the unknown parameters $\theta = (q, r, Q, R)$; then, using the Maximum Likelihood Estimation, its estimates $\hat{\theta}$ can be calculated as follows

$$\hat{\theta}^{MLE} = \arg \max_{\theta} \{ \ln[L(q, r, Q, R|Z_k, X_k)] \} \quad (13)$$

Note that the likelihood function of θ is $L(q, r, Q, R|Z_k, X_k)$, which can be expanded as

$$L(q, r, Q, R|Z_k, X_k) = p(Z_k, X_k|q, r, Q, R) = p(X_k|q, Q, r, R)p(Z_k|X_k, q, r, Q, R) \quad (14)$$

Since $X_k = [x_0, \dots, x_k]$, $Z_k = [z_1, \dots, z_k]$, and Eq. (1) refers to the first-order of the Markov process, the factorized form of Eq. (14) is

$$p(Z_k, X_k|\theta) = p[x_0] \prod_{i=1}^k p[x_i|x_{i-1}, q, Q] \prod_{i=1}^k p[z_i|x_i, r, R] \quad (15)$$

Next, by considering that the prior knowledge complies with Gaussian distribution, then Eq. (15) can be rewritten as follows

$$\begin{aligned} p(Z_k, X_k|q, r, Q, R) &= \frac{1}{(2\pi)^{-\frac{k(n+m)+n}{2}}} |P_0|^{-\frac{1}{2}} |Q|^{-\frac{k}{2}} |R|^{-\frac{k}{2}} \\ &\times \exp \left\{ -\frac{1}{2} \left[\|x_0 - \hat{x}_0\|_{P_0^{-1}}^2 + \sum_{i=1}^k \|x_i - f(x_{i-1}) - q\|_{Q^{-1}}^2 \right. \right. \\ &\left. \left. + \sum_{i=1}^k \|z_i - h(x_i) - r\|_{R^{-1}}^2 \right] \right\} \end{aligned} \quad (16)$$

Then by taking logarithm Eq. (16), it yields

$$\begin{aligned} \ln[L(q, r, Q, R|Z_k, X_k)] &= -\frac{k(n+m)+n}{2} \ln(2\pi) - \frac{1}{2} \ln(|P_0|) - \frac{k}{2} \ln(|Q|) - \frac{k}{2} \ln(|R|) \\ &- \frac{1}{2} \left[\|x_0 - \hat{x}_0\|_{P_0^{-1}}^2 + \sum_{i=1}^k \|x_i - f(x_{i-1}) - q\|_{Q^{-1}}^2 + \sum_{i=1}^k \|z_i - h(x_i) - r\|_{R^{-1}}^2 \right] \end{aligned} \quad (17)$$

3.1. Expectation-Maximization (EM) Estimation

According to Eq. (1) – Eq. (17) and aiming to estimate noise statistics about the process and measurement together with the corresponding covariances, the principle of Expectation-Maximization is involved. Estimating particular function based on EM are done by taking the expectation of the objective function, and sequentially maximizing its result [7], [40]–[43].

3.1.1. Expectation Process (E-Step)

The expectation process can be done by first taking the conditional expectation and sequentially equating the result to zero, as shown below.

$$\begin{aligned}
 E[\ln[L(q, r, Q, R|Z_k, X_k)]] & \quad (18) \\
 &= -\frac{k(n+m)+n}{2} \ln(2\pi) - \frac{1}{2} \ln(|P_0|) - \frac{k}{2} \ln(|Q|) - \frac{k}{2} \ln(|R|) \\
 &\quad - \frac{1}{2} E \left[\|x_0 - \hat{x}_0\|_{P_0^{-1}}^2 + \sum_{i=1}^k \|x_i - f(x_{i-1}) - q\|_{Q^{-1}}^2 \right. \\
 &\quad \left. + \sum_{i=1}^k \|z_i - h(x_i) - r\|_{R^{-1}}^2 \right]
 \end{aligned}$$

Now by supposing that

$$C = -\frac{k(n+m)+n}{2} \ln(2\pi) - \frac{1}{2} \ln(|P_0|) - \frac{1}{2} E \left[\|x_0 - \hat{x}_0\|_{P_0^{-1}}^2 \right] \quad (19)$$

And applying Eq. (19) into Eq. (18), the compact form of Eq. (18) can be written as follows

$$\begin{aligned}
 E[\ln[L(q, r, Q, R|Z_k, X_k)]] & \quad (20) \\
 &= C - \frac{k}{2} \ln(|Q|) - \frac{k}{2} \ln(|R|) \\
 &\quad - \frac{1}{2} E \left[\sum_{i=1}^k \|x_i - f(x_{i-1}) - q\|_{Q^{-1}}^2 + \sum_{i=1}^k \|z_i - h(x_i) - r\|_{R^{-1}}^2 \right]
 \end{aligned}$$

It is known that by definition $\|a\|_{b^{-1}}^2 = a^T b^{-1} a$. Therefore, by applying the identity $\text{tr}(a^T a) = \text{tr}(a a^T)$, Eq. (20) can be calculated as

$$\begin{aligned}
 E[\ln[L(q, r, Q, R|Z_k, X_k)]] & \quad (21) \\
 &= C - \frac{k}{2} \ln(|Q|) - \frac{k}{2} \ln(|R|) \\
 &\quad - \frac{1}{2} \sum_{i=1}^k E \{ \text{tr}[Q^{-1}(x_i - f(x_{i-1}) - q)(x_i - f(x_{i-1}) - q)^T] \} \\
 &\quad - \frac{1}{2} \sum_{i=1}^k E \{ \text{tr}[R^{-1}(z_i - h(x_i) - r)(z_i - h(x_i) - r)^T] \}
 \end{aligned}$$

3.1.2. Maximization Process (M-Step)

Up to this point, the unknown parameters relative to the noise can be approximated by maximizing $E[\ln[L(q, r, Q, R|Z_k, X_k)]]$. It can be done by calculating its partial derivative concerning all elements of the unknown parameter θ and equating it to zero. Correspondingly, the suboptimal of θ are determined as follows

$$\hat{q}_k = \frac{1}{k} \sum_{i=1}^k x_{i|k} - f(x_{i-1|k}) \quad (22)$$

$$\hat{r}_k = \frac{1}{k} \sum_{i=1}^k z_i - h(x_{i|k}) \quad (23)$$

$$\hat{Q}_k = \frac{1}{k} \sum_{i=1}^k (x_{i|k} - f(x_{i-1|k}) - q)(x_{i|k} - f(x_{i-1|k}) - q)^T \quad (24)$$

$$\hat{R}_k = \frac{1}{k} \sum_{i=1}^k (z_i - h(x_{i|k}) - r)(z_i - h(x_{i|k}) - r)^T \quad (25)$$

According to Eq. (22) – Eq. (25), it can be evaluated that the multistep smoothing term of $x_{i|k}$ and $x_{i-1|k}$ seems unobservable. Therefore, as the effort to proceed derivation process and prevent solution from inefficiency, $x_{i|k}$ and $x_{i-1|k}$ are respectively replaced by $x_{i|i}$ and $x_{i-1|i}$. Thus, the new forms of suboptimal solutions are obtained as

$$\hat{q}_k = \frac{1}{k} \sum_{i=1}^k x_{i|i} - f(x_{i-1|i}) \quad (26)$$

$$\hat{r}_k = \frac{1}{k} \sum_{i=1}^k z_i - h(x_{i|i}) \quad (27)$$

$$\hat{Q}_k = \frac{1}{k} \sum_{i=1}^k (x_{i|i} - f(x_{i-1|i}) - q)(x_{i|i} - f(x_{i-1|i}) - q)^T \quad (28)$$

$$\hat{R}_k = \frac{1}{k} \sum_{i=1}^k (z_i - h(x_{i|i}) - r)(z_i - h(x_{i|i}) - r)^T \quad (29)$$

Although the suboptimal formulation relative to the noise statistics are calculated already, they contain the lack of estimates values, $x_{i-1|i}$, which is unavailable from the original form of SVSF. For this reason, the SVSF is smoothed and improved using a one-step smoothing point [7], [15], [20]. Using Eq. (3) – Eq. (10), one lag smoothed values $\hat{x}_{k-1|k}$ and its covariance $P_{k-1|k}$ are computed as follows

$$\hat{x}_{k-1|k} = \hat{x}_{k-1|k-1} + K_k^{SVSF} \hat{e}_{z,k|k-1} \quad (30)$$

$$P_{k-1|k} = (I - K_k^{SVSF} H) P_{k-1|k-1} (I - K_k^{SVSF} H)^T + K_k^{SVSF} R_k K_k^{SVSF T} \quad (31)$$

Instead of using the prior $\hat{x}_{k-1|k-1}$, in this point $\hat{x}_{k-1|k}$ in Eq. (30) is applied into the transition function $f(\cdot)$ in Eq. (3); then, the SVSF is essentially smoothed and improved already. Moreover, once Eq. (30) and Eq. (31) are determined, the estimated values $\hat{x}_{k|k}$ and $P_{k|k}$ can be computed. It is noted that the prediction steps in Eq. (3) and Eq. (4) of the second step are using the following definition.

$$\hat{x}_{k|k-1} = f(\hat{x}_{k-1|k}, u_k) + q \quad (32)$$

$$P_{k|k-1} = FP_{k-1|k}F^T + Q \quad (33)$$

Now, the estimate values $x_{i-1|i}$ in the sequence forms of Eq. (22) – Eq. (25) can be replaced by Eq. (30).

3.2. Unbiased Estimate Noise Statistic

Up to this point, it seems to have clear derived formulation, but the simplification shown in Eq. (26) – Eq. (29) might reduce the quality as well as leads to bias condition. For this reason, the unbiased estimation is approached to guarantee the optimality of Eq. (26) – Eq. (29). This stage can be sequentially conducted as follows; By definition, it is known that

$$x_i - f(x_{i-1|i}) = K_i^{SVSF} e_{z,i|i-1} + q \quad (34)$$

Now, by substituting Eq. (34) into $z_i - h(x_{i|i})$

$$z_i - h(x_{i|i}) = z_i - h(x_{i|i-1} + K_i^{SVSF} e_{z,i|i-1}) = (I - HK_i^{SVSF}) e_{z,i|i-1} + r \quad (35)$$

then the equivalent form of Eq. (26) – Eq. (29) are respectively presented as follows

$$\hat{q}_k = \frac{1}{k} \sum_{i=1}^k K_i^{SVSF} e_{z,i|i-1} + q \quad (36)$$

$$\hat{r}_k = \frac{1}{k} \sum_{i=1}^k (I - HK_i^{SVSF}) e_{z,i|i-1} + r \quad (37)$$

$$\hat{Q}_k = \frac{1}{k} \sum_{i=1}^k K_i^{SVSF} e_{z,i|i-1} e_{z,i|i-1}^T K_i^{SVSF^T} \quad (38)$$

$$\hat{R}_k = \frac{1}{k} \sum_{i=1}^k (I - HK_i^{SVSF}) e_{z,i|i-1} e_{z,i|i-1}^T (I - HK_i^{SVSF})^T \quad (39)$$

Since the innovation $e_{z,k|k-1}$ and its covariance $e_{z,k|k-1} e_{z,k|k-1}^T$ are the parts on the process and measurement noise estimator, it is clear to have

$$e_{z,i|i-1} = h(\tilde{x}_{i|i-1}) + v_i - r \quad (40)$$

and the expectation of the innovation error $e_{z,k|k-1}$ as well as its corresponding covariance $e_{z,k|k-1} e_{z,k|k-1}^T$ are respectively obtained as follows

$$E[e_{z,k|k-1}] = 0 \quad (41)$$

$$E[e_{z,k|k-1} e_{z,k|k-1}^T] = HP_{k|k-1}H^T + R \quad (42)$$

Therefore, the expectation of all the suboptimal Eq. (36) – Eq. (39) are

$$E[\hat{q}_k] = q_k \quad (43)$$

$$E[\hat{r}_k] = r_k \quad (44)$$

In order to obtain the expectation form of the error covariance noise statistic for both the process and measurement, the Joseph covariance form is used.

$$P_{i|i} = P_{i|i-1}(I - K_i^{SVSF}H) = P_{i|i-1} - P_{i|i-1}K_i^{SVSF}H \quad (45)$$

It is clear, once the unbiased estimates are also satisfying $e_{z,i|i-1}e_{z,i|i-1}^T = HP_{i|i-1}H^T + R$, therefore, the following forms are determined

$$K_i^{SVSF}e_{z,i|i-1}e_{z,i|i-1}^T = H^T P_{i|i-1} \quad (46)$$

$$(K_i^{SVSF}e_{z,i|i-1}e_{z,i|i-1}^T)^T = HP_{i|i-1} \quad (47)$$

Then all expectation values of θ relative to the error matrices are

$$E[\hat{Q}_k] = \frac{1}{k} \sum_{i=1}^k (FP_{i-1|i-1}F^T + Q)H^T K_i^{SVSF^T} \quad (48)$$

$$E[\hat{R}_k] = R_k + \frac{1}{k} \sum_{i=1}^k HK_i^{SVSF}HP_{i|i-1}H^T - HP_{i|i-1}H^T \quad (49)$$

Up to this point, the expectation of all the noise statistic are obtained. Note that, q_k, r_k, Q_k, R_k in Eq. (46) – Eq. (49) and Eq. (36) – Eq. (39) are the representation of Eq. (26) – Eq. (29), respectively. Hence, the unbiased noise statistic properties can be calculated as follows

$$\hat{q}_k = \frac{1}{k} \sum_{i=1}^k K_i^{SVSF}e_{z,i|i-1} + q \quad (50)$$

$$\hat{r}_k = \frac{1}{k} \sum_{i=1}^k (I - HK_i^{SVSF})e_{z,i|i-1} + r \quad (51)$$

$$\hat{Q}_k = \frac{1}{k} \sum_{i=1}^k (FP_{i-1|i-1}F^T + K_i^{SVSF}e_{z,i|i-1}e_{z,i|i-1}^T K_i^{SVSF^T})H^T K_i^{SVSF^T} \quad (52)$$

$$\begin{aligned} \hat{R}_k &= \frac{1}{k} \sum_{i=1}^k (I - HK_i^{SVSF})e_{z,i|i-1}e_{z,i|i-1}^T (I - HK_i^{SVSF})^T - HP_{i|i-1}H^T + HK_i^{SVSF}HP_{i|i-1}H^T \\ &= \frac{1}{k} \sum_{i=1}^k (I - HK_i^{SVSF})e_{z,i|i-1}e_{z,i|i-1}^T (I - HK_i^{SVSF})^T \\ &\quad - (I - HK_i^{SVSF})HP_{i|i-1}H^T \end{aligned} \quad (53)$$

3.3. Time-Varying Unbiased Noise Statistic

Once, the unbiased form are calculated, the time-varying forms can also be calculated. According to Eq. (50) – Eq. (53), they are respectively expressed as follows

$$\hat{q}_k = \hat{q} + \frac{1}{k} (K_i^{SVSF}e_{z,i|i-1}) \quad (54)$$

$$\hat{r}_k = \hat{r} + \frac{1}{k} \left((I - HK_i^{SVSF}) e_{z,i|i-1} \right) \quad (55)$$

$$\hat{Q}_k = \hat{Q} \frac{k-1}{k} + \frac{1}{k} \left(FP_{i-1|i-1} F^T + K_i^{SVSF} e_{z,i|i-1} e_{z,i|i-1}^T K_i^{SVSF T} \right) H^T K_i^{SVSF T} \quad (56)$$

$$\hat{R}_k = \hat{R} \frac{k-1}{k} + \frac{1}{k} \left((I - HK_i^{SVSF}) e_{z,i|i-1} e_{z,i|i-1}^T (I - HK_i^{SVSF})^T - (I - HK_i^{SVSF}) HP_{i|i-1} H^T \right) \quad (57)$$

where \hat{q} , \hat{r} , \hat{Q} , and \hat{R} are q_{k-1} , r_{k-1} , Q_{k-1} , and R_{k-1} , respectively. Moreover, as an effort to keep its stability, the exponential $\frac{1}{k}$ in Eq. (54) – Eq. (57) are replaced with the weighting coefficient d_k [7], [15], [18], [22], [30], [37]. Additionally, the use of Innovation Covariance Estimator (ICE) is involved to depress the possibility of negative definite matrices Eq. (56) – Eq. (57). Then, the final formulation for covariance matrices relative to the noise statistic of the process and measurement are expressed as follows

$$\hat{Q}_k = (1 - d_k) \hat{Q}_{k-1} + d_k \left(FP_{k-1|k-1} F^T + K_k^{SVSF} ICE_k K_k^{SVSF T} \right) H^T K_k^{SVSF T} \quad (58)$$

$$\hat{R}_k = (1 - d_k) \hat{R}_{k-1} + d_k \left((I - HK_k^{SVSF}) ICE_k (I - HK_k^{SVSF})^T - (I - HK_k^{SVSF}) HP_{k|k-1} H^T \right) \quad (59)$$

Once, the adaptive SVSF is designed with addition of the smoothing formulation (see Eq. (1) – Eq. (12) and Eq. (32) – Eq. (33)) and the time-varying of the noise statistic Eq. (54) – Eq. (55) and Eq. (58) – Eq. (59), the adaptive SVSF-based SLAM algorithm can also be designed. The design involves all the configuration and completeness that have been introduced in [15]. It is noted that this involvement includes the motion model, direct point-based observation, and inverse point-based observation. Accordingly, the compact psuedo-code of this algorithm can be described as follows:

Algorithm ASVSF-Based SLAM

Require : Initial State Estimate, Covariance, Convergence Rate, and Initial Error

- 1: **loop**
 - 2: **Prediction Step: If proprioceptive data is available**
 - 3: Propagate the state estimate
 - 4: Compute the Jacobian of $f(\cdot)$
 - 5: Propagate the covariance relative to the state
 - 6: **Update: If the observation data is available**
 - 7: Compute the innovation sequence error
 - 8: Calculate Gain
 - 9: Update the State, and Covariance
 - 10: Compute the noise statistic
 - 11: **endloop**
-

4. RESULT AND DISCUSSION

In order to validate its stability, the proposed method is realistically simulated before it is compared to the conventional one. All the parameters relative to the robot configuration are adopted from Turtlebot2, as stated below.

$$W_r = 33cm, d_{ls} = 14cm, \gamma = 15e - 2, e_{z,0} = [0.1; 0.5\pi/180]$$

Furthermore, the initial state and its error covariance are defined as follows.

$$\hat{x}_0 = \begin{bmatrix} 0 \\ 0 \\ \frac{35\pi}{180} \end{bmatrix}, P_0 = \begin{bmatrix} (1.5)^2 & 0 & 0 \\ 0 & 1^2 & 0 \\ 0 & 0 & \left(\frac{2.5\pi}{180}\right)^2 \end{bmatrix}$$

It is also assumed, the robot is also completed with a 2D-LIDAR used to get the measurement data, distance and bearing. According to the initial noise statistics, there would be two different simulation cases presented in this paper.

- **First Test** The initial process and measurement noise are considered as follows

$$\hat{q}_0 = \begin{bmatrix} 0.03 \\ \frac{\pi}{180} \end{bmatrix}, \hat{r}_0 = \begin{bmatrix} 0.2 \\ \frac{3\pi}{180} \end{bmatrix}, \hat{Q}_0 = \begin{bmatrix} 0.03^2 & 0 \\ 0 & \left(\frac{\pi}{180}\right)^2 \end{bmatrix}, \hat{R}_0 = \begin{bmatrix} 0.2^2 & 0 \\ 0 & \left(\frac{3\pi}{180}\right)^2 \end{bmatrix}$$

These noises will be executed once initially, and for the next iteration, they will be recursively provided by the proposed algorithm. To validate the effectiveness and robustness of the proposed method some comparative results are presented as follows.

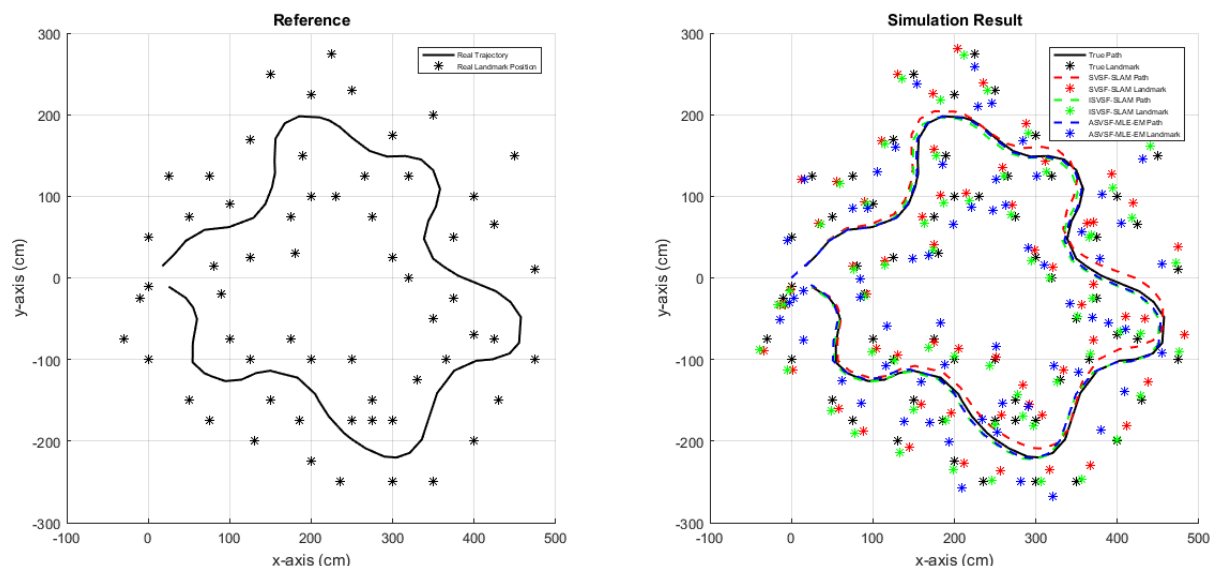


Fig. 1. Performance of Different SLAM-Based Algorithm (First Test)

Fig. 1 demonstrates different filter performances in solving the SLAM problem of wheeled mobile robots. It verifies that the proposed method's properness is satisfied with locating the robot position and mapping the features. Graphically, it is hard to evaluate the difference, so that Fig. 2 and Fig. 3 are presented.

Fig. 2 shows that the proposed method has been successfully presenting the better-estimated path than then SVSF-SLAM algorithm. Although the small difference between ISVSF-SLAM, ASVSF-MLE-EM cannot be observed from this figure. So that to ease our analysis, Table 1 is presented.

Additionally, the algorithms mentioned above are also compared in terms of RMSE for the estimated map. Fig. 3 demonstrates that the proposed method has been reducing the RMSE given by the SVSF-SLAM algorithm. Thus, it can be noted that the ASVSF-SLAM based on MLE-EM has been successful in upgrading the quality of the classical method.

Moreover, according to Fig. 3, the effectiveness of one-step smoothing has been proven to stably the SVSF-SLAM algorithm.

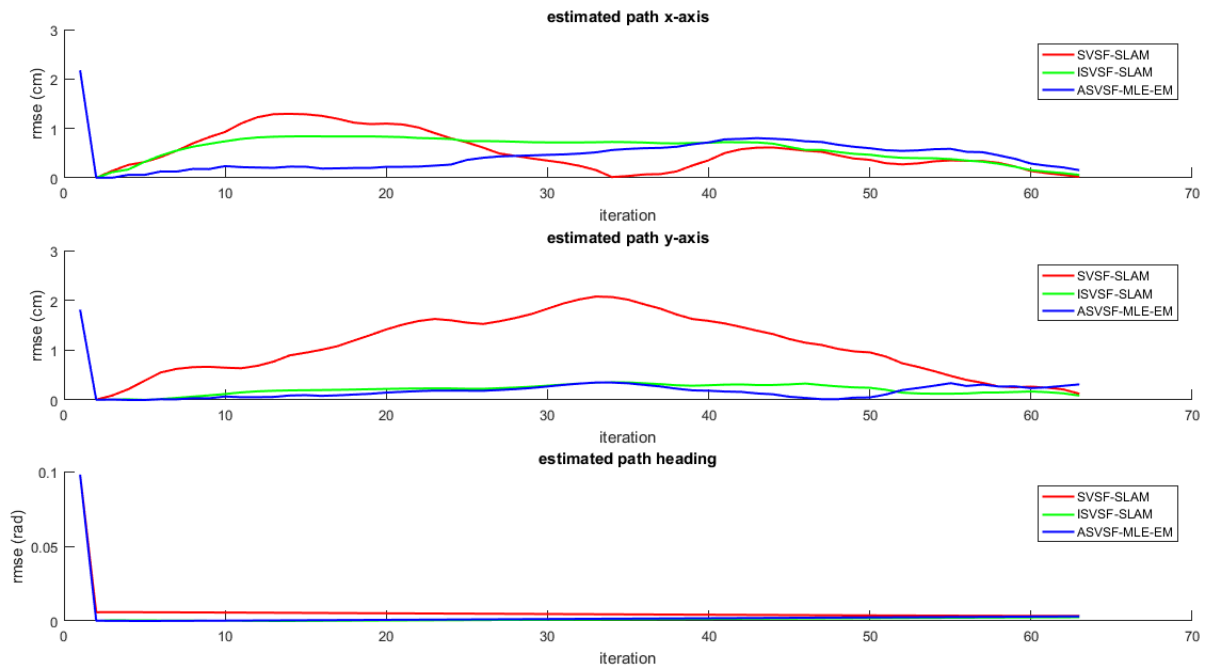


Fig. 2. RMSE of Estimated Path Coordinate of Different SLAM-Algorithm (First Test)

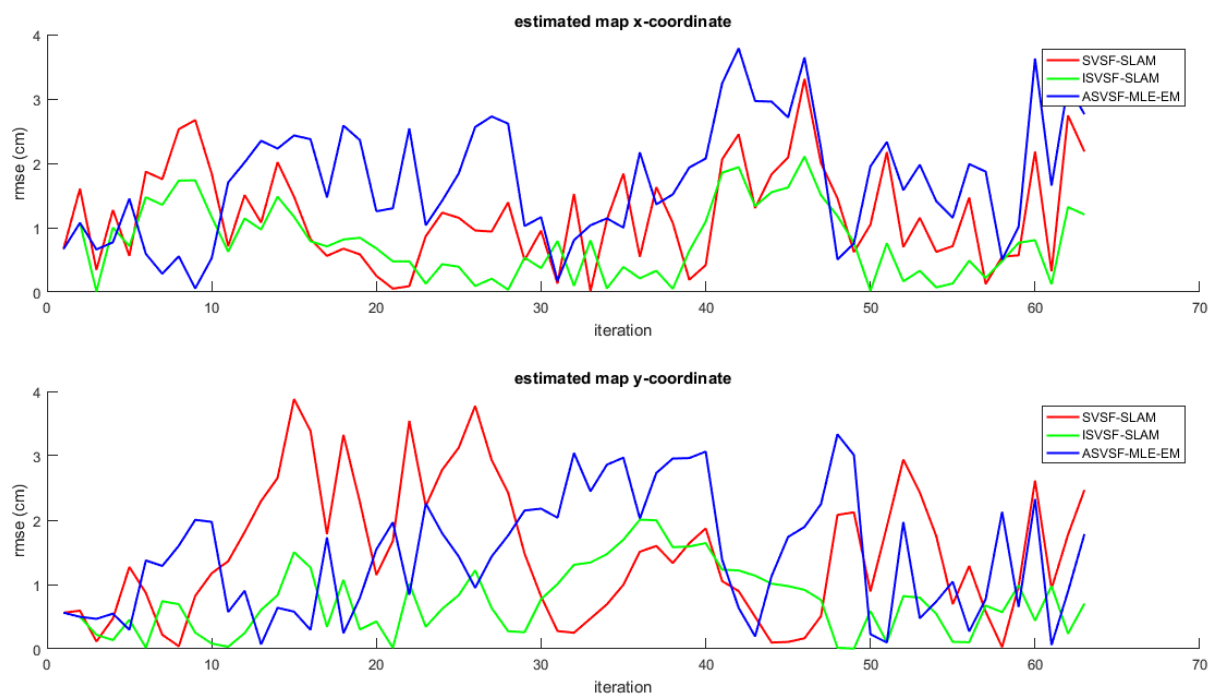


Fig. 3. RMSE of Estimated Map Coordinate of Different SLAM-Algorithm (First Test)

Table 1: RMSE of Different SLAM-Based Algorithm (First Test)

SLAM-Based Algorithm	x-EPC [cm]	y-EPC [cm]	θ -EPC [rad]	x-EMC [cm]	y-EMC [cm]
SVSF	5.5823	9.7952	0.1045	11.2296	14.4148
ISVSF	5.4492	2.5447	0.0985	7.5200	14.2128
ASVSF	4.2798	2.3807	0.0989	15.4925	13.5943

- **Second Test** The initial process and measurement noise are considered as follows.

$$\hat{q}_0 = \begin{bmatrix} 0.08 \\ \left(\frac{5\pi}{180}\right) \end{bmatrix}, \hat{r}_0 = \begin{bmatrix} 0.8 \\ \left(\frac{3\pi}{180}\right)^2 \end{bmatrix}, \hat{Q}_0 = \begin{bmatrix} 0.08^2 & 0 \\ 0 & \left(\frac{5\pi}{180}\right)^2 \end{bmatrix}, \hat{R}_0 = \begin{bmatrix} 0.8^2 & 0 \\ 0 & \left(\frac{3\pi}{180}\right)^2 \end{bmatrix}$$

In the second case, the initial noise statistics both for process and measurement were increased. It aims to examine the stability of the proposed algorithm under an uncertain predetermined noise statistic.

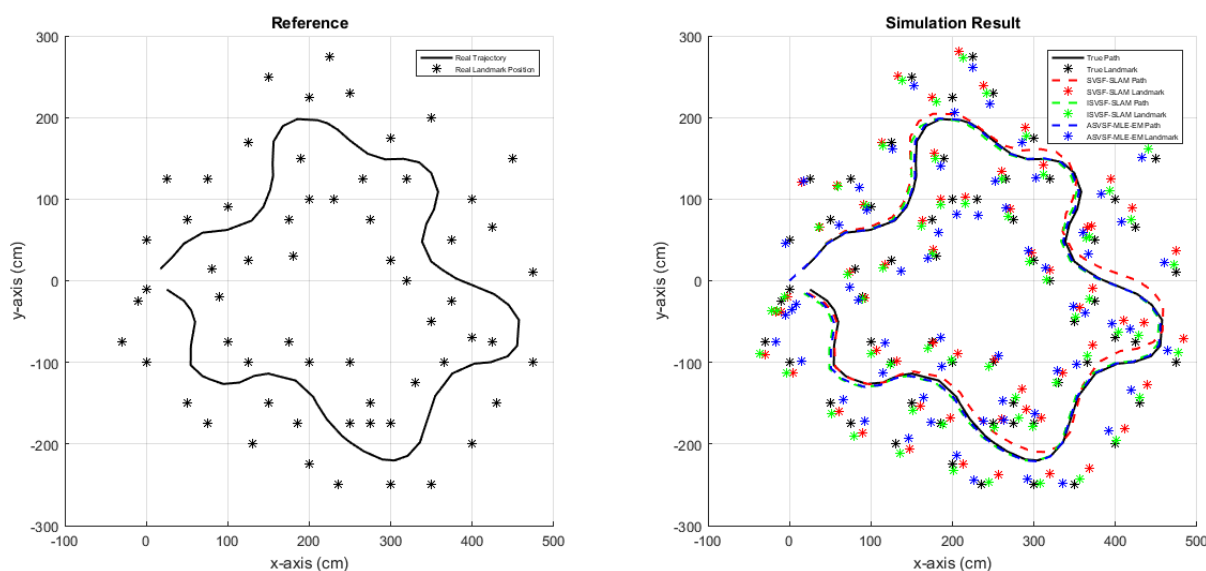


Fig. 4. Performance of Different SLAM-Based Algorithm (Second Test)

Similarly, Fig. 4 also demonstrates different filter performances in solving the SLAM problem of wheeled mobile robots. It also verifies that the proposed method's properness is satisfied with locating the robot position and mapping the features even there is an increment of small additive noise to both the process and measurement.

According to Fig. 5, it can be noted that the increment of the defined noise statistic has no effect on the proposed method stability. It is shown by its ability to reduce RMSE of the SVSF-SLAM algorithm. At this point, it can be stated that the proposed method can guarantees stability better than the classical one. Next, to validate the proposed algorithm stability, the different approaches in estimating map are compared (see Fig. 6).

Fig. 6 illustrates that the stability of the proposed method in mapping the feature is satisfied even after increasing the statistics of the initial noise. According to Fig. 6, the proposed method also presents better quality compared with the SVSF-SLAM algorithm. The

effectiveness of one-smoothing is again proven, referring to its best achievement in estimating the map. Similarly, to clearance the differences in the simulation results discussed above, Table 2 is presented.

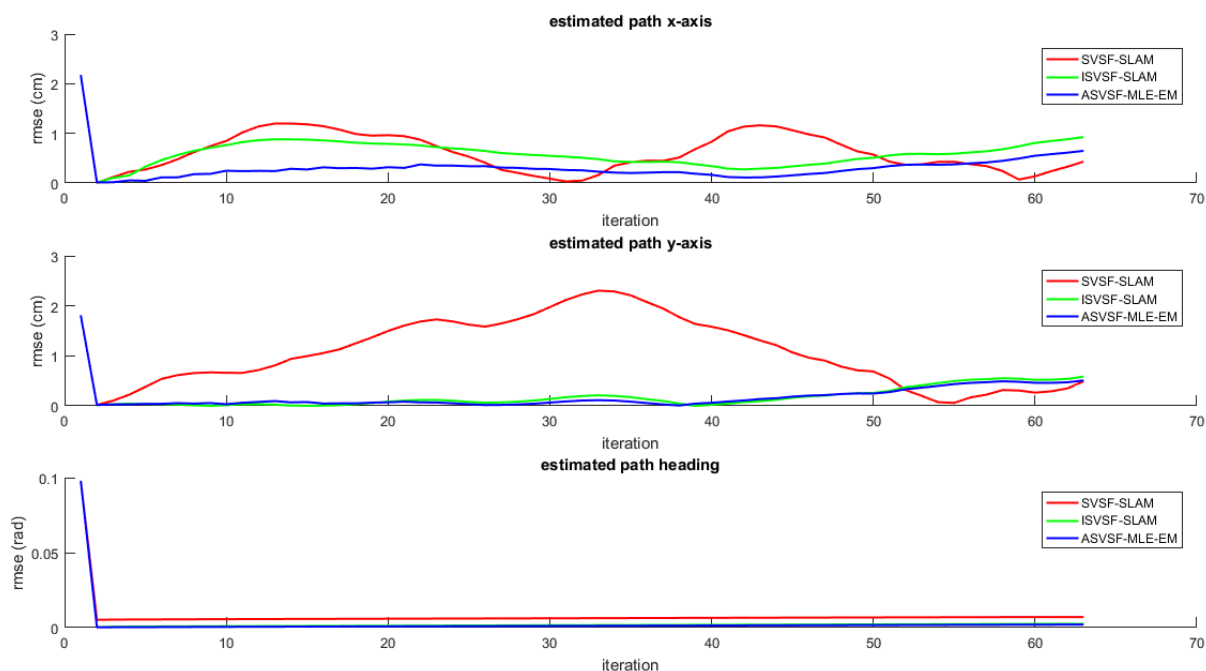


Fig. 5 RMSE of Estimated Path Coordinate of Different SLAM-Algorithm (Second Test)

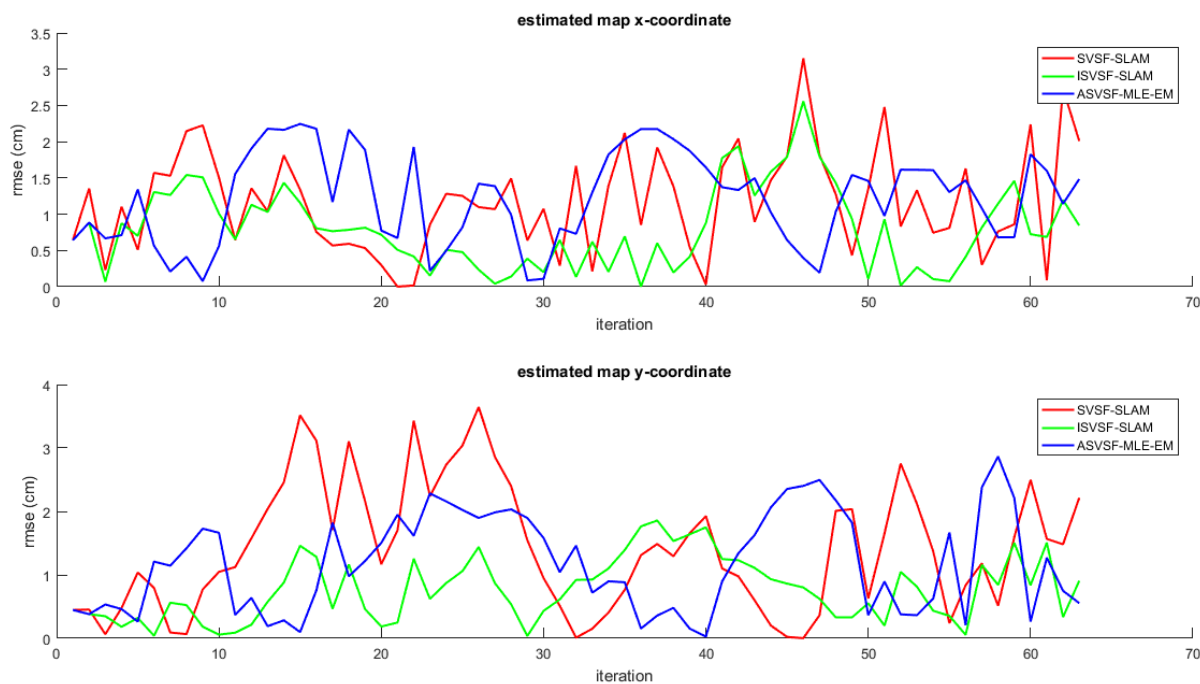


Fig. 6. RMSE of Estimated Map Coordinate of Different SLAM-Algorithm (Second Test)

Table 2: RMSE of Different SLAM-Based Algorithm (Second Test)

SLAM-Based Algorithm	x-EPC [cm]	y-EPC [cm]	θ -EPC [rad]	x-EMC [cm]	y-EMC [cm]
SVSF	5.9065	10.0448	0.1099	10.8078	13.6891
ISVSF	5.3109	2.6691	0.0989	7.7296	7.2725
ASVSF	3.2337	2.5043	0.0985	10.8512	11.1995

According to Table 1 and Table 2, the smallest RMSE is shown by the ISVSF-Based SLAM algorithm. It verifies that the one-step smoothing technique has been successfully enhancing the classical SVSF without losing the SVSF characteristic. However, since it can estimate the noise statistic, its performance cannot guarantee effectiveness when applied in the real application. Regarding these differences, the proposed method has been presenting excellent performance.

- **Third Test ASVSF-SLAM Algorithm Based on MLE-EM with and without ICE**

In order to evaluate the existence of Innovation Covariance Estimation, the following figures (see Fig. 7 and Fig. 8) are presented. These results refer to the initial noise statistic as defined in the Second Test above.

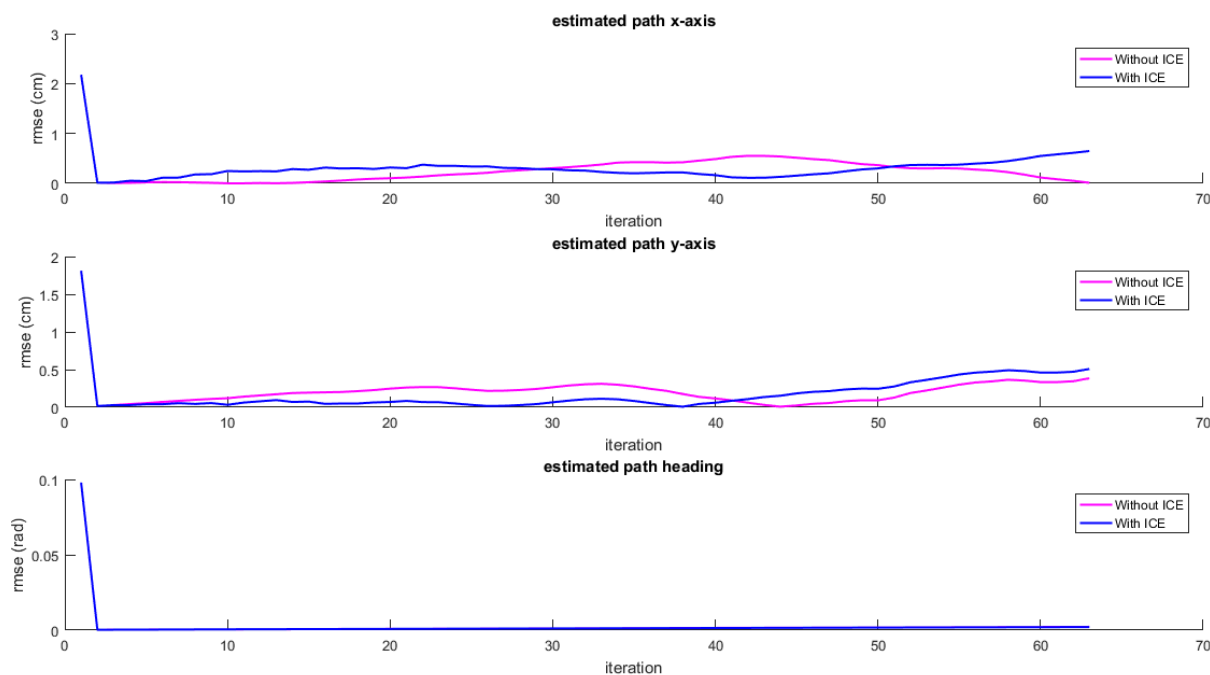


Fig. 7. RMSE of Estimated Path Coordinate of Different SLAM-Algorithm (Third Test)

Fig.7 confirms that the simplification of the first formulated covariance of the measurement noise statistic does not negatively affect the final solution. It can be proven as well in Fig. 8.

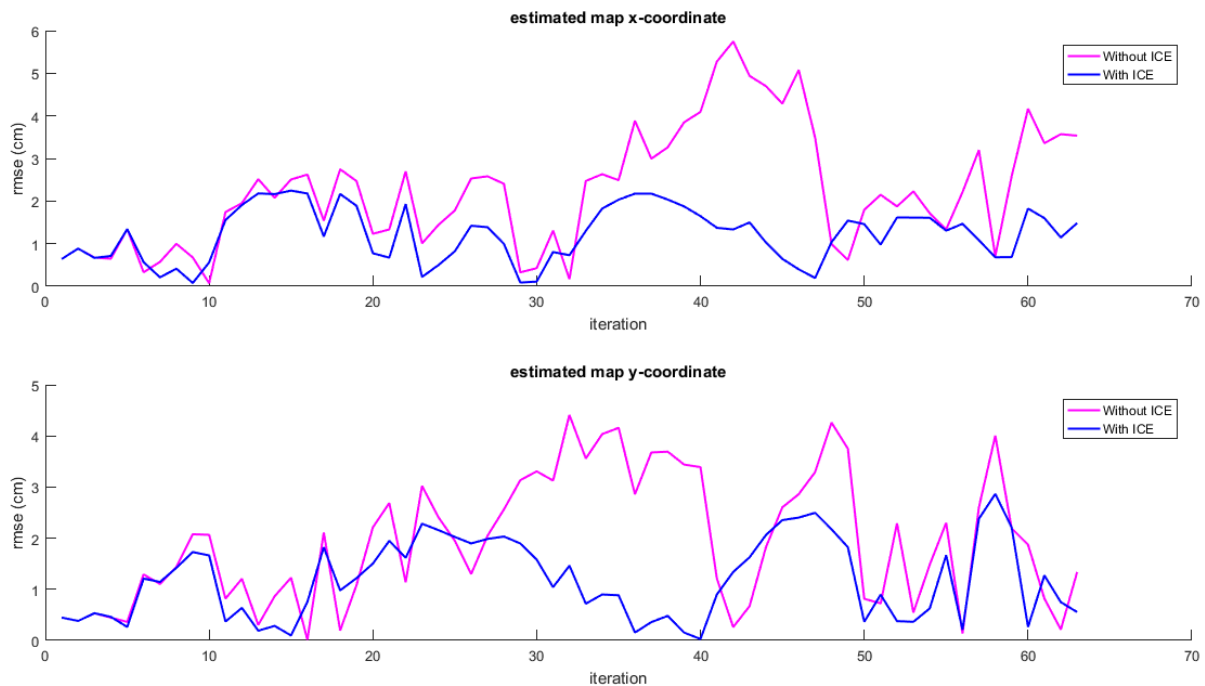


Fig. 8. RMSE of Estimated Map Coordinate of Different SLAM-Algorithm (Third Test)

At this point, it can be noted that the differences depicted by Fig. 7 and Fig. 8 verify that the Innovation Covariance Estimator (ICE) has been successfully reducing RMSE of the original ASVSF-SLAM algorithm. To ease our analysis, Table 3 is also presented

Table 3: RMSE of Different SLAM-Based Algorithm (Second Test)

ASVSF-SLAM-Based Algorithm	x-EPC [cm]	y-EPC [cm]	θ -EPC [rad]	x-EMC [cm]	y-EMC [cm]
Without ICE	3.1637	2.4950	0.0985	20.9206	18.3115
With ICE	3.2337	2.3807	2.5043	10.8512	11.1995

According to Table 3, the proposed method with ICE has been showing better performance compared to other algorithm in term of RMSE of EPC and EMC

5. CONCLUSION

This paper presents a proposed method termed as ASVSF-SLAM Based on MLE-EM creation. The contributions can be summarized as follows; improving the normal SVSF based on a one-step smoothing method, providing an ability to estimate the noise statistic to normal SVSF, providing the time-varying unbiased noise statistic; completing the recursive unbiased noise statistic with innovation covariance estimation. Following all the stages and validating the ASVSF-SLAM algorithm's performance in terms of RMSE has been proving the robustness and effectiveness of the proposed method. Additionally, by referring to the convergence result, which is shown by its performance in different and increment of the initially predetermined noise statistic, the proposed method guarantees the stability compared to the conventional one.

ACKNOWLEDGEMENT

Research was supported by Special Plan of Major Scientific Instruments and Equipment of the State (Grant No.2018YFF01013101), National Natural Science Foundation of China (61704102), the IOT Innovation and Development Special Foundation of Shanghai (2017-GYHLW01037) and Project named “Key Technology Research and Demonstration Line Construction of Advanced Laser Intelligent Manufacturing Equipment” from Shanghai Lingang Area Development Administration, Shanghai University, and Mercu Buana University, Jakarta, Indonesia.

REFERENCES

- [1] Suwoyo, H., Tian, Y., Deng, C., & Adriansyah, A. (2018). Improving a Wall-Following Robot Performance with a PID-Genetic Algorithm Controller. *Proceeding of the Electrical Engineering Computer Science and Informatics*, 5(1), 314-318.
- [2] Adriansyah, A., Suwoyo, H., & Tian, Y. (2019). *Jurnal Teknologi IMPROVING ROBOT*. 3, 119–126.
- [3] Afshari, H. H., Gadsden, S. A., & Habibi, S. (2017). Gaussian filters for parameter and state estimation: A general review of theory and recent trends. *Signal Processing*. <https://doi.org/10.1016/j.sigpro.2017.01.001>
- [4] Ahmed, R., El Sayed, M., Gadsden, S. A., Tjong, J., & Habibi, S. (2016). Artificial neural network training utilizing the smooth variable structure filter estimation strategy. *Neural Computing and Applications*, 27(3), 537–548. <https://doi.org/10.1007/s00521-015-1875-2>
- [5] Akhlaghi, S., Zhou, N., & Huang, Z. (2018). Adaptive adjustment of noise covariance in Kalman filter for dynamic state estimation. *IEEE Power and Energy Society General Meeting*, 2018-January, 1–5. <https://doi.org/10.1109/PESGM.2017.8273755>
- [6] Al-Shabi, M., & Habibi, S. (2011). Iterative smooth variable structure filter for parameter estimation. *ISRN Signal Processing*, 2011(1). <https://doi.org/10.5402/2011/725108>
- [7] Bailey, T. (2002). Mobile Robot Localisation and Mapping in Extensive Outdoor Environments. *Philosophy*, 31(August), 212. [https://doi.org/10.1016/S0921-8890\(99\)00078-0](https://doi.org/10.1016/S0921-8890(99)00078-0)
- [8] Bailey, T., & Durrant-whyte, H. (n.d.). Simultaneous Localisation and Mapping (SLAM): Part II State of the Art. 1–10.
- [9] Bar-Shalom, Y., Li, X.-R., & Kirubarajan, T. (n.d.). Estimation with Applications to Tracking and Navigation.
- [10] Benzerrouk, H., Nebylov, A., & Salhi, H. (2016). Quadrotor UAV state estimation based on High-Degree Cubature Kalman filter. *IFAC-PapersOnLine*. <https://doi.org/10.1016/j.ifacol.2016.09.060>
- [11] Chen, S., Shi, Z., & Ding, J. (2017). Application of the 2nd-order Smooth Variable Structure Filter algorithm for SINS initial alignment. *2017 Forum on Cooperative Positioning and Service, CPGPS 2017*, (1), 43–49. <https://doi.org/10.1109/CPGPS.2017.8075095>
- [12] Choset, H., Lynch, K., Hutchinson, S., Kantor, G., Burgard, W., Kavraki, L., & Thrun, S. (2006). *PRINCIPLES OF ROBOT MOTION, Theory, Algorithms and Implementations*, by Howie Choset et al., MIT Press, 2005. xix + 603 pp., index, ISBN 0-262-03327-5, 433 references (Hb. £38.95) . *Robotica*, 24(2), 271–271. <https://doi.org/10.1017/s0263574706212803>
- [13] Demim, F., Nemra, A., & Louadj, K. (2016). Robust SVSF-SLAM for Unmanned Vehicle in Unknown Environment. *IFAC-PapersOnLine*. <https://doi.org/10.1016/j.ifacol.2016.10.585>
- [14] Fethi, D., Nemra, A., Louadj, K., & Hamerlain, M. (2018). Simultaneous localization, mapping, and path planning for unmanned vehicle using optimal control. *Advances in Mechanical Engineering*, 10(1), 1–25. <https://doi.org/10.1177/1687814017736653>
- [15] Gadsden, S. A., Al-Shabi, M., Arasaratnam, I., & Habibi, S. R. (2014). Combined cubature Kalman and smooth variable structure filtering: A robust nonlinear estimation strategy. *Signal Processing*, 96 (PART B), 290–299. <https://doi.org/10.1016/j.sigpro.2013.08.015>
- [16] Gadsden, S. Andrew, & Afshari, H. H. (2015). A review of smooth variable structure filters: Recent advances in theory and applications. *ASME International Mechanical Engineering*

- Congress and Exposition, Proceedings (IMECE), 4A-2015. <https://doi.org/10.1115/IMECE2015-50966>
- [17] Gadsden, S. Andrew, Habibi, S. R., Dunne, D., & Kirubarajan, T. (2011). Combined particle and smooth variable structure filtering for nonlinear estimation problems. *Fusion 2011 - 14th International Conference on Information Fusion*, 1552–1559.
- [18] Gadsden, S. Andrew, & Lee, A. S. (2017). Advances of the smooth variable structure filter: square-root and two-pass formulations. *Journal of Applied Remote Sensing*. <https://doi.org/10.1117/1.jrs.11.015018>
- [19] Gadsden, Stephen Andrew. (2011). *Smooth Variable Structure Filter Theory and Application.pdf*. McMaster University.
- [20] Gao, B., Gao, S., Gao, L., & Hu, G. (2016). An adaptive UKF for nonlinear state estimation via maximum likelihood principle. *ICEIEC 2016 - Proceedings of 2016 IEEE 6th International Conference on Electronics Information and Emergency Communication*, (4), 117–120. <https://doi.org/10.1109/ICEIEC.2016.7589701>
- [21] Gao, B., Gao, S., Hu, G., Zhong, Y., & Gu, C. (2018). Maximum likelihood principle and moving horizon estimation based adaptive unscented Kalman filter. *Aerospace Science and Technology*. <https://doi.org/10.1016/j.ast.2017.12.007>
- [22] Gao, W., Li, J., Zhou, G., & Li, Q. (2015). Adaptive Kalman filtering with recursive noise estimator for integrated SINS/DVL systems. *Journal of Navigation*, 68(1), 142–161. <https://doi.org/10.1017/S0373463314000484>
- [23] Gao, Z., Mu, D., Zhong, Y., Gu, C., & Ren, C. (2019). Adaptively random weighted cubature kalman filter for nonlinear systems. *Mathematical Problems in Engineering*, 2019. <https://doi.org/10.1155/2019/4160847>
- [24] Grisetti, G. (2004). *Towards a PhD Thesis on Simultaneous Localization and Mapping*. 1–38. Retrieved from <http://citeseerx.ist.psu.edu/viewdoc/download?doi=10.1.1.106.4683&rep=rep1&type=pdf>
- [25] Habibi, B. S. (2007). Structure Filter. *Proceedings of the IEEE*, 95(5).
- [26] He, J., Chen, Y., Zhang, Z., Yin, W., & Chen, D. (2018). A hybrid adaptive unscented Kalman filter algorithm. *International Journal for Engineering Modelling*, 31(3), 51–65. <https://doi.org/10.31534/engmod.2018.3.ri.04d>
- [27] Huang, Y., Zhang, Y., Xu, B., Wu, Z., & Chambers, J. A. (2018). A New Adaptive Extended Kalman Filter for Cooperative Localization. *IEEE Transactions on Aerospace and Electronic Systems*, 54(1), 353–368. <https://doi.org/10.1109/TAES.2017.2756763>
- [28] Kim, K. H., Lee, J. G., & Park, C. G. (2009). Adaptive two-stage extended kalman filter for a fault-tolerant INS-GPS loosely coupled system. *IEEE Transactions on Aerospace and Electronic Systems*, 45(1), 125–137. <https://doi.org/10.1109/TAES.2009.4805268>
- [29] Kim, T., Wang, Y., Sahinoglu, Z., Wada, T., Hara, S., & Qiao, W. (2014). State of charge estimation based on a realtime battery model and iterative smooth variable structure filter. *2014 IEEE Innovative Smart Grid Technologies - Asia, ISGT ASIA 2014*, 132–137. <https://doi.org/10.1109/ISGT-Asia.2014.6873777>
- [30] LaViola, J. J. (2003). A Comparison of Unscented and Extended Kalman Filtering for Estimating Quaternion Motion. *Proceedings of the American Control Conference*, 3, 2435–2440.
- [31] Levitan, E., & Herman, G. T. (1987). A Maximum A Posteriori Probability Expectation Maximization Algorithm for Image Reconstruction in Emission Tomography. *IEEE Transactions on Medical Imaging*, 6(3), 185–192. <https://doi.org/10.1109/TMI.1987.4307826>
- [32] Li, Z., Yang, W., & Ding, D. (2017). Time-Varying Noise Statistic Estimator Based Adaptive Simplex Cubature Kalman Filter. *Mathematical Problems in Engineering*, 2017. <https://doi.org/10.1155/2017/5349879>
- [33] Mohamed, A. H., & Schwarz, K. P. (1999). Adaptive Kalman filtering for INS/GPS. *Journal of Geodesy*, 73(4), 193–203. <https://doi.org/10.1007/s001900050236>
- [34] Outamazirt, F., Fu, L., Lin, Y., & Abdelkrim, N. (2016). A new SINS/GPS sensor fusion scheme for UAV localization problem using nonlinear SVSF with covariance derivation and an adaptive boundary layer. *Chinese Journal of Aeronautics*. <https://doi.org/10.1016/j.cja.2016.02.005>

- [35] Shao, X., He, B., Guo, J., & Yan, T. (2016). The application of AUV navigation based on adaptive extended Kalman filter. *OCEANS 2016 - Shanghai*. <https://doi.org/10.1109/OCEANSAP.2016.7485592>
- [36] Suwoyo, H., Deng, C., Tian, Y., & Adriansyah, A. (2018). Improving a wall-following robot performance with a PID-genetic algorithm controller. *International Conference on Electrical Engineering, Computer Science and Informatics (EECSI), 2018-Octob*, 314–318. <https://doi.org/10.1109/EECSI.2018.8752907>
- [37] Thrun, S. (2002). Probabilistic robotics. *Communications of the ACM*, 45(3), 52–57. <https://doi.org/10.1145/504729.504754>
- [38] Tian, Y., Suwoyo, H., Wang, W., & Li, L. (2019). An ASVSF-SLAM Algorithm with Time-Varying Noise Statistics Based on MAP Creation and Weighted Exponent. *Mathematical Problems in Engineering*, 2019, 28–34. <https://doi.org/10.1155/2019/2765731>
- [39] Tian, Y., Suwoyo, H., Wang, W., Mbemba, D., & Li, L. (2019). An AEKF-SLAM Algorithm with Recursive Noise Statistic Based on MLE and EM. *Journal of Intelligent and Robotic Systems: Theory and Applications*. <https://doi.org/10.1007/s10846-019-01044-8>
- [40] Wan, E. A., & Van Der Merwe, R. (2000). The unscented Kalman filter for nonlinear estimation. *IEEE 2000 Adaptive Systems for Signal Processing, Communications, and Control Symposium, AS-SPCC 2000*, 153–158. <https://doi.org/10.1109/ASSPCC.2000.882463>
- [41] Wang, Hairong, Deng, Z., Feng, B., Ma, H., & Xia, Y. (2017). An adaptive Kalman filter estimating process noise covariance. *Neurocomputing*. <https://doi.org/10.1016/j.neucom.2016.10.026>
- [42] Wang, Hongjian, Fu, G., Li, J., Yan, Z., & Bian, X. (2013). An adaptive UKF based SLAM method for unmanned underwater vehicle. *Mathematical Problems in Engineering*, 2013. <https://doi.org/10.1155/2013/605981>
- [43] Wang, X., Song, B., Liang, Y., & Pan, Q. (2017). EM-based adaptive divided difference filter for nonlinear system with multiplicative parameter. *International Journal of Robust and Nonlinear Control*, 27(13), 2167–2197. <https://doi.org/10.1002/rnc.3674>
- [44] Woo, R., Yang, E. J., & Seo, D. W. (2019). A fuzzy-innovation-based adaptive Kalman filter for enhanced vehicle positioning in dense urban environments. *Sensors (Switzerland)*, 19(5). <https://doi.org/10.3390/s19051142>
- [45] Yang, J. N., Pan, S., & Huang, H. (2007). An adaptive extended Kalman filter for structural damage identifications II: Unknown inputs. *Structural Control and Health Monitoring*, 14(3), 497–521. <https://doi.org/10.1002/stc.171>
- [46] Yang, Jann N., Lin, S., Huang, H., & Zhou, L. (2006). An adaptive extended Kalman filter for structural damage identification. *Structural Control and Health Monitoring*, 13(4), 849–867. <https://doi.org/10.1002/stc.84>
- [47] Yi, B., Kang, L., Tao, S., Zhao, X., & Jing, Z. (2013). Adaptive two-stage extended kalman filter theory in application of sensorless control for permanent magnet synchronous motor. *Mathematical Problems in Engineering*, 2013. <https://doi.org/10.1155/2013/974974>
- [48] Yong, S., Chongzhao, H., & Yongqi, L. (2009). Adaptive UKF for target tracking with unknown process noise statistics. *2009 12th International Conference on Information Fusion, FUSION 2009*, (1), 1815–1820.
- [49] Yu, F., Sun, Q., Lv, C., Ben, Y., & Fu, Y. (2014). A SLAM algorithm based on adaptive cubature Kalman filter. *Mathematical Problems in Engineering*, 2014. <https://doi.org/10.1155/2014/171958>
- [50] Zeng, Z., Zhang, S., Xing, Y., & Cao, X. (2014). Robust adaptive filter for small satellite attitude estimation based on magnetometer and gyro. *Abstract and Applied Analysis*, 2014. <https://doi.org/10.1155/2014/159149>

SYSTEM OF AUTOMATIC CONTROL OF THE LEVEL OF STEAM POWER GENERATORS ON THE BASIS OF THE REGULATION CIRCUIT WITH SMOOTHING OF THE SIGNAL

UMURZAKOVA DILNOZA MAXAMADJONOVNA*

*Department of Information Processing Systems and Management,
Tashkent State Technical University, 100097 Tashkent, Uzbekistan*

Corresponding author: umurzakovadilnoz@gmail.com

(Received: 25th March 2020; Accepted: 3rd September 2020; Published on-line: 4th January 2021)

ABSTRACT: The purpose of this article is to develop high-quality combined automatic control systems (ACS) for the water level in the drum of steam boilers of thermal power plants (TPPs), which can significantly improve the quality of regulation and increase the efficiency of TPPs in a wide range of load changes. To improve the quality of water level control in the drum of steam generators of nuclear power plants with a pressurized water-cooled power reactor (PWPR), it is proposed to use a combined automatic control system based on a control loop with a correcting PI-controller tuned to a symmetrical optimum, with smoothing the reference signal and device compensation of the most dangerous internal and external measurable disturbances. A technique has been developed for assessing the impact of changes in the quality characteristics of transients of combined self-propelled guns by the water level in the drum of steam boilers and steam generators on the safety, reliability, durability, and efficiency of thermal power equipment of thermal power plants. Comparison was made of direct indicators of the quality of three ACS (typical and three-pulse, digital system with an observer state, and the proposed combined ACS). The simulation results of transients of the proposed and typical three-pulse self-propelled guns confirmed the advantages of the first.

ABSTRAK: Artikel ini bertujuan bagi membina sistem kombinasi automatik (ACS) berkualiti tinggi bagi aras air dalam drum dandang stim tenaga terma loji kuasa (TPP). Ini dapat meningkatkan mutu peraturan dan meningkatkan kecekapan TPP secara signifikan dengan pelbagai perubahan beban. Bagi meningkatkan kualiti kawalan aras air dalam drum penjana wap loji kuasa tenaga nuklear dengan reaktor berpendingin air bertekanan (PWPR). Gabungan sistem kawalan automatik berdasarkan gelung kawalan dengan pembedahan PI telah dicadangkan dan diselaraskan simetri secara optimum, dengan melancarkan isyarat rujukan dan pembedahan peranti dari gangguan yang boleh diukur dari dalam dan luar. Satu teknik telah dibina bagi menilai kesan perubahan ciri kualiti transien gabungan berjentera pada aras air di tong dandang stim dan drum penjana wap pada keselamatan, kebolehpercayaan, ketahanan dan kecekapan peralatan tenaga terma loji janakuasa. Perbandingan dibuat pada kualiti tiga ACS (sistem digital khas dan tiga signal dengan keadaan pemerhati dan gabungan ACS yang dicadangkan). Hasil sistem simulasi transien yang dicadangkan dan tiga signal biasa berjentera mengesahkan kelebihan pada yang pertama.

KEYWORDS: *combined automatic control system; steam boiler drum; steam generator; controller; adaptive system; heat power industry*

1. INTRODUCTION

Currently widespread in the field of automation, heat and power processes in thermal and nuclear power plants (TPPs and NPPs) received standard three-pulse automatic control systems (ACS). As a result of their wide distribution, the problem of “technical contradiction” arises between the speed and stability of the system. The existing ACS with the water level in the boiler drum and their modifications, which have become widespread at TPPs and NPPs, but significant load changes turned out to be insufficiently effective. An increase in the steam production of boilers, the parameters of superheated steam at the outlet of the latter, as well as the need for boilers to operate in the peak and half-peak parts of the electrical loads of the power system, actualizes the problem of a significant increase in the quality of water level control in the drum in the entire range of load variation of heat power facilities during deep disturbances.

A comparison of steam production technologies at TPPs and NPPs shows that they are similar to each other: in essence, the difference is that the reactor and the primary circuit take on the role of the furnace in the boiler of TPPs at nuclear power plants. Therefore, the schemes for automatic control and regulation of nuclear power units in general coincide with the schemes for regulating power units of TPPs. The similarity of steam and electricity production technologies at TPPs and NPPs leads to the similarity of their automatic control and regulation schemes. One of the main ACS of nuclear power plants that determine the safety and reliability of power units is self-propelled guns for the water level in the drum of the steam generator. Despite attempts to use single-pulse level control systems in the drum of a steam generator of nuclear power plants [1], typical three-pulse self-propelled guns have currently gained maximum popularity at thermal power plants and nuclear power plants, which cannot provide the required quality level maintenance in the drum under deep load changes [2].

To eliminate this drawback, it is proposed to use a combined self-propelled gun for objects without self-leveling with the allocation of an equivalent external disturbance [3], which is characterized by increased fluctuations in the flow rate of feed water when disturbed by the steam flow. In [4], it was proposed to use combined self-propelled guns with a limitation of the maximum value of the corrective action at the output of the equivalent external disturbance compensation device.

Steam generators of NPP with pressurized water power reactor (PWPR) are complex control objects, on the reliable operation of which safety depends and the reliability of the entire power plant. The main controllable parameter in the steam generator (SG) is the water level, which is subject to rigid requirements. Inaccurate maintenance of the water level in the steam generator drum leads to an increase in humidity steam, increases the wear of the turbine blade and reduces the power of the power unit. The control of the water level in the drums of boilers of TPP and SG of NPP is carried out by three-pulse ACS [5,6].

2. RESEARCH METHODS

A typical three-pulse ACS with the water level in the boiler drum has the following disadvantages:

- the presence of a static control error at the end of the transient process, first of all, when there is an external disturbance by the steam flow with the phenomenon of “level swelling”;

- the presence of three measurement sensors (level, steam, and feed water consumption);
- large deviations of the water level in the boiler drum beyond the established limits with large load changes, which lead to the boiler shutdown by protection in case of overflow.

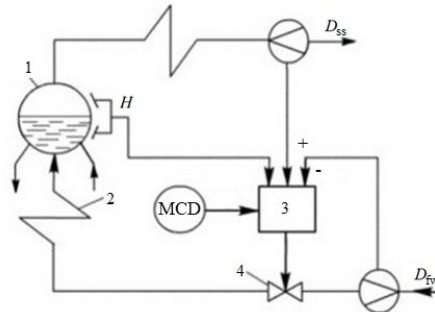


Fig. 1: Typical three-pulse ACS with water level in the drum: 1 - boiler drum; 2 - water economizer; 3 - controller; 4 - regulating feed valve; MCD - manual control dial; H - level water; D_{fw} - consumption of feed water; D_{ss} - superheated steam flow rate.

The specified ACS under deep disturbances in the system does not provide the required quality regulation, which leads to unloading or shutdown of the power unit and economic losses [7].

To improve the quality of the control of the steam generator PGV-1000 level at NPP with PWPR a digital PI controller with one water level instead of three in the standard ACS, which ensures an improvement in the quality of control in the case of external and internal disturbances in comparison with the typical system [8]. In this regard, the task of further improving the quality of comparison with the optimal ACS with a state observer is based on express methods of structural and parametric optimization of dynamic systems of heat and power processes of NPP and TPP with using the principles of the theory of invariance [9]. One of the implementation options for such systems is shown in Fig. 2 [10].

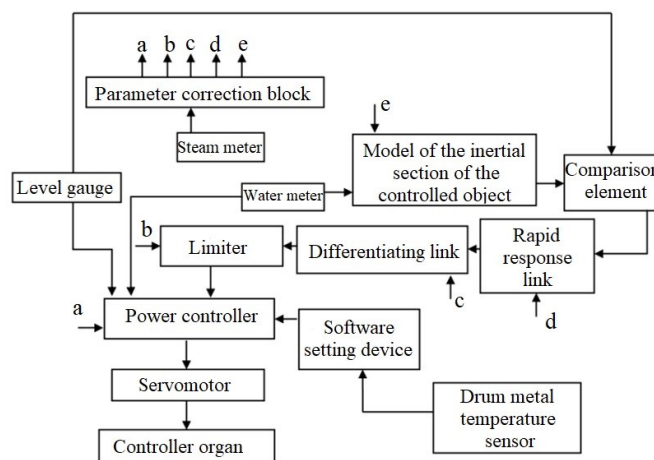


Fig. 2: Scheme of implementation of the combined ACS by the water level in the boiler drum.

The specified combined ACS with the extraction of an equivalent external disturbance provides a decrease in the maximum dynamic error of regulation by the water level in the drum under external disturbance with steam consumption by 36% compared to a typical ACS with differentiator. In this case, the time for working out the disturbance with the steam consumption is 200 s.

To further improve the quality of maintaining the water level in steam generators of TPPs based on standard controllers, it is proposed to use self-propelled guns based on a control loop with reference signal smoothing (Fig. 3). Designations adopted in Fig. 3: $y(t)$, $y_1(t)$ - respectively, the main (water level in the drum) and intermediate (feed water flow) controlled values; x_{st1} , x_{st2} - assignment of intermediate and main controlled quantities; x_{st2}^s - smoothed setpoint to the correction knob; $x_c(t)$, $x_r(t)$ - corrective and control effects; f_1 , f_2 - internal and external disturbances; k_{le} - coefficient transmission; $e^{-\tau_1 s}$ - pure lag; transfer functions: $W_{le}(s)$ - leading site of the object; $W_1(s)$ - inertial section of the object; $W_2(s) - W_3(s)$ - the difference between the inertial link and the ideal integrating link, which describes the dynamics of the phenomenon of “swelling” of the water level with increasing steam flow from the steam generator; $W_{cd}^{f_1}(s)$, $W_{cd}^{f_2}(s)$ - compensation devices for measured internal and external disturbances.

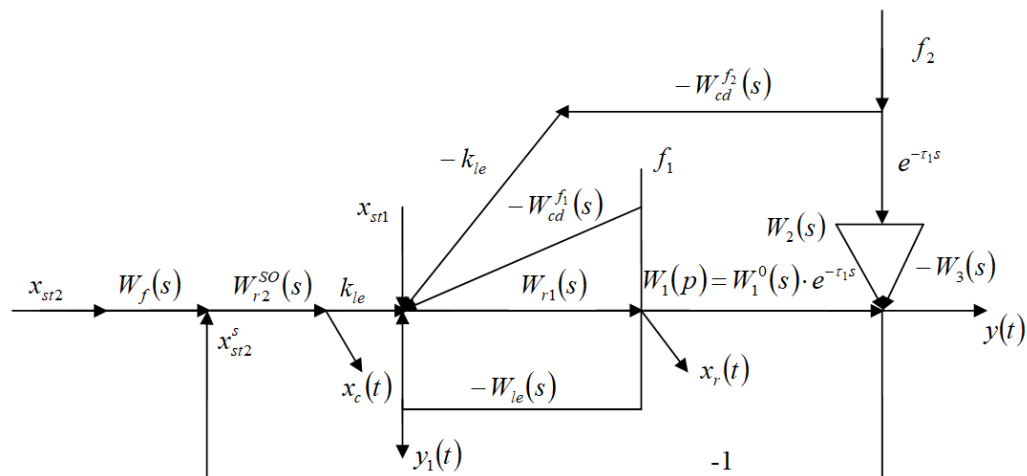


Fig. 3: Structural diagram of the combined PGV-1000 steam generator automatic level control system with a correcting PI controller tuned to a symmetrical optimum, with a smoothing of the reference signal.

The numerical values of the transfer functions developed by the combined ACS of the level of the steam generator PGV-1000 TPP with WWPR-1000 are shown in the structural diagram of the simulation in Fig. 4.

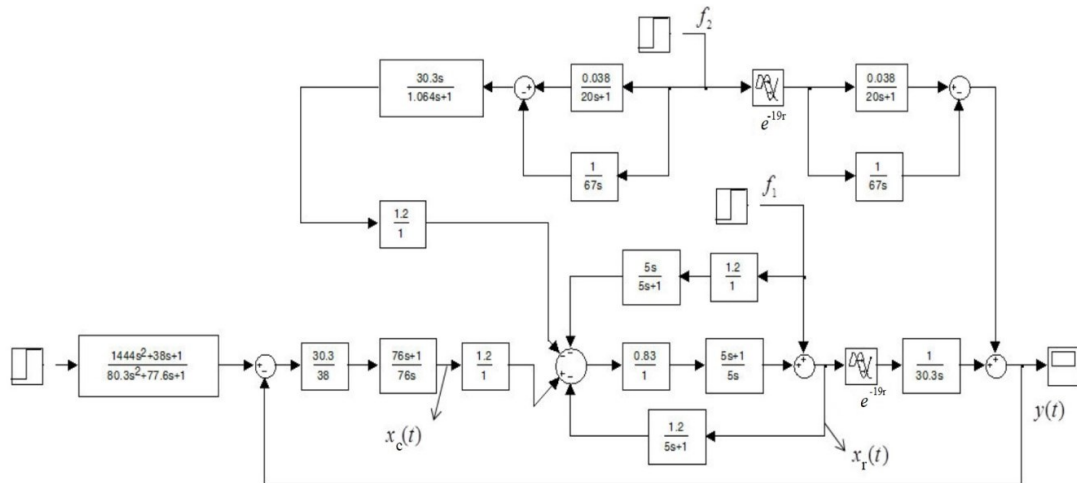


Fig. 4: Transient simulation modeling of combined ACS with a water level in the PGV-1000 drum with a PI controller tuned to a symmetric optimum with smoothing of the reference signal.

The following notation of transfer functions is accepted here:

- leading section:

$$W_{le}(s) = \frac{k_{le}}{T_{le}s + 1} = \frac{1,2}{5s + 1}; \quad (1)$$

- inertial section:

$$W_1(s) = W_1^0(s) \cdot e^{-\tau_1 s} = \frac{e^{-19s}}{30,3s}; \quad (2)$$

- inertial link of the first order:

$$W_2(s) = \frac{k_2}{T_2s + 1} = \frac{0,038}{20s + 1}; \quad (3)$$

- ideal integrating link:

$$W_3(s) = \frac{k_2}{T_3s} = \frac{1}{67s}; \quad (4)$$

- stabilizing PI controller:

$$W_{c1}(s) = \frac{k_1(T_{I1}s + 1)}{T_{I1}s} = \frac{0,83(5s + 1)}{5s}; \quad (5)$$

- corrective PI controller:

$$W_{c2}(s) = \frac{k_2(T_{I2}s + 1)}{T_{I2}s} = \frac{0,797(76s + 1)}{76s}; \quad (6)$$

- smoothing filter:

$$W_f(s) = \frac{4\tau_1^2 s^2 + 2\tau_1 s + 1}{(4\tau_1 s + 1)(T_{st2}s + 1)} = \frac{1444s^2 + 38s + 1}{80,3s^2 + 77,06s + 1}, \quad (7)$$

where T_{st2} - a dynamic tuning parameter aligning the order of the numerator and denominator of the filter transfer function;

- compensation devices for measured internal disturbance

$$W_{cd}^{f_1}(s) = \frac{k_{D1}T_{D1}s}{T_{D1}s + 1} = \frac{1,2 \cdot 5s}{5s + 1}; \quad (8)$$

- compensation devices for measured extreme external disturbance by steam flow:

$$W_{cd}^{f_2}(s) = [W_2(s) - W_3(s)] \frac{T_1s}{T_{st3}s + 1} = \left[\frac{0,038}{20s + 1} - \frac{1}{67s} \right] \cdot \frac{30,3s}{1,064s + 1}, \quad (9)$$

where T_{st3} - a dynamic tuning parameter aligning the order of the numerator and denominator of the transfer differentiator of the device for compensating extreme external disturbances by the steam flow rate.

It is required to form such an ACS structure, which significantly (at times) will reduce the maximum permissible level control error when disturbed by the steam flow compared to a typical three-pulse ACS, to achieve complete invariance when working out the most dangerous measured internal disturbance, and also to eliminate large overshoot (up to 43.4%) when working out the jump in task x_{st2} , inherent ACS with a correcting PI controller tuned to a symmetrical optimum [11].

In order to form the ACS structure that satisfies the given requirements, we will start by choosing the stabilization structure of the controller as the product of the inverse transfer function of the leading section and the transfer function of the open system in the form of an ideal integrating link taking into account (1) [12]:

$$W_{r1}(s) = [W_{le}(s)]^{-1} \cdot W_{st1}^{OS(n=1)}(s) = \frac{T_{le}s + 1}{k_{le}T_{st1}(s)} = \frac{5s + 1}{1,2 \cdot 5s} = 0,83 \frac{5s + 1}{5s}, \quad (10)$$

where $T_{st1} = T_{le}$ - parameter of dynamic adjustment of the stabilizing controller.

In this case, the internal circuit of the system with a stabilizing controller during the completion of task x_{st1} can be replaced by a first-order inertial unit that plays the role of a quality criterion:

$$W_{st1}(s) = \frac{1}{T_{st1}s + 1}. \quad (11)$$

If between the output of the correction and the input of the stabilizing controllers there is an amplifier with the transmission coefficient $k_{am} = k_{le}$, then the corrective action $x_c(t)$ will be equal to the regulating $x_r(t)$. As a result, the dual-circuit system turns into a single-loop system with a correcting controller and an inertial section of the object (2). If, at the same time, we select and measure the most dangerous internal disturbance f_1 using an additional sensor, the output of which is connected to the input of the compensation device for this disturbance, then the ACS will have complete invariance with respect to f_1 if the following condition is satisfied [13]:

$$W_{cd}^{f_1}(s) \cdot W_{r1}(s) = 1. \quad (12)$$

From where, taking into account (5), we obtain the transfer function of the compensation device for the measured internal disturbance in the form of a real differentiator:

$$W_{cd}^{f_1}(s) = \frac{1}{W_{r1}(s)} = \frac{T_{I1}s}{k_{r1}(T_{I1}s + 1)}. \quad (13)$$

For high-quality testing of internal unmeasured disturbances, the dynamic adjustment of the correcting PI controller should be performed at a symmetrical optimum with respect to the transfer function of the object (2) [14]:

$$T_{I2} = 4\tau_1 = 76s. \quad (14)$$

$$k_{r2} = \frac{1}{2k_{in}\tau_1} = \frac{30,3}{2 \cdot 19} = 0,797. \quad (15)$$

At the same time, with the high-quality processing of internal disturbances, the graph of the transition characteristic for the water level in the drum of the steam generator in relation to the task at the entrance to the correcting controller will have the following direct quality indicators: the first time of regulation $t_{r1} = 3\tau_1 = 3,1 \cdot 19 = 58,9s$; time of final entry into the tolerance band $\pm 2\%$ $t_{r2} = 16,5 \cdot 19 = 313s$; the maximum overshoot in this case will be 43.4% [15].

To eliminate overshoot and improve system performance when working out a task, a smoothing filter with a transfer function of this form is installed between the setter and the correction controller

$$W_f(s) = \frac{4\tau_1^2 s^2 + 2\tau_1 s + 1}{(4\tau_1 s + 1)(T_{st2} s + 1)} = \frac{1444s^2 + 38s + 1}{80,3s^2 + 77,06s + 1}, \quad (16)$$

where T_{st2} - a dynamic filter setting parameter that aligns the order of the numerator and denominator of the filter transfer function (16), with a decrease in the numerical value which increases the ACS speed during mining x_{st2} .

To improve the quality of working out extreme external disturbances during a planned change in the load of the power unit, we measure the steam flow rate with an additional sensor, the output of which is fed to the input of the external disturbance compensation device, the dynamics of which is described by the transfer function $W_{cd}^{f_2}(s)$. The output of the compensation device through the amplifying link k_{le} is connected to the input of the stabilizing controller with the opposite sign. As a result, the invariance condition with a planned change in the load $y(t)$ with respect to the measured external disturbance takes the following form [16, 17]:

$$W_{cd}^{f_2}(s) \cdot W_1^0(s) \cdot e^{-\tau_1 s} = [W_2(s) - W_3(s)] \cdot e^{-\tau_1 s}. \quad (17)$$

Here, the delay link in the right-hand side of equality (17) is implemented programmatically in the automatic unit power generator, which, with a planned daily change in load, first generates the corresponding signal at the input to the external disturbance compensation device, and after the control action reaches the system output at time $t = \tau_1$, the power unit automatically switches to a different load level. In this case, the numerical value of τ_1 is adjusted as a function of the load of the power unit [18].

Taking into account (2) and (17), the transfer function of the external disturbance compensation device, as well as the physical implementation condition, will take

$$W_{cd}^{f_2}(s) = [W_2(s) - W_3(s)] \cdot \frac{T_1 s}{T_{st3} s + 1}, \quad (18)$$

where T_{st3} - a parameter of dynamic adjustment of an external disturbance compensation device aligning the order of the numerator and denominator of the transfer function of the differentiator.

3. RESULTS AND DISCUSSION

Transient graphs combined by an ACS combined with the water level in the PGV-1000 drum with a PI controller tuned to a symmetrical optimum under basic influences confirming the achievement of specified requirements are shown in Fig. 5.

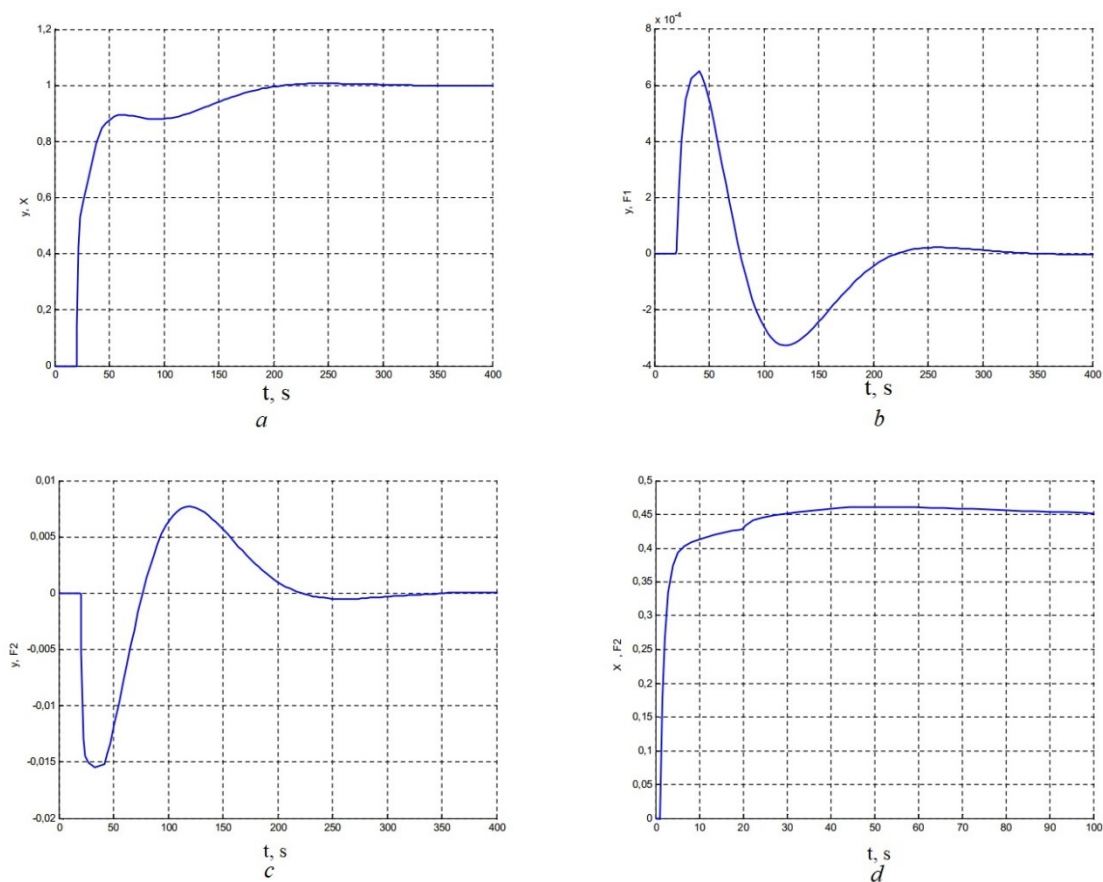


Fig. 5: Graphs of transient processes of combined ACS with the water level in the PGV-1000 drum with the adjustment controller set to a symmetric optimum: a - testing the jump of the setting action x_{st2} ; b - development of internal disturbance f_1 ; c - development of external disturbance by steam flow f_2^* ; d - changes in the control action $x_r(t)$ during the development of an external disturbance by the steam flow rate; t - is time.

Three combined ACS of the water level in the drum of the PGV-1000 steam generator for a planned load change and complete invariance with respect to the most dangerous internal disturbance with the measurement of the external disturbance by the steam flow

rate: ACS using the main feedback compensator during the processing of the driving signal, have been developed for steam generators of power units of PWPR TPPs with PWPR; ACS with smoothing the reference signal and using a PI controller tuned to a symmetric optimum (SO); ACS based on optimal controllers. In these ACSs, the structure and dynamic settings of the stabilizing controllers due to the additional amplifier at the output of the correcting controller ensure the equality of the correcting $x_c(t)$ and control $x_r(t)$ actions, as well as the complete invariance of the development of internal perturbations and invariance accurate to ε when working out external perturbations by the steam flow rate. Direct indicators of the quality of transients of the two proposed ACSs in comparison with a typical three-pulse ACS and digital ACS with a state observer are shown in Table 1.

Table 1: Quality indicators of transients of the compared ACS

Name of ACS	Quality indicators			
	$\Delta y/y_N$	ΔH_b	t_r, s	$\overline{X_r^m}$
typical three-pulse ACS	0,034	83,6	160	0,454
digital ACS with state observer	0,031	76,0	130	+0,61
combined ACS with signal smoothing and the use of a PI controller (SO)	0,016	41,0	200	+0,46
combined ACS based on optimal controllers	0,024	61,5	75	+0,475

From the analysis of the data in Table 1 it follows that the proposed combined ACS provides the best direct quality indicators in relation to a typical three-pulse ACS, and digital ACS with a state observer. The following notation has been adopted here: $\Delta y/y_N$ - the relative deviation of the water level in the drum from the nominal; ΔH_b - absolute deviation of water level 13; t_r - regulation time; $\overline{X_r^m}$ - the maximum value of the control impact.

4. CONCLUSION

The results of this research made it possible to formulate the following practical recommendations for improving the quality of drum water level control in steam boilers and steam generators:

- refinement of task x_{st2} is carried out without overshoot. The control time is 200 s instead of 313 s without a smoothing filter.
- when working out the measured internal disturbance, the complete invariance of the ACS is achieved.
- the maximum dynamic level deviation in a combined ACS using a PI controller tuned to a symmetrical optimum is 0.016 relative units, which corresponds to 41 mm of water, which is 2 times less than in a typical three-pulse ACS.
- the maximum change in the controller action in the combined ACS decreased by 22.1% compared to the ACS with a state observer

- the mathematical model for assessing the quality of ACS transient processes the water level for partial and complete load shedding of the boiler can be used to clarify the settings for the operation of technological protections without carrying out field tests of the systems.

REFERENCES

- [1] Siddikov IX, Umurzakova DM, Bakhrieva HA. (2020) Adaptive system of fuzzy-logical regulation by temperature mode of a drum boiler. *IIUM Engineering Journal*, 21(1): 185-192. <https://doi.org/10.31436/iiumej.v21i1.1220>.
- [2] Siddikov IX, Umurzakova DM. (2019) Mathematical Modeling of Transient Processes of the Automatic Control System of Water Level in the Steam Generator, *Universal Journal of Mechanical Engineering*, 7(4): 139-146. doi: 10.13189/ujme.2019.070401.
- [3] Siddikov IX, Umurzakova DM. (2019) Synthesis of Adaptive Control Systems of a Multidimensional Discrete Dynamic Object with a Forecasting Models. *International conference on information science and communications technologies applications, trends and opportunities (ICISCT 2019)*. Tashkent University of information technologies named after Muhammad al-Khwarizmi. –Tashkent. 4-6 November, 2019. DOI: 10.1109 / ICISCT47635.2019.9012033
- [4] Siddikov IX, Umurzakova DM. (2019) Neuro-fuzzy Adaptive Control system for Discrete Dynamic Objects. *International conference on information science and communications technologies applications, trends and opportunities (ICISCT 2019)*. Tashkent University of information technologies named after Muhammad al-Khwarizmi. –Tashkent. 4-6 November, 2019. DOI: 10.1109/ICISCT47635.2019.9012027.
- [5] Siddikov IX., Umurzakova DM. (2020) Fuzzy-logical Control Models of Nonlinear Dynamic Objects // *Advances in Science, Technology and Engineering Systems Journal*, Vol. 5, No. 4, 419-423 (2020). DOI: 10.25046/aj050449.
- [6] Demchenko VA. (2001) *Avtomatizacija i modelirovanie tehnologicheskikh processov AJeS i TJeS*. Odessa: Astroprint, 308 s.
- [7] Pletnev GP. (2007) *Avtomatizacija tehnologicheskikh processov i proizvodstv v teplojenergetike: uchebnik dlja studentov vuzov*. M.: Izd. dom MJeI, 352 s.
- [8] Rotach, V. Ya. (2008) *The Theory of Automatic Control*. Moscow: Publishing House Moscow Power Engineering Institute, 396 p.
- [9] Zhu X, Zhang H, Cao D, Fang Z. (2014) Robust control of integrated motor-transmission powertrain system over controller area network for automotive applications, *Mechanical Systems and Signal Processing*, 58: 15-28.
- [10] Zulfatman, Rahmat MF. (2009) Application of self-tuning Fuzzy PID controller on industrial hydraulic actuator using system identification approach, *International Journal on Smart Sensing and Intelligent Systems*, 2(2): 246-261.
- [11] Das S, Pan I, Halder K, Das S, Gupta A. (2013) LQR based improved discrete PID controller design via optimum selection of weighting matrices using fractional order integral performance index, *Applied Mathematical Modelling: Simulation and Computation for Engineering and Environmental Systems*, 37(6): 4253-4268.
- [12] Gasbaoui B, Nasri A. (2012) A novel multi-drive electric vehicle system control based on multi-input multi-output PID controller, *Serbian Journal of Electrical Engineering*, 9(2): 279-291.
- [13] Has Z, Muslim AH, Mardiyah NA. (2017) Adaptive-fuzzy-PID controller based disturbance observer for DC motor speed control, in *Proceedings of the 2017 4th International Conference on Electrical Engineering, Computer Science and Informatics (EECSI)*, pp. 1-6, Yogyakarta, September.
- [14] Hu S, Liang Z, Zhang W, He X. (2018) Research on the integration of hybrid energy storage system and dual three-phase PMSM Drive in EV, *IEEE Transactions on Industrial Electronics*, 65(8): 6602-6611.

- [15] Iplikci S. (2010) A comparative study on a novel model-based PID tuning and control mechanism for nonlinear systems, *International Journal of Robust and Nonlinear Control*, 20(13): 1483-1501.
- [16] Kumar SMG, Deepak J, Anoop RK. (2010) PSO based tuning of a PID controller for a high performance drilling machine, *International Journal of Computer Applications*, 1(19): 12-18.
- [17] Malwatkar GM, Khandekar AA, Nikam SD. (2011) PID controllers for higher order systems based on maximum sensitivity function, 2011 3rd International Conference on Electronics Computer Technology.
- [18] Pelusi D. (2012) PID and intelligent controllers for optimal timing performances of industrial actuators, *International Journal of Simulation: Systems, Science and Technology*, 13(2): 65–71.

ASSIST AS NEEDED CONTROL STRATEGY FOR UPPER LIMB REHABILITATION ROBOT IN EATING ACTIVITY

NORSINNIRA ZAINUL AZLAN* AND NURUL SYUHADAH LUKMAN

*Department of Mechatronics Engineering, Kulliyah of Engineering,
International Islamic University Malaysia
Jalan Gombak, 53100 Kuala Lumpur, Malaysia*

**Corresponding author: sinnira@iium.edu.my*

(Received: 20th May 2020; Accepted: 18th August 2020; Published on-line: 4th January 2021)

ABSTRACT: The slacking behaviour or lack of participation from impaired patients during robotic rehabilitation therapy is one of the factors that slow down their recovery. The implementation of Assist As Needed (AAN) control law in the robotic assisted rehabilitation treatment may alleviate this problem and encourage the patients to be actively involved in the rehabilitation exercises. This paper presents a new Assist As Needed control strategy for an upper limb rehabilitation robot in assisting subjects with various levels of capabilities to regain their original upper limb's functionality in realizing basic motions in eating activity. The controller consists of Proportional, Integral, Derivative (PID) controller in the feedback loop, with an adjustable gain K that varies according to the user's level of capability. A Force Sensing Resistor (FSR) is used to identify the user's upper extremity capability level. The controller regulates the necessary amount of assistance provided by the robot based on the information obtained from the sensor. The automatic adjustment of the robot's assistance to the subjects leads them to put in their own effort in accomplishing the desired movements. The proposed control strategy is simple, easy to program, and mathematically less complicated. A prototype of the wearable upper limb rehabilitation robot has been built and a Graphical User Interface (GUI) has been developed using MATLAB software to facilitate the rehabilitation process and for progress monitoring. The simulation and experimental results have proven that the proposed control strategy is successful in regulating the necessary amount of robot assistance according to the patients' level of capability. The proposed controller has effectively driven the upper limb rehabilitation robot to achieve the desired trajectory with zero steady state error, percentage overshoot less than 8% and settling time below 6 seconds, whilst providing the correct amount of robotic assistance in accordance to the subjects' capability level.

ABSTRAK: Reaksi kurang respon dari pesakit kurang keupayaan semasa terapi pemulihan robotik adalah satu faktor melambatkan kadar pemulihan. Pelaksanaan teknik kawalan Bantu Apabila Diperlukan (AAN) dalam rawatan pemulihan dengan bantuan robot dapat membantu dan mendorong pesakit terlibat secara aktif dalam latihan pemulihan. Artikel ini membentangkan strategi kawalan baru, iaitu Bantu Apabila Diperlukan oleh robot pemulihan bagi anggota atas pesakit yang mempunyai pelbagai tahap kemampuan, dalam mengembalikan fungsi asas gerakan tangan seperti aktiviti makan. Teknik kawalan terdiri daripada kawalan Berkadar, Integral, Terbitan (PID) dalam lingkaran tindak balas, dengan pemboleh ubah K mengikut tahap kemampuan pesakit. Alat pengukur Resistan Daya Rasa (FSR) digunakan bagi mengenal pasti tahap kemampuan maksima pesakit dalam menggerakkan tangan. Berdasarkan maklumat yang diperolehi daripada sensor, teknik kawalan akan menghantar maklumat kepada robot bagi membantu pesakit. Bantuan automatik yang dibekalkan robot kepada pesakit akan mendorong pesakit berusaha melakukan gerakan yang diperlukan. Strategi kawalan yang dicadangkan ini adalah

ringkas, mudah diprogramkan dan kurang rumit dari segi matematik. Sebuah prototaip robot pemulihan anggota tangan telah dibina dan sebuah platform grafik bagi pengguna (Antara Muka Grafik Pengguna, GUI) telah dibangunkan menggunakan perisian MATLAB bagi memudahkan proses pemulihan dan pemantauan kemajuan pesakit. Hasil simulasi dan eksperimen membuktikan bahawa strategi cadangan kawalan ini berjaya mengatur jumlah bantuan daripada robot bersesuaian dengan tahap kemampuan pesakit. Teknik kawalan yang dicadangkan telah berjaya menggerakkan robot pemulihan tangan bagi mencapai lintasan gerakan yang diinginkan dengan ralat sifar pada keadaan stabil, peratusan ayunan berlebihan kurang daripada 8%, masa penyelesaian bawah 6 saat dan pada masa sama, memberikan maklumat bantuan robot yang tepat, bersesuaian dengan tahap kemampuan pesakit.

KEYWORDS: *assist-as needed control; upper limb rehabilitation robot; control input regulation; PID controller and eating activity*

1. INTRODUCTION

Stroke is a devastating disease and remains a major health concern worldwide as it is one of the leading causes of disability and mortality. According to Global Burden of Diseases, Injuries and Risk Factors Study (GBD) in 2010, stroke is ranked as the third top disease with greatest burden based on the disability-adjusted life-years (DALYs). In Malaysia, the scenario is equally debilitating as the prevalence of data from 2007 to 2017 shows that the disease is the third prominent cause of fatality among Malaysians. According to Malaysia Health Minister in 2007, six new cases of stroke occurred every hour and 17,909 stroke victims were admitted into hospitals in 2005 [1]. The number had increased to 45,000 in-patients and 31000 outpatients receiving stroke treatments at various hospitals and medical institutions nationwide in 2016 [2]. Statistics revealed that 85% of post-stroke survivals are left with various deficiencies in their hand and wrist areas [3]. The stroke victims' upper limbs weaken and as a result, they lose their arm's capability to perform tasks. One of the most important activities in daily living that is done frequently every day is eating [4,5]. It is very frustrating for the patients with upper limb impairment due to stroke to be unable to eat by themselves at any time that they want, at any place and at their own pace. They have to depend a lot on the caregiver to feed themselves. The disease does not only distress the patients, but the caregivers and family members are also severely affected in many ways including time, energy, and finances. Thus, a great socioeconomic impact is left to the nation after the occurrence of a stroke.

Rehabilitation therapy facilitates patients' ability to regain upper limb function and get back to performing ordinary and essential tasks of daily living. Intensive, massed, and repeated practice in the rehabilitation process modifies neural organization and leads to the recovery of functional motor skills [6]. Robotic rehabilitation therapy automates the manual rehabilitation treatment and offers the advantages of providing a high level of repetitive movements without the need to increase the therapist's supervision time [7]. It also provides a more consistent movement that can increase the recovery rate and speed.

One of the challenges in a robotic rehabilitation therapy is the slacking behaviour of the patients who have partially regained their motor functions, where they stay passive throughout the rehabilitation process without putting any effort into the exercise. Nonetheless, clinical studies have shown that the simultaneous contribution of both patients' voluntary effort and assistive torque from the robot aid in a higher recovery rate and a more effective treatment [8]. One of the methods to achieve this is by the implementation of Assist As Needed (AAN) control strategy that emphasizes patient's active participation [9]. The

main feature in this control technique is that the robot's assistive torque is regulated according to the patients' limb capability or impairment level, which is estimated a priori or during the training. Under the assistive scheme, the patient performs the prescribed task independently while the robot provides assistance to facilitate the patient only as deemed necessary [10]. Adjusting the robot's assistance based on the patient's ability will encourage them to put an effort in moving their limbs to accomplish the specified motions in the exercise. Their own movement initiative will lead to cognitive processing in the brain and stimulate neuroplasticity. Therefore, a greater recovery performance can be achieved under the Assist As Needed control scheme.

Several Assist As Needed control techniques have been formulated for lower and upper limb rehabilitation treatments for various types of patients [11-25]. Gui et al. introduced the progressive Assist As Needed (pAAN) controller for a lower limb exoskeleton system. In this technique the subjects' voluntary input torque is estimated using an electromyography (EMG) signal. The relationship between the patient's effort torque and EMG signal is established using an unsupervised learning algorithm. The method is able to predict the subject's effort and finally encourage their active participation in the robotic assisted training [11]. An Assist As Needed (AAN) control with adjustable assistance level for robotic orthoses has been developed by Asl et al. [12]. An experiment on a lower extremity robotic exoskeleton was conducted. The controller provides a freedom zone for the user by lowering the control effort and allowing adjustable tracking errors [12].

The Assist as Needed control scheme for upper limb rehabilitation [13-25] was included in the works by Pérez-Rodríguez et al. [13]. It was composed of three subsystems: (1) biomechanical prediction, (2) assistance decision, and (3) command generation. The biomechanical prediction subsystem estimated the current state of the biomechanical evolution of the subject; the assistance decision subsystem determined the exact amount of assistance needed by the subject; and the command generator subsystem excited the exact output to the robot. Kapsalyamov et al. proposed a brain-computer interface in the Assist As Needed upper limb rehabilitation training paradigm. An electroencephalography sensor was used in the brain-computer interface implementation. The technique enabled the patients to move the robot utilizing the limited motion and strength that they had and the robot assisted for the remaining course of trajectory that they were unable to perform by themselves. [14]. The major challenge in AAN control strategy is to effectively determine the patients' movement/functional ability, and then to adjust the robot assistance consistently with the changes in the patients' movement abilities [15,16]. Agarwal and Deshpand [17] introduced the learned force-field control that establishes the relationship between the subject's torque and joint angular displacement in an off-line setting. It is used to assist the finger's movement along a targeted trajectory. The AAN control algorithm presented by Stroppa et al. tunes the robot assistance in real time. The performance indices of the subject in an upper limb rehabilitation is extracted accurately and correlated to the amount of robot's assistance to be supplied. The information of the patients' clinical status is not necessary in this algorithm [18]. Taheri et al. proposed an AAN control method that learns the subject's neuromuscular impairment adaptively [19]. In the Greedy AAN (GAAN) control scheme presented by Luo et al. [10], a Gaussian RBF with weight vectors and challenge level modification algorithm are used in the rehabilitation training of the neurologically impaired subjects. The function of the Gaussian RBF network is to model the functional capability of the patients and therefore, assign the corresponding a tailored task challenge. Wolbrecht et al. [20] implemented an adaptive controller with Gaussian Radial Basis Function (RBF) to estimate the patients' capability level. The RBF is integrated with a forgetting factor to vary the robotic assistance with respect to the subject's effort.

Bower et al. [21] and Guidali et al. [22] have improved the technique by proposing a directionally dependent RBF in quantifying the patients' capability. In the works by Pehlivan et al. [23], the patients' ability has also been predicted using RBF. The subject's positional error bounds have been manipulated to correlate patients' input estimation and engagement. A Function Ability Index (FAI) has been introduced by Mounis et al. [24,25] to describe the patients' adequacy in performing elbow flexion/ extension based on the patient's quality of movement and speed. A statistical normalized function and a spline equation have been used in categorizing the patients' impairment stages and then associating them to the available (Wolf Motor Function Test) WMFT and Action Research Arm Test (ARAT) clinical scales.

Several Assist As Needed control techniques have been presented in the literature, however, these methods are difficult and mathematically complicated. A huge sample of subjects are needed in learning the patients' functionality level and establishing a mathematical equation to describe their capability. This may influence the controller performance for real time implementation. Many of the existing control methods also rely heavily on the plant's model in which the inaccuracy in the modelling may affect the system performance. The existing controller designs and programming also become more difficult with the increasing complexity and number degrees of freedom (DOF) in the robot structure.

Therefore, this paper presents a new simple, easy to programme and mathematically less complicated Assist As Needed (AAN) control strategy. It is suitable for the real time hardware implementation. The proposed control scheme consists of an adjustable gain K and PID control feedback loop, focusing on the 4 movements in eating, which are the elbow and wrist flexion/ extension motions.

2. UPPER LIMB REHABILITATION ROBOT MECHANISM AND OPERATIONAL SEQUENCE FOR EATING

This study focuses on the formulation of Assist As Needed control law for an upper limb rehabilitation robot. At this stage of work, the upper limb rehabilitation robot prototype for the eating task, as shown in Fig. 1, has been built for controller development and testing. The prototype is an improved version of the previously wearable motion assist robot for eating, developed in the WISE Lab, IIUM [26]. It has 2 degrees of freedom (DOF) and is made of 3 links, namely the arm, elbow, and wrist linkages, focusing on the 2 important upper extremity movements in eating: (1) elbow flexion/extension and (2) wrist flexion/extension motion. Among these 3 links, only the elbow and wrist linkages are actuated by the motors to realize the required feeding movements. The arm link is kept stationary. Arm/elbow holders made of 3D printed material with the slots for a Velcro strap are installed at the arm and elbow links to attach the robot to the user's upper limb. Eating utensils such as a spoon or fork can be fixed at the end of the wrist link to scoop or transfer food to the mouth. The mechanical drawing of the robot from various views is illustrated in Fig. 2.

The 12 V 120 RPM 18 kgfcm (1.76 Nm) planetary direct current (DC) geared motor (product code: IG42E-49K) and 12V 22RPM 7kgfcm (0.687 Nm) brushed DC geared motor with encoder (product code: SPG30E-200K) from Cytron Technologies [27] have been chosen for actuating the elbow and wrist joints respectively. The choice was made mainly based on the amount of torque that is needed from each motor, in which the elbow joint needs at least 1.31 Nm (13.36 kgfcm) of torque to operate and the wrist joint requires a minimum torque of 0.30 Nm (3.06 kgfcm) for the wrist flexion/extension. The detailed calculation on these necessary motor torques can be found in [28] and the specification of

the motors are listed in Table 1. These DC motors are also equipped with encoders that are used to measure the angular displacement of each joint.

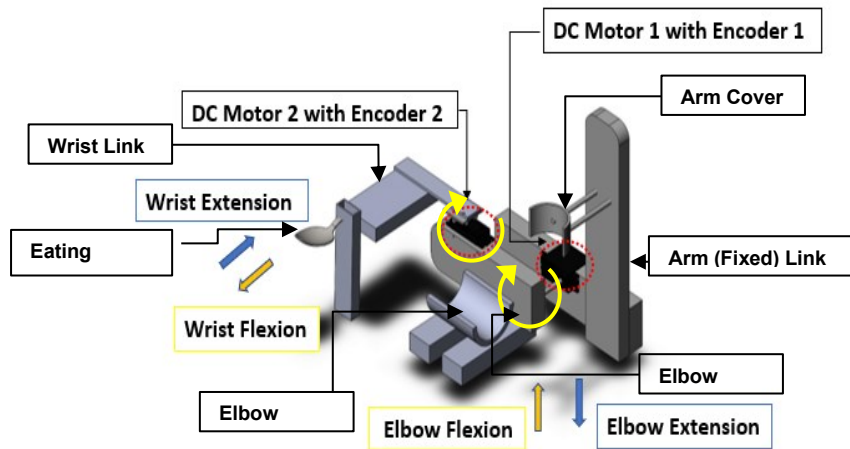


Fig. 1: Upper limb rehabilitation robot for eating.

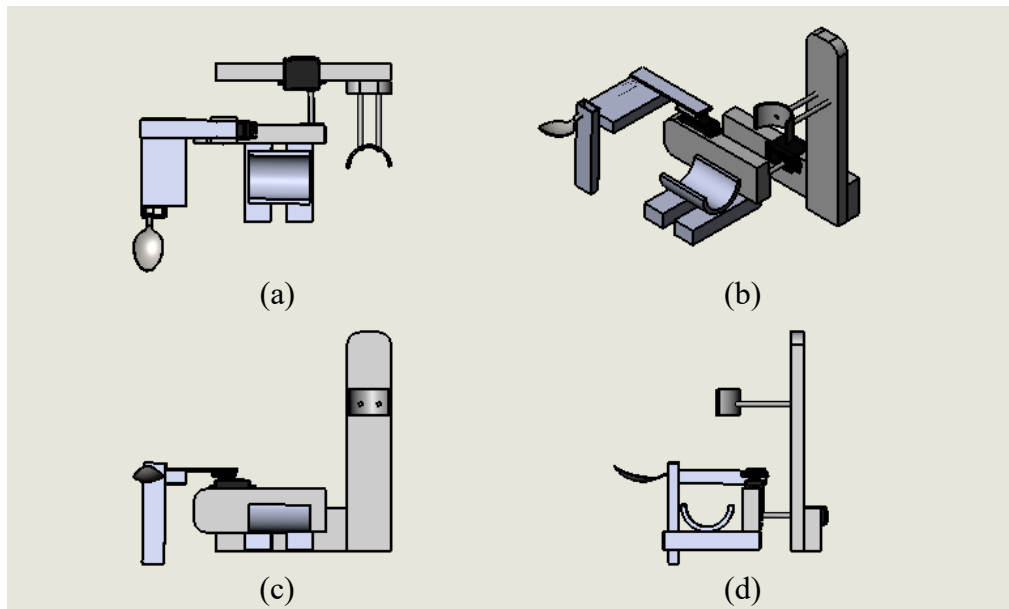


Fig. 2: Proposed design for the upper limb rehabilitation robot from (a) top, (b) isometric, (c) side and (d) front views.

Table 1: Specification of the DC motors with encoder
 (Retrieved from <https://www.cytron.io/> [27])

Specifications	DC Motor 1 (Elbow Joint Motor)	DC motor 2 (Wrist Joint Motor)
Rated Torque	18 kgf.cm (1.76 Nm)	0.687 Nm (7 kgfcm)
Voltage	12 VDC	12 VDC
Rated Current	5.5 A	< 0.6 A
Rated Power output	41.3W	37 mm
Rated Speed	120 RPM	< 50 RPM
Encoder Output	245 pulses per rotation, single channel output	7 pulses per rear shaft revolution.

The force sensor resistor (FSR), from [29] (product code: FSR01CE) has been selected to measure the user's forearm payload that indicates their capability in lifting their own hand

from the encoders and they are fixed to pin D2 PWM, D3 PWM, D18 TX1 and D19 RX1 of the Arduino microcontroller board. The complete prototype of the upper limb rehabilitation robot for the eating task in shown in Fig. 4.



(a)

(b)

Fig. 4: Prototype of the upper limb rehabilitation robot for eating activity
 (a) front view (b) side view.

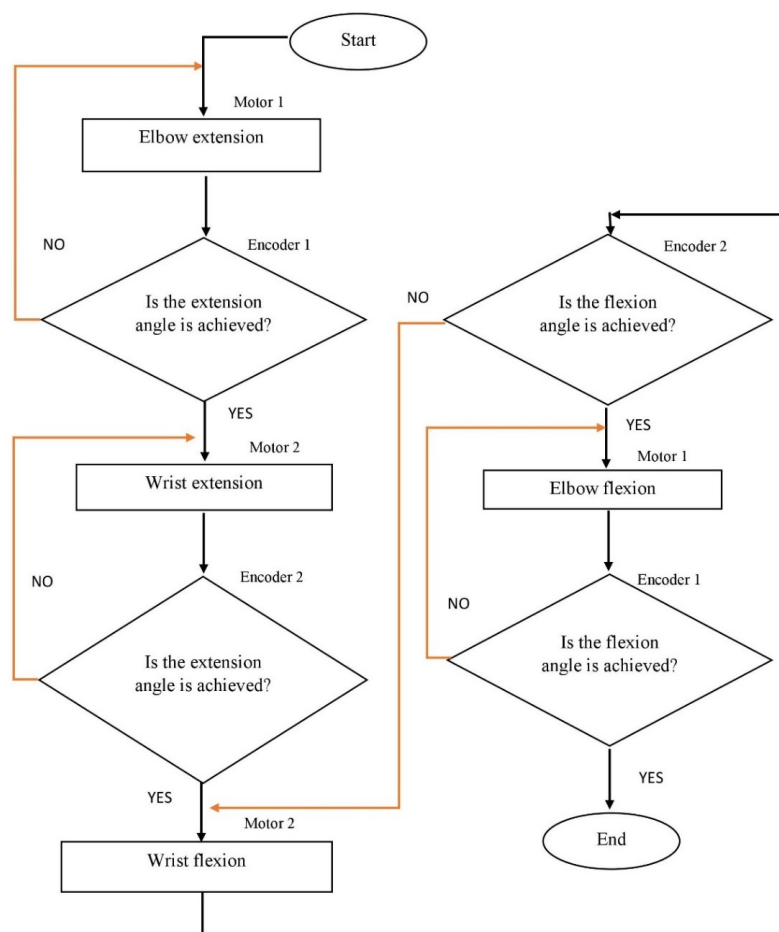


Fig. 5: Operational sequence.

The operational sequence of the system for one eating cycle is shown in Fig. 5. Firstly, DC motor 1 extends the elbow from its rest position to reach the food container as can be seen in Fig. 6 (a). Encoder 1 will measure whether the joint has achieved the desired position. Then, DC motor 2 performs the wrist extension movement, as shown in Fig. 6 (b), until it attains the predefined angular displacement indicated by encoder 2. Next, the wrist joint will be flexed by DC motor 2 towards the centre as depicted in Fig. 6 (c). Finally, DC Motor 1 performs elbow flexion motion to bring the food to the user's mouth as illustrated in Fig. 6 (d).

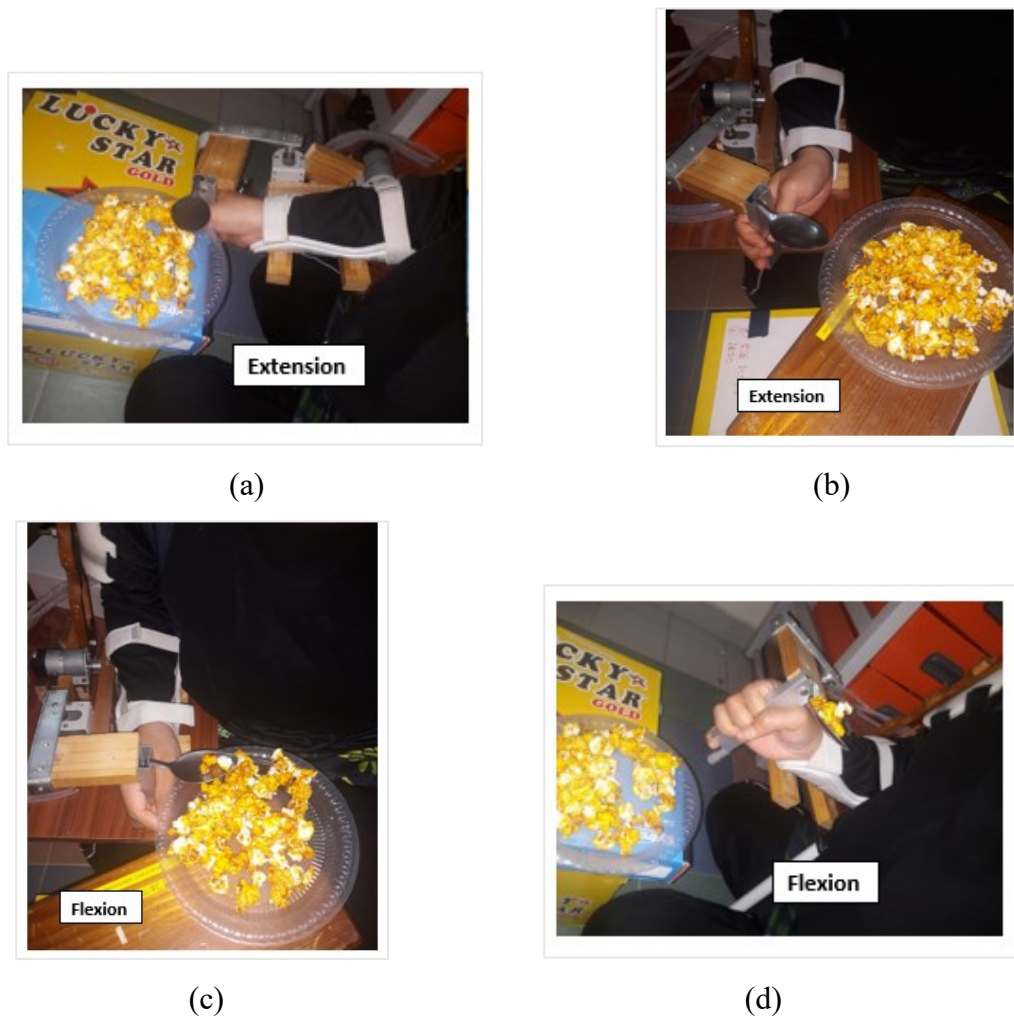


Fig. 6: Upper limb rehabilitation robot movement during eating
(a) elbow extension (b) wrist extension (c) wrist flexion (d) elbow flexion.

3. DYNAMIC MODELLING OF THE ROBOT

For the purpose of simplifying the mathematical model derivation and since the elbow and wrist joints do not move simultaneously in the eating procedure, the dynamic modelling representing the load torque for each motor with respect to the physical quantities of the two robot joints are conducted separately. The next subsection will describe the mathematical modelling for the elbow flexion/extension, wrist flexion/extension and DC motors.

3.1 Dynamic Modelling for the Elbow Flexion/Extension (in Y-Z plane)

In this dynamic modelling, it is assumed that: (1) the elbow and wrist linkages are a single body, (2) the wrist joint is at its original position and (3) the wrist motor is stationary for simplicity. DC motor 1 moves the combined body of elbow and wrist linkages.

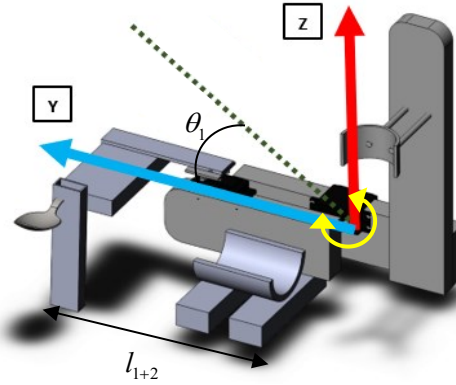


Fig. 7: Dynamic modeling for elbow flexion/extension.

Referring to Fig. 7, the velocity of the y and z components can be written as

$$\dot{y} = \frac{1}{2} l_{1+2} \dot{\theta}_1 \sin \theta_1 \quad (1)$$

and,

$$\dot{z} = \frac{1}{2} l_{1+2} \dot{\theta}_1 \cos \theta_1 \quad (2)$$

where l_{1+2} is the total length of the combined body of the elbow and wrist linkages. Taking the summation of square for Eqs. (1) and (2), gives v_1^2 , where

$$v_1^2 = \dot{y}_1^2 + \dot{z}_1^2 = \frac{1}{4} l_{1+2}^2 \dot{\theta}_1^2 \quad (3)$$

The angular velocity can be represented as,

$$w_1 = \dot{\theta}_1 \quad (4)$$

The moment of inertia can be approximated as,

$$I_1 = \frac{1}{12} m_{1+2} (l_{1+2})^2 \quad (5)$$

where m_{1+2} is the total mass of the elbow and wrist linkages combined. Using Eqs. (3) – (5), the kinetic energy, K_1 and potential energy, P_1 can be written as,

$$K_1 = \frac{1}{2} m_{1+2} v_1^2 + \frac{1}{2} I_1 w_1^2 = \frac{1}{6} m_{1+2} (l_{1+2})^2 \dot{\theta}_1^2 \quad (6)$$

and,

$$P_1 = mgh = \frac{1}{2} m_{1+2} g l_{1+2} \sin \theta_1 \quad (7)$$

Subtracting Eq. (7) from Eq. (6) gives,

$$L_1 = K_1 - P_1 = \frac{1}{6} m_{1+2} (l_{1+2})^2 \dot{\theta}_1^2 - \frac{1}{2} m_{1+2} g l_{1+2} \sin \theta_1 \quad (8)$$

Using Eq. (8), the torque for lumped elbow and wrist link can be expressed as,

$$T_1 = \frac{d}{dt} \left(\frac{\partial L_1}{\partial \dot{\theta}_1} \right) - \left(\frac{\partial L_1}{\partial \theta_1} \right) = \frac{1}{3} m_{1+2} l_{1+2}^2 \ddot{\theta}_1 + \frac{1}{2} m_{1+2} g l_{1+2} \cos \theta_1 \quad (9)$$

3.2 Dynamic Modelling for the Elbow Flexion/Extension (in X-Y plane)

In this modelling part, the elbow joint is assumed to be stationary and only the wrist joint is rotating. The load torque for DC motor 2, in driving the wrist, is derived by considering the structure in the X-Y plane, from the top view as shown in Fig. 8.

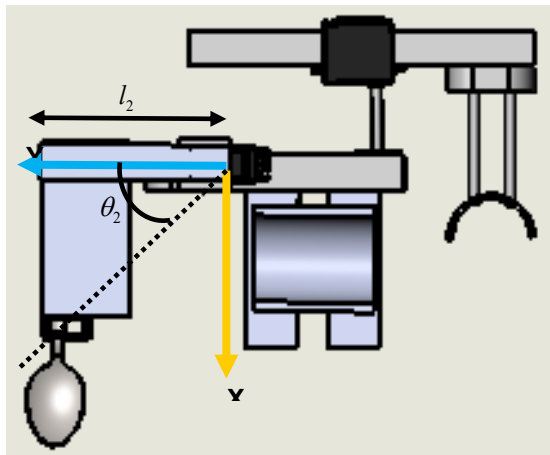


Fig. 8: Dynamic modelling for wrist flexion/ extension.

The velocity of the x and y components can be written as,

$$\dot{x} = -\frac{1}{2} l_2 \dot{\theta}_2 \sin \theta_2 \quad (10)$$

and,

$$\dot{y} = \frac{1}{2} l_2 \dot{\theta}_2 \cos \theta_2 \quad (11)$$

Taking the summation of square Eq. (10) and (11), gives v_2^2 where

$$v_2^2 = \dot{x}_2^2 + \dot{y}_2^2 = \frac{1}{4} l_2^2 \dot{\theta}_2^2 \quad (12)$$

The value of angular velocity can be represented as,

$$w_2 = \dot{\theta}_2 \quad (13)$$

The moment of inertia can be expressed as,

$$I_2 = \frac{1}{12} m_2 (l_2)^2 \quad (14)$$

Utilizing Eqs. (12)-(14), the kinetic energy, K_2 and potential energy, P_2 can be written as,

$$K_2 = \frac{1}{2}m_2v_2^2 + \frac{1}{2}I_2\omega^2 = \frac{1}{6}m_2(l_2)^2\dot{\theta}_2^2 \quad (15)$$

and,

$$P_2 = mgh = 0 \quad (16)$$

Subtracting Eq. (16) from (15), yields

$$L_2 = K_2 - P_2 = \frac{1}{6}m_2(l_2)^2\dot{\theta}_2^2 \quad (17)$$

Using Eq. (17), the load torque for the wrist or DC motor 2 can be expressed as,

$$T_2 = \frac{d}{dt} \left(\frac{\partial L_2}{\partial \dot{\theta}_2} \right) - \left(\frac{\partial L_2}{\partial \theta_2} \right) = \frac{1}{3}m_2l_2^2\ddot{\theta}_2 \quad (18)$$

Equations (9) and (18) represent the load torque from the upper limb rehabilitation robot at the elbow and wrist joints respectively. The next subsection will describe the mathematical model of the DC motors in actuating the upper limb rehabilitation robot.

3.3 Mathematical Model of the Motor

In the simulation, the mathematical model of the motors needs to be integrated with the dynamic model of the linkages in Eqs. (9) and (18) to simulate the complete upper limb rehabilitation robot for eating. The mechanical behaviour of the motors can be described by [30].

$$J_n\ddot{\theta}_{mn} + b_n\dot{\theta}_{mn} + T_n = T_{mn} \quad (19)$$

where J_n is the n th motor's inertia, b_n is the n th motor's viscous friction, T_{mn} is the n th motor's torque, T_n is the load torque for n th motor which are governed by Eqs. (9) and (18), $\dot{\theta}_{mn}$ and $\ddot{\theta}_{mn}$ are the n th motor's angular velocity and acceleration respectively, where the n th motor's shaft angular displacement. θ_{mn} is related to the angular displacement of n th joint, θ_n by $\theta_{mn} = \theta_n / N$, in which N is the gear ratio and $n=1$ and 2 for DC motor 1 (for the elbow) and DC motor 2 (for the wrist) respectively.

The electrical part of the motors can be represented by the mathematical equation [30]

$$\frac{di_n}{dt} = \frac{1}{L_n} (-R_n i_n + v_n - K_n b_n \dot{\theta}_{mn}) \quad (20)$$

where i_n is the current in the n th motor, v_n is the voltage supplied to n th motor, R_n is the resistance in the n th motor, and K_n is the back emf constant of the n th motor.

Finally, the mechanical and electrical subsystems for each motor as described in Eqs. (19) and (20), respectively, are combined using the n th motor's torque constant, k_{tn} where

$$T_{mn} = k_{tn}i_n \quad (21)$$

Equations (9), (18) – (21) will be used in the computer simulation of the upper limb rehabilitation robot and its controller. The block diagrams representing these equations will be drawn in Matlab Simulink software to test the proposed control strategy before implementing it on the real hardware.

4. ASSIST AS NEEDED CONTROL STRATEGY

Assist As Needed control strategy aims to encourage an active participation from patients in the rehabilitation exercise rather than just relying completely on the robot. The method has been proven to facilitate the patients' recovery of their original motor functions faster and more effectively [9]. This objective can be achieved by regulating the amount of assistance provided by the robot according to the patients' capability level or level of impairment. If the patient's impairment level is high, the robot will provide high assisting torque and in case the patient's impairment level is low, the robot will provide a lower level of assistance. The combination of the patient's effort torque and the assistance torque supplied by robot moves the upper limb to reach the pre-set desired angular displacement. By this technique, the patient will need to put his/her own effort in moving his/her upper limb based on his/her capability level rather than just totally depending on the robot to complete the exercise. As a result, slacking behaviour may be avoided and the patient may be able to successfully recover in a shorter duration.

This study proposes a simple and easy AAN control strategy for upper limb rehabilitation as illustrated in Fig. 9. The proposed method is computationally faster and uncomplicated to program, which makes it suitable for real time applications. The proposed control method is modified from [24,25]. It basically consists of a PID feedback control loop and adjustable gain, K , that is tuned based on the patients' level of capability (LOC), indicated by the Force Sensitive Resistor (FSR) measurement. In the feedback loop, the operator may set the desired angular position at the control input. The actual displacement is measured by the encoder and the value is compared with the predefined desired position. The difference between the desired and actual positions (error) will be used in the PID control algorithm to compute the control output signal which is then multiplied by the adjustable gain, K . The resulting output is then supplied to the motor and finally it actuates the combined patient's upper limb and rehabilitation robot mechanism plant accordingly.

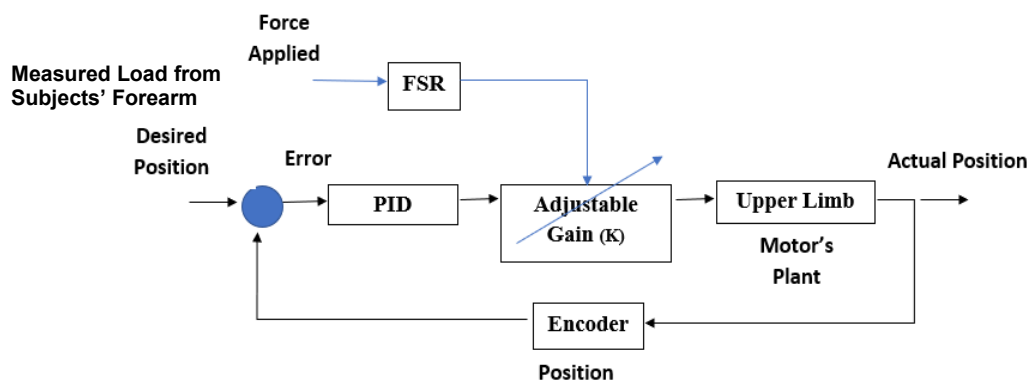


Fig. 9: Proposed AAN control framework.

The adjustable gain K regulates the amount of the assistance that the robot needs to supply to the patients using the value of resistance measured by the Force Sensitive Resistor (FSR). The sensor is attached to the patient's forearm, at the location where the forearm rests on the elbow cover of the upper limb rehabilitation robot (in between the patients' forearm and the robot's elbow cover) as shown in Fig. 10. It measures the force exerted by the forearm load onto the robot's elbow cover. The identification of patient's capability level is conducted before the exercise begins. In this stage, the patient is requested to flex his/her elbow for 100 seconds without any assistance from the robot and the FSR will measure the amount of resistance that is proportional to the load from the forearm. If the patient has low

capability level, the load from the forearm on the elbow cover will be high since the patient has no strength and is unable to lift his/her forearm, giving a high FSR resistance value. On the contrary, in case the patient has a higher level of capability, he/she has the ability to flex his/her forearm on his/her own, and therefore, the load exerted on the elbow cover is lower, giving a smaller FSR resistance. A voltage divider circuit has been constructed using the FSR. The voltage across the FSR, which is proportional to its resistance value, is supplied to the Arduino board.

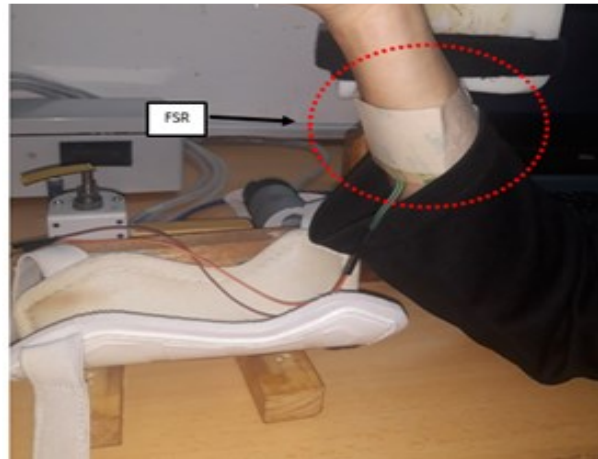


Fig. 10: Attachment of the FSR to the forearm.

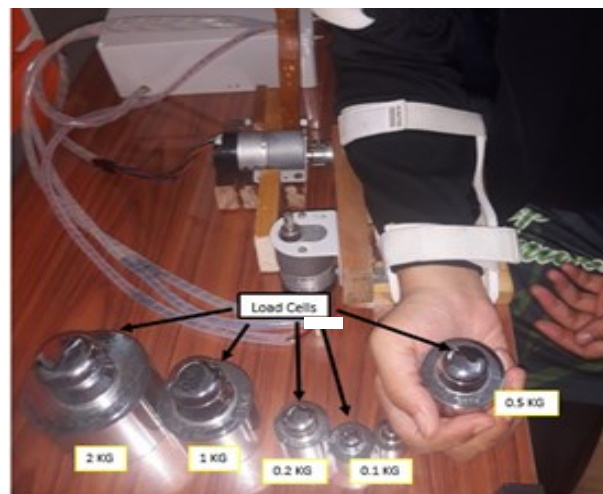


Fig. 11: FSR calibration process with load cells.

The gain, K needs to be calibrated according to the level of voltage across the FSR, which represents the patient's level of capability. Ideally, the calibration needs to be done using real patients with various levels of capability. However, at this stage of study, the calibration is conducted using a healthy person with different loading to imitate disabled patients. Four healthy subjects have been recruited for the simple calibration. They were requested to hold loads with different weights as shown in Fig. 11 while performing flexion movement and the value of the voltage across the FSR during the motion is recorded by the Arduino board. Then, the value of the gain, K is assigned for each level of capability (or loads carried) based on the voltage readings obtained. The different loads carried by the healthy person during the identification stage represent the forces that may be induced by the patients with various levels of impairment. The higher the weight of the load denotes a

higher level of impairment, which will give a higher average FSR resistance and voltage across it, and vice versa. The outcome from the calibration is summarized in Table 2.

Table 2: Value of gain K with respect to the patient’s level of capabilities (LOC) and voltage across FSR.

LOC	Force [N]	Voltage Range, V [V]	Gain, K	Assistance
0	20	$V \geq 4.4$ V	1	Need maximal assist
1	10	$4.10 \text{ V} \leq V \leq 4.39$ V	0.75	Needs assist
2	5	$3.50 \text{ V} \leq V \leq 4.09$ V	0.5	Needs minimal assist
3	2	$3.20 \text{ V} \leq V \leq 3.49$ V	0.25	Needs very minimal assist
4	1	$0.00 \text{ V} \leq V \leq 3.19$ V	0	Assist not required at all

Referring to the Table 2, if the voltage across the FSR is more than or equal to 4.4 volts, it means that the resistance across the FSR is high and the patients is unable to lift his/her hand by himself/herself at all (his/her level of capability, LOC=0). Therefore, the value of gain K is assigned to 1, in which he/she needs the complete or maximum level of assistance from the robot to perform the eating function. In contrast, the case where the voltage across the FSR is lower than 3.20 V denotes that the patient has the full ability to lift up his/her elbow by himself/herself (LOC=4), where only a small value of resistance is detected by the FSR. Therefore, the gain K is set to be 0 and no assistance needs to be provided to the recovered patient. Since the main focus of the study at this stage is on proving the concept of the proposed controller and the experiments are conducted in the laboratory only, this method of calibration is sufficient in setting the value of gain K. However, for the real implementation and clinical testing of the proposed control system in the future, the calibration needs to be conducted based on real patients with various levels of capability (LOC) or impairment.

The PID control law in the feedback loop is governed by the well-known formula, where

$$u_{PIDn}(t) = K_{pn}e_n(t) + K_{dn}\frac{de_n(t)}{dt} + K_{in}\int_0^t e_n(\tau)d\tau \quad (22)$$

where $u_{PIDn}(t)$ is the control signal of the n th joint, $e_n(t)$ is the position error for the n th joint, K_{pn} , K_{dn} and K_{in} are the proportional, derivative and integral gains respectively for n th joint, t is the time and $n=1$ and 2 for the elbow and wrist joints respectively. The control input to the plant, $u_n(t)$ is then calculated by

$$u_n(t) = Ku_{PIDn}(t) \quad (23)$$

where the value of K is governed by the patient’s level of capability or calibrated voltage across the FSR as listed in Table 2.

The proposed control strategy in this study is simple and easy. The derivation of the control law does not require a complex system model that may be subjected to modelling errors, uncertainties, and complexity. Due to the simple nature of the control strategy, the method is not difficult to program and the computational speed is higher since there are fewer components to be computed in the control law. These factors make it appealing for real time implementation of the robotic assisted rehabilitation therapy.

5. GRAPHICAL USER INTERFACE (GUI)

A graphical user interface (GUI) has been developed as a medium to help the patient and the therapist to better understand and control the processes flow involved in the therapy session. The GUI also aids in the observation and analysis of the patients' progress. It has been developed using MATLAB software and starts with the welcoming window as in Fig. 12 (a). After clicking the "START" button, the next window, as shown in Fig. 12 (b), will pop up and give 4 options to the user, which are either to: (1) identify the patients' level of capability based on the Force Sensitive Resistive (FSR) data or (2) to start the training without any assistance from the robot or (3) to start the training with the assistance from the robot based on the identified patients' level of capability or (4) to exit the program.

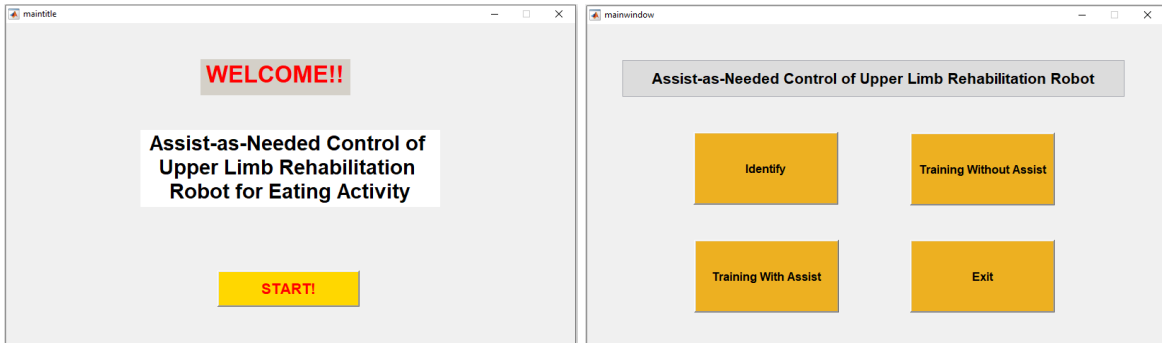


Fig. 12: GUI (a) startup window (b) main window for options.

Clicking the 'Identify' button in the main window as shown in Fig. 12 (b) will pop up the "IDENTIFY CAPABILITY" window as illustrated in Fig. 13, where the patients' level of impairment or capability can be detected. The identification session starts once the 'START' button is pressed. As mentioned in Section 4, the patient will be instructed to flex his/her elbow for 100 seconds. The FSR that is attached below the patients' forearm will detect the amount of force that is exerted on the elbow cover during the movement. The FSR is installed in a voltage divider circuit and the resulting voltage will be plotted in the graph in real time. This amount of voltage represents the patients' level of capability (LOC) as summarized in Table 2 and the detected level will be shown in the window as can be seen in Fig. 13. The graph can be saved by clicking the 'SAVE' button and the 'RETURN' button can be used if the operator would like to return to the main window in Fig. 12 (b).

The 'TRAINING WITHOUT ASSIST' and 'TRAINING WITH ASSIST' buttons as depicted in Fig. 14 and Fig. 15 respectively will appear once the 'Training without Assist' or 'Training with Assist' as in Fig. 12 (b) is pressed respectively. These windows enable the operator to set the desired angular displacement that upper limb rehabilitation robot's need to reach during the exercise based on the therapist's or doctor's recommendation. The patient's progress can be monitored in real time from the graph and can be saved for analysis purpose by clicking the "SAVE" button. The compilation of the MATLAB coding for building this GUI can be found in [28].

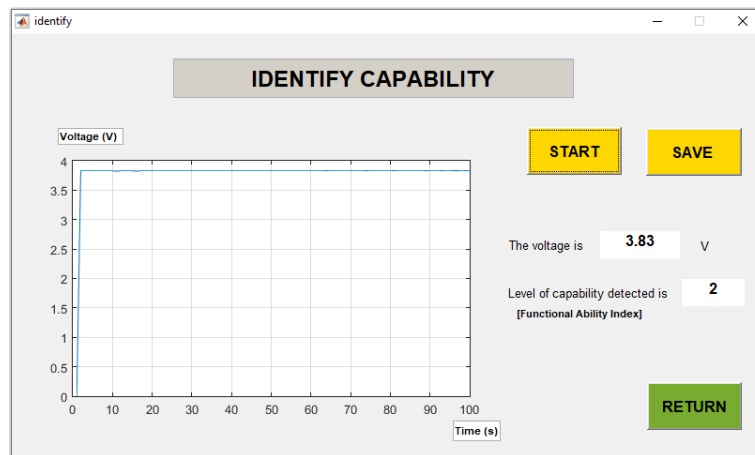


Fig. 13: 'IDENTIFY CAPABILITY' GUI window.

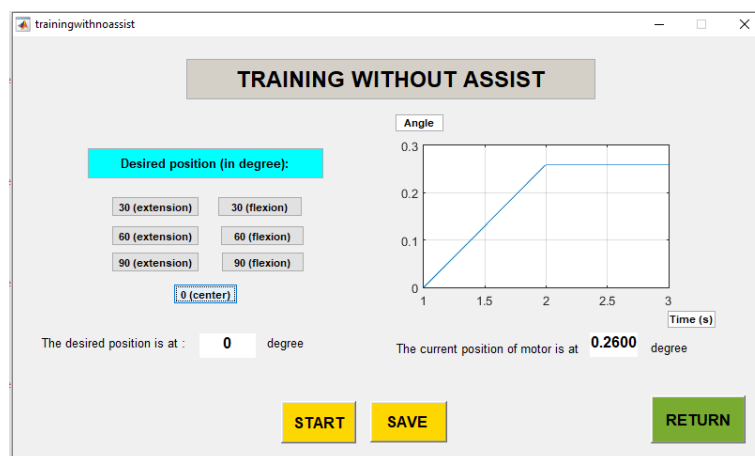


Fig. 14: 'TRAINING WITHOUT ASSIST' GUI window.

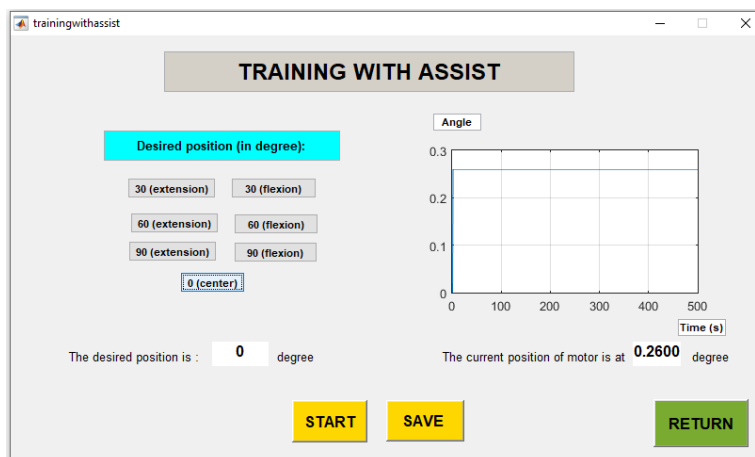


Fig. 15: 'TRAINING WITH ASSIST' GUI window.

6. RESULTS AND DISCUSSION

Simulation and experimental tests have been conducted to verify the effectiveness of the proposed controller to achieve the desired angular displacement whilst regulating the necessary amount of assistance to the patients according to their level of capability. The simulation tests have been conducted in Matlab Simulink environment, while the developed

prototype as explained in Section 2 is used in the experimental test. This research has obtained ethics approval from the IIUM (International Islamic University Malaysia) Ethics Committee, with the approval number: IREC 2018-256 to conduct the experimental test.

6.1 Simulation Results

The simulation starts with the testing of the elbow and wrist movements of the integrated motor and upper limb rehabilitation robot under PID controller without incorporating gain K of the Assist As Needed algorithm. Separate simulation block diagrams for the wrist and elbow motors, as in Fig. 16, have been constructed in Matlab Simulink Software using the integrated upper limb rehabilitation model in Eqs. (9), (18) – (21). In this simulation, the effort from the human arm is not incorporated in the system since the main purpose of the simulation test is to check the feasibility of the proposed controller and to determine the suitable values of PID gain, and besides, the human arm effort should be obtained from experimental hardware. The PID gain for DC motor 1 (elbow motor) has been tuned manually to $K_{p1} = 40$, $K_{i1} = 0.0001$ and $K_{d1} = 50$, and for DC motor 2 (wrist motor) $K_{p2} = 45$, $K_{i2} = 0.00001$ and $K_{d2} = 10$. Figures 17 and 18 show the simulation results of the closed loop system for the elbow and wrist motors respectively, under the PID control. From the figures, it can be seen that the PID controller is feasible in controlling both the robot's elbow and wrist joints to reach the desired position controller. The control system has successfully met meets the design specification where the percentage overshoot is less than 8%, steady state error is below 5% and settling time is less than 6 seconds.

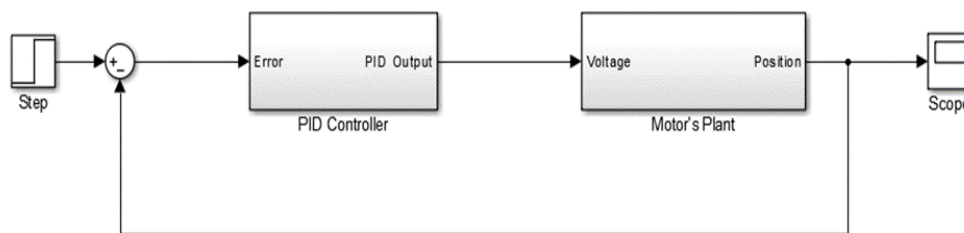


Fig. 16: Closed-Loop System of Motor with PID Controller (Wrist linkage-DC Motor 2).

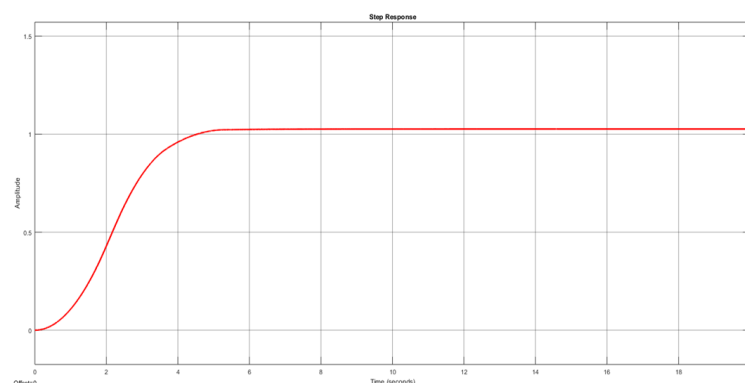


Fig. 17: Position response of the elbow motor under PID controller.

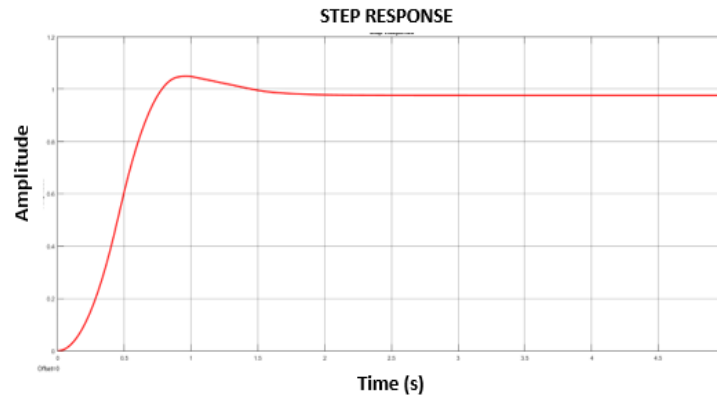


Fig. 18: Position response of the wrist motor under PID controller.

Therefore, the tuning effort and time may be reduced since the PID gains do not need to be readjusted for different capability levels or gain K . From the figure, it can also be observed that lower value of gain K reduces the system speed in achieving the targeted angular displacement and increases the percentage of overshoot. In this case, the simulation results have demonstrated that with the increase in gain K , the controller degrades the transient performance of the system instead of regulating the right amount of assistance from the robot whilst maintaining the same transient response. This situation occurs since actual human effort is not included in the simulation test. However, the right regulation of the robot assistance under the proposed Assist As Needed control strategy can be seen in the hardware experimental test with the incorporation of actual human effort as will be described in the next subsection.

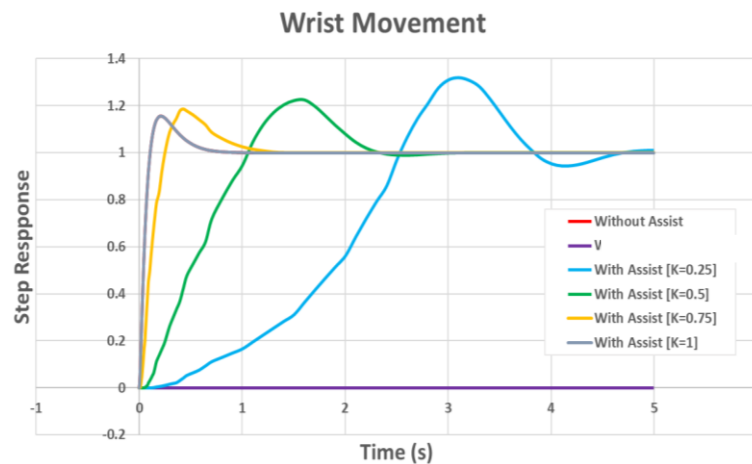


Fig. 19: Position response of the wrist motor under the proposed AAN controller.

6.2 Experimental Hardware

In the hardware experimental test, the user wears the upper limb rehabilitation robot prototype described in Section 2 and is requested to be in sitting position as shown in Fig. 20. The wearable robot is linked to both the developed GUI in Matlab environment and the Arduino. The selected operation mode has been entered in to the GUI and the proposed Assist As Needed (AAN) control law has been programmed in the Arduino command line interface.

The subject's level of capability or impairment has been firstly identified in the experiment by clicking the "Identify" button in the command window. In this step, the subject has been requested to flex his/her elbow to 20° as illustrated in Fig. 20. The GUI displays the identified subject's level of capability as depicted in Fig. 13 and passes the information to the Arduino programming, where the value of gain K is invoked based on the identified level of capability. Then, the training is started by clicking the "Training with Assist" button as illustrated in Fig. 12 (b). This experimental test has focused on the training of four upper limb movements in eating which are the elbow extension (EE), elbow flexion (EF), wrist extension (WE) and wrist flexion (WF). The desired angular displacement for EE, WE and WF have been set in the "Training with Assist" window, as shown in Fig. 15, to 30° and the required position for EF has been selected to be 70° . At this stage of study, the experiments have been conducted in the laboratory on healthy humans. Their hands have been loaded with the payloads as explained in Section 4 to imitate the disabled with various levels of capabilities.

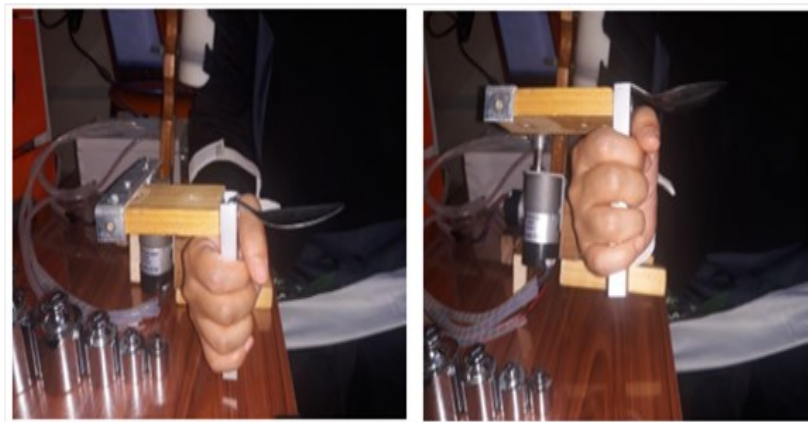


Fig. 20: Identification of the user's upper limb capability level.

Figures 21-24 illustrate the experimental results of the average actual angular displacement of the EE, EF, WE, and WF in reaching the desired position. The corresponding average proposed controller output supplied to the integrated upper limb rehabilitation robot and human arm for each joint are depicted in Fig. 25-28. From Figs. 21-24, it can be seen that under the proposed control law, the upper limb rehabilitation robot has successfully assisted the human arm to reach the desired angular joint displacements in the elbow extension, elbow flexion, wrist extension, and wrist flexion that are needed in the eating rehabilitation exercise respectively. The results have verified that the proposed control law is able to drive the upper limb rehabilitation robot in assisting the user's elbow and wrist joints to achieve the desired angular displacement regardless of their level of capability. Under the proposed control law, the integrated human arm and upper limb rehabilitation robot achieves zero steady state error and meets the specified transient response: (1) percentage overshoot is less than 8% and (2) settling time less than 6 seconds for all level of capabilities. It is evident from Figs. 25-28 that the proposed control technique has successfully regulated the necessary amount of robot assistance according to the user's level of capability. For the subjects with higher level of capability, the value of the gain K is lower, giving a lower level of robot assistance, thus encouraging the subject to put in his/her effort to reach the desired target. The level of assistance as indicated by the proposed controller signal to the plant in Figs. 25-28, decreases as the subject's capability level gets higher. The combination effort from the patients and upper limb rehabilitation robot pushes the system to reach the desired transient and steady state response. Contrary to the

simulation outcomes in Fig. 19, the experimental results of the proposed AAN controller in Figs. 21-24 have shown that the control system transient response (percentage overshoot and settling time) is not compromised by the increase in the value of gain K . This is because in the experiment, the total effort from the regulated upper limb rehabilitation robot's assistance and impaired human arm moves the integrated plant to reach the desired position, whereas the in the simulation, the results depicts the outcome resulting from the upper limb rehabilitation robot only, without any input from the disabled's or patients' effort.

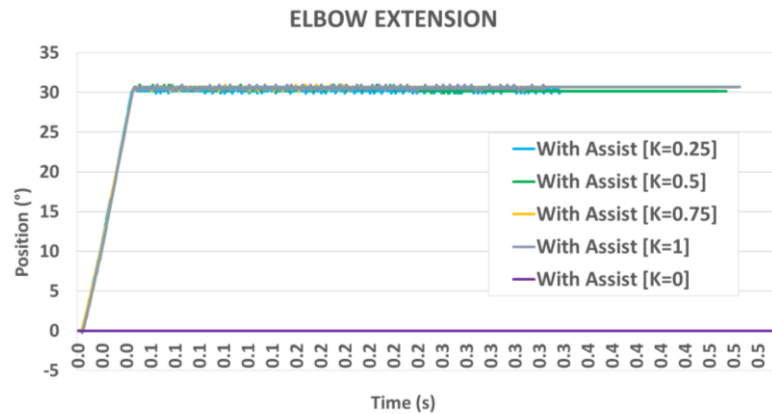


Fig. 21: Experimental results of the elbow extension for various levels of capability.

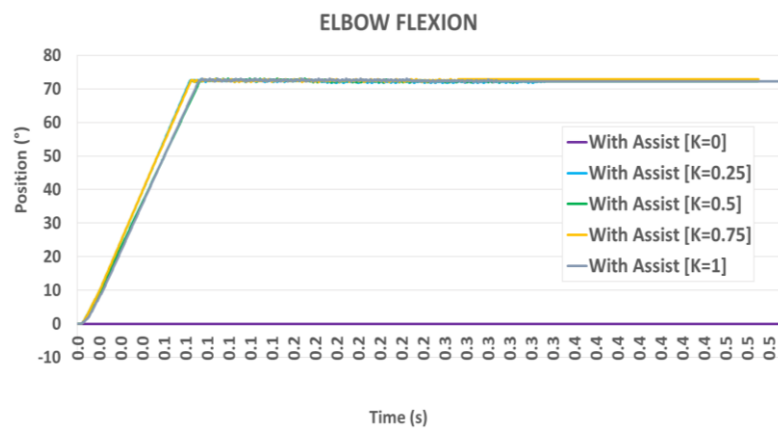


Fig. 22: Experimental results of the elbow flexion for various levels of capability.

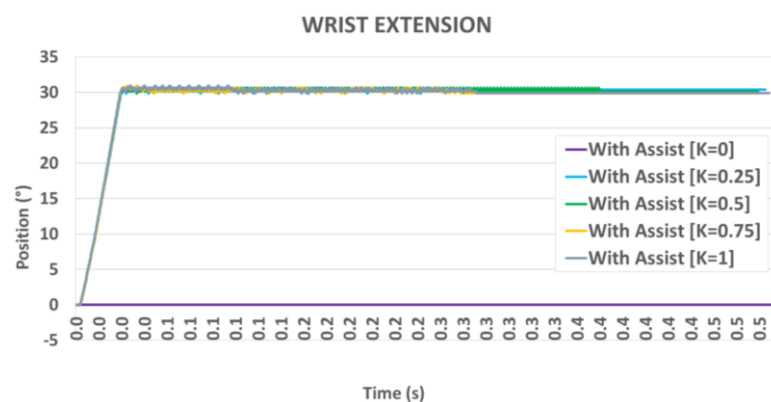


Fig. 23: Experimental results of the wrist extension for various levels of capability.

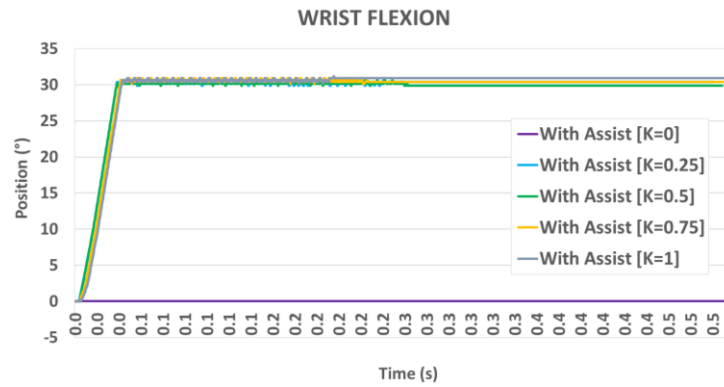


Fig. 24: Experimental results of the wrist flexion for various levels of capability.

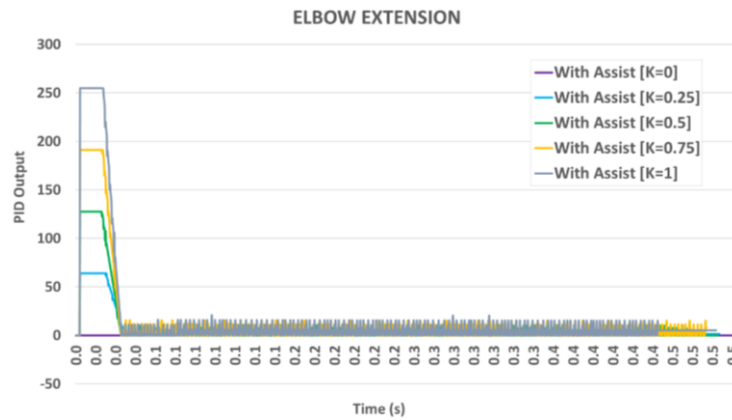


Fig. 25. Proposed controller output for elbow extension.

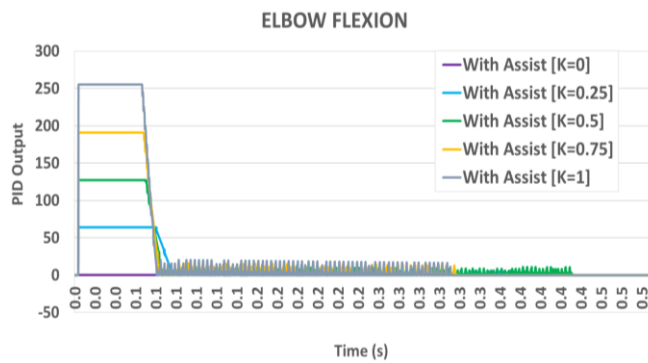


Fig. 26: Proposed controller output for elbow flexion.

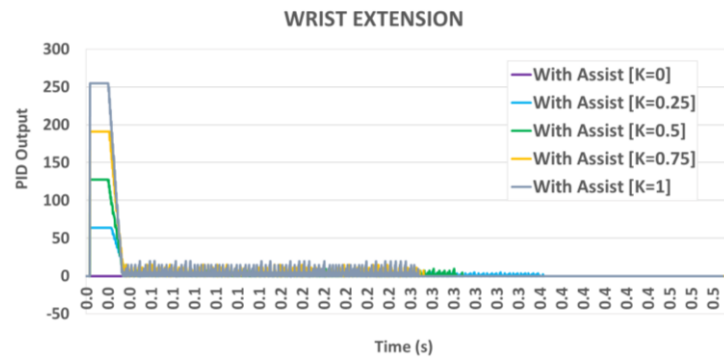


Fig. 27: Proposed controller output for wrist extension.

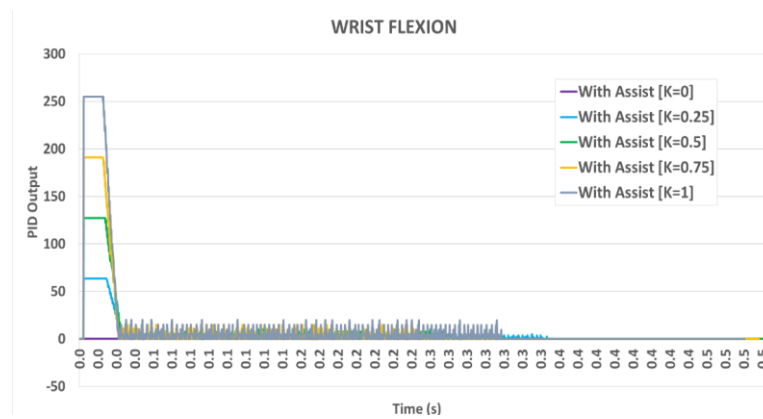


Fig. 28: Proposed control output for wrist flexion.

In comparison to the existing methods in the literature, the proposed method is simple, easy to be programmed and mathematically less complicated. The direct regulation of the robot assistance using the FSR resistance (denoted by the voltage across the resistor) eliminates the complicated estimation of the patients' capability using computationally time consuming and complex mathematical equations. The developed GUI facilitated the rehabilitation therapy and monitoring very well. At this stage of study, the calibration of gain K , identification of the patient's capability level and experimental test have been conducted in the university laboratory based on healthy human beings, imitating the patients. The experimental set up and results have successfully demonstrated and proven the effectiveness of the proposed controller in regulating the needed level of assistance according to the user's ability. However, for the real implementation of the system in future, gain K must be calibrated based on actual patients or disabled with various level of capabilities. The capability level identification, testing and real time implementation of the upper limb robot under the proposed AAN control strategy have to be conducted on actual patients in a clinical setting to study its practicality and performance in real application.

7. CONCLUSION AND FUTURE WORK

This paper presents a new Assist As Needed (AAN) control strategy for an upper limb rehabilitation robot for eating. The mechanism has been upgraded from the previous wearable robot version with the enhancement in the elbow and wrist movements. The mechanism is simple and focuses on four main motions in eating, which are the elbow and wrist flexion/extension. A GUI has been developed to facilitate the operation of the rehabilitation exercise procedure and progress monitoring. The proposed AAN control strategy consists of a PID controller in feedback loop and a newly introduced gain K that is assigned based on the patients level of capability, which is indicated by the FSR resistance or voltage across it. The simulation results have proven that the proposed AAN controller has successfully regulated the necessary amount of robot assistance according to the user's level of capability and drives the integrated robot and human arm to achieve the desired angular displacement under the specified transient response. It is evident from the experimental results that under the proposed control strategy, the amount of the control input to the plant are automatically adjusted depending on the identified user's capability level. The control strategy is simple, easily programmed, and mathematically less complicated. Future works involve the calibration of gain K based on actual patients or disabled with various level of capability and testing the proposed system on them in a real clinical setting, while performing the eating task. Future study will also focus on the effectiveness of the

proposed control law in aiding the patient's rehabilitation process in eating various types of food. The mechanism may also be upgraded with higher degree of freedom joints to accommodate a more natural human eating motion and other activities. In this way, the usage of the developed upper limb rehabilitation robot may not be restricted to sitting position only. The patients' feedback while utilizing the upper limb rehabilitation robot under the proposed control system may also be collected to enhance the system and increase their comfort in using the upper limb rehabilitation robot system.

ACKNOWLEDGMENT

The authors would like to thank the International Islamic University Malaysia for supporting this research under the research grant number: P-RIGS18-019-0019.

REFERENCES

- [1] Krishnamoorthy M. (2007) Killer stroke: Six Malaysians hit every hour. In *The Star*, April 24, 2007. [<https://www.thestar.com.my/news/nation/2007/04/24/killer-stroke-six-malaysians-hit-every-hour/>]
- [2] RM300 juta setahun rawatan pesakit strok. In *Bernama*, October 28, 2016. [<https://www.freemalaysiatoday.com/category/bahasa/2016/10/28/rm300-juta-setahun-rawatan-pesakit-strok/>]
- [3] Palmer KT. (2003) Pain in the forearm, wrist and hand. *Best Pract. Res. Clinical Rheumatol*, 17(1): 113-135. [https://doi.org/10.1016/S1521-6942\(02\)00100-6](https://doi.org/10.1016/S1521-6942(02)00100-6)
- [4] Hussain Z, Azlan NZ, Yusof AZ. (2018) Human hand motion analysis during different eating activities. *Applied bionics and biomechanics*: 2018: 1-12. <https://doi.org/10.1155/2018/8567648>
- [5] Hussain Z, Azlan NZ. (2017) Human lower arm analysis during different eating activities. In *Proceedings of the 2017 IEEE 8th Control and System Graduate Research Colloquium (ICSGRC): 3-5 August 2017; Shah Alam*. pp 93-98. doi: 10.1109/ICSGRC.2017.8070575.
- [6] Chiri N, Vitiello F, Giovacchini S, Roccella F, Vecchi, Carrozza MC. (2012) Mechatronic design and characterization of the index finger module of a hand exoskeleton for post-stroke rehabilitation. *IEEE/ASME Transactions on Mechatronics*, 17(5): 884-894. doi: 10.1109/TMECH.2011.2144614.
- [7] Squeri V, Basteris A, Sanguineti V. (2011) Adaptive regulation of assistance "as needed" in robot-assisted motor skill learning and neurorehabilitation. In *Proceedings of the IEEE International Conference on Rehabilitation Robotics: 29 June – 1 July 2011; Zurich, Switzerland*. pp. 1-6, doi: 10.1109/ICORR.2011.5975375.
- [8] Houwink A, Nijland RH, Geurts AC, Kwakkel G. (2013) Functional recovery of the paretic upper limb after stroke: who regains hand capacity? *Archives of physical medicine and rehabilitation*, 94(5): 839-844. 10.1016/j.apmr.2012.11.031
- [9] Hussain S, Jamwal PK, Ghayesh MH, Xie SQ. (2016) Assist As Needed control of an intrinsically compliant robotic gait training orthosis. *IEEE Transactions on Industrial Electronics*, 64(2): 1675-1685. doi: 10.1109/TIE.2016.2580123.
- [10] Luo L, Peng L, Wang C, Hou ZG. (2019) A greedy Assist As Needed controller for upper limb rehabilitation. *IEEE transactions on neural networks and learning systems*, 30(11): 3433-3443. doi: 10.1109/TNNLS.2019.2892157.
- [11] Gui K, Tan U, Liu H, Zhang D. (2020) Electromyography-driven progressive Assist As Needed control for lower limb exoskeleton. *IEEE Transactions on Medical Robotics and Bionics*, 2(1): 50-58. doi: 10.1109/TMRB.2020.2970222.
- [12] Asl HJ, Narikiyo T, Kawanishi M. (2017) An Assist As Needed control scheme for robot-assisted rehabilitation. In *Proceedings of the 2017 American Control Conference (ACC): 24 - 26 May 2017; Seattle, Washington*. pp 198-203. doi: 10.23919/ACC.2017.7962953

- [13] Pérez-Rodríguez R, Costa C, Cáceres C, Tormos JM, Medina J, Gómez EJ. (2014) Anticipatory assistance-as-needed control algorithm for a multijoint upper limb robotic orthosis in physical neurorehabilitation. *Expert Systems with Applications*, 41(8): 3922-3934. <https://doi.org/10.1016/j.eswa.2013.11.047>
- [14] Kapsalyamov A, Hussain S, Sharipov A, Jamwal P. (2019) Brain-computer interface and Assist As Needed model for upper limb robotic arm. *Advances in Mechanical Engineering*, 11(9): 1-9. <https://doi.org/10.1177/1687814019875537>.
- [15] Frullo JM, Elinger J, Pehlivan AU, Fitle K, Nedley K, Francisco GE, O'Malley MK. (2017). Effects of Assist As Needed upper extremity robotic therapy after incomplete spinal cord injury: a parallel-group controlled trial. *Frontiers in Neurorobotics*, 11(26): 1-34. <https://doi.org/10.3389/fnbot.2017.00026>.
- [16] Peng L, Wang C, Luo L, Chen S, Hou ZG, Wang W. (2018) A CPG-inspired Assist As Needed controller for an upper-limb rehabilitation robot. In *Proceedings of the 2018 IEEE Symposium Series on Computational Intelligence (SSCI)*: 18-21 November 2018; Bangalore, India. pp 2200-2206. doi: 10.1109/SSCI.2018.8628896
- [17] Agarwal P, Deshpande AD. (2017) Subject-specific Assist As Needed controllers for a hand exoskeleton for rehabilitation. *IEEE Robotics and Automation Letters*, 3(1): 508-515. <https://doi.org/10.1109/lra.2017.2768124>
- [18] Stroppa F, Loconsole C, Marcheschi S, Mastronicola N, Frisoli A. (2018) An improved adaptive robotic assistance methodology for upper-limb rehabilitation. In *Proceedings of the International Conference on Human Haptic Sensing and Touch Enabled Computer Applications*: 13 – 16 June 2018; Pisa, Italy. Edited by: Prattichizzo D, Shinoda H, Tan H, Ruffaldi E, Frisoli A; pp 513-525. https://link.springer.com/chapter/10.1007/978-3-319-93399-3_44
- [19] Taheri H, Reinkensmeyer DJ, Wolbrecht ET. (2016) Model-based assistance-as-needed for robotic movement therapy after stroke. In *Proceedings of the Annual International Conference of the IEEE Engineering in Medicine and Biology Society, EMBS*: 17 – 20 August 2016; Florida, USA. pp 2124-2127. doi: 10.1109/EMBC.2016.7591148.
- [20] Wolbrecht ET, Chan V, Reinkensmeyer DJ, Bobrow JE. (2008) Optimizing compliant, model-based robotic assistance to promote neurorehabilitation. *IEEE Transactions on Neural Systems and Rehabilitation Engineering*, 16(3): 286-297. doi: 10.1109/TNSRE.2008.918389.
- [21] Bower C, Taheri H, Wolbrecht E. (2013) Adaptive control with state-dependent modeling of patient impairment for robotic movement therapy. In *Proceedings of the 2013 IEEE 13th International Conference on Rehabilitation Robotics (ICORR)*: 24-26 June 2013; Seattle, USA. pp. 1-6, doi: 10.1109/ICORR.2013.6650460.
- [22] Guidali M, Schlink P, Duschau-Wicke A, Riener R. (2011) Online learning and adaptation of patient support during ADL training. In *Proceedings of the 2011 IEEE International Conference on Rehabilitation Robotics*: 29 June - 1 July 2011; Zurich, Switzerland. pp 1-6, doi: 10.1109/ICORR.2011.5975434.
- [23] Pehlivan AU, Sergi F, O'Malley MK. (2015) A subject-adaptive controller for wrist robotic rehabilitation. *IEEE/ASME Transactions on Mechatronics*, 20(3): 1338-1350. doi: 10.1109/TMECH.2014.2340697
- [24] Mounis SYA, Azlan NZ, Sado F. (2019) Assist As Needed control strategy for upper-limb rehabilitation based on subject's functional ability. *Measurement and Control* 52 (9-10): 1354-1361. <https://doi.org/10.1177/0020294019866844>
- [25] Mounis SYA, Azlan NZ, Sado F. (2017) Progress based Assist As Needed control strategy for upper-limb rehabilitation. In *Proceedings of the 2017 IEEE Conference on Systems, Process and Control (ICSPC)*: 15-17 December 2017; Malacca, Malaysia. pp 65-70. doi: 10.1109/SPC.2017.8313023
- [26] Kashtwari U, Azlan NZ, Shahdad I. (2020) Wearable upper limb motion assist robot for eating activity. *Applied Research and Smart Technology (ARSTech)* 1 (1), pp 1-10. <https://doi.org/10.23917/arstech.v1i1.28>
- [27] Cytron marketplace [<https://www.cytron.io/>]

- [28] Lukman NS. (2019) Assist As Needed Control of upper limb rehabilitation robot for eating activity. Final Year Project Report. International Islamic University Malaysia, Kulliyah of Engineering.
- [29] Digi-key electronics [<https://www.digikey.com/>]
- [30] DC motor speed: System modeling
[<http://ctms.engin.umich.edu/CTMS/index.php?example=MotorSpeed§ion=SystemModeling>].

IMPROVED CONSTRAINT HANDLING APPROACH FOR PREDICTIVE FUNCTIONAL CONTROL USING AN IMPLIED CLOSED-LOOP PREDICTION

MUHAMMAD ABDULLAH¹, JOHN ANTHONY ROSSITER²,
AND ALIA FARHANA ABDUL GHAFFAR^{1*}

¹*Department of Mechanical Engineering, International Islamic University Malaysia,
Jalan Gombak, 53100 Kuala Lumpur, Malaysia*

²*Department of Automatic Control and Systems Engineering,
The University of Sheffield, S1 3JD, UK*

*Corresponding author: aliafarhana@iium.edu.my

(Received: 6th July 2020; Accepted: 24th September 2020; Published on-line: 4th January 2021)

ABSTRACT: Predictive Functional Control is a simple alternative to the traditional PID controller which has the capability to handle process constraints more systematically. Nevertheless, the most basic form of PFC has suffered from ill-posed prediction due to its simplicity in formulation and assumption of constant future input dynamics. Although some constraints can be satisfied, nevertheless the performance may be very conservative due to this issue. The main objective of this paper is to improve the constrained performance of a PFC controller with a minimum modification of the existing formulation. Specifically, a novel constraint handling approach for PFC is proposed based on an implied closed-loop prediction. Instead of assuming a constant input as deployed in the conventional open-loop prediction, the implied closed-loop input dynamics are utilised to detect future constraint violations. In addition, a future perturbation is introduced into the prediction structure as an extra degree of freedom for satisfying the constraints. Two simulation results confirm that the proposed approach gives far less conservative constraint handling and thus better control performance compared to the nominal PFC. Furthermore, this novel implementation also alleviates the well-known tuning difficulties and prediction inconsistency issues that are associated with conventional PFC when handling constraints.

ABSTRAK: Kawalan Kefungsian Ramalan adalah alternatif mudah kepada kawalan tradisional PID yang mempunyai kekangan keupayaan bagi mengawal proses secara lebih tersusun. Namun, keadaan paling asas pada kesan PFC adalah daripada ramalan tak terajurapi yang disebabkan oleh formula ringkas dan anggapan dinamik input yang sama bagi masa depan. Walau kekangan ini dapat diatasi, namun prestasi akan berubah secara konservatif disebabkan oleh isu ini. Objektif utama kajian ini adalah bagi membaiki kekangan prestasi kawalan PFC dengan modifikasi minimum formula yang ada. Secara spesifik, pendekatan nobel kawalan PFC dicadangkan berdasarkan ramalan lingkaran-tertutup. Selain anggapan input tetap seperti yang dilakukan pada ramalan lingkaran-terbuka yang konservatif, dinamik input yang dibuat pada lingkaran-tertutup telah digunakan bagi mengesan kekangan masa depan yang bertentangan. Tambahan, gangguan yang bakal berlaku pada masa depan telah diperkenalkan ke dalam struktur ramalan sebagai tambahan darjah pada kebebasan bagi mengatasi kekangan. Dua dapatan simulasi kajian menyetujui pendekatan yang dicadangkan dan menyebabkan sangat kurang kekangan pengendalian pada sistem konservatif, oleh itu kawalan yang lebih bagus pada prestasi berbanding pada PFC nominal. Selain itu, pendekatan nobel ini juga

menghilangkan kesukaran pelarasan yang dikenali ramai dan ramalan isu tidak konsisten yang terdapat pada PFC konvensional apabila mengendalikan kekangan.

KEYWORDS: *predictive functional control (PFC); constraints handling; implied closed-loop prediction; constrained predictive controller*

1. INTRODUCTION

Advances in the industrial revolution triggered the need for advanced control methods that can work within a constrained environment. Generally, constraints can be classified into two categories: i) a hard constraint refers to a physical limitation of process hardware which typically is in terms of input and output rates and ii) a soft constraint refers to a state or output limit which may be violated to some extent when required or perhaps when unavoidable. Satisfying all of these constraints can provide several benefits such as lower maintenance costs, maximisation of profits, and a safer control environment [1]. Nevertheless, dealing with constrained systems poses several challenges. For example, one often needs to deploy a classical controller such as Proportional Integral Derivative (PID) and ensuring this control loop does not violate the limits may not be straightforward or systematic in general. The more systematic, but far more expensive alternative, is to implement Model Predictive Control (MPC); this approach utilises predictions explicitly and optimises the expected behaviour by minimising a quadratic cost function subjected to predictions satisfying process constraints [2, 3]. However, conventional MPC solutions [4] are expensive and computationally demanding and hence may not be viable for applications where the costs and complexity need to be similar to those of PID.

An alternative prediction-based method which is computationally simple and relatively inexpensive is Predictive Functional Control (PFC) [5-7]. Whereas a conventional MPC algorithm uses optimisation of a quadratic cost function and the entire prediction trajectory, the most basic PFC utilises the prediction at just one point in the future, which is far simpler to compute, and avoids optimisation by forcing its future prediction to match the desired target trajectory (often first order dynamics) at a specific coincidence horizon. Again, for simplicity, a well-known assumption is that the predicted future input dynamics are taken to be constant, as this simplifies the control law definition into the solution of a single degree of freedom (d.o.f) equality expression. Thus, programming the algorithm will be simple and it can be used on a low cost processor including a Programmable Logic Controller (PLC) [5,8]. Of course, as a consequence, PFC performance is suboptimal in general (e.g. measured against typical MPC objective functions), but because it provides straightforward tuning, implementation, and constraint handling, it can be effective for a number of Single Input Single Output (SISO) processes when compared to both PID and MPC considering its low computation demand and simple coding requirement [6,9]. Indeed, these features explain the widespread acceptance and successful implementation of PFC in many real industrial applications ranging from aerospace, automotive, and chemical processes [5,10].

The current implementation of PFC in handling input and rate constraints is by simply applying a clipping or saturation method. If the current manipulated input is violating the limits, then a maximum or minimum value will be sent to the plant. This simple framework can alleviate issues such as integral wind-up, due to its use of predictions, although it may still be suboptimal [5]. As for state and output constraints, the traditional PFC approach uses multiple controllers in parallel whereby the primary regulator is tuned to track the target trajectory while the other one is tuned to satisfy the limits [11], as shown in Fig. 1. A real-time prediction is made based on the primary input by a supervisor and if it violates the limits, then the input will be switched. Although this simple concept often works and

provides a fast control solution, it can nevertheless be considered obsolete with modern computing facilities and moreover lacks sufficient rigour. Besides, it is easy to formulate scenarios where this approach fails or leads to significant performance degradation [12] and thus improvements are needed.

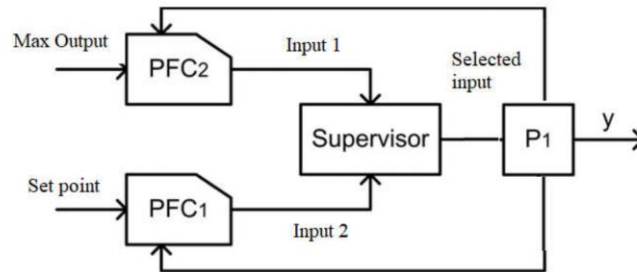


Fig. 1: Schematics of traditional PFC when handling output constraint.

A core aspect of efficient and accurate constraint handling is to ensure that the optimised predictions and the expected closed-loop behaviour are consistent [1,3, 12-13]. When there is inconsistency, ensuring that the model predictions meet constraints may be a poor reflection of whether the resulting closed-loop responses satisfy constraints, leading to either unpredicted constraint violations or the controlled response becomes very conservative in satisfying the constraints. In fact, the core weakness of the traditional PFC is its conventional assumption of its future input predictions being constant; in reality, this assumption is often inconsistent with the resulting closed-loop input to a significant degree [12]. Hence, even though PFC can check the expected constraint violations over a long prediction horizon, yet due to the prediction mismatch, the control law will produce a very conservative solution.

In previous work [12], an alternative parameterisation of the d.o.f. had been introduced within the PFC framework in order to improve the predictions and closed-loop behaviour's consistency, thus resulting in more accurate constraint handling and systematic tuning. Specifically, a Laguerre based parameterisation of the predicted future input replaced the conventional constant input assumption of PFC. This modification showed improvements in the prediction consistency with low order models and thus enabled less conservative constraint handling [14]. However, the use of a simple first order Laguerre function is still somewhat limited, and for higher-order systems, significant prediction inconsistency may still exist. While it is possible to increase the order of the Laguerre polynomial [15], this is not straightforward in general [16] and not in line with the simplicity concept which is an essential facet of PFC.

In summary, the specific objective of this new work is to propose a novel constraint handling concept for PFC, which can be applied to higher order systems and which minimises the prediction inconsistency, thus ensuring that the inequalities used for constraint handling are as accurate as possible and reducing conservatism and risk. In real applications, this is very beneficial as the system can be pushed to work nearer to its high profit boundary region without causing unexpected violations and thus fatigue damage. A core research gap in PFC is that there are no attempts in deploying the well-known concept from dual-mode MPC [3] whereby the predictions are made up by assuming a known feedback control law is in place for the asymptotic part of the predictions. In the case of PFC, a nominal control law is available for the constraint-free case and thus a simple proposal is to exploit this control law within the prediction formulation used for constraint handling. Nevertheless, the nominal PFC control law also needs to be modified further by

introducing a new slack variable or degree of freedom (d.o.f.) in the formulation to be utilised for handling the constraints. Thus, this paper will make two main contributions: (i) first, it will demonstrate how an effective d.o.f. can be incorporated alongside a suitable dual-mode formulation and (ii) second, it will show how the constraint handling can be implemented.

2. BACKGROUND ON PREDICTIVE FUNCTIONAL CONTROL

A brief review of the key assumptions, notations, and principles of conventional Predictive Functional Control laws together with a constraint handling method as proposed in [12] is described in this section.

2.1 Target Trajectory and Control Law Definition

A core principle of PFC is, at sample k , a desired target trajectory $r(k + i|k)$ is defined, where $i = 1, 2, \dots$ for future samples $k + i$ based on a desired steady-state target R . The target trajectory is defined as a *first-order-response* from the current process output $y_p(k)$ to R , hence:

$$r(k + i|k) = (1 - \lambda^i)R + \lambda^i y_p(k), \quad i = 1, 2, \dots \quad (1)$$

where, λ is the implied desirable pole position. For industrial users, one can use a desired settling time, T_s and determine λ from the relationship [5]:

$$\lambda = e^{-\frac{3T}{T_s}} \quad (2)$$

with the sampling period, T . The second core principle in PFC is to force the system prediction, that is $y_p(k + n|k)$, to match the target n samples into the future, where n is representing the coincidence horizon (second tuning parameter) [5]. Hence, the control law can be summarised as:

$$r(k + n|k) = (1 - \lambda^n)R + \lambda^n y_p(k) = y_p(k + n|k) \quad (3)$$

This is shown in Fig. 2 for clarity. The two *tuning parameters* or user choices are the desired closed-loop pole, λ , and the coincidence horizon, n .

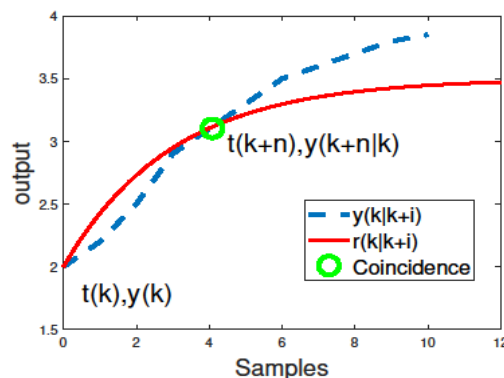


Fig. 2: PFC control law definition.

Remark 2.1: For clarity of formulation, this work will not discuss the PFC framework that is related to a delay control problem and non-constant targets because these issues require more complex algebra and moreover have no effect on the core concepts proposed in this paper. Details are available in the references [2,5].

2.2 Prediction Structure and Degrees of Freedom

For solving the control law in Eq. (3), it is necessary to define the output prediction $y_p(k + n|k)$ and its dependence on the control signal $u(k|k)$. Prediction is standard in the literature [1] so just a brief illustration is given here. It is noted that this formulation ensures unbiased prediction in the steady-state and therefore offset free tracking.

Without loss of generality, the formulation in this paper utilises a state space model as it is easier to demonstrate the proposed control law in the next section. The one-step ahead prediction for a state-space model with states, inputs and output $x(k), u(k), y_m(k)$ can be formed as:

$$x(k + 1) = Ax(k) + Bu(k); \quad y_m(k + 1) = Cx(k + 1) \quad (4)$$

Note the use of subscript m to denote model. Typically, the real process output y_p differs from the model y_m , so process predictions are estimated using the measured signal $d(k)$ given in the structure illustrated in Fig. 3. Hence:

$$d(k) = y_p(k) - y_m(k) \quad \rightarrow \quad y_p(k + i|k) = y_m(k + i|k) + d(k) \quad (5)$$

Consequently, the predicted plant output with the assumed predicted constant future input ($u(k) = u(k + 1|k) = u(k + 2|k), \dots$) can be written as:

$$y_p(k + i|k) = CA^i x_k + [CB, CAB, \dots, CA^{i-1}B] \begin{bmatrix} 1 \\ \vdots \\ 1 \end{bmatrix} u(k) + d(k) \quad (6)$$

Remark 2.2: For constraint handling it is convenient to stack the output predictions into matrix form over some prediction horizon and hence one can define:

$$\begin{aligned} \vec{y}_p(k + n|k) &= Fx(k) + Hu(k) + Ld(k) \quad (7) \\ \vec{y}_p(k + n|k) &= \begin{bmatrix} y_p(k + 1|k) \\ y_p(k + 2|k) \\ \vdots \\ y_p(k + n|k) \end{bmatrix}; \quad F = \begin{bmatrix} CA \\ CA^2 \\ \vdots \\ CA^n \end{bmatrix}; \quad H = \begin{bmatrix} CB & 0 & 0 & \dots \\ CAB & CB & 0 & \dots \\ \vdots & \vdots & \vdots & \ddots \\ CA^{n-1}B & CA^{n-2}B & CA^{n-3}B & \dots \end{bmatrix} \end{aligned}$$

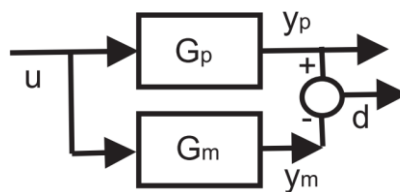


Fig. 3: Structure of an Independent Model (IM).

2.3 The PFC Control Law

The conventional PFC control law is defined by substituting the predictions in Eq. (6) into the control law definition Eq. (3). It is understood that one must first choose the desired closed-loop pole, λ ($0 < \lambda < 1$), and the coincidence horizon, n . In fact, the choice of n is less simple in general [13], but that discussion is outside the focus of this paper. Defining the n^{th} row of matrices F, H to be F_n, H_n respectively, the control law Eq. (3) is defined by solving the following for u_k (this form would be used in real implementation):

$$H_n Lu(k) + F_n x(k) + d(k) = (1 - \lambda^n)R + \lambda^n y_p(k) \quad (8)$$

Equation (8) can be solved to determine u_k but, in order to facilitate some loop analysis (nominal case), this can also be expressed by substituting $y_p(k) = y_m(k) + d(k) = Cx(k) + d(k)$. Hence, the control law Eq. (3) is presented as:

$$(1 - \lambda^n)(R - d(k)) = H_n Lu(k) + F_n x(k) - \lambda^n Cx(k) \quad (9)$$

Thus, the required control input can be represented as an augmented state feedback:

$$u(k) = \underbrace{\begin{bmatrix} \frac{-(F_n - C\lambda^n)}{H_n L} & \frac{(1 - \lambda^n)}{H_n L} \end{bmatrix}}_K \underbrace{\begin{bmatrix} x(k) \\ (R - d(k)) \end{bmatrix}}_{\bar{x}(k)} \quad (10)$$

where K is the state feedback gain and \bar{x}_k is the augmented state.

Remark 2.3: The main reason why PFC is attractive is due to its simplicity in computing the control law of Eq. (10). Since $H_n L$ and F_n are only needed for a single horizon, n , the required computation is relatively straightforward and indeed can be calculated off-line [2, 5].

2.4 Conventional Constraint Handling with Open-loop Predictions

A good constraint handling approach for PFC should be systematic and also simple enough to avoid the usage of common optimisers deployed in more expensive MPC algorithms and reference governor strategies [11, 17]. Let the rate, input and output constraints at every sample be defined respectively as:

$$\underline{\Delta u} \leq \Delta u(k) \leq \overline{\Delta u} ; \underline{u} \leq u(k) \leq \overline{u} ; \underline{y_p} \leq y_p(k) \leq \overline{y_p} \quad (11)$$

As discussed before, the classical PFC algorithm deploys a saturation method to deal with input and rate constraints [1,5], but that can be severely suboptimal in practice due to the difference between the input prediction and the implied closed-loop evolution. This inaccuracy is even more notable when output/state constraints are introduced in the optimised open-loop predictions, [14], as detailed next. The constraint handling procedure of PFC, as proposed by [12], is outlined as:

- (1) Given a suitably long validation horizon, n_i (horizon used to check a future limit violation), the whole set of future predictions as formulated in Eq. (7) is computed.
- (2) Group all the constraints (input, rate, and output) and the system predictions into a single set of linear inequalities as:

$$Mu(k) \leq f(k) \quad (12)$$

$$M = \begin{bmatrix} 1 \\ -1 \\ 1 \\ -1 \\ HL \\ -HL \end{bmatrix} ; f(k) = \begin{bmatrix} \overline{u} \\ -\underline{u} \\ \overline{\Delta u} \\ -\underline{\Delta u} \\ L\overline{y_p} \\ -L\underline{y_p} \end{bmatrix} - \begin{bmatrix} 0 \\ 0 \\ u(k-1) \\ -u(k-1) \\ Fx(k) + Ld(k) \\ -Fx(k) - Ld(k) \end{bmatrix}$$

where $f(k)$ depends on the states and the limits. It is advisable that the output predictions horizon, $y_p(k+n)$, and the row dimension of H , need to be long enough in order to capture all the important dynamics [17].

- (3) It is noted that the predictions will satisfy constraints if the selected input $u(k)$ satisfies Eq. (12), that is, inequalities $Mu(k) \leq f(k)$ can be used explicitly to determine this condition.

Next, a modern PFC constraint handling algorithm is given. This concept utilises a simple “for” loop to choose the $u(k)$, that is nearest to the unconstrained solution shown in Eq. (10) but does not violate the limits in Eq. (12).

Algorithm 2.1. *At each time step or sample:*

- (1) Compute the unconstrained input $u(k)$ as defined in Eq. (9).
- (2) Define the vector $f(k)$, from Eq. (13) where vector M is fixed.
- (3) A simple for loop is utilised to inspect each row of M , here:
 - (a) The i^{th} constraint; represented by the i^{th} row of $Mu(k) \leq f(k)$, is checked using $a_i = M_i u(k) - f_i(k)$.
 - (b) If $a_i > 0$, then $u(k) = f_i(k)/M_i$; else the original value of $u(k)$ is retained.

It has been proven in [14] that for the nominal case where $d(k)$ is assumed constant and also for stable open-loop systems, a recursive feasibility property for Algorithm 2.1 is guaranteed where $u(k)$ converges to a feasible value nearest to the unconstrained choice.

Remark 2.4: *Since Algorithm 2.1 utilises a straightforward for-loop, the programming, coding, and computation becomes far simpler and faster compared to more demanding MPC approaches based on optimisation of a quadratic program. In addition, the algorithm is more systematic and faster than most of the conventional PID methods. However, it should be noted that the usage of PFC is often limited to a single-input-single-output (SISO) process and is rarely used for multi-input, multi-output (MIMO) systems [5].*

2.5 Limitations of Conventional PFC Constraint Handling

The main reason behind the popularity of PFC in industrial processes is due to its transparent tuning parameters. Here, one only needs to select the desired closed loop time constant, which is equivalent to λ . Then, the different choices of coincidence horizon, n , can be quickly explored using a computer while displaying the associated responses. Thus, a user can then select a suitable coincidence horizon, n , for their system. Nevertheless, there are two major trade-offs that need to be considered [8, 13, 15]:

- (1) Smaller values of coincidence horizon, n , drive the output response closer to the target trajectory where the effect of tuning parameter, λ , becomes more significant. However, smaller, n , typically leads to poorer consistency between the predicted and actual responses, and thus inaccurate constraint handling and potentially less desirable behaviour.
- (2) Conversely, larger, n , improves the prediction consistency, yet the closed-loop behaviour then approaches open-loop dynamics which decreases the significance and efficacy of λ as a tuning parameter.

Prediction mismatch is potentially catastrophic for reliable constraint handling as predictions satisfying constraints need not imply that the resulting closed-loop responses will satisfy constraints, and vice versa. Consequently, the constraint handling algorithm may be either highly conservative [12, 14] and/or overly aggressive.

Remark 2.5: It is well noted that one of the weaknesses of conventional PFC algorithm is its prediction mismatch [1] between its optimised predictions and the closed-loop behaviour that results. This inconsistency arises mainly due to the assumed constant future input prediction. Consistency between predictions and actual behaviour is needed to ensure good behaviour, especially for cases dealing with higher order systems.

3. PFC CONSTRAINT HANDLING BASED ON AN IMPLIED CLOSED-LOOP PREDICTION

The main weakness of conventional PFC, as indeed with many conventional MPC algorithms, is its assumption of a constant future input. This assumption is typically inconsistent with the actual closed-loop behaviour, and thus incorrect constraint handling decisions are made [12]. To some extent, dual-mode approaches [18] can overcome this issue by ensuring the predictions are as close as possible to the actual closed-loop behaviour, but of course these are computationally demanding. The main contribution here is to exploit a similar concept, that is, to use implied closed-loop predictions for constraint handling, but in a simplified manner to maintain the core selling benefits of PFC. The proposal is novel in that dual-mode approaches still use *open-loop* predictions in transients, but with a long-term input trajectory that emulates the implied closed-loop after transients. Conversely, we will predict the expected closed loop behaviour explicitly for the entire horizon.

In summary, the expected benefits of this proposal are:

- More accurate predictions when checking output/state constraints implies less conservative decision making.
- A smaller coincidence horizon (n) can be selected without worrying about the prediction inconsistency which will retain more tuning capability.
- The proposed approach only requires a simple modification in the offline computations required for constraint handling.

3.1 Closed-loop Prediction PFC (CL-PFC) with Constant Input Perturbation

In order to use closed-loop predictions for constraint handling, an extra d.o.f. is required in the predictions. The proposal here is to add a constant perturbation to the implied closed-loop input [1] as this structure has been found to be effective elsewhere. Hence, based on the control law of Eq. (10), the closed-loop prediction model combines the open-loop model and control law, with a constant input perturbation, $c(k)$, as the new d.o.f. Thus:

$$\{\bar{x}(k+1|k) = \bar{A}\bar{x}(k) + \bar{B}u(k); u(k) = K\bar{x}(k) + c(k); c(k+i|k) = c(k), i > 0\} \quad (13)$$

\bar{A}, \bar{B} are the augmented model with respect to \bar{x}_k . The implied closed-loop predictions take the following form (for clarity of presentation, we define $\phi = [A + \bar{B}K]$):

$$\begin{bmatrix} y_p(k+1|k) \\ y_p(k+2|k) \\ \vdots \\ y_p(k+n|k) \end{bmatrix} = \underbrace{\begin{bmatrix} C\phi \\ C\phi^2 \\ \vdots \\ C\phi^n \end{bmatrix}}_{P_c} \bar{x}(k) + \underbrace{\begin{bmatrix} C\bar{B} & 0 & 0 & \dots \\ C\phi\bar{B} & C\bar{B} & 0 & \dots \\ \vdots & \vdots & \vdots & \ddots \\ C\phi^{n-1}\bar{B} & C\phi^{n-2}\bar{B} & C\phi^{n-3}\bar{B} & \dots \end{bmatrix}}_{H_c} Lc(k) \quad (14)$$

$$\begin{bmatrix} u(k|k) \\ u(k+1|k) \\ \vdots \\ u(k+n|k) \end{bmatrix} = \underbrace{\begin{bmatrix} -K \\ -K\phi \\ \vdots \\ -K\phi^{n-1} \end{bmatrix}}_{P_{cu}} \bar{x}(k) + \underbrace{\begin{bmatrix} I & 0 & 0 & \dots \\ -K\bar{B} & C\bar{B} & 0 & \dots \\ \vdots & \vdots & \vdots & \ddots \\ -K\phi^{n-2}\bar{B} & C\phi^{n-3}\bar{B} & C\phi^{n-4}\bar{B} & \dots \end{bmatrix}}_{H_{cu}} Lc(k) \quad (15)$$

$$\begin{bmatrix} \Delta u(k|k) \\ \Delta u(k+1|k) \\ \vdots \\ \Delta u(k+n|k) \end{bmatrix} = P_{cDu} \bar{x}(k) + H_{cDu} c(k) + Q_{cDu} u(k) \quad (16)$$

Remark 3.1: For the unconstrained case, the value of perturbation as in Eq. (13) will be $c(k) = 0$ since the term $u(k) = K\bar{x}_k$ is derived from the original control law. Thus, a non-zero $c(k)$ is required solely for constraint handling and the underlying loop tuning is based on the original PFC law.

3.2 Constraint Handling

For constraint handling, a similar procedure as discussed in Section 2.4, will be employed. The prime conceptual improvement here is the d.o.f., which is now expressed in terms of perturbation $c(k)$ instead of the input $u(k)$ and one needs to consider the entire input prediction and not just the first value. Thus:

$$\bar{M}c_k \leq \bar{f}_k, \quad (17)$$

$$\bar{M} = \begin{bmatrix} H_{cu}L \\ -H_{cu}L \\ H_{cDu}L \\ -H_{cDu}L \\ H_cL \\ -H_cL \end{bmatrix}; \quad \bar{f}(k) = \begin{bmatrix} L\bar{u} \\ -L\bar{u} \\ L\bar{\Delta u} \\ -L\bar{\Delta u} \\ L(\bar{y}_p - d(k)) \\ -L(\bar{y}_p - d(k)) \end{bmatrix} - \begin{bmatrix} P_{cu}\bar{x}_k \\ -P_{cu}\bar{x}_k \\ P_{cu}\bar{x}_k + Q_{cDu}u(k-1) \\ -P_{cu}\bar{x}_k + Q_{cDu}u(k-1) \\ P_c\bar{x}_k \\ -P_c\bar{x}_k \end{bmatrix}$$

In a similar manner to Algorithm 2.1, the goal is to select the d.o.f. $c(k)$ that is closest to its unconstrained value while satisfying the constraints in Eq. (11) (equivalently inequalities (17)).

Algorithm 3.1. At each sample:

- (1) Set $c(k) = 0$.
- (2) Define vector \bar{f}_k as in Eq. (17) with the assumption that \bar{M} does not change.
- (3) A simple loop is utilised to inspect each row of \bar{M} , where:
 - (a) The i^{th} constraint represented by the i^{th} row of $\bar{M}c(k) \leq \bar{f}(k)$ is checked with $a_i = \bar{M}_i c(k) - \bar{f}_i(k)$.
 - (b) If $a_i > 0$, then $c(k) = \bar{f}_i(k) / \bar{M}_i$, else use the existing $c(k)$.
- (4) Define the input from $u(k) = -K\bar{x}_k + c(k)$.

One can argue that better prediction consistency and more accurate constraint handling is obvious (and will be demonstrated in the examples section). Nevertheless, it is also important to establish that the proposed algorithm does indeed retain feasibility, that is the recursive feasibility property in the nominal case and moreover subject to changes in the target R .

Theorem 3.1: When there is no change in $d(k)$ and also in the nominal case, Algorithm 3.1 can guarantee recursive feasibility with any desired target, R .

Proof: Assume at sample $k-1$, the solution is feasible, then with no change in R , the choice $c(k) = c(k-1)$ must retain feasibility as the implied predictions at the previous and current

sample would then be identical. Hence, it remains only to show that $c(k)$ can be chosen to retain feasibility, irrespective of any changes in R . Consider then the nominal control law given in Eq. (10) and augment this with the proposed perturbation term $c(k)$ as in Eq. (13), hence:

$$u(k) = \begin{bmatrix} \frac{-(F_n - C\lambda^n)}{H_n L} & \frac{(1-\lambda^n)}{H_n L} & 1 \end{bmatrix} \begin{bmatrix} x(k) \\ R - d(k) \\ c(k) \end{bmatrix} \quad (18)$$

It is clear that the terms R and $c(k)$ both act as scaled additive terms to $u(k)$, and thus any change in R can be countered by a suitable scaled change in $c(k)$ so that the predictions at sample k match those from sample $k - 1$. In other words, recursive feasibility is guaranteed!

Corollary 3.2: *In practice, Algorithm 2.1 uses the smallest perturbation $c(k)$ possible so that performance is as close as possible to that desired. This also means that, if it is feasible, then $c(k)$ is driven to zero and offset free tracking will be ensured.*

The reader will note that we have not attempted to guarantee recursive feasibility subject to parameter uncertainty and disturbance changes as the literature on that area is far more complicated than would fit with the PFC philosophy: that is, simple coding and implementation. Of course, in practice, all MPC algorithms have some inherent degree of robustness and thus this lack of a guarantee is rarely a problem except for exceptional and challenging cases where one is unlikely to use PFC anyway.

4. METHODOLOGY FOR RESULT ANALYSIS

In this paper, the developed formulation will be used to set up the control algorithm for an arbitrary SISO system with constraints. Instead of quantitative analysis, this paper adopts a qualitative analysis since the main objective is to show the improvement between the proposed PFC with a conventional PFC. The control performance can be evaluated by observing its convergence speed to the desired setpoint within the constrained environment. Besides, for clarity of presentation, the obtained simulation results will not be compared with other types of controllers as that is not the main contribution of this paper and moreover, those comparisons are already well known in the existing literature. Indeed PFC performance cannot be contrasted with more comprehensive MPC alternatives as those deploy more complicated algorithms and are far more costly to implement and maintain. Interested readers can refer to these references on the comparison between MPC, PID and PFC [19, 20].

5. NUMERICAL EXAMPLES

This section provides two numerical examples with the characteristics of typical industrial processes to highlight the effectiveness of the proposed Algorithm 3.1 compared to the traditional PFC algorithm such as Algorithm 2.1. For clarity, the following comparisons are made:

- (1) Investigation of the prediction behaviour of the two algorithms and their associated consistency with the resulting closed-loop dynamics.
- (2) Comparison of the closed-loop controller performance when dealing with output constraints.
- (3) Demonstration of the ability of the proposed controller to handle multiple constraints and uncertainties.

In order to emphasise a variety of characteristics, the examples use two second order dynamics systems as follows:

- (1) A second order over-damped system model (pole at 0.4 and another pole at 0.8), with constraints of $\underline{u} = 0.12$, $\Delta u = 0.05$, and $\bar{y} = 1.5$:

$$G_1 = \frac{z^{-1} + 0.3z^{-2}}{1 - 1.2z^{-1} + 0.32z^{-2}}; n = 2; \lambda = 0.7 \quad (19)$$

and to include the model uncertainty in the analysis, the real process representation is given by:

$$G_{1,p} = \frac{z^{-1} + 0.28z^{-2}}{1 - 1.21z^{-1} + 0.3z^{-2}} \quad (20)$$

- (2) A second order non-minimum phase model (zero at 1.6 and poles at 0.6 and 0.85, respectively), with constraints of $\underline{u} = -3$, $\Delta u = -1$, and $\bar{y} = 1.5$:

$$G_2 = \frac{0.1z^{-1} - 0.16z^{-2}}{1 - 1.45z^{-1} + 0.51z^{-2}}; n = 5; \lambda = 0.7 \quad (21)$$

and its real process representation is given by:

$$G_{2,p} = \frac{0.11z^{-1} - 0.15z^{-2}}{1 - 1.44z^{-1} + 0.5z^{-2}} \quad (22)$$

The reader is reminded that λ is selected based on the user preference, which is associated to the desired closed-loop time response (CLTR). The selection range is between $0 < \lambda < 1$. In principle, a smaller λ gives faster convergence and vice versa. Normally, the coincidence horizon, n , is taken to be at the low end of the values which gives good performance as this ensures that λ is also an effective tuning parameter.

5.1 Effect of Prediction Consistency when Identifying Future Constraint Violations

In this subsection, only the output constraint will be considered to highlight the performance improvement where the output limit for both examples is set to $\bar{y} = 0.8$. In addition, the plant transfer function is set to be equal as the model $G_p = G$. Notably, and as expected, the unconstrained control law for both PFC and CL-PFC for examples 1 and 2 are the same as shown in Figs. 3 and 4, respectively. Since PFC is a discrete controller, the results are plotted in terms of sampling instant instead of time.

However, in the presence of output constraints, their performances may differ since the adjustment is linked to different inequalities shown in Eq. (12) and Eq. (17), respectively. The first example is based on open-loop predictions, while the second example is based on implied closed-loop predictions. In this section, we present the *optimised* predictions for each algorithm, with and without constraint handling, and demonstrate the differences in the resulting decision making. The core observations are as follows:

- The unconstrained predictions at the first sample (same for both approaches) violate output constraints for large prediction horizons (refer to Figs. 5 and 6).
- Based on Fig. 7 and Fig. 8, Algorithm 2.1 (PFC, red dotted line) reduces the choice of constant $u(k)$ substantially to ensure that the maximum value of $y_p(k+i|k)$ satisfies the constraints, but the consequence is a small initial value of $u(k)$ and a much slower responding output prediction for both examples 1 and 2 respectively.

- Conversely, Algorithm 3.1 (CL-PFC, blue dashed line) recognises that future inputs will change, thus the predictions used for constraint handling can retain the fast transients while not exceeding the constraints.

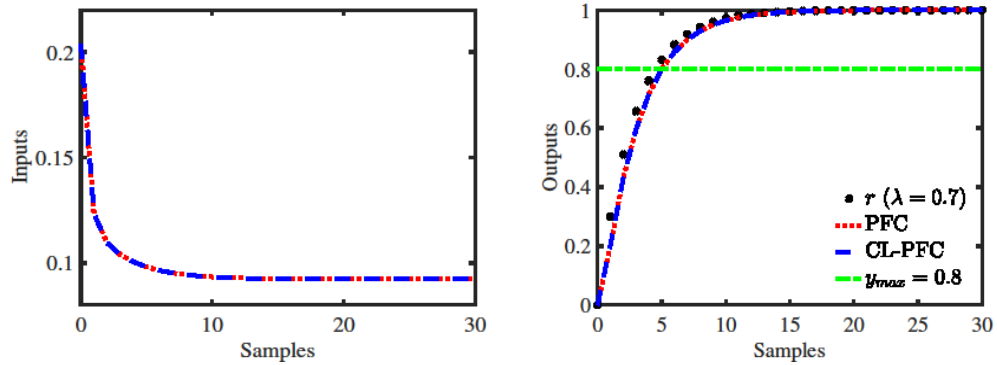


Fig. 3: Unconstrained closed-loop input and output of PFC and CP-PFC for example G_1 .

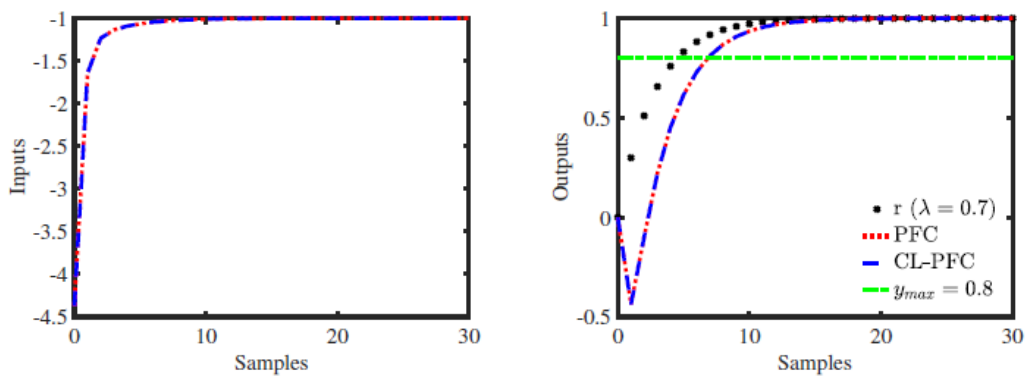


Fig. 4: Unconstrained closed-loop input and output of PFC and CP-PFC for example G_2 .

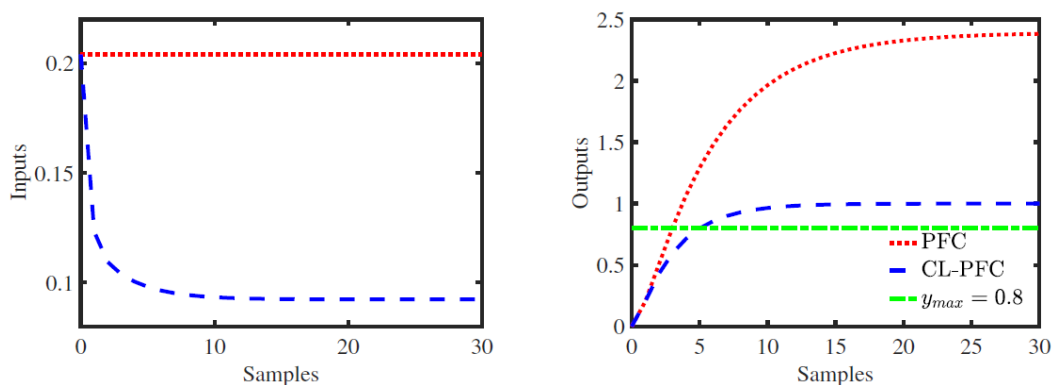


Fig. 5: Input and output predictions at the first sample of PFC and CP-PFC for example G_1 .

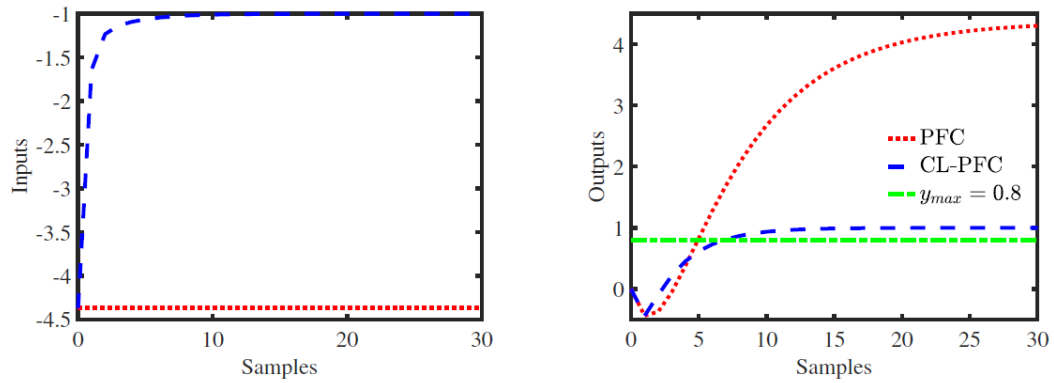


Fig. 6: Input and output predictions at the first sample of PFC and CP-PFC for example G_2 .

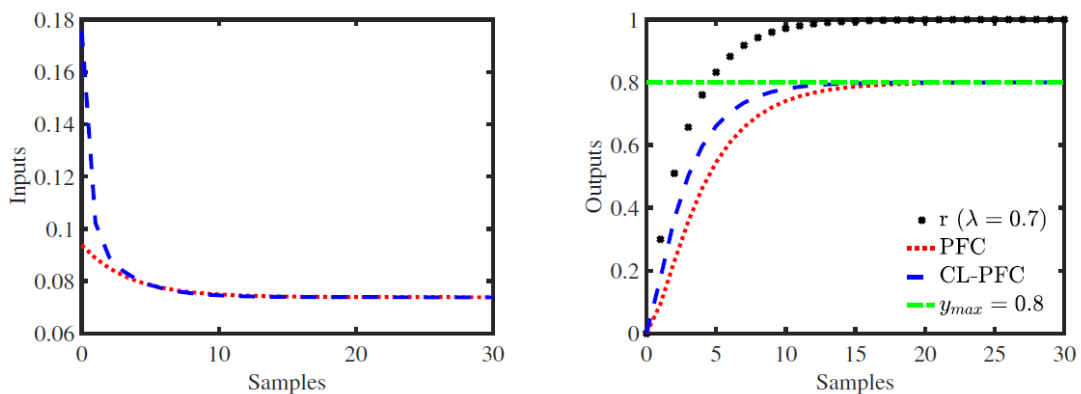


Fig. 7: Constrained input and output behaviour of PFC and CL-PFC for example G_1 .

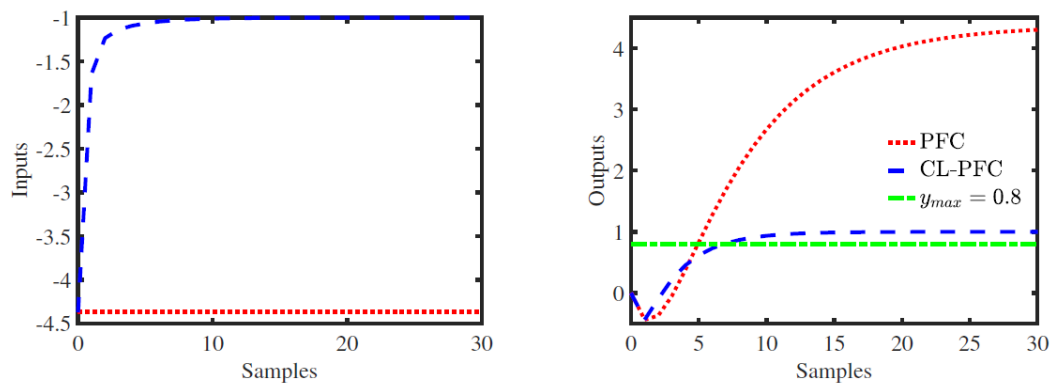


Fig. 8: Constrained input and output behaviour of PFC and CL-PFC for example G_2 .

In summary, due to significant prediction mismatch in the open-loop predictions and the corresponding closed-loop behaviour in Algorithm 2.1, the constraint handling is highly conservative/suboptimal. Conversely, the proposed Algorithm 3.1 removes this mismatch thus ensuring effective and accurate constraint handling, therefore, no more loss of performance than necessary.

5.2 Handling Multiple Constraints and Uncertainties

In this section, the CL-PFC algorithm is tested with multiple constraints that include input, input rate, and output constraints to demonstrate that Algorithm 3.1 deals effectively

with all of these simultaneously. Moreover, some parameter uncertainties are introduced to demonstrate inherent robustness as discussed before in the introduction part of Section 4. In addition, to demonstrate the recursive feasibility properties more strongly, the examples include a switch from a feasible to an infeasible R . Figures 9 and 10 show the constrained closed-loop performance of CL-PFC for both example 1 and 2, respectively. It is noted that all the constraints are satisfied without a conflict and good performance is retained even in the presence of uncertainty while the system converges to the closest feasible output.

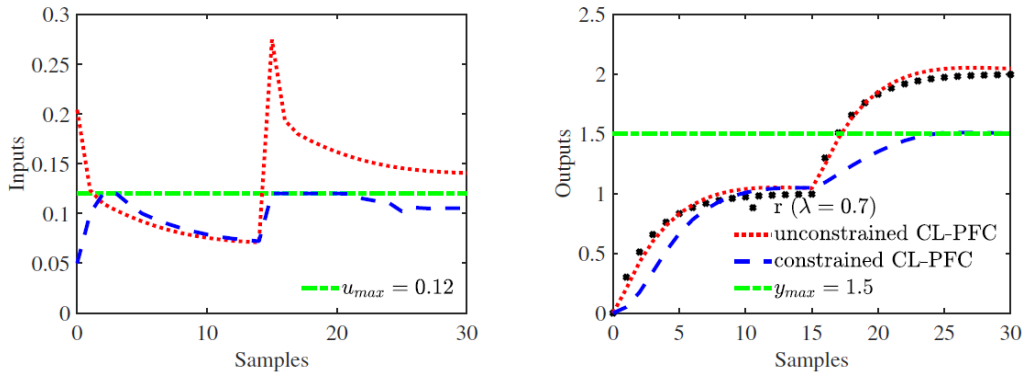


Fig. 9: Constrained and unconstrained performance for example G_1 .

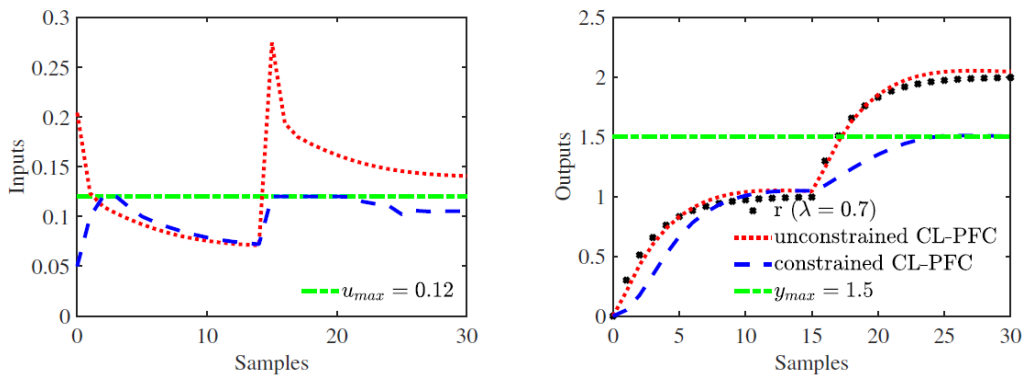


Fig. 10: Constrained and unconstrained performance for example G_2 .

5.3 Possible Application and Practical Significance

As discussed in Section 1, PFC is a simple and practical controller that can be implemented in any processor with a few lines of coding. The main attraction of PFC is that it can provide a satisfactory control performance when handling constraints with minimum computation and transparent tuning parameter of the desired closed-loop time constant. It should be noted that this work does not claim that PFC is better than MPC and in fact, it can never be, due to the simplification of the algorithm. For low order processes and SISO systems, PFC can work well whereas the implementation of MPC will be very expensive for a simple application.

With the proposed framework, the user can get a less conservative control performance compared to a traditional PFC. For example, if this controller is implemented in a car, the car will slow down at the right time before cornering. Conversely, with a traditional PFC, the car will slow down long before the corner which will make it unnecessarily conservative/slow. Given the nominal performance is the same as conventional PFC, the authors expect that application of CL-PFC to real systems will demonstrate similar benefits [3, 17] in the constrained case; this constitutes future work.

6. CONCLUSIONS

This work presents a novel constraint handling approach for PFC that employs some of the recent ideas from a more conventional MPC. Specifically, by utilising the concept of an implied closed-loop prediction one can make the constraint handling decisions more accurate. With this modification, the constraint handling performance becomes more consistent and reliable when compared with the nominal PFC, as demonstrated in the numerical example simulations. With this finding, a simple system can work nearer to its constraints limits, but without constraint violation or sacrificing the desired dynamic performance. It is also worth highlighting that the required modifications for deploying this method are simple, thus in-line with the key requirements for PFC. In a real application, this benefit may be translated in terms of more production profit and a safer working environment as well as simple coding and maintenance.

Nevertheless, it should be noted that the constrained control performance is not claimed to be optimal. The underlying algorithm is still based on a simplified and far cheaper version of conventional MPC so the performance is not expected to be comparable. A few aspects which can be addressed next may include the rigorous extension of this approach to handle more challenging open-loop dynamics such as unstable, marginally stable, and oscillating systems. In addition, a more systematic and robust tuning procedure in selecting a suitable coincidence horizon in the presence of parameter uncertainty, noise and disturbances also needs to be investigated. A systematic sensitivity analysis that describes the relationship between the PFC tuning parameter and those uncertainties may provide useful information to a user before deploying this controller.

ACKNOWLEDGEMENTS

The author would like to acknowledge the International Islamic University Malaysia Research Acculturation Grant Scheme 2018 (IRAGS18-013-0014) and Ministry of Higher Education Malaysia for funding this work.

REFERENCES

- [1] Rossiter, J. A. (2018). A first course in predictive control. CRC press.
- [2] Haber, R., Bars, R., & Schmitz, U. (2012). Predictive control in process engineering: From the basics to the applications. John Wiley & Sons.
- [3] Mayne, D. Q., Rawlings, J. B., Rao, C. V., & Scokaert, P. O. (2000). Constrained model predictive control: Stability and optimality. *Automatica*, 36(6), pp 789-814.
- [4] Clarke, D. W., & Mohtadi, C. (1989). Properties of generalized predictive control. *Automatica*, 25(6), pp 859-875.
- [5] Richalet, J., & O'Donovan, D. (2009). Predictive functional control: principles and industrial applications. Springer Science & Business Media.
- [6] Richalet, J., & O'Donovan, D. (2011). Elementary predictive functional control: A tutorial. In 2011 International Symposium on Advanced Control of Industrial Processes (ADCONIP): May 2011; pp 306-313.
- [7] Richalet, J., Rault, A., Testud, J. L., & Papon, J. (1978). Model predictive heuristic control. *Automatica (Journal of IFAC)*, 14(5), pp 413-428.
- [8] Khadir, M., & Ringwood, J. (2008). Extension of first order predictive functional controllers to handle higher order internal models. *International Journal of Applied Mathematics and Computer Science*, 18(2), pp 229-239.

- [9] Haber, R., Rossiter, J. A., & Zabet, K. (2016). An alternative for PID control: predictive functional control-a tutorial. In 2016 American Control Conference (ACC): July 2016; pp. 6935-6940
- [10] Richalet, J., Lavielle, G., Mallet, J., & Dreyfus, G. (2005). *La commande prédictive*. Eyrolles.
- [11] Fiani, P., & Richalet, J. (1991). Handling input and state constraints in predictive functional control. In Proceedings of the 30th IEEE Conference on Decision and Control: December 1991; pp. 985-990.
- [12] Abdullah, M., & Rossiter, J. A. (2019). Using Laguerre functions to improve the tuning and performance of predictive functional control. *International Journal of Control*, pp 1-13.
- [13] Rossiter, J. A., & Haber, R. (2015). The effect of coincidence horizon on predictive functional control. *Processes*, 3(1), pp 25-45.
- [14] Abdullah, M., Rossiter, J. A., & Haber, R. (2017). Development of constrained predictive functional control using Laguerre function based prediction. *IFAC-PapersOnLine*, 50(1), pp 10705-10710.
- [15] Khan, B., & Rossiter, J. A. (2013). Alternative parameterisation within predictive control: a systematic selection. *International Journal of Control*, 86(8), pp 1397-1409.
- [16] Muehlebach, M., & D'Andrea, R. (2017). Basis functions design for the approximation of constrained linear quadratic regulator problems encountered in model predictive control. In 2017 IEEE 56th Annual Conference on Decision and Control (CDC): December 2017; pp. 6189-6196.
- [17] Gilbert, E. G., & Tan, K. T. (1991). Linear systems with state and control constraints: The theory and application of maximal output admissible sets. *IEEE Transactions on Automatic control*, 36(9), pp 1008-1020.
- [18] Scokaert, P. O., & Rawlings, J. B. (1998). Constrained linear quadratic regulation. *IEEE Transactions on automatic control*, 43(8), pp 1163-1169.
- [19] Valencia-Palomo, G., & Rossiter, J. A. (2012). Comparison between an auto-tuned PI controller, a predictive controller and a predictive functional controller in elementary dynamic systems. online publication, research gate.
- [20] Haber, R., Rossiter, J. A., & Zabet, K. (2016). An alternative for PID control: predictive functional control-a tutorial. In 2016 American Control Conference (ACC): July 2016; pp. 6935-6940.

FECTION OF FERRO ELECTRIC THICKNESS ON NEGATIVE CAPACITANCE FET

MUHAIMIN BIN MOHD HASHIM, AHM ZAHIRUL ALAM AND
NAIMAH BINTI DARMIS

*Dept. of Electrical and Electronic Engineering,
International Islamic University Malaysia,
Kuala Lumpur, Malaysia*

**Corresponding author: zahirulalam@iium.edu.my*

(Received: 19th September 2020; Accepted: 16th December 2020; Published on-line: 30th January 2021)

ABSTRACT: Conventional Field Effect Transistor (FET) are well known to require at least 60mV/decade at 300K change in the channel potential to change the current by a factor of 10. Due to this, 60mV/decade becomes the bottleneck of this day transistor. A comprehensive study of the Negative Capacitance Field Effect Transistor (NCFET) is presented. This paper shows the effect of ferroelectric material in MOSFET structure by replacing the insulator in the conventional MOSFET. It should be possible to obtain a steeper subthreshold swing (SS) compared to the one without a ferroelectric material layer, thus breaking the fundamental limit on the operating voltage of MOSFET. 27% of the subthreshold slope reduction is observed by introducing ferroelectric in the dielectric layer compared to the conventional MOSFETs. Hence, the power dissipation in MOSFET can be mitigated and shine to a new technology of a low voltage/low power transistor operation.

ABSTRAK: Transistor Kesan Medan Konvensional (FET) terkenal memerlukan sekurang-kurangnya 60mV / dekad pada 300K perubahan pada saluran yang berpotensi untuk mengubah arus dengan faktor 10. Oleh kerana itu, 60mV / dekad menjadi hambatan transistor hari ini. Kajian komprehensif mengenai Negative Capacitance Field Effect Transistor (NCFET) dikemukakan. Makalah ini menunjukkan kesan bahan ferroelektrik dalam struktur MOSFET dengan mengganti penebat dalam MOSFET konvensional. Sebaiknya dapatkan swing subthreshold (SS) yang lebih curam berbanding dengan satu tanpa lapisan bahan ferroelektrik, sehingga melanggar had asas pada voltan operasi MOSFET. 27% pengurangan cerun subthreshold diperhatikan dengan memperkenalkan ferroelektrik di lapisan dielektrik berbanding dengan MOSFET konvensional. Oleh itu, pelepasan daya dalam MOSFET dapat dikurangkan dan bersinar dengan teknologi baru operasi transistor voltan rendah / kuasa rendah.

KEYWORDS: *NCFETs, Ferroelectric, Subthreshold*

1. INTRODUCTION

Moore's Law drove the scaling trend of Metal-Oxide-Semiconductor Field-Effect Transistor (MOSFET). Moore's idea was that the transistor's size would double every 18 months, making the transistor consume less power, become smaller in size, and perform at high speed [1]. Though the downscaling of MOSFET for the past decades continues to grow, it causes another problem to arise, such as short-channel effect, higher power consumption, and gate oxide tunneling effect [2].

However, researchers have come out with many possible solutions to make sure Moore's Law can be held for the long run. Feedback FET [3], Tunnel FET [4], and Impact-ionization MOSFET [5] are some technologies introduced to hold MOS scaling limits. Yet, Moore's Law is almost reaching its fundamental limit [6]. Therefore, new technologies and physics are needed to cope with the MOS scaling. The voltage scaling of the supply voltage (V_{DD}) almost stopped as a further reduction of the device size, and hence the threshold voltage (V_{TH}) causes the exponential increase in the OFF state current (I_{OFF}). This is a direct consequence of the non-scalability of the subthreshold swing (SS) to below 60 mV/decade. The negative capacitance FET (NCFET) has been proposed by Salahuddin et al. [7-8] as an alternative steep slope transistor to overcome the classical limit of 60mV/dec, and has been extensively studied [8-16].

In this paper, the effect of ferroelectric thickness and doping concentration in NCFETS is analyzed to observe the device's performance, which may give further insight for future device consideration.

2. DEVICE STRUCTURE

The NCFET is designed considering 20nm gate length. Figure 1 and Table 1 shows the device structure and its parameters, respectively.

The S/D depths were designed to be shallow (10nm) is to avoid punch-through occurs which typically occurs at lower voltage with a deeper source-drain junction depth. Silicon doped hafnium oxide (Si: HfO₂) was used as a ferroelectric material layer due to its superior performance, such as nonvolatility, hysteresis-free, and compatible with complementary metal-oxide-semiconductor transistor (CMOS) technology [17]. A buffer layer is used to reduce the gate leakage current and improve the electrical properties of the NCFET [17].

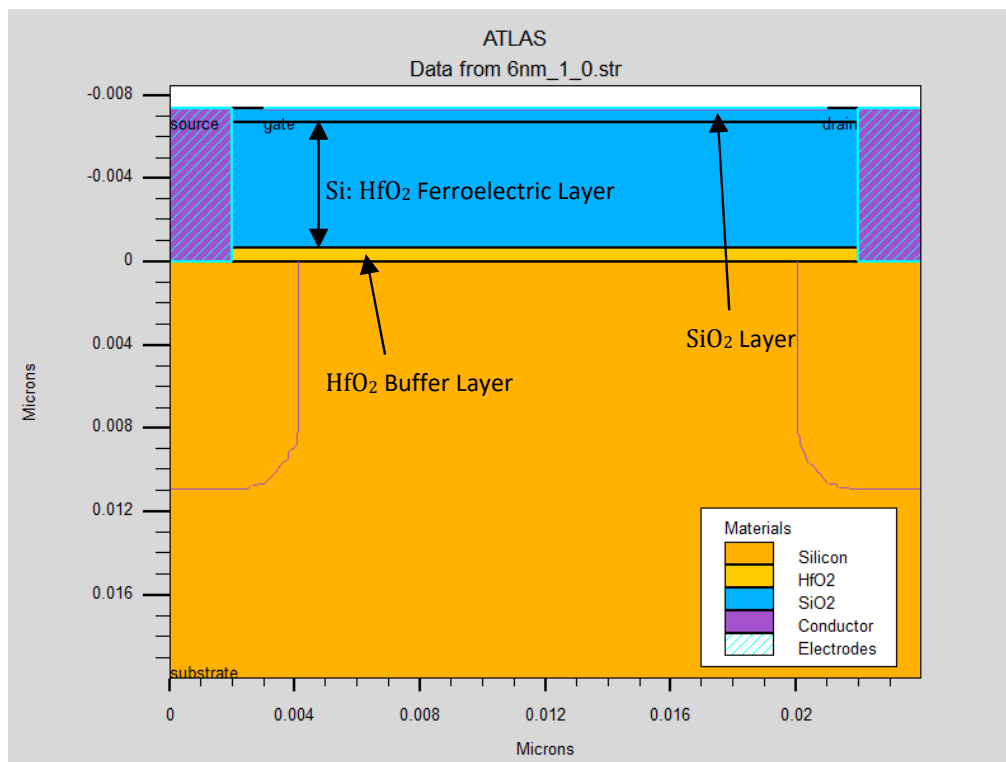


Figure 1: NCFET structure (dimension in microns)

Table 1: Parameters used for the simulation

Parameter	Value
P-well Doping (cm^{-3})	1×10^{15}
Source/Drain Doping (cm^{-3})	1×10^{20}
Junction depth (nm)	10
Gate Metal Length (nm)	20
HfO ₂ Buffer Layer Thickness (Å)	7
Ferroelectric Layer	Si: HfO ₂

In this paper, five different ferroelectric material layers were used as mentioned in Table 2, various parameters for the thickness are shown. Pseudocode is developed to calculate the parameters of any given thickness of ferroelectric material based on Miller [18].

Table 2: Ferroelectric material parameters for different thickness

Ferroelectric Thickness (nm)	Remanent polarization, P_r ($\mu C/cm^2$)	spontaneous polarization, P_s ($\mu C/cm^2$)	E_c (MV/cm)	ϵ_f
2	11.8	12.50	1.18	34.8
4	11.1	11.75	1.16	34.1
6	10.4	11.00	1.14	33.4
8	9.7	10.25	1.12	32.7
10	9.0	9.50	1.10	32.0

As the ferroelectric material's thickness increases, the parameters related to the ferroelectric material; remanent polarization, spontaneous polarization, critical electric field, and zero-field relative permittivity decreased. As a result, it can be concluded that the ferroelectric properties are inversely proportional to ferroelectric thickness. This information will help us determine the ferroelectric material parameters when designing a gate structure of MOSFET with the ferroelectric material.

3. RESULTS AND DISCUSSION

The performance of the NCFETs is observed for different thickness of the ferroelectric thickness, the source-drain doping concentration in I-V characteristics, and subthreshold behavior of the MOSFETs.

3.1 Effect of Ferroelectric Layer Thickness on I-V Characteristics ions

Five transistors with different ferroelectric material layer thickness, as mentioned in Table 2, were created using the simulator. All these devices have a buffer layer of 7 Å of HfO₂. The simulation on the devices with different ferroelectric material layers is carried out by using Silvaco TCAD to investigate the effect of thickness of the ferroelectric material layer on the I-V characteristics of the devices with 0.5V, 1.0V, and 1.5V gate voltages. Figure 2 shows the I-V characteristics of the devices for various ferroelectric thicknesses.

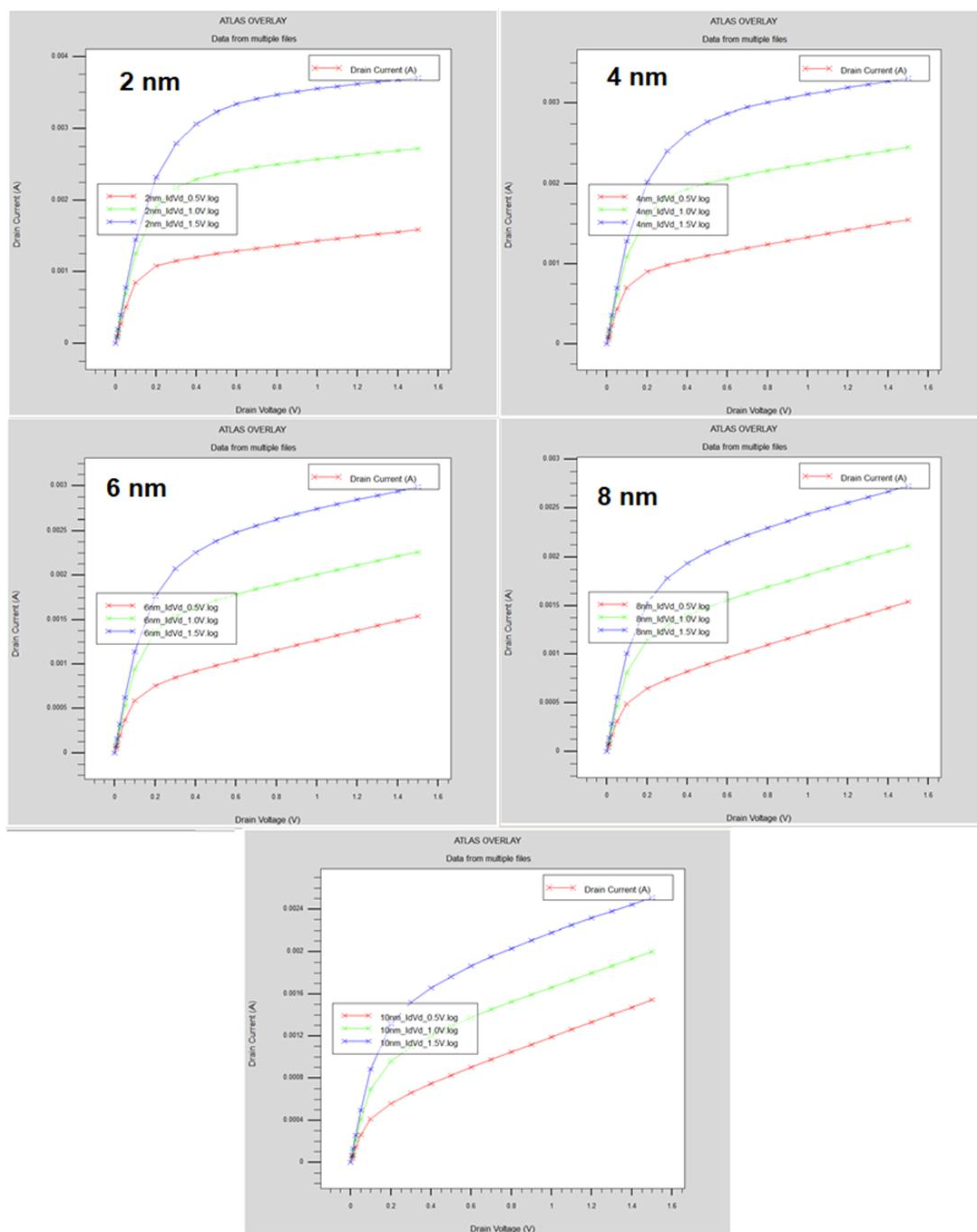


Fig. 2. I-V Characteristics of the NCFET for 2 nm to 10 nm ferroelectric layer.

The simulation shows that the saturation slope is decreasing while the current density was increasing. As the thickness increases, the variation of the slope of the drain current increases, and instead of saturation current the behavior of the transistors are moral-less resistive.

Figure 3 shows the variation of maximum drain current at $V_{DS} = 1.5$ V for different gate voltages and the slope at saturation with the ferroelectric thickness variation. It is observed that there is not much increment in drain current for 10nm, 8nm, and 6nm. But as the thickness of ferroelectric material decreased, in this case, 4nm and 2nm, the drain current also increased considerably. For example, for 10nm, 8nm, and 6nm cases, when the gate voltage is bias with 0.5V, there is not much increment. Figure 2 shows that as the thickness of ferroelectric material

decreased, the current increase from 1.55mA to 1.59mA for a 0.5V gate bias voltage. The same case can be seen when the gate bias voltages are 1.0V and 1.5V, the drain current increase from 2.46mA to 2.73mA and from 3.31mA to 3.7mA, respectively. It can be concluded that the thickness of ferroelectric material plays a vital role in the performance of the NCFET.

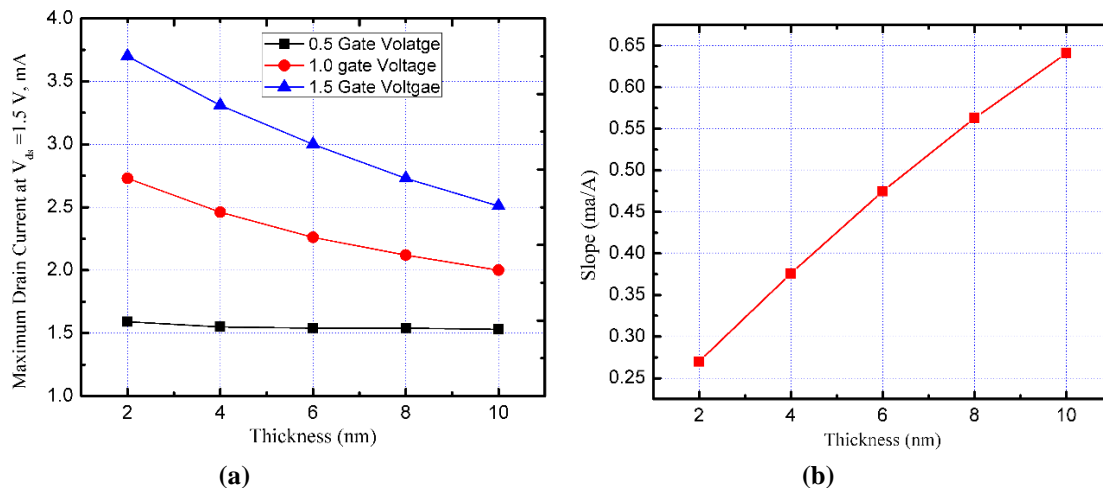


Fig. 3 (a) Variation of the maximum drain current at $V_{DS} = 1.5$ V for different gate voltages and (b) slope at saturation with the variation of the ferroelectric thickness.

3.2 Effect Of Source Drain Doping Concentration To The I-V

For this simulation, 2nm ferroelectric material thickness is chosen as it gives a higher drain current at lower drain voltage, and source and drain concentration are varying, and the effect of doping concentration on the I-V characteristics are observed and shown in Fig. 4.

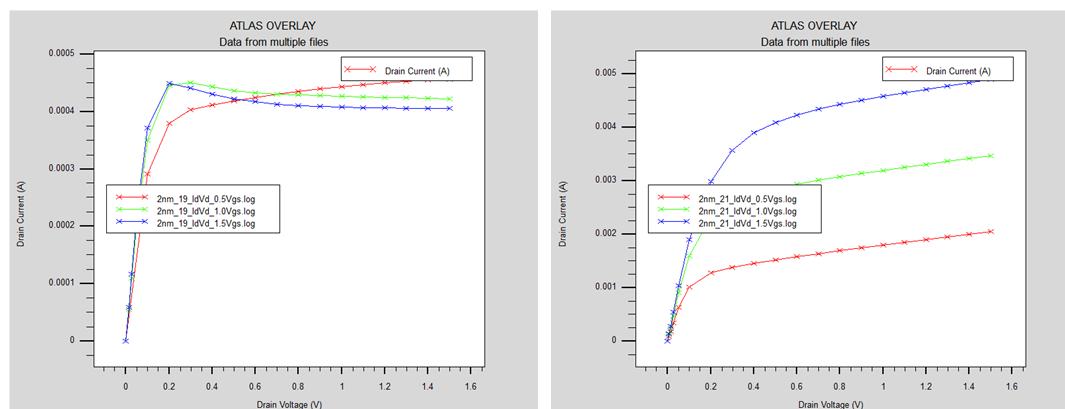


Fig. 4. I-V characteristics of 2nm ferroelectric layer NCFET for $1 \times 10^{19} \text{ cm}^{-3}$ and $1 \times 10^{21} \text{ cm}^{-3}$ source drain doping concentration respectively.

It is observed that the doping concentration of source-drain increased, the drain current density also increased. However, when the concentration is at $1 \times 10^{19} \text{ cm}^{-3}$, there is a high current density observed for 0.5V and 1.0V gate bias voltage, but at a certain point, the current drop and become constant afterward. This effect is said to be a short channel effect due to the results of two-dimensional potential distribution and high electric fields in the channel region. For a given channel doping concentration, as the channel's length is reduced, the depletion layer width of source and drain becomes equal or comparable to the channel length. Failing current

saturation due to the punch-through effect [19]. These results show that the doping concentration of source-drain plays a vital role in the performance of the NCFET.

3.3 Subthreshold Slope Behavior

For a Field-Effect transistor, the minimum voltage swing needed to turn a transistor from on to off is an important parameter that can be used to define the power dissipated by the device. Drain current with the variation of gate voltage (I_d versus V_g) are shown in Fig. 5 for the V_{DS} of 0.05 V, 0.5 V, and 1.0 V, respectively, with different views by scaling up.

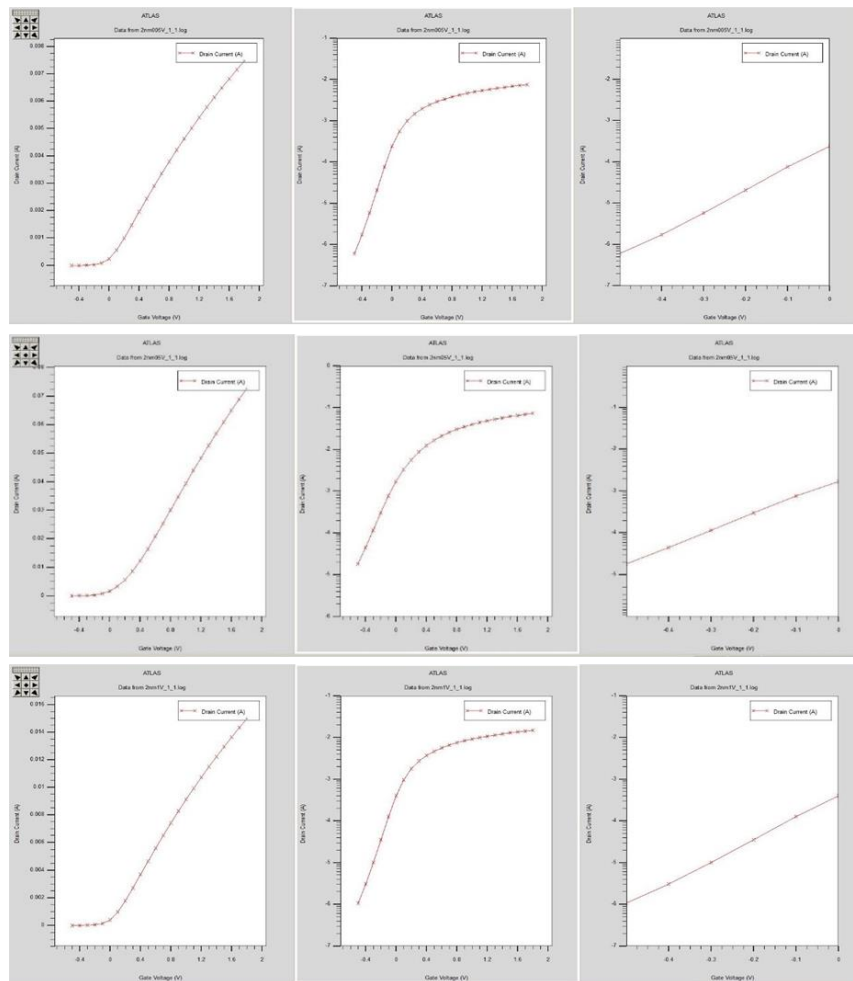


Fig. 5. I_{DS} versus V_{GS} for V_{DS} 0.05 V, 0.5 V, and 1.0 V.

Table 3. Result for different drain bias voltage and subthreshold slope

Drain Bias Voltage (V)	Subthreshold Slope (mV/dec)
0.05	270.323
0.5	348.37
1.0	481.67

The results are tabulated in Table 3, and it is observed that with a lower drain bias voltage, the subthreshold also decrease. This means NCFET can give a steeper subthreshold slope at a lower drain bias voltage.

The input characteristics of the NCFETs and MOSFETs are shown in Fig. 5 in linear and logarithm scale. The NCFETs gives a larger drain current compared to MOSFETs. The NCFET and MOSFET subthreshold slope are 348.37 mV/dec and 446.45 mV/dec for the same device dimensions. The subthreshold slope for the one without ferroelectric material is much higher than the one with the ferroelectric material layer. This shows that, by introducing the ferroelectric material layer to the structure of MOSFET, it is possible to get a steeper subthreshold swing, thus improving the device's performance.

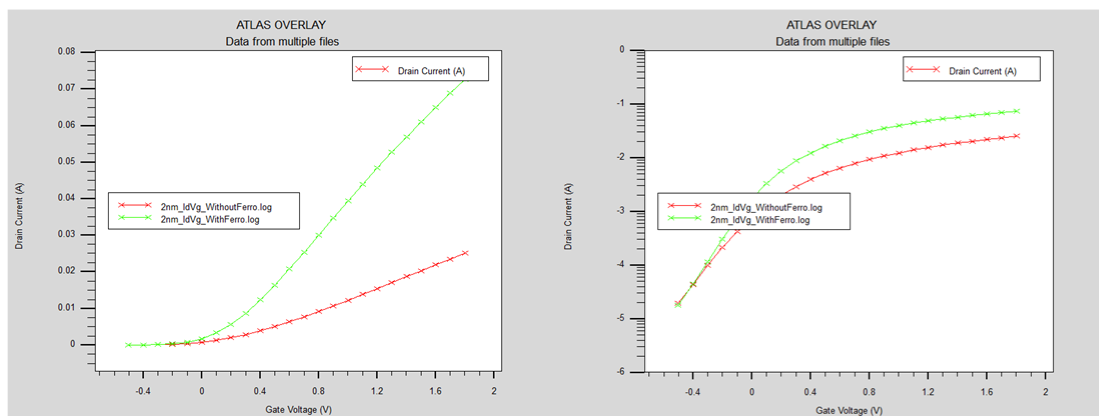


Fig. 5. $I_D - V_{GS}$ graph the structure with ferroelectric material and without a ferroelectric layer.

4. CONCLUSION

In conclusion, a steeper subthreshold slope for NCFET compared to conventional MOSFET has been demonstrated. It is also shown that the performance of NCFET is affected by the thickness of ferroelectric material and source/drain concentration doping. As the thickness of the ferroelectric material layer decreased, a steeper $I_D - V_{DS}$ is observed. While as the source/drain concentration doping increased, a steeper $I_D - V_{DS}$ graph is noticed. It is remarkable that by manipulating the ferroelectric material's thickness and the source/drain doping concentration, the transistor performance can be improved for the NCFET.

ACKNOWLEDGEMENT

This paper is financially supported by the Ministry of Higher Education Malaysia (MoHE) through the Research Centre, International Islamic University Malaysia under the Fundamental Research Grant Scheme (FRGS), Ministry of Higher Education, Malaysia. (IIUM/504/RES/G/14/3/2/1/ FRGS19-050-0658).

REFERENCES

- [1] G. M. Moore (1965) Moore's Law, Electronics. Electronics 38(8): 114. [Online]. Available: <https://newsroom.intel.com/wpcontent/uploads/sites/11/2018/05/moores-law-electronics.pdf>.
- [2] S. Chopra and S. Subramaniam (2015) A Review on Challenges for MOSFET Scaling. Int. J. Innov. Sci. Eng. Technol. 2(4): 1055–1057. [Online]. Available: www.ijiset.com.
- [3] C. W. Yeung (2014) Steep On / Off Transistors for Future Low Power Electronics.

- [4] U. E. Avci, R. Rios, K. J. Kuhn, and I. A. Young (2011) Comparison of power and performance for the TFET and MOSFET and considerations for P-TFET. *Proc. IEEE Conf. Nanotechnol.* pp. 869–872. doi: 10.1109/NANO.2011.6144631.
- [5] K. E. Moselund, D. Bouvet, V. Pott, C. Meinen, M. Kayal, and A. M. Ionescu (2008) Punch-through impact ionization MOSFET (PIMOS): From device principle to applications. *Solid State. Electron.* 52(2): 1336–1344. doi: 10.1016/j.sse.2008.04.021.
- [6] M. Kobayashi, Kyokai Joho Imeji Zasshi (2016) More than moore. *Journal Inst. Image Inf. Telev. Eng.* 70(3): 324–327. doi: 10.3169/itej.70.324.
- [7] S. Salahuddin and S. Datta (2018) Can the subthreshold swing in a classical FET be lowered below 60 mV/decade?" *Tech. Dig. Int. Electron Devices Meeting.* pp. 693–696
- [8] S. Salahuddin and S. Datta (2018) Use of Negative Capacitance to Provide Voltage Amplification for Low Power Nanoscale Devices. *Nano Lett.*, 8 (2): 405–410.
- [9] X. Li, J. Sampson, A. Khan, K. Ma, S. George, A. Aziz et al. (2018) Enabling Energy-Efficient Nonvolatile Computing With Negative Capacitance FET. *IEEE Transactions on Electron Devices.* 64(8): 3452-3458. <https://doi.org/10.1109/TED.2017.2716338>
- [10] S. C. Chang, U. E. Avci, D. E. Nikonov and I. A. Young (2017) A Thermodynamic Perspective of Negative-Capacitance Field-Effect Transistors. *IEEE Journal on Exploratory Solid-State Computational Devices and Circuits.* 3(1): 56-64.
- [11] Ko E, Shin J, Shin C (2018) Steep switching devices for low power applications: negative differential capacitance/resistance field effect transistors. *Nano Convergence.*5(1):2.
- [12] A. Sharma and K. Roy (2017) Design Space Exploration of Hysteresis-Free HfZrOx-Based Negative Capacitance FETs. *IEEE Electron Device Letters.*38(8):1165-1167.
- [13] A. I. Khan, K. Chatterjee, B. Wang, S. Drapcho, L. You, C. Serrao, S. R. Bakaul, R. Ramesh, and S. Salahuddin (2015) Negative capacitance in a ferroelectric capacitor. *Nature Materials.* 14(2): 182-186.
- [14] Saptarshi Das (2016) Two Dimensional Electrostrictive Field Effect Transistor (2D-EFET): A sub-60mV/decade Steep Slope Device with High ON current. *Scientific Reports.* 6: 34811 (2016)
- [15] S. H. Le, B. R. Salmassi, J. N. Burghartz, P. M. Sarr (2004) Characterization of ferroelectric thin films materials for FeRAM. *Proc SAFE & Prorisc Veldhoven*, pp. 710-713.
- [16] Fei Liu, Yan Zhou, Yijiao Wang, Xiaoyan Liu, Jian Wang and Hong Guo (2016) Negative capacitance transistors with monolayer black phosphorus. *npj Quantum Materials.* 2016: 16004: 1-6. <http://dx.doi.org/10.1038/npjquantmats.2016.4>
- [17] L. Tu, X. Wang, J. Wang, X. Meng, and J. Chu (2018) Ferroelectric Negative Capacitance Field Effect Transistor," *Adv. Electron. Mater.* 4(11):1–17. doi: 10.1002/aelm.201800231.
- [18] S. L. Miller and P. J. McWhorter (1992) Physics of the ferroelectric nonvolatile memory field effect transistor. *J. Appl. Phys.*72(12):5999–6010. doi:10.1063/1.351910.
- [19] Faculty of NPTEL, "Module 2 : MOSFET Lecture 8 : Short Channel Effects," p. 6, [Online]. Available: <http://nptel.ac.in/courses/117101058/downloads/Lec-8.pdf>.